Yield Criterion for Sequentially Excavated Tunnels in Heavily Overconsolidated Fissured Soils

by

David Elton Yeats Elwood

A thesis submitted in partial fulfillment of the requirements for the degree of

Doctor of Philosophy

in

Geotechnical Engineering

Civil and Environmental Engineering
University of Alberta

Abstract

This thesis presents the formulation of geo-mechanical design parameters using a combination of laboratory and insitu test results in the heavily overconsolidated cohesive till formation in the city of Edmonton. These data were then used in the design of the recently constructed North LRT twin tunnels.

This study initially focuses on the geology local to the test site as observed in a deep excavation constructed as part of a foundation and cut and cover tunnel section. During excavation of the North LRT twin tunnels, regular face mapping was carried out and several geological structures, not previously identified have been observed. The presence of these formations is discussed in terms of their potential genesis and the potential impact on stability of the unsupported tunnel cutting.

The yield criterion of the major stratigraphic units were then explored using a detailed reassessment of previous laboratory experiments as well as new data obtained from a series of insitu testing. The previous studies indicated the importance of the stress path in terms of the displacements measured around an excavation. What was not determined was the role the stress path had on the yield strength and the strains required to achieve a state of plasticity. This study has ascertained that not only the stress path and strains to yield are critical to the strength of the soil, but also the state of stress prior to testing. These data indicate that the conventional upper and lower strength bounds of drained and undrained strength might not be the dominating failure state in hard, fissured soils like the Edmonton till. Because the typical construction rates were less than 0.1 m /hour per tunnel and should result in drained conditions around the tunnel cavity. Additional in-situ test methods for heavily overconsolidated soils have been developed in order to shed light on parameters that are conventionally very difficult to obtain. These

new methods shed light on limitations of previous test methods and how the results of analysis may be influenced by the unsaturated state of the soil.

These data were then supplemented by displacement measurements recorded during the twin tunnel construction. Regular monitoring of both surface and in-tunnel displacements provided a basis for analysis to determine the extent of ground movement into the tunnel cavities as well as the influence of the second, lag tunnel on the constructed lead tunnel. The presence of a variable spacing between the twin tunnels (pillar width) provided a basis for comparison of the stresses and displacements associated with the lag tunnel influence. These displacement data provided the basis for a numerical back analysis as well as determining the efficacy of the tunnel construction methods.

Finally a numerical back analysis of the measured displacements was undertaken and compared to the relevant yield criterion. This demonstrated that the influence of a closely spaced tunnel on a previously constructed tunnel is not as extensive within heavily overconsolidated soils as previously reported. Knowledge of the stress path and the associated yield strains, relevant yield criterion are assigned to the ground in order to illustrate where and how yielding of an unsupported tunnel cutting will occur. This also suggests that non-conventional methods of analysis should be employed as part of the design process to determine the size and shape of translational failure expected within a fissured underground opening.

Acknowledgements

When undertaking a project such as this, the work is never really completed by just one person. It takes an effort by everyone that is in the life of the candidate. It is to these people that I would like to extend my gratitude and thanks. All of you have made this experience one to remember and I will forever be in debt to all of you for your help and encouragement in the bad times and more importantly, your willingness to celebrate in the good times.

First I would like to thank my advisor Dr. Derek Martin. Dr. Martin has been incredibly patient with me throughout this entire process including my unending neuroses. He always pushed for better work but granted the freedom to explore. He also understands when it is necessary to motivate and when to back off and give some space.

No one should leave this faculty without a word of thanks to the ladies who make this place run like a top. To Sally and Christine, you two are lifesavers, shoulders to cry on and facilitators. This place is going to shut down upon both of your retirements. I am just glad I got to see it during its hay-day (when you two were taking care of the administration and in the labs). You love your work and the students and it shows and I cannot express enough gratitude for your help through the years here.

Next, I would like to thank my friends here in Alberta who have been some of the best I have had. Barb and I will miss you dearly when we leave. Renato and Kristen, you two were great to have around and awesome at making me laugh when there really wasn't anything to be laughing about. I love you guys and thank you for making these last years what they were. I am pretty sure I would have packed it in long ago were it not for you guys.

Finally, to my wife Barb, you have a level of patience like no other human being and for this I am very thankful. These lines most definitely would not be written were it not for you and your constant encouragement (and occasional threat!). Your help in deciding the next phase of our life together has been immense. Even through your troubles, you managed to stay strong and keep me focused on writing. I love you more than anything in the world and always will. Thank you for being there.

"*Hung up waiting for a windy day…*" Robert Hunter

Table of Contents

List of Tables

List of Figures

List of Equations

1.0 Introduction

1.1 Research Problem

When constructing underground transportation systems in urban environments, tunnelling is often the option, which results in the least impact on the day-to-day workings at the ground surface. In such an environment the twin-tunnel alignment has to respect existing surface and subsurface infrastructure. To reduce the costs associated with interfering with the existing infrastructure, designers try to minimize the footprint of the tunnel alignment as much as practicable. This usually translates into reducing the separation distance between the twin-tunnels, i.e., the pillar width. While this may appear as an obvious solution, the consequences of reducing the pillar width may exceed the consequences of interfering with the existing infrastructure. The potential damage to existing infrastructure resulting from tunnel construction is generally quantified by assessing the ground deformations and structure interaction resulting from those deformations. This potential problem is exacerbated when the ground conditions and the impact of the interactions between the two excavations are unknown.

It is well understood that tunnel construction alters the properties of the ground around the excavated cavity. In cases where the influence zones of twin tunnels overlap, the ground performance can vary considerably from the single tunnel case. These changes in the ground performance can be difficult to predict both at the ground surface and around the tunnel cavities. When the tunnels are to be constructed in heavily overconsolidated soils, determining appropriate strength and deformation criteria can be particularly problematic. Because these soils are generally state dependent and possess structural features that may or may not be represented in test samples, a true understanding of their characteristics is hard to ascertain. Equally, the number of assumptions that are required to predict the interactions and resulting deformations poses additional risk to the tunnel design. These interactions not only have a negative impact on the surface and near surface infrastructure, but also can have implications regarding the actual tunnel construction methodology. Therefore the potential concerns with spacing twin tunnels closely together are twofold: first, the surface settlements may negatively impact existing infrastructure since displacements can greatly exceed the anticipated "greenfield" values; and second, the tunnel construction methodology may need to be altered in the second tunnel due to differing ground conditions and ongoing yielding despite the geology being similar to that of the first tunnel. Both of these results can have tremendous implications in terms of additional costs following completion of tunnel construction. As such, it is important for tunnel designers to predict to the best of their ability how twin tunnel construction will differ from single tube tunnel projects. Moreover, designers must understand the potential impact that minor changes to the pillar width can have on surface and in-tunnel deformations.

Pillar width is defined as the ground between the springlines of multiple tunnels. The pillar is conventionally the vertical piece of ground left by side-by-side tunnels, but can also be the ground left between stacked tunnels. Tunnel lag is defined as the spacing along the tunnel axis between consecutively constructed tunnel headings. Two methods are typically employed for tunnel excavation, either mechanised methods (tunnel boring machines) or sequentially excavated methods (SEM). This research will focus only on SEM tunnel construction. SEM tunnels utilize the observational method and can adapt the tunnelling methodology to suit the ground conditions as needed. SEM tunnelling methods involve the sequential excavation of a section of tunnel or 'round' with support being added following round excavation. This suggests that the sequencing of round excavation can vary considerably from one round to the next. Figure 1.1 illustrates the definitions of pillar width, tunnel lag and shows a sequenced face round excavation (header/bench/invert).

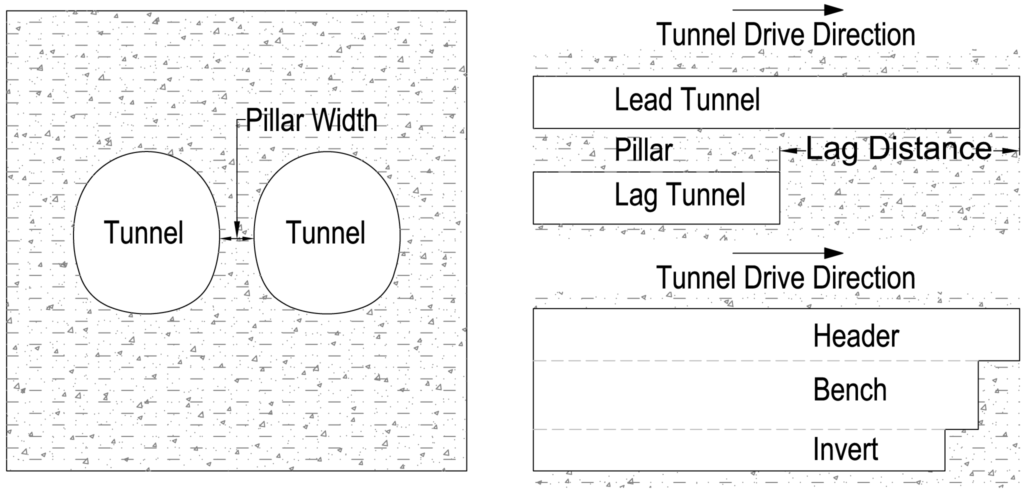

Figure 1.1. Definition of tunnel aspects

While there have been many historical studies examining the performance of hard fissured materials, none are known to have measured the interaction with pillar widths less than 0.75 the tunnel diameter. Current knowledge of the interactions between closely spaced tunnels has been measured in either soft (normally to lightly overconsolidated) soils or rock tunnels where the effects are more obvious. Moreover, studies that have considered the effects of changing the pillar width have only focused on the problem numerically with little to no field verification. As a result, no physical data have been obtained from tunnels within heavily overconsolidated (fissured) soils that can be used to compare the performance of a variable pillar width along the same alignment. Also, there are no known numerical simulation or field verification studies of a tunnel face passing through two geologic formations with differing characteristics with respect to the influence of the pillar width. The near field effects of mixed face conditions can strongly influence not only the safety inside the tunnel, but also the surface settlement profiles. This is particularly relevant in sequentially excavated tunnels where the excavation sequence can have a profound influence on the stability and safety of the unsupported cutting. Variable ground conditions within the same round may also require changes to the tunnel construction methodology in the same round in order to handle the ground response of two different materials.

Peck (1969,b) in his Rankine lecture discussed the importance of understanding the ground being constructed in. He also stressed the need for actively monitoring the ground movements during tunnelling activities to update and confirm/refute the initial hypotheses regarding the ground reaction. Once the ground characteristics were showing discernable trends, adjustment of the construction methods to suit the ground could be made as needed. Peck and Terzaghi both stressed the importance of designing the excavation to suit the ground conditions and not force the ground to suit the building methods. Therefore, in order to reasonably predict the performance of the ground during tunnel construction, it is integral to research the engineering geology throughout the tunnel alignment. This should include a basic depositional history as well as the physical properties of the various deposits where available which must be confirmed in the field during construction. The structure of the soil can greatly impact the performance of the ground, particularly if the material is fissured, as the local discontinuities can dominate the failure mechanisms when unsupported.

Terzaghi (1943) was the first to document his observations of the interaction between closely spaced tunnels in a soft clay. Terzaghi observed that the liner displacements of the first tunnel were strongly influenced by the construction of the second tunnel indicating an interaction. Peck (1969,a) discussed his observations of settlement and a method of estimating ground loss from over-excavation of single and twin tunnels. He suggested that an inverted Gaussian curve would accurately represent the settlement profiles observed at the ground surface. Peck also found that the effects of the tunnel construction extended approximately one tunnel diameter ahead of the face and up to two tunnel diameters behind the heading. This inverted Gaussian curve creates a three dimensional trough that is best represented as an elongated settlement trough as illustrated below in Figure 1.2.

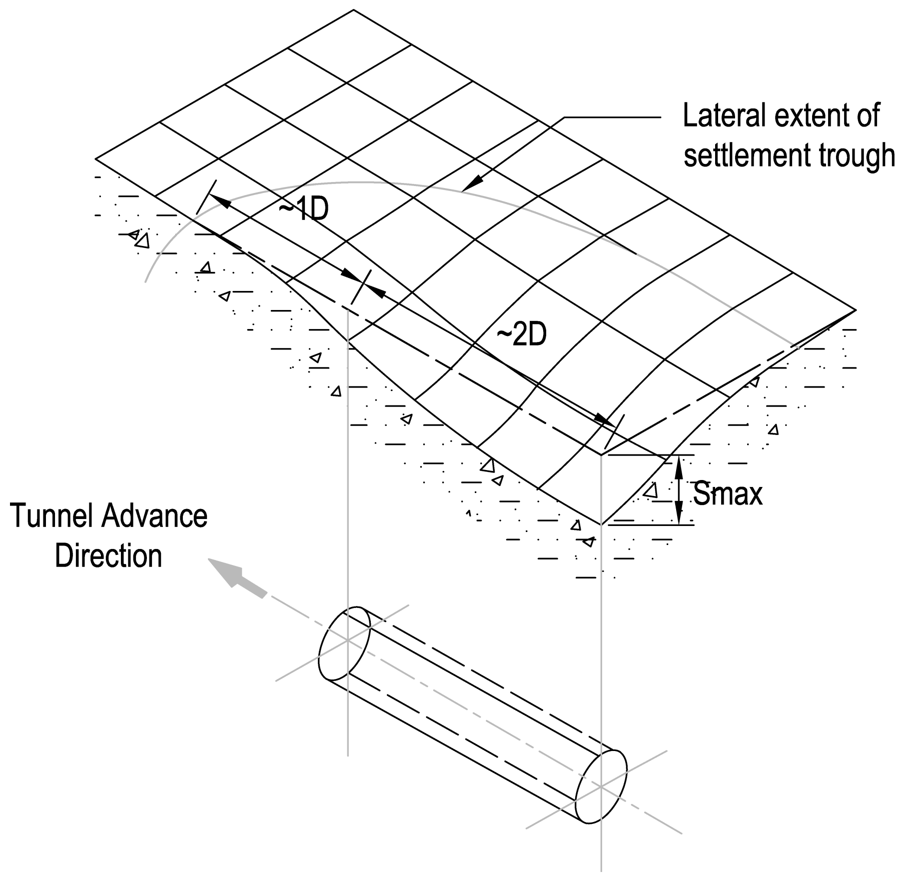

Figure 1.2. Three dimensional settlement trough from tunnel construction (adapted from Mair and Taylor, 1997)

Numerical simulation of the influence of narrow pillars on the surface settlement profiles was first presented by Barla and Ottoviani (1974). They attempted to determine the influence of pillar width in terms of the near field stresses and surface settlements. This study was followed up by Ghaboussi and Ranken (1977) who examined the influence of the tunnel spacing, tunnel depth and construction method (fully supported or unsupported) on the stresses around the tunnel cavity. Most recently, Ng et al. (2004)

numerically assessed the influence of tunnel staggering of twin, side by side, sequentially excavated tunnels. None of the studies considered the near field stress paths around the tunnel during the excavation sequence. More importantly, they never addressed how changes to the pillar width, geology or construction methodology would affect the collapse mechanisms around the tunnel cavities.

A number of researchers at Cambridge University in the 1970's (Potts, 1976; Atkinson, Potts and Schofield, 1977; Mair, 1979; and Atkinson and Mair, 1981) attempted to understand collapse mechanisms of unsupported cuttings. They assessed the stability of several unsupported cutting lengths for a single tunnel heading in soft clay and sand. Their tests were carried out in a centrifuge using an inflatable bladder within the tunnel cavity to provide stability of the heading. By slowly reducing the bladder pressure while being loaded, they were able to model the collapse mechanism at the tunnel face and within the unsupported heading. All of this work was for single, full face excavations in an ideal, homogeneous soil formation.

Anagnostou and Kovári (1996) developed a series of numerical models designed to assess the minimum pressure required to maintain a stable face within cohesionless and cohesive materials. Their study was followed up by Vermeer, Ruse and Marcher (2002) who carried out a series of numerical simulations to assess the stability of the face and the unsupported cutting length. Their models were carried out using a three dimensional, finite element model designed to simulate the laboratory experiments discussed briefly above. Based on these results, they found a very strong agreement between the values recommended by Anagnostou and Kovári (1996) and the collapse values reported by the researchers at Cambridge University. To date, these studies have defined the methodology for predicting tunnel stability for single tunnels constructed in ideal homogeneous materials. Interactions between twin closely spaced tunnels within complex overconsolidated or mixed face soils have not been considered.

Based on the above, it would appear that with respect to the construction of closely spaced, twin tunnels in heavily overconsolidated soils, there is a lack of understanding of the following:

- A need to provide usable yield criteria for the ground based on an understanding of the factors that contribute to failure in test samples and how this applies to construction;
- The measurement of the impact of the pillar width on the displacement fields at the ground surface; ahead of, during and following construction of the tunnels. This includes a basic understanding of the extent of the excavated damage zone in heavily overconsolidated soils and how it influences the stability of the pillar;
- There is no known monitoring data to provide a physical comparison of the effect of pillar width on the displacement fields within the ground needed to verify the previous numerical simulations. This can potentially shed light on appropriate SEM construction methods for variable pillar widths, thereby potentially increasing the efficiency and rate of tunnel construction;
- How the construction sequence of a sequentially excavated tunnel round can impact the stability and displacement fields within a narrow pillar; the unsupported cutting and tunnel face. This is considered particularly pertinent in excavations through mixed geological formations with differing characteristics; and
- An understanding of how the construction sequence and the pillar width influence the stress paths of points surrounding the tunnel. To date, the final stress states around closely spaced tunnels for either full face or sequenced excavations are well known. However, the performance of either construction method has not been

formally compared; nor have the impacts of either method effectively been assessed with respect to the incremental changes in the state of stress with excavation. Knowledge of the evolution of stress paths around twin tunnel cavities would potentially lead to optimization of construction sequencing for differing materials as well as optimal stability of the unsupported cutting.

1.2 Research Objectives

This research uses field data collected from twin tunnels constructed within the City of Edmonton, with the following objectives:

- Investigate the geologic history of the City of Edmonton to help understand how the past depositional sequences may influence the performance of the ground. This information will be used to help better understand the structural geology of the local sediments and how they can influence the stability of a tunnel heading;
- Assemble a compilation of the previous geotechnical work throughout the City of Edmonton to develop up to date failure and deformation criteria;
- Monitor ground deformations resulting from the construction of closely spaced, SEM twin tunnels within heavily overconsolidated soils. Attention will be given to the performance of the narrow pillars and the displacements within the lead tunnel during the approach and passage of the lag tunnel;
- Develop a three dimensional numerical model to back calculate the results obtained from the monitoring data based on the ground parameters developed in the past studies. The monitoring program will be used to validate the numerical model and the geotechnical parameters used;
- Use the calculated data to determine the efficacy of a sequenced face excavation versus a full-face excavation. This study will focus on the change in stress path

associated with each method as well as the changes to the associated displacement fields around the tunnel cavity; and

- Draw conclusions regarding the preferred method of tunnelling within heavily overconsolidated materials for various pillar widths. Emphasis will be given to the narrow pillar performance and the associated tunnel interactions; the influence of mixed face conditions both in the face and the narrow pillar; the displacements and stability of the tunnel face and unsupported cutting; potential failure mechanism observed for all of the above based on the calculated stress paths.

1.3 Research Methodology

The methodology of this research is to approach the problem from a designer's perspective. This means that the goal will be to help future designers choose an appropriate construction methodology for a given alignment geometry and geology. The research will focus on ascertaining how closely tunnels spaced in hard fissured soils influence the heading stability and surface interactions, and more importantly, how the construction sequencing can optimize the overall stability of the heading.

The internal (micro) failure mechanisms of the soils are hypothesized based on data measured in the field but are not determined in a laboratory setting. Questions related to the "most probable" failure and deformation criteria as well as anticipated ground performance will be addressed based on a review of previous work and the findings of a field monitoring program. From this information, a working model will be developed as it relates to observations of the ground performance. This model will then be used to illustrate the impact of changes in the ground due to a number of factors outlined above.

1.4 Thesis Outline

This thesis has been organized into eight chapters and three Appendices. The first chapter has introduced the problems encountered in closely spaced twin, sequentially excavated tunnels. A discussion is provided on the development of the research program considering the nature of the ground conditions and pillar widths. Finally, the objectives, scope and methodology to achieve the objectives have also been discussed.

Chapter 2 presents a literature review related to the development of the understanding of the influence of pillar width and methods used to determine tunnel stability. The review considers both an unsupported cutting and the face as it relates to SEM tunnels. This is followed by a brief discussion on the history of assessing the ground displacement fields around tunnels in order to shed light on the meaning and interpretation of settlement data measured during construction.

In Chapter 3, an outline of the geology within the region of Edmonton is provided. This section reviews the existing studies on the depositional history of the various overburden settlements. It also provides an update of observations of the ground made during the excavation of the Epcor Tower foundations as well as those made during the construction of the North LRT twin tunnels. These observations shed additional light into the physical nature the till and provide evidence of the possible formation of the intra-till sand pockets.

Chapter 4 provides a detailed analysis of the strength and stiffness of the Edmonton till and Empress Sand using a pre-bore Camkometer style pressuremeter. This chapter provides an assessment of both the drained and undrained parameters of each formation and discusses the relevance of each method employed. Finally, two new methods of analysis of pressuremeter data are provided. These methods provide for the estimation of consolidation parameters from constant stress holding tests; as well as an estimation of the total volume change of the ground surrounding a pressuremeter probed due to the compression of occluded pore-air pockets.

Chapter 5 involves a detailed analysis of existing laboratory and insitu data for both the Edmonton till and the Empress Sand. The focus of this chapter is to shed light onto the mechanisms of failure within each sediment as well as providing definitions of yielding and how these criteria can be effectively applied to actual projects.

Chapter 6 presents the design assumptions, layout and results of the field monitoring program. The data are interpreted and an explanation of the observed displacement fields is provided. Because the monitoring program is to include several instruments that had not been previously used in this fashion, monitoring methodologies and verification of the collected data will be provided. Finally, conclusions on the efficacy of the various instruments will be drawn based on the measured results.

In Chapter 7, numerical models have been used to back analyse the results of the field-monitoring program at three key monitoring sections. The construction of the various numerical models and the modelling approach will be outlined. Results of the models will be compared to the actual field monitoring results for each section assessed. Based on the results, conclusions will be drawn regarding the effectiveness of the model and the developed yield criterion.

Finally, Chapter 8 presents the conclusions of the research program and provides recommendations for future research. This chapter summarizes the research program and its results and how they may be applied to future research programs.

2.0 Tunnel Stability and Ground Behaviour

2.1 Introduction

The literature review will provide background information on the design of tunnels and underground space within soft ground (soils). The chapter will be divided into sections that review the performance and current state of knowledge of heavily overconsolidated soils; processes to estimate the overall stability of the ground during excavation; the ground response due to excavation; and past experience in the City of Edmonton with large diameter tunnels.

The literature review will first examine the current state of knowledge of heavily overconsolidated soils and how their geotechnical performance relates to construction. This will provide a review of previous investigation methods and studies of the associated failure mechanisms in fissured ground and how the discontinuities influence the overall performance of the ground.

The second section in this chapter describes the state of tunnel stability research as it is currently understood. Each section will address a different facet of assessing a tunnel's stability. The methods range from the undrained and drained stability of the tunnel face as well as the unsupported profile. Another important aspect will be how cohesionless deposits respond to excavation when subjected to seepage forces.

Next a discussion will be provided on the previous work carried out to determine the overall performance of a tunnel as it relates to ground loss and surficial settlements. Since limiting disruption to society at the ground surface is the main reason why tunnels are constructed in urban environments, it is important to understand how the performance of the ground is assessed. Any negative impacts related to the surrounding infrastructure are considered beyond the scope of this work. This section will focus on the assessment of measured settlement profiles and the research that has been carried out by others to better quantify the physical response to the ground above tunnels before, during and following excavation. Special attention will be paid to cohesive materials and twin tunnels. Where possible, the research will highlight studies on twin, side-by-side tunnels constructed with narrow pillars and within hard, fissured clays.

The final section of the literature review will examine previous projects and studies carried out in previously constructed tunnels within the City of Edmonton. Local engineers and academics have documented the experiences of contractors and monitored the performance of the ground during construction of several major projects throughout the city. This background will help illustrate the past performance of the various geologic formations and shed light on the anticipated performance of subsurface excavations within hard fissured soils and heavily overconsolidated sands similar to those encountered in Edmonton.

The literature review presented in this section provides a brief synopsis of work by others and should not be considered exhaustive.

2.2 Performance of Heavily Overconsolidated Soils

In heavily overconsolidated soils, the internal mechanisms, which occur when subjected to shear forces, are poorly understood. Though the strains associated with these internal changes are extremely small (less than 0.1%), understanding of the internal changes can help shed light on the overall performance.

Many studies have been carried out on the London Clay over the years. These studies were developed based on experiments carried out within a laboratory setting, Hight et al. (2003) provides a detailed summary of the previous work.

Several of the studies have focused on the difference between the intact strength and strength of the soil mass as a whole. Skempton et al. (1969) found that the shear strength along the surface of fissures was slightly greater than the measured residual strength of the soil itself when tests carried out on intact and fissured samples of the London Clay. This low friction angle was a result of simply shearing the irregularities from the fissure surface. Studies carried out on exposed slope cuttings demonstrated that the presence of fissures within the mass strongly influenced the strength of the ground. Marsland (1971a) carried out a number of full-scale field tests to determine the influence of the fissures on the intact shear strength of the London and Barton Clays. He found that when tested using a small and large plate loading apparatus, that the smaller plates tended to not exhibit a peak strength while the larger plate tests demonstrated a slight peak before approaching a residual value. During large scale drained and undrained shear box tests carried out on the Barton Clay, Marsland (1971b) found that the pore pressure variation within the fissured soil strongly influenced its peak strength. In the only quick test carried out (4 hours to peak shear), he found that the pore suctions exceeded the peak shear stress while in the drained test (5 to 8 days to peak shear) the suctions were only about 11% of the peak stress.

Lo, Adams and Seychuk (1970) demonstrated the effect of sample disturbance on test results of stiff fissured soils. They found that despite the best efforts of researchers to recover "undisturbed" samples, there was always some degree of state dependence that could not be reproduced in the laboratory. Morgenstern and Thomson (1971) also showed the impact of sampling technique on the measurement of the intact shear strength of a glacial till. They also found that the undrained shear strength was highly dependent on the natural moisture content owing to internal suctions of partially saturated soils. Hight et al. (2003) examined the effectiveness of using suction and shear wave velocities on samples of the London Clay to determine the degree of disturbance. They found that most rotary cored samples (similar to the Pitcher Sampler described by Morgenstern and Thomson, 1971) fell within the limits of most insitu tests. They also found that most Shelby tube samples tended to fall outside of these limits suggesting disturbance. Therefore they concluded that any of the rotary cored samples that fell outside of the insitu data, were considered to be disturbed and therefore not suitable for testing.

The other aspect that is synonymously difficult to ascertain with any certainty in stiff fissured clays is the coefficient of lateral earth pressure at rest (K_o). Bishop (1958) suggested that the measurement of K_o is relatively easy provided that the lateral strain in a sample is monitored during shear. Once a lateral strain was detected, the spherical stress was increased in order to return the lateral strain to zero. The difference between the vertical and spherical stress (less pore pressures) was the K_o. It is common knowledge now that the ideal scenario described by Bishop is not in fact reality and the subject is considerably more complicated. Lacasse and Lunne (1982) demonstrated the difficulties of obtaining the insitu K_o from self-bore pressuremeter tests. Hight et al. (2003) indicated that there was some success in determining the K_o of the London Clay using a Marchetti dilatometer, though the results are by no means conclusive or exhaustive.

Considering the above, there is a considerable number of studies that have examined the performance of heavily overconsolidated soils. Most of which have only resulted in more questions as to how best to understand the influence of the micro and macro structure on the overall performance of the ground as a whole.

2.2.1 Effective Stress of Overconsolidated Soils

Changes of the effective stress on a micro scale cannot be effectively monitored and subsequently the strains associated with these internal stress changes are not well understood. In a partially saturated material like most cohesive glacial tills, these small changes in the pore pressures subjected to shear stresses are thought to play a considerable role. Bishop et al. (1975) demonstrated the role that internal suctions play in the stress strain profiles of partially saturated, heavily overconsolidated soils. They demonstrated that under conventional triaxial compression tests, most overconsolidated soils responded as either a lightly overconsolidated or normally consolidated material by exhibiting strain hardening tendencies. Once the internal suction within the sample was accounted for, the materials exhibited strongly brittle behaviour, as would be expected for a sample subjected to a considerable stress history like most glacial tills. No discussion was provided on the formation or performance of fissures within the samples and it is assumed that no discontinuities were present within the samples tested.

Fredlund and Morgenstern (1977) suggested that the internal structure of a partially saturated material is not a three phase system as suggested by Skempton (1960), but rather a four phase system. The presence of a meniscus between the occluded air and water pore fluids is considered a discernable phase which fluctuates under changes in applied stress. The presence of the meniscus termed the contractile skin by Fredlund and Morgenstern (1977) accounts for the presence of tensile stresses within a partially saturated soil during unloading. These tensile stresses coupled with the presence of microscopic fissures can greatly impact the performance of the material when subjected to conventional engineering strains. Bishop and Blight (1963) discussed the stress paths of partially saturated soils under compression. They suggested that under compression, the occluded air pockets compress, subsequently reducing the area of the contractile skin, which increases the saturation. This would eventually lead to a compressed state where the material is nearly or fully saturated and therefore responds according to Terzaghi's effective stress theory.

Little is known about this stress path when subjected to unloading in scenarios such as tunnelling applications. It is not uncommon for pore pressures to increase ahead of the tunnel face during the approach of tunnel boring machines (TBM). This pore pressure increase is followed by an abrupt decrease in pore pressure once the tunnel face has passed and the material is within the unloaded excavated damage zone (EDZ). It is expected that during the convergence of a tunnel cavity (prior to and immediately following support installation), the dilation of the ground (volume increase) surrounding the tunnel(s) would result in negative pore pressures around the cavity. This negative pore pressure should be roughly equal to the stress release that occurred during the excavation process according to saturated soil mechanics. In reality, because the ground is partially saturated, a suction equal to the unloading will not be realized. The influence of this internal change in effective stress over the strain fields within the tunnel cavity are currently unknown. More importantly, the role that the fissures and micro-fissures play in this negative pore pressure formation and eventual dissipation as well as the accompanying strain fields is also unknown.

With respect to volume change of partially saturated soils, Blight (1965) suggests that the volume change measured in unsaturated soils during shear tests can be highly deceptive in that the air voids within unsaturated soils are compressible and can initially result in volumetric changes within the sample upon the start of shearing. Bishop et al. (1975) indicated that when a sample of the London Clay was consolidated, it underwent a high degree of consolidation and was then allowed to return to atmospheric pressure, the volumetric expansion was approximately 6% while the volume of the air voids were measured to be approximately 5.7%. The same authors (Bishop et al., 1975) also found that when soil suction was not accounted for in triaxial tests, that the typical stress/strain curves of heavily overconsolidated materials were typically strain hardening which is very similar to what Medeiros (1979) and Whittebolle (1983) found. When Bishop et al. (1975) accounted for the soil suction, they found that the failure mechanism was brittle as would be expected. In addition, they found that as suction was eliminated from the tests, the samples became increasingly brittle with the degree of overconsolidation, again as expected. This study agrees well with earlier theories that in heavily overconsolidated, glacially deposited materials, that are at least partially unsaturated, conventional triaxial tests should be used with caution.

2.2.2 Small Strain of Heavily Overconsolidated Soils

It has been known for years that the reliable measurement of deformation moduli in heavily overconsolidated soils has been notoriously difficult to obtain. State dependence, sample disturbance, representative samples all play a considerable role in the measured results. Most engineering applications are subjected to strains within the 1 to 10% range. Therefore insitu tests like the pressuremeter which provide stress-strain profiles within a similar strain range are useful for most engineering applications. These instruments can provide reliable results for designers trying to comprehend the likely ground performance under normal construction scenarios, though they shed little light on the internal performance of the ground when subjected to loading.

Bishop et al. (1965) provided commentary on laboratory experiments on samples of the London Clay recovered from the Ashford Common shaft. They noted that there was a distinct transition in the stress-strain curves between low and high stress ranges. They determined that a cohesion intercept defining the low stress yield surface of these materials should be applied with extreme caution. They suggested instead that the use of a curved failure envelope in the very low stress range would be more appropriate than simply extending the intercept of the high stress range back to zero confining stress. This also suggests that the strain profiles at very low confining stresses differ considerably than those at higher stress states.

Gasparre et al. (2007) carried out a series of laboratory tests to help understand the performance of the heavily overconsolidated London Clay. They determined that though they were hard to recognize prior to testing, fissures accounted for 70% of the recorded failures when tested in extension. Of their tests on the influence of structure on the performance of the London Clay, they observed that in general, the material performed as a strain softening material that dilated when sheared. Most importantly, they concluded that throughout the test process, strain localization at the fissures would truncate the dilation process. Because local slip planes would develop along the fissures, none of the samples obtained the peak shear strength or strain levels measured in the intact samples.

Hight et al. (2007) carried out a detailed investigation to determine the anisotropic modulus of the London Clay influenced the construction of the London Heathrow Terminal 5 expansion. As part of their study, they measured the coefficient of lateral earth pressure by measuring the internal effective stress of recovered core samples using a high pressure tensiometer. By assuming that the unloading of the test samples would result in suctions that would indicate the effective stress in the ground, they demonstrated that the values measured compared well with those reported by Bishop et al. (1965) from the Ashford Common shaft. Hight et al. (2007) did not report the duration of the suction tests nor the detailed interpretation of the results. It is well understood that suctions typically are equal to the unloading of stresses during recovery in saturated soil mechanics, but the impact on partially saturated soils is not completely understood. This suggests that some form of correction should have been applied to account for the removal of the spherical stress of the sample at the ground surface. It is unclear whether this correction was applied by Hight et al. (2007).

Cross borehole seismic testing at the terminal site indicated that the very small strain shear modulus was highly anisotropic within the London Clay. This was due to the high coefficient of lateral earth pressure at rest (K_o). Despite there being considerable scatter in the data, Hight et al. (2007) reported that the general trend was representative of the in-situ ground conditions.

Hight et al. (2007) also commented briefly on the brittle nature of the London Clay. Their discussion simply mentioned that the brittle stress paths measured in their experimental program was controlled by the presence of fissures. Samples that possessed higher fissure concentrations, responded in a more ductile fashion. It was found by Medieros (1980) and Whittebolle (1983) that the stress strain profiles suggested that the glacial till in the Edmonton area was a strain hardening material. Though it was not discussed in detail by Medieros or Whittebolle, it was likely that the samples that were tested possessed some form of micro-fissuring which dominated the measured stress strain profiles of the test samples. These fissure structures would not necessarily be discernable to the naked eye, but influenced the experimental results none the less.

2.3 Tunnel Stability

Tunnel stability can be divided into three categories:

a) Undrained conditions (short term $\phi=0^{\circ}$);

b) Cohesionless soils subjected to seepage forces; and

c) Drained conditions.

In each of the above categories, the base method for analysis assumes a shape of collapse mechanism above the tunnel and the formation of a collapse wedge into the tunnel face.

Typically it is assumed that settlement at the surface occurs by movement of a cylindrical soil mass moving downward from the ground surface. It is reported by Vermeer and Ruse (2000) that the first publication of a silo theory was by Horn in 1961, though Terzaghi and Jelinek also purportedly considered the same failure shape in 1954. As both of the original publications are in German and translations are not readily available, this review provides a summary of their work as described by others.

In each of the categories for assessing the tunnel stability given above, the theory of stability is similar to that of slope stability in that it relies on limit equilibrium methods and therefore only the onset of failure. Actual displacements cannot be obtained from any of the methods described below.

The basic theory of face stability assumes that a cylindrical soil mass above the tunnel displaces vertically downward into the tunnel cavity. To obtain the stresses required for mobilization to occur, the stresses acting on an infinitely thin strip of soil with radius R should be considered. The stresses acting on the strip are shown below in Figure 2.1.

.

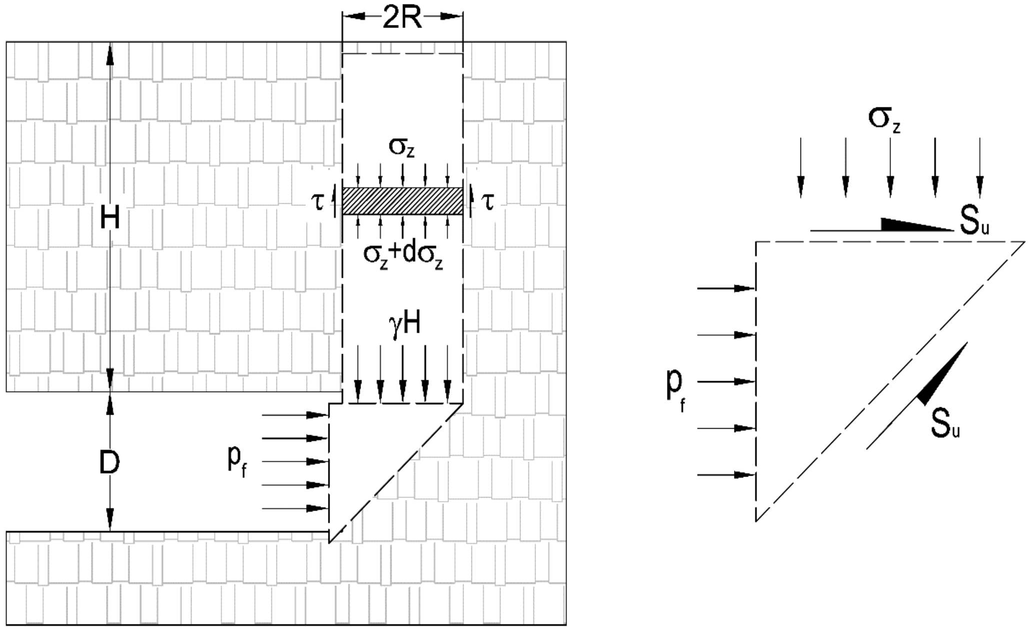

Figure 2.1. Stresses acting on a silo wedge (modified from Vermeer and Ruse, 2000)

The stress acting along the sides of the strip is given as $\tau = c_u + K_o\sigma_z.\tan\phi$ where K_o is the coefficient of lateral earth pressure at rest; c_u is the cohesion of the soil and ϕ is the coefficient of friction. If equilibrium is assumed for the above free body diagram of the silo, then Equation 2.1 below is obtained.

$$\frac{d\sigma_z}{dz} = \gamma - \frac{2c_u}{R} - \frac{2K_o \tan\phi}{R}\sigma_z$$

Equation 2.1

The above Equation 2.1 is applicable for cohesive-frictional material acting as a driving force of soil above a tunnel moving into the tunnel face. Actual failure mechanisms into the tunnel face (representing face collapse) are also illustrated in Figure 2.1.

In order to resist sliding and thereby maintain a stable working face or unsupported cutting length, a pressure must be applied to the exposed soil surface (P_f) as shown in the figures above.

Atkinson and Mair (1981) assumed that the calculation of P_f would occur at the centre of the tunnel face. As a result, the pressure at the face would exceed that at the crown and the upper portion of the face, but would be less than the actual pressure at the invert of the tunnel. It is more common now to calculate P_f as a triangular distributed load that will slightly exceed the minimum required P_f value in order to achieve a factor of safety greater than 1.

Using a 3D Finite Element Model, Vermeer, Ruse and Marcher (2002) illustrated the distribution of stress around a fully lined tunnel and the nature of collapse considering various material properties. They demonstrated that undrained materials (ϕ=0) tended to exhibit considerable distribution of the collapse zone. This suggests that squeezing into the tunnel opening (assuming a fully lined tunnel) is the dominant failure mechanism. The distribution of the principal stresses throughout the soil mass confirms that there is little stress concentration around the opening and the support pressure must be high. In cohesionless deposits with low friction angles ($\phi \leq 20^\circ$), the degree of arching around the tunnel face is minimal, but some stress redistribution around the face takes place and confines the collapse zone to a narrow silo above the face as hypothesized by Horn (1961). When the friction angle is high ($\phi > 20^\circ$), the effect of arching is clear and the zone of collapse is nearly zero. Considering this, it stands to reason that the face pressure needed to maintain stability is also nearly zero.

2.3.1 Undrained Tunnel Stability

The stability of a tunnel face in undrained conditions (short term) can be estimated using the approach given by Vermeer and Ruse (2000). The face pressure (P_f) required for stability is a function of the undrained shear strength (S_u), the unit weight of the soil (γ), the tunnel radius (R) and the depth of the tunnel crown below the ground surface (H). The stresses resulting in shear failure are shown on the right of Figure 2.1.

The face pressure required for face stability (P_f) is given by Equation 2.2 below.

$$P_f = \gamma R - 3S_u + (\gamma R - 2S_u)\, H/R$$

Equation 2.2

For SEM tunnelling, the face pressure P_f is taken as zero and the stability of the face is solely reliant on the undrained shear strength of the ground. This also assumes a critical sliding plane acting at an angle of 45° and an isotropic, homogeneous soil layer acting above the tunnel crown. If multiple layers of soil are above the tunnel, the weighted average unit weight would be assumed. The stability of the face assumes that the tunnel liner is installed at the face and no collapse of the heading can occur. Vermeer, Ruse and Marcher (2002) investigated the numerical solution for an SEM tunnel case where the tunnel liner is installed at some distance behind the tunnel face.

Physical modelling of the undrained failure phenomenon was carried out at Cambridge University in the 1970's as presented in the 1980 Rankine Lecture by Schofield. Schofield (1980) provided a commentary on the nature of failures in tunnels in an overconsolidated clay with cuttings (unsupported rounds) of various lengths. Potts (1976), Atkinson, Potts and Schofield (1977) and Mair (1979) provided the basis for the centrifugal studies to determine the nature and extent of failures in supported (fully lined) and unsupported tunnels at depth. They found that the stability of the face for a fully lined tunnel (liner to the tunnel face) failed in a manner similar to that described by Vermeer and Ruse (2000). This suggests that a plug of soil at the face was pushed into the tunnel cavity with the failed column of soil above following the plug into the cavity. When cuttings (unsupported lengths) were left at the face, similar to SEM tunnelling methods, the collapse mechanism included some form of failure of the tunnel crown similar to squeezing as the soil above the tunnel moved into the cavity. Images from

Schofield's 1980 Rankine Lecture illustrating the various failure mechanisms are shown below in Figure 2.2.

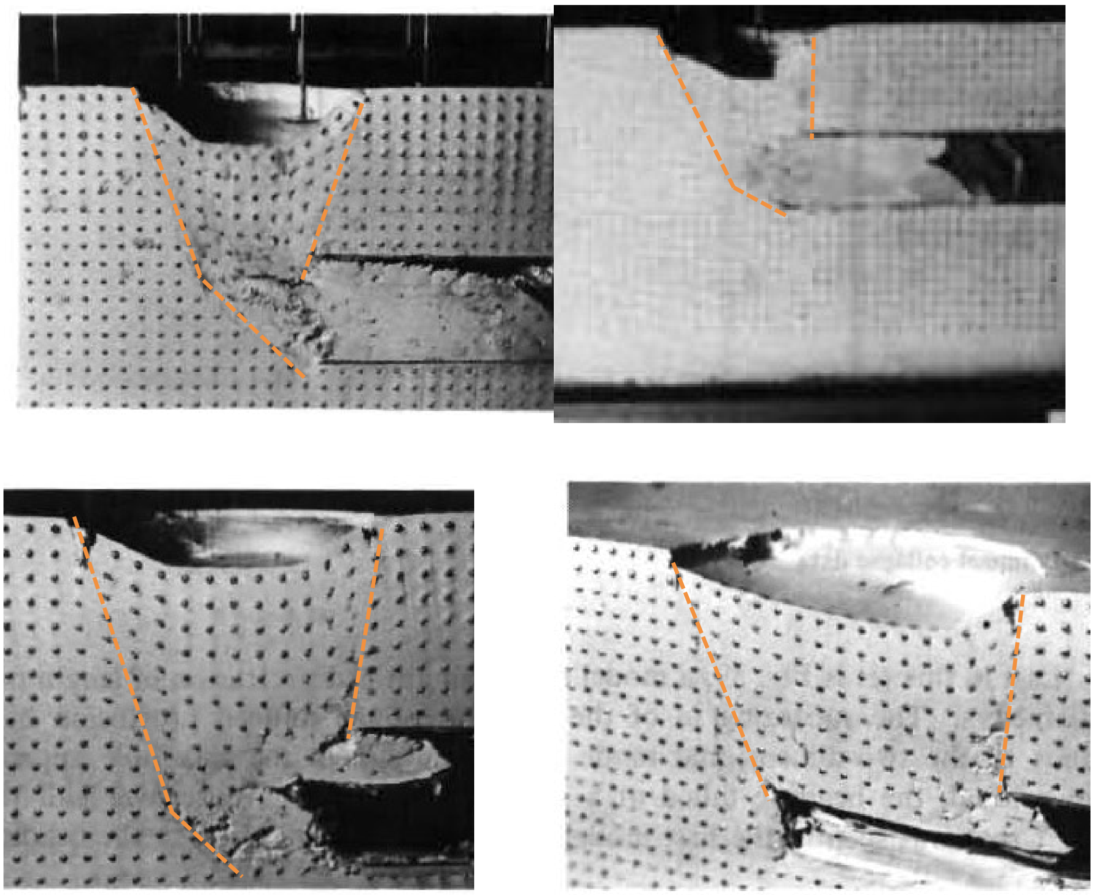

Figure 2.2. Face and cutting failures in an overconsolidated clay. Clockwise from top left: fully lined; cutting length 1/2D; cutting length 2D; cutting length 1D (adapted from Schofield, 1980)

In order to assess the stability of the face for an SEM tunnel (P_f=0), Vermeer and Ruse (2000) recommend obtaining a critical cohesion number ($S_u/\gamma D$). The critical cohesion number (after Vermeer and Ruse, 2000) is given as Equation 2.3 below.

$$(D+2H)/(6D+8H)$$

Equation 2.3

For values of S_u less than the critical cohesion number, a face pressure must be applied in order to maintain stability of the face. The face pressure can consist of either pressurized air or face dowels (for SEM tunnels) or a slurry shield / earth pressure balance machine.

Another alternative would be to express the stability in terms of a factor of safety against the onset of movement which would be described as the ratio between the available undrained shear strength (S_u) versus the S_u required to result in a unsupported face pressure (P_f =0). By examining the assumed "most probable" S_u versus a range of S_u, a plot illustrating the Factor of Safety (FoS) of the material against collapse may be obtained. This plot would illustrate the possible range of FoS for the "most probable", best and worst case scenarios for S_u.

2.3.2 Drained (Effective Stress) Face Stability

Assessment of whether a tunnel face will respond as either drained or undrained is given by Anagnostou and Kovári (1996). They describe that drained conditions occur when the permeability of the soil is higher than 10^{-7} to 10^{-6} m/s and the net excavation rate is less than 0.1 to 1 m/hour. Anagnostou and Kovári (1994) assumed the failure mechanisms described by Horn (1961) except that the shape of the driving silo above the tunnel will be rectangular and not cylindrical. At the face, the failure is still assumed to be a triangular wedge similar to the clay. The major difference between the two methods is that the undrained shear strength (S_u) has been substituted with the drained (effective) shear stress (τ_f). A graphical representation of the assumed collapse mechanism is shown below as Figure 2.3.

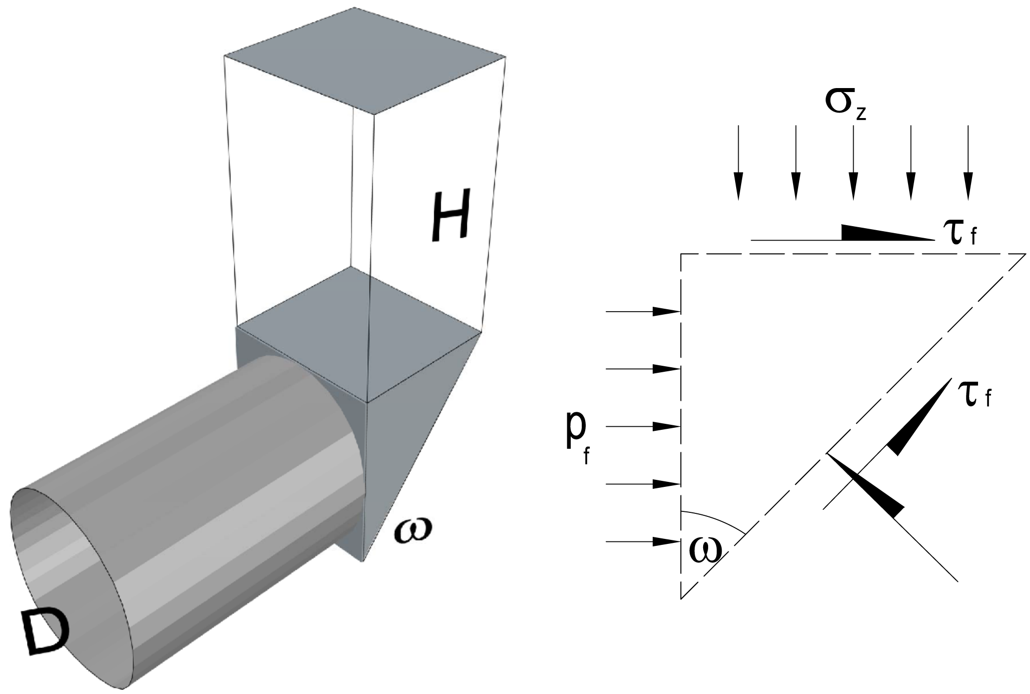

Figure 2.3. Undrained tunnel face stability (modified from Vermeer and Ruse, 2000)

It is reported by Vermeer and Ruse (2000) that the collapse mechanism provided by Anagnostou and Kovári (1994) was not kinematically admissible in that the shear stress acting on the top of the wedge was omitted. Vermeer and Ruse (2000) subsequently corrected the omission and provided a solution for the face collapse as shown above in Figure 2.3 on the right.

Vermeer and Ruse (2000) provide the equations of face collapse for a tunnel constructed assuming drained (effective) stress conditions. The critical aspect of the equations given by Vermeer and Ruse is the calculation of the vertical stress acting on the wedge (σ_z). The key factor in this calculation is the radius of the depression at the ground surface (R). In the case of Equation 2.4 below, R is assumed equal to the radius of the tunnel cavity. Equation 2.4 results in equilibrium of the forces given on the right of Figure 2.3 above.

$$\sigma_z = \frac{(\gamma R - 2c)}{(2K_o \tan\phi)}\left(1 - e^{-2K_o - \tan\phi H/R}\right)$$

Equation 2.4

The above equation assumes that the cutting length (unsupported round length) is equal to zero, the tunnel liner is installed at the face and the angle of ω is equal to ω=45˚+ϕ/2. In reality the angle ω will vary based on the shear stress acting on the top of the wedge, but Vermeer and Ruse (2000) assume the above for simplicity. Considering the above assumptions, the equation given by Vermeer and Ruse (2000) for a minimum required stabilizing pressure needed to prevent face collapse in a drained material is given as Equation 2.5.

$$P_f = \left(\frac{1}{2}\gamma D + \sigma_z\right)K_a - (3c + \sigma_z \tan\phi)\sqrt{K_a}$$

Equation 2.5

where K_a is the Rankine active earth pressure $K_a = \frac{1-sin\varphi}{1+sin\varphi} = tan^2(45 - \frac{\varphi}{2})$. In the case where ϕ=0, the equation reduces to that of the undrained condition.

2.3.3 Stability of an Unsupported Cutting Length (SEM Tunnel Construction)

2.3.3.1 Solution Based on Physical and Numerical Models

When an SEM tunnel is being considered in soft ground, it is necessary to consider the potential collapse of the unsupported cutting. In the images provided by Schofield (1980) above, it is clear that the length of the cutting plays a critical role in cohesive materials in terms of collapse. The equation used to assess the stability of a tunnel face with an unlined cutting in undrained conditions was first reported by Atkinson and Mair (1981). Atkinson and Mair described the face pressure (P_f) for partially unlined, SEM tunnels using a "tunnel stability number" (T_c). The stability number was used similarly to the N parameters for foundation design and was based on the depth and diameter of the tunnel as well as the length of unsupported cutting. Based on these factors, the stability number (T_c) was obtained from the chart shown below in Figure 2.4 and substituted into Equation 2.6

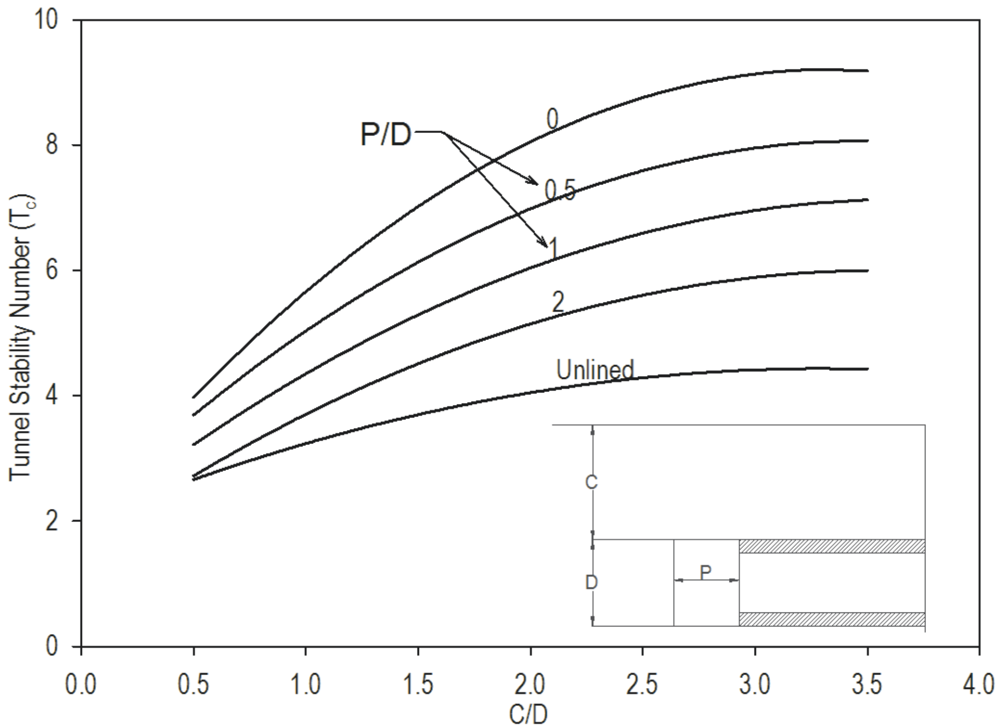

Figure 2.4. Stability number (T_c) estimation (adapted from Atkinson and Mair, 1981)

$$P_f = \sigma_s - \frac{s_u}{F_s} T_c + \frac{1}{2}\gamma D\left(1 + \frac{2s_u}{D}\right)$$

Equation 2.6

where σ_s is any surcharge acting at or slightly below the ground surface (foundation loads); s_u is the undrained cohesion (for drained, s_u would be effective c') and F_s is the required factor of safety against collapse.

Figure 2.4 indicates that the application of the stability number suggested by Atkinson and Mair (1981) begins to become difficult to apply at depth to diameter ratios less than one. The curves have been extended to shallower depths in order to illustrate the inherent limitations of comparable empirical methods.

Anagnostou and Kovári (1996) recommended a similar method using stability terms similar to that of Atkinson and Mair (1981), but in the case of Anagnostou and Kovári (1996), a stability term was assigned for each of the three components. The values for the stability factors were suggested based on numerical modelling assessing the nature of face collapse subjected to seepage and earth pressures. The terms were later refined by Vermeer, Ruse and Marcher (2002) and were renamed to correspond more closely with the familiar bearing capacity terms. The updated equation is shown below in Equation 2.7.

$$P_f = -c' N_c + qN_q + D\gamma N_\gamma$$

Equation 2.7

The stability terms (N_c, N_q and N_γ) given in Equation 2.7 are analogous with the bearing capacity factors for footings and are related to the friction angle of the ground (ϕ'). Vermeer, Ruse and Marcher (2002) also found that the factors are independent of tunnel depth (H) when the friction angle is greater than 20˚. Any surface loading is accounted for by the surcharge parameter (q), the mass of the soil within the collapsed zone and silo is a function of the soil unit weight (γ) and the tunnel diameter (D). Finally, the effective cohesion of the ground is given as c'. In contrast to fully lined tunnels (solely face collapse), Vermeer, Ruse and Marcher (2002) found that the coefficient of lateral earth pressure at rest (K_o) only influenced the calculated displacements but had little effect on the collapse pressure. This implies that the frictional forces acting along the length of the collapsed silo of soil are negligible.

In order to validate the assumptions made for their model, Vermeer, Ruse and Marcher (2002) numerically reproduced the findings of Potts (1976), Atkinson, Potts and Schofield (1977) and Mair (1979). by In a numerical experiment similar to that of the centrifuge tests carried out in Cambridge in the 1970's, Vermeer, Ruse and Marcher (2002) numerically created a cavity that was supported by an internal pressure at the face and any cutting length. By incrementally reducing the pressure along the unsupported length of tunnel, they were able to simulate the nature of collapse for fully lined and partially lined tunnels.

Vermeer, Ruse and Marcher (2002) reported that the evaluation of the two stability numbers may be carried out based on the ratio of the cutting length (d) to the tunnel diameter (D) and the effective friction angle of the soils (ϕ') as shown in Figure 2.5.

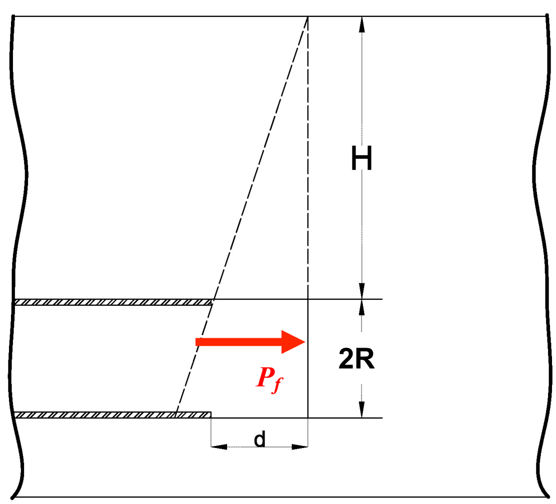

Figure 2.5. SEM cutting and face stability theory (modified from Vermeer, Ruse and Marcher, 2002)

Based on the numerical modelling, the stability factors used in the calculation of the minimum required face stability pressure are given as

$N_c = cot\varphi'$, $N_q \sim 0$; and $N_\gamma = \frac{2+3(d/D)^{6tan\varphi}}{18tan\varphi} - 0.05$

2.3.3.2 Solution Based on Back Calculated Field Results

Another method of determining the stability number of tunnels constructed in plastic clays at depths greater than 4D was proposed by Broms and Brennermark (1967). The overall stability number was based on the findings of Bjerrum and Eide (1956) for heave into braced excavations relative to the undrained shear strength of soil. Broms and Brennermark (1967) found that shear failure occurred in circular holes cut into sheetpiles (or tunnel faces) when the overburden exceeded the undrained shear strength by 6 times. The equation Broms and Brennermark (1967) proposed is given below in Equation 2.8.

$$\left(\gamma z - P_a\right) / S_u$$

Equation 2.8

where S_u is the undrained shear strength of the ground being tunnelled through and P_a is the pressure required at the tunnel face to maintain stability.

The method for assessing the face stability proposed by Broms and Brennermark (1967) assumed that any in-tunnel pressure (P_a) to support the face and cutting length provided added stability by increasing the pore pressure (u) in the soil. This has the effect of reducing the effective overburden pressure near the tunnel opening and thereby reducing the driving force.

Broms and Brennermark (1967) demonstrated the efficacy of the method using several laboratory tests as well as comparing the findings with several successful and unsuccessful tunnelling projects in Sweden. They found that all successful projects were completed where the stability number (N) was less than 6 and all unsuccessful projects were not.

Of key interest was the role that drainage played in their analysis. Broms and Brennermark (1967) often referred to the method as undrained, but consistently alluded to the accumulation of pore pressure gradients and how the migration of pore pressures would locally increase or reduce the shear strength with time. This would imply that their method, though it uses the undrained shear strength as a metric, is in actuality a drained analysis of clays subjected to extrusion. Considering this, the method's effectiveness is not known for unsaturated, hard, fissured clays. Broms and Brennermark (1967) briefly discussed the implications of applying the method in unsaturated soils and suggested that Equation 2.8. would ultimately result in pore pressure gradients into the opening. These gradients would be manifested as seepage forces into the cavity thereby reducing the factor of safety of the unsupported cutting.

Peck (1969) suggests that a stability number of 4 or less would result in relatively stable tunnelling conditions. Numbers in excess of 4 would likely result in difficulties with tunnel squeezing of one fashion or another (face or profile). Ward and Thomas (1965) suggests that for stability numbers less than 2, that tunnels may be driven unsupported for some distance with little concern.

Deere et al. (1969) provided an assessment of a variety of ground conditions assuming a range of stability numbers. Based on the total strains calculated from an elasto-plastic model, he determined that for a stability number of 1 or less, the ground will remain elastic and the volume loss (as a function of tunnel diameter) will be between

0.5 to 1.5%. The volume loss ratio was considered by Deere et al. (1969) to be independent of the construction method (TBM vs SEM) as the solutions were for fully unlined/unshielded tunnels.

Deere et al. (1969) provided general stability observations for a number of tunnels constructed in clay and found that most tunnels with a stability number of 2 or less were generally stable. They also suggested that ductile materials (stability factor >6) were more likely to accommodate large strains when compared to stiffer materials. This factor plays a significant role in determining how much ground loss occurs ahead of the tunnel face during excavation. A ductile material that can sustain large plastic deformations will undergo greater volume loss prior to round excavation due to ground movement into the tunnel at the face than a stiffer soil. This finding is in agreement with the numerical models presented by Vermeer, Ruse and Marcher (2002) who illustrated the general displacement fields ahead of a tunnel face for soils of various stiffnesses. The general stiffness of the material would thus in theory be detectable based on the settlement profile of a tunnel approaching and passing a point. For settlements less than about 50% of the total displacements (for an SEM tunnel) occurring when the monitoring point is at the tunnel face, the material may be considered to be relatively stiff and little movement into the face is taking place. For softer materials or stiffer materials that are undergoing yielding, it would then be expected that the recorded settlements greater than 50% of the total settlements or higher prior to the passage of the tunnel face.

2.3.4 Critical Strain

Sakurai (1981) was the first to suggest that a critical strain be applied to determine the cohesion and friction angle for back calculation of tunnel displacements. Sakurai (1981) suggested that the critical strain (ε_o) could be defined as the uniaxial compressive strength (UCS) divided by the initial Young's modulus of the material in question. He also found that the critical strain decreased with an increase in the UCS. This means that the critical strain is much lower for hard rocks (~0.1 to 1%) versus soft rocks and soils (~1 to 5%). This stands to reason as it would be expected that hard rocks behave as brittle materials, while soft rocks and soils would be more ductile. There were no comments as to the anticipated critical strains for hard, fissured soils.

Chern et al. (1998) compiled the convergence data from a series of tunnels and assessed the general stability of the excavations based on the measured convergence strains (relative to tunnel diameter). Based on the measured strains and the UCS of the rock, they established categories defining a stable to unstable excavation based on three levels of safety. Though still in rock, the empirical safety criterion developed by Chern et al. (1998) provides an additional check for stability similar to that of the stability factor given by Broms and Brennermark (1967). The data presented by Chern et al. (1998) is shown below in Figure 2.6.

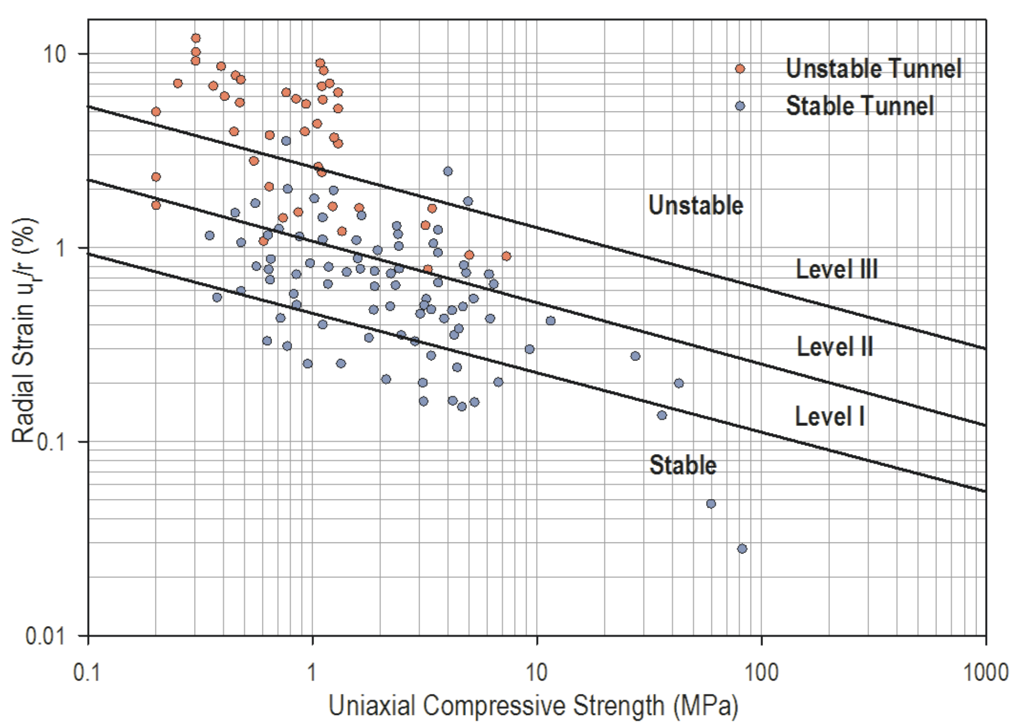

Figure 2.6. Tunnel stability as a function of critical radial strain (adapted from Chern et al., 1998)

Hoek (2001) found it interesting that nearly all of the failures that were recorded by Sakurai (1983), Chern et al. (1998) and Hoek (2001) took place when the radial strain/UCS values were Level II or above. Therefore the use of the radial strain as an empirical method to assess the overall stability of the tunnel cavity can be quite useful for most materials.

It would be expected that for heavily overconsolidated, cohesive soils the tolerance for shear strain should be considered before establishing a safety criteria. Peck (1969) discussed how the stiffness of the soil would directly influence the degree of convergence that could occur in an unsupported cutting before rupture initiated. Because most stiff fissured soils do not typically fail in conventional shear, the application of the methods provided by Chern et al. (1998) are not clear. Also, because the definition of unstable excavations was variable and included the translation of blocks relative to one another, the application of the critical strain method in stiff fissured soils should be evaluated on a case by case basis.

2.3.5 Narrow Pillar between SEM Tunnels

Very few studies have been carried out to examine the physical interactions of narrow pillars between twin, side by side tunnels. It is commonly known that closely spaced, parallel tunnels will interact with one another resulting in differing ground conditions from one excavation to the next. This implies that the settlements above two adjacent and parallel tunnels will be greater than the sum of those measured above each tunnel individually. Because there can be significant interactions between parallel tunnels, an understanding of how stress changes within the pillar will impact the nearby surface structures is essential. Furthermore, most studies have been carried out considering only homogeneous soil formations.

2.3.6 Field Observations / Site Investigations

The first observations of the influence of multiple tunnel tubes adjacent to one another may have been made by Terzaghi (1943). The subway tunnels were constructed as horseshoe shaped, using sequential excavation methods within a firm to soft clay and with a pillar width of 0.425D. All measurements were taken during the approach and passage of the second tunnel tube. Terzaghi (1943) found that during construction of the second of twin subway tubes, the shape of the first tunnel springline deformed almost 5 mm nearest to the pillar and only 1 mm on the far side of the first tunnel. In addition, measurements of the liner stress were made in the first tunnel. These measurements indicated an increase in ground pressure acting on the first tunnel liner following passage of the second tunnel. This resulted in differential stress profiles around the tunnel opening (from the pillar side to the far springline) which remained until the completion of monitoring.

Hansmire and Cording (1985) reported their findings for twin tunnels constructed in the Washington D.C. area in the early 1970's. The ground consisted of a post-glacial sand and gravel which was excavated using an open face TBM with rib and lagging temporary support. It was disclosed by the authors that for the construction of the first tunnel, the construction methodologies were not adequate to control the ground displacements and therefore considerable displacements occurred around the first tunnel. Of importance were their observations of the pillar performance when the tunnels were spaced at distances of 0.6D. They found that there was considerable stress increases within the pillar during passage of the second tunnel. These increased stresses resulted in yielding of the ground and a volumetric decrease (contraction) within the pillar and above each tunnel following passage of the second tunnel. Hansmire (1975) found that during excavation of the first tunnel, the ground underwent considerable volume increases due to loosening of the ground above the tunnel crown. This dilation of the soils within the centre of the settlement trough for the first tunnel effectively reduced the measured volume of the displaced soils. As a result, they determined that evaluation of the volume loss due to overexcavation (as a function of the tunnel face area) was not always representative of the actual loss at the ground surface. Estimation of the dilation was carried out by measuring the actual ground loss volume versus the volume of the surface settlement. It is generally assumed that the excavated volume will be equal to the volume of soil removed during a given round length (tunnel cavity) plus the volume of the measured settlement trough at the ground surface. As there was a deficiency in the volume of the settlement profile versus the actual volume loss, it was concluded that the low volume loss at the surface due to the first tunnel was compensated for by the ground dilating upon excavation. During the excavation of the second tunnel, the settlements were in excess that of the in-tunnel volume loss. This was due to ground loss during excavation of the second tunnel as well as compression of the recently dilated disturbed soils around the first tunnel. The vertical compression was also accompanied by lateral compression which further increased the measured volume loss. Because the stresses increased substantially within the pillar at narrow widths, considerable recompression of the previously dilated ground would contribute to the measured volume loss at the surface. The degree of settlements measured from the construction of the lag tunnel was influenced by the pillar width and tunnel depth (Hunt, 2004). The depth of overburden over the tunnel crowns was a key factor because with increased depth, there was more loosened ground to compress. Cording and Hansmire (1975) concluded that the only way to ascertain the settlements associated with stress increases in the pillar is to install deep settlement points immediately outside the tunnel envelope and at an elevation equal to or less than that of the tunnel crown. This effectively measures the settlements outside of the tunnel face and would therefore only represent those settlements associated with compression of the ground due to increased vertical stresses at the tunnel springline within the pillar. Measurements of the liner thrust during construction of the second tunnel were not conclusive. It was reported that in general, the thrusts measured on the ribs of the first tunnel increased during the approach and passage of the second tunnel. There were no measurements on the displacement of the temporary liner during the passage of the second tunnel. Hansmire and Cording (1985) did report measurements on the final liner which indicated that the influence of the second tunnel on the final concrete liner shape was minor and not a concern with respect to long term serviceability of the liner.

Mohamad (2008) provided the results of fibre optic, Brillouin Optical Time Domain Reflectometry (BOTDR) of twin tunnels through chemically weathered granites that were comprised of clayey to sandy silts. The focus of his research was to investigate the response of the previously constructed lead tunnel during the approach and passage of the lag tunnel. The minimum pillar width was 2.3 m or approximately 0.4D. Mohamad (2008) observed that the measured compressive strains within the lead tunnel were on the order of 0.07% following completion of the lag tunnel through the test section. The compressive strains at the pillar springline exceeded the tensile strains recorded at the crown which resulted in a net ovalization of the lead TBM tunnel lining. Finally, the strains within the first tunnel during the approach of the lag tunnel were recorded before any surface settlements were observed. Mohamad (2008) did not provide any discussion on the performance of the ground during his investigation, but rather kept his focus on the structural interactions of the liner with the ground resulting from a narrow pillar. As such, the actual influence of the tunnel interactions and the pillar performance/stability and its associated implications of the overall pillar width were not discussed.

2.3.7 Numerical Assessment of Pillar Performance

Several numerical studies have been carried out to assess the effect of spacing between tunnels. The first study on the effect of closely spaced tunnels using numerical methods was produced by Barla and Ottoviani (1974). They examined the stresses around two cavities spaced at distances ranging from 0.25D to greater than 1D (R/2 to >2R). They assumed a homogeneous, isotropic elastic (linear and hyperbolic elastic) soil mass for their models. When the linear elastic models were compared, Barla and Ottoviani (1974) noticed that the settlements were greater for the narrow pillar (0.25D) versus the wider pillars. They were the first to demonstrate numerically that in an elastic half space, pillar widths greater than 1D resulted in little interaction between the two tunnels.

When Barla and Ottoviani (1974) examined the stresses around the cavities, they found that the stress at the crown was more influenced by the depth of the tunnel as opposed to the pillar width. With respect to the springlines, they reported that the far springline was minimally influenced by either the depth of the tunnel or the width of the pillar. The pillar springlines, however, were highly influenced by the spacing of the tunnels. In fact, Barla and Ottoviani (1974) reported that for tunnels at the same depth (H=3D), the maximum principal stress at the inner springline increased approximately 150% for pillar widths ranging from 0.25D to 1D. When the depth of the tunnel was reduced to H<2D, the found that the stresses at the crown went into tension. The stress distributions were also the same regardless of the elastic model (linear or non-linear) at shallow depths. The coefficient of lateral earth pressure at rest (K_o) was not reported by the authors and was assumed to be equal to one.

Ghaboussi and Ranken (1977) also examined the effects of spacing between twin tunnels, numerically assuming a homogeneous, isotropic, linear elastic medium. Ranken (1978) suggests that carrying out an elastic model when considering the measured settlement data is important because the elastic model cannot predict the volume changes. Therefore, the settlements in excess of the elastic solution can only be attributable to localized shear failure and volumetric changes in the soil. Therefore, the elastic model provides an excellent method for determining the extent of plastic deformations around parallel tunnel openings during construction. For their model, a K_o value of 0.5 was assigned to the materials.

The tunnels were modelled with a liner installed either at the tunnel heading (same step as the tunnel excavation) or a step following excavation of the tunnel face. The former only accounts for displacements of the liner and the ground interactions with the liner as deformations of the ground are immediately constrained. The latter allows for the elastic deformations of the ground to take place and therefore indicates the stresses within the pillar due to the ground movements only.

Because Barla and Ottoviani (1974) indicated that tensile stresses form around the tunnels at shallow depths, Ranken (1978) considered not only the pillar width, but also the depth of the tunnel given as the ratio of H/D where H is the tunnel depth to the crown in his analyses. Ranken (1978) found that with excavation of deep (H/D>2) unlined tunnels with a pillar width of 0.25D, the principal stress in the springline at the pillar was approximately 1.5 times that of the springline on the far tunnel side. In addition, he also demonstrated that the shear stresses in the pillar were approximately 1.7 times those on the opposite side of the tunnel.

Ranken (1978) also found that the vertical stress is a maximum at the tunnel springline, and a minimum at the centre of the pillar. Despite the stresses being a minimum at the springlines of the pillar, the vertical stresses are still slightly above geostatic conditions at a pillar width of 1.2D. The point where no interaction between the tunnels occurs can be estimated by evaluating where the vertical stresses approach geostatic conditions. The data provided by Ghaboussi and Ranken (1977) suggests that at a spacing of approximately 2D there should no longer be any interactions between the two tunnels. It is important to note, however, that the stresses are near geostatic at a spacing of 1D and should be sufficient to assume little to no interactions under most circumstances as suggested by Ranken (1978).

Addenbrooke and Potts (2001) considered a series of small diameter (4.1 m) tunnels with several pillar widths within the heavily overconsolidated London clay. In all cases, the numerical models were constructed wholly within the London clay and did not consider the interactions of the underlying Lambeth Group sands.

Their numerical models evaluated the effects of consolidation and a non-linear elastic-perfectly plastic constitutive model. However, the spacings between the tunnels modelled were significant and were (at their smallest) between 0.92D to 1.4D.

Addenbrooke (1996) demonstrated the influence of K_o on the degree of yielding around a cavity. He found that for high values of K_o (K_o>1.5), yielding occurred around the crown and invert of the tunnel, while in a low K_o environment (K_o<0.5), that yielding occurred around the springlines of the tunnel. He also showed that the use of a non-linear elastic material severely restricted the extent of the yielding around the tunnel, while an anisotropic linear elastic model had little to no effect on the extent of yielding.

With respect to in-tunnel deformations, Addenbrooke and Potts (1996) found that the shortening in tunnel height and increase in tunnel width for pillars widths less than 0.5D were respectively on the order of 0.2 and 0.3% of the original tunnel diameter. Based on their numerical models, they concluded that for twin tunnels to be constructed as two, virgin tunnels (no interaction), a minimum pillar width of 7D would be required. This is considerably higher than the minimum 2D suggested by Ghaboussi and Ranken (1977) and Ranken (1978) and is indicative of the degree of yielding occurring within the modelled pillar. Further studies on a model identical to that of Addenbrooke and Potts (1996) by Koungelis and Augarde (2004) confirmed that it was indeed the overlapping of elements on the yield surface that resulted in the extensive tunnel interactions. This would explain the suggested tunnel interaction distances reported by Addenbrooke and Potts (1996) when compared to the elastic model reported by Ghaboussi and Ranken (1977) and Ranken (1978).

Ng et al. (2004) numerically examined the influence of tunnel heading lag for non-circular, SEM tunnels in the London clay. They developed a 3D anisotropic elastic perfectly plastic numerical model that was fully coupled with respect to seepage forces. As a result, consolidation was permitted to occur as long as drainage was allowed (liner installation effectively stopped all drainage for that portion of the model).

Ng et al. (2004) found that when the tunnel faces were excavated simultaneously i.e. with no lag between the headings, the displacements within the pillar were essentially vertically down. This finding agrees well with the stress predictions provided by Ghaboussi and Ranken (1978) in that the vertical stresses increase while the lateral stresses in the pillar decrease. When the tunnels were constructed assuming a lag, Ng et al. (2004) found that the displacements in the horizontal direction were strongly influenced by the lag separation. They reported that the reduction in the horizontal diameter at the springline with respect to the change in lag distance was approximately related linearly with the total lag distance. Ng et al. (2004) indicated that the change in stress was solely in the horizontal direction as the vertical deformations did not change appreciably with the differing lag distances. This suggests that the lag distance between tunnel faces only plays a role increasing the horizontal stress and not the vertical stress within narrow pillars for heavily overconsolidated soils.

2.4 Surface Settlements

2.4.1 Analytical Settlement Estimations

An empirical (analytical) method for assessing the settlements at the ground surface was first discussed by Peck (1969) and is given as Equation 2.9

below.

$$S_{\max} = {Vs}\Big/{\sqrt{2\pi i}}$$

Equation 2.9

where $V_s = V_l \frac{\pi D^2}{4}$ and S_{max} is the maximum settlement; *i* is horizontal distance from the tunnel centre-line to the point of inflection of the settlement trough; V_s and V_l represent the volume loss of the settlement trough and the volume of ground loss relative to the excavated tunnel area (as a percentage), respectively.

The actual vertical settlement at any distance from the tunnel centreline is given by Equation 2.10 below.

$$S_v = s_{\max}{}^{(-y^2/2i^2)}$$

Equation 2.10

where *y* is the horizontal distance from the centreline of the tunnel; and S_v is the vertical settlement at the distance *y* from the tunnel centreline.

Peck (1969) suggested that for estimation of the settlement trough of very closely spaced twin tunnels the above empirical method could be used, provided an equivalent tunnel radius was determined. The effective tunnel radius (R') is given for open faced excavations as R' = R +d/2 where d is given as the centre to centre spacing of the two tunnels. It has also been common in practice to simply calculate the empirical settlement troughs for each tunnel individually and superimpose them together to get the final trough due to twin tunnel construction. Mair, Taylor and Burland (1996) describe this method as being highly conservative, as it tended to overestimate the actual settlements. It should be added that they suggested that the superposition method was useful for determining the possibility of damage to nearby structures, since it effectively provided an upper bound on the surface settlements. Addenbrooke and Potts (1996) suggested that the superposition method was satisfactory when used in heavily overconsolidated soils. This is provided that an appropriate offset factor is applied to the maximum settlement of the second profile prior to superposition as suggested by Addenbrooke (1996).

Hansmire (1975) reported the results of several twin tunnel subway projects throughout North America. Of key interest were two test sections of twin tunnels with narrow pillars (<1D) in the Washington, D.C. area. He found that the displacement profiles for twin tunnels differed considerably from the commonly used method of superposition. Hansmire (1975) and Hunt (2004) determined that when two tunnels are excavated side by side in soft ground (soils), the settlement trough will be skewed towards the first tunnel. This greatly differs from the conventional superposition method where the greatest settlements will be estimated to occur along the centreline of the pillar.

Rankin (1988) reports that the superposition of the empirical settlement troughs is acceptable for tunnels constructed in stiff to hard clays, unless the pillar width is narrow. Rankin (1988) does not stipulate what constituted a narrow pillar, thus leaving its use open for interpretation. He also clearly states that the superposition method is not applicable for twin tunnels constructed in soft to firm clays or cohesionless soils as the method cannot account for the associated volume changes. This suggests that the superposition method is acceptable for situations where the stability number is less than 2 and the ground will likely remain elastic following excavation. If any plastic strains are likely, the empirical method cannot realistically be expected to capture the anticipated ground movements of twin side by side tunnels.

Suwansawat and Einstein (2007) describe another method of superposition based on Peck's inverted Gaussian curve to estimate the actual volume loss (as a function of the tunnel area) based on settlement measurements at the ground surface. This method is not useful for the prediction of surface settlements prior to tunnelling, but rather a more accurate method for determining the volume loss following passage of twin tunnels. They suggest to calculate the volume loss at the ground surface for the first tunnel using the conventional inverted Gaussian curve recommended by Peck (1969). Once the second tunnel passes, the overall settlement trough is then used to estimate the shape of the settlement trough created by the second tunnel alone. This is done by subtracting the settlement trough created by the first tunnel from the total settlement profile. The difference between the two profiles represents the total settlement created by the passage of the second tunnel. Once an inverted Gaussian curve fit has been made to both the first and second tunnel settlement troughs, the two curves could be superimposed together to generate the final curve. The result was found to closely represent the final settlement curve as generated by both tunnels. The total area under this curve represents the volume loss with respect to the tunnel face area.

2.4.2 Laboratory Testing of Settlement Profiles

Though Equation 2.10 is given to estimate the settlements above an SEM tunnel, as described by Peck (1969) and Mair and Taylor (1997), others have suggested that the settlement profile is independent of the tunneling method. Kimura and Mair (1981) demonstrated from centrifuge tests of tunnels constructed in clay that the width of the trough is independent of the support methods and is therefore independent of the tunneling method.

Hunt (2004) and Chapman, Ahn and Hunt (2007) carried out a series of centrifuge experiments to help illustrate and predict the degree of skew during twin tunnel excavation. By measuring the overlap of the disturbed zone about side by side tunnels, Chapman et al. (2003) and Hunt (2004) determined a skew factor to shift the results of the superimposed analytical method proposed by Peck (1969) towards the first tunnel. Unfortunately, this skew method requires the assumption of 3 additional parameters above and beyond those assumed for the Peck method. By providing an additional level of unknowns to the analytical method, it is doubtful that the recently proposed methods may be used as a predictive model, but rather only for back analysis of measured settlement troughs.

Chapman, Ahn and Hunt (2007) also carried out a series of laboratory experiments within a reconstituted Kaolin slurry to examine the effectiveness of the conventional inverted Gaussian method proposed by Peck (1969). They examined the movement of the settlement trough above several side by side tunnels constructed following consolidation of the material. With an OCR = 2.7 and a minimum pillar width of 1.6D, they found that by applying a skew factor to the summed Gaussian curves, a more representative analytical method could be obtained for multiple side by side tunnels. Again, the application of the skew factor required the assumption of additional parameters suggesting that the application is only good for back calculation.

2.4.3 Numerical Modelling of Settlement Profiles

Addenbrooke (1996) examined the changes in the settlement profiles for a series of 2D numerical models carried out assuming a number of twin tunnel construction geometries. Addenbrooke (1996) modelled the heavily overconsolidated London Clay using a coefficient of lateral earth pressure at rest (K_o) of 0.5. He found that the settlement trough was offset from the pillar centreline following the passage of the second tunnel. As the pillar with was reduced, the point of maximum settlement was found to move towards the crown of the first (previously constructed) tunnel. This was due to the assumptions of Peck (1969) and Hansmire (1975) which concluded that the dilated soil above the first tunnel underwent consolidation during the approach and passage of the second tunnel. This dilation followed by recompression of the ground above the lead tunnel would result in additional settlements above the lead tunnel not measured initially.

Ng et al. (2004) report that the combined settlement profiles for twin tunnels are actually opposite those reported by others (Hansmire, 1975; Addenbrooke, 1996 and Addenbrooke and Potts, 2001). Ng et al. (2004) suggest that the largest combined settlements should shift from above the first tube to nearly over top of the second tube. The key difference between the work of Ng et al. (2004) and Addenbrooke (1996) is the coefficient of lateral earth pressure. Ng et al. (2004) modeled the London Clay using a $K_o = 1.5$ while Addenbrooke (1996) used a K_o of 0.5.

The results reported by Hansmire (1975), Addenbrooke (1996) and Addenbrooke and Potts (2001) utilized actual field data to validate their results. Ng et al. (2004) did not present their results in the context of the actual Heathrow trial tunnels, but rather used the geometry and the ground parameters as the base for his model. No validation of their results or explanation of the assumptions was discussed.

2.5 Historical Tunnel Excavations in Downtown Edmonton

Since the early 1900's, the City of Edmonton has been constructing tunnels within the heavily overconsolidated soils throughout the city for drainage and transportation purposes. Edmonton has advanced well over 350 km of tunnels within the city since

1909 and has employed TBMs (moles) since the mid 1960's. Most of the tunnels have been advanced by sequentially excavated hand methods and generally consist of steel rib and wood lagging support systems. They are predominantly excavated in the glacial till due to its high strength and ability to stand open unsupported for relatively long periods of time. In most cases, there is little difficulty with construction of these smaller diameter tunnels and ultimately there is little to no impact on the surrounding community despite many being advanced through heavily populated urban environments.

Over the years, the City of Edmonton has developed techniques to help handle any unfavourable ground conditions such as seepage from cohesionless intra-till sand pockets and has even adapted several open face TBMs to advance drainage tunnels through the geologic conditions common to the city. In fact, for many years, the moles did not use tail shields to protect the workers from roof failures (Eisenstein and Thomson, 1978). The moles would leave at least a 1.2 to 1.5 m space unsupported in tunnels up to 6 m in diameter for some time while the workers installed the temporary support system.

These tunnels had a history of being stable for long periods of time with the only indication of progressive ground failure occurring along the discontinuities within the glacial till. Most failures would initiate at the interface with the cohesionless intra-till sand pockets which are randomly present throughout the formation. Tunnel cavities that either encountered the sand at the surface of the crown or sidewalls, were commonly the source of tunnel overbreak/overexcavation. In terms of safety, it has been known by local tunnellers that the hazards of falling till blocks can occur if there is a wet intra-till sand pocket behind a thin layer of clay till. This would provide a cohesionless discontinuity along the till and effectively remove any cohesion along one or more surfaces of the till block. With a reduced cohesion along one or more surfaces, the unloading of confining stresses within the tunnel cavity would result in joint dilation and block translation. Once one block would fall out and the sand was exposed, the sand would drop out and the process would continue until confinement was achieved and the geometry was stable. This failure process had not been reported to readily occur in the tunnel face during excavation and appears to be confined mainly to the tunnel profile.

2.5.1 Historical Tunnel Roof Failures in Edmonton

2.5.1.1 163 Street and 79A Avenue Roof Failure

Throughout the history of tunnelling in the City of Edmonton, there have been several minor roof failures that resulted in either time lost in terms of construction schedule or in minor ground loss at the ground surface.

One such failure occurred in 1969 during the construction of the 5.3 m diameter trunk sewer tunnel near 163 St and 79A Ave. At the time of the collapse, a representative from the University of Alberta was onsite to take photos as part of his research project. Matheson (1969) was informed upon arrival by the tunnel foreman that the roof was showing signs of distress and that the tunnelling crew did not want to stop installation of the temporary liner because they were in ‘bad ground’. Upon inspection of the tunnel roof, Matheson reported that the tunnel roof was composed of glacial till and intra-till sands. There were no obvious signs of seepage initially from the roof; however a small portion of sand had been encountered near the floor on one side which had shown signs of seepage and flowing conditions resulting in minor overbreak in that portion of the tunnel.

Shortly after arrival and inspection of the tunnel, a large cavity opened above the springline of the tunnel. Inspection of the cavity indicated that a block of till had fallen out and was surrounded by intra-till sand. The block had appeared to fail preferentially along the surface of the sand layer and fissures within the glacial till. Further observation of the unsupported portion of the tunnel indicated that there was a large intra-till sand pocket that was initially the source of the roof collapse. Approximately 15 minutes after arrival, Matheson reported that several cracks running parallel to the tunnel axis began to open. Shortly after opening, these cracks resulted in the formation of several small blocks measuring around 150 to 300 mm in length which began to individually fall out.

Once a small cavity was opened from the block failure, the crew attempted to add wood lagging between the mole and the closest rib in order to prevent a general roof failure. The general roof failure took place approximately 7 minutes following the installation of the lagging and resulted in larger blocks measuring around 600 mm in length and 100 mm thick falling from the roof. Finally, several other much larger blocks fell from the roof completing the general roof failure. The final blocks were considerably larger than before and measured roughly 1 m by 1 m by 0.6 m thick and the weight of the till blocks was sufficient to break at least one piece of wood lagging that was used as temporary support.

Following completion of the failure, the overbreak appeared to extend approximately 1 m above the original crown of the tunnel. Observation of the surface of the roof failure suggested that there were no irregularities to the roof shape implying that the blocks freely broke off from the roof along the pre-existing fissures that simply allowed blocks to slide relative to one another.

2.5.1.2 SLRT Extension 104 St. Roof Failure

In early 1981, construction began for the SLRT extension from Central to Corona Stations as reported by Branco (1981). Construction of the tunnel was carried out by a modified open face TBM owned and operated by the City of Edmonton. Tunnelling was to be wholly within the glacial till with intermittent contact with the intra-till sands. Near the start of tunnelling, the TBM contacted and damaged a multi-point extensometer prompting the installation of a fourth monitoring point some 80 m down chainage of the damaged point. This auxiliary multi-point extensometer was anchored within an intra-till sand pocket located within the crown of the future tunnel.

As the TBM approached the instrument, ground heave on the order of 3 mm was detected in the multi-point extensometer (as was typical for most deep settlement points along this alignment) followed by a dramatic drop to around 90 mm. As the TBM contacted the intra-till sand pocket, a large volume of the sand flowed into the cutting head and was ultimately overcut from the face resulting in a cavity in the roof of around 1.5 m^3. The monitoring point that was anchored within the sand, was lost into the tunnel during the collapse.

The displacements resulting from the collapse were generally confined to within the section of the roof failure. The extensometer indicated that the chimney appeared to propagate approximately only 3.4 to 4.5 m above the crown. The propagation of the settlement was indicated by the uppermost extensometer location which only showed around 11 mm of settlement which was fairly consistent with the near surface settlement measurements for much of the tunnel. Following collapse of the roof, the surface settlements were also shown to be mainly confined immediately above the tunnel crown as shown by measured settlements of around 8.5 mm at a settlement rod located nearby, but outside of the tunnel alignment.

2.5.1.3 SLRT North and South Portal Roof Failures

For the construction of the SLRT from Corona Station to University station, several contracts for construction of the tunnelled sections were let out to various tunnelling contractors. A portion of the tunnels were completed by the City of Edmonton using a modified open face TBM, another was carried out using a closed face slurry shield TBM while two other sections were carried out using conventional SEM construction methods. The open faced TBM had been modified such that the gates could be closed as required should unstable or wet, flowing ground conditions be encountered. It effectively permitted for the cutting face to be held in position to allow drainage of any intra-till sand pocket that were encountered. Once the pocket was drained, tunnelling operations were commenced. The proposed LRT alignment was to pass through three of the major geologic units encountered throughout the city. Of main concern was the presence of the upper outwash sand and silt. The outwash sands consists of variably graded, dry sand and silt in the upper horizons and are wet near the contact with the underlying clay till. Because of its nature, the sand was expected to run freely when excavated near the surface and flow near the lower horizons of the formation when left unsupported (Eisenstein and Sorenson, 1986)

Approximately four days into construction, the TBM crown broke out from the clay shale bedrock and was partially within the post glacial outwash sands. The percentage of each material within the mixed face was not reported. A roof collapse occurred resulting in the closing of the cutter head gates and a stop in production. Tweedie et al. (1989) reported that settlement in the area had been measured to exceed 200 mm above the crown of the tunnel and had in fact damaged one of the deep settlement rods by coming into contact with it. These settlements were reported as being chimney like and did not extend more than 10 m laterally from the centreline of the tunnel. This was indicated by the various instruments including settlement rods and inclinometers installed within the anticipated settlement trough, but away from the tunnel crown.

During a time that the TBM was under repair, it was concluded that the TBM would not be able to excavate the tunnel within the post glacial sands without some form of soil improvement. Initially, chemical grouting techniques were explored, however due to the fine grained nature of the sand, the permeation and overall treatment of the sands was not adequate to provide the necessary stabilization of the soils and permit further tunnelling. A series of cast in place, fillcrete piles were constructed from the ground surface ahead of the tunnel face. This method was effective in stabilizing the outwash sands for construction, but was considered too costly financially to install for the entire 150 m tunnel section. In the end, a series of jet grout (soilcrete) columns were advanced from the ground surface ahead of the tunnel face in a fan pattern.

As the tunnel advanced, additional ground loss was realized due to the TBM breaking the base of the unconnected soilcrete piles above the crown causing pile fallouts. These fallouts resulted in settlements at the ground surface of up to 40 mm, however in the end additional face collapses were avoided. In order to minimize the impact and lateral extent of the surface settlement, additional post construction pressure grouting was used to stabilize the soils above the crown and ultimately recover some of the measured settlements. One area in particular where the surface settlements were considered excessive occurred at a previous manhole had been constructed above the crown of one of the tunnels and had been backfilled with sand. Upon contact with the backfill by the TBM, the relatively loose sand simply ravelled into the TBM cutting chamber.

A second failure occurred during the construction of the LRT tunnels during the SEM excavation of the tunnels between the south river bank portal and University Station. Like the TBM collapse, the SEM collapse occurred within the glacial till and initiated at a contact with an intra-till sand pocket. The ground loss into the tunnel was so rapid, that the contractor did not have time to apply a skin coat of shotcrete to the roof prior to failure. The contractor did not anticipate any negative ground conditions, and did not possess any pre-support equipment as recommended in the contract.

The contractor decided to attempt further excavation without additional support with further ground loss occurring during each round advancement. Ultimately, the ground loss was controlled by using an active dewatering system consisting of vacuum well points installed within the intra-till sand formation and the installation of the designed pipe umbrella.

2.5.2 Performance of the Glacial Till during Tunnelling in the City of Edmonton

Published papers (Eisenstein and Thomson, 1978; Branco, 1981; El-Nahhas (1981); Eisenstein and Sorenson, 1986 and; Phelps and Brandt, 1989) suggest that the tunnels excavated within the glacial till an generally performed with regard to surface settlement. The performance of the first side by side LRT twin tunnels in the downtown area excavated within the glacial till was initially assessed by Eisenstein and Thomson (1978). While the surface settlements were small they did report a difference in the ground behaviour between the first drive and the second drive. Their experience is summarized as:

> "The first tunnel, driven through the undisturbed till, relieved the existing ground stresses. This led to opening of the adjacent joints and hence reduced the stiffness of the soil mass. Thus the second tunnel was driven through a till, which, in terms of its mechanical response, differed appreciably from the till encountered along the first tunnel.
>
> Evidence of this phenomenon was not too difficult to find. At the face of the tunnel in front of the mole in the second tunnel, blocks of till were observed to fall rather frequently from the crown area. The blocks were bounded by joints. No similar occurrences were observed in the first tunnel."

The above tunnels were constructed using an open face TBM with ribs and lagging installed behind the face. The excavation was left unsupported until the temporary liner was in installed (Eisenstein and Thomson, 1978). Based on the undrained ground parameters reported by Eisenstein and Thomson (1978) for the glacial till and the tunnel geometry (S_u=250 kPa and H≤12 m), a stability number of around 1 was realized.

Branco (1981) reported on the performance of the twin, side by side LRT tunnels within the glacial till between Central and Corona Stations. He found that, much like in the previously constructed tunnels, the glacial till performed well, but significant over-excavation occurred during contact with the intra-till sands.

Branco (1981) noted that there was negligible settlement ahead of the tunnel face (and in some cases heave up to 3 mm was observed). Most of the settlements were completed within 15 m of the tail shield of the tunnel corresponding with a distance of around two tunnel diameters. In general, the maximum measured displacement at the ground surface was around 10 mm suggesting excellent control of the ground. The measured ground loss (as a percentage of the total face excavation) was estimated by Branco (1981) to be on the order of 1.9% which is considerably higher than most other tunnelling projects documented within the city. He also reported that approximately 96% of the ground loss occurred immediately above the tunnel crown.

Phelps, Brandt and Eisenstein (1988) reported that the ground control above the TBM driven tunnels improved considerably within the glacial till with typical surface settlements on the order of 20 mm compared to settlements around 40 mm within the treated outwash sands. They also found that the settlement profile was "gentle" with the lateral extent of the trough equal to roughly 1 diameter to either side of the tunnel alignment. They also noted that the majority of the settlement that occurred during the TBM tunnelling took place following passage of the tail shield and relaxation of the soil into the tail gap created by the cutter head and the temporary liner. Finally, they reported that when the TBM encountered the intra-till sand pockets, the ground control was not as good as in the glacial till alone. Overbreak of the tunnel whenever the intra-till sand pockets were encountered was generally higher than in the glacial till alone.

El-Nahhas et al. (1981) reported on the construction of a test tunnel within the glacial till. The TBM utilized expanders to place segments of a pre-cast concrete liner into contact with the surrounding ground following passage of the TBM shield. The use of a mechanical expander was designed so that back grouting of the annular space would not be needed as the liner segments would be brought directly into contact with the ground. Based on the extensive measurements taken in the till during the advancement and passage of the TBM, El-Nahhas et al. (1981) found that shear strains in excess of 1 to 2% resulted in plastic deformation. There was no discussion as to how the strains were assessed in the field; whether the vertical displacements relative to the tunnel diameter or inclinometer displacements over a given length etc. The range of strains required for failure to occur was based on the results of a series of samples subjected to either triaxial extension or active compression as reported by Medeiros (1979) and El-Nahhas (1981). The upper bound is suggested for points in the ground that are subjected to that of a conventional triaxial test El-Nahhas (1981).

With the exception of El-Nahhas et al. (1981), none of the previous studies examined the extent of the plastic zone (if any) surrounding the tunnels. El-Nahhas et al. (1981) suggested that the zone of plastic deformations was not circular around the cavity, but rather concentrated at locations around the crown, invert and away from the springlines of the tunnels. They deduced that the concentrations of shear stress would explain the nature of the failures observed by Matheson (1970). Eisenstein et al. (1981) measured the ground pressures acting on both the precast lining described by El-Nahhas

(1981) and the rib and lagging liners. They found that because the rib and lagging liner was very flexible relative to that of the pre-cast concrete liner, the measured stresses acting on the rib and lagging liner were considerably less than those measured on the concrete liner. This indicates that the larger deformations of the liner and ground resulted in the mobilization of shear strength within the till and thereby resulted in greater activity of the ground support ring.

2.5.3 Narrow Pillar Construction

Typically the tunnels have been constructed as side-by-side twin tunnels with a minimum spacing of at least three quarters of a tunnel diameter between the springlines. During the construction of the SLRT extension from Corona Station to University Station, SEM tunnelling was undertaken for a portion of the tunnel alignment. Approximately 100 m of SEM tunnel was constructed immediately adjacent to a yet to be driven TBM tunnel. This was reportedly (Phelps, Brandt and Eisenstein, 1988) the first soft ground SEM tunnel constructed in North America at the time. To make the construction more complicated, the pillar width through a good portion of this section was considerably less than for other previously constructed LRT tunnels, and in some sections, the pillar width was reduced to around 300 mm. The SEM tunnels were constructed using a heading and bench sequence.

Based on an enhanced monitoring program, the surface and in-tunnel monitoring points suggested that the TBM tunnelling methods and liner design performed well and no damage was observed within the existing tunnel, the pillar or at the ground surface. The maximum overall settlement at the ground surface above the two tunnels was measured to be around 55 mm which was slightly higher than initially estimated but still within acceptable limits.

2.5.4 Historical LRT Surface Settlements

The surface settlements measured during tunnelling projects associated with the LRT extensions have been reported using various monitoring methods. In some cases, the settlement troughs were measured using deep and shallow settlement points, while others used more sophisticated multi-point extensometers. In the case of the first LRT tunnels, the settlement trough was reported based on survey targets fixed to a masonry structure at ground surface.

In most cases, the settlement troughs were measured for an open faced TBM with and without a shield. In one case, a settlement trough for an SEM excavated tunnel was reported. For the SLRT extension, settlements were reported for twin bored tunnels using an Earth Pressure Balance (EPB) TBM. In order to estimate the volume loss for the various projects, the reported settlement troughs were digitized based on the discrete settlement measurements (where data were not available) and the analytical methods for twin tunnels given by Peck (1969);Mair and Taylor (1997) and Suwansawat and Einstein (2007) were used to match as closely as possible the measured settlement trough.

Based on the above, the maximum settlements (S_{max}), distance to the point of inflection (i) and the volume loss relative to the excavated tunnel volume (as a percentage) is given below in Table 2.1.

Project	**Year**	**Excavation Method**	**Maximum Settlement (mm)**	**Inflection Point (m)**	**Volume Loss (%)**

North LRT	1977	Open TBM	24.3	16	0.65
SLRT	1988	Open TBM Till	15.9	7	0.22
SLRT	1988	Open TBM Intra-Till Sand	56.6	7	0.47
SLRT	1988	Open TBM Outwash Sand	186	7.5	2.25
SLRT	1988	SEM Till	15.7	10	0.32
SLRT Ext	2003	EPB TBM Outwash Sand	34.5	4	0.42

Table 2.1: Historical ground loss for various LRT tunnels

As is shown above, despite several difficulties with the modified open face TBM excavating within the intra-till sand pockets, it appears that typical ground loss percentages are between 0.2 to 0.5%. It should be noted the ground loss of 2.25% within the outwash sands and the open face TBM. The ground control within the outwash sand was effective when using the EPB TBM for the construction of the SLRT from University to Jubilee Station.

2.6 Conclusions

This chapter summarizes the various approaches of tunnel designers when approaching a Sequentially Excavated tunnel design in heavily overconsolidated soils. It provides a background on the following:

- A brief history of the determination of the engineering properties of heavily overconsolidated soils has been presented, illustrating the inherent difficulties of working with highly variable and state dependent sediments.
- Very small strain soil mechanics has also been briefly discussed with the intention to understand that the materials common to the Edmonton area do not perform according to conventional soil mechanics. The presence of micro and

macro fissures within the soil mass can strongly influence the shear planes that develop within the materials when subjected to shear stresses.

- Various analytical, empirical and numerical techniques that are typically employed to assess the face and heading stability in a variety of ground conditions;
- Methods used to assess the ground surface settlement profiles as well as the volume losses due to the tunnelling methods in terms of measured ground displacements. This was discussed in terms of a single tunnel as well as multiple, side-by-side tunnels;
- The nature and extent of the interaction between closely spaced, side-by-side tunnels within soils. This includes the likely zone of influence around the first tunnel cavity as well as the performance of the soil above the tunnel crown;
- A brief history of tunnelling in the City of Edmonton through the various geologic formations and using several tunnelling techniques. This includes a summary of the documented failures and problematic tunnelling techniques applied over the years.

In general, tunnelling within the heavily overconsolidated "soft" sediments within the City of Edmonton has been very successful in the past. There have been few documented face or header collapses that resulted in any major time delays in terms of construction. Historically, there has also been very good control of the ground by the various contractors resulting in little ground loss as measured at the ground surface. There is still however, a need to better understand the interactions of closely spaced, side by side twin tunnels in heavily overconsolidated and fissured soils.

3.0 Edmonton Regional Geology and Observations of Two Excavations

3.1 Introduction

There have been numerous studies throughout the City of Edmonton focused on the regional sediments and the glacial activity which deposited the surficial soils. To date, very little has been done to establish the engineering characteristics in terms of geologically controlled performance. The work carried out during this portion of the research examined the surficial geology within the downtown area of the City of Edmonton. The research has observed the impact of any pre-glacial, englacial and/or postglacial activities that may have direct relevance of the characteristics and performance of the surficial soils. This study will provide insight into the nature of cohesionless deposits within the glacial till. Details related to the structure of the fissures within the glacial till and their impact on heavy civil construction. Finally, attention has been paid to the structurally controlled movements of the ground during heavy civil construction.

In order to supplement the previous geological studies, additional field observations have been carried out along the North LRT tunnel alignment. These observations included a study of the exposed ground during the construction of the foundations for the Epcor tower and the associated North LRT box structure. This very large excavation was essentially a 22 m deep test pit located in the city centre. It provided insight into the ground structure of a large excavation within all of the Edmonton sediments. In addition, as the North LRT tunnel was being sequentially excavated, geologic maps were generated and key observations are provided. These observations have led to the identification of several unique structures within the Edmonton till that had not been previously observed.

3.2 Regional Surficial Geology

The surficial geology of the Edmonton area was first reported by Bayrock and Hughes (1962). They attempted to identify the majority of the surficial features and comment on the various geologic formations in the area. The study area was quite broad and included many of the outlying areas surrounding Edmonton as well as the city centre itself. In total, they assessed a region of approximately 3600 km^2 with Edmonton located in the centre of the study area. Their study identified nine key physiographic regions within the area (excluding the city) and are as follows (from Bayrock and Hughes, 1962):

- North Saskatchewan River valley
- Sturgeon River valley;
- Gwynne outlet;
- Ground moraine;
- Hummocky dead-ice moraine area;
- Lake Edmonton area;
- Pitted deltas;
- Early North Saskatchewan area; and
- Dune areas.

Within the city limits of Edmonton, only the Lake Edmonton area and the North Saskatchewan River valley are of relevance. It should be noted that these physiographic regions represent only the uppermost strata within the geologic sequence. In reality, the ground moraine, hummocky dead-ice moraine and Early North Saskatchewan areas are of relevance as they underlie other surficial deposits throughout the city centre.

As a result of the last major glaciation in the central Alberta area, the soil stratigraphy throughout the City of Edmonton is fairly consistent. The advancement and subsequent melt out of the Laurentide ice sheet during the Wisconsinan ice age (May and Thomson, 1978) locally eroded the bedrock; deposited sands and gravels as part of an ancient braided stream; which were then overlain by a thick layer of glacial till as well as alluvial and lacustrine deposits.

Within the downtown Edmonton area, the main stratigraphic units of concern are the pro-glacial Lake Edmonton clay and outwash deposits; ground moraine (cohesive till); pre-Laurentide (tertiary) early Saskatchewan River sand and gravel deposits all overlying the Upper Cretaceous bedrock. Past researchers have identified many of the landforms throughout the city and have developed several working theories as to the geologic history of the various formations.

Slight variations are known to occur throughout the city, particularly near the North Saskatchewan River valley, but in general, the subsurface conditions summarized below and illustrated in Figure 3.1 have been encountered throughout the City of Edmonton. Details of the extent and general thickness of each formation are described by Bayrock and Hughes (1962), Bayrock and Berg (1966); Westgate (1969) and Kathol and McPherson (1975).

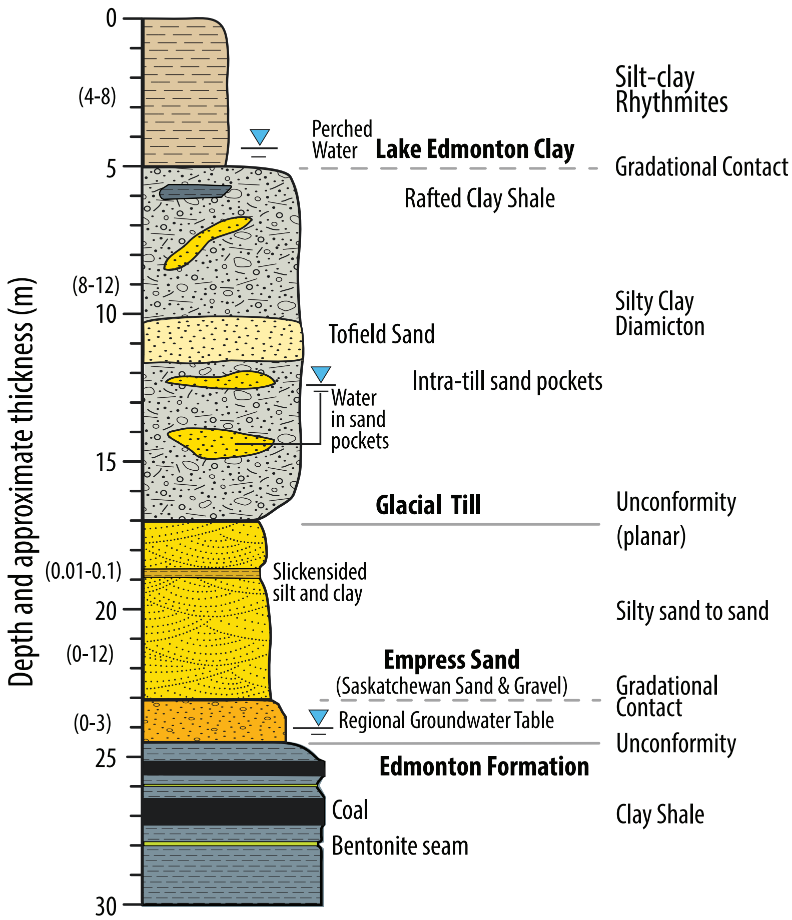

Figure 3.1. Generalized stratigraphic profile encountered with the City of Edmonton

3.2.1 Glacio-Lacustrine Clay

The majority of the surficial materials throughout the city consist of a glacio-lacustrine silt and clay known as the Lake Edmonton Clay. Ice damming near the southern limit of the city resulted in a short-lived glacial lake that deposited soft cohesive sediments on the surface of the glacial deposits (Bayrock and Hughes, 1962). The silt and clay is generally firm to stiff and is typically about 4 to 6 metres thick. The glacio-lacustrine clay is rhythmically bedded though the spacing of the varves are generally quite wide and are typically very difficult to observe visually. In many areas throughout the city, the Lake Edmonton clay is overlain by a thin layer of fill that generally consists of a reworked material that is similar to that of the glacio-lacustrine clay or the underlying glacial till. In general, the fill is variable in thickness but does not typically extend through the full depth of the Lake Edmonton Clay. Fredlund and Dahlman (1971) provide a concise description of the deposition of the Lake Edmonton Clay and is as follows:

> "Pro-glacial Lake Edmonton was formed in contact with the ice during de-glaciation when the, natural north-easterly drainage was blocked by ice. Water was impounded and the lacustrine sediments were deposited. Subsequently the lake was drained by outlets to the south of the city."

The Lake Edmonton sediments are known to be highly variable in composition spatially due to differential depositional energies relative to the previous shoreline. Typically the deposits are coarser to the north of the city where the overland glacial meltwater entered the lake. To the south of the city near the Gwynne Outlet, the thickness of the clay is thinned due to erosion following breach of the ice dam. Within the city centre, the sediments are typically composed of silts and clays. Ice rafted gravel and slabs of the Edmonton Formation bedrock are also found occasionally within the deposits.

3.2.2 River Terraces

Previous river terraces have been observed throughout the North Saskatchewan River valley. Like the Lake Edmonton sediments, the composition and extent of the river terraces are highly variable depending on the energy state of the water during deposition. Westgate (1969) reports that the alluvial deposits vary from fine to coarse aggregates associated with regular periods of degradation followed by aggradation. The different depositional patterns were thought to likely be influenced by the position of the advancing and retreating ice sheets that subsequently influenced the level of the pro-glacial Lake Edmonton. Considering this, at least four terraces have been identified throughout the river valley. The relief of the uppermost terrace is nearly 20 m above the existing river level. Kathol and McPherson (1975) indicate three types of terrace formation, one is pre-glacial and is located below glacially derived sediments within local valleys within the bedrock, while the remaining two are near the current river valley. Within the river valley, there are terraces associated with changes in the energy level following the lowering of glacial Lake Edmonton and the river terraces associated with the current and ongoing down-cutting of the existing river valley.

Westgate (1969) reports that the age of the terrace deposits is between 10,000 to 12,500 years as determined by animal remains recovered from within the formations. Unlike Stalker (1968), there was no evidence of older sediments that were deposited during impounding of a pro-glacial lake during glacial advancement similar to those encountered near Cochrane, AB. The exception to this may be in the terrace formations found in the upper reaches of the river valley deposited in bedrock valleys also known as the Outwash Sands. These formations may be closer to tertiary in age rather than quaternary and may have been deposited during periods of lower energy due to impounding during the advance of the Laurentide ice sheet as described by Stalker (1968) and Kathol and McPherson (1975).

Mostly in the southern parts of the city, a layer of fine to medium grained (5% to 15% silt), uniformly graded sand is encountered immediately below the Lake Edmonton Clays. Outwash sands are in-filled channels of the pre-Laurentide terrace fine sands. Kathol and McPherson (1975) indicate that the outwash sands are likely a reworked pre-glacial (Empress) sand that was deposited in either super-glacial or englacial drainage systems. The formations typically are found in contact with the river valley or areas where local water discharge from the receding glaciers was possible. They are relatively continuous in that the cohesionless formation may extend for hundreds of meters to kilometers, though the composition, and subsequently, their physical characteristics can change considerably over very short distances.

Typically the sand is compact to very dense and was encountered throughout the alignment of the University to Jubilee South LRT stations. The thickness of the outwash sands along the South LRT alignment was reported to vary from between 8 to 11 m, though thicker deposits exist in several areas further south of Whitemud Drive. Groundwater is commonly encountered within the outwash sands, though the drainage properties are dictated by the percentage of fines within the formation. The groundwater within the outwash sand is generally confined between the overlying Lake Edmonton clay and the underlying glacial till.

3.2.3 Glacial Till

The genesis of the glacial till in Edmonton has been debated for many years. Bayrock and Berg (1966) suggested that the glacial till has two colours to it. The colour change is simply a function of long-term oxidation and not the indication of differing units. They emphatically stated that in their opinion the change in colour with depth is not a change in composition. Westgate (1968 and 1969), however felt that there were two distinct units of the till, each representing an advance and retreat of the Laurentide ice sheet. Thomson et al. (1982) agreed with Westgate and attributed local ice advances and retreats to the presence of two till sheets referred to as the upper and lower tills. Shaw (1982) suggested that the glacial till was deposited by the melt out of stagnant ice and not due to lodgement of advancing ice sheets. Frequent knob and kettle land forms are observed to the southeast of the city center and are indicative of stagnant ice breaking off and becoming embedded within the upper horizons of the till. Where present, Lake Edmonton sediments have worked to partially conceal the hummocky terrain in many locals. Shaw (1982) has noted the presence of Cretaceous bedrock that had been plucked from the local bedrock and deposited within the till. These bedrock slabs were found to be intact and could have only have been deposited as super-glacial formations following the melting of stagnant ice. Cobbles and coal fragments are encountered throughout the formation and, like the sand pockets, are randomly located throughout the deposit. In some cases, the cobbles are oriented in the direction of glacial advancement though most researchers have determined that the sole markings found where the till is in direct contact with the Empress Sand is an accurate indicator of glacial advance direction. Otherwise, use of the clastic orientation has been called into question. This is because only the sole markings at the unconformity with the Empress Sand, indicates a northeast to southwest trend that coincides with regional fluting. Westgate (1969) indicates that cobble orientation within the glacial till trending from the northwest to southeast is in fact indicative of a second ice sheet advancement. Several authors (Bayrock and Hughes, 1962; Bayrock and Berg, 1966; and Shaw, 1982) disagree with this hypothesis and point to the dead ice moraine around the city and that there are no obvious recessional moraines in the region indicating a gradual retreat of the ice front. Their thinking is that the glacial till was deposited from a stagnant ice sheet that melted out in place, depositing its englacial sediments basally as the glacier melted down. The presence of floating slabs of the Edmonton formation bedrock also suggests that plucked slabs were incorporated onto the glacier. Because the soft rock is still found intact throughout the deposit, they must have been transported only short distances either englacially or supraglacially before being deposited wholly intact within the till.

The glacial till deposit in the Edmonton area is approximately 6 to 16 metres thick and generally very stiff to hard. The till was laid down on the surface of the Saskatchewan Sands and Gravels in pre-glacial channels or in contact with the bedrock in the upland areas. Pockets of intra-till sand with a highly variable percentage of coarse and fine particles are randomly encountered within the glacial till. The size and extent of the sand pockets can vary significantly from tens of centimetres to several metres in length and thickness. Boulders up to 500 mm in diameter are also present within the soil matrix, though are not frequently encountered. The interface between the glacial till and the glacio-lacustrine clay is gradational (where the outwash sands are not present) whereas the unconformity with the underlying sand and gravel formation is generally sharp and planar.

The upper horizons of the glacial till are brownish and columnar-jointed suggesting that they have been oxidized. The lower till has a thickness of approximately 6 m and is greyish in colour with prominent rectangular jointing. Westgate (1969) and Shaw (1982) observed the presence of a cohesionless deposit between the two tills, commonly referred to as the Tofield sand (Warren, 1954). The Tofield sand is composed of both quartzite and shield clasts suggesting a combination of the pre-Laurentide sands and glacial deposits. The formation is up to 6 to 8 m thick (Westgate, 1969) but is typically on the order of 1 to 2 m. It commonly exhibits cross bedding and regular faulting. Shaw (1982) attributes the faulting observed in the upper horizons of the lower till, the Tofield sand and the lower horizons of the upper till to consolidation of lower sediments deposited during the melt out of the glacier. The presence of dipirism in the upper horizons of the lower till suggests ice contact and thaw-consolidation. Shaw (personal communication) suggests that the presence of the underlying Saskatchewan Sand encountered within the till at moderate angles suggests that the glacier plucked frozen slabs of underlying sand that were subsequently incorporated into the till and deposited during melt out. Shaw further detailed that the overwhelming evidence that the sub-glacial flows resulted in a decoupled environment that would have deposited glacially derived sediments within the formations resulting in a mixture of the underlying sands with clasts originating in the Canadian Shield. The occasional presence of sand pockets exhibiting convex upper surfaces, point to frequent meltwater drainage events.

3.2.4 Empress Formation (Saskatchewan Sand and Gravel)

Below the glacial clay till, the pre-Laurentide sand and gravel deposits are encountered. These deposits have been observed at depths greater than 15 m below the ground surface. The Empress sands were deposited as the continental Laurentide ice sheet advanced up the regional slope resulting in a change in direction of rivers flowing from the Rocky Mountains in the west to the Arctic Ocean in the north (Bayrock and Berg, 1966). This change in flow and continual displacement of the river location resulted in gradual aggradation of the rivers and the subsequent deposition of the Empress Sands throughout much of Alberta and Saskatchewan.

Bayrock and Berg (1966) carried out an extensive drilling program in the downtown area in order to map the location and thickness of the Empress Sand. They found that the sand deposits were typically thicker within buried pre-glacial channels and absent in areas of high bedrock relief. Specifically, they did not encounter the Empress Sand in small areas to the southwest and southeast of the downtown area. Bayrock and Berg (1966) identified a long ridge within the Empress Sand, starting around 104 Avenue and 100 Street and extending northeast. The local relief of this ridge was reported by Bayrock and Berg (1966) to be around 7 m. There was no evidence of the ridge presented in their work, but they suggested that its presence might be a result of glacial push deforming the bedrock and the overlying sediments.

These cohesionless soils are generally dense to very dense and tend to fine upwards towards the contact with the overlying glacial till suggesting a change in depositional energy near the completion of the aggradation process. The lower horizon of the formation generally consists of coarser sand and gravel and typically coincides with the long-term, regional groundwater surface. The mid to upper horizons are frequently cross-bedded with coarser deposits of sand and gravel and also with silts, clays and organics. The sand and gravel is composed of quartzitic sands and gravels with minor percentages of silts and clays that are thought to originate from the Cordilleran (Shaw, 1982). The Empress is easily differentiated from the overlying till by the lack of igneous clasts originating from the Canadian Shield. It is not uncommon to encounter laminations of high plastic clay and deposits of silt and organics within the sands varying between 10 and 100 mm thick. Slickensided clay laminations were observed at Elevation 643 m within the Station Lands Cavity excavation. These discontinuous bedded clay laminations recovered from boreholes drilled through the Station Lands indicated 30 percent silt sizes and 70 percent clay sizes, with liquid limits ranging between 72 and 82 percent and plastic limits between 24 and 27 percent. Samples recovered during the North LRT tunnel construction indicated that the formation depth was highly variable and was discontinuous in all directions. This meant that one fine grained deposit could be observed extending through one tunnel face, and not be encountered in the second face at the same location; or the beds may be exposed in one round and the next, they were not present. The discontinuous nature of the material is thought to be consistent with that of a braided river system that would have both high and low energy deposits throughout the channel width at any given time.

3.2.5 Bedrock

The Edmonton Formation Bedrock consists of soft sedimentary deposits of claystone, sandstone and siltstone with varying thicknesses is encountered below the Empress Formation. This sequence is commonly referred to as clay shale. The Edmonton Formation was deposited in a relatively shallow saline to freshwater inland sea (Eisenstein and Thomson, 1978). The contact with the Empress Sand above is sharp and for the most part planar with a slight dip to the northeast within the city. Intermittent coal beds of variable thickness and aerial extent are known to be present within the Edmonton Formation and historical mines are located throughout the North Saskatchewan River valley. The Edmonton Formation also contains up to centimeter thick bentonite layers (volcanic ash) in the upper horizons of the bedrock that were deposited during intermittent volcanic eruptions. These layers are exposed in the river valley and often form part of the rupture surface for river valley landslides.

3.2.6 Groundwater

Perched groundwater is occasionally encountered on the surface of the glacial till near the interface with the glacio-lacustrine clay. Where this occurs, the overlying glacio-lacustrine clay is generally softer and can make excavations through these horizons difficult with accumulation of groundwater within the excavation occurring over a period of days following exposure. Typically though, groundwater is most commonly encountered within the intra-till sand pockets. These saturated sand pockets are the major source of seepage and soil instabilities during most excavations through the glacial till. Groundwater seepage rates of 4 to 5 L/min have been measured when these sand pockets are encountered, though they can be much higher depending on the gradation of the pocket. In general, these sand pockets are fairly small in aerial extent and possess a relatively low storativity and therefore, may readily yield groundwater upon exposure. The seepage however will be of relatively short duration, usually tapering off over a period of minutes to hours (Matheson, 1970; Eisenstein and Thomson, 1978). Due to the limited size of the sand pockets and the low permeability of the till in which they are contained, it is unlikely that they are readily recharged during precipitation or seasonal events.

Where the Empress Formation is encountered it often acts as an under-drain for the overlying soils with the groundwater occurring as a perched water table metres above the surface of the clay shale bedrock. This perched groundwater level generally represents the regional groundwater level and is usually contained within the coarser portion of the Empress Sand.

3.3 Observations at the Station Lands Excavation

3.3.1 Glacial Till – Empress Formation Contact

As stated in the regional geology section, the contact between the glacial till and the underling Empress Formation is a sharp unconformity that was clearly observed in the Station Lands Cavity. The contact elevations were documented in the Station Lands excavation to be at EL 647.8 m at the eastern portion of the site and EL 646.5 m at the western limit of the excavation. This suggests a nearly horizontal contact over the 170 m long excavation. There was a slight dip towards the west as shown below in Figure 3.2. The elevations of the unconformity in the north to south direction were not measured due to the presence of the soldier pile wall along the southern limit designed to support the CN Tower. It is thought that there is a gentle dip to the south (towards the river valley).

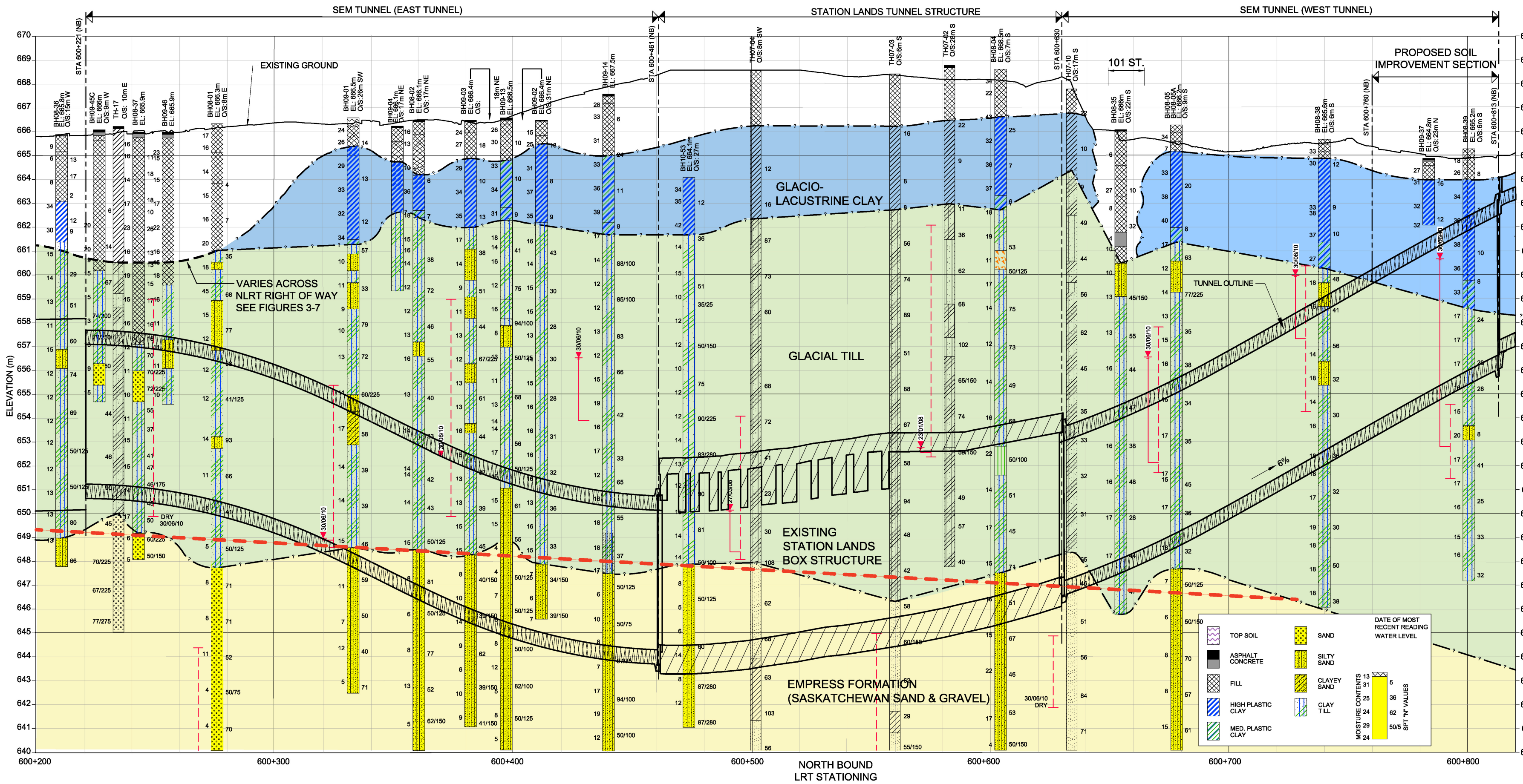

Figure 3.2. Elevation of the Till/Sand Contact from the Epcor foundation (adapted from Soliman et al., 2010)

Plate 3.1 Exposure of the Till-Sand contact in the Epcor foundation. The contact was planar with no evidence of shearing. The photo was taken looking towards the West (with permission from Martin, 2010)

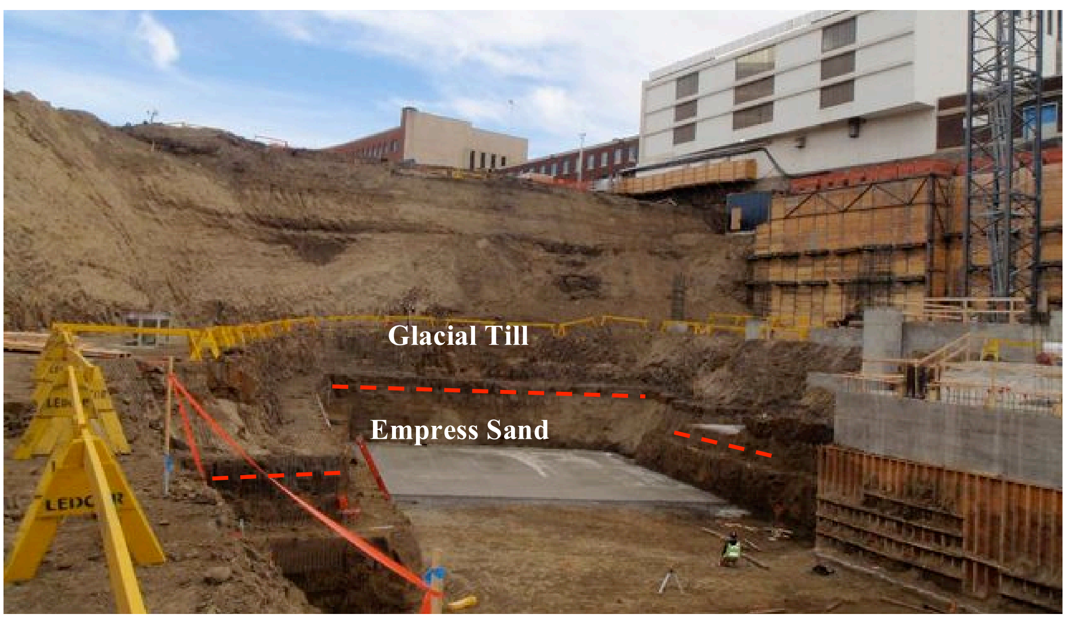

Plate 3.2. Unconformity between the glacial till and Empress Sand (facing east) (adapted from Martin, 2010)

3.3.2 Stand-up Time

Due to the length of the construction activities at the Station Lands Cavity, observations of the stand-up time of both the glacial till and the Empress Sand were possible. Conventional geotechnical engineering would require most excavations open more than several weeks be cut back at a slope of close to 3H:1V in order to minimize the risk of instabilities and the potential for injury to workers within the excavation. In the Station Lands, the excavations within the glacial till were cut at a 45˚ angle if sloped at all. In most cases, the excavations were cut nearly vertical and benched to the contact with the Empress Sand. Within the Empress Formation, the depth of excavation was on the order of 3 to 5 m below the unconformity with the glacial till. In order to get to the base of the excavation, the Empress Sands were cut vertically with one bench approximately 1/3 of the total depth to the base of the excavation and left exposed for several months. During the time that the Empress Sands were left exposed, they were unsupported and subjected to weathering.

Over the duration of open excavation, small instabilities within the glacial till resulted in the formation of small debris piles of till. These failures resulted from blocks sliding relative to one another along the pre-existing fissures as shown below in Plate 3.3. Before a block falls, the sand and till form a single, continuous face. After the failure and removal of a till block, they still form a single face, set back from the original face. So, the till block failure takes a chunk of sand with it and possibly shears the sand face to be continuous with the overlying till face. It is likely that the till blocks which are nearly separated from the soil mass due to the presence of fissures, adds weight to the unsupported underlying Empress Sand, causing the sand formation to shear and fail. As a result the sand and till fail as a single mass regressing back to a meta-stable state at the newly separated joint surface.

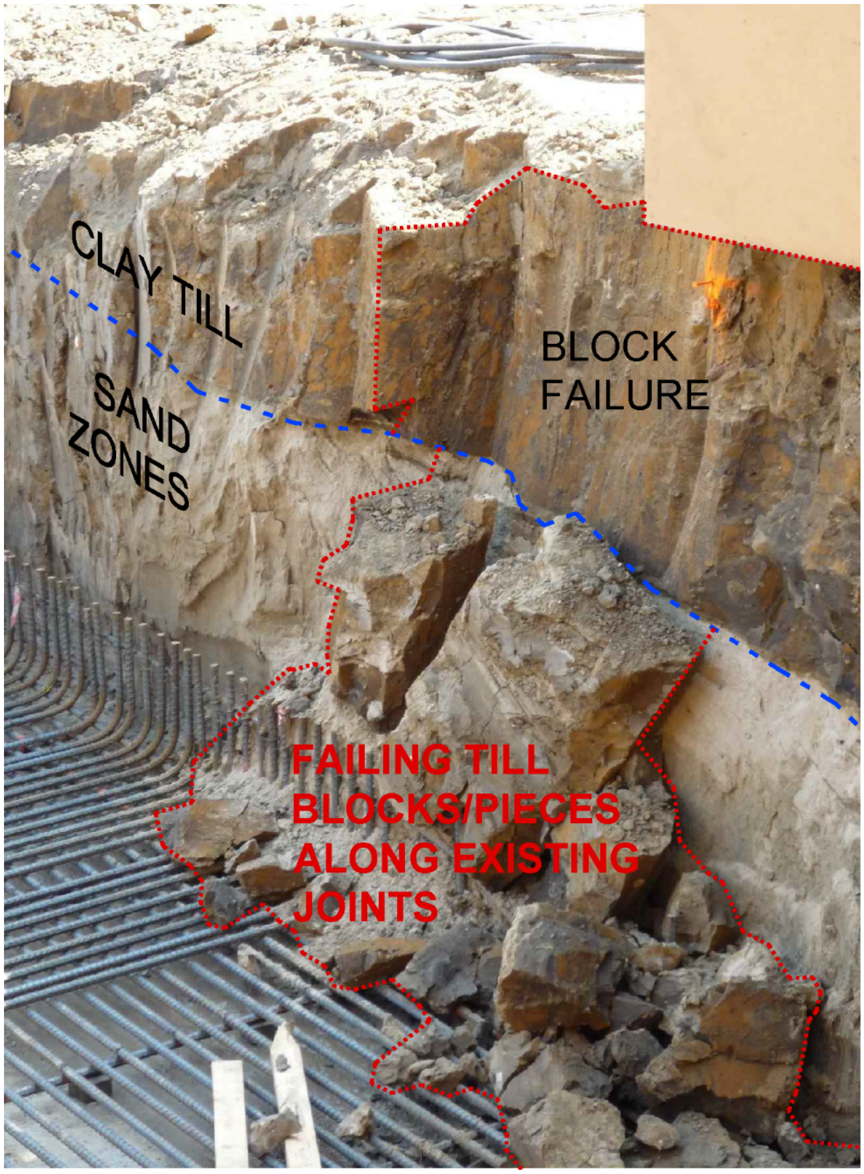

Plate 3.3. Block failure at the contact with the Empress Sand (with permission from Soliman et al., 2010)

Within the Empress Sands, the walls remained vertical for a minimum of several months despite the changing of seasons from the summer to winter and back to spring. The seasonal changes in precipitation appeared to have little effect on the stability of the sand. When instabilities occurred they tended to be small isolated failures that were more like local slabbing or ravelling as opposed to a conventional circular slip failure. The ravelling failures would progress only as far back as the contact with the glacial till. Once the sand was beneath the till, a sufficient overburden pressure was present and the ravelling ceased.

An example of the stand-up time of the two materials is shown below in Plate 3.4 illustrates the base slab excavation for the North LRT Station Lands Cavity during the placement of the reinforcing steel. From the image, it is clear that the sidewalls were unsupported and cut vertically in the vicinity of the cavity structure. The time required to complete the excavation, prepare the foundation and begin to place the reinforcing steel suggests the walls had been stable for at least five to six months if not longer when the photograph was taken.

Plate 3.4. Unsupported vertical sidewalls of glacial till and Empress Formation within the Station Lands Cavity excavation (with permission Soliman et al., 2010)

In general the two heavily overconsolidated materials encountered within the Station Lands Cavity appeared to exhibit a sufficient stand-up time for durations of several months.

3.3.3 Glacial Till Fissures at Station Lands

Visual observations made in the excavation of the Station Lands cavity showed extensive fissuring in the till as shown in Plate 3.5. In almost every photo taken of the glacial till within the Station Lands, some form of oxidation staining on the nearly vertical faces of the till is shown. In most cases, the planar faces tended to be oriented in a regular fashion suggesting that the fissures were in general consistently orientated spatially and, more importantly, ubiquitous throughout the formation. Wedge failures were also common in the station lands near to the Empress Sand contact (Plate 3.6). Plate 3.6 also indicates the presence of a horizontally bedded sand deposit approximately mid-height of the photo. This is indicative of periodic decoupling of the glacier from the basal deposits. This added discontinuity would also pose an additional shear surface when excavated and left unsupported.

Bayrock and Hughes (1962) suggested that two till sheets were partially differentiated by the joint orientations of two layers. In the upper formation, they indicated that the fissures were more frequent and oriented in a columnar fashion. The lower till was observed to have distinct joint sets which tended to form relatively uniform sized blocks with planar surfaces when exposed. Phelps and Brandt (1989) indicated that the glacial till was identified to have two, nearly vertical, mutually perpendicular joint sets spaced approximately 0.6 m apart. Within the Station Lands Cavity, the orientation of the fissures within the upper horizons of the till was not immediately clear. Where observed, the fissures were randomly oriented throughout the soil mass.

Plate 3.5. Planar and nearly orthogonal nature of the joint sets within the glacial till at the Empress Sand contact (adapted from Martin, 2010)

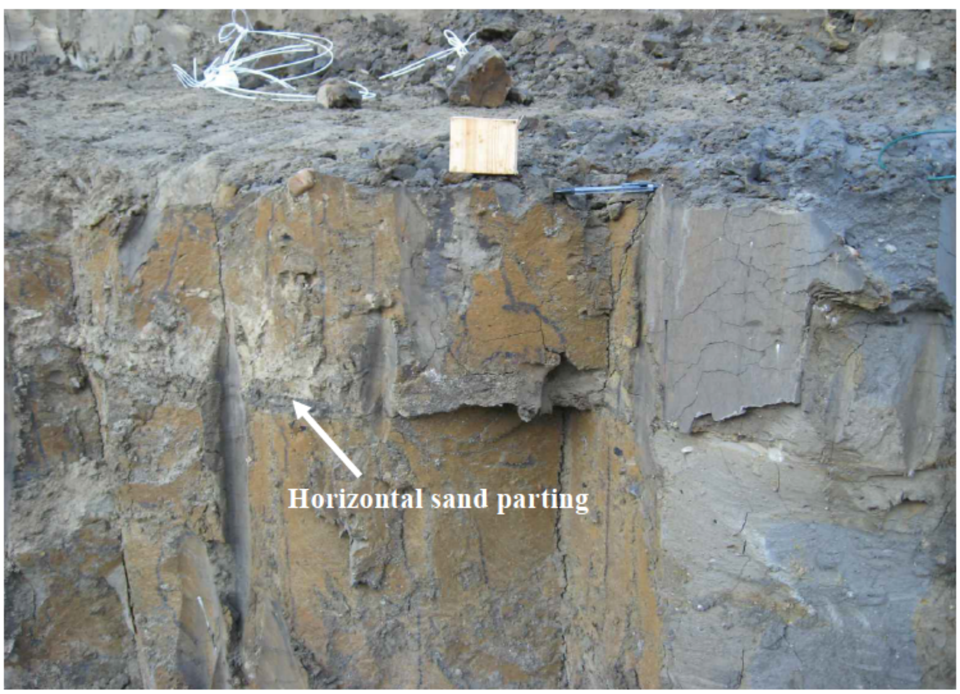

Plate 3.6. Wedge failure of the glacial till within the Station Lands excavation (with permission from Soliman et al., 2010)

The heavily fissured nature of the glacial till was also evident in the methods used by the contractor to excavate the glacial till in the Station Lands Cavity. In most cases, the glacial till was too hard to simply cut or dig with a conventional excavator, but instead, was readily broken and pulled apart using an exposed face and the pre-existing joint sets. By excavating in this manner, small block slides were initiated and the material could then be readily removed once broken from the soil mass.

Several photos taken from the site by Soliman et al. (2010) and Martin (2010) show that, when excavated as described above, the material tended to behave in a manner similar to weak rocks. An example of this is shown in Plate 3.7 below.

Plate 3.7: Excavation of glacial till within the Station Lands Cavity (with permission from Martin, 2010)

Plate 3.8. Debris pile of till following a minor failure within the Station Lands (with permission from Martin, 2010)

Piles of large blocks suggest that the primary failure mechanism of the glacial till is sliding of blocks over one another. Sliding would occur following either a release or dramatic reduction of confining stresses (such as exposure during excavation). The stress release resulted in joint dilation and residual friction along the joint surface. Blocks would then translate relatively freely relative to one another.

Observations of the cobbles and boulders encountered during the excavation of the Station Lands indicated that the majority of the clasts consist of 75 to 150 mm sized igneous and metamorphic cobbles. Some boulders were also excavated from the Station Lands excavation, though the greatest dimension did not exceed 500 mm in diameter. The cobbles and boulders were typically rounded to sub-rounded. Finer gravel does provides additional resistance to sliding, both for the intact till as well as along the fissures. Most gravel was generally angular to sub-angular in shape and, like the cobbles was igneous or metamorphic in origin.

3.3.4 Sand Pockets in the Glacial Till

The open excavation at the Station Lands allowed observation of the general size, shape and position of the intra-till sand pockets. These visual observations allowed for an analysis of the percentage of intra-till sand formations expected to be encountered throughout the glacial till. During numerous site visits, Soliman et al. (2010) recorded photographs that documented the size, shape and location of some sand pockets. If groundwater was present within the formation, the nature of the ground conditions when fully exposed. They also showed that the excavated pockets exhibit a reasonable stand-up time even when wet. An example of an intra-till sand pocket with dimensions is shown (Plates 3.9 and 3.10).

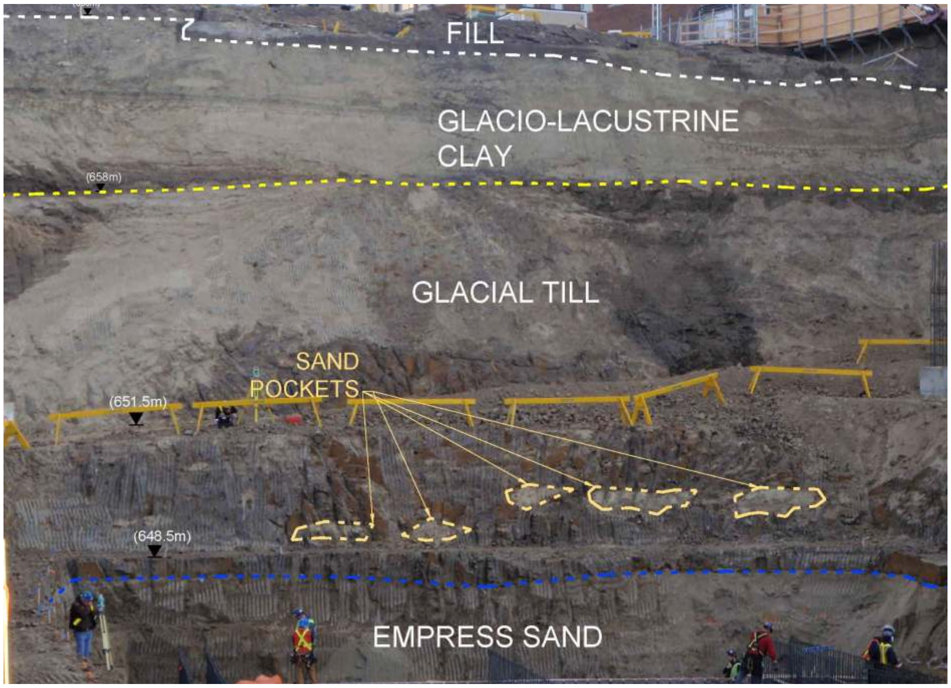

Plate 3.9. Location and spatial distribution of intra-till sands within the glacial till (with permission from Soliman et al., 2010)

Plate 3.10. Intra-till sand pocket size observed within the Station Lands excavations (with permission from Soliman et al., 2010)

Based on the photos taken from the Station Lands Cavity excavation, the intra-till sand appeared to occur as pockets that varied in size from approximately 0.3 to 2.5 m in thickness and from 0.4 to greater than 3 m in length. The sand was not excavated into the exposed face to determine the depth into the till in order to minimize the risk of localized slope failure. It is suspected that the length of the sand layers into the face is proportional to the length exposed at the face. Plate 3.11 provides some insight into this by showing a sand pocket that formed a cavity due to seepage following exposure. Observation of the contact between the till and the intra-till sand indicates a distinct unconformity suggesting a different deposition process for the two formations. The spacing between the pockets was highly variable and ranged from less than 0.3 m to greater than 10 m.

In most cases, the intra-till sand pockets were wet and resulted in groundwater seepage upon exposure. While these sands contained groundwater, the storativity of these pockets was found to be more or less limited to the size of the deposit. One larger pocket encountered near the base of the Station Lands excavation was filled with confined groundwater that was immediately released upon excavation. Once the water was released, piping occurred resulting in the opening of a 2 m diameter void within the till formation.

The relative discontinuity of the intra-till sand pockets was reported by Doohan and McLean (1975) when a pumping test was carried out as part of the original North LRT open cut construction. They found that when dewatering activities were initiated, the formation tended to readily yield its stored groundwater and recovery was slow suggesting little recharge. This statement is considered to be an oversimplification of the ground conditions as the observations of the sand pockets within the Station Lands were highly variable in gradation and may not yield free groundwater every time a wet formation was encountered. A good percentage of the sand pockets were found to be composed mainly of sand and silt with an appreciable percentage of clay within the soil mass. A photo of the large void that formed due to the confined groundwater release in the Station Lands is shown below in Plate 3.11.

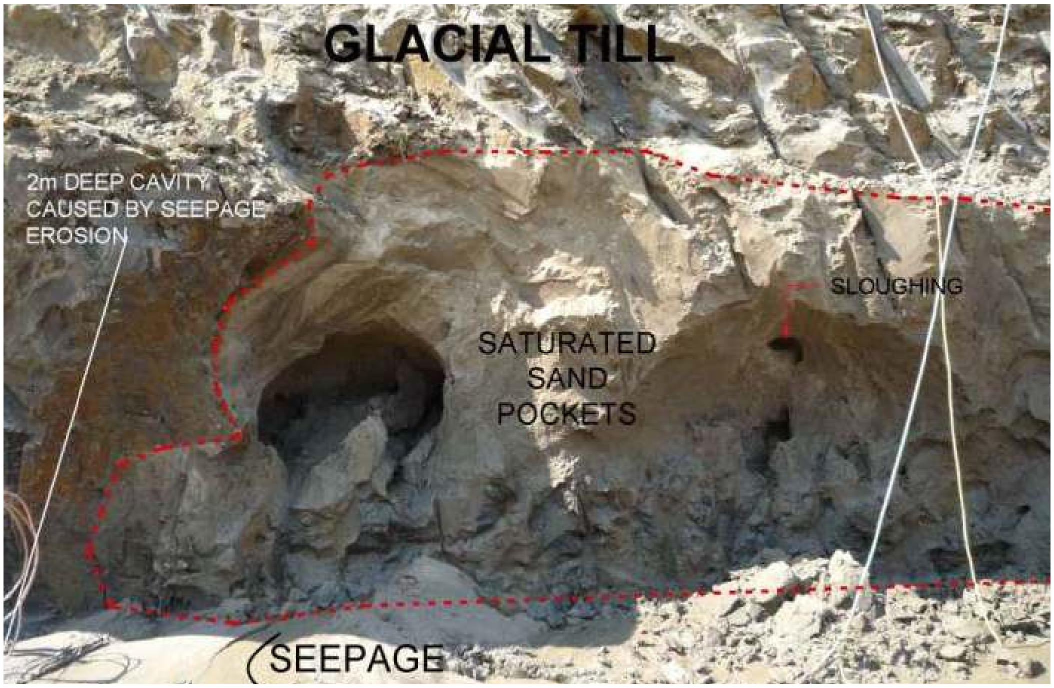

Plate 3.11. Cavity caused by seepage from intra-till sand (with permission from Soliman et al., 2010)

3.4 Ground Behaviour Observations from the North LRT Twin Tunnels

Observations of the ground conditions encountered immediately following excavation of each tunnel round were made during the construction of the North LRT twin tunnels. The observations included detailed geologic mapping of the exposed face. This included noting the composition of the encountered material; measurements of size of larger intra-till sand pockets (greater than 1 m in length); observation of uncontrolled seepage and/or instabilities associated with the intra-till sand pockets; instabilities of the soil mass in general (either local or global); and mapping of any discontinuities if encountered.

The purpose of the site documentation was to obtain detailed mapping of the sand pockets and fissure sets as they were encountered. The nature of the fissures was focused on how they related to the hypothesis of two separate till sheets within the downtown Edmonton area as described by Westgate (1969). The study of the sand pockets was to document their presence and prevalence and what influence they have on the overall SEM tunnelling methodology when dry or when wet.

To this end, the study was intended to provide an understanding of how the heavily overconsolidated soils perform under conventional tunnelling methods. This includes the performance and stability of the narrow pillar throughout the western leg and the first 50 to 75 m of the eastern portion of the twin tunnels where the alignment was within mixed face conditions. It was also intended to consider providing an understanding of the role of the fissures in the overall stability of the glacial till during tunnelling operations.

3.4.1 Fissures within the Glacial Till

Geologic mapping of the tunnel face was seldom carried out on previous tunnelling projects as they were typically excavated using mechanical methods. The two LRT tunnels constructed using conventional methods in the mid 1980's and early 1990's apparently did not require face mapping as part of the contract documents as no documentation of the mapping were found during this study. As such, most of the documented mapping of the geology in the region has been carried out by either aerial interpretation; from the various river valley exposures located throughout the region or from other construction projects in the area. This limits the observations in terms of the ground behaviour as the river valley exposures are subject to sliding and natural stabilization over time and therefore, the actual short-term ground behaviour characteristics are not readily observed. Notes from deep excavations for foundations are generally restricted to the small exposures left between soldier piles prior to the installation of wood lagging needed to provide the temporary support of the exposure.

3.4.2 General Observations during Construction

The stiff cohesive nature of the till as shown by the laboratory properties discussed in Chapter 5 was confirmed by the face conditions observed during tunnelling and (Plate 3.12). Despite the cohesive matrix, jointing in the Edmonton glacial till was well known and documented by many authors in the city (Bayrock and Hughes, 1962; Bayrock and Berg, 1966; Westgate, 1968 and 1969; May and Thomson, 1978 and Shaw, 1987). As noted previously, Westgate (1969) suggested that there were likely two till sheets present in the Edmonton area. It was therefore expected that the two sheets would be encountered these along the tunnel alignment. Westgate (1969) suggested that the fissures in the upper or "brown" till were typically columnar in nature while the fissures were more regular and rectangular in the lower "grey" till. Hence there was the expectation that jointing in the till would become evident upon exposure throughout the tunnel construction and as the tunnels progressed deeper below the ground surface.

Plate 3.12. Example of the cohesive nature of the glacial till observed in the tunnel face

Despite the cohesive face conditions the blocky nature of the till became obvious during the mucking cycle (Plate 3.13). It was also observed that the joint patterns between the upper and lower horizons were slightly different than the observations made by May and Thomson (1978). The upper horizon was not found to have any distinct and regular joint patterns. Most of the fissures appeared to be randomly located throughout the soil mass if discernable at all. For the most part, the till appeared to be mainly cohesive with major fractions of silts within the overall matrix. Many of the exposed faces exhibited teeth marks from the excavator and a shine following removal of the soil suggesting a high clay content likely on the order of 20 to 30%. Unlike in the Station Lands, the till was easily cut by the excavator and was generally shaved from the face instead of digging it. When the material was first removed from the face, the till would consist of blocks measuring roughly 0.3 to 0.5 m in diameter. These blocks would continually break up with further excavation and clearing from the working face by the excavator until cobble sized fragments remained. These would generally form a uniform debris pile at the face prior to mucking as shown below (Plate 3.13).

Plate 3.13. Blocky mass of till following excavation from the face and prior to mucking

In the lower horizon of the till, the fissure patterns became more obvious and regular as shown below (Plate 3.14). The fissures were most obvious at the boundary with the underlying Empress Sands, especially when the till comprised a small portion of the bench.

Plate 3.14. Wedge failures in the lower horizon of the glacial till

In all, there were four sets of fissures that were measured in the lower portion of the till where the fissures were common and regular. Typically the fissures were spaced between 10 to 30 cm though could extend up to 2 m in some cases. Three of the identified sets were steeply dipping, and were measured to be at angles between 70 to 85˚ from the horizontal. The fourth set was nearly horizontal, dipping between 5 to 15˚ from the horizontal. Spacing of the nearly horizontal fissures were not readily measurable as these fissures tended to remain closed unless located near the top of the bench where overlying material could be easily removed by hand. A stereonet show the orientation of the fissures measured in the North LRT twin tunnels within the lower horizon of the tunnel sections is shown below as Figure 3.3. For reference, the orientation of the tunnels through the western leg of the North LRT is provided. Since the number of measured fissures comprising the fourth set was limited, only the measurement points are shown on the stereonet in Figure 3.3.

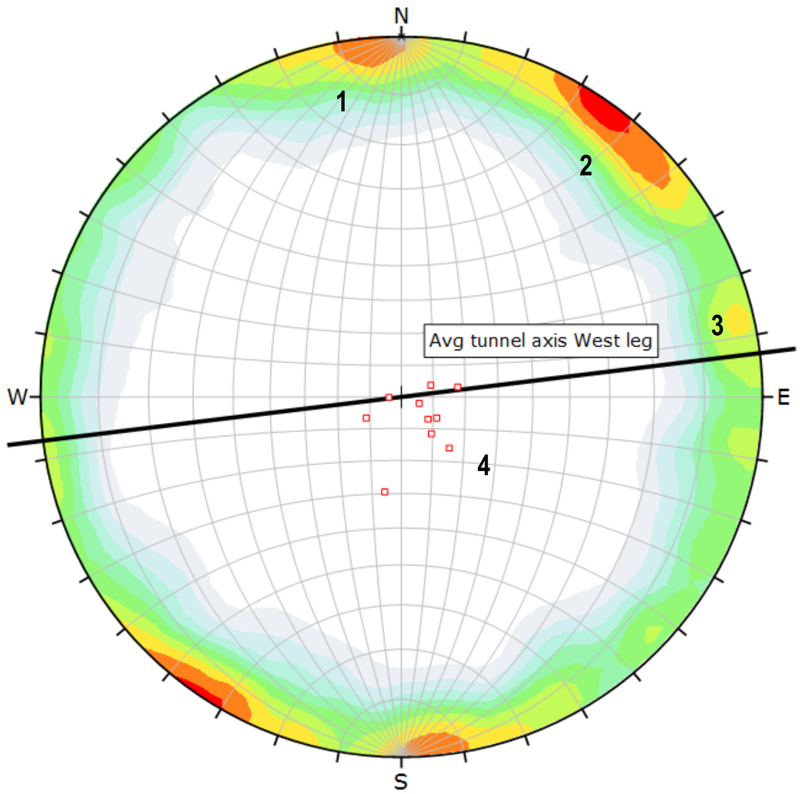

Figure 3.3. Stereonet showing fissure orientation in the North LRT twin tunnels

The fissures that were readily observable during tunnelling (Sets #1 and 3) were generally orthogonal to each other. Set #2 was found to bisect the orthogonal sets at around 40° forming triangular wedges. The fissures intersecting at nearly 90˚ to one another (sets 2 and 3) would readily form wedges when exposed that would separate from the tunnel face. The typical wedge size was approximately 0.1 to 0.3 m^3 and shaped as prismatic triangles as shown in Plate 3.14. The wedge formation was a function of nearly complete separation from the soil mass due to the intersection of the nearly planar surface of the fissures and the removal of confinement normal to the fissures.

3.4.3 Fissure Surfaces

Examination of the joint surfaces indicated that they were smooth to slightly undulating and oxidized. An example of the planar nature of the fissures is shown below in Plate 3.15. This photo was taken of the exposure in the Station Lands where the depth and shape were more easily measured. When dry, the surfaces of the fissures were found to be in good contact. Typically the fissure gaps were closed, though apertures of the gaps up to 5 mm in width (depending on confinement) were observed. If the fissure surfaces were wet, the oxidized surfaces tended to become slick and would reduce the effective frictional resistance along the fissure surface.

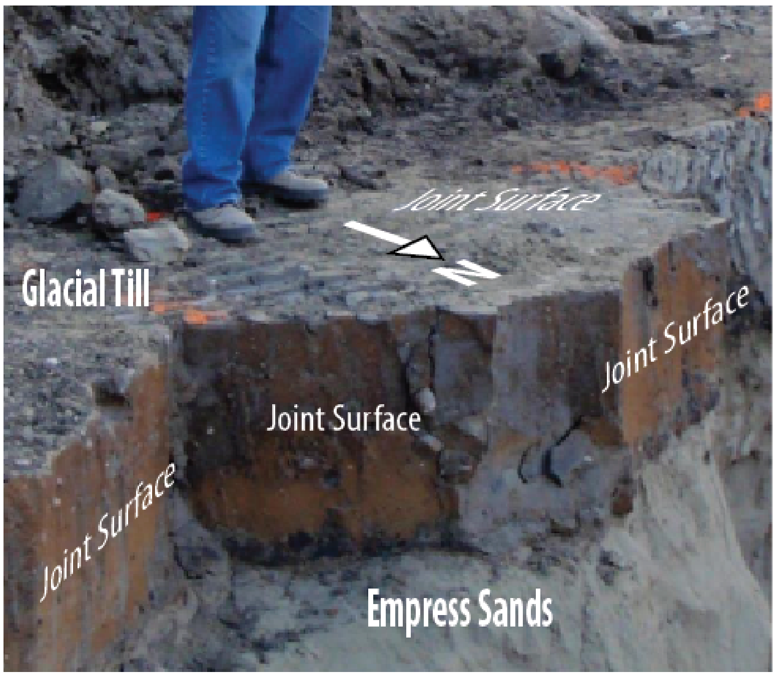

Plate 3.15. Exposed fissure surfaces (with permission from Martin, 2010)

In some instances, the fissures appear to be glacio-tectonically bent such as those shown in Plate 3.16. This phenomenon was not observed frequently as the method of excavation rarely permitted for small advancements of the excavation (less than 0.3 m into the face). However, following a slabbing event in the Empress Sand when the face retrogressed behind the bench and beneath the glacial till, the remaining till cantilever subsequently collapsed exposing the bent and partially foliated nature of the fissures. Plate 3.16 shows the first large wedge failure at this location and the surface of the fissures following collapse. Note the planar surfaces of the blocks in the bottom of the image that had broken away from the bench. For scale purposes, the thickness of the till overhang within the bench is approximately 0.75 m and the depth of the overhang (into the tunnel face) is 1 m. Plate 3.17 shows the final till overhang with the bent and foliated fissures exposed following completion of the collapse.

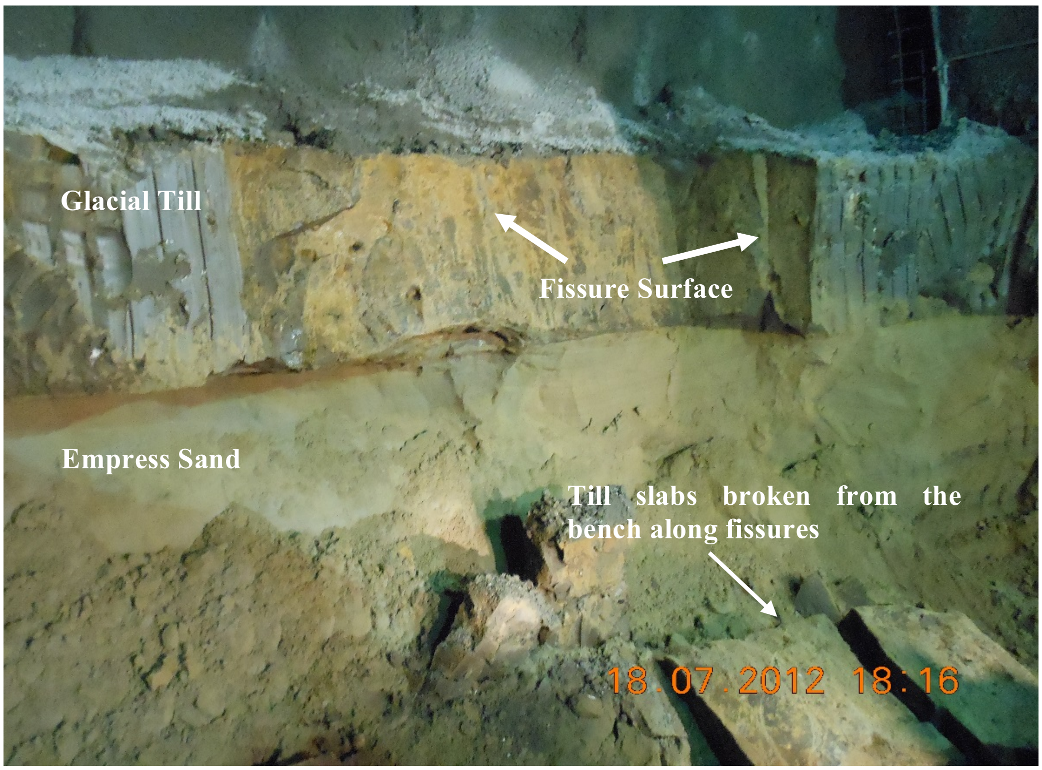

Plate 3.16. Large wedge failure in bench following progressive slabbing/ravelling of the Empress Sand to beneath the tunnel header

Plate 3.17. Glacio-tectonically altered fissure surfaces within the glacial till

The fissures are bent as shown by the arcs in photo, and the vectors normal to the fissure surface are inclined towards the ground surface as opposed to parallel to the tunnel axis. The upward orientation of the fissures tended to resist additional displacement of the blocks along the surface by using the weight of the blocks to resist sliding. As the excavator attempted to remove the loosened debris from the face and this formation was exposed, the face became very stable and mechanical excavation was extremely difficult.

As noted above, Westgate (1969) and May and Thomson (1978) suggested that there are likely two till sheets in the vicinity of the tunnel alignment. They proposed that there is a thin sheared zone or a thin sand layer (Tofield Sands) between the two formations indicating where the second glacier overrode the first till sheet. Observations within the North LRT tunnels did not confirm these findings in as much that there is no distinct unconformity indicating an upper and lower till. There was a gradual transition between the "brown" and "grey" tills however it was observed that the grey till would oxidize rapidly following excavation. The grey till turned brown in a matter of tens of minutes, making differentiation of the two till sheets difficult. This suggests that the difference between the grey and brown tills is a function of exposure to oxygen. It is likely that progressive drainage through the fissures in the till have introduced oxygen to the upper horizons altering the colour of the formation in the long term. This reduced pore water may also contribute to the highly fractured nature of the upper till in that it is slightly more desiccated than the lower horizons.

3.4.4 Genesis of Fissures

Neal et al. (1968) found that when the mineralogy of desiccated clay playas were examined, locations that were highly susceptible to polygonal desiccation possessed high percentages of illites and montmorilonites. Any non-clay minerals in susceptible soils consisted of high quantities of quartzites and feldspars. Neal et al. (1968) determined that the areas with the most desiccation demonstrated plastic limits of 22±4% and liquid limits between about 40 to 48%. Additional tests on surficial samples also indicated that the most fissured materials possessed natural moisture contents at or below the shrinkage limit and could no longer deform plastically. The moisture content with depth was also reported to be slightly higher at depth when compared to the moisture content at the ground surface. Despite the slightly higher moisture contents, the natural water content at depth was still below the plastic limit. It is commonly understood that when the natural moisture content is below the plastic limit, the soil is unsaturated and likely heavily overconsolidated.

The glacial till in the Edmonton area has been shown to possess all of the above findings for desiccation susceptible soils. The mineralogy of the till is discussed below in Section 6.2, but in general, the main clay component is illite with kaolinite as the minor clay component. Overall, the clay component of the till is found to only be around 5% of the total makeup. The majority of the non-clay minerals are quartzite and albite (plagioclase feldspar). When the natural moisture content of the glacial till is observed, it is typically around 15 to 20% which is generally about 5% below the plastic limit. The Atterberg limits are typically between around 18 and 40% for the plastic and liquid limits respectively. Therefore it is safe to assume that the glacial till is highly susceptible to desiccation cracking when subjected to drying as defined by Neal et al. (1968).

Next, the orientation of the desiccation patterns was examined. Neal et al. (1968) considered the polygonal pattern classification outlined by Lachenbruch (1962) and determined that oriented or orthogonal polygonal patterns typically form in anisotropic environments. The anisotropy could be a result of thermal gradients within the periglacial region (Lachenbruch, 1962), or due to desiccation gradients near the surface (Neal et al., 1968). In the development of the theory, Lachenbruch suggests that most ice wedge polygons begin as irregular polygonal patterns, which eventually form regular, orthogonal patterns as fissuring continues. The process continues until the width of the fracture approaches the width of the stress relief within the ground. Neal et al. (1968) indicate that within the playa formations, the predominant polygonal pattern from desiccation is irregular (not orthogonal) however in older, more defined regions, regular patterns approach near 90° orthogonal intersections within the major initial polygon.

Kerfoot (1972) conducted a study of the regular polygonal pattern formation in surficial soils subjected to permafrost in the Canadian arctic. He found that the majority of angles measured between polygonal ground formations were orthogonal, with the polygons radiating from the banks of a nearby water body such as a river or lake. This initial fracture would act as a primary fracture appearing to be similar to a desiccation fracture like those identified by Neal et al (1965). Thus, primary cracks near rivers would typically form perpendicular to the river and radiate out from the water body. Additional secondary fractures would then form perpendicular to the primary fracture resulting in orthogonal polygons. Kerfoot (1972) also found that when the angles differed from 90°, they were due to the intersection of two primary fractures and typically resulted in angles between the cracks of either 40° or 60°. Considering this, it is likely that the regular fissuring identified in the exposures of the glacial till was due the formation of two primary fractures (Sets #1 and 3). These fractures were then followed by the formation of a secondary crack (Set #2). Set #3 is nearly perpendicular to the North Saskatchewan River (albeit nearly 750 m north of the river bank), while Set #1 is nearly perpendicular with the theorised flow direction of the Laurentide Ice Sheet. Because Set #2 is nearly orthogonal to Set #3, it is assumed that #2 is a secondary feature. Set #4 is assumed to strictly be a function of vertical stress relief (isostatic rebound) following deglaciation.

3.4.5 XRD and SEM Tests on the Glacial Till

In Samples of the glacial till were collected and submitted for bulk X-ray Diffraction Analysis (XRD), elemental analysis by X-ray Energy Dispersive Spectrometry (EDS), Scanning Electron Microscopy (SEM) and Particle Size Analysis. In order to determine the mineralogy and composition of the glacial till, two samples were collected from the upper and lower horizons of the formation. One sample was collected from an elevation close to the surface of the till and another from near the unconformity with the Empress Sand. The sample locations were designed to ensure that representative samples of the “upper” and “lower” tills were recovered for testing. To ensure that the sample near the surface was till (as opposed to Lake Edmonton Clay) oxidation staining and regular gravel sized particles were used to identify the material. The upper and lower samples were respectively collected at elevations of 665 m and 647 m. The samples were submitted to GR Petrology Consultants Inc. of Calgary, Alberta for testing. The results are included in Appendix 1 and are summarized below.

The results of the laboratory testing of the mineralogy of the glacial till suggest that the primary mineral in the composition of the samples was quartzite as indicated by percentages of nearly 70% SiO_2. Minor fractions of aluminum, iron and potassium also suggest that the Laurentide ice sheet likely deposited the material since these elements typically make up minor fractions of granites typical to the Canadian Shield. Differentiation of the clasts between metamorphosed sedimentary versus igneous origins was not possible in the XRD tests. This differentiation was carried out visually on the recovered samples of the glacial till. Based on these observations, there were clearly quartzic clasts within the till matrix near the surface as well as at the base. The majority of the clasts though were predominately felsic granites and appeared to be composed mainly of either grey-black gneissic (albite rich) granites or pink orthoclase granites. Therefore, since the shield rocks are felsic in origin, it would be impossible to differentiate the origin of the minerals based on the elemental composition alone.

From the Scanning Electron Microscopy (SEM) images and the particle size analyses, it does appear that the upper till is slightly better graded ranging from sand to clay sized particles when compared to the lower till. The upper till is also slightly finer grained than the lower till as indicated by the median and minimum particle sizes, which are respectively 21.4 μm and 0.1 μm in the upper till and 19.55 μm and 0.33 μm in the lower tills. Finally, the percentages of illite is moderately higher in the upper till which is given as 3.3% compared to 2.2% in the lower till, while the percentage of kaolinite is only slightly higher in the lower till (1.5% compared to 1.6% in the lower till) which also suggests that the upper till is slightly finer than the lower deposit. Images from the SEM analyses of the upper and lower tills are shown below in Plate 3.18 and Plate 3.19.

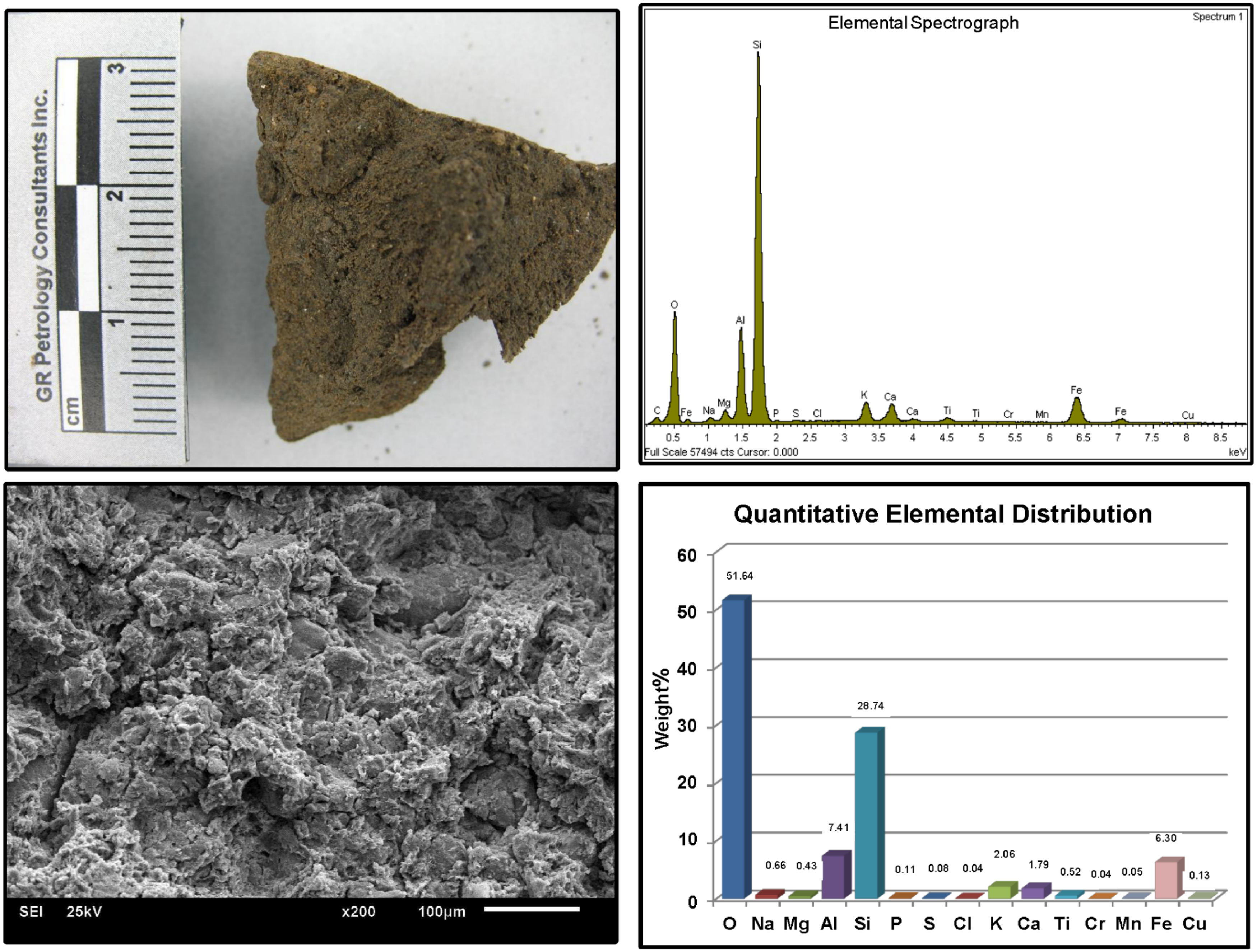

Plate 3.18. SEM and XRD results of the upper till

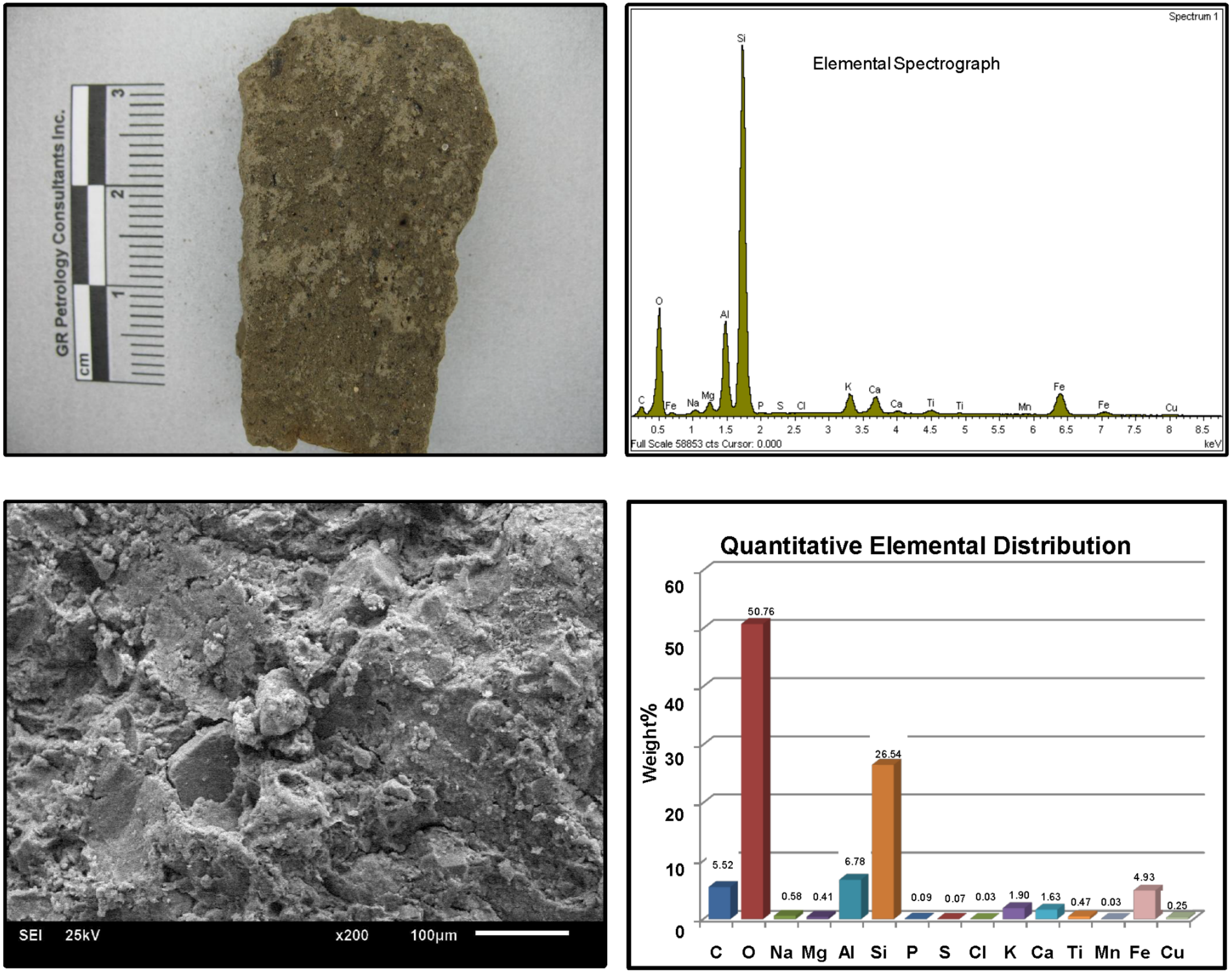

Plate 3.19. SEM and XRD results for a sample towards the base of the till

Based on the various laboratory experiments, it is likely that both samples were deposited by the same glacier and are ultimately from the same till sheet. The mineralogy of the till does not differ significantly despite its colour change and minor fabric differences. This information agrees well with the initial theory that the glacial till originates from the basal deposition from the gradual melt out of stagnant dead ice (Bayrock and Hughes, 1962; and Bayrock and Berg, 1966).

3.4.6 Sand Pockets in the Glacial Till

As noted by many researchers in the past (Bayrock and Hughes, 1962; Bayrock and Berg, 1966; Westgate, 1968, 1969; Kathol and McPherson, 1975; May and Thomson, 1978; and Shaw, 1982, 1987; Catto 1984), the glacial till possesses frequent, randomly located intra-till sand pockets. The sand pockets are known to be persistent throughout the formation and are frequently water charged. Observations within the North LRT tunnels did not suggest that these sand pockets were different than those described previously. Their prevalence throughout the formation was consistent with the findings of others.

The sequential excavations in the twin tunnels did however indicate two findings that have not previously been observed. First, nearly every round encountered an intra-till sand pocket of some kind. For the most part, these pockets would consist of thin veins of sand that were highly discontinuous and did not pose any stability issues other than to form a local discontinuity within the till soil mass. The second observation was that the sand pockets were found to be dipping at angles between 25 to 35° to the south. This trend was only observed in the western leg or the North LRT tunnels. It would appear that this leg of the tunnels was being driven nearly parallel to the strike of this anomaly.

The constant presence of the sand pockets is slightly different than most observations in the past, which may have discounted their presence as simply part of the till matrix. To account for the presence of the intra-till sand inclusions, Shaw (1982) suggests that the intra-till sand pockets may be blocks of Empress Sand that were incorporated into the till matrix. Shaw (1982) hypothesized that during glacial flow slabs of frozen Empress Sand were plucked from the upper beds of the formation and carried into the glacier. He concluded that the slabs were incorporated into the till matrix during melt out from regionally stagnant ice sheet as opposed to gradual retreat of an active Laurentide ice sheet. Because there is strong evidence that the moraine was deposited under stagnant ice conditions (Bayrock and Berg, 1965; Kathol and McPherson, 1975 and Shaw, 1982) these frozen blocks of Empress Sand would be randomly located in the soil mass instead of being disaggregated and incorporated into the soil matrix. In order to not fully destroy the frozen blocks of the sand following plucking from the bed, the distances that the blocks were carried had to be minimal.

In order to investigate this theory, the appearance and the general composition of the intra-till sand pockets was examined. Visual observations of the intra-till sand indicate that the gravel within the formations is typically quartzic in nature with no clear presence of shield clasts. In addition, the sand inclusions appeared to be graded to occasionally cross bedded. This also strongly suggests a similar origin to that of the Empress Sands. Since the glacial and pre-glacial rivers that deposited the Empress Sands were subjected to considerable change in energy level over space and time, the grain sizes have been shown to vary considerably spatially as discussed above. In addition to the regular cross bedding and highly variable composition of the intra-till pockets, occasional faults were observed within the sand. These faults and shear zones would suggest differential settlement due to thaw consolidation or groundwater infiltration. Shaw

(1982) had also observed similar faults within the intra-till sands. Plate 3.20 presents an example of faulting in the intra-till sand. It should also be noted that the general trend of the dark seam in the sand pocket shown in Plate 3.20 also indicates the 30° dipping of the sand pocket.

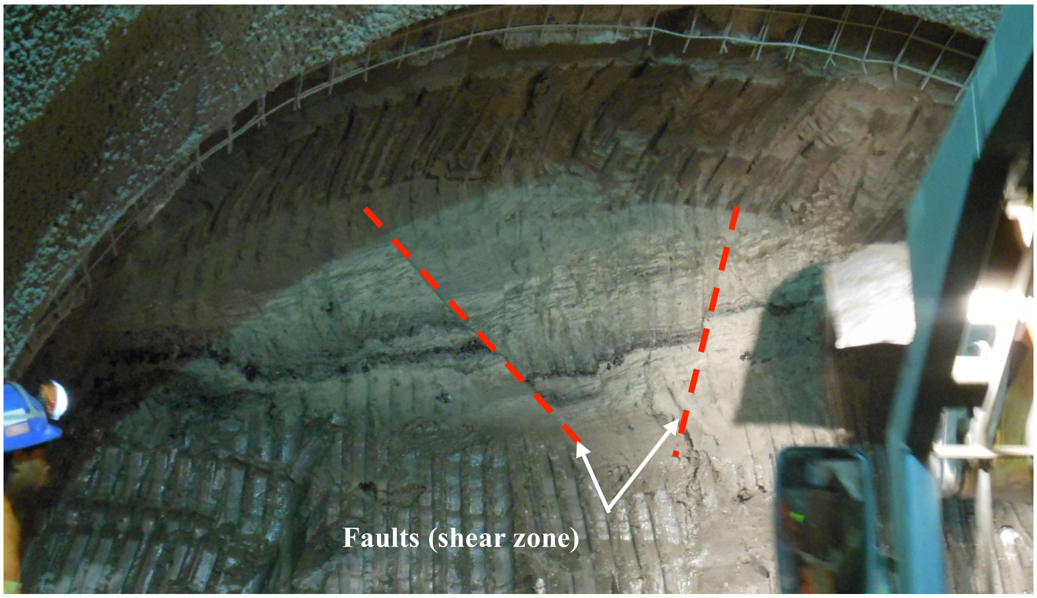

Plate 3.20. Fault zones observed in North LRT intra-till sand pockets

It is now believed that they were formed as diapirs, within larger sand blocks. At this time, it would be appropriate to define the terms “vein(s)”; “beds”; and “pockets”. Veins are defined as sand inclusions that are long (minimum 2 m in length) and thin in cross section (less than 0.1 m across). Typically veins were encountered in groups that generally appeared to be a pocket of sand that was either sheared with clay filling in the resulting shear planes; or had clay injected into the sand pocket dividing the pocket into many thin sections. They are usually uniformly graded within an individual vein, but may be well graded across the series of veins. Their position was random and typically located along oxidized discontinuities. Very rarely was groundwater present within these veins unless they were connected with larger, water bearing sand pockets. Intra-till sand veins were usually dipping in the face at angles between 25 and 30° along the western tunnel drive. This characteristic was only observed to occur at depths ranging from 3 to 10 m into the glacial till formation. Because the inclination of the beds was not observed in the eastern leg of the tunnels, the orientation of the dipping was probably parallel to the path of glacial flow that is about north-northeast to south-southwest. Inclined veins did not extend through the entire depth of the till formation to the Empress Sand.

A bed is defined as an intra-till sand vein that was oriented horizontally or a dip less than 10°. They were indicative of periods of de-coupling of the glacier from the basal till. An example of a bed is shown in Plate 3.6.

Finally, an intra-till sand pocket is defined as a continuous block of sand that was greater than 0.1 m in thickness and greater than 0.5 m in length. These sand pockets were typically water charged and would release ground water upon exposure. The sand pockets were generally well graded and often exhibited signs of faulting or boudinage.

The dipping of the near surface materials suggests that the interface between the overlying ice-sheet may have been periodically fully coupled to the thick till bed. This means that the glacier was frozen to the surface of the till. The additional weight of the glacier bearing down on the till, as opposed to isolation during decoupling, would result in extrusion of the clay till into blocks of frozen Empress Sand. This pressure and intrusion of the moderately plastic clay till also would result in stretching and necking of the sand blocks (boudinage). As mentioned above, the coupled process may have been seasonal or short lived. This agrees with the findings of Shaw (personal communication) that there were clearly short periods where the till and ice sheet were decoupled, though the predominant case was one of a coupled scenario.

Photos of the zones of boudinage and the clay intrusion (diapirs) forming intra-till sand veins are shown below in Plates 3.21 to 3.23. The photos were taken in the Southbound tunnel of the western leg at the stations indicated below for the photos. This type of formation was found to be prevalent throughout the western leg. The shine on the surface of the till and presence of teeth marks from the excavator indicate inclusions that were predominately cohesive. This would further support the theory that the more plastic clay till was extruded into blocks of the Empress Sand resulting in till diapirs. These formations are not dissimilar to other diapirs observed in tills within the Athabasca region as shown in Plate 3.24.

Plate 3.21. Dipping sands in header at Sta. 700+637 (crown 7 m below ground surface)

Plate 3.22. Dipping sands in header at Sta. 700+627 (crown 7.5 m below ground surface)

Plate 3.23. Dipping sands in header at Sta. 700+589 (crown 9.3 m below ground surface)

Plate 3.24. Till diapirs in the region of Athabasca (with permission from Shaw)

3.5 Empress Formation

Observation of the Empress Formation sand was also made throughout the first 135 m of the eastern leg of the North LRT tunnels. The sand was encountered immediately following breakout from the Station Lands to Sta. 600+326 (Northbound) and Sta. 700+323 (Southbound).

The Empress Sand appeared to be consistent with observations made at other locales throughout the city. It was consistent in its grain size with cross-bedding common observed. The unsupported sand had a stand up time of approximately one hour. It should be noted that the Empress Sand was only encountered in the bench and invert of the tunnels. The short stand up time can likely be attributed to the construction of the bench. By removing the overburden in the header, confinement was removed and therefore the internal shear strength of the sand was greatly reduced. The stress paths of the sequenced excavations given in Chapter 5 illustrate the cause of the shear failures within the sand bench. When failures were documented, the sand would tend to either ravel or slab (overturn or topple in slabs). These types of failures would be progressive and would generally retrogress until the sand face was positioned below the glacial till header. Only on two occasions did the sand face ravel to a distance of approximately 1 m behind the till header. This resulted in an undercutting of the till header that had to be subsequently removed.

During exposure, it became clear that there were two primary coloured materials. The first was the commonly encountered yellow sand while the second was grey which was slightly finer grained and moist. Whenever face loss was observed, it was noticed that the grey sand was usually the location where failure would initiate. Once toppling occurred, the surrounding materials would follow suit and failure would retrogress beneath the tunnel heading. Plate 3.24 shows a photo of the coloured bedding of the Empress Sands. There is some rippled cross bedding observed in the upper regions to the centre of the photo.

Plate 3.25. Graded bedding of the Empress Sand with some ripple formations near the top

The Empress Sand appeared to overturn in massive slabs rather than break apart and flow to the angle of repose and would be expected for a relatively dry sand. Plates 3.25 and 3.26 illustrate the presence of a grey sand graded bedding with the yellow sand prior to and following a failure where the sand face progressed behind the till header.

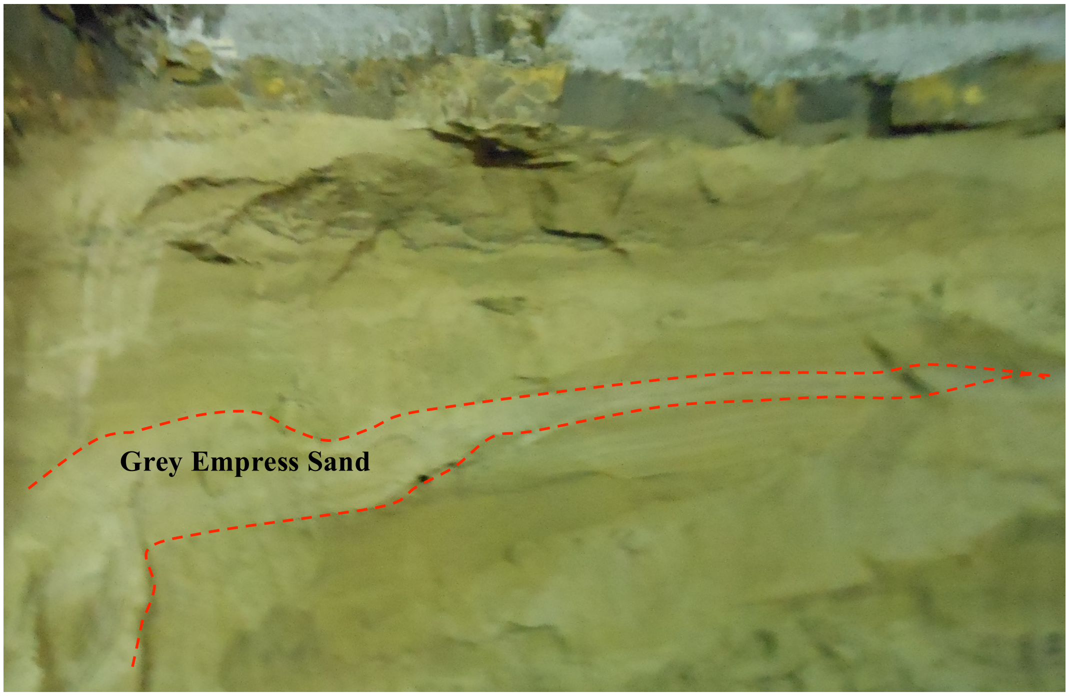

Plate 3.26. Graded bedding of grey sand prior to failure

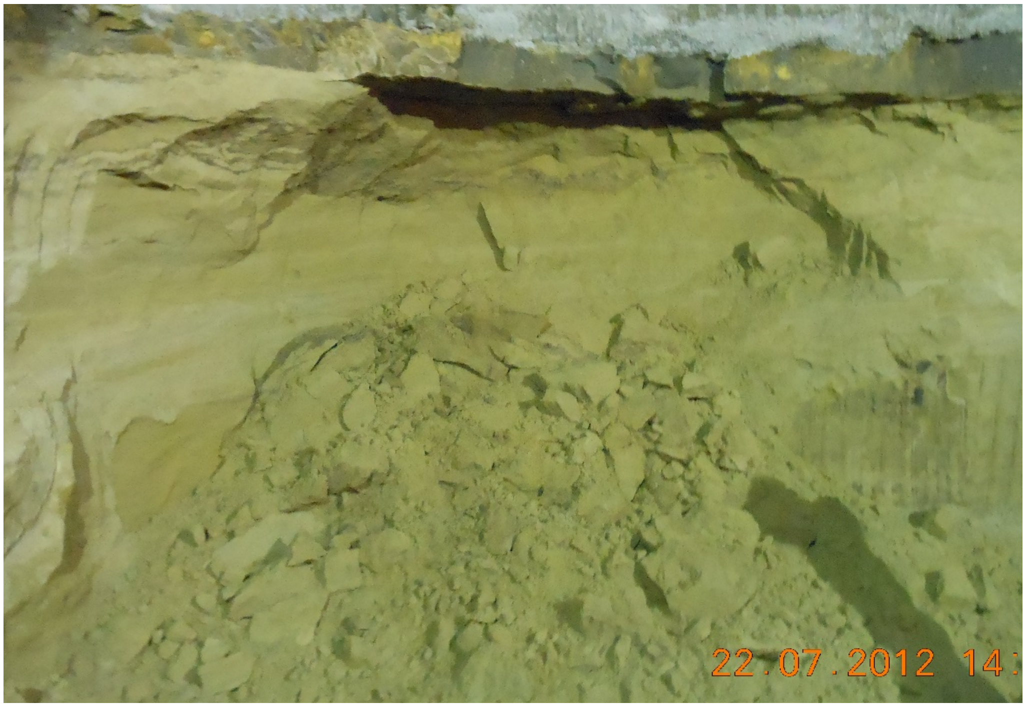

Plate 3.27. Sloughing of Empress Sand bench

The slabbed sand first progressed to a point where the Empress Sand was immediately below the till header as shown in Plate 3.25. Once the contractor attempted to further shape the face, additional failure commenced until the face of the bench was approximately 0.5 m behind the till header as shown in Plate 3.26. In all cases where the Empress Sand progressed behind the till face, the failures occurred in the lag (Northbound) tunnel.

To illustrate the slabbing mechanism, note that the debris of the sand in Plate 3.26 consists of distinct blocks that have toppled and translated relative to one another. There are clearly Empress Sand blocks on the surface of the debris pile. This indicates that there is either a high degree of internal suction or a high degree of interlocking of the grains. Cementation of the sands has been ruled out since the material can easily be reduced to the individual grains when contacted.

Near the surface of the Empress Sand, a highly discontinuous layer of fine-grained materials including silts, clays and organics was encountered. This formation would be present in one round and not in the next (continuity was less than 1 m). Visual observation of the formation suggests that it was probably deposited in an anastomosing stream system in which organic sediments accumulate in wetlands between channels. Photos of the fine-grained beds are shown below in Plates 3.27 and 3.28.

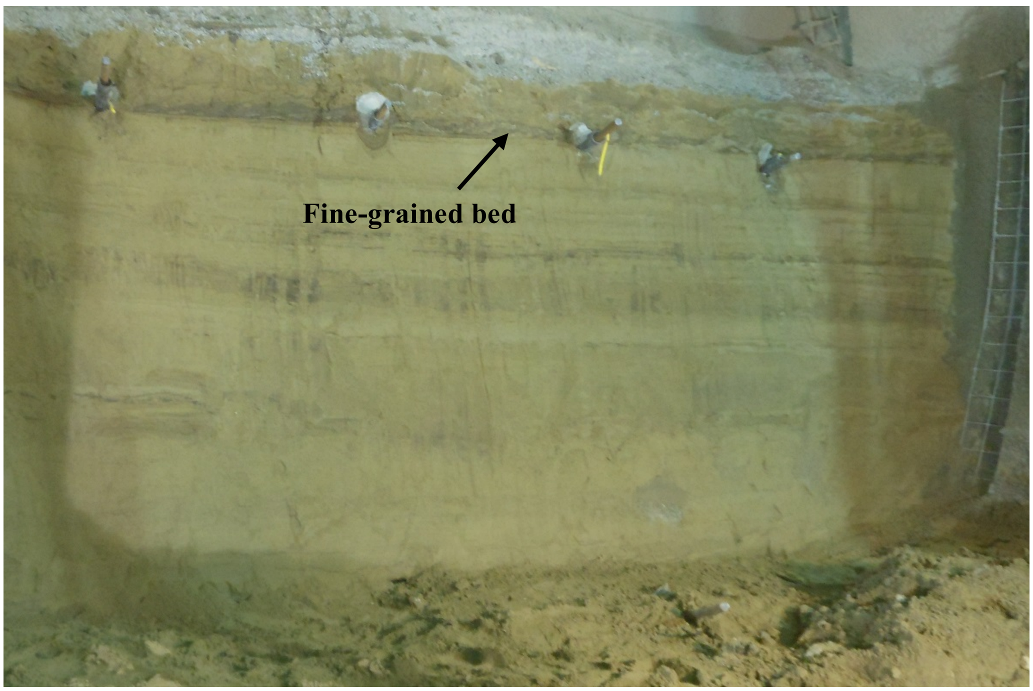

Plate 3.28. Fine grained beds in the Empress Sand

Plate 3.29. Close up of a fine-grained bed in the Empress Sand (note that sand is loaded into the fine bed indicating density instability at the time of deposition).

These fine-grained beds are very dense such that penetration with a finger or pencil was not possible.

The final observation of the Empress Sand involved the presence of collapse structures similar to those observed in the intra-till sands. In several locations, fault zones were observed. These fault zones were considerably smaller than those in the intra-till sand and spanned distances of tens of centimeters instead of meters. The location of the fault zones was always in the upper 2 m of the Empress Sand. These fault zones are thought to be an indication of permafrost conditions within the sand as the collapse structures could have only occurred during the thawing of ice lenses within the soil matrix resulting in differential settlement. Plate 3.29 shows a photo of one these fault zones observed in the Empress Sand. Shaw (personal communication) has also documented similar fault zones within the Empress Sand throughout the City of Edmonton and surrounding areas.

Plate 3.30. Fault zone in the Empress Sand

3.6 Conclusions

Observations of the nature and performance of the various surficial deposits throughout the City of Edmonton has been discussed. This study considered the possible cause of the geologic structure of the till and Empress Sand and how the depositional history would impact the overall performance of the material.

- The shear and fissure patterns within the till point to deep reaching permafrost conditions that were later subjected to shear and compression during coupled conditions. A possible hypothesis for the formation of the nearly vertical fissures within the clay till has also been presented. It is hypothesised that the fissures are a function of desiccation of the clay till during permafrost conditions. The theory of desiccation is supported by historical research that suggests that desiccation cracking occurs as primary fractures that tend to intersect one another at angles of 40 to 60° while secondary fractures tend to intersect primary fractures at 90°. These fracture patterns strongly resemble the patterns of the fissures within the glacial till observed in the North LRT tunnels.

- The presence of local faults within the cohesionless deposits also support the theory of frozen ground conditions during glaciation. Progressive melting would result in differential settlements as internal ice lenses melted in warmer climates. The compressive force of the glaciers is also indicated by the frequent presence of diapirs within the till. As the glaciers exerted pressure on the underlying sediments, the clay was extruded into blocks of the Empress Sand that had been incorporated into the basal region of the glacier. This extrusion resulted in the highly discontinuous nature of the intra-till sand pockets and the presence of formations that have been classified as sand veins, beds and pockets. Each of the classifications are based on the size and extent of the sand within the till matrix. This theory is supported by the presence of formations that resemble boudinage within sand pockets. This suggests that the clay was exerting stress on the stiffer sands that ultimately thinned the sand and extended its length within the till. Ultimately, the softer till was extruded into the sand pocket, periodically bisecting the pocket and creating two intra-till sand pockets of the same sand formation.
- Suction forces within the Empress Sand are suspected to be extremely high as demonstrated in the nature of failure within the North LRT tunnels. Because the sand exhibited a high "cohesion" until it was disturbed, the attractive forces between the sand grains must be extremely high. The Empress Sand typically demonstrates a

native moisture content of approximately 6 to 10% and is unsaturated. The negative pressures of the contractile skin, therefore greatly improve the short-term shear strength of the Empress Sand. Upon prolonged exposure to atmospheric pressure or stresses that break down the structure of the soil, the Empress Sand collapsed. The primary failure mechanism in the short-term within the North LRT tunnels was found to be that of slabbing and overturning of sand blocks, that subsequently disintegrated to blocks and loose sand.

- The presence of fine-grained beds within the Empress Sand suggests the presence of an anastomosing stream system that deposited fine grained and organic sediments locally within the stream channel at random locations. The fine-grained beds were found to be very stiff to hard and possessed slickensided shear zones indicating post-depositional stresses during the subsequent glaciation(s). These beds were highly discontinuous in nature and could occasionally host perched ground water if the beds were concaved upwards. The fine-grained beds presented a stabilizing factor in the Empress Sand by providing a confining layer for the rounds that encountered it.

4.0 Pressuremeter Testing in Stiff Fissured Soils

4.1 Introduction

Pressuremeter tests were carried out in the heavily overconsolidated glacial and pre-Laurentide sediments in downtown Edmonton. The tests were extended through the depth of the glacial till and into the deeper horizons of the Empress Sand. The purpose of these tests was to determine the stress strain criteria of the ground as they relate to partially saturated soils. In addition to determining the strength and stiffness profiles, simplified methods for determining the coefficient of horizontal consolidation (c_h) and coefficient of horizontal hydraulic conductivity (k_h) are proposed.

Lastly, a method for calculating the volume change within the plastic region for partially saturated soils has been developed. Conventional pressuremeter interpretation assumes that the soil surrounding the probe is fully saturated and responds as an undrained soil (clays). When the soil is partially saturated, volume changes associated with compression of the occluded air will occur, rendering the assumptions used in the analytical assessment of the stress strain profile invalid. The proposed method uses the degree of saturation, initial void ratio and the coefficient of volume change (m_h) calculated from the pressuremeter hold test to determine the transition from a partially saturated (four phase) soil mass to a saturated (two phase) soil mass.

4.2 Background

One of the major challenges of working with stiff fissured soils is the accurate measurement of the strength and stiffness parameters of the soil. Due to the high degree of state dependence, sample disturbance and sample size (Lo, 1970; Morgenstern and Thomson, 1971; Marsland, 1968, 1971 a, and 1971 b and Bishop, 1967), representative data are often difficult to obtain. Insitu test methods are often sought out in order to minimize disturbance, maintain insitu stresses as close to the native state of stress as possible. Another key aspect is to incorporate a sample size large enough to measure the characteristics of the soil fabric and subsequently, the soil mass as a whole. Use of the pressuremeter can provide detailed information regarding the shear modulus, horizontal earth pressure, undrained shear strength and coefficient of horizontal consolidation for most soil masses.

Interpretation of pressuremeter results assumes that all displacements are in the radial and circumferential directions. Since there are no displacements in the z direction, the test is considered as plane strain. As a result, the results may be interpreted analytically using various closed form cavity expansion solutions for a pre-existing circular opening in an infinite mass. Typically, pressuremeters are assessed assuming a linear elastic-perfectly plastic medium (clays) as described by Gibson and Anderson (1961) or as a purely frictional material as described by Hughes et al. (1977). Other more complicated models can also be incorporated; however each model introduces a new unknown and therefore another degree of uncertainty. Carter, Booker and Yeung (1986) describe a cohesive frictional model with a non-associated angle of dilation (Ψ). All methods assume that the ideal model can be manipulated by varying one or several parameters to fit the measured stress strain data. Once fitted, the parameters used in the analysis are assumed to be representative of those insitu. In all cases, the insitu horizontal stress (σ_h) and the shear modulus must be known. The horizontal stress is assessed based on the lift off pressure for self-bore pressuremeters as described by Lacasse and Lunne (1982) or by calculating the overconsolidation ratio (OCR). The shear modulus is assessed based on the slope of the post yield unload-reload curves. In cases of high hysteresis or highly non-linear unload-reload curves, the modulus is assessed incrementally and a range of shear moduli are determined with the lowest value being selected. Assessment of the shear modulus should not be carried out for cases of unloading where the release of shear stress is greater than $2S_u$. In this case, plastic strains will occur and result in unrepresentative moduli.

The short term (undrained) shear strength of the soil mass can be roughly estimated from the initial loading curve based on the first break in the curve. This method should only be used for roughly determining the limits of unloading during testing. Gibson and Anderson (1961) observed that when the stress strain curve recorded during testing is plotted on a semi-log graph, that the slope of the curve at high stresses very closely represents the undrained shear strength. Houlsby et al. (1986) developed a method to assess the undrained shear strength based on the data recorded during the unloading cycle of the pressuremeter. Because the stress release during unloading is greater than $2S_u$, shear failure occurs during the cavity contraction. They found that by inverting the unloading curve, the conventional curve fitting methods could be used to ascertain the undrained shear strength. It is common practice to utilize several of the analytical methods to determine the undrained shear strength and use the average of the values obtained.

Marsland and Randolph (1977) compared the results of pressuremeter tests with deep plate loading tests carried out in the London Clay. They found that the undrained shear strengths estimated from the pressuremeter ranged from equal to up to greater than three times those estimated from the plate load tests. Contributing factors were the insitu stresses, interpretational error and the soil fabric. Marsland and Randolph (1977) suggested that the usage of the Gibson and Anderson (1961) elasto-plastic cavity expansion model resulted in reasonable values provided an accurate limit pressure and insitu horizontal stress were known. They also stated that methods for determining the undrained shear strength which utilized the limit pressure (theoretical point of pure plasticity) were much lower than the undrained shear strength obtained from conventional curve fitting methods. This is typically contrary to the findings of most other practitioners (Hughes, personal communication). Palmer (1972) developed a method for plotting the principal stress ratio relative to the shear strain for the pressuremeter test. Because the stress path of a pressuremeter test is not the same as a triaxial test, comparisons between the two tests should be made with extreme caution. However, as a means for determining the onset of yield, the method of plotting the principal stress ratio versus the shear strain should indicate the transition from elastic to plastic shear strains. Marsland and Randolph (1978) give the shear stress (τ) based on the change in volume of the pressuremeter (for a Camkometer) as Equation 4.1

$$\tau = \frac{dp}{d(\ln(1 - 1/(1+\varepsilon_c)^2)}$$

Equation 4.1

where,
τ is the shear strength;
dp is the change in applied pressure;
ε_c is the circumferential strain at the cavity wall given as $(a - a_o)/a_o$;
a and ao are the current and initial borehole radii respectively.

By assuming that the applied pressure is the major principal stress once it exceeds the insitu horizontal stress, then the principal stresses can be calculated from the shear stress. The incremental shear strain is calculated from the method described by Palmer (1972).

Bolton and Whittle (1999) developed a solution to determine the shear strain required for the onset of plasticity (γ_y). In many stiff fissured clays the yield strains can be very small and difficult to ascertain graphically. Bolton and Whittle used a power law fit to the unload/reload data to determine the reduction in stiffness throughout the elastic range with strain. By plotting the unload/reload curves using log-log scales, they found that the trend could be defined well by a linear line of best fit. Using the slope of the trendline, the limit pressure and undrained shear strength, the yield shear strain is calculated as given in Equation 4.2.

$$\gamma_y = \exp[(\frac{p_{\lim} - p_o}{s_u}) - \frac{1}{\beta}]^{-1}$$

Equation 4.2

where,
γ_y is the yield shear strain;
p_{lim} is the limit pressure;
p_o is the insitu horizontal stress;
s_u is the undrained shear strength; and
β is the slope of the line of best fit to the unloading data.

Bolton and Whittle suggested neglecting the initial unload reload cycle as it may be subject to scatter in the data, likely a result of minor sample disturbance. It is for this reason also that the tangent modulus calculated from the initial loading stage is also typically neglected. In pre-bore pressuremeter tests, this stage represents the recompression of rebounded material that may or may not have undergone shear failure following borehole construction.

Clarke et al. (1979), Clarke (1995) and Randolph and Wroth (1979) initially proposed methods for determining the coefficient of horizontal consolidation from the Camkometer pressuremeter test. They suggested holding the peak strain until pore pressures at the borehole wall had dissipated to at least 50% of the initial value. Because the Cambridge Insitu Camkometer is equipped with a pore pressure transducer on the inflatable membrane, measurement of the pore pressure decay at a given applied pressure is possible. Because not all Camkometer style pressuremeters are fitted with pore pressure transducers, this method is not always feasible.

4.3 Limitations of Pressuremeter Tests in Stiff Fissured Soils

Within stiff fissured materials similar to the Edmonton till, usage of the pressuremeter is not without its limitation. Due to the highly fractured nature of the till, the soil mass may not always be capable of developing high tensile hoop stresses around the borehole during loading. Contact with fissures that have no tensile strength can result in immediate drop in σ_3 and ultimately make interpretation very difficult. Typically when cracking or fissures are a concern, there is a sharp increase in stress with little change in strain followed by a large jump in strain with no increase in applied stress similar to those observed during hydrofracture. This results in a stress-strain curve that appears discontinuous throughout the test duration.

In addition to the fractures within the soil, another layer of difficulty in terms of interpreting pressuremeter data in material like the Edmonton till is the presence of occluded air within the sample voids. Because most pressuremeter tests in clay formations are considered undrained provided the bulk hydraulic conductivity $< 10^{-9}$ m/s, volume changes within the plastic region are neglected. This is not the case with heavily overconsolidated, partially saturated materials. In these materials, the test may still be undrained, however volume change can occur as the occluded air can compress forcing the test sample towards saturation at a constant water content. To date, there has not been any known attempt to account for the initial volumetric changes that occur during compression of a test pocket of partially saturated soils.

Hilf (1948) presented a method for determining the degree of consolidation of partially saturated soils under one dimensional loading. This method accounted for the initial compression of the occluded pore air pressure within the soil matrix followed by the eventual compression of the soil mass due to pore water pressure reduction. During initial loading of a test pocket by a pressuremeter in a partially saturated soil, there is a transition from a partially saturated state where the occluded air compresses and volume change must be considered to one of a saturated state where the conventional undrained closed form solutions apply.

4.4 Field Investigation and Test Methodology

As part of the North LRT detailed geotechnical investigation, a single borehole was advanced from the ground surface approximately 20 m east of the temporary retaining structure known as the East Headwall within the EPCOR Station Lands. The borehole was drilled to a depth of 24.5 m below the ground surface and was tested at intervals of 0.75 m using a pre-bore high pressure pressuremeter supplied and operated by InSitu Engineering of Snohomish, Washington.

The pressuremeter consisted of a modified Cambridge Insitu Pressuremeter (Camkometer), which utilizes nitrogen gas to apply a pressure to the borehole walls which is monitored using a pressure transducer installed within the instrument. Radial displacements are monitored during the pressurization of the borehole walls by means of spring loaded feeler arms that are connected to strain gauges and are positioned at 120° from one another. The movement of the feeler arms and the applied pressure are monitored in real time by the operator at the ground surface using a specially designed data logger and software. An image of the Camkometer used for the insitu testing is shown below in Figure 4.1.

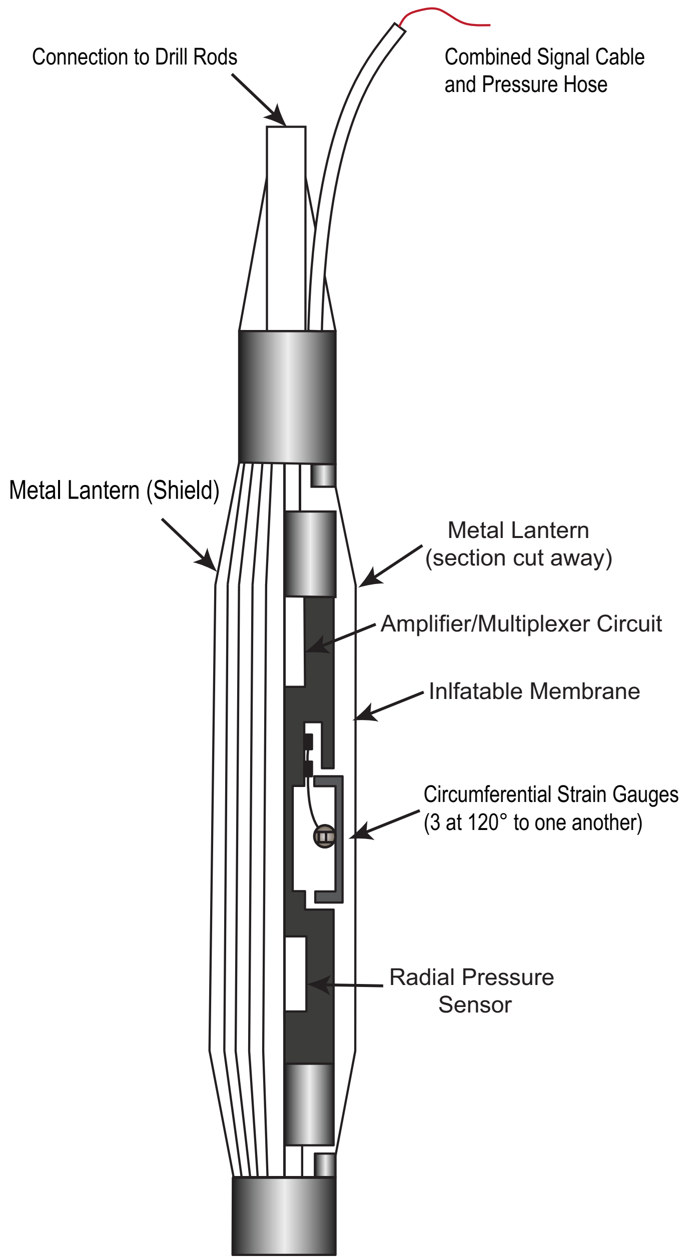

Figure 4.1 Typical pre-bore Camkometer (with permission from InSitu Engineering Inc.)

The purpose of the pressuremeter work was to accurately measure the in-situ shear modulus and undrained shear strength of the glacial till and the Empress Sand. To ensure that the testing was within the glacial til, the borehole was advanced to a depth of 6 m from the ground surface before pressuremeter testing began.

Each of the tests except the last 4 were conducted within a pre-bored, 1.5 m long test pocket. The last four tests were conducted within a 3.0 m long test pocket in order to better document the softening due to relaxation of the Empress Sand. Each test pocket was drilled using a 73 mm diameter tri-cone bit and wet rotary methods by Mobile Augers and Research of Edmonton, Alberta. Following advancement of the test pocket, the drill tooling was removed from the borehole and the pressuremeter probe was lowered to the bottom of the test pocket for testing. Following completion of the first test, the probe was lifted approximately 0.75 m and a second test was conducted within the test pocket. Upon completion of the two tests, the pressuremeter was removed from the borehole and the borehole was advanced another 1.5 m.

Pressure was applied to the probe from the ground surface while the resulting radial stress/circumferential strain curve was observed. Pressure was applied to the probe past the observed yield point and until the circumferential strain reached approximately 10% at which time, the test was terminated. Early termination also occurred if one or more feeler arms extended more than 6 mm from the probe or if disproportionate expansion of the probe was detected. Disproportionate expansion was indicated by one feeler arm moving 2 or 3% more or less than the others. Typically this type of displacement is indicative of the presence of gravel within the test pocket. Each test was subjected to three to four unload-reload curves in order to assess the elastic shear modulus. In cases of minor borehole disturbance, as determined by the initial rate of strain relative to other tests, only two unload-reload tests were carried out as the maximum borehole strains were achieved at lower loads. Unload-reload tests were only carried out once yielding was determined to have occurred. Yielding was assumed based on a general break in the initial slope of the stress/strain curve. This ensured that recompression of the disturbed region surrounding the borehole was nearly complete and the response of the ground would be entirely elastic. Care was taken during unloading to not reduce the borehole pressure more than twice the observed yield pressure ($2S_u$). In theory, these cycles would exhibit little to no hysteresis and all be parallel corresponding with the elastic shear modulus of the soil. The degree of hysteresis and consistency of the interpreted unload-reload slope was used as an indication of reliability of the results.

During the test, typically at around 3% radial strain, the applied pressure was held constant for 3 minutes. This portion of the test is indicated by a radial expansion at a constant applied pressure. The results of the hold tests were then used to assess the coefficient of horizontal consolidation (c_h). The coefficient of horizontal consolidation is analogous with that of the coefficient of consolidation (c_v). Because the Camkometer used during this study was not equipped with a pore pressure transducer, pore pressure decay measurements could not be made.

Following completion of the testing, the data was downloaded to a text file and corrected for the thickness of the membrane based on calibrations performed in a steel casing by In-Situ Engineering.

4.4.1 Short Term Shear Strength

The undrained shear strength of the glacial till was initially assessed from the pressuremeter tests using the Gibson Clay Model (Gibson and Anderson, 1961) fitted to the loading stress-strain curve. The undrained shear strength was also assessed following inversion of the measured stress-strain curve and applying the Gibson Clay Model to the unload curve and dividing the resultant undrained shear strength by two as suggested by Houlsby et al. (1986). Next, the undrained shear strength calculated by using the log method as described by Gibson and Anderson (1961). By plotting the loading curve past the yield strength (less the unload-reload curves) versus the log of the radial strain, the slope of the curve represents the undrained shear strength. Finally, the short term shear strength was assessed using the iterative, limit pressure method also described by Gibson and Anderson (1961). This is generally considered to be the least conservative of the methods and is typically used as an upper bound for the undrained shear strength.

The cohesive frictional model for an associated, isotropic soil given by Carter, Booker and Yeung (1986) was used to assess the drained shear strength of the glacial till. The cohesive-frictional model was selected because the results of the tests within the glacial till suggested that there was some frictional component within the till for the upper samples. This was indicated by the gradual increase in applied pressure throughout the test. A purely cohesive material would exhibit a nearly perfectly plastic response of increased strain at the peak applied pressure. This elastic perfectly plastic response is well illustrated in tests carried out in the lower 3 m of the glacial till while the partially frictional response is demonstrated in the upper horizons of the glacial till.

Within the Empress Sand, the test is assumed to be drained during loading. Unloading however took place over a course of 3 minutes and is assumed to be undrained. Considering this, the inversion method given by Houlsby et al. (1986) was used to determine the short term shear strength of the Empress Sand. For these tests the Gibson Clay model was used to assess the short term strength of the Empress Sand. The undrained response calculated from fitting to the unload data were then compared to the results of the log and limit pressure methods.

4.4.2 Glacial Till Response

4.4.2.1 Undrained Loading Curve Fit

The ideal Gibson Clay model was initially used to fit the loading curve data for the glacial till. This model assumes an undrained response for an elastic perfectly plastic soil. It was found during the course of interpretation that only a select number of test samples were well represented by the Gibson Clay model. Comparisons between the actual and the ideal model were made by using the measured circumferential strains as input into the Gibson model and calculating the associated radial stress. The calculated stresses were then compared to the applied stresses to obtain an incremental percent difference. It is important to note that during loading, there was at least one to two hold tests carried out which resulted in measured radial strains without an increase in applied load. Observation of the fitted curves indicates that these sections were the source of greatest error.

In order to accurately represent the lift off pressure or to account for any disturbance resulting from borehole advancement, the measured data was shifted towards the ordinate. This ensured that the strains associated with initial lift off (at zero applied pressure) of the measured values were similar to those estimated from the ideal models. To account for the hydrostatic pressure, the final "zero" pressure following complete unloading of the probe was used to shift the measured stress strain curve vertically downward. This is based on the assumption that the pressure transducer within the pressuremeter would measure the hydrostatic pressure on the membrane when the internal gas pressure is fully released. Typical loading curves with the associated Gibson Clay Model fit are shown below in Figure 4.2 and Figure 4.3.

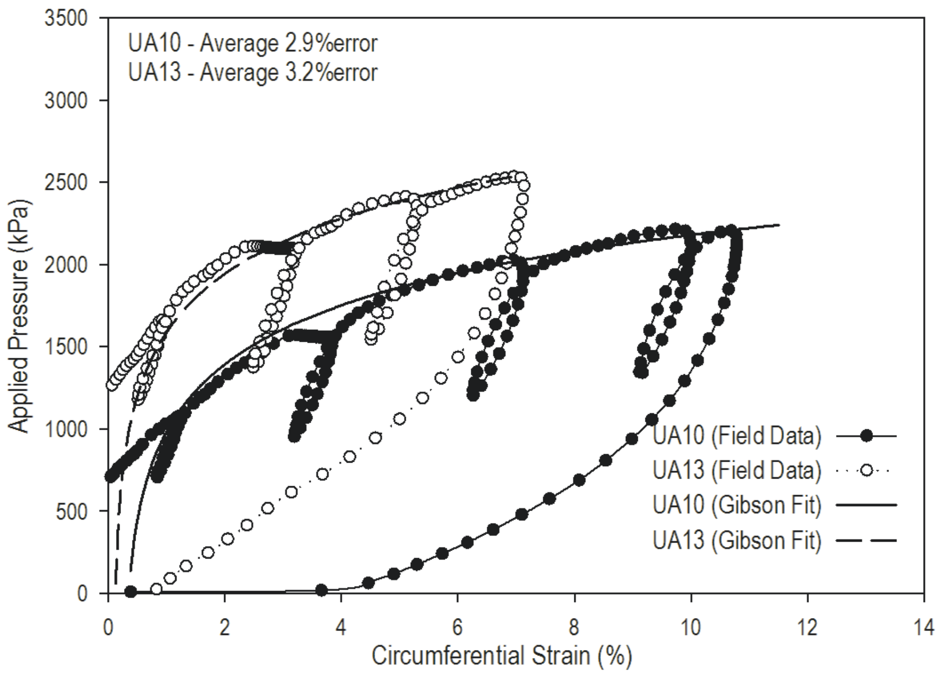

Figure 4.2 Typical loading curve with good Gibson Clay Model fit

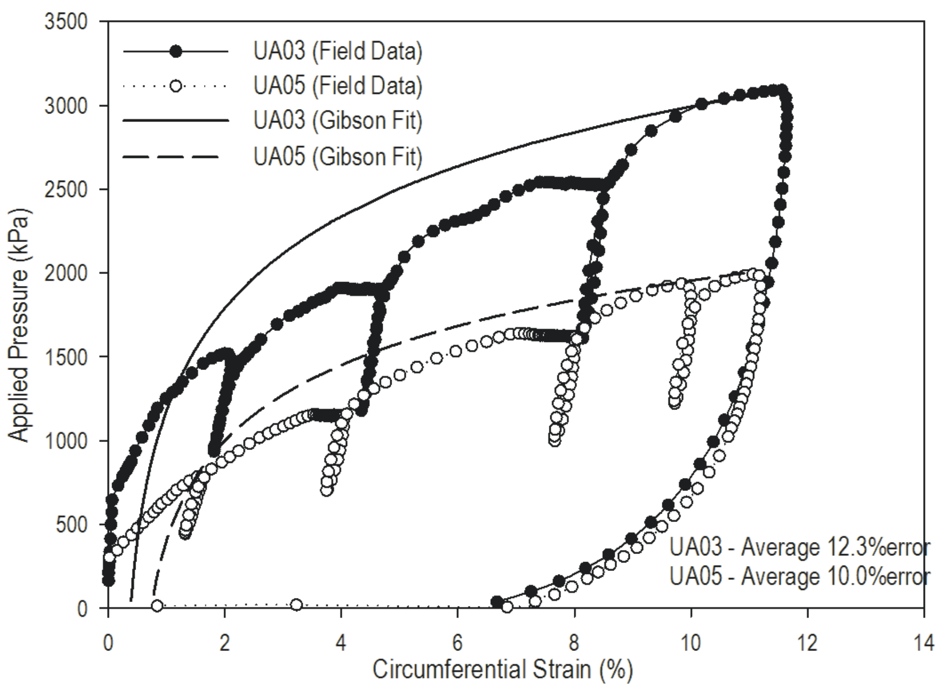

Figure 4.3 Typical loading curve with poor Gibson Clay Model fit

4.4.2.2 Drained Loading Response

When the ideal Gibson Clay Model did not provide a reasonable fit as shown in Figure 4.3, the cohesive-frictional model derived by Carter, Booker and Yeung (1986) was used. This model was selected due to the apparent accumulation of applied stress with strain in post yield conditions. Like the Gibson Clay Model, yield in the cohesive-frictional model is dictated by the cohesion of the soil. The subsequent plastic strains are then controlled by a combination of the cohesion and the frictional components. Examples of the improvement to the loading curve prediction are shown below in Figure 4.4, where the tests which resulted in a poor Gibson Clay Model, were recalculated using the cohesive frictional model of Carter, Booker and Yeung (1986).

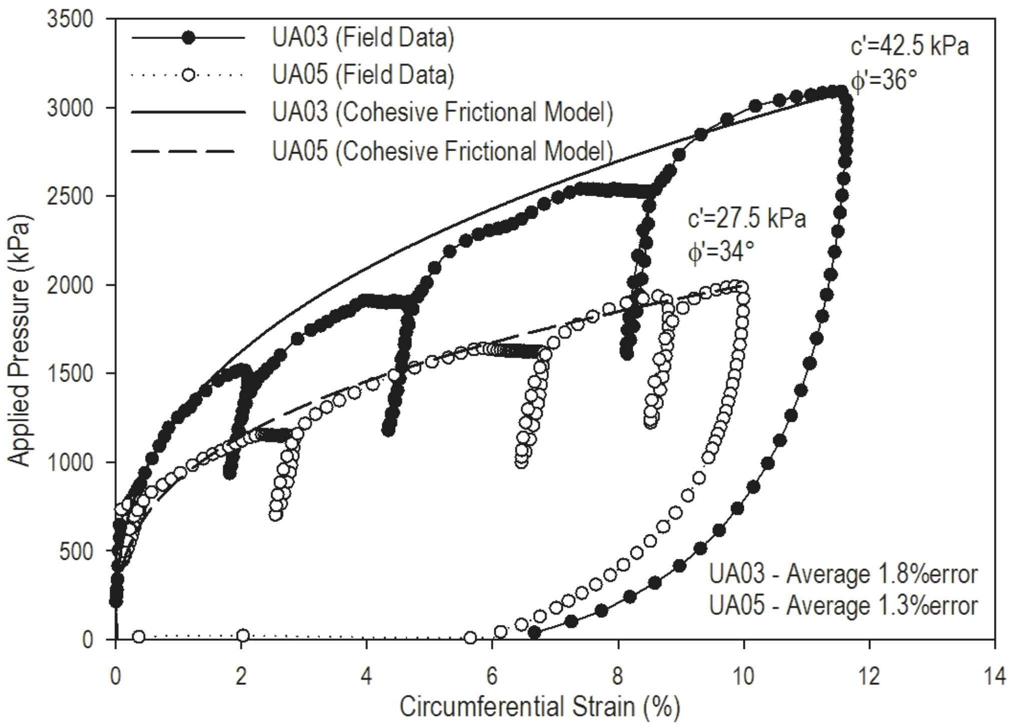

Figure 4.4 Typical loading curve with a good Cohesive-Frictional Model fit

Based on the strength of the cohesive-frictional model fit to the field data, the failure envelopes were evaluated for each test that was considered feasible. The profile of assessed undrained shear strengths and cohesive-frictional as well as frictional (Hughes Sand Model) fits are shown in Figure 4.5. Interpreted piezocone values are shown for reference.

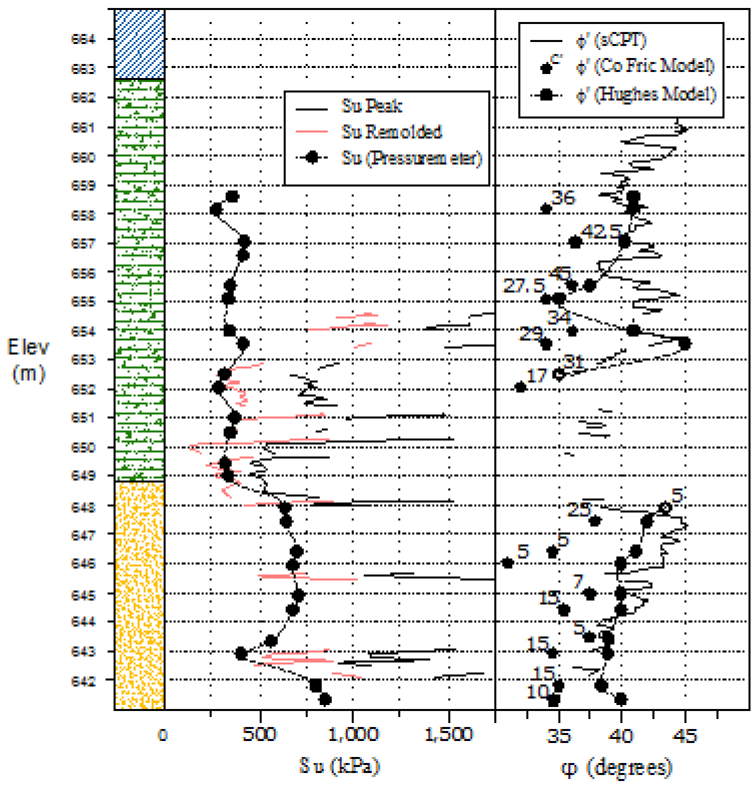

Figure 4.5 Soil strength profile through the depth of the pressuremeter test hole

The use of a cohesive-frictional model assumes drained conditions and dilation within the plastic region. Therefore the permeability of the soil must be sufficiently high or the loading sufficiently slow to permit drainage throughout the duration of the test. In the model derived by Carter, Booker and Yeung (1986), the dilation flow rule is often selected to be associated, though does not have to be.

The applicability of the cohesive-frictional model may be reasonable within the glacial till provided that the test pocket was intersected by some portion of the intra-till sand. The borehole advanced adjacent to the pressuremeter testhole did not indicate discernable quantities of the intra-till sand throughout the depth of the boring. Historically, the intra-till sand has been thought to consist of isolated pockets within the glacial till. Observations of the ground conditions within the North LRT tunnels indicated that the intra-till sand was more commonly encountered as frequent, thin laminar-like inclusions that were ubiquitous throughout. The intra-till sand was more commonly encountered in the upper horizons of the glacial till which became more cohesive with depth. Considering this, it is felt that the assumption of partial drainage during the test is reasonable.

For the analysis of the pressuremeter tests using the cohesive-frictional model, several assumptions other than partial drainage were made. The additional assumptions are as follows:

- Dilation of the soil was assumed to be minimal and was maintained between 3 and 5°;
- The shear modulus was selected to be equal to the average of the unload-reload curves;
- Poisson's ratio was selected to range between 0.33 and 0.35;
- In order to reduce the number of unknowns, the effective cohesion was arbitrarily selected to be 10% of the undrained shear strength; and
- The effective friction angle was initially selected as 34°.

Each of the selected parameters and assumptions had varying influence on the calculated circumferential strains. Some of the assumptions were found to play a more important role than others, and were kept constant if possible. The dilation angle had a strong influence on the stiffness of the ground. A 10% increase in the dilation angle resulted in a 12% increase in the calculated circumferential strain while a 100% increase in dilation resulted in a 260% increase in the calculated circumferential strain. When the influence of the dilation angle is plotted, a quadratic function is found to fit the data well with a coefficient of determination (R^2) of 0.998. Because the shear modulus of the material was generally fixed, the dilation angle was initially selected to reasonably represent the initial slope of the field data.

The shear modulus was assumed to be fixed and the most accurate of the parameters used as input in the closed form solutions. Because the initial tangent modulus was typically less than the unload-reload curves, only the average of the post yield unload-reload curves were used. Increasing the shear modulus resulted in a reduced strains within in the elastic region of the predicted curve, though changes could be observed within the post yield portion as well. When the stiffness was increased by 25%, there was a 22% reduction in the calculated strains. When the increase was 50%, the strains were reduced by 40%. When the data were plotted, it suggested that the influence of the stiffness was well defined by a power law as suggested by Bolton and Whittle (1999).

Poisson's ratio had a nearly 1:1 influence over the calculated circumferential strains. A 10% change resulted in a 10.2% change in the circumferential strains. Considering that the variance of Poisson's ratio was less than 10%, and typically less than 5%, the overall influence on the results was considered as minimal.

The effective cohesion and friction angle played a considerable role in the shape and final strains of the ideal model. It was for this reason that the effective cohesion was selected to be relatively fixed and kept at 10% of the undrained shear strength (±0.5% S_u). The cohesion played an important role as to when plasticity initiated in the cavity expansion model. As would be expected at lower confining stresses where friction would not have as an important role. The friction angle tended to influence the post-yield strains by either increasing or decreasing the slope of the predicted curve with increases or decreases in the friction angle. In terms of influence, when the cohesion was increased by 25%, the calculated strains were reduced by approximately 18%, while a 100% increase in cohesion resulted in a reduction in strain by 35%. The frictional response was highly influential as would be expected as it dominated the plastic strains. A 25%

reduction in friction resulted in a 288% increase in the calculated strains while a 10% increase in friction resulted in a 28% reduction in the calculated strains. Clearly by reducing the frictional resistance, the strains could be greatly overestimated.

4.4.2.3 Unloading Response

The undrained shear strength of the glacial till was also calculated by fitting the Gibson Clay Model to the final unloading curve. Because the stresses start from a yielded state for an elastic-perfectly plastic material, the stress path is such that the undrained shear strength used to fit the unloading curve is actually equal to $2S_u$. Figure 4.6 illustrates the stress path of a typical pressuremeter test from initial loading to complete unloading.

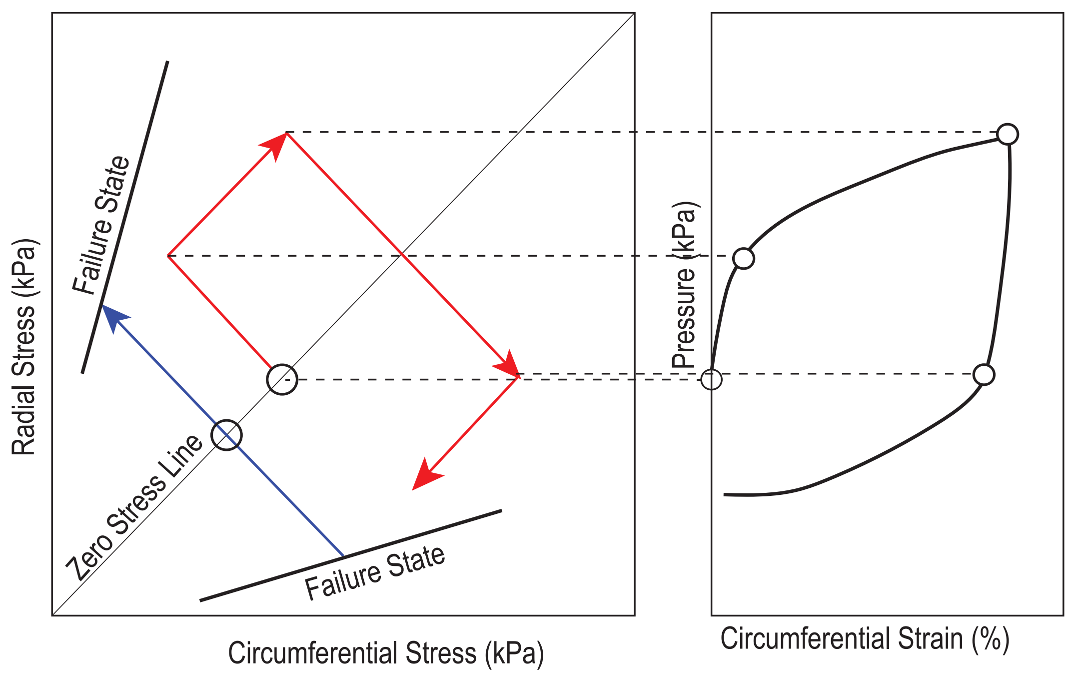

Figure 4.6 Stress path of pressuremeter test and typical field data results

The unloading curve fit was considered to be truly an undrained response due to the rapid unloading rate. Typically, complete unloading was completed within 3 to 4 minutes. In addition, the peak-applied stresses should have forced any occluded air within the soil into solution putting the ground in a fully saturated state. This effect would ensure that no volume changes occurred throughout unloading. As a result, the undrained shear strength was considered the most representative of all of the methods used. Within the glacial till, the Gibson Clay Model represented the unloading curves very well as shown below in Figure 4.7 and Figure 4.8.

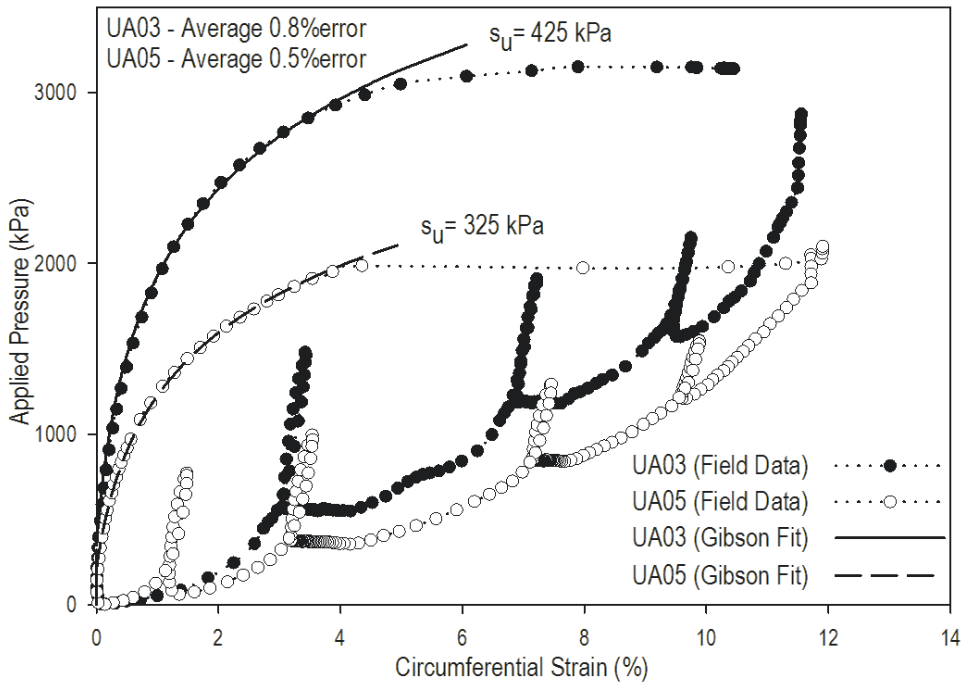

Figure 4.7 Representative unloading field data curves with Gibson Clay Model fits

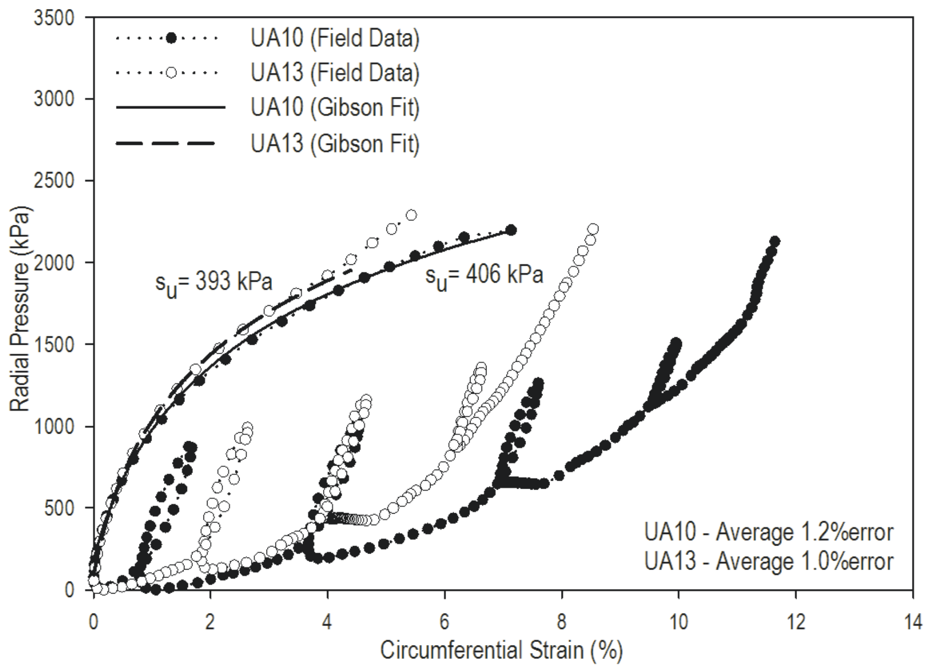

Figure 4.8 Representative unloading field data curves with Gibson Clay Model fits

When the degree of error was examined, it appeared that the samples that suggested a partially drained response during loading, were best represented by an undrained response upon unloading. This suggests that there was some influence by the pore air volume (degree of saturation) on the interpretation of the loading curve. It also suggests that upon completion of loading, that the occluded air was forced into solution, making the yielded soil surrounding the probe fully saturated.

4.4.2.4 Log Method

The next method employed to determine the undrained shear strength was the log method. Gibson and Anderson (1961) demonstrated that by plotting the loading curve in semi-log space, the slope of the curve at high stress will indicate the undrained shear strength of the soil tested. In addition, extrapolation of the line to the ordinate would indicate the limit pressure. In each case the loading curve was plotted as the loading pressure versus the log circumferential strain and the slope of the curve at high stress was calculated. Examples of the application of the Log Method are shown in Figure 4.9 for the demonstration samples used above.

The undrained shear strength of the glacial till interpreted from the Log Method resulted in values that were very similar to those obtained from the unloading method. This would appear to validate the undrained shear strengths obtained from the unloading curve fitting method.

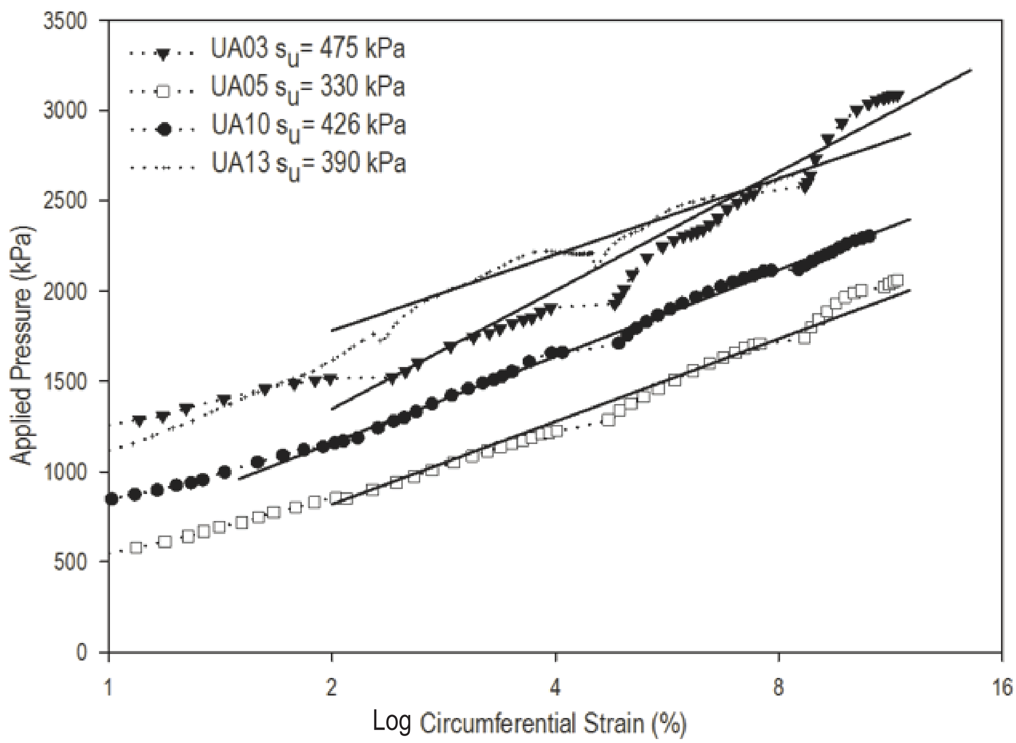

Figure 4.9 Undrained shear strength of the glacial till from Log Method

4.4.3 Empress Sand

The shear strengths of the Empress Sand were calculated using the Hughes Sand Model (Hughes et al., 1977) to interpret the loading curve and the Gibson Clay Model to interpret the unloading curve. The undrained model was not used to assess the loading curve because the loading rate was sufficiently slow and the permeability of the sand was sufficiently high, that it was that assumed drained conditions prevailed. In addition to the unloading curve assessment, the short-term shear strength was also interpreted using the log method for the loading curve.

4.4.3.1 Drained Response – Hughes Sand Model

The drained parameters were first assessed for the loading curves within the Empress Sand using the Hughes Sand Model. The Hughes Model (Hughes et al., 1977) assumes a fully drained soil that is homogeneous, isotropic and shears with a flow rule that is associated with the critical friction angle. This terminology is not to imply that the dilation angle is set equal to the critical friction angle, but rather that the ratio between the peak and critical state friction angles influence the rate of dilation post yield. The dilation ratio (M) is given below in Equation 4.3.

$$M = \left({1 - \sin\phi_p} \middle/ {1 + \sin\phi_p} \right) \left({1 + \sin\phi_{cr}} \middle/ {1 - \sin\phi_{cr}} \right)$$

Equation 4.3

where,

ϕ_p and ϕ_{cr} are the peak and critical state friction angles.

Finally, the model assumes that the elastic strains within the plastic region are neglected as they are minor relative to the plastic strains. Carter, Bookerand Yeung (1984) have demonstrated that this assumption can lead to considerable error. Despite this, industry standard is to use the Hughes Sand Model as it tends to represent the response of dense sands better than any existing model (Clarke, 1995).

The Hughes Sand Model is by far the simplest model and requires the least number of variables to determine an ideal curve fit for dense frictional soils. In most cases, the only parameters that are required are the shear modulus, pore water pressure, the insitu stress and the peak and critical state friction angles. Most of these parameters are easily determined from the pressuremeter test itself, while the critical state friction angle is related to the mineralogy of the soil and does not vary significantly, making its assumption relatively trivial. As a result, the Hughes model leaves the only unknown as the peak friction angle itself.

For the interpretation of the field data, the insitu horizontal stress was calculated based on an historical coefficient of lateral earth pressure (K_o) of 0.65. The static pore water pressure was measured by the pressuremeter probe as the measured deflated probe pressure obtained following complete unloading at each test location. The critical state friction angle was assumed as 34° based on the mineralogy of the Empress Sand. This value is considered to be typical for quartizic sands as given by Terzaghi et al. (1996). Based on the above assumptions, typical examples of the drained curve fitting within the Empress Sand are shown below in Figure 4.10.

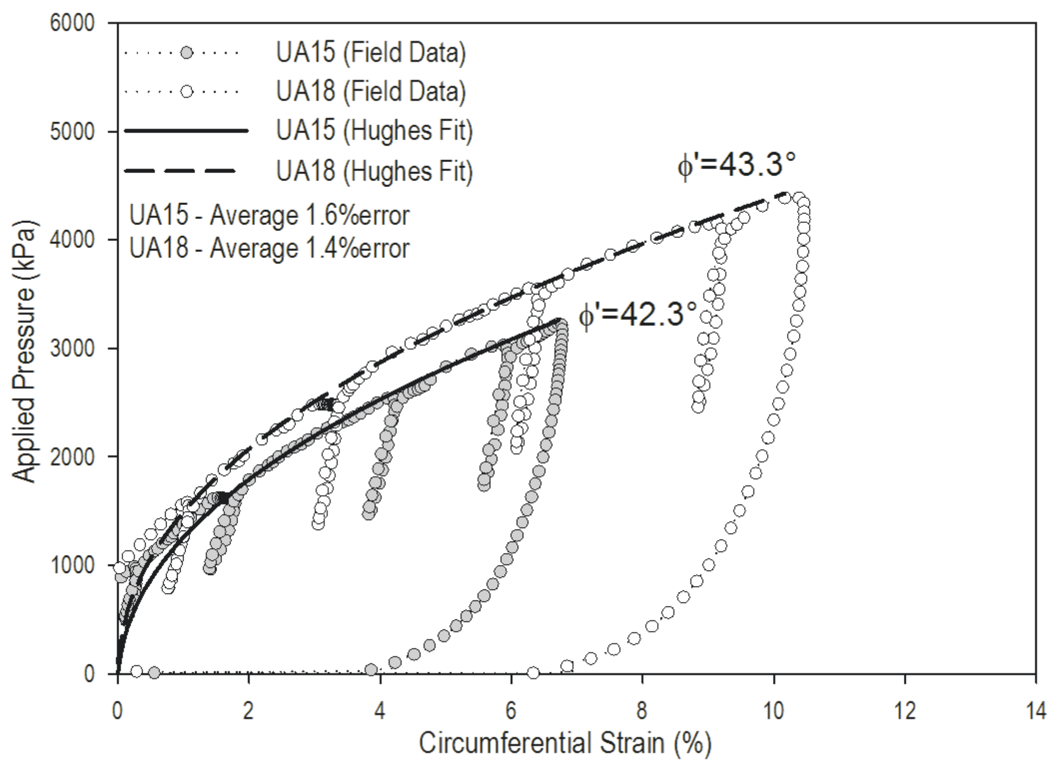

Figure 4.10 Empress Sand field data and associated Hughes Sand Model fit

Figure 4.10 illustrates that the use of the Hughes Sand Model is highly effective in the Empress Sand. The average percent difference between the actual and predicted curves was found to always be less than 5% for the test samples that were not disturbed prior to testing. It should be noted that the initial loading (pre-yielding) was excluded from the goodness of fit analysis as every loading curve was shifted to account for the pre-boring process.

From the overall analyses, the friction angles are all quite consistent with an average peak friction angle of 41.1° and a standard deviation of 1.4°. The maximum and minimum values were found to be 43.3 and 39.4° respectively. Figure 4.5 illustrates the interpreted friction angles with depth through the Empress Sand.

4.4.3.2 Unloading Response

The undrained or more appropriately, the very short term shear strength of the Empress Sand was assessed by fitting the Gibson Clay Model to the unloading field data. It was assumed that the rate of unloading was such that drainage into the plastic region around the probe was not permitted and the undrained conditions were relevant. Examples of the undrained analyses are shown below in Figure 4.11.

As with the glacial till, the Gibson Clay Model fit to the unloading curves within the Empress Sand were quite strong. The undrained strengths were also found to be on the order of 40% higher than those of the glacial till. Figure 4.5 illustrates the interpreted undrained shear strengths through the Empress Sand with depth.

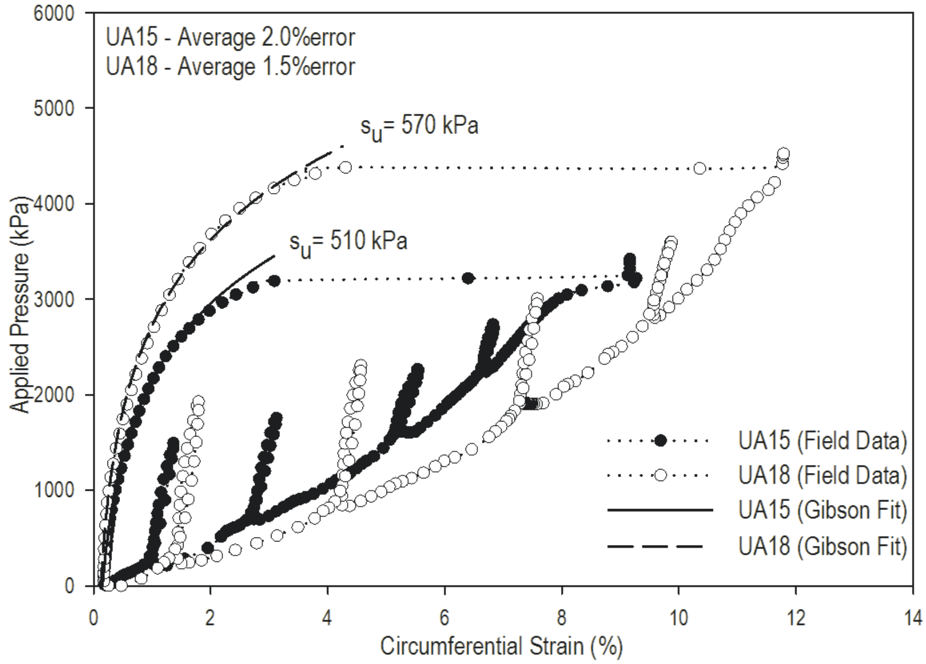

Figure 4.11 Unloading curves within the Empress Sand and Gibson Clay Model fit

4.4.3.3 Log Method

The next method of interpretation for the undrained response was the calculation of the slope of the applied pressure / log circumferential strain curve. The undrained shear strengths obtained for the Empress Sand using the Log Method were approximately 1.5 times those interpreted from the unloading curves. Examples of the log method interpretation within the Empress Sands are shown below in Figure 4.12.

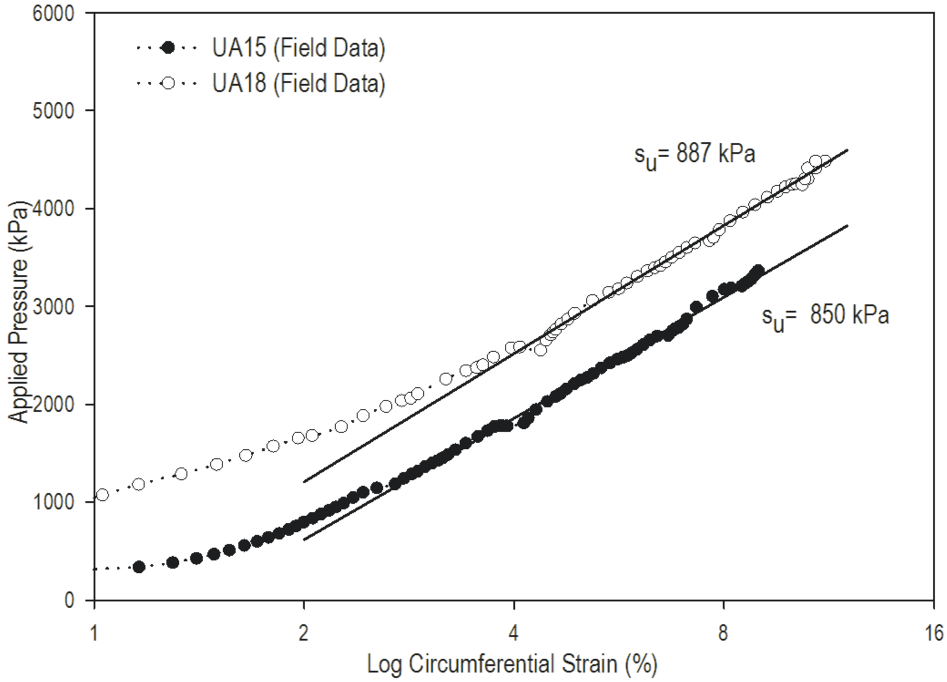

Figure 4.12 Undrained shear strength of the Empress Sand from Log Method

Limit Pressures

Limit pressures were calculated for each test carried out through the depth of the borehole. The limit pressure is the true point of perfect plasticity where the applied pressuremeter volume expands indefinitely.

The limit pressure is best calculated by plotting the inverse of the measured circumferential strain with respect to the applied pressure. When this curve is plotted, a line of best fit is constructed through the large strain portion of the graph and extended to the intersection with the ordinate. The intersection is coincident with the limit pressure for that test. Calculated limit pressures with respect to the geologic profile at the testhole location is given in Figure 4.13. Another method of interpretation of the limit pressure was described in a previous section. It involves extension of the applied pressure / log circumferential strain curve to the ordinate and that intersection is equal to the limit pressure for that test.

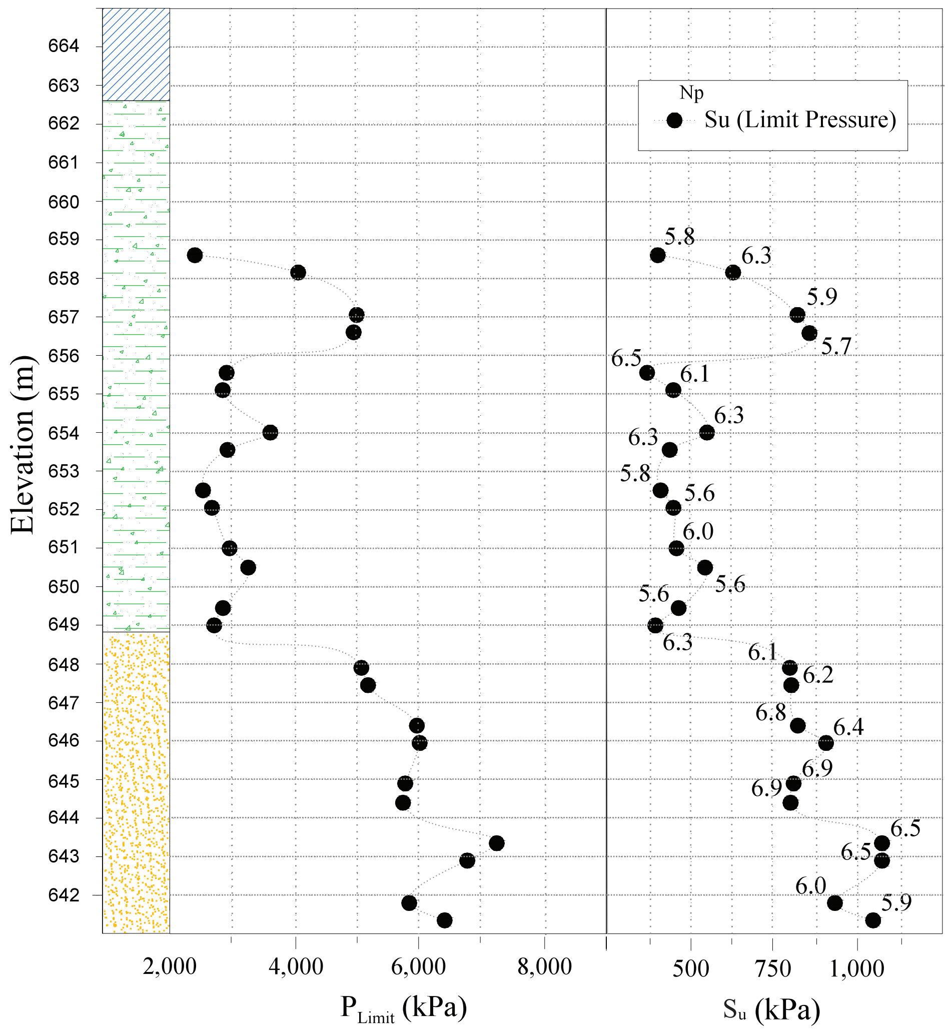

Figure 4.13 Limit pressures and undrained shear strength based on limit pressure

For a given limit pressure and shear modulus, the undrained shear strength may also be obtained. Marsland and Randolph (1977) provide a method for estimating the undrained shear strength by assuming a pressuremeter constant (N_p) related to the shear modulus and undrained shear strength. From the limit pressure, the undrained shear strength of the soil mass may be estimated using Equation 4.4.

$$s_u = \left(p_{\lim} - \sigma_{ho}\right) / N_p$$

Equation 4.4

where,

p_{lim} is the limit pressure;
σ_{ho} is the insitu horizontal stress; and
N_p is the pressuremeter constant given as $N_p = 1 + \ln\left({}^{G}/_{s_u}\right)$.

Equation 4.4 suggests that calculation of the undrained shear strength is an iterative process. Marsland and Randolph (1978) reported that the pressuremeter constant N_p is equal to 6.2 based on plate loading tests. Use of 6.2 as a reasonable constant was tested during this study. Using the iterative method to solve for s_u, the pressuremeter constant (N_p) was back calculated. The back calculations indicated that a value of 6.2 is a reasonable approximation for the field data obtained from the current investigation as it was the mean of all tests. As expected, the pressuremeter constant was a function of the measured soil stiffness and higher values were calculated within the Empress Sand than within the glacial till. The undrained shear strengths obtained from the estimated limit pressures are shown on Figure 4.13. The corresponding pressuremeter constants (N_p) for each test were plotted adjacent to the undrained shear strengths for reference.

The undrained shear strengths obtained from the limit pressure method suggest that these values are less conservative than the other methods. This is because the limit pressure model assumes a perfectly plastic state. To this end, this method was recommended (Hughes personal communication) to be used as an upper bound for the undrained shear strength of a soil.

4.5 Shear Modulus

The elastic shear moduli were measured for each test by applying a line of best fit to the initial loading curve and through the apexes of the unload-reload curves. When the difference between unload and reload cycles was greater than 20%, the incremental modulus was calculated using the finite difference method. In these cases, (seven in total) the minimum value was assumed. Graphs showing the assumed lines of best fit are shown in Appendix A while the calculated range of values as well as the average from the slope of the line of best fit are shown below in Figure 4.14. Note that the shear moduli have been converted to Young's Modulus assuming a Poisson's ratio of 0.34. The Young's moduli calculated from the seismic CPT are also shown for comparison.

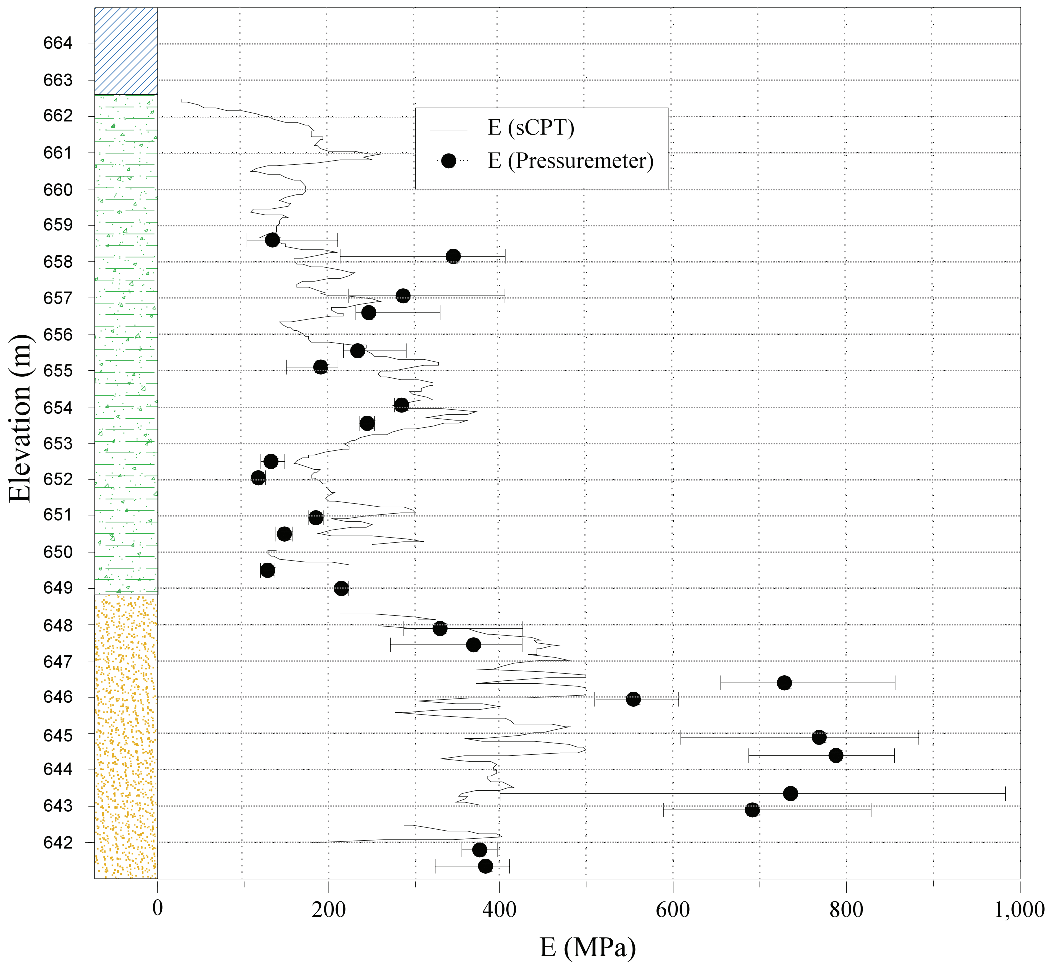

Figure 4.14 Calculated Young's moduli from pressuremeter tests (in MPa)

A table showing all of the calculated hysteresis values for each test is provided in Appendix A. In each case, the maximum, minimum, average and standard deviation of the curves is shown. The difference between each curve was calculated as a percent difference of pressures for a given radial strain based on second order polynomial curve fits to the actual data. All curve fits had a minimum R^2 value of 0.99 indicating an exact match.

Within the glacial till, none of the unload-reload cycles indicated hysteresis greater than 20%. Within the Empress Sand, differences between the unload-reload curves greater than 20% occurred in seven of thirty seven instances or 19% of tests carried out within the sand. The larger degree of hysteresis was found to have only occurred in the third and fourth unload-reload cycles or when the applied pressure was greater than 60% of the limit pressure. This suggests that there was some degradation to the ground structure as the applied pressure began to approach the limit pressure of the soil either through dilation or particle realignment. Considering that there were little changes in the total hysteresis of the unload-reload cycles within the clay till, it is likely that the changes were as a result of volumetric changes during dilation. Because the glacial till is considered to be undrained, and at higher pressures, the ground will have become saturated and the assumption of zero volume change during shear would be valid. Within the Empress Sand however, this would not be the case and at high pressures and strains, dilation would occur changing the structure of the ground within the plastic region.

4.5.1 Glacial Till

The range and average shear moduli of the glacial till are shown in Figure 4.14. Based on the stiffnesses calculated within the glacial till shown in Figure 4.14, there appears to be a trend of maximum stiffness near the surface of the formation. It then gradually reduces approximately 3 m above the interface with the underlying Empress Sand. This change is likely attributed to a higher clay content within the soil matrix. The testhole advanced adjacent to the pressuremeter testhole did not indicate any obvious reasons for this decrease in stiffness, nor was there any grain size analyses carried out through this section to confirm any increase in clay content. Examination of the actual stress-strain curves however do suggest that the soil matrix through this section is likely more clayey. Because the stress-strain curves appeared to exhibit elastic-perfectly plastic trends relative to the overlying samples, it suggests that the material was more cohesive in nature.

The maximum and minimum values of the shear modulus within the glacial till is shown below in Table 4.1. Figure 4.14 and Table 4.1 show that the average initial tangent modulus within the glacial till is 31 to 38% that of the unload-reload cycles as would be expected. Since the pressuremeter was not a self-boring pressuremeter, some stress release following borehole construction was inevitable. In most cases, it is likely that the surrounding soil had undergone some form of plastic yielding in extension following borehole construction.

	Initial	Cycle #1	Cycle #2	Cycle #3
Maximum	45.5	105.2	151.7	151.5
Minimum	9.7	26.3	45.5	42.7
Average	26.2	69.0	80.0	82.1
Std Dev	11.2	22.2	29.1	31.7

Table 4.1 Shear modulus key values from pressuremeter tests in the glacial till (in MPa)

In most cases, the interpreted moduli from the first cycle tended to be slightly lower than the latter two unload-reload cycles. This would suggest that the soil surrounding the borehole had not completely yielded prior to carrying out the first unload-reload cycle.

Observation of the post-yield stiffness measurements indicated that there was little change in the shear modulus with strain within the glacial till. This would also suggest a material that was subject to undrained loading (zero volume change) once yielding has occurred. If the soil experienced volume change, dilation would have resulted in loosening of the soils immediately adjacent to the borehole while compression would result in re-alignment of particles and a stiffer response following unloading.

4.5.2 Empress Sand

The stiffnesses of the Empress Sand are shown in Figure 4.14. The measured shear moduli indicated that the Empress Sand is 1.8 to 2.9 times stiffer than the overlying glacial till. As with the glacial till, the average initial tangent modulus was less than the post yield shear moduli. Based on the average values, the initial tangent modulus was between 18 to 25% that of the post-yield unload-reload shear moduli. Table 4.2 presents the key values for the initial tangent modulus and post yield shear moduli obtained from the unload-reload cycles for each test.

	Initial	Cycle #1	Cycle #2	Cycle #3	Cycle #4
Maximum	66.2	307.8	280.3	365.6	407.7
Minimum	34.8	118.3	90.3	129.4	152.3
Average	47.1	189.1	190.5	236.6	257.3
Std Dev	12.0	64.2	69.2	91.6	91.0

Table 4.2 Shear modulus key values from pressuremeter tests in the Empress Sand (in MPa)

Because there was hysteresis greater than 20% in seven of the unload-reload cycles, the tangent shear modulus was calculated incrementally using the finite difference method from the initial release of stress until the continuation of the loading curve. Tests numbered 17 through 20 all experienced maximum differences from between 20.3 to 26.1% of the third and fourth unload-reload cycles. The one exception is the third unload-reload cycle for test number 18, which only measured a difference of 18.9%.

Using the finite difference method to calculate the tangent shear modulus of the unload-reload cycles resulted in a wide range of moduli. These ranged from greater than 3 GPa to values similar to that of the interpreted line of best fit. In each case, the lowest calculated shear modulus was within 10% of the shear modulus estimated from the line of best fit shown on Figure 4.14. Table 4.3 presents the minimum shear moduli calculated using the finite difference method for the unload-reload cycles for tests 17 through 20. The percent differences are from the shear moduli predicted from a line of best fit through the tip and tail of the unload-reload cycle.

Test #	Cycle #3	Cycle #4	% Difference (cycle)	% Difference (line of best fit)
17	334.1	323.7	5.0%	1.8%
18	-	201.9	-	7.1%
19	289	350.1	6.3%	6.4%
20	314.2	320.5	1.1%	0.8%

Table 4.3 Calculated minimum tangent shear moduli from unload-reload cycles (GPa)

Considering the strong correlation with the line of best fit through the unload-reload curve, it was assumed that the line of best fit can be reasonably used to determine the shear modulus provided that the hysteresis of the unload-reload cycle is below 25%.

4.6 Yield Shear Strain

One of the key aspects of this research was to obtain an understanding of what percentage of radial strain resulted in the onset of plastic deformations. Due to their strength, stiff fissured soils have been shown to exhibit plastic deformations when subjected to very low strains under specific stress paths (Medeiros, 1979). Because the stress paths are an important aspect of the yield criterion, the yield shear strains were calculated for the pressuremeter tests in both compression and extension. These stress paths are similar but not identical to plane strain triaxial tests as discussed by Medeiros (1979).

Using the method described by Bolton and Whittle (1999) discussed in the introduction, the yield shear strains in extension were determined. This was carried out only on the unloading curve as at high stresses realized upon test completion, the glacial till was considered to be saturated. This implies that the unload tests did not undergo volume changes and would therefore be representative of undrained extension tests. The extensional results were then compared to the compressive results obtained using the methods described by Palmer (1972) and Marsland and Randolph (1978) in which the field data was plotted in terms of the principal stress ratio / shear strain for the loading curve. For an ideal homogeneous isotropic material where stress path does not influence the yield strain, the yield shear strain in compression should be similar in extension.

4.6.1 Glacial Till Yield Shear Strain

The yield shear strain in the glacial till was obtained by plotting the results of the unloading log stress / log strain curve in Cartesian space. From this curve, a linear trendline was fit to the resulting function and the correlation (R^2) and the equation associated with the line of best fit were obtained. As described by Bolton and Whittle, the correlations of the trendline to the data were very strong and ranged from 0.97 to 0.99 with the lower values corresponding with test samples that were clearly disturbed. Based on the strong correlations of the fit curve to the field data, the equations are considered to be representative of the unloading trend. Using the slope of the trendline as β and Equation 4.2, the yield strains were calculated in active extension for each unloading test.

The yield strains associated with passive compression were then calculated using the method described by Palmer (1972) and Marsland and Randolph (1978). To obtain the yield shear strains in compression, the principal stresses and strains were calculated incrementally throughout each test. The incremental shear stress was calculated using the Palmer method. The calculated incremental shear stress was then converted to the incremental principal stresses by assuming that the applied pressure is the major principal stress (σ_1). The assumption of the applied pressure as the major principal stress is correct provided it is greater than the insitu horizontal stress, which is taken as the initial pressure

(p_o) for each test. The incremental shear strain was then calculated as described by Marlsand and Randolph (1978). For a conventional Camkometer pressuremeter, the incremental shear strain is simply twice the incremental circumferential strain measured by the probe during the test. The peak compressive strains were obtained by plotting the ratio of shear to confining stresses (q/p) with respect to the measured shear strain in total stress space. In most cases this plot resulted in a peak at a shear strain less than 5% and subsequently stabilized at larger shear strains. Typical principal stress ratio and shear stress plots for the glacial till and the Empress Sand are shown below in Figure 4.15.

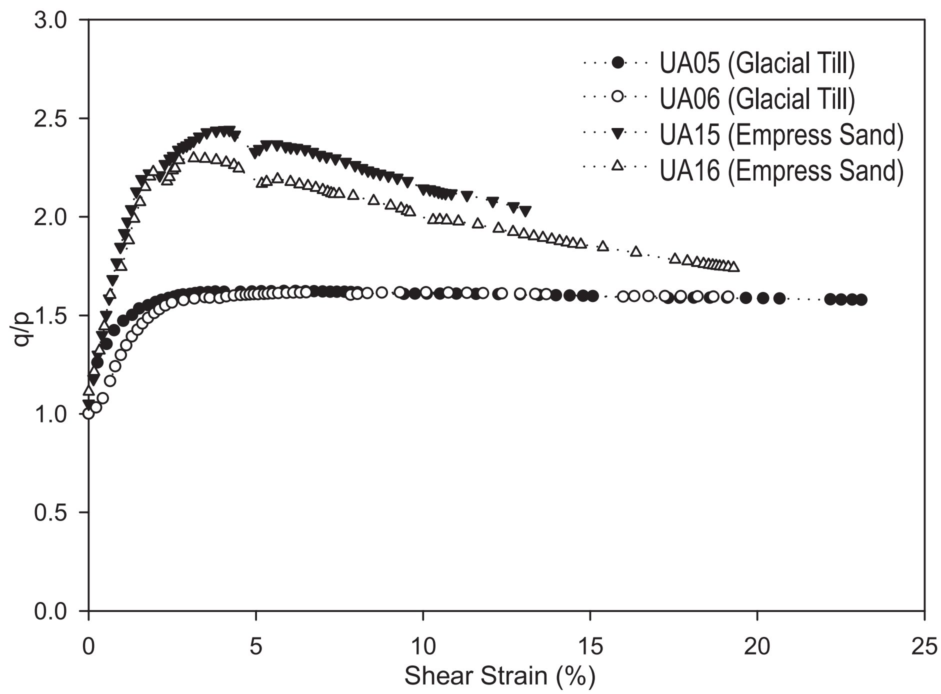

Figure 4.15 Stress ratio profiles for the glacial till and Empress Sand

In tests where there was appreciable disturbance as determined by the initial strains prior to accumulating load, the stress ratio plots did not necessarily reach a peak but rather tended to increase with increased shear strain. In these cases, the yield point was determined from an apparent break in the stress ratio curve. Disturbance also had the effect of shifting the yield shear strain by the amount of measured disturbance. Once the yield shear strain was ascertained, the disturbance strain was subtracted from the interpreted yield shear strain to obtain the true yield shear strain for that test.

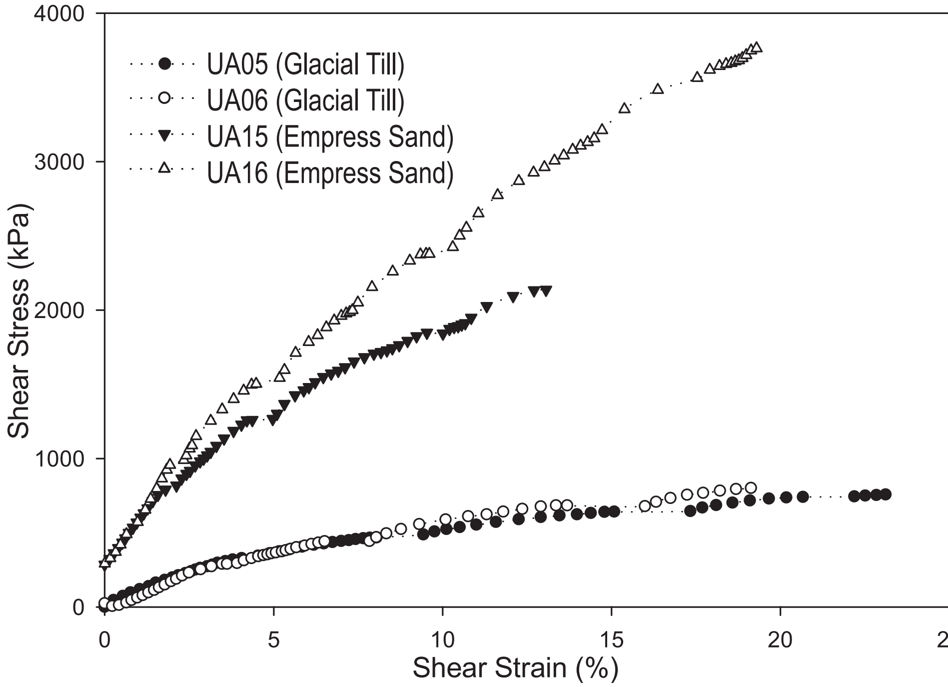

Figure 4.16 Shear stress versus shear strain for the glacial till and Empress Sand

The calculated yield shear strains for each test are shown below in Table 4.4. Note that the sample numbers labelled UA01 to UA14 are within the glacial till while samples UA15 to UA 24 are within the Empress Sand. The compressive yield shear strain measured during each test is denoted as γ_y (comp).

Test No.	Depth (m)	β	S_u (kPa)	p_{limit} (kPa)	p_o (kPa)	γ_y (%)	γ_y (comp) (%)
UA01	6.85	0.4714	275	2,435	100.3	0.17	6.05
UA02	6.4	0.5109	360	3,250	93	0.21	4.85
UA03	8.4	0.6487	420	3,580	125.8	0.2	0.49
UA04	7.95	0.5951	425	3,425	118.1	0.17	3.07
UA05	9.9	0.5565	340	2,545	150.9	0.17	3.79
UA06	9.45	0.6404	350	2,866	143.8	0.2	3.47
UA07	11.45	0.4973	420	3,605	175.5	0.21	3.28
UA08	11	0.5684	345	2,940	168.4	0.19	3.66
UA09	12.95	0.5367	290	2,580	200.1	0.18	3.43
UA10	12.5	0.6141	320	2,700	193	0.18	1.13
UA11	14.5	0.5903	350	2,975	225.8	0.21	3.99
UA12	14	0.5291	375	3,265	217.6	0.2	2.82
UA13	16	0.6776	340	2,870	250.4	0.2	3.42
UA14	15.55	0.7263	325	2,735	243	0.19	2.95
UA15	17.55	0.6529	640	5,065	225.3	0.24	2.49
UA16	17.1	0.5736	635	5,175	219.1	0.23	1.93
UA17	19.05	0.5538	675	5,790	245.7	0.17	1.09
UA18	18.6	0.5791	695	6,015	239.6	0.14	1.42
UA19	20.6	0.5772	675	5,780	266.9	0.16	1.22
UA20	20.1	0.6338	705	5,745	260.8	0.2	1.42
UA21	23.65	0.6399	850	7,270	308.5	0.18	2.05
UA22	23.2	0.5853	800	6,790	302.4	0.17	2.2
UA23	22.1	0.625	410	4,990	287.4	0.11	5.13
UA24	21.65	0.6152	560	4,840	281.2	0.15	1.17

Table 4.4 Soil parameters related to yield calculated from the pressuremeter tests

The compressive yield shear strains varied considerably depending on the type of soil. Within the glacial till, the yield shear strains were typically between 2.8 and 4.0% with an average of 3.4%. Evaluation of the extensional yield strains suggested that the glacial till reached the onset of plastic deformations at shear strains of approximately 0.18 to 0.22%. The plane strain triaxial tests carried out by Medeiros (1979), compare quite well with the extensional yield shear strains despite the stress paths being different. Medeiros (1979) indicated that the yield strains occurred between 0.35 to 0.5% in plane strain active compression and between 3 to 4% in passive compression. The compressive values obtained during the pressuremeter tests are also slightly higher than those reported by El-Nahhas, (1980) and Whittebolle (1982). They suggested that the onset of yield within the glacial till occurred when shear strains reached values on the order of 1 to 2%. As with Medeiros, the yield shear strains obtained by El-Nahhas (1980) and Whittebolle (1982) are not directly comparable, though would suggest a bound for compressive behaviour.

When the shear stress curves are examined, the glacial till typically appears to be an elasto-plastic (cohesive-frictional) material while the Empress Sand appears to be a strain hardening material. The nature of the shear stress-shear strain curve will influence the selection of the appropriate ideal model used to interpret the data. The elasto-plastic nature of the glacial till suggests that a cohesive-frictional model similar to the model presented by Carter, Booker and Yeung (1986) should be used when interpreting the data.

Figure 4.16 clearly shows a break in the glacial till shear stress-shear strain curve with minor stress accumulation following this break. This implies that the initial portion would be a result of the cohesion while the second region is a function of the material friction. Due to the consistent strength accumulation of the Empress Sand, the selection of the purely frictional Hughes Sand Model (Hughes et al., 1977) would be the most applicable.

As previously discussed, caution should be used in the selection of the ideal model as with each degree of complexity added, the number of unknown and assumed variables increases. It is for this reason that simpler models like the Gibson Clay Model (Gibson and Anderson, 1961) and the Hughes Sand Model (Hughes et al., 1977) have been widely used as industry standards over other methods.

4.7 Consolidation

One of the major challenges with stiff fissured soils is determining representative soil parameters. Due to the high degree of state dependence, sample disturbance and sample size, consistent and reliable laboratory data is often difficult to obtain (Lo, 1970; Morgenstern and Thomson, 1971; Marsland and Butler, 1968; Marsland, 1971 a, and b; and Bishop, 1967). Insitu test methods are often sought out in order to minimize disturbance and to maintain the insitu stresses as close to the native state as possible. Historically, the pressuremeter has been used to provide detailed information regarding the shear modulus, horizontal earth pressure coefficient as well as the drained and undrained shear strength of the soil.

Consolidation tests using a pressuremeter are typically conducted by holding the maximum strain (approximately 10%) constant (Clarke et al., 1979). During this test, the soil pore pressure decay at constant borehole strain is monitored to determine the pore pressure response with time. This requires the operator to continually adjust the pressure in order to maintain a near constant strain of the pressuremeter probe. This has the same effect as a pore pressure dissipation test for a CPTu pushed into a cohesive deposit. At high pressures however, this decay can be rapid and the rate of pressure correction is often difficult to maintain. This test also requires the presence of a pore pressure transducer on the surface of the dilatometer that is in intimate contact with the surrounding soil. This is not always feasible since not all Camkometers are equipped with pore pressure transducers.

Kjartanson et al. (1990) proposed the use of pressuremeter hold tests in order to estimate the creep characteristics of ice. These tests were typically run for 8 to 24 hours in order to allow for complete stress redistribution within the ice sheets tested. Since then, the observation of creep within soils and soft rocks has been assessed using short duration hold tests. These hold tests simply indicated the general plasticity of the soil and allowed for easy differentiation between cohesive and cohesionless soils. In general, these tests are around 3 to 5 minutes in duration and conducted immediately after yielding and prior to an unload-reload loop as illustrated by Withers et al. (1989). The hold tests have the effect of providing a break in what would be an otherwise smooth loading curve as shown in Figure 4.17. To date, no known assessment of the consolidation characteristics have been calculated from these short duration hold tests in stiff to hard cohesive formations.

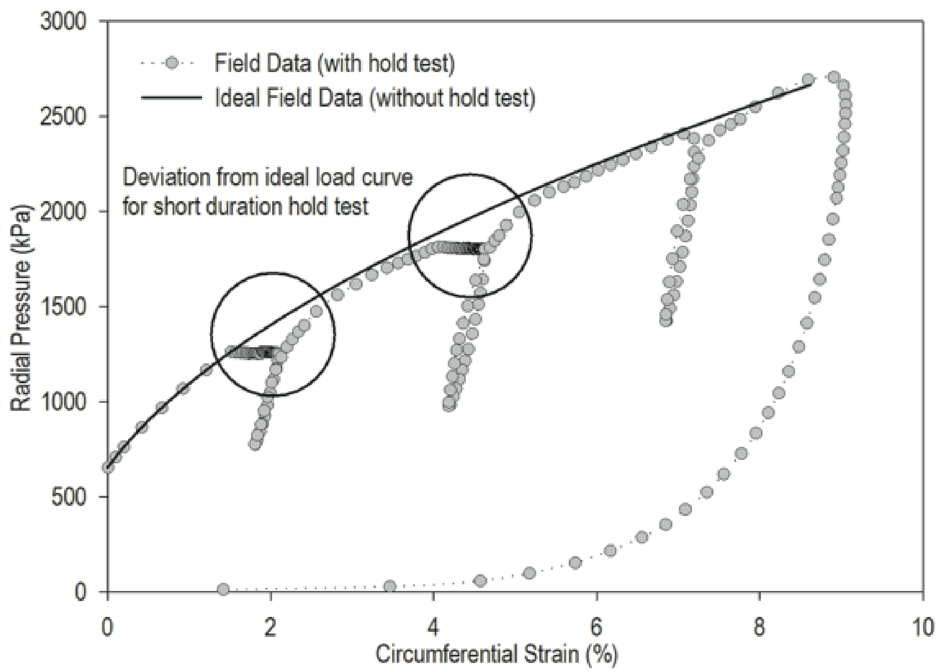

Figure 4.17 Difference between field data with hold tests and ideal field data without hold tests

4.7.1 Consolidation Parameters from a Pressuremeter Hold Test

Pressuremeter analysis using cavity expansion theory, assumes the conditions of plane strain, consequently the displacements in the vertical direction are assumed to be zero. The analysis also assumes that the soil surrounding the borehole is saturated and that pore pressures only develop within the plastic region as described by Carter et al.

(1979). Randolph and Wroth (1979) demonstrated that the pore pressure dissipation could be assumed to be linear with the logarithm of the radius from the borehole wall. Subsequently, it is assumed that the maximum excess pore pressure (Δu_{max}) occurs at the borehole wall and dissipates to zero at the interface of the elastic-plastic regions as shown in Figure 4.18.

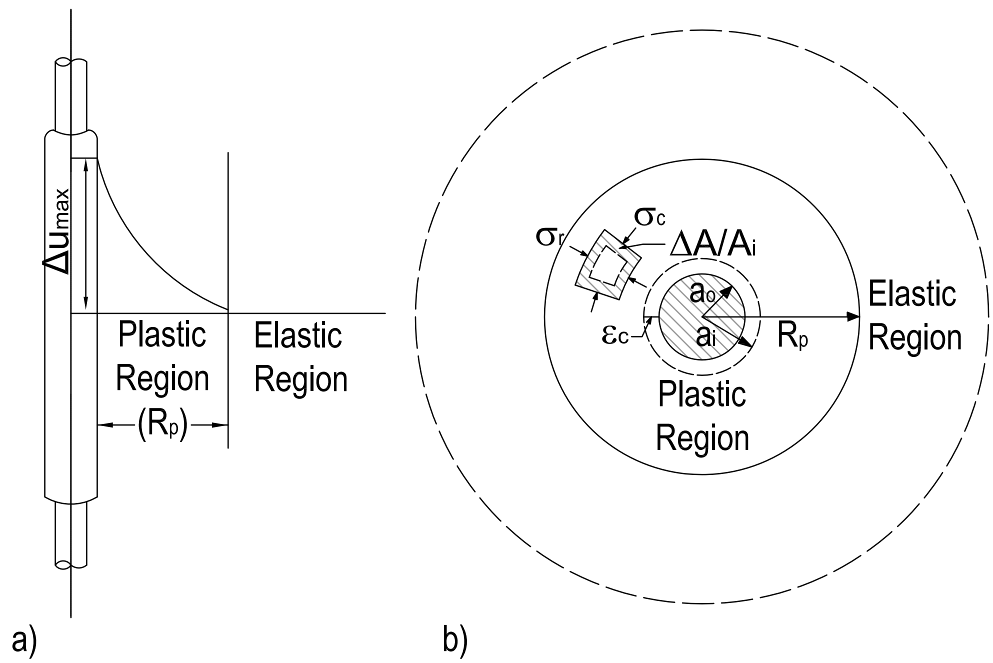

Figure 4.18 Consolidation boundary conditions: a) Excess pore pressure (modified from Carter et al., 1979); b) Assumed strain fields

It is assumed that the soil behaves elastically during consolidation. This was first postulated by Randolph et al. (1979) and has been shown by Clarke et al. (1979) that this assumption results in minimal error. This assumption stems from the fact that consolidation around a sheared borehole is in the form of unloading. Because unloading is taking place, the stress path results in a decreasing deviator stress (q), which results in elastic deformation. Because if the borehole strain is kept constant as suggested by Clarke et al. (1979), the applied radial pressure must decrease with time in order to maintain a constant borehole radius. This confirms that indeed unloading is taking place and that the soil is deforming elastically as long as the unloading pressure needed for constant strain is not greater than $2c_u$. Finally, it is assumed that any increase in the plastic radius is negligible under constant pressure and that all strains measured during the hold test are solely a result of excess pore pressure dissipation and the associated particle realignment. The assumed boundary conditions are illustrated in Figure 4.18.

The proposed interpretive method uses the Taylor Method (root time) for interpreting the constant stress test where pore pressures are not monitored. The Taylor method of consolidation estimation assesses that the rate in change of borehole radius with respect to the square root of time. The Taylor method is adequate for the calculation of primary consolidation only and cannot be used for estimation of secondary compression. By plotting the measured change in radial displacement with the square root of time, the times to 50 and 90% consolidation (t_{50} and t_{90}) are easily determined.

Once the time to 50% consolidation is obtained, the maximum theoretical excess pore pressure at the borehole wall, derived by Clarke et al. (1979) must be calculated in order to obtain the non-dimensional time factor to 50% pore pressure dissipation (T_{50}) as described by Carter et al. (1979). The maximum excess pore pressure is given as Equation 4.5.

$$\Delta u_{\max} = s_u \left[\ln\left(\frac{G}{s_u}\right)\left(\frac{\Delta V}{V}\right) \right]$$

Equation 4.5

where,

Δu_{max} is the maximum excess pore pressure at the borehole wall;
G is the shear modulus of the soil;
s_u is the undrained shear strength of the soil; and

$\Delta V/V$ is the change in probe volume over the current probe volume, for a Camkometer, this term is equivalent to $\Delta V/_V = 1 - \left(\frac{1}{1+\varepsilon_c}\right)^2$.

It is important to note that the calculated maximum excess pore pressure is applicable for a given load and will vary considerably for higher applied borehole pressures.

The non-dimensional time factor for 50% pore pressure decay (T_{50}) is determined using the chart derived by Carter et al. (1979) and the curve adapted for pressuremeter loading of Clarke et al. (1979) is shown as Figure 4.19.

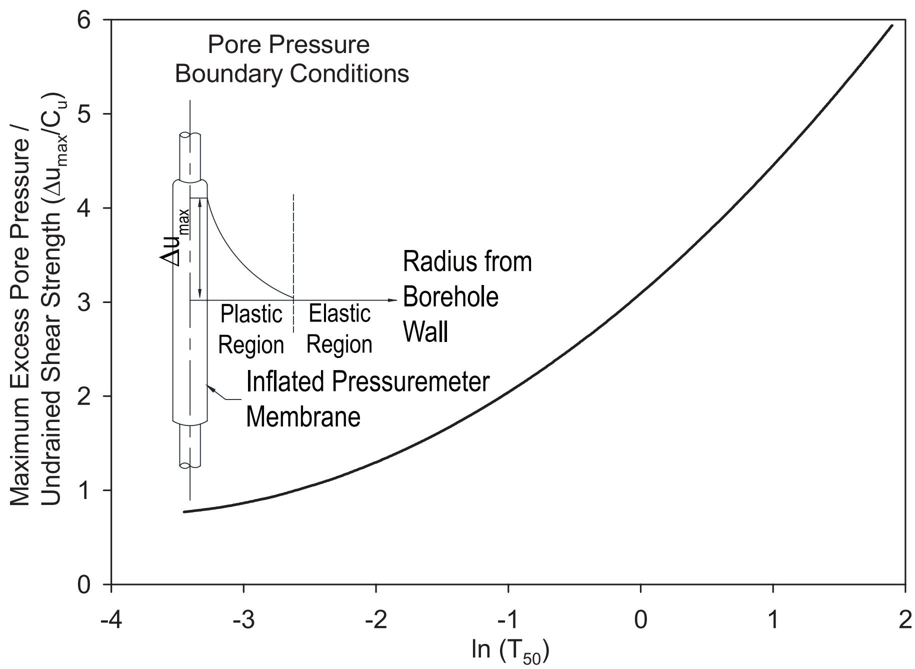

Figure 4.19 Time to 50% pore pressure dissipation (after Carter et al., 1979)

Once the T_{50} had been determined, the coefficient of horizontal consolidation (c_h) may then be calculated from the time to 50% consolidation and the borehole radius at the start of the hold test. The derivation for c_h based on pore pressure dissipation tests is provided by Clarke (1995) and is given as Equation 4.6.

$$c_h = \left(T_{50} a_{max}^2 / t_{50} \right)$$

Equation 4.6

where,

a_{max} is the radius of the borehole at the start of the consolidation test; and

t_{50} is the time to 50% consolidation obtained from the Taylor method.

Like the estimation of the maximum excess pore pressure, the coefficient of consolidation is a function of the state of stress applied to the borehole at the time of the hold test. Because a_{max} is a function of the applied borehole pressure, the borehole radius can be considerably larger for hold tests conducted at the later stages of the loading curve. This aspect has a significant impact on the calculated coefficient of consolidation as will be demonstrated later.

Once the coefficient of horizontal consolidation has been calculated, that value may then be substituted into Equation 4.7 in order to calculate the horizontal coefficient of hydraulic conductivity (k_h) for a given load case.

$$k_h = \left(c_h \gamma_w / M \right)$$

Equation 4.7

where,

γ_w is the unit weight of water; and

M is the constrained modulus given as $M = \left[2G(1-\upsilon) / (1-2\upsilon) \right]$

where,

G is the shear modulus of the soil; and
υ is the Poisson's ratio.

As described by Terzaghi et al. (1996), it is assumed that the coefficient of permeability is a constant for each load increment and throughout the duration of the test.

This assumption has been shown by Schiffman and Gibson (1964) to not be the case. For the purposes of parameter calculation however, the assumption of constant permeability with consolidation is assumed valid and is used throughout.

Because of the assumption of elastic strains during consolidation, Clarke (1995) suggests that the coefficient of horizontal volume change (m_h) may be calculated by simply taking the inverse of the constrained modulus and is given as Equation 4.8 This means that m_h is simply a function of the measured elastic properties (shear modulus *G* and Poisson's ratio, υ).

$$m_h = 1/M = k_h / c_h \gamma_w$$

Equation 4.8

Since the coefficient of volume change defines the compression characteristics of the soil structure, it is important to determine when the soil achieves a truly saturated state. Prior to this point, the coefficient of volume change will be a function of compression of the occluded air within the voids as well as changes to the soil structure. It is for this reason that for best results, that the consolidation test is held at least two points in the loading cycle, preferably immediately after the onset of yielding and midway through the loading process.

During each pressuremeter test within the glacial till, hold tests were carried out following the onset of yield and prior to an unload-reload cycle. The hold tests consisted of maintaining the applied borehole pressure while monitoring the resulting change in circumferential strain. In most cases the tests were carried out at strains of approximately 3 to 4%, while for tests that resulted in lower strains at higher applied stresses, additional hold tests were carried out at strains of approximately 7%. The ability to conduct one or two hold tests must be determined for each loading test and is solely dependent on the strain rate of the borehole during loading.

4.7.2 Interpretation of Test Results

The determination of the consolidation parameters for two creep tests carried out at a depth of 10 m below the ground surface is described below to illustrate the methodology. The applied pressure – circumferential strain plot for these two hold tests is shown in Figure 4.20. In each case the hold-test data has been highlighted to show the detailed response.

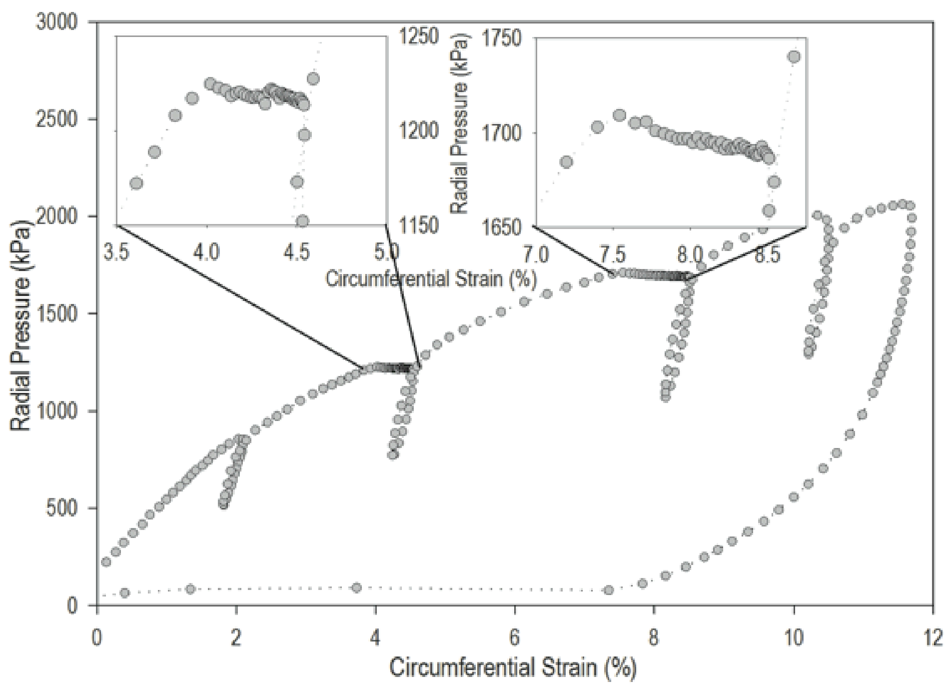

Figure 4.20 Field data of pressuremeter hold test in glacial till

These two tests were carried out with applied radial pressures of roughly 1,220 and 1,700 kPa for the first and second tests respectively. Figure 4.21 and Figure 4.22 illustrate the change in radial borehole displacement relative to the square root of time. The corresponding t_{50} and t_{90} values were determined in accordance with the ASTM standards for a conventional oedometer tests (ASTM D2435-11).

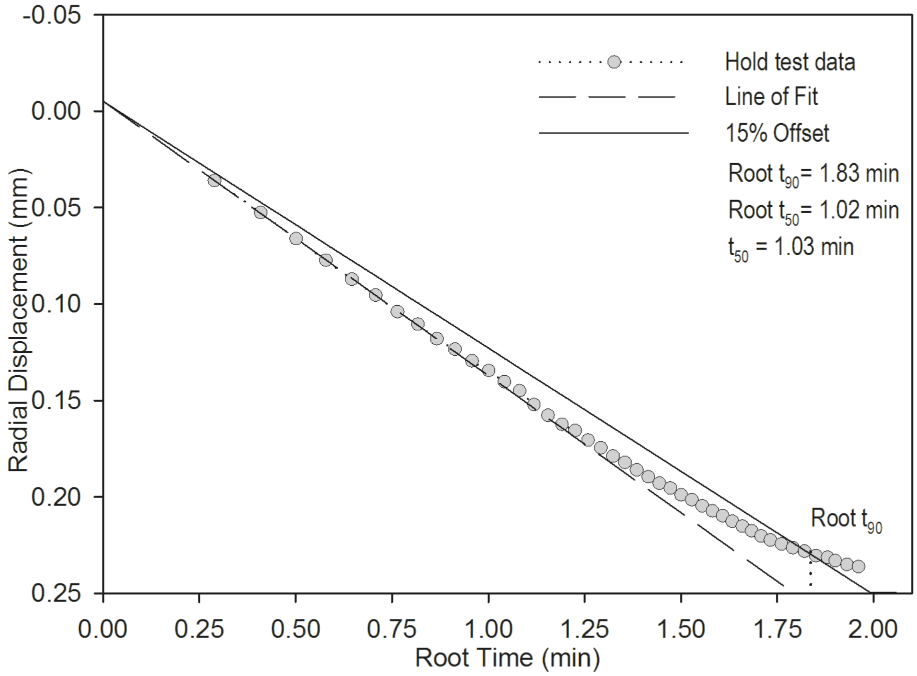

Figure 4.21 Taylor method application of the first hold test to determine consolidation parameters

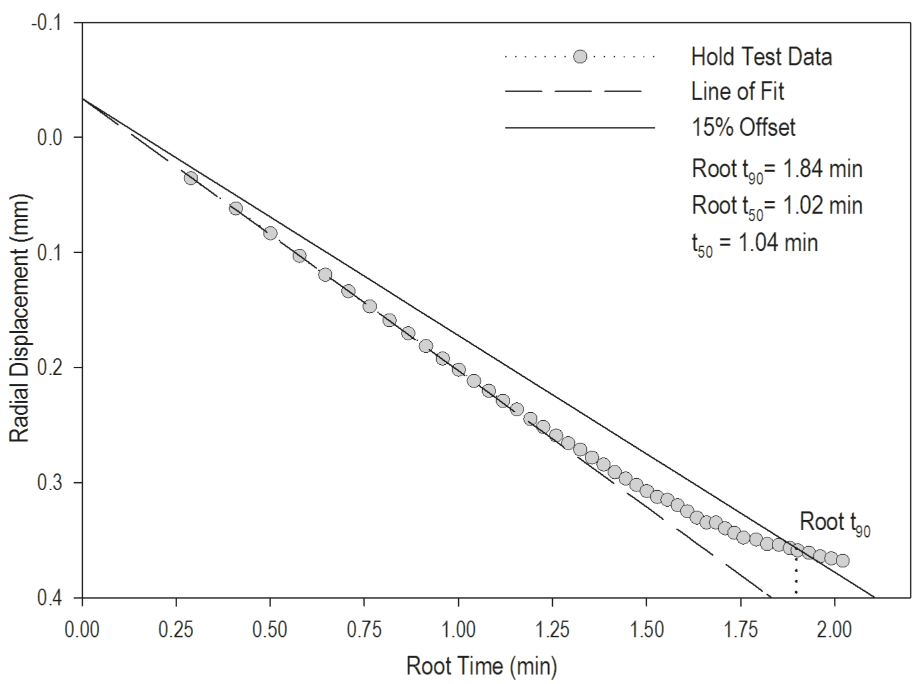

Figure 4.22 Taylor method application of the second hold test to determine consolidation parameters

The tests indicate that the $\sqrt{t_{90}}$ and t_{50} times were 1.83 and 1.03 for the first hold test and 1.84 and 1.04 minutes for the second hold test. Using Equation 4.5, the maximum excess pore pressure at the start of the first hold test for an elastic shear modulus of 87.2 MPa and an undrained shear strength of 350 kPa was calculated to be 1,020 kPa. The maximum excess pore pressure for the second hold test, using the same parameters as the first test but for a larger borehole radius was calculated as 1,231 kPa.

These maximum excess pore pressures where then used to calculate a ratio of maximum excess pore pressure relative to the undrained shear strength in order to determine the time to 50% dissipation of the excess pore pressures (T_{50}). Using the chart developed by Carter et al. (1979) (Figure 4.19), the time factors for 50% pore pressure dissipation for the first and second tests are approximately 0.86 and 1.13. Using these terms as input for Equation 4.6, the coefficients of horizontal consolidation (c_h) are 0.872 and 1.105 m^2/year. These values are in good agreement with the findings of Morgenstern and Thomson (1971) who estimated the range for the glacial till to be between 0.26 to 1.59 m^2/year at for a pressure increment between 190 to 380 kPa.

Using Equation 4.7, coefficients of horizontal permeability (k_h) of 7.5 x 10^{-7} and 3.0 x 10^{-6} cm/s were calculated assuming a Poisson's ratio of 0.34. The hydraulic conductivity (k_v) values given by Morgenstern and Thomson (1971) averaged 1.5 x 10^{-9} cm/s.

Using the inverse of the constrained modulus, coefficients of horizontal volume change (m_h) of 2.8 x 10^{-6} and 8.7 x 10^{-6} kPa^{-1} were estimated for the first and second hold tests. The first hold test estimation agrees well with the vertical coefficient of volume change average value of 3.1 x 10^{-6} kPa^{-1} for an applied load of 1,150 kPa, reported by Morgenstern and Thomson (1971).

4.7.3 Discussion of Consolidation Tests

The results from the pressuremeter hold tests in stiff glacial till discussed above were in good agreement with the laboratory results from high quality samples. However, there are limitations to the application of the Taylor Method in order to interpret the consolidation parameters from a 3 to 5 minute pressuremeter hold test. In order for this method to be applicable, the soil must be heavily overconsolidated and the coefficient of consolidation (c_h) of the soil is less than 2 m^2/year.

It is important to note that the coefficient of horizontal consolidation can only be obtained for tests that appeared to be elastic-perfectly plastic in nature. The appropriate constitutive model is demonstrated by the degree of fit by the conventionally used Gibson Clay Model (Gibson and Anderson, 1961). In the case of these tests, the error associated with the Gibson Clay Model relative to the actual stress-strain curve was less than 5% for a given point on the field data curve. Where a drained cohesive-frictional model such as the one presented by Carter et al. (1984), represents the ground response with an error less than 5%, the consolidation parameters cannot be obtained using the Taylor Method. Examination of the change in strain / root time curves indicated that for the most frictional materials, there was very rarely a break in the strain / root time curve.

The borehole pressure at the start of the hold test used to calculate the corresponding consolidation values plays a critical role in the estimated parameters. Because the maximum excess pore pressure to undrained shear strength ratio was higher in the second test than the first, the estimated T_{50} time factor was increased by approximately 27%. This then had a cascading effect on the calculated parameters (c_h, k_h and m_h), despite the Taylor method indicating nearly identical t_{50} times. This suggests that the method proposed by Clarke et al. (1979) may in fact over estimate the consolidation and hydraulic conductivity parameters as their tests are conventionally carried out at the end of the loading curve.

In order to compensate for this potential error, it is suggested that for hold tests started at shear strains that exceed the compressive yield shear strain (Palmer, 1972), by more than 50% the coefficient of horizontal consolidation should be calculated based on the yield shear strain as proposed by Palmer, 1972. This effectively makes the consolidation calculations solely a function of the applied radial pressure and the associated strain rate measured during the hold test. For example using Palmer's methodology, a compressive yield strain of 3.786% resulted in c_h, k_h and m_h values of 0.821 m^2/yr, 2.2×10^{-7} cm/s and 8.7×10^{-6} kPa^{-1} respectively, which agree very well with the results of the first hold test.

A plot of the calculated consolidation parameters from the tests within the glacial till are shown in Figure 4.23. The values obtained from correcting the initial test radius to that of the yield radius are also shown. When the radius corresponding with the onset of plasticity is used, the test results in parameters are consistent with those obtained from the hold test carried out immediately following the onset of yield as shown on Figure 4.23. Using the compressive yield strain as the starting point of the test, forces the consolidation parameter calculations to become a function of the calculated time to 50% consolidation (t_{50}). Excluding the points outside of the range of values calculated by Morgenstern and Thomson (1971) shown on Figure 4.23, the average c_h, k_h and m_h values are 0.725 m^2/year, 9.3×10^{-8} cm/s and 4.2×10^{-6} kPa^{-1} respectively. Based on the values of c_h, k_h and m_h given by Morgenstern and Thomson (1971) the estimated averaged differ by 16.6, 22.6 and 2.5% respectively.

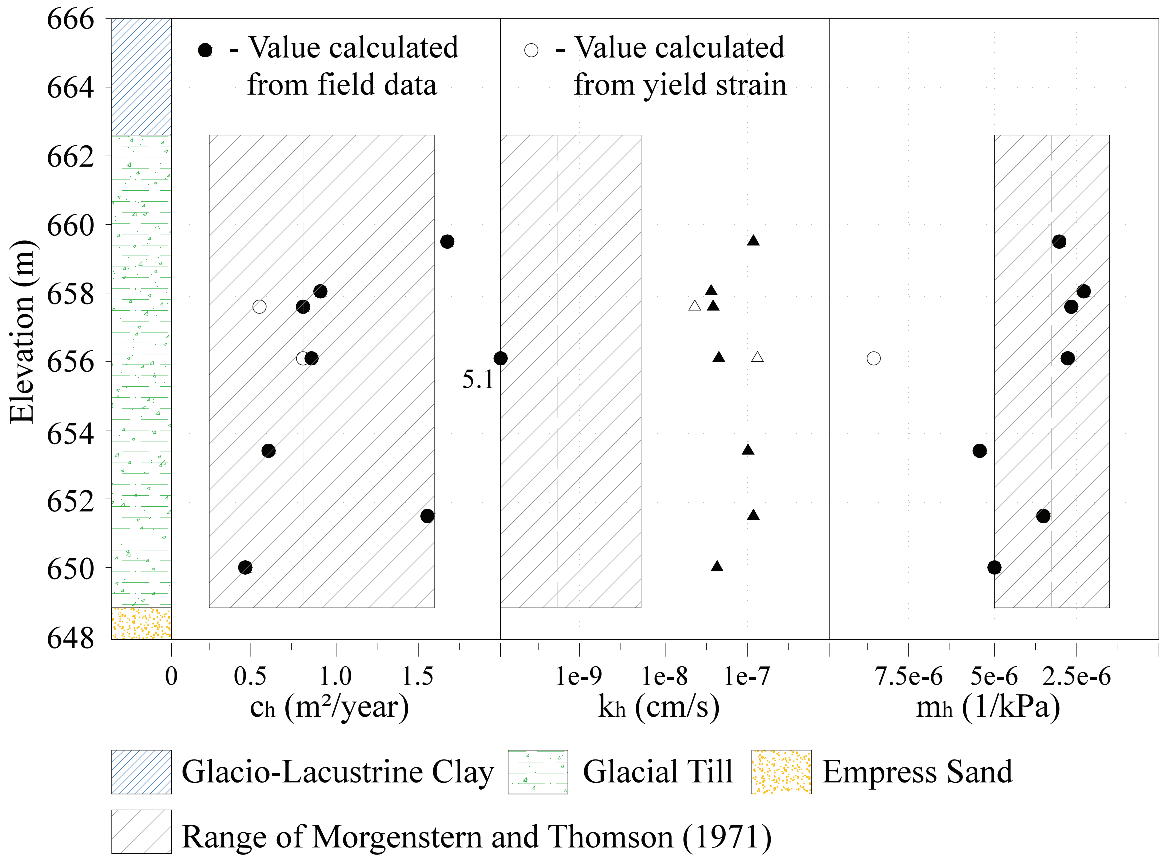

Figure 4.23 Consolidation parameters from pressuremeter hold tests with depth

The difference between the horizontal conductivity values from the hold tests and those reported by Morgenstern and Thomson (1971) may have to do with the sample size used for consolidation testing by the previous authors. Despite the till being a relatively heterogeneous formation in terms of grain size and composition, it is homogeneous in terms of its depositional history. Unlike lacustrine or alluvial deposits, which typically exhibit rhythmic depositional patterns, the Edmonton glacial till in laboratory scale samples, do not generally possess high anisotropy in terms of hydraulic conductivity. With that in mind, it is unlikely that the differences are a result of anisotropy between the k_v and k_h directions, but rather a function of sand content within the test.

4.8 Unsaturated Ground Response

The interpretation of pressuremeter test results assumes that the soil is saturated and the rate of loading is such that undrained conditions apply. When the soil is not saturated, there will be volume changes associated with compression of the occluded air. Consequently, assuming the soil is saturated introduces inaccuracies into the analysis of the pressuremeter test results and the interpretation of the stress-strain profile.

This section presents a method for interpreting pressuremeter test results in a heavily overconsolidated, unsaturated soil. The proposed methodology makes use of the degree of saturation (S_o), porosity (n_o), and the coefficient of volume change (m_h) calculated from a pressuremeter hold-test to determine the transition from unsaturated to saturated soil conditions. A solution is presented for the determination of the total volume change within the plastic region. Volume change is attributed to the compression of the air in the voids under undrained loading conditions, prior to achieving complete saturation. It is important to determine the point at which saturation is reached in order to ascertain the transition from unsaturated to saturated conditions. In other words, the volume change behaviour becomes consistent with undrained cavity expansion once saturation is achieved.

4.8.1 Background

Terzaghi's (1936) theory of consolidation is based on the assumption that the soil is saturated and that excess pore-water pressures increase linearly with the application of an applied pressure. Skempton (1954) provided an equation defining the change in pore pressure of a soil when subjected to spherical and shear stresses. The change in pore pressure, Δu as a function of confining (spherical) and shear stresses is given as Equation 4.9.

$$\Delta u = B\left[\Delta\sigma_3 + A\left(\Delta\sigma_1 - \Delta\sigma_3\right)\right]$$

Equation 4.9

where:

Δu is the change in pore pressure;

$\Delta\sigma_1$ and $\Delta\sigma_3$ are the major and minor principal stresses respectively;

A is the pore pressure contribution to shear stress; and

B is the pore pressure parameter contribution due to the applied confining stress.

Skempton (1954) defined a '*B*' pore pressure parameter to relate changes in the pore-water pressure in a soil to the applied isotropic stress change. When the soil was subjected to shear stress, Skempton (1954) introduced a second pore pressure parameter; namely, the '*A*' parameter. Bishop (1954) demonstrated that when the '*B'* pore pressure parameter was less than unity, the '*A'* pore pressure parameter would also be less than unity and also likely close to zero. This implies that when an unsaturated soil is subjected to shear stresses, the undrained pore-water pressure response will likely be considerably less than assumed by Gibson and Anderson (1961) in the development of their undrained pressuremeter solution. A drained response would be anticipated even under relatively fast loading conditions and a low permeability soil mass.

The method presented here is applicable for either a pre-bore or self-bore pressuremeter test using a conventional Camkometer. During the loading of the borehole, the circumferential strains are monitored in real time by three spring loaded strain gauges positioned at 120° to one another. It is possible to use a Menard type pressuremeter for the interpretation, but because the data is recorded manually rather than by a data logger, the accuracy of the results is limited. The interpretation was based on data recorded by a pre-bore pressuremeter in a very stiff to hard glacial till.

4.8.2 Hilf's Method of Pore Pressure Prediction

Hilf (1948) assumed that when the matric suction in an unsaturated soil was negligible, the change in pore-air pressure was equal to the change in pore-water pressure during loading. Consequently, the saturation of a soil could be defined as the point where the pore-air pressure was equal to the pore-water pressure as described by the matric suction variable, (u_a - u_w) (Fredlund and Morgenstern, 1977). The change in pore-air pressure required to achieve saturation can be defined by the variable, $\Delta u_{a(sat)}$ and calculated using the equation derived by Fredlund et al., (2012).

$$\Delta u_{a(sat)} = \left(\frac{1 - S_o}{S_o h} \right) u_{ao}$$

Equation 4.10

where:

S_o is the initial saturation of the soil,

h is Henry's coefficient of solubility of air into water, assumed as 0.02; and

u_{ao} is the initial pore-air pressure, (usually assumed to be atmospheric, (101.3 kPa).

Fredlund et al., (2012) evaluated the graphical methods proposed by Hilf (1948) and developed the following equation which accounted for the volume change of the soil within the plastic region during loading.

$$\Delta u_a = \left[1 \Big/ 1 + \frac{(1 - S_o + hS_o) n_o}{\left[(u_{ao} + \Delta u_a) m_h \right]} \right] \Delta \sigma_r$$

Equation 4.11

where:

$\Delta\sigma_r$ is the change in applied radial pressure,

n_o is the initial porosity of the soil prior to consolidation,

m_h is the coefficient of horizontal volume change for the soil skeleton; and

Δu_a is the change of pore-air pressure with a change in applied stress.

When the stress path of the ground surrounding a pressuremeter is considered, the boundary conditions related to the pore-air and pore-water response must be developed. Randolph and Wroth (1979) first reported the boundary conditions of pore-water pressure accumulation (and dissipation) around a pressuremeter borehole. It was demonstrated that the maximum excess pore-water pressure occurs at the borehole wall, while dissipation could be assumed to be linear with the logarithm of the radius from the borehole wall (Figure 4.24). The maximum change in pore-air pressure will also occur at the borehole wall when the pore-air pressure boundaries are considered for an unsaturated soil. The pressure will vary linearly with the logarithm of radius as per Randolph and Wroth (1979), but to a minimum of u_{ao}. The minimum pore-air pressure will be equal to atmospheric pressure and occur at the boundary between the plastic and elastic regions (Figure 4.24). This condition can then be used to determine the change in matric suction, (u_a - u_w), around the pressuremeter probe. The suction will increase from saturation at the borehole wall to the *in situ* state at the boundary of the plastic and elastic zones. As saturation is achieved ($\Delta u_a = \Delta u_w$), and the plastic region continues to grow, the saturated zone within the plastic region will progressively extend away from the borehole wall. In turn, the pore-air pressure gradient from $\Delta u_{a(sat)}$ at the limit of the saturated and unsaturated soils to u_{ao} at the interface with the elastic region will move with the saturation zone away from the borehole wall (Figure 4.24).

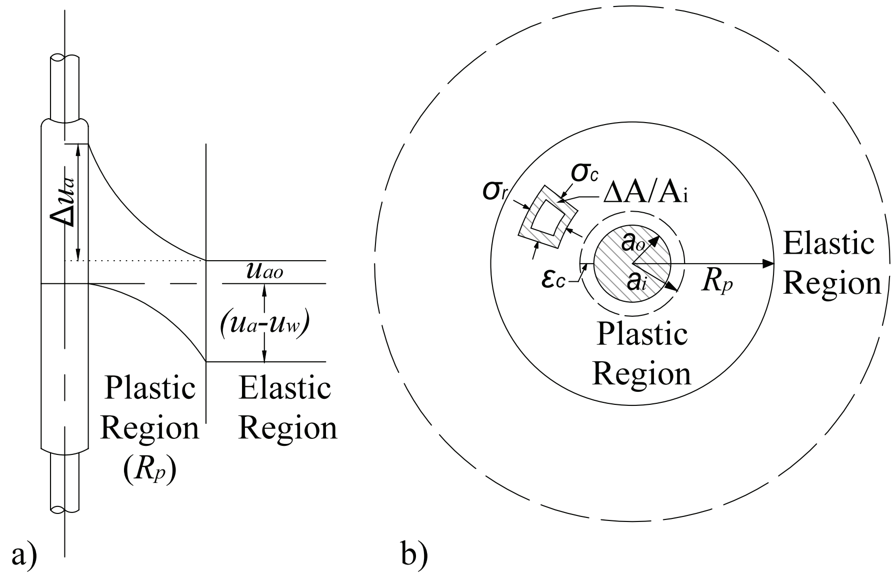

Figure 4.24 a) Pore-air pressure boundary conditions around the pressuremeter probe; and b) Volume change due to compression of pore-air around pressuremeter probe

The boundary conditions described by Carter et al. (1979) can be used to determine the volume changes which occur due to compression of the occluded pore-air. The net stress change is zero since the circumferential and radial stresses are equal and opposite within the elastic zone. This implies that volume changes can only occur following initial yield of the ground around the pressuremeter probe. Figure 4.24 (b) illustrates the nature of the compression within the plastic region during loading of the pressuremeter prior to saturation.

4.8.3 Influence of Degree of Saturation on Volume Change in the Pressuremeter Test

The change in area of the plastic region must be considered so that the plane strain changes in volume around a pressuremeter due to compression of the air-filled voids can be assessed. This change can be expressed in terms of a change in area with respect to the current borehole area, $\Delta A/A$, and can be calculated for the Camkometer style pressuremeter (Wroth and Hughes, 1973) using Equation 4.12.

$$\Delta A/A = 1 - 1/(1+\varepsilon_c)^2$$

Equation 4.12

where,

$\Delta A/A$ is the ratio of change in area within the plastic region over the current borehole (or probe) area; and

ε_c is the average circumferential strain measured by the three spring loaded strain gauges.

The volumetric strain of the plastic region around a loaded pressuremeter is quantified for plane strain conditions (i.e., zero change in the vertical direction). The change in volume of the plastic region for various saturation levels and porosities can be determined using the change in volume of a sample due to the compression of the air-filled voids, ($\Delta A/A$) to the point of saturation (Fredlund et al., 2012). The change in volume due to the compression of air-filled voids (i.e., change in porosity, Δn) at a given saturation is given by Fredlund et al. (2012) in Equation 4.13.

$$\Delta A/A = \left(\Delta u_a/u_{ao} + \Delta u_a\right)(1 - S_o + hS_o)n_o$$

Equation 4.13

When

Equation 4.13 is plotted with respect to the change in pore-air pressure, (Δu_a), a trend emerges that indicates the approach of saturation. Figure 4.25 illustrates an example rate and total change in volume of the plastic region, ($\Delta A/A$) of a generic soil with an initial porosity of 0.2, for a change in pore-air pressure, (Δu_a) and initial degrees of saturation ranging from 85 to 97.5%. The predicted saturation pressures can be calculated using Equation 4.10 and are also shown on Figure 4.25 as the single points (diamonds) on each curve. In each case, the volumetric changes associated with 100% saturation were subtracted from each curve. Subtraction of the volume changes at saturation removes any effect related to elastic strains within the soil structure or consolidation resulting from the displacement of pore-water. Clarke et al., (1979) and Randolph et al., (1979) assumed that consolidation around a pressuremeter probe was elastic and therefore the correction applied to the calculations in Figure 4.25 for 100% saturation effectively eliminated the elastic strains from within the plastic region.

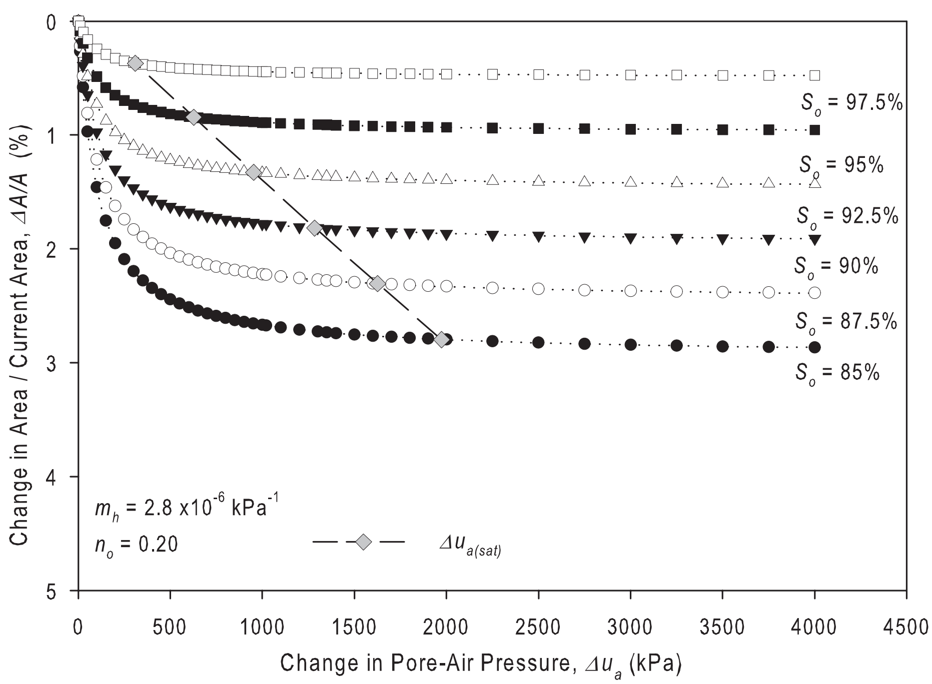

Figure 4.25 Change in $\Delta A/A$ (i.e., porosity) with respect to change in pore-air pressure (n_o = 0.20)

The results in Figure 4.25 appear to indicate that up to the change in pore-air pressure required to attain saturation indicated by the diamonds, there are some volume changes taking place. After the predicted saturation pore-air pressure is reached, the volume changes approach zero for any increase in pore-air pressure. The change in volume suggests that there is ongoing consolidation within the plastic region around the borehole due to the compression of the air within the voids until saturation is reached. At this point, the change in pore-air pressure is equal to the change in pore-water pressure, ($\Delta u_a = \Delta u_w$), and consolidation becomes a function of the excess pore-water pressure and the compressibility of the soil particles. Alternatively, if the hydraulic conductivity of the soil is sufficiently low to not permit drainage of excess pore-water pressures, then the ground response is undrained and volume change is absent. The proposed model then conforms to the assumption of a saturated clay formation under undrained conditions postulated by Gibson and Anderson (1961). This then suggests that the ground will develop positive pore pressures under increased loading and volume changes are negligible. When these assumptions apply, then the closed form analytical solution given by Gibson and Anderson (1961) are considered correct.

Based on the findings of Figure 4.25, a chart has been developed to establish the degree of volume change that occurs around a pressuremeter probe during loading. Figure 4.26 illustrates the volumetric changes per unit length within the plastic region for a wide variety of pore-air saturation pressures, $\Delta u_{a(sat)}$, and initial porosities, n_o. Provided the change in pore-air pressure required for saturation given as Equation 4.10 and the porosity is known, the total volumetric changes during initial loading may be predicted.

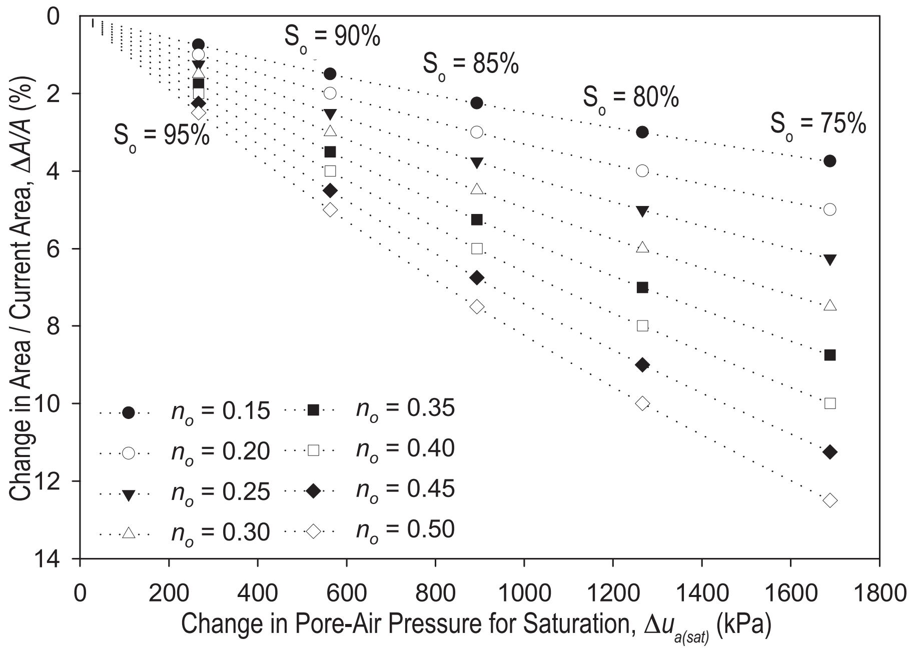

Figure 4.26 Volumetric changes of air-filled voids to the point of saturation

Once the volumetric change with respect to changes in pore-air pressure have been calculated, the overall response of the ground in terms of both total and effective stresses can be calculated. These stress components are only valid within the unsaturated zone. Once saturation is attained, the Skempton (1954) '*B*' pore pressure parameter is equal to 1.0 and the change in pore-water pressure is equal to the change in applied normal stress. At this point the Skempton '*A*' pore pressure parameter relating the excess pore-water response to the applied shear stress also becomes a maximum. This analysis only considers the case of the pore-air response when the material is unsaturated and therefore, the positive pore-water response with respect to borehole loading is considered to be beyond the scope of this research.

The influence of the coefficient of horizontal volume change, m_h, on the applied borehole pressure was also investigated. The purpose was to determine at what m_h the ground would respond as a saturated material regardless of the degree of saturation. In order to bound the solution, the initial porosity, n_o, for each case was varied from 0.2 to

0.45. The m_h was then varied from 2.5×10^{-6} to 1×10^{-3} kPa^{-1} and the degree of saturation was varied from 80 to 95%. Because the calculation of the change in area (drained compression) is iterative based on the change in pore-air pressure, Δu_a; the coefficient of horizontal volume change, m_h; and the applied pressure, $\Delta \sigma_r$, one of the three parameters had to be selected as static. The change in pore-air pressure was therefore selected as the change in pore-air pressure at saturation, $\Delta u_{a(sat)}$. Figure 4.27 demonstrates how the applied borehole pressure to achieve saturation varies with respect to the coefficient of horizontal volume change, m_h.

Figure 4.27 shows that for coefficients of horizontal volume change, m_h, greater than 10^{-4} kPa^{-1}, the ground generally responds as a saturated material regardless of the degree of saturation. Since the borehole pressure approaches the minimum saturation pressure regardless of the initial void ratio, the applied pressure is immediately equal to that needed to achieve the change in pore-air pressure for saturation, $\Delta u_{a(sat)}$. The immediate collapse suggests that the air-filled voids are soft and rapidly compresses under loading resulting in instant saturation. It is also important to note that for values of m_h less than 1×10^{-6} kPa^{-1}, it is unlikely that saturated conditions will ever be achieved for soils with a degree of saturation less than 90% and a porosity, n_o, greater than 0.25. This is because the required borehole pressure would be greater than is reasonably achievable by most pressuremeter equipment. Therefore the applicability of the Hilf method is bounded for coefficients of horizontal volume change between 10^{-6} kPa^{-1} and 10^{-4} kPa^{-1}. Usage of the above method for soils with m_h values less than 10^{-6} $kPa^{-}1$ is not realistically feasible. Additionally, its application is irrelevant for soils with m_h values greater than 10^{-4} kPa^{-1} as these soils respond as fully saturated.

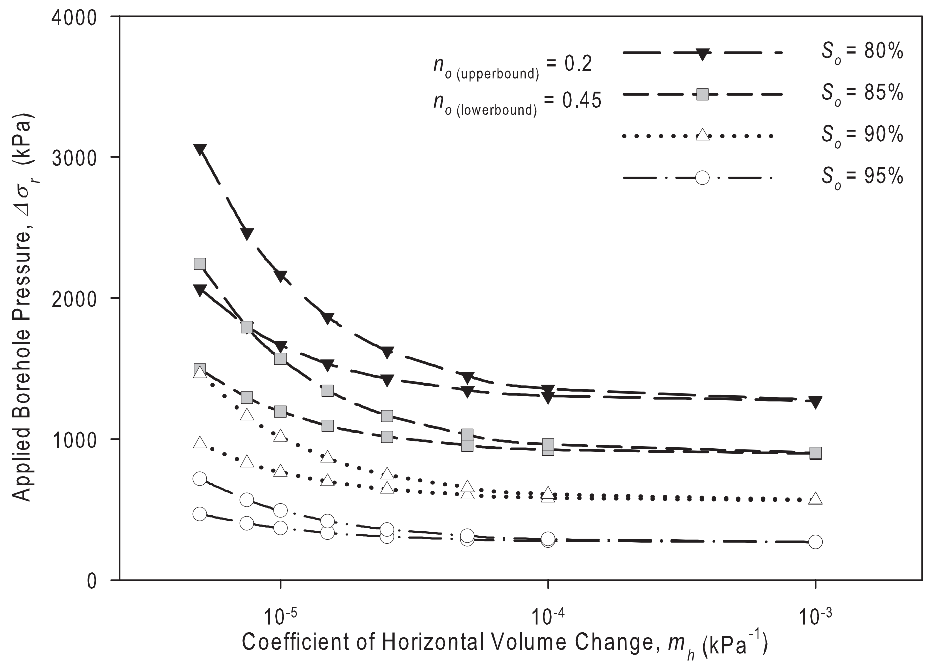

Figure 4.27 Influence of m_h on the saturation borehole pressure

In order to demonstrate the bounding limits of m_h above, the change in pore-air pressure, Δu_a, was compared with the change in applied borehole pressure, $\Delta\sigma_r$. Saturation has been shown (Skempton, 1954) to occur when the slope of the line ('*B*' parameter) is equal to 1.0. A coefficient of horizontal volume change, m_h, above 10^{-4} kPa^{-1} results in a '*B'* parameter equal to 1.0, 10^{-4} kPa^{-1} which can be considered to be an upper bound for unsaturated volume change around a pressuremeter probe. The response of a ground with a porosity of 0.275 and values of m_h ranging from $5\text{x}10^{-6}$ to $5\text{x}10^{-5}$ kPa^{-1} is shown in Figure 4.28. The degree of saturation was varied from 75 to 95% in all cases.

Figure 4.28 shows that for unsaturated soils with a lower m_h, the borehole pressure required to achieve a '*B'* value of 1.0 is much higher. For the soils with saturations above 85% and an m_h of $5\text{x}10^{-5}$ kPa^{-1}, a '*B'* parameter of 1.0 is achieved after loading the borehole past 500 kPa which is generally lower than the undrained shear strength of the ground for most soils within this range of coefficient of horizontal volume change, m_h.

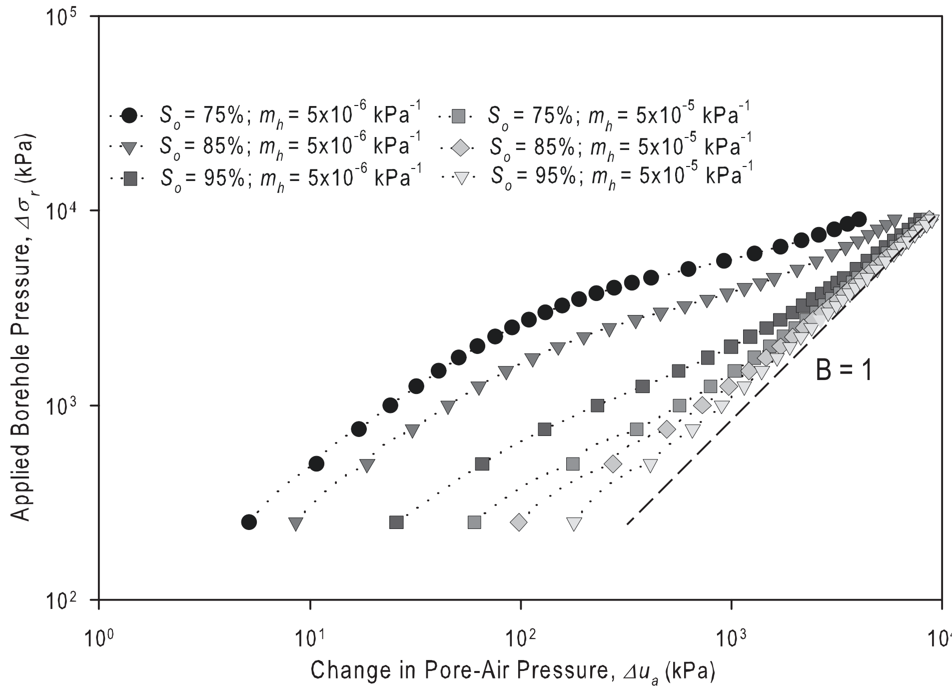

Figure 4.28 Applied borehole and change in pore-air pressure for m_h = 5x10^{-4} to 5x10^{-5} kPa^{-1}

The total change in volume up to saturation is the same regardless of m_h. This suggests that the total volume change is solely a function of the porosity, n_o, and initial degree of saturation, S_o. The coefficient of horizontal volume change only affects the borehole pressure required to achieve saturation. Figure 4.29 demonstrates the influence of m_h on the change in volume within the plastic zone. For the case of m_h = 5x10^{-6} kPa^{-1}, it is clear that the total volume change is the same as that of 5x10^{-5} kPa^{-1} but the applied pressure to achieve saturation, (i.e. 'B' = 1.0), is between two to three times higher.

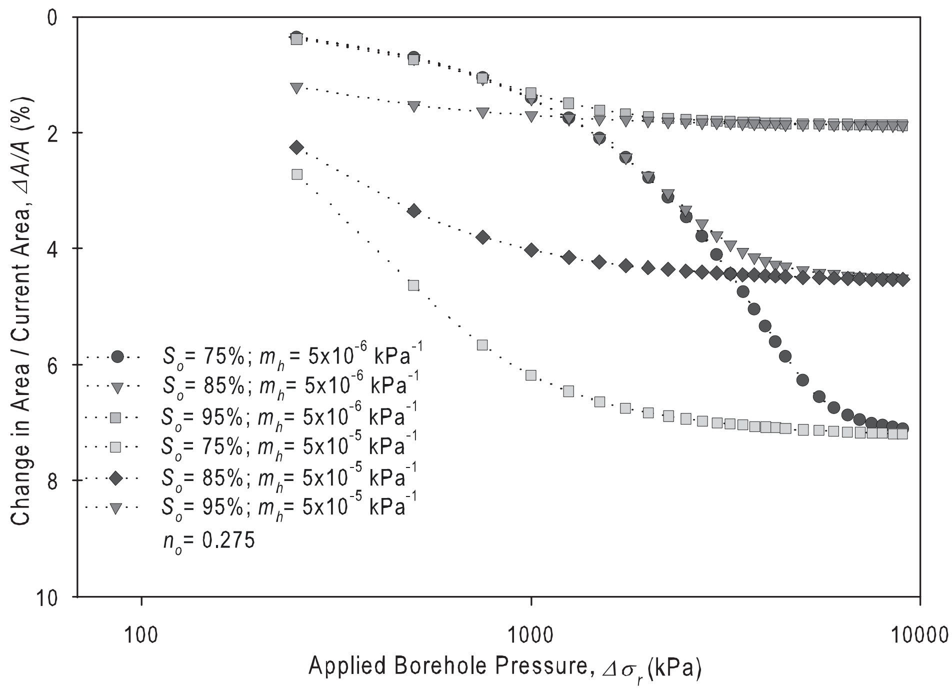

Figure 4.29 Influence of m_h on the change in volume due to the applied borehole pressure

A review of the sensitivity of the value of m_h shows that it is generally controlled by the permeability of the soil rather than the compressibility. If the coefficient of horizontal consolidation, c_h, is examined as a function of m_h, Whittebolle (1982) suggested that the maximum range of c_h for the Edmonton till would be between 0.1 to 3 m^2/year. Figure 4.23 shows that c_h varies from around 0.5 to 1.5 m^2/year, with a typical value around 0.85 m^2/year in the Edmonton till. In order for m_h to vary by an order of magnitude or more, the permeability of the ground must be the controlling factor. Considering this, soils with a low m_h are considered to respond as drained during initial loading to the point of saturation.

To determine the sensitivity of the total volume change to the porosity of the soil, the upper bound of porosity for the glacial till (n_o = 0.3) has been selected to replot the information provided in Figure 4.25. The volumetric changes calculated for a porosity of 0.3 and for a range of degrees of saturation are shown in Figure 4.30. Based on Figure 4.25 and Figure 4.30, the porosity appears to be the most significant variable affecting the maximum change in volume for degrees of saturation between 85 and 95%. The difference between the total volume change of soils with porosities of 0.2 and 0.3 and saturations of 85 and 95% are 40 and 12% respectively. This suggests that a soil with a saturation of 95% will not be as dependent on an accurate determination of porosity as a sample with a lower saturation.

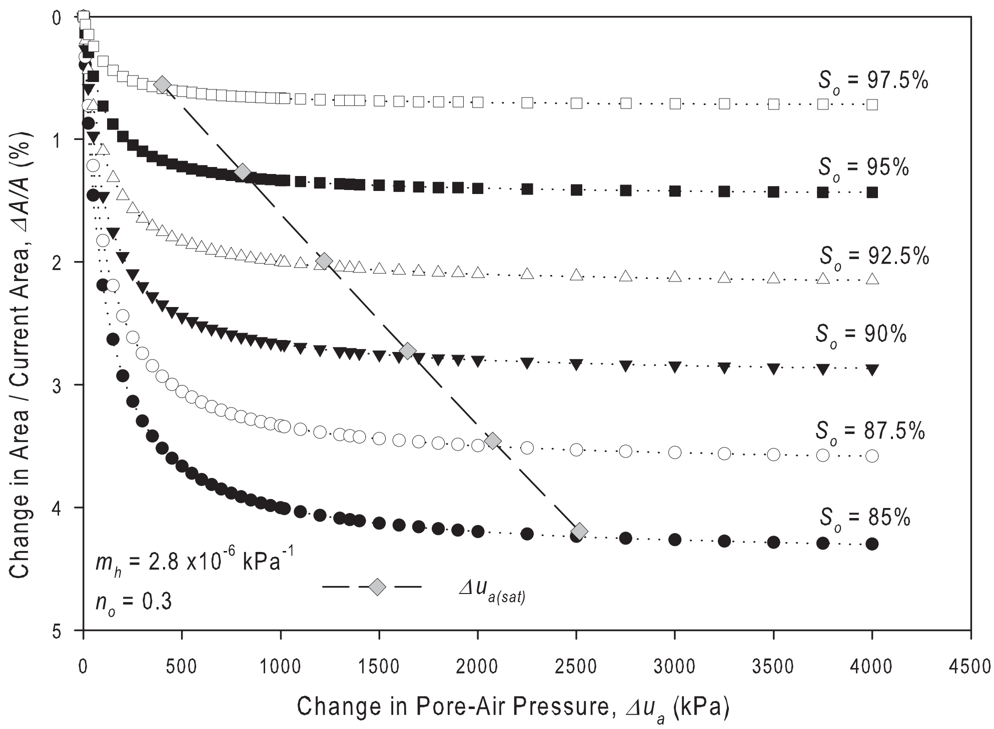

Figure 4.30 Change in $\Delta A/A$ (i.e., porosity) with respect to change in pore-air pressure (n_o= 0.30)

In order to determine the borehole pressure required to attain the change in pore-air pressure for saturation at a given saturation, the values were plotted for coefficients of horizontal volume change (m_h) ranging from $5x10^{-4}$ to $5x10^{-6}$ kPa^{-1}. Figure 4.31 illustrates the change in borehole pressure required to attain saturation for a range of saturations.

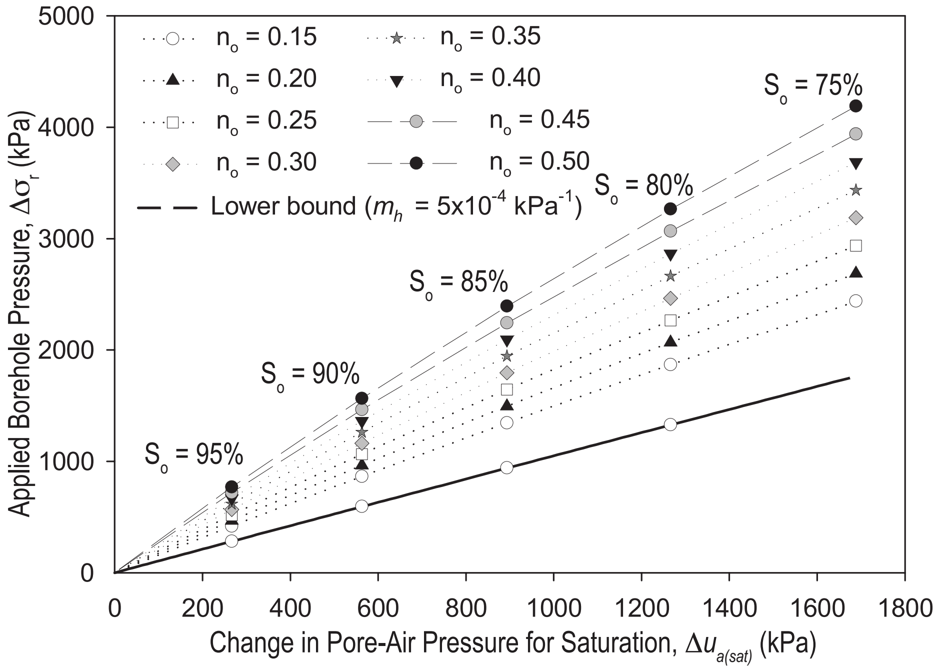

Figure 4.31 Borehole pressure required for saturation for $m_h = 5 \times 10^{-4}$ to 5×10^{-6} kPa^{-1}

4.8.4 Application to Field Data

The calculation of the saturation point and the associated volume change during loading of the heavily over-consolidated cohesive till in Edmonton can be performed as follows. The change in applied radial pressure can be calculated using Equation 4.11 for the case where the pore-air pressure required for saturation, Δu_a, given by Equation 4.10 is known. The incremental change in volume during loading can be calculated once the radial borehole pressure for saturation is known. Plotting the change in pore-water pressure with applied radial stress then illustrates the point of near zero volume change for a given change in radial stress or the saturation point. Figure 4.32 provides a flow chart illustrating the steps required to assess the saturation point of the soil; the radial borehole pressure required for saturation and the total volume change that occurs due to compression of the air-filled voids within the soil.

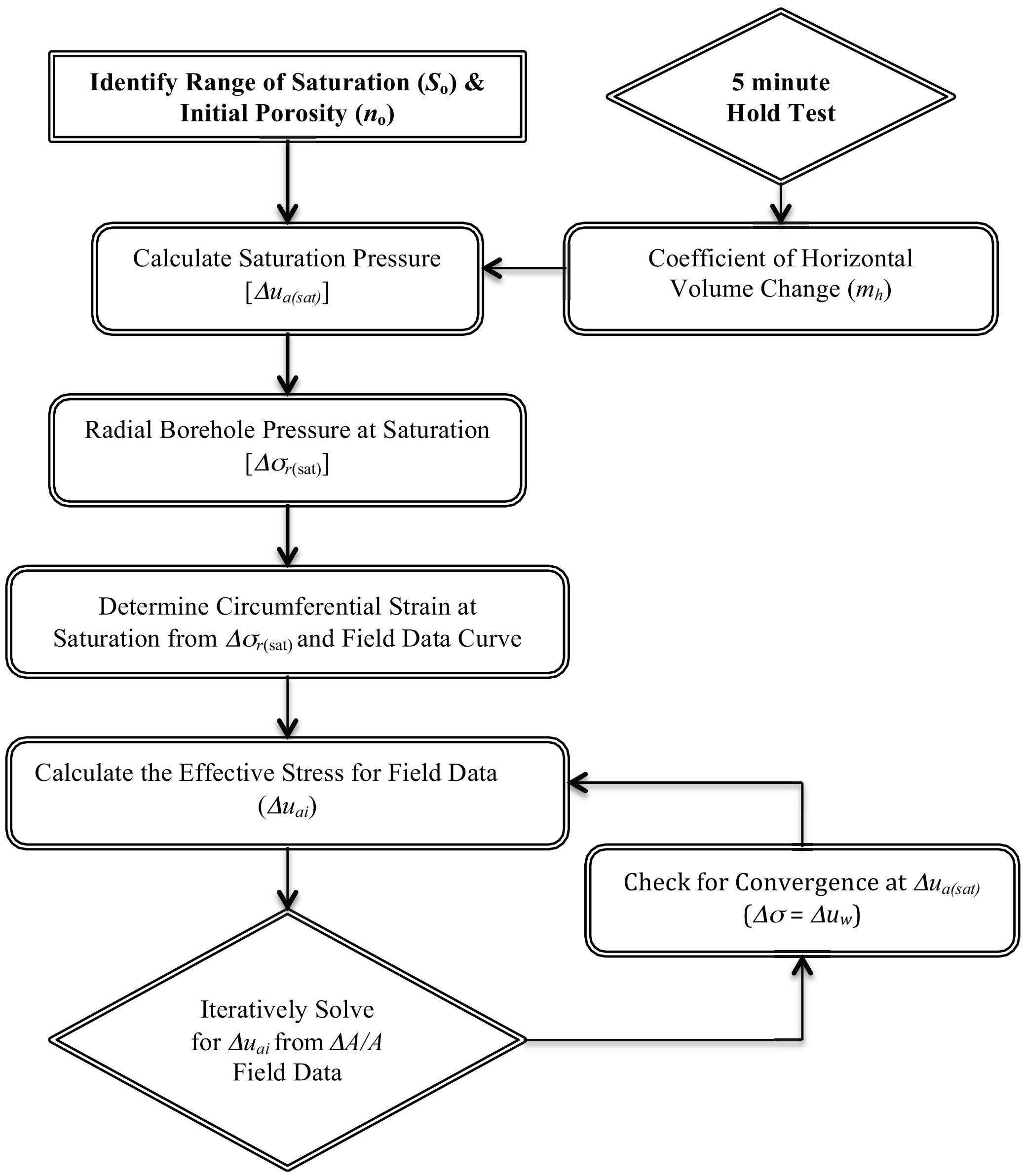

Figure 4.32 Flow chart for determination of saturation point and total volume change from a pressuremeter test in unsaturated soils

Pressuremeter tests UA05 and UA13 at respective depths of 9.9 and 16.0 m within the Edmonton glacial till have been selected as representative samples to demonstrate the application of the proposed method. The consolidation parameters, m_h, were determined using the method described in Section 4.7 and were taken as 2.77×10^{-6} and 5.0×10^{-6} kPa^{-1} for UA05 and UA13 respectively. The saturation of the ground was assumed to be uniform with depth and was selected as the historical average of 90.7%. Therefore a single change in pore-air pressure at saturation [$\Delta u_{a(sat)}$] of 519.3 kPa for each pressuremeter test can be calculated using Hilf's method.

The results for a test performed at a depth of 9.9 m below the ground surface (UA05) are shown in Figure 4.33. For porosities ranging from 0.26 to 0.3, the radial pressure applied by the pressuremeter required to compress the soil to the point of saturation is between 1,391 to 1,525 kPa. For UA13, the borehole pressure required to achieve saturation is between 1,002 to 1,076 kPa for porosities ranging from 0.26 to 0.3. The loading curve and the expected saturation point for UA13 are shown on Figure 4.34.

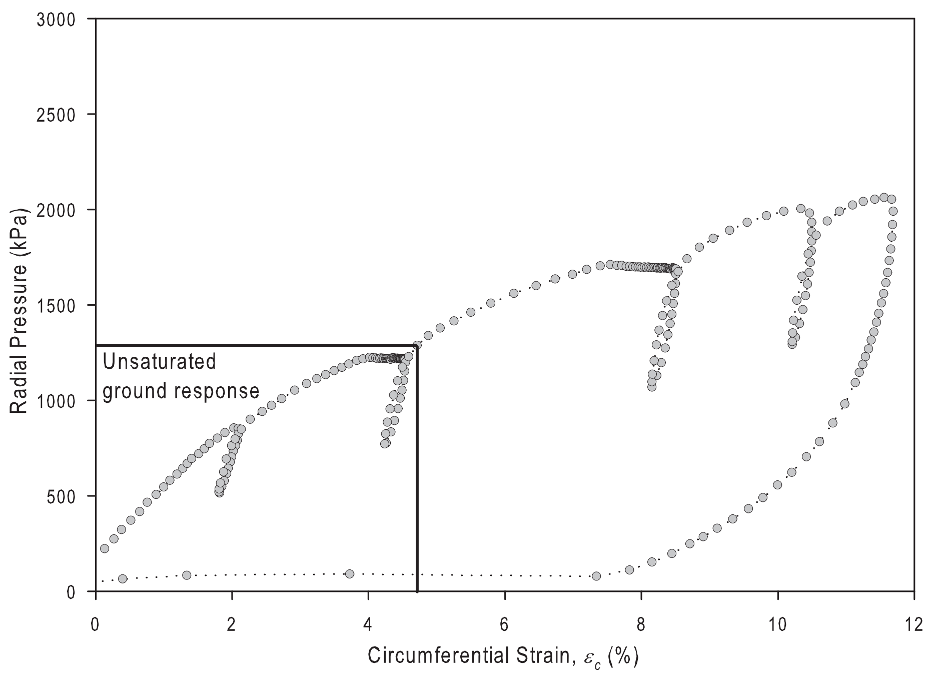

Figure 4.33 Field data and unsaturated response from Edmonton till at a depth of 9.9 m

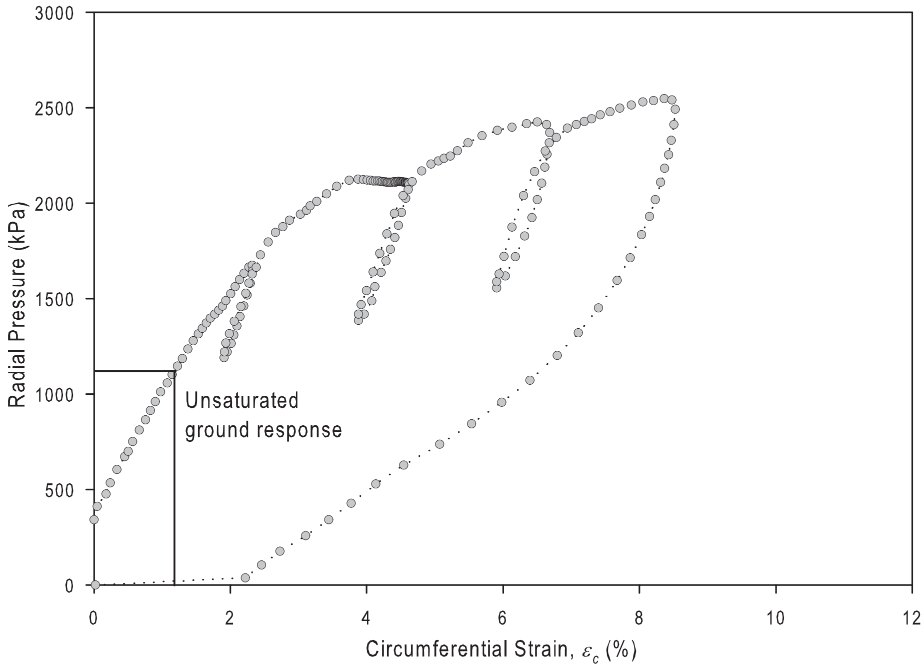

Figure 4.34 Field data and unsaturated response from Edmonton till at a depth of 16.0 m

Assuming that Hilf's method provides an accurate estimation of the saturation point of the soil, minimum radial pressures of 1,391 and 1,002 kPa must be applied to UA05 and UA13 respectively for the soil to achieve a truly undrained response. The corresponding volumetric changes per unit length, $\Delta A/A$, which occurs prior to saturation, are a function of the coefficient of volume change, m_h and the applied borehole pressure. The volumetric changes that are calculated to occur prior to saturation for UA05 and UA13 are 2.7 and 2.2% respectively. The resulting change in volume with change in pore-air pressure during the initial loading of the pressuremeter for the test at a depth of 9.9 m (m_h = 2.8 x 10^{-6} kPa^{-1}) is shown in Figure 4.33 while the curves for the test at 16.1 m depth (m_h = 5.0 x 10^{-6} kPa^{-1}) are shown in Figure 4.34.

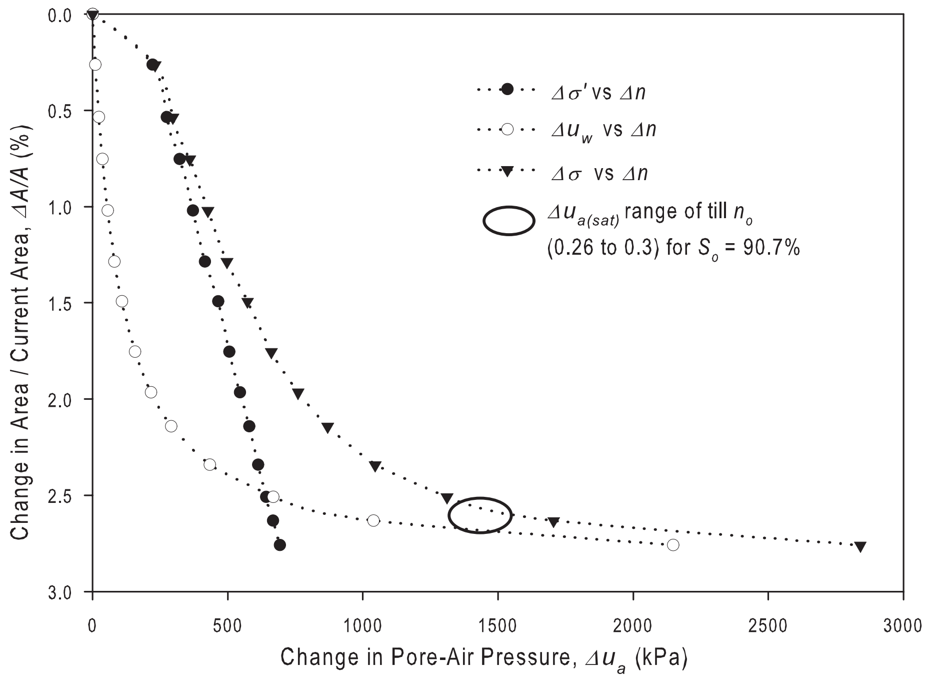

Figure 4.35 Stress components of a pressuremeter loading test in an unsaturated glacial till (UA05)

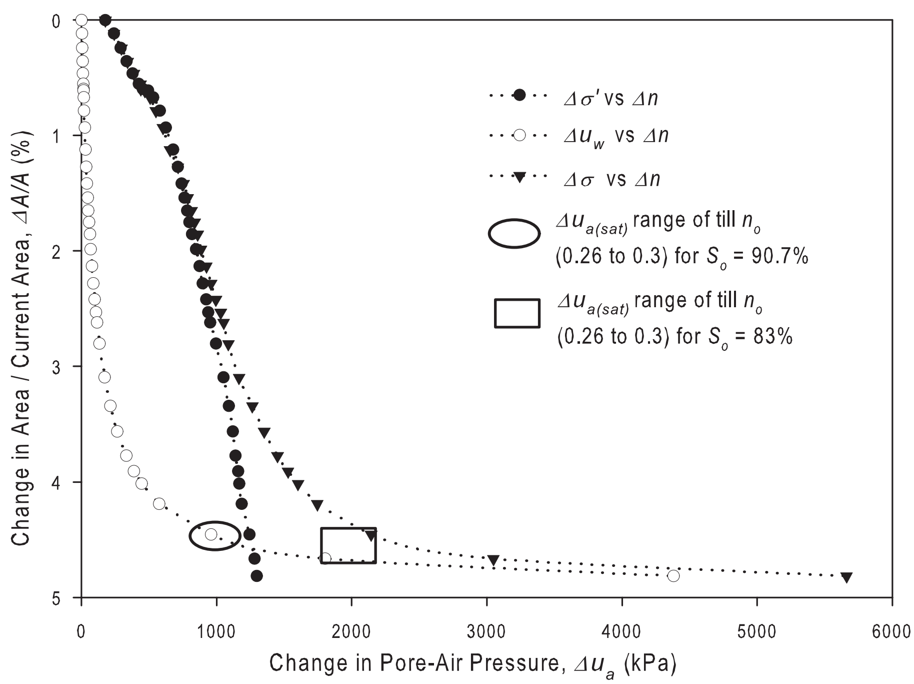

Figure 4.36 Stress components of a pressuremeter loading test in an unsaturated glacial till (UA13)

The stress component curve within the unsaturated region of loading can then be determined once the curve indicating the change in volume with respect to the change in pore-air pressure has been calculated. Using the loading curve as the effective stress response, the pore-water pressure, total and effective stress components of the loading curve within the unsaturated region can be calculated. The results for UA05 and UA13 are shown in Figure 4.35 and Figure 4.36.

The use of Hilf's method of analysis to estimate the point of saturation in a pre-bore pressuremeter test appears to be valid based on the results presented in Figure 4.35 and Figure 4.36. The estimated change in pore-air pressure required to attain zero volume change appears reasonable given the range of likely porosities for the glacial till. Though the slopes of the calculated curves are not zero between the last two points, the change in slope of the data is clearly trending towards zero. The slopes of the pore-water and effective stress curves are a function of the sample rate of the pressuremeter during loading. The saturation point was overstepped because measurements were recorded at 5 second intervals. The corresponding curves may have better illustrated that the slope is approaching zero if more data points had been recorded between the last two measurements. Because two points were recorded past the saturation point in UA13, the slopes of the pore-water pressure and effective stress curves clearly approach zero.

Figure 4.35 and Figure 4.36 indicate that the calculated change in pore-air pressure estimated from Equation 4.11. Equation 4.11 is valid as it is essentially the intersection of the change in total stress, $\Delta\sigma_r$, and the change in pore-water pressure, Δu_w, curve. The definition of the saturation point is based on Hilf's equation.

4.9 Conclusions

With respect to the pre-bore pressuremeter testing carried out within the lower two stratigraphic units in the City of Edmonton, the following can be deduced:

- Pre-bore pressuremeters may be an effective testing method for determining detailed ground characteristics within heavily overconsolidated cohesive and frictional soils
- Borehole disturbance was detected but did not play a critical role in the assessment of the parameters except where the disturbance was found to exceed 4%;
- The undrained shear strength was accurately estimated using a combination of several interpretive methods. Values obtained through the depths of the various formations were relatively consistent. Preference to methods that utilized the post-yield data to estimate the undrained shear strength was shown;
- Within the glacial till, the drained strength parameters were best represented by the cohesive-frictional model presented by Carter, Booker and Yeung (1986). Usage of the fully undrained elastic-perfectly plastic model by Gibson and Anderson (1961) tended to over predict the shear strength of the material at low stresses;
- The cohesive-frictional model proved highly versatile in being able to account for the elastic region, the yield strength (at low applied pressures) as well as the high pressure region post yield. This suggests that the glacial till should be considered as a cohesive-frictional material for longer term applications like cuts;
- Within the Empress Sand, the Hughes Friction Model (Hughes et al., 1977) very closely represented the measured stress/strain curves. This was indicated by the highly consistent frictional values obtained through the depth of the formation;
- Usage of the iterative method based on the calculated limit pressure to predict the undrained shear strength were not considered to be conservative nor reasonably representative of the short term strengths of the various formations;

- A pressuremeter constant (N_p) of 6.2 as suggested by Marsland and Randolph (1978) proved to be a reasonable approximation, though was not used in the current analysis;
- The shear modulus was accurately measured through the depth of the glacial till as indicated by the lack of hysteresis or shear degradation throughout each test. Some degradation occurred within the Empress Sand as hysteresis occasionally exceeded 20% for the last two unload-reload cycles. This is likely a function of the change in soil structure related to dilation;
- The non-linear yield shear strain for unloading (borehole extension) was found to be very small within both the glacial till and the Empress Sand. These yield shear strains were on the order of 0.2% and corresponded well with the plane strain, active compression tests carried out by Medeiros (1979);
- Compressive yield shear strains were determined by plotting the principal stress ratio versus the incremental shear strain. Typical compressive yield shear strains were typically on the order of 3 to 5% which were much higher than the passive compression tests carried out by Medeiros (1979);
- The glacial till appeared to respond mainly as an elastic-perfectly plastic soil, while the Empress Sand suggested brittle behaviour with a well-defined peak and residual stress regions when plotted as a function of the shear stress ratio;
- In terms of shear stress versus shear strain, the glacial till was best represented by a cohesive-frictional material as indicated by the clear break in the initial curve at the yield stress followed by a gradual increase in shear strength with shear strain. The Empress Sand was best represented by a frictional material as demonstrated by the continuous and steep increase in shear strength with shear strain;

- A new method to determine the horizontal consolidation characteristics has been developed for heavily overconsolidated cohesive soils. Using the data from 3-minute hold tests carried out during post yield conditions, the time to 50% consolidation (t_{50}) may be reasonably assessed. In softer ground, it may be necessary to extend the test duration, however this will strain the borehole without increasing the stress-strain curve;
- The coefficient of horizontal consolidation (c_h) is assessed using the Taylor (root time) method to determine the t_{50} while the T_{50} is assessed from the maximum excess pore pressure/undrained shear strength ratio. From this, the coefficient of horizontal permeability (k_h) and the coefficient of horizontal volume change (m_h) may also be ascertained;
- Using the values obtained during the consolidation assessment, the pore pressure response of a partially saturated soil may be evaluated. The change in pore air pressure needed to attain saturation and volume change within the plastic region during loading may also be calculated. This will better explain the changes within the plastic region for an effective stress analysis of partially saturated soils where the assumption of an undrained response is not valid until the presence of air within the void spaces is forced into solution;
- This new method seamlessly indicates when the volume change within the plastic region approaches zero indicating the onset of undrained conditions;
- Charts have been developed that will illustrate the change in volume within the plastic zone resulting from a change in air pressure for a given coefficient of horizontal volume change, porosity and saturation. This may be used to predict the volume changes within the plastic region for a range of values;

5.0 Strength of Heavily Overconsolidated Glacial Till and Empress Sands

The City of Edmonton has constructed numerous tunnels throughout the city as the primary means of providing drainage and transportation to the public. The majority of these tunnels are constructed within the heavily overconsolidated glacial till, common throughout the city. The glacial till has been frequently sampled but has not been extensively tested to determine its actual failure mechanisms. The recovered samples from studies for the various LRT tunnels (Doohan and McLean, 1975; Eisenstein and Thompson, 1977; and Soliman et al., 2010) have primarily been subjected to only unconfined compression tests on select (intact) samples. Others (DeJong, 1971; Medeiros, 1979 and Whittebolle, 1983) have conducted advanced laboratory experiments, however they all reported difficulties with their experiments. The problems they reported primarily stemmed from the presence of discontinuities (fissures) within the samples. This made sample recovery, preparation and testing extremely difficult. Each series of tests provided a yield surface, though no true definition of yielding was provided. Additionally, none of the previous researchers discussed the overall implications on the yield envelopes on full-scale excavations in underground cavities such as tunnels. Because of the difficulty in sampling and testing of the tills, a re-examination of the previous test results was conducted to better define when the onset of yielding occurs and between what limits these criteria are applicable.

Within the Empress sands, even fewer tests have been conducted. This is mainly due to the overall depth to the strata and that most structures do not extend into the Empress sand. Because the strength of the overlying glacial till is quite favourable for most heavy civil applications, most investigations did not even consider the presence or influence of the Empress sand. Like the glacial till, the sampling and recovery of the Empress sand has been historically very difficult. Since the insitu water content is quite low, freezing and sampling of the sand is not possible. Block samples are also difficult to recover and even harder to prepare for testing.

Because of the history of these two materials, and the lack of clarity as to their typical failure mechanisms, they are solely the focus of this chapter. The strength and strain characteristics of the Lake Edmonton clay and the Edmonton Formation bedrock are not considered in this study.

5.1 Glacial Till

The glacial till in the downtown Edmonton area has been well documented over the last 40 years. Comprised of a heterogeneous mixture of clay, silt and sand, the till has been extensively encountered and has historically been viewed as an ideal material for heavy civil construction. Starting in the late 1960's, researchers at the University of Alberta have sampled and tested as well as observe the overall performance of the glacial till. One of the most important aspects of the glacial till is the discontinuous nature of the soil mass. Researchers such as DeJong (1971); Westgate (1969); Eisenstein and Thomson (1977); May and Thomson (1978); Medeiros (1979); Whittebolle (1982) and El-Nahhas (1982) have all discussed the nature of the fissuring in the glacial till. Westgate (1969) reported the presence of two till sheets in the city and suggested that the fissures in the lower till (bottom 10 m) were frequent and resulted in angular blocks when separated. Westgate (1969) also reported that the upper till was characterized partially by the columnar nature as well as the heavily oxidized surface of the fissures.

Eisenstein and Thomson (1977) commented on the response of the ground due to the presence of the fissures within the glacial till in large diameter tunnels. They found that during construction of the lead tunnel, the fissures tended to remain closed and block failure was not generally observed. During the construction of the second (lag) tunnel however, they found that the ground had loosened due to unloading during construction of the lead tunnel. As a result, the fissures were opened and block translation was common.

May and Thomson (1978) indicated that the upper 1 m of the “lower” till was highly sheared and subsequently highly fractured. They also presented the observation of regular shear zones within the lower horizons of the glacial till which they attributed to glacial drag. May and Thomson (1978), were also the first to suggest that the nature of the fissures likely had a considerable impact on the measured strength of laboratory samples.

5.1.1 Sampling of the Glacial Till

Because of the heavily overconsolidated and highly fissured nature of the glacial till, sampling has traditionally been a problem for most researchers. Researchers have historically made a concerted effort to recover high quality samples of the till where possible. A number of researchers have recovered block samples from open excavations (DeJong, 1971; Medeiros, 1979) or from the face of tunnel excavations (Morgenstern and Thomson, 1971). Others have recovered samples by rotary coring methods (Morgenstern and Thomson, 1971; Whittebolle, 1983), though most have used thin walled tube sampling methods (Matheson, 1969; Morgenstern and Thomson, 1971; DeJong and Harris, 1971; Doohan and McLean, 1975; Soliman and Cherniawski, 2010).

Morgenstern and Thomson (1971) provide a detailed discussion on the degree of disturbance between sampling the glacial till using the three methods given above. They found that a specially designed coring tool, tended to result in unconfined compression values that were very similar to those measured in samples recovered using thin walled Shelby tubes. The major difference was that sample recovery was far more likely with the coring tool than with pushed thin walled tubes. Use of thin walled tubes in the glacial till has the potential for the tube sampler to become stuck or damaged during advancement (Morgenstern and Thomson, 1971; Soliman and McRoberts, 2010) or destroyed during extraction (Morgenstern and Thomson, 1971).

DeJong (1971) and Morgenstern and Thomson (1971) also suggest that contrary to conventional thinking, block samples tended to result in the lowest measured strength and stiffness values. This was mainly due to sample disturbance during excavation that resulted in the dilation of pre-existing micro fissures. Another problem associated with the usage of block samples, was the low recoverability of the samples following preparation for triaxial or oedometer testing. All researchers who recovered block samples reported large sample losses when trimming the samples in preparation for testing. This was mainly due to fissures encountered within the sample (DeJong, 1971; Whittebolle, 1983) or the presence of small pebbles along the cutting plane (DeJong, 1971; and Medeiros, 1979). Whittebolle (1983) overcame the problems associated with the presence of gravel within the soil matrix by using diamond coring and cutting tools, which sawed through the clasts resulting in reduced sample loss.

With respect to sample size, since most block samples were on the order of 0.5 m in length, the samples were capable of capturing some macro fissures within the sample. Whittebolle (1983) reported difficulties in recovering samples with a core barrel diameter greater than 100 mm. This however was not a constraint of the lateral fissures, but rather, associated with the spacing of the vertical fissures, which were found to be approximately 100 to 125 mm apart. By restricting the core barrel diameter to 100 mm, samples with length to diameter ratios of 1:1 could be obtained with minimal post sampling preparation. Most tube samples and rotary core methods recover samples with a diameter of approximately 70 to 100 mm. Based on the spacing of the fissures reported in Chapter 3, it is unlikely that the samples would have encountered appreciable numbers of fissures through the depth of the boreholes.

5.1.2 Laboratory Properties

5.1.2.1 Grain Size

Grain size is one of the most commonly carried out experiments on recovered samples of the glacial till. As a result there is an abundance of data within the Edmonton glacial till. In most cases of reports reviewed for this research, only a range of values was reported for each study. Historically, it has been found that there is very little difference in gradation between the "upper" and "lower" tills (Westgate, 1969) and conventionally, differentiation has been based on the presence of a roughly 1 m thick sand layer (Toefield Sand) and pebble orientation (Westgate, 1969). It is important to note that the Toefield Sands are not extensive throughout Edmonton and are more commonly encountered to the north of the city limits. More recently, Shaw (1982) has suggested that there is not two different till sheets, which would explain the similar appearance of the material through its depth. The historical and current breakdown of the grain size of the glacial till is provided below in Table 5.1.

	Minimum	Average	Maximum	Standard Deviation
Historical Clay (% Passing)	15	20 - 25	42	-
North LRT Clay (% Passing)	16	26.3	31	5.5
Historical Silt (% Passing)	25	27 - 32	38	-
North LRT Silt (% Passing)	32	37.8	51	6.7
Historical Sand (% Passing)	35	35 - 40	50	-
North LRT Sand (% Passing)	32	35.8	39	2.9

Table 5.1 Historical and current (North LRT) grain sizes of the Edmonton glacial till

With respect to the plastic limits of the glacial till, there is little difference in the indices with depth. A summary of the historical and current (North LRT) Atterberg limits and natural moisture content are given below in Table 5.2.

	Minimum	Average	Maximum	Standard Deviation
Historical Liquid Limit (%)	22	30 - 35	66.8	-
Historical Plastic Limit (%)	9	15 - 20	22.7	-
North LRT Liquid Limit (%)	25	35	42	6
North LRT Plastic Limit (%)	13	15	17	1
Historical Moisture Content (%)	9.4	15 - 20	28.7	-
North LRT Moisture Content (%)	6	15	45	3

Table 5.2 Atterberg limits and natural moisture content of the Edmonton glacial till

These values indicate that the natural moisture content of the glacial till is near to or slightly lower than the measured plastic limit suggesting a partially saturated, heavily overconsolidated material. The measured plasticity indices and natural moisture content of each sample subjected to Atterberg Limits testing is shown below in Figure 5.1.

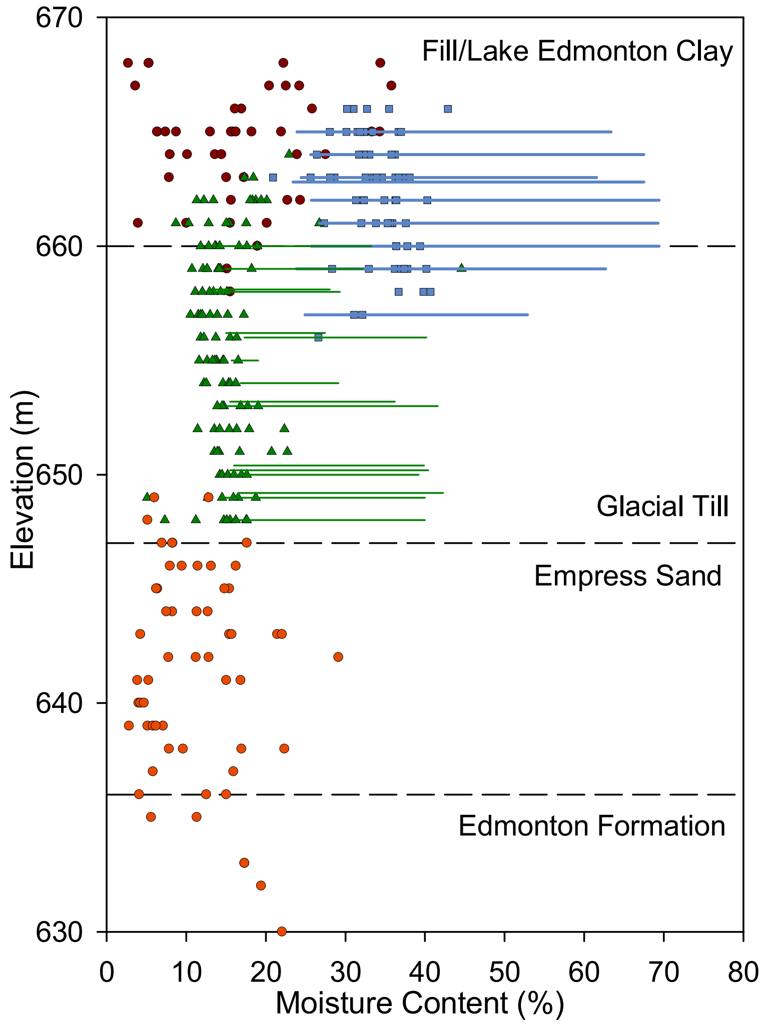

Figure 5.1. Moisture content relative to the Atterberg limits (adapted from Soliman et al. (2010))

The degree of saturation of the glacial till has been reported by several authors, (Matheson, 1969; DeJong and Harris, 1971; Doohan and McLean, 1975; and El-Nahhas, 1978) and is between 75 and 95%. Typically though the degree of saturation is between 87 and 92%.

Most investigators did not readily measure the relative density of the glacial till in the past. In most cases, a range of densities was provided for design purposes based on past experience and correlations with SPT 'N' values. Of researchers that did investigate the relative density of the glacial till, DeJong and Harris (1971) measured the density glacial till to be between 20 and 22 kN/m^3 with an average of 21.4 kN/m^3; while Eisenstein and Thomson (1978) estimated the density to range between 20.6 and 21.2 kN/m^3 and Whittebolle (1983) reported values between 21.1 and 21.9 kN/m^3.

Due to the difficulty in attaining realistic insitu values, most researchers rarely reported the permeability of the glacial till. In most cases, coefficients of permeability (k) were obtained in the laboratory for a specific stress state based on consolidation tests. These values are indicative of the hydraulic conductivity of an assumed fully saturated sample of the glacial till fabric. Based on the size of the samples used in the testing, there was no way to determine the bulk permeability of the soil mass that takes into account the presence of fissures. Morgenstern and Thomson (1971) carried out a large number of consolidation tests on samples recovered using a variety of methods. They reported that values obtained from block samples were considerably higher than those measured from samples recovered from boreholes, while those recovered from boreholes showed little variation of permeability with depth. Morgenstern and Thomson (1971) reported that the hydraulic conductivity ranged from 2.4×10^{-9} to 5.3×10^{-10} cm/s with an average of 1.5×10^{-9} cm/s. As shown in Chapter 4, calculations of pre-bore pressuremeter test results suggest a coefficient of horizontal hydraulic conductivity within the glacial till indicate hydraulic conductivities ranging from 7.5×10^{-7} and 3.0×10^{-6} cm/s were calculated assuming a Poisson's ratio of 0.34.

For the most part, the presence of the intra-till sand pockets dictates the hydraulic conductivity of the glacial till. Because the sand pockets are generally small and not interconnected, the overall storativity is quite small occasionally resulting in relatively high flow rates that taper off over short periods of time. Doohan and McLean (1975) reported that a pumping well dried after approximately 3 hours following the startup of a pumping test. The pumping test was carried out approximately 150 m east of the North

LRT alignment. The recovery time of the well took approximately two days, however full recovery was not reported. Because there was apparently no interference with any monitoring wells during the pumping test, Doohan and McLean (1975) could not report a measured hydraulic conductivity of the intra-till sand. Boone et al. (2002) reported that the hydraulic conductivity of the intra-till sand was approximately $1\text{x}10^{-3}$ to $4\text{x}10^{-3}$ cm/s. These values were determined based on the results of a pumping test carried out as part of the South LRT (University Line) tunnel design. The storativity of the deposit was also estimated to be between 0.0005 and 0.03 while the transmissivity was between 0.5 to 1.5 cm^2/s. The seepage of a large intra-till sand pocket encountered within a TBM launch shaft near to the three-cell structure of the North LRT was assessed based on baling rates. Recharge of the sand pocket was provided by a ruptured water line that intersected the sand pocket away from the launch shaft. Flow rate measurements were based on groundwater removal following approximately 12 hours of seepage, which suggested a hydraulic conductivity of approximately $1\text{x}10^{-6}$ cm/s. Falling head permeability tests were carried out during this study on sand recovered from the above TBM launch shaft, which was subject to the prolonged seepage. These tests indicated that the permeability of the intra-till sand ranged from $8.4\text{x}10^{-6}$ to $9.7\text{x}10^{-7}$ cm/s with an average of $4.9\text{x}10^{-6}$ cm/s, which agreed well with the observed flow rates into the shaft.

5.1.3 Laboratory Strength Testing

5.1.3.1 Undrained Strength

Many researchers and practitioners have investigated the undrained shear strength of the glacial till over the last 40 years (Morgenstern and Thomson, 1971; DeJong, 1971; Doohan and McLean, 1975; Medeiros, 1979; Whittebolle, 1983; and Soliman and McRoberts, 2010). The majority of the tests were carried out as unconfined compression (UC) tests, while a limited number were conducted as unconsolidated undrained (UU) tests. DeJong (1971) and Whittebolle (1983) both carried out a series of isotropically consolidated undrained (CU) tests on the glacial till. Morgenstern and Thomson (1971) demonstrated that the sampling method used to recover the test specimens and the moisture content of the sample strongly influenced the undrained shear strength. The above triaxial tests (UC, UU and CU) apply a passive compression, which historically resulted in the most ductile response of the various triaxial stress paths as shown by Medeiros (1979). The historical (total) stress-strain curves from available UC and CU test data are shown below in Figure 5.2.

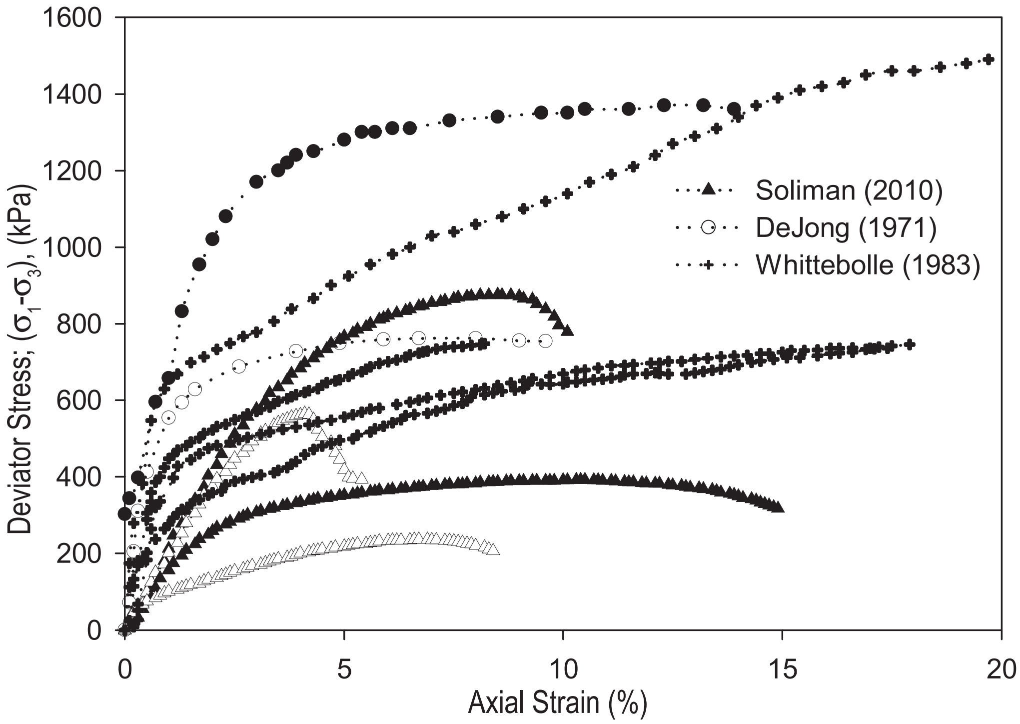

Figure 5.2. Historical undrained stress-strain curves of the Edmonton glacial till

Figure 5.2 demonstrates an interesting trend for the samples subjected to confinement. The test results shown in Figure 5.2 suggest that for confining stresses less than 500 kPa, the peak stress is roughly 600 kPa. For the two tests carried out above this confining pressure, the peak stress was approximately 1,450 kPa. In the two unconfined cases that failed at shear stresses less than 400 kPa, the samples reportedly failed preferentially along existing discontinuities. Whittebolle (1983) observed that the pore pressure response of the test samples initially went up but subsequently dropped at strains of greater than 1 to 3%. Though not discussed by Whittebolle (1983), the reduction in pore pressures suggests an increase in suction with strain following dilation of the soil.

When the test method and confining stress data were available, the Mohr circles for undrained shear strength were plotted to give a range of values. As there were only a total of 10 tests with complete data as shown in Figure 5.2 the number of Mohr circles are considered limited. Figure 5.3 illustrates the constructed Mohr circles with the maximum, minimum and average undrained shear strengths plotted for reference.

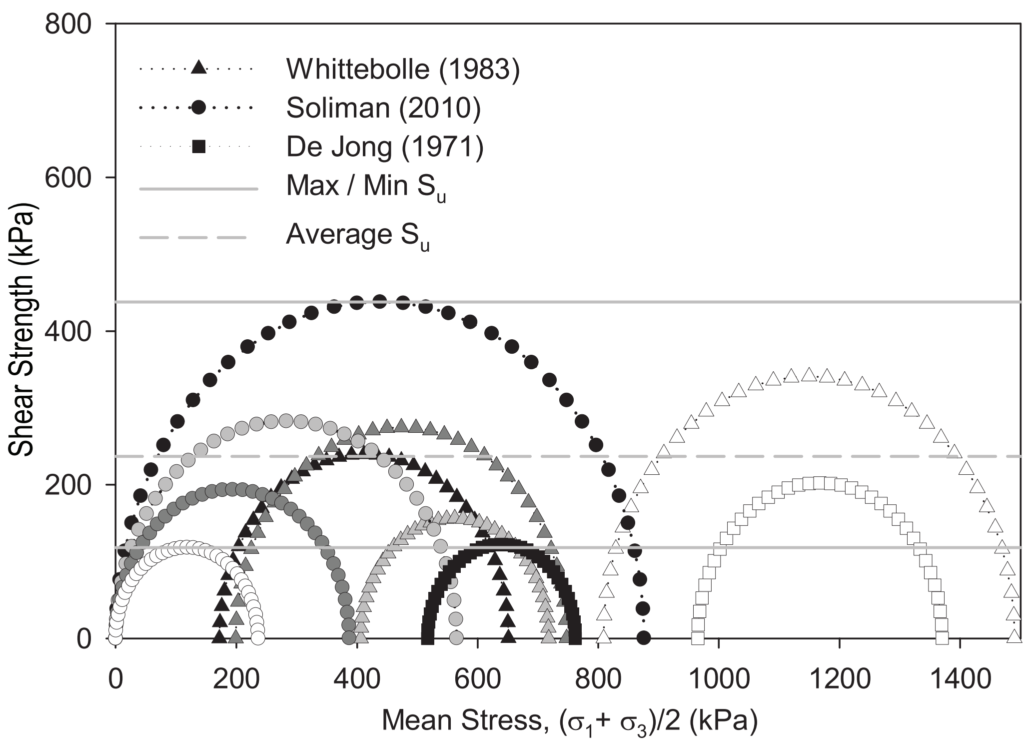

Figure 5.3 Total stress Mohr circles for the glacial till

Figure 5.3 shows that the undrained shear strength is between 438 and 118 kPa with an average and standard deviation of 236 and 100 kPa respectively. Because there are two tests that indicate undrained shear strengths above 300 kPa, the average undrained shear strength is slightly skewed. If the values above 300 kPa are excluded, the average undrained shear strength becomes 198 kPa and the standard deviation becomes 64 kPa.

Figure 5.4 demonstrates a compilation of the available historical undrained triaxial testing with respect to the measured moisture content. The average trendline shown in Figure 5.4 should be used with caution since the coefficient of determination (R^2) of the line is approximately 0.2 indicating little to no correlation with the dataset. In this case, the upper and lower bounds should be used to provide a feasible range of undrained shear strength based on the insitu moisture content.

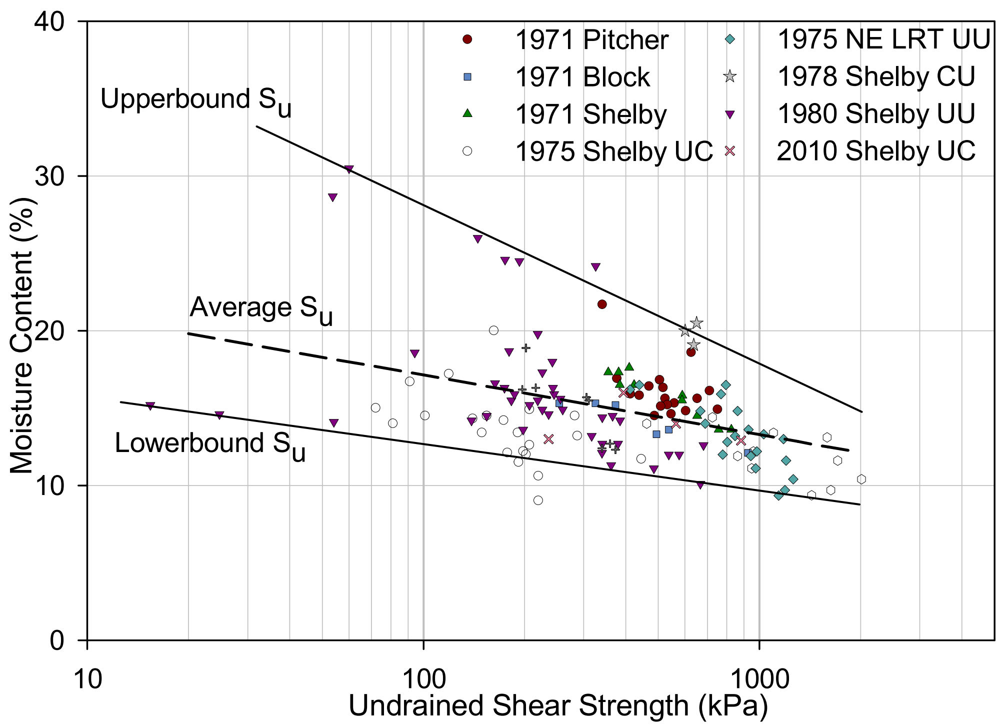

Figure 5.4. Undrained shear strength with respect to moisture content

5.1.4 Drained Strength

Two previous researchers (Medeiros, 1979; and Whittebolle, 1983) have studied the drained failure envelope of the glacial till with mixed results. Medeiros (1979) carried out a series of drained analyses of the glacial till using a variety of different stress paths to probe the failure envelope. Medeiros reported that the strains required for the onset of yielding were highly stress path dependent. By plotting the drained stress-strain curves together, the effect of the pore pressure on the high stress sample by Whittebolle (1983) is well illustrated. Figure 5.5 shows the drained stress-strain profiles of the passive compression tests (conventional triaxial and plane strain) by Medeiros (1979) and the four conventional triaxial tests (effective stress) on undisturbed glacial till by Whittebolle (1983).

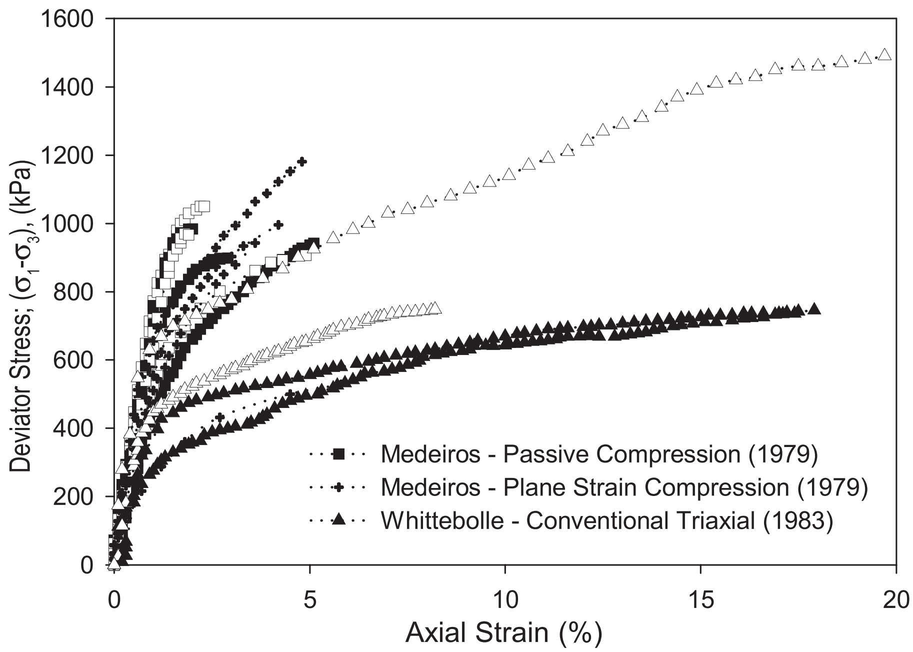

Figure 5.5. Stress-strain response of the glacial till for drained tests (Medeiros, 1979) and Consolidated Undrained tests with pore-pressures measurements (Whittebolle, 1983)

Whittebolle (1983) measured the pore pressure response for the consolidated undrained tests and these results are shown below in Figure 5.6 for the four tests.

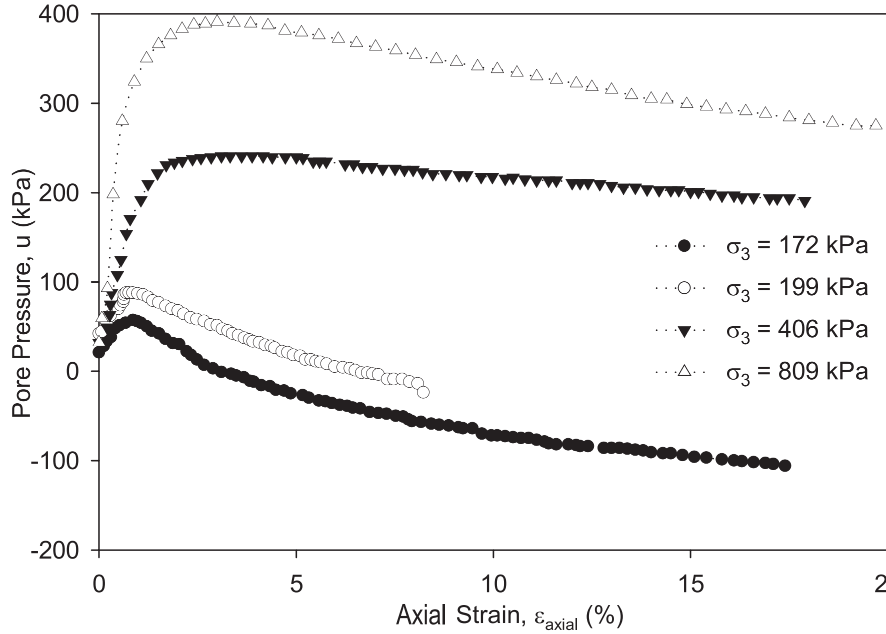

Figure 5.6 Pore pressure response of the glacial till during consolidated undrained testing (after Whittebolle, 1983)

Medeiros (1979) conducted drained compression tests and therefore the excess pore pressures were in theory always zero. Medeiros (1979) instead monitored the volumetric change of the samples by measuring the flow of pore-water from and into each sample during shearing. The results of the volumetric changes of the samples are shown below in Figure 5.7. The volumetric changes under drained conditions are analogous with the pore pressure responses of Whittebolle (1983) as compression would be indicative of positive pore pressures while dilation would be indicative of negative pore pressures.

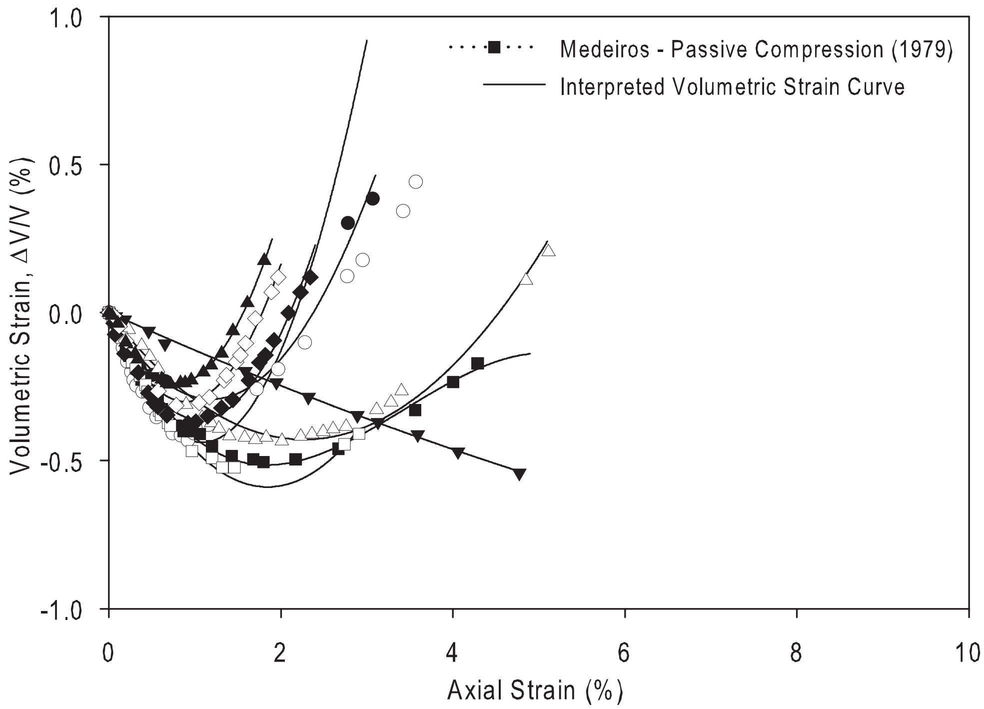

Figure 5.7 Volumetric strain of the glacial till in drained triaxial tests (after Medeiros, 1979)

Clearly the pore pressures demonstrate the trend typical to heavily overconsolidated soils. Initially there is a compression of the soil mass, followed by dilation. The measurements demonstrated that there was a pore pressure accumulation up to strains between 1 and 3% after which the pore pressures began to decline. This suggests that yielding of the till typically takes place at shear strains of approximately 1 to 3% in compression. Failure in this case is associated with the transition from positive to negative pore pressures (compression to dilation).

The angle of dilation was calculated for each test for both the compressive and dilative phases of volume change and is shown on Table 5.3. In each case, the shear strains at which the maximum angle of dilation was also recorded and is shown on Table 5.3. These values represent the peak angles of dilation and the corresponding shear strains for both the compressive (initial) and dilative (post peak) phases within the glacial till.

Parameter	Lowest Value	Mean	Highest Value	Standard Deviation
Compressive Dilation Angle (°)	17.7	26.6	37.6	5.4
Yield Shear Strain (%)	0.8	1.4	2.3	0.55
Expansive Dilation Angle (°)	4.6	38.9	59.5	17.9
ϕ_{mob} Shear Strain (%)	2.4	2.65	2.9	0.19

Table 5.3 Peak angles of dilation for the glacial till

Medeiros (1979) also modified the stress path applied to the glacial till in order to probe the effect of stress path on the failure envelope. Other than passive compression and plane strain compression tests shown above, Medeiros (1979) also conducted active compression tests. The tests involved isotropically consolidating the soil samples to the desired effective stress. Once consolidation was complete, the samples were progressively unloaded by incrementally reducing the confining stress (σ_3). In order for the test samples to fail, the axial stress (σ_1) was incrementally increased as the confining stress was reduced. In order to interpret and reproduce Medeiros' data, which was presented only as deviator stress by axial strain, it was assumed that for each point recorded that the increase in axial stress is exactly equal to the decrease in confining stress. The stress-strain curves of the active compression tests are shown below in Figure 5.8.

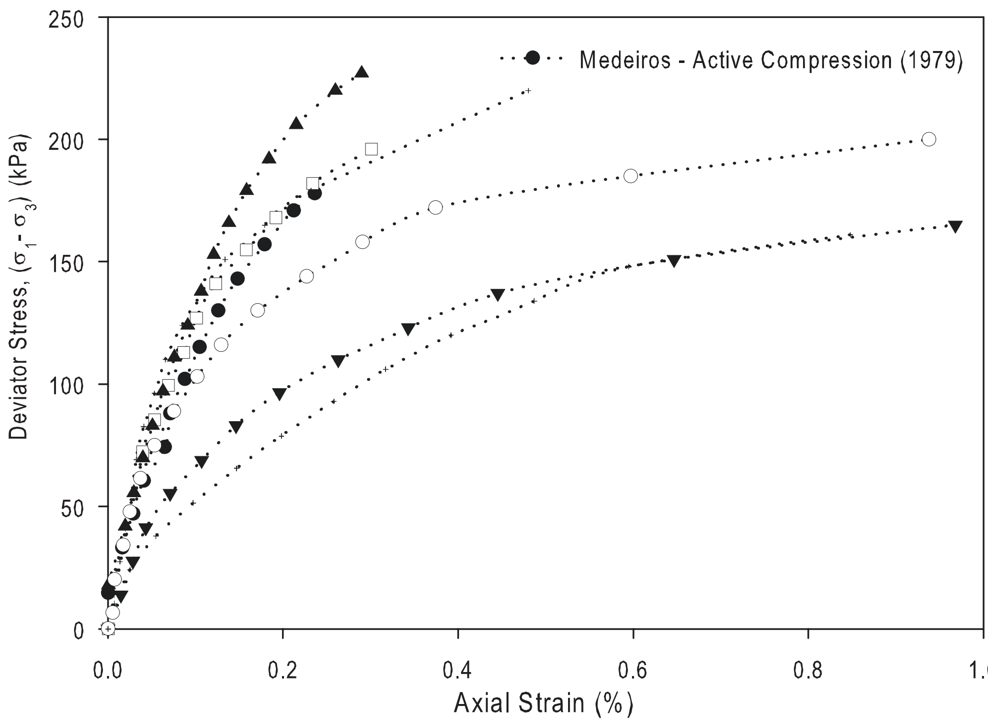

Figure 5.8 Active drained compression stress-strain curves (after Medeiros, 1979)

It is important to note that the scales have been changed for the active compression tests in order to visualize the shape of the curves. The total shear stress and shear strain are both approximately 20% that of the conventional triaxial tests given in Figure 5.5. Medeiros (1979) stated that there was no way to effectively monitor the volumetric strain during these experiments as the changes of the cell volume far exceeded that of the sample volume change. Therefore, yielding is assumed to occur at the approximate end of the linear region of the stress-strain curve.

Using the peak values obtained from each of the passive compression drained and effective stress test, an effective stress envelope has been constructed. The effect of the plain strain passive compression test is not seen to be influential on the peak strength. This is demonstrated in Figure 5.9 by the strong correlation with the peak effective stress results produced by Whittebolle (1983).

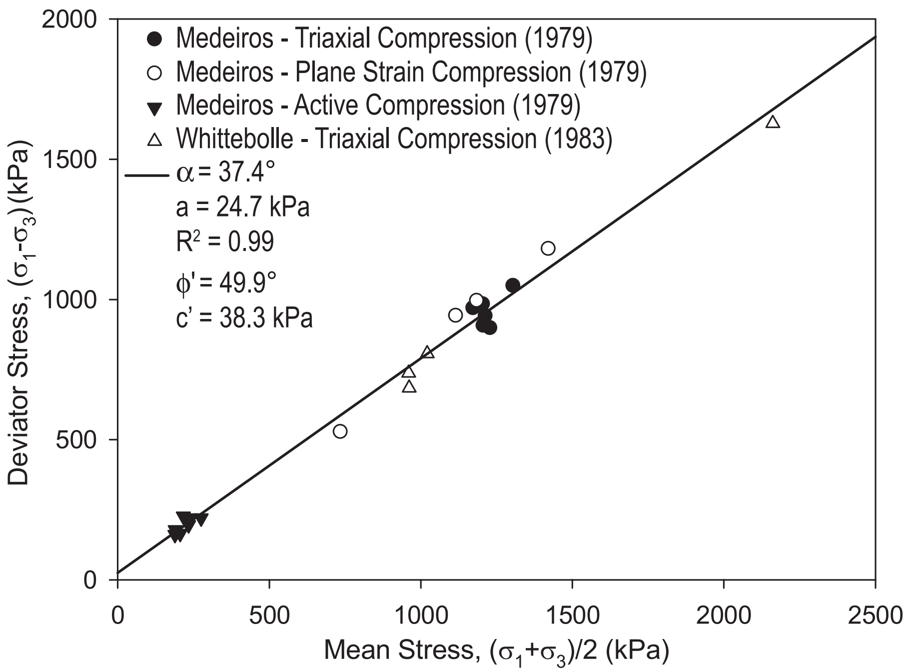

Figure 5.9. Effective peak Mohr-Coulomb failure envelope for the glacial till

Figure 5.9 provides summary of data from Whittebolle (1983) and Medeiros (1979). The linear best line to the data is shown in Figure 5.9 and when converted to Mohr-Coulomb parameters give c' = 38.3 kPa and ϕ' = 49.9°. El-Nahhas (1980), suggested that the onset of failure in compression for the Edmonton glacial till is fixed at a axial strain no greater than 2%. If the failure strain is set to 2% for the data set in Figure 5.9, the friction angle for failure envelope is only reduced by 0.1° and the coefficient of determination is reduced by 1.3%.

5.1.4.1 Residual (Large Strain) Strength of the Glacial Till

Of all of the laboratory experiments conducted on the glacial till, only those carried out by Whittebolle (1983) were strained sufficiently to define the residual strength of the soil matrix. The onset of the critical state could not be determined based on the volume change measured during the tests by Whittebolle, as the pore pressure changes did not appear to approach a constant value nor was a final void ratio reported. As the material approaches the residual strength, the cohesion will have been completely broken down and the mobilized friction of the soil grains provides the only resistance to shear stress. In order to assess the residual strength parameters of the glacial till, the data of Whittebolle (1983) were plotted in p' - q space (where p' = $(\sigma_1+2\sigma_3)/3$) in order to observe the stress path and the slope of the critical state friction angle (*M*). The data were then plotted in terms of the triaxial stress ratio (q/p') to determine the shear strain required for the onset of residual conditions. The principal stress ratio should indicate the point where shear stresses approach a common value. In theory, critical state should be achieved when the change in the shear stress ratio is constant for any given effective confining stress. It should be at this point when the change in volume of the test specimen is zero and the sample is shearing at constant volume. The plots of the effective stress paths and the triaxial stress ratios are shown below in Figures Figure 5.10 and Figure 5.11.

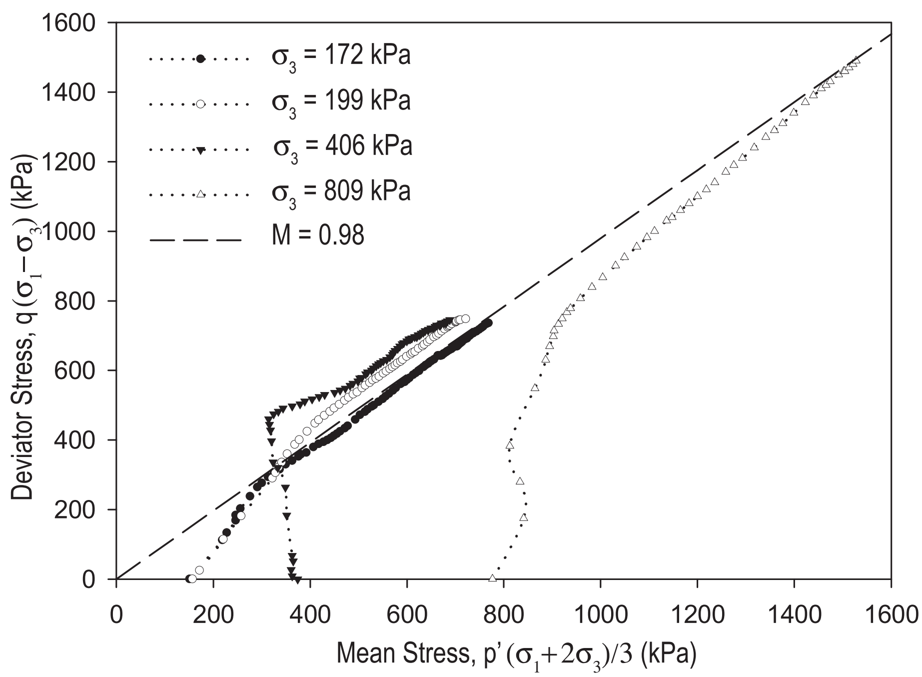

Figure 5.10. Effective consolidated undrained stress paths of the glacial till and critical state line

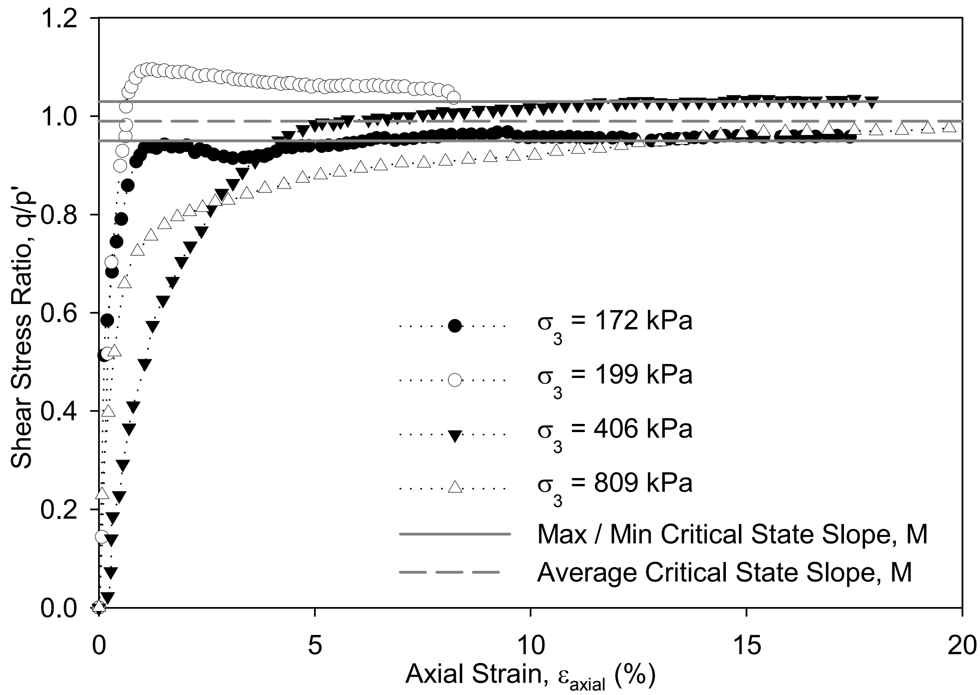

Figure 5.11. Triaxial stress ratio versus the axial strain of glacial till

The above figures show that the test samples were likely at critical state upon completion of the test though the final void ratio was not known. The triaxial stress ratio indicates the slope of the critical state line (*M*) between 0.95 and 1.03 with an average slope of 0.99. This suggests a critical state friction angle between 43.5 and 45.8° with an average of 44.4°. Figure 5.11 illustrates the stress path with respect to axial strain. The samples subjected to low confining stresses exhibited a peak followed by a reduction to critical state. This is indicative of a heavily overconsolidated material. The samples subjected to confining stresses greater than 400 kPa tended to approach the critical state as a normally consolidated material. This suggests that the pre-consolidation pressure is somewhere between 200 and 400 kPa for the samples tested. This is in good agreement with the average pre-consolidation pressure determined by Morgenstern and Thomson (1971) to be 300 kPa. Morgenstern and Thomson (1971) provided a minimum, maximum and standard deviation (respectively) of the pre-consolidation pressure for the glacial till of 101, 556 and 120 kPa.

5.1.5 Insitu Properties

The insitu properties of the glacial till were determined during the current study using data obtained from seismic CPTu test holes and a pre-bore pressuremeter test hole. The seismic CPTu test holes were advanced throughout the alignment while the pressuremeter test hole was advanced through the station lands adjacent to a previously advanced CPTu test hole.

5.1.5.1 Seismic CPTu

A total of ten undrained, seismic cone penetration tests (CPTu) were advanced from the ground surface throughout the North LRT alignment in order to better classify the overburden profile. The CPTu with pore pressure measurement were advanced by ConeTec using an integrated electronic cone system equipped with a triaxial geophone to record seismic waves. All soundings were performed using compression type cone penetrometers as shown below in Figure 5.12.

The cone used consisted of a 20-ton instrument with a tip area of 15 cm^2, a friction sleeve area of 225 cm^2 and a tip capacity of 150 MPa and a pore pressure capacity of 5 MPa. The CPT cone was designed with an equal end area friction sleeve and a tip end area ratio of 0.80. A porewater pressure filter constructed of porous plastic measuring 5.0 mm in thickness was located directly behind the cone tip. Prior to the start of testing, the contractor saturated the porewater pressure filters within the tip under a vacuum. At pre-determined times, the advancement of the cone was ceased and porewater pressure dissipation data was recorded at 5 second intervals. The cone system was capable of recording the following parameters:

Tip Resistance (*qc*);

Sleeve Friction (*fs*);

Pore Pressure (u);

Temperature (T); and

Cone Inclination (I).

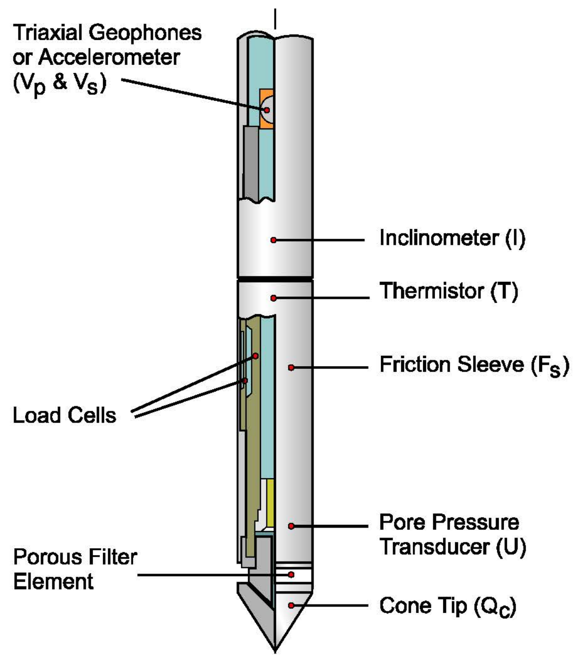

Figure 5.12. Compression cone penetrometer (with permission from ConTec)

The cones were statically driven using a drilling rig provided by Mobile Augers Ltd. at a constant rate as per ASTM D-5778-95. In the event that refusal was encountered prior to completion of the test hole, the CPTu tooling was extracted from the test hole and the borehole was reamed out with solid stem augers.

The very small strain shear moduli were measured by means of seismic testing at regular intervals of 1 m throughout the depth of the test holes. The seismic waves were generated using a sledgehammer impacting a steel H-beam that was coupled to the ground by under the outriggers of the drilling rig. The impact of the sledgehammer on the beam acts as an electrical contact trigger, initiating the recording of the seismic wave traces. The offset of the beam from the cone was taken into account during calculation of the seismic wave velocities. Each sounding was carried out on each side of the H-beam in order to generate equal, and opposite shear waves in order to check the consistency of the waveforms. The seismic wave receiver used was a horizontally active geophone located in the body of the cone penetrometer. The geophone was reported located approximately 0.2 meters behind the cone tip and the offset was accounted for in the interpretation of the data. Data were sampled at a frequency of 20 kHz with a total of 5000 points being recorded per wave trace. To maintain the desired signal resolution, the input sensitivity (gain) of the receiver was increased with depth. All data were downloaded following completion of the test hole and entered into specialized cone software (CPeT-it) for interpretation and plotting.

5.1.5.2 Undrained Shear Strength

Based on the data directly recorded by the sCPTu, correlations have been used to determine the peak and remoulded undrained shear strengths of cohesive soils; the friction angle of cohesionless soils; and the permeability and the elastic modulus of both soil types. Because the interpretation employs the use of empirical methods based on the tip resistance, vertical stress and a factor based on soil sensitivity and plasticity, it was not always possible to determine values throughout the depth of the test hole. The sensitivity of the soil is estimated by the ratio of the peak undrained shear strength relative to the remoulded shear strength. For sCPTu testing, the remoulded undrained shear strength is assumed equal to the sleeve friction stress. Robertson et al. (2012) provide the interpretation of the undrained shear strength and potential modifications to the cone factor value (N_{kt}). Because N_{kt} is selected as a constant for each test, occasionally the remoulded strength was interpreted to be higher then the peak shear strength, which is theoretically impossible. The equation for the peak undrained shear strength as given by Robertson et al. (2012) is given as

$$s_u = {q_t - \sigma_v}/{N_{kt}} \qquad \text{Equation 5.1}$$

where,

s_u is the undrained shear strength;

q_t is the measured cone tip resistance;

σ_v is the calculated vertical total stress at the point of assessment;

N_{kt} is the cone factor.

An example of the interpretation of the undrained shear strength of the soil profile (CPT09-06) with respect to depth is shown below in Figure 5.13. The undrained shear strength profiles of other test holes are included in Appendix A.

The undrained shear strength of the glacial till as interpreted by the empirical correlations of the CPT vary from between 11.1 to 2228 kPa but are generally between 250 to 500 kPa with an overall average of 377 kPa and a standard deviation of 344 kPa. Undrained shear strengths greater than 1 MPa were assessed in several test holes, though was usually restricted to the upper 4 m of the glacial till formation. These sections were also usually highly discontinuous in nature suggesting that the material was on the borderline between cohesive and frictional.

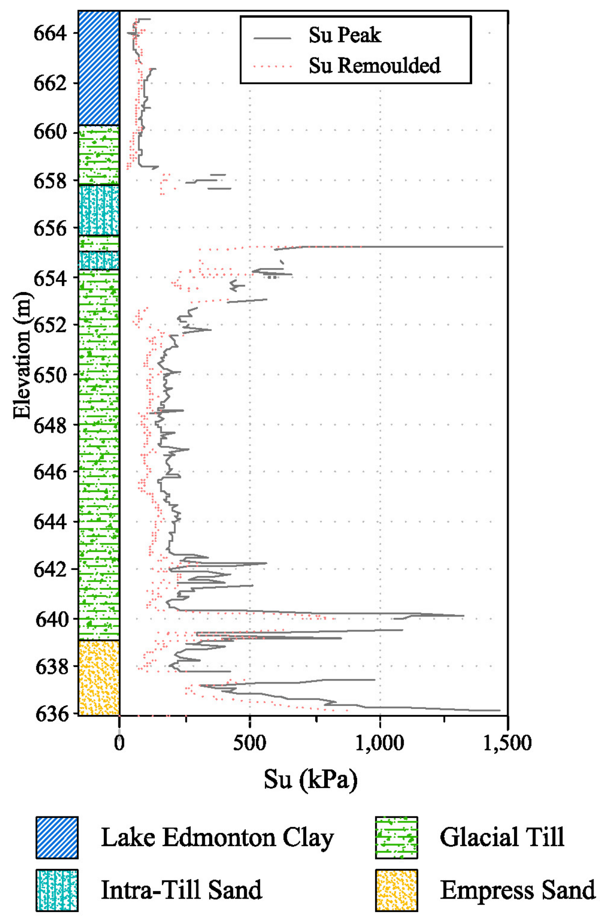

Figure 5.13. Interpreted undrained shear strength (CPT09-06)

5.1.5.3 Frictional (Drained) Shear Strength

The frictional shear strength of the glacial till was assessed from the sCPTu tests using empirical correlations from the tip resistance measurements and insitu vertical stress. There are a number of methods that can be used, but the most common methods are those given by Robertson and Campanella (1983) and Kulhawy and Mayne (1990). In the case of the CPTe-it software, it calculates the effective friction angle (ϕ') using the method given by Kulhawy and Mayne (1990). This method calculates a normalized tip resistance (Q_{tn}) based on correlations for clean, rounded, uncemented quartz sands and very high quality test holes. Using the normalized tip resistance, the effective friction angle is assessed using:

$\phi' = 17.6 + 11 \log (Q_{tn})$ Equation 5.2

where,

$$Q_{tn} = \left(q_t - \sigma_{vo} \middle/ \sqrt{\sigma'_{vo} \cdot \sigma_{atm}} \right)$$

From Equation [5.2], the effective friction angles (ϕ') for the various formations through the depth of the soil profile have been interpreted. The friction angle with depth for all of the recently advanced the sCPTu test holes are shown below in Figure 5.14.

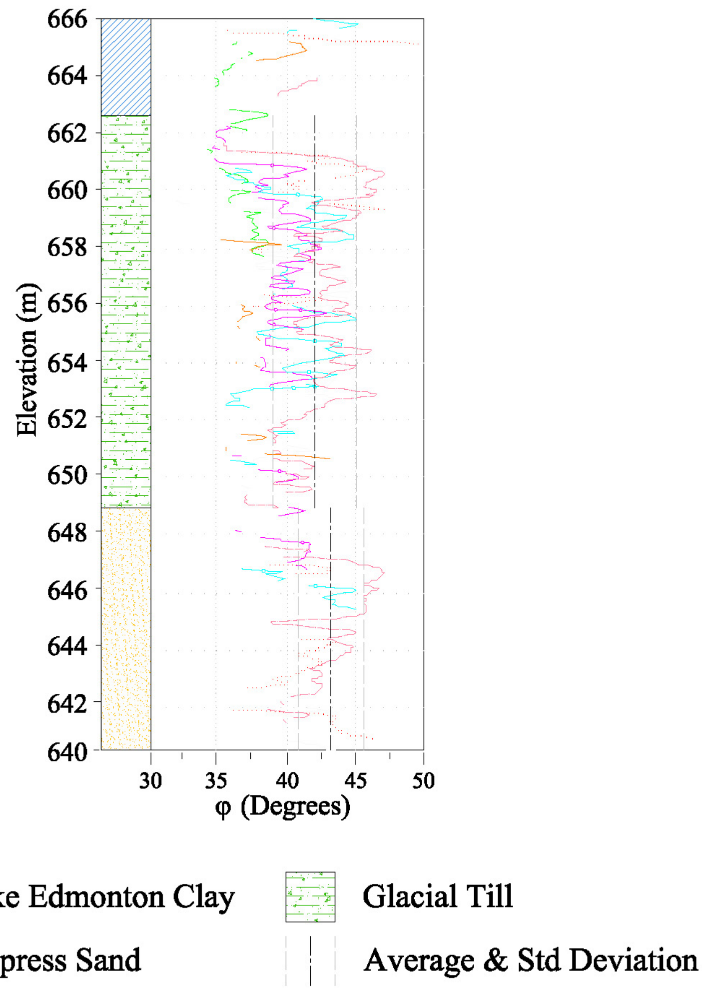

Figure 5.14. Profile of effective friction angle (ϕ') with depth from sCPTu

Through the glacial till, the effective friction angle is generally consistent ranging from a minimum of 32° to a maximum of 49°. The average effective friction angle and standard deviation are 41.9° and 3.1° respectively. It is important to note that the friction angles are generally higher in the upper horizons of the glacial till relative to the lower regions.

5.1.6 Pre-Bore Pressuremeter (Camkometer)

As part of the North LRT detailed geotechnical investigation, a single borehole was advanced from the ground surface approximately 20 m east of the temporary retaining structure known as the East Headwall within the EPCOR Station Lands. The borehole was drilled to a depth of 24.5 m below the ground surface and was tested at intervals of 0.75 m using a pre-bore high-pressure pressuremeter supplied and operated by In-Situ Engineering of Snohomish, Washington. Testing commenced at an initial depth of 6 m below the ground surface to ensure each test was within the glacial till. This section only summarizes the findings of the investigation. Details of the testing, methodology and interpretation of the results can be found in Chapter 4.

As detailed in Chapter 4, the pre-bore pressuremeter indicated that the glacial till was well represented by either a fully undrained model (Gibson and Anderson, 1961) or by a cohesive-frictional model (Carter, Booker and Yeung, 1984). The applicability of either of the models was assumed to be a function of the soil composition within the test pocket. In sections where the ground was more cohesive (higher percentage of clay), the stress-strain curves were well represented by an undrained model (elastic-perfectly plastic) derived by Gibson and Anderson (1961). In sections where the percentage of clay was lower or intra-till sand pockets were likely encountered, then the drained, cohesive-frictional model was considered to best represent the stress-strain curves. The characterization of the soil was obtained from a conventionally sampled borehole and an sCPTu test hole advanced adjacent to the pressuremeter test hole. Considering these findings, the shear strength of the glacial till was reasonably bounded by the pressuremeter test results.

5.1.6.1 Undrained Shear Strength

The undrained shear strength of the glacial till was best determined by fitting an ideal undrained curve model (Gibson and Anderson, 1961) to the unloading curve as suggested by Houlsby et al. (1986). The assumptions and parameters used in the interpretation of the pressuremeter tests are given in Chapter 4. The results of the undrained analyses on the glacial till are provided in Table 5.4. In general, the undrained shear strength varied from between 175 to 848 kPa with an average value of 412 kPa and a standard deviation of 122 kPa.

Test ID	Unloading Fit (kPa)	Loading Fit (kPa)	Log (kPa)	Limit Pressure (kPa)
UA01		Disturbed		
UA02	352.5	375	485	624
UA03	425	377	420	814
UA04	350	515	525	848
UA05	325	550	330	370
UA06	342.5	377	345	448
UA07	290	370	390	547
UA08	315	355	395	437
UA09	387.5	455	375	410
UA10	287.5	300	426	448
UA11	350	410	370	456
UA12	227	455	415	541
UA13	393	490	390	463
UA14	262.5	340	365	394

Table 5.4 Undrained shear strength interpreted from pressuremeter testing in the glacial till

As discussed in Chapter 4, the quality of the analyses should be considered when assessing the undrained shear strength of the ground. The order of the presentation in Table 5.4 indicates the values for the method of greatest confidence (left column) to the least confidence (right column). With this in mind and preference being given to the results obtained from the unloading curve, then the range of undrained shear strengths is from 175 to 425 kPa with an average and a standard deviation of 309 and 74 kPa respectively.

5.1.6.2 Drained Shear Strength

As described in Chapter 4, the drained shear strength of the glacial till was determined by fitting the cohesive-frictional model developed by Carter, Booker and Yeung (1984) to the loading curve. It was found during the analyses that the model was not considered to be applicable to all of the tests within the till. The applicability of the model was related to the degree of fit to the loading curve by the undrained model. In cases where the undrained model represented the loading stress-strain curve well, the drained cohesive-frictional model did not generally correlate well with the data. The assumptions and interpretation of the pressuremeter results considering a drained response of the glacial till is provided in Chapter 4. One assumption of note is that in each case, the cohesion was set as 10% of the average undrained shear strength. This minimized the number of assumed parameters in the curve fitting process.

The drained parameters obtained from the curve fitting to the loading curve using the cohesive-frictional model of Carter, Booker and Yeung (1984) are given below as Table 5.5.

Test ID	c' (kPa)	ϕ' (°)	Ψ (°)
UA01		Disturbed	
UA02	36	35	3.0
UA03	43	36	0
UA04	48	38	2.5
UA05	25	34	4.5
UA06	34	34	2.0
UA07	29	34	4.3
UA08	32	36	3.7
UA09	32	36	2.2
UA10	35	38.5	2.0
UA11	41	34	2.0
UA12		N/A (cohesive / undrained)	
UA13		N/A (cohesive / undrained)	
UA14		N/A (cohesive / undrained)	

Table 5.5 Drained parameters obtained from pressuremeter tests in the glacial till

Chapter 4 discusses the influence of each parameter on the shape of the ideal curve. In general, the friction angle is from between 34 to 38.5° with an average and standard deviation of 35.5 and 1.7° respectively. The effective cohesion is between 29 and 47.5 kPa with an average of 35.8 kPa and a standard deviation of 6.8 kPa.

5.2 Empress Sand

The Empress Sands are a pre-Laruentide glacio-fluvial deposit present throughout the City of Edmonton below the glacial till. The cohesionless deposits are typically encountered in pre-glacial valleys that were incised in the soft, claystone bedrock. In areas where the bedrock surface is higher, the Empress Sand is generally absent. Typically, the Empress Sand is coarser near the lower 1.2 m of the formation, which is composed of sand and gravel. The Empress Sands are readily differentiated from overlying till by its quartzic composition and lack of igneous rocks originating from the Canadian Shield. Finally the Empress Sand has been reported to have a maximum thickness of 19.8 m (Bayrock and Berg, 1966), though is typically around 12 to 15 m in thickness.

Historically, there has not been a significant amount of strength testing on the Empress Sands, as the depth to the strata is considerable and most heavy civil and large diameter tunnelling projects have not encountered the sand. Because of this, the historical data within the Empress Formation is extremely limited.

DeJong (1971) recovered several samples of the Empress Sand from the downtown area below the Avord Arms building. The samples were recovered as block samples carved from the foundation excavation. The block samples were then further trimmed to smaller 38.1 mm diameter samples for triaxial testing. DeJong (1971) did not report any difficulties in terms of sample recovery or preparation for testing.

Medeiros (1979) also recovered block samples of the Empress Sand from within excavations for the Churchill and Central LRT Stations during their construction. Following the advancement of shallow excavations into the Empress Sand, Medeiros (1979) pushed sharpened metal boxes into the sand and carved the bottom from the formation. The samples were preserved in the field with polyethylene wrap and paraffin wax. Prior to trimming, the block samples were placed into a cold room at -5 °C and frozen. However because the Empress Sand is only partially saturated, the samples could not be effectively frozen and most samples reportedly cracked during preparation. Medeiros then hand carved the samples in an unfrozen state and then froze the carved samples prior to mounting. Since there were severe difficulties in sample preparation and significant sample loss, only four compressive and four extension triaxial tests could be carried out on the relatively undisturbed Empress Sands.

An attempt was made during the current study to obtain samples for triaxial testing to help augment the meager data set with little success. Soil samples were recovered using conventional 70 mm diameter thin walled tube samplers (Shelby tubes). Due the high relative density of the Empress Sand, many of the thin walled tubes were either crushed under the pull down weight required to advance them or were pulled apart during extraction attempts. In all, 3 samples were recovered out of 7 attempts.

Additional sampling was attempted using a Laskey sampler which recovered 60 mm diameter soil samples in plastic liners placed within 85.7 mm (3 3/8") inner diameter threaded hollow stem augers. The plastic liner was attached to an adapter that was fed into the hollow stem augers on AW rods. The method is not dissimilar from the Pitcher sampler described by Morgenstern and Thomson (1971) that used spring loaded Shelby tubes within an adapted core barrel. These core samples were preserved in the field and transferred to the university where they were immediately sealed in polyethylene wrap, tinfoil and paraffin wax. The preserved samples were then placed into a temperature controlled moisture room for storage.

5.2.1 Laboratory Properties

5.2.1.1 Grain Size

The grain size of the Empress Sand is commonly obtained when encountered during site investigations. Unlike the clay till, most of the tests obtained for this study were conducted as part of research investigations, which were focused on other aspects other than the physical composition. As a result, most studies only reported the range of gradations for the tested samples. Based on these limited findings, the Empress Sand is reported to have a sand content ranging from 90 to 95% and a fines content from 5 to 10%. Of the historical studies, only Bayrock and Berg (1966) determined that the fines consisted of 3% silt and 6% clay content.

More information has been obtained however during the most recent study for the North LRT. Based on 12 grain size analyses carried out on the Empress Sand, the gradations measured on samples recovered from boreholes are shown below in Table 5.6.

Parameter	Lowest Value	Mean	Highest Value	Standard Deviation
Natural Moisture Content (%)	3	10	29	5
Sand (% Passing)	53	80	97	13
Silt (% Passing)	3	17	40	10
Clay (% Passing)	0	14	16	4

Table 5.6 Soil parameters of the Empress Sand in the downtown Edmonton area

Due to the negligible clay content within the Empress Sand, Atterberg limits tests could not be carried out. However, a thin cohesive layer was observed within the Empress Sand in several boreholes and within the exposed North LRT tunnel face. The clay laminations were highly discontinuous and varied from 10 to 100 mm in thickness. In the single sample that was tested, the material was best classified as a silty clay with silt and clay fractions of 30 and 70% respectively. Atterberg limits testing carried out on the single sample indicated plastic limits ranging from 24 and 27% and liquid limits between 72 and 82%. This results in a plasticity index between 45 and 58%, which corresponds with a high plasticity clay.

5.2.1.2 Unit Weight

A detailed review of the existing literature indicates that only Doohan and McLean (1975) and Medeiros (1979) attempted to measure the unit weight of the Empress Sand. The measured unit weights ranged from 18.3 to 19.6 kN/m^3. These values are relatively low when compared to estimates made based on SPT blow counts between 25 to greater than 50 blows/300 mm of penetration. These blow counts suggest the range of the unit weight should be between to 20.4 to 23.6 kN/m^3 (Bowles, 1996) and is typically assumed as being between 20.5 to 21.5 kN/m^3.

5.2.1.3 Hydraulic Conductivity

The permeability of the Empress Sand has not been formally measured in any documented investigation. This is primarily due to the depth of the sand formation and its near dry state in the upper horizons. Considering the variable gradation of the Empress Sand, it stands to reason that the lower horizons have a higher coefficient of permeability when compared to the finer upper reaches. Using basic empirical correlations based on the maximum, minimum and average D_{10} grain sizes, the maximum, minimum and average permeabilities as estimated by the Hazen method (Bowles, 1996) are 10^{-2}, 10^{-4} and 10^{-3} cm/s respectively.

5.2.2 Laboratory Strength Testing

Very limited laboratory experiments have been conducted on the Empress Sand. Only Medeiros (1979) examined the strength of relatively undisturbed samples in both compression and extension. Because the data set was so sparse, it is difficult to draw definitive conclusions as to the performance of the Empress Sand in the lab. What was clear was that there was a dramatic difference in the shear strains at the onset of yielding between compression and extension. This observation is very similar to that of the glacial till testing. Medeiros (1979) reported that axial strains on the order of 2.5 to 3% were required for yielding to occur in the sand when subjected to compressive forces. The stress-strain curves that resulted from the strength testing of Medeiros (1979) are shown below in Figure 5.15.

Because the compressive tests were conducted under drained conditions, Medeiros (1979) reported the volumetric changes of each sample as opposed to the pore pressure response. These results indicated a clear trend of volumetric compression, followed by rapid dilation after approximately 1.1% strain as shown in Figure 5.16. These trends agree well with the observation of the Empress Sand consisting of a heavily overconsolidated material in its undisturbed state.

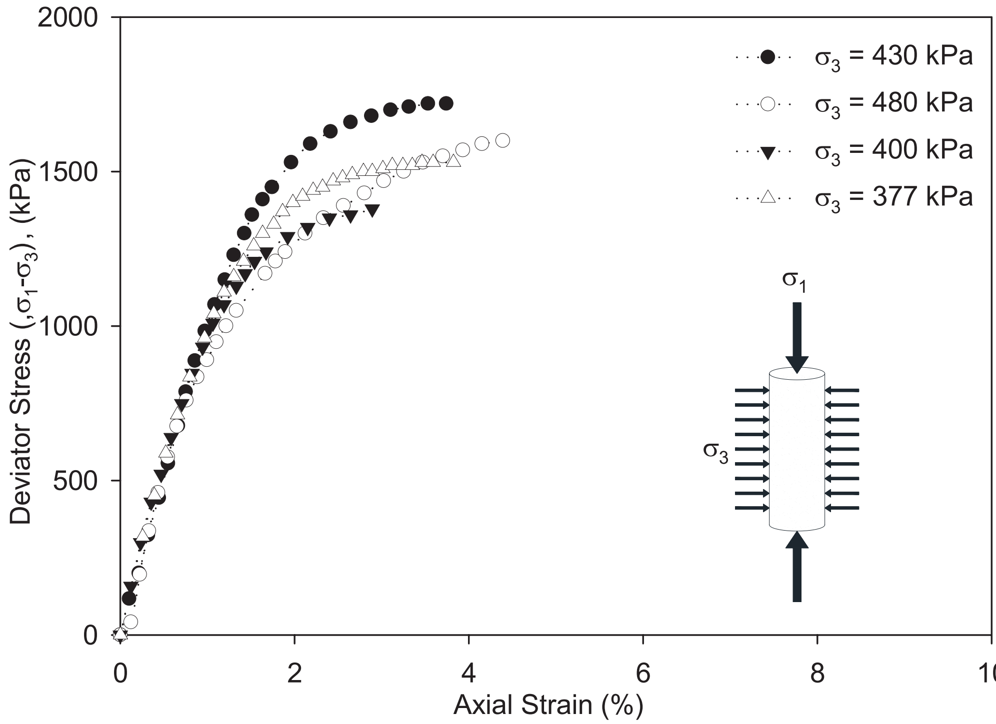

Figure 5.15 Compressive stress-strain curves for the Empress Sand (adapted from Medeiros, 1979)

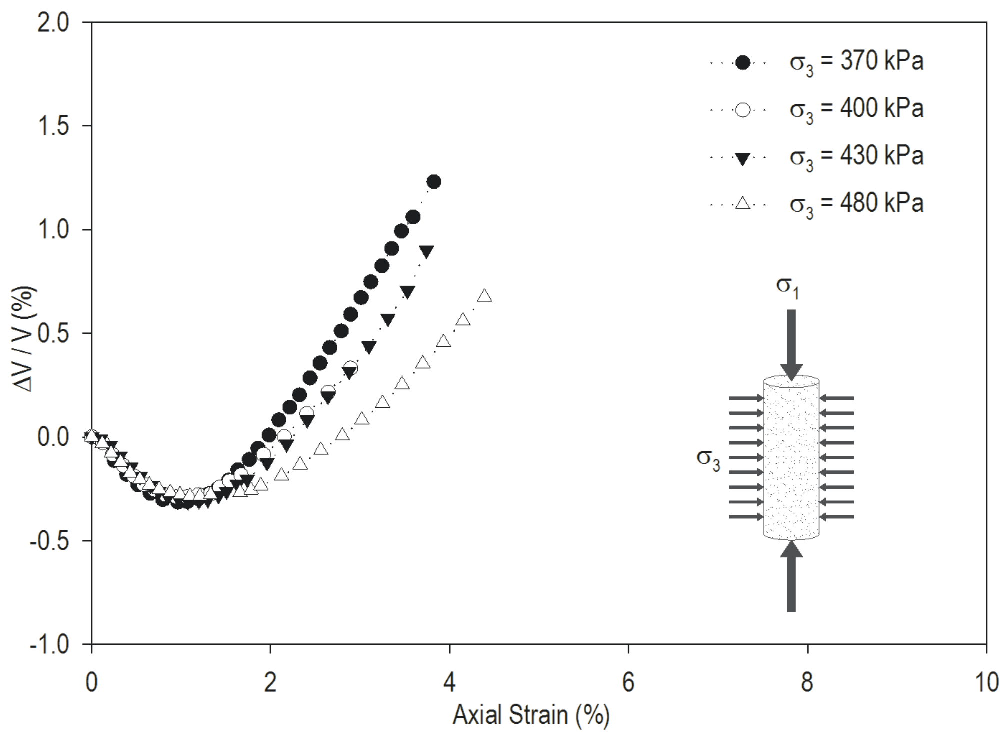

Figure 5.16 Volumetric changes in compressive samples (adapted from Medeiros, 1979)

The angle of dilation was calculated for each test for both the compressive and dilative phases of volume change and is shown on Table 5.7. In each case, the axial strains at which the maximum angle of dilation was also recorded and is shown on Table 5.7. Because the confining stress is very similar for each test, the low degree of scatter in the data suggests that the results are representative of the Empress Sand for that stress state. These values represent the peak angles of dilation and the corresponding shear strains for both the compressive (initial) and dilative (post peak) phases within the sand.

Parameter	Lowest Value	Mean	Highest Value	Standard Deviation
Compressive Dilation Angle (°)	25.9	26.6	27.2	0.6
Axial Strain (%)	0.96	1.05	1.1	0.06
Expansive Dilation Angle (°)	25.1	33.0	43.0	9.2
Axial Strain (%)	2.9	3.48	4.4	0.73

Table 5.7 Peak angles of dilation for the Empress Sand

In extension, the onset of yield also occurred at shear strains very similar to that of the glacial till when subjected to either extension or active compression. Of the three tests, the onset of yielding took place at strains of roughly 0.4 to 0.5%. Unlike the compressive tests, Medeiros (1979) did not monitor the volumetric changes during the extension tests and therefore the angles of dilation could not be determined. The stress-strain curves recorded by Medeiros (1979) for the extension tests on the Empress Sand are shown in Figure 5.17.

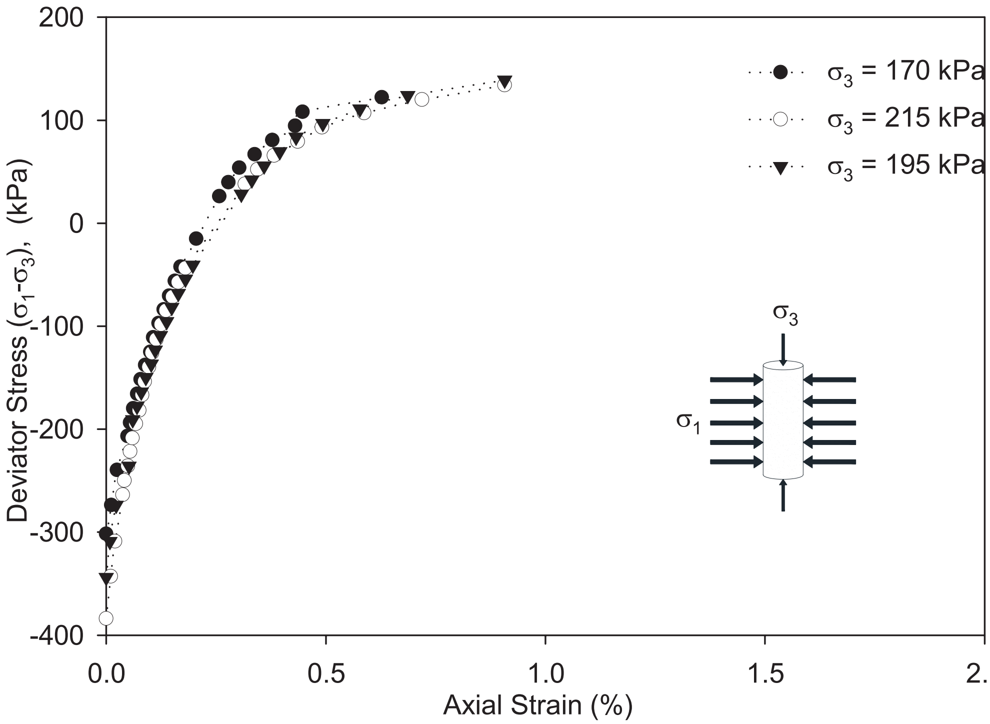

Figure 5.17 Extension stress- strain curves for the Empress Sand (adapted from Medeiros, 1979)

Additional shear strength testing was carried out during this study. A single borehole was drilled from the ground surface to a depth of 27 m. 63 mm diameter, relatively undisturbed samples were collected using a Laskey core barrel as described in Section 5.2. Upon testing, the samples were removed from the preservative and trimmed accordingly.

Direct shear testing was selected, as the sample diameter was the same as the direct shear machines reducing the amount of trimming and exposure to atmosphere prior to testing. In all cases, the samples were cut to a thickness of approximately 35 to 37 mm and had a final diameter of approximately 63.5 mm. Prior to mounting, the samples were weighed and a representative portion was measured for the water content. The samples were loaded and the associated confining pressure was applied in one step. The confining pressures used were 50, 150, 250, 300 and 400 kPa. Once the initial compression of the sample was completed, which was typically around 5 to 10 minutes in duration; the shearing forces were applied. The samples were initially sheared at a rate of 0.0667 mm/min. The samples were tested in a wet state with water added to the reservoir during consolidation. The typical initial moisture contents measured ranged from 6.6 to 18.6%. When compared to the moisture contents measured upon completion of the testing, there was approximately a 7.2% increase in the final moisture content. The samples would have been tested in a dry state, however, it was not possible to effectively preserve the moisture content in the test chamber and the additional strengths attributed to negative pore pressures could not be determined. The measured stress-strain curves for the five tests are shown below in Figure 5.18.

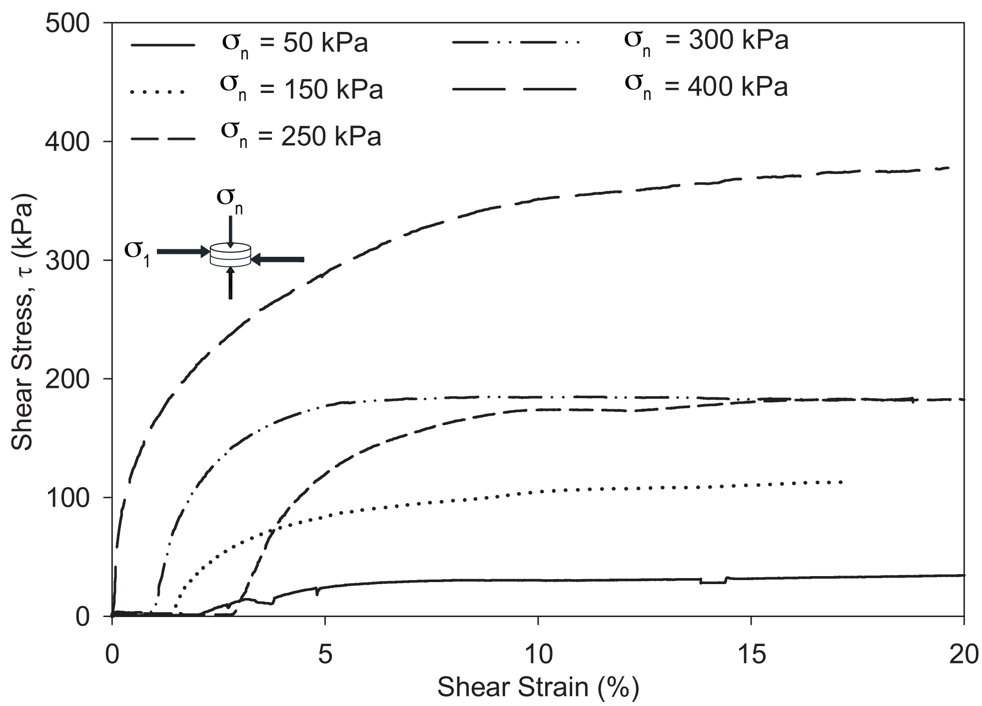

Figure 5.18 Direct shear stress-strain curves for the Empress Sand

The vertical changes of the Empress Sand during direct shear was also monitored. The change in volume of the sample during shear was calculated by dividing the incremental volume by the sample volume at the start of shearing. The results of the volumetric strain with shear are shown in Figure 5.19. All tests but the test conducted at a confining stress of 50 kPa appeared to approach a constant volume. It was however expected that the sample subjected to a low confining stress would compress with increased shear. The sample sheared at a confining stress of 400 kPa exhibited an odd behaviour by compressing at a near constant rate to a shear strain of 2% at which time there is a distinct break in the rate of volume change and the sample compresses at a slower but still constant rate thereafter.

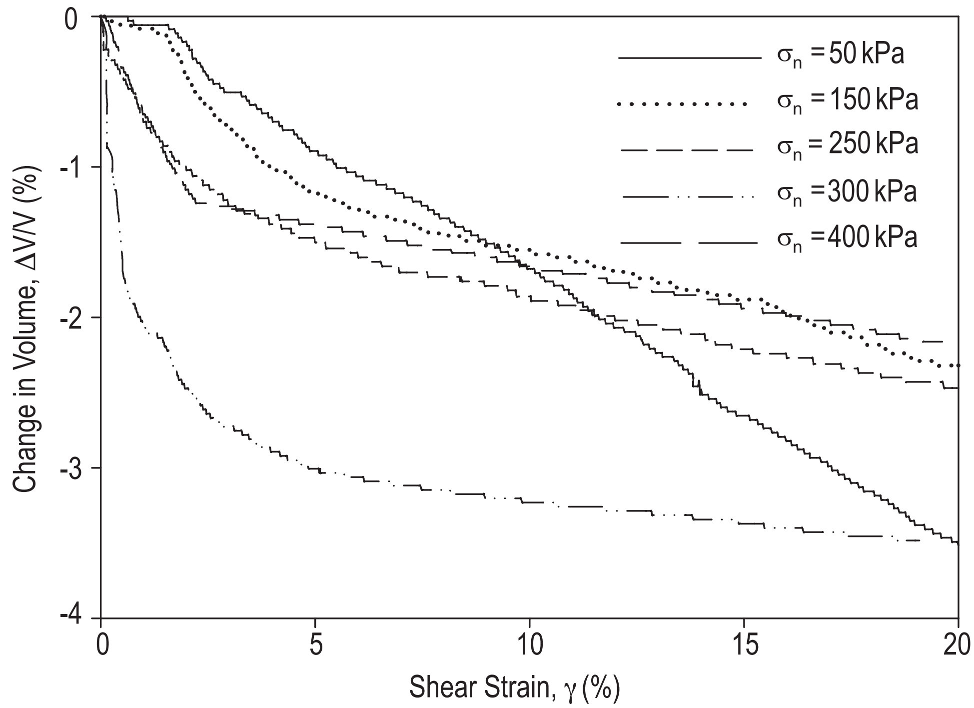

Figure 5.19 Volumetric change (ΔV/V) of the Empress Sand in direct shear

Medeiros (1979) did not plot the Mohr-Coulomb failure envelopes resulting from either the compression or extension tests on the Empress Sand. In the work by Medeiros (1979) an effective friction angle of 40.5° was reported for the tests carried out in compression. No values were reported for the extension tests except to say that the friction angles "were similar to the compressive values since the Empress Sand is a cohesionless formation" (Medeiros, 1979). During the current investigation, the peak values were replotted in p'-q space and the resulting Mohr-Coulomb failure envelopes were fit using a linear line of best fit. Based on these lines of best fit, two distinct failure envelopes were obtained, one for compression with an α = 39.6° which agreed well with the one calculated by Medeiros (1979) and one for extension (α' = 23.9°) which was considerably lower than the compressive envelope. The two yield criterion are shown in Figure 5.20. The R^2 value of each line was greater than 0.95.

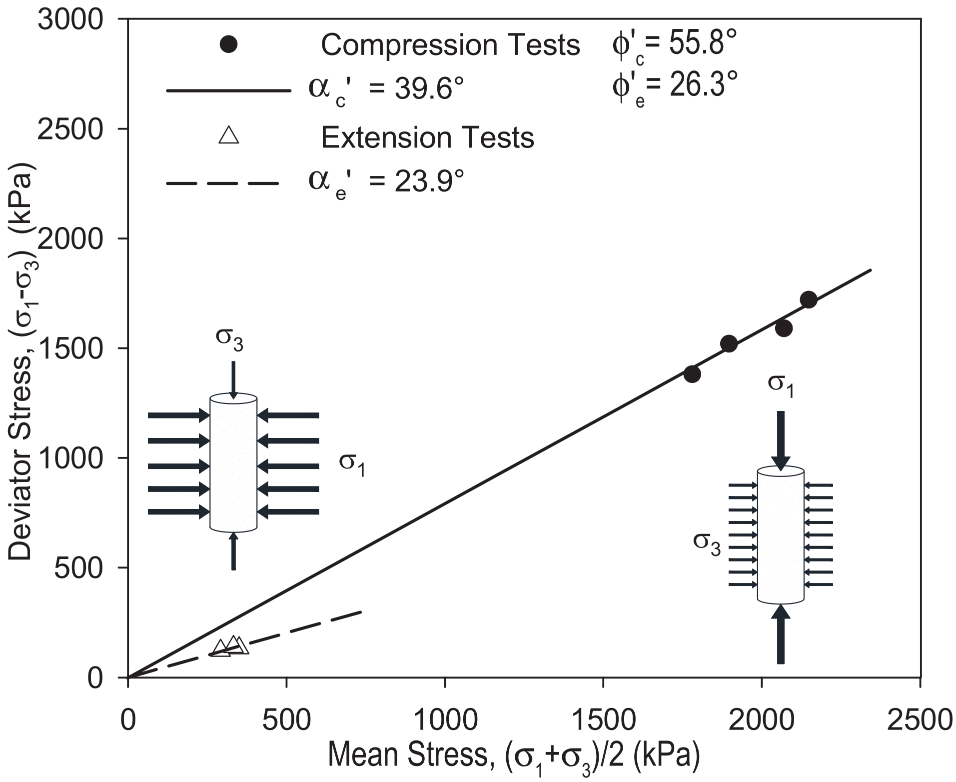

Figure 5.20 Compression and extension peak shear stress failure envelopes for the Empress Sand (after Medeiros, 1979)

As with the glacial till, the usage of the peak shear stress values (α) in p'- q space has resulted in an drained friction angle that is slightly higher than is calculated from the tangential shear stress circles which consider all of the tests together. By assuming a cohesion of zero and attempting to find a line that contacts the tangent of most Mohr circles of stress constructed from the various lab tests, an drained friction angle of 55.8° is determined. The Mohr circles constructed from the triaxial tests by Medeiros (1979) and the direct shear tests recently conducted are shown below in Figure 5.21. It is unclear which effective angle of friction best represents the Empress Sand since the lower friction angle is very closely related to the friction angles obtained from the pressuremeter testing. Knowledge of the stress history however suggests that the higher friction angle may be more representative of the Empress Sand in its confined state.

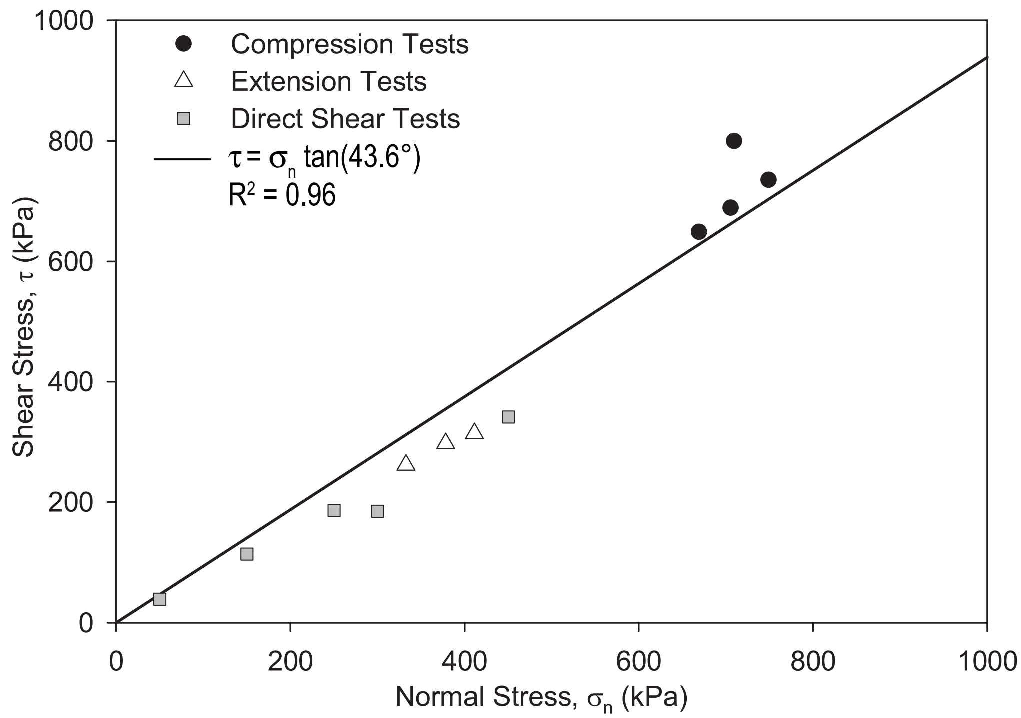

Figure 5.21 Drained Mohr circles for the Empress Sand.

5.2.3 Residual Strength of the Empress Sand

The residual strength of the Empress Sand was probed during the direct shear tests carried out during the current investigation. In each test, the samples were sheared a minimum of 18% in order to achieve a constant volume during shear. Based on Figure 5.19, 4 of the 5 tests appeared to approach a constant volume. Because the effective stress paths have a constant confining stress, the stress path could not be used to determine the critical state friction angle (*M*) or the point of onset of residual conditions. Examination of the stress-strain curves shown in Figure 5.18 suggests that the residual shear strength is approximately equal to the peak shear strength, as all tests appeared to be strain hardening in nature. Calculation of the larger strain shear strength (shear strains >15%) indicates that the residual friction angle is approximately 37.7°. This friction angle is approximately 87% of the peak value. In each case shown below, the residual strength was averaged between strains starting at 15% through to completion of the test.

Because the volume change of the Empress Sand during shear was only approximately constant for two of the samples, it is not considered correct to term the residual shear strength as the critical state. Historically though, once the friction angle in a sand is fully mobilized as it appears to be at large strains, this would typically coincide with the critical state for that material. The measured residual friction angle is slightly higher than the typical critical state upper bound of 35° for quartzic sands as given by Terzaghi et al (1996).

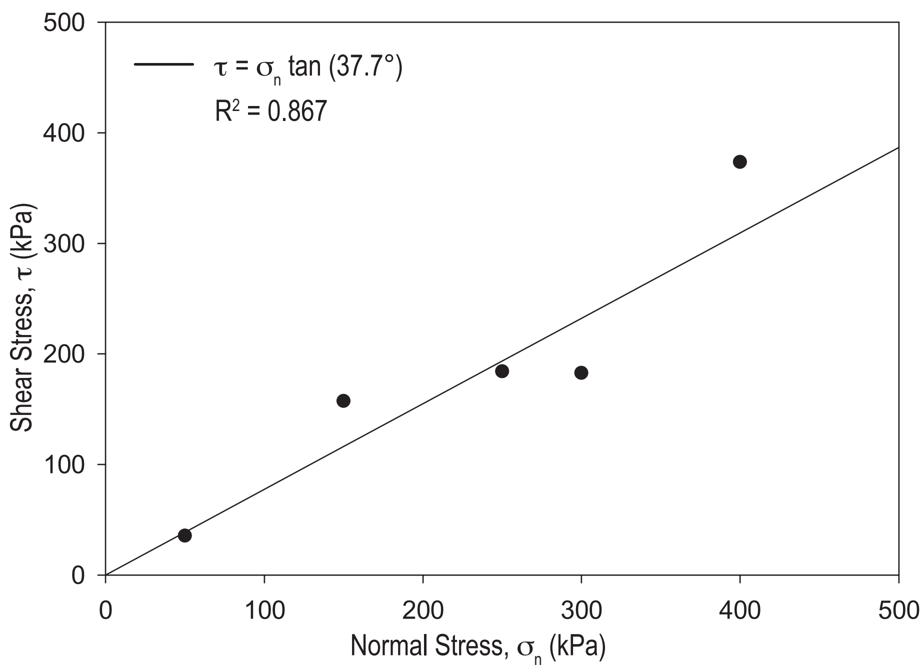

Figure 5.22 Average residual strength for the Empress Sand from direct shear tests.

The shear strain required to achieve the residual state for the Empress Sand was assessed to occur when a given sample achieved the average larger-strain (>15% strain) strengths shown above. Based on these criteria, the maximum, minimum and average shear strains required to achieve the average residual state are 23, 4.9 and 12.8% respectively. The standard deviation of the residual shear strains is 6.9%.

5.2.4 Insitu Strength

5.2.4.1 Seismic CPTu

The insitu strength of the Empress Sand was assessed using the seismic CPTu described in Section 5.1.5.1. Of all of the sCPTu test holes advanced as part of the North LRT investigation, all but 09-3, 09-3B, and 09-7 penetrated into the Empress Sand, and two (09-4 and 09-5) were only pushed up to 2.5 m into the sand deposit. As a result, the data is somewhat limited when compared to the glacial till. It should also be noted that in test holes 09-1 and 09-2, the cone was deemed to achieve refusal and was removed from hole and the test hole was augered out. The CPT was continued following augering of the hole. Details of the sCPTu data and the associated logs are provided in Appendix A.

5.2.4.2 Drained Shear Strength

The drained shear strength of the Empress Sand was determined as described above in Section 5.1.5.3. Because there are thin layers of cohesive and fine-grained soils within the Empress Sand, there are some sections that were not considered as cohesionless and therefore the entire depth of the Empress Sand does not show as a frictional material. The typical frictional response from test hole sCPTu 10-08 is shown below in Figure 5.23. The remaining CPT profiles are included in Appendix C for reference.

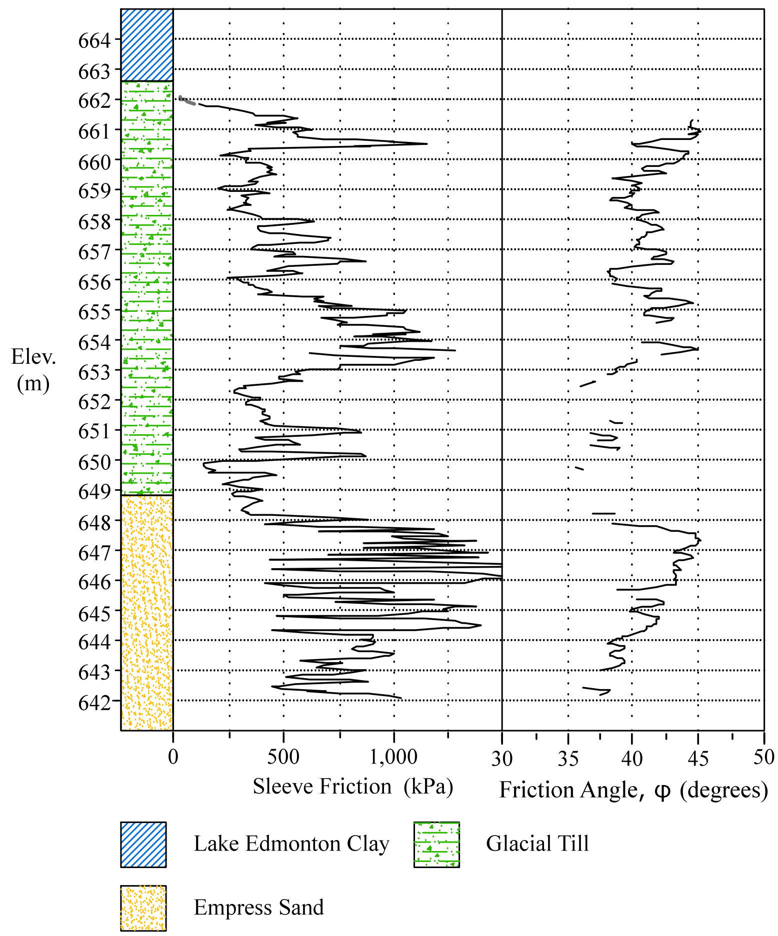

Figure 5.23 Frictional parameters from sCPTu tests of the Empress Sand within the Station Lands

Figure 5.23 shows that substantial friction is accumulated within the Empress Sand with an average frictional component of approximately 850 kPa along the 225 cm^2 sleeve. Based on the tip resistance equation given as Equation [3.2], the angle of internal friction of the Empress Sand is between 36 and 45° with an average of around 41°. This is in very good agreement with the laboratory testing. When the peak friction angle from Figure 5.20 is used, the difference between the peak friction and the sCPTu is only 3.5%. When the friction angle tangent to the Mohr circles from Figure 5.21 is used the difference between it and the sCPTu friction angle is 13.9%.

5.2.5 Pre-Bore Pressuremeter (Camkometer)

The pre-bore pressuremeter test hole extended through the glacial till into the underlying Empress Sand. In all, a total of 9 tests were carried out within the cohesionless deposit. It is important to note that there was considerable disturbance of the last two tests due to the length of time between the tests and when the final test section was drilled. Because the pressuremeter was a high pressure, pre-bore pressuremeter, it required the advancement of the borehole in 1.5 m increments (test pocket) prior to the insertion of the pressuremeter probe. The final test pocket was advanced 3 m in order to expedite the test process and observe the rate of strength and stiffness degradation with time. Details of the testing and assessment of the shear moduli and shear strength are provided in the Chapter 4. This section is designed to briefly summarize the methods of assessment and the final results of the pressuremeter testing within the Empress Sand.

5.2.5.1 Short-Term (Undrained) Shear Strength

The short-term shear strength of the Empress Sand was assessed by curve fitting the undrained model developed by Gibson and Anderson (1961) to the unloading portion of the stress-strain curve. It was only during unloading that the strain rate was sufficient to result in conditions that did not permit complete drainage between measurements. Use of the unloading curves is also convenient in that the degree of initial disturbance is irrelevant. Since the borehole is in a failed state, the unloading curve was always complete and easy to interpret. Also, because the material was quite clearly a very dense, cohesionless deposit based on its loading curve, application of the undrained model or even the cohesive frictional model by Carter, Booker and Yeung (1984) was not possible.

The undrained shear strengths obtained from the unloading curves within the Empress Sand using the three of the four methods detailed in Section 5.1.6.1 (unloading, log method and limit pressure method) are summarized below in Table 5.8.

ID	Unloading Fit	Log Method	Limit Pressure
UA15	575	700	792
UA16	660	877	796
UA17	672.5	630	815
UA18	575	655	898
UA19	662.5	568	802
UA20	650	760	794
UA21	700	980	1062
UA22	775	746	989
UA23	407.5	415	923
UA24	660	782	1037

Table 5.8 Short term (undrained) shear strength of the Empress Sand from pre-bore pressuremeter tests

Table 5.8 shows that the undrained shear strength of the Empress Sand is generally consistent with depth. The single low (minimum) shear strength at UA23 was the test where there was considerable disturbance following borehole advancement. Overall the unloading curve assessment shows maximum and minimum strengths of 775 and 407.5 kPa respectively. The average strength and standard deviation are 633 and 98 kPa respectively. These strengths represent a 105% increase in undrained shear strength when compared to the overlying glacial till.

5.2.5.2 Drained Shear Strength

The drained shear strength of the Empress Sand was assessed using only the Hughes frictional model (Hughes, 1977). Since the formation is a very dense deposit, the Hughes frictional model was considered ideal for interpreting the loading stress-strain curves. In each case, the critical state friction angle was selected to be 35° which is given by Terzaghi et al. (1966) as the upper bound for quartzic sands. This is slightly lower than the findings of the recent direct shear tests that indicated that the critical state friction angle was 41.3°. The static critical state friction angle was selected in order to eliminate additional variables from the interpretation of the data. The analyses indicated that the effective friction angle is strongly influenced by the dilation angle. The dilation angle in the Hughes frictional model is actually a function of the ratio between the effective friction angle and the critical state friction angle. The range of dilation angles was found to be between 34.5 and 39.5°. This also agrees well with the findings of the post peak (dilation) dilation angles given by Medeiros (1979) that were determined to be between 25 and 43° with an average of 33°. The good agreement between the two sets of dilation angles indicates that the use of a critical state friction angle of 35° was not overly detrimental to the analyses.

Representative curve fits are provided in Chapter 4 as well as in Appendix A. The frictional parameters of the Empress Sand are provided below in Table 5.9.

ID	ϕ' (°)	Ψ (°)
UA15	43.3	34.5
UA16	41.2	37.2
UA17	40.2	38.5
UA18	42.3	35.8
UA19	40.3	38.4
UA20	39.5	39.4
UA21	40.4	38.2
UA22	43.2	34.7
UA23	41.4	36.9
UA24	39.4	39.5

Table 5.9 Frictional parameters of the Empress Sand from pre-bore pressuremeter tests

Table 5.9 indicates that the range of effective friction angles is very close with the maximum and minimum effective friction angles being 43.3 and 39.4° with an average of 41.1°.

As described in the previous chapter, the fit of the Hughes frictional model was determined by using the method of least squares. Setting the error between the field data and the ideal model to a minimum optimized the curve fitting. This was accomplished by making the effective friction angle the variable and using the solver function in excel to set the average error to a minimum.

5.3 Defining Yield Criteria in Over-Consolidated Soils for Tunnelling

5.3.1 Yield Characteristics

In order to establish a definition of yielding of the glacial till, the triaxial data of Whittebolle (1983) has been replotted in several different ways to better illustrate the response throughout the shearing process. The first method was to plot the pore pressure response, u with respect to the principal stress ratio, σ_1/σ'_3. Plotting the data in this fashion illustrates the transition from positive to negative pore pressures in a much clearer manner. These paths represent the transition from compressive to dilative volume change during shear. Figure 5.24 shows the measured change in pore pressure with respect to the effective stress ratio. In each case, the pore pressure response has been plotted relative to the initial backpressure. As a result, negative pore pressures indicate pore pressures that are less than the initially applied backpressure and are not actually negative.

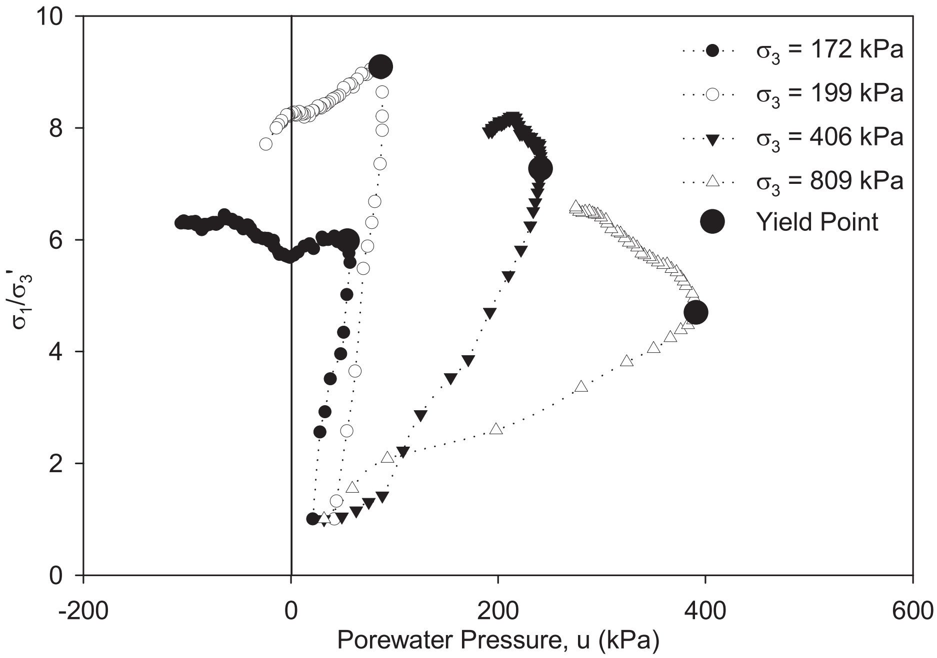

Figure 5.24 Pore pressure response as a function of the principal stress ratio

From Figure 5.24, there is a clearly a transition from a contractile (compressive) state to a dilative state. The end of compression (positive pore pressures) and the onset of dilation is marked by the gradual reduction of pore pressures with ongoing strain. In the two samples with low confinement, the transition appears to occur at axial strains of 0.85%. In the two samples with confining stresses of 406 and 809 kPa, the transition occurs at axial strains of 3.3 and 3% respectively. When these strains are compared with the peak values shown in Figure 5.11, the values correspond with the peak in the curve in the tests at lower confinement. It is interesting to note that the two samples sheared under low confining stresses both exhibited final pore pressures less than the initially applied backpressure suggesting considerable dilation post-peak. It is expected that as dilation (volume increase) occurs, that the pore volume increases, thereby reducing the measured pore pressures and resulting in suction. In the tests subjected to confining stresses greater than 400 kPa, the strains that the pore pressure reversal occurs is at the point where the incremental increase in the shear stress ratio (q/p') approaches zero. There is still some increase to the shear ratio following the transition, but the pore pressure reversal point represents the point where the incremental rate of increase in the shear ratio is 0.01 or less.

Another way to plot the data is to plot the effective principal stress ratio with respect to the effective minor principal stress. Figure 5.25 illustrates how the confining stresses are influenced by the change in pore pressure throughout the shearing of the sample. In this case, it appears that the two samples subjected to low confinement (176 and 199 kPa) follow roughly the same path during loading. This suggests that the pore pressure response is nearly identical during loading. The peak principal stress ratio of the sample with a confining stress of 176 kPa however is 66% that of the sample at a confining stress of 199 kPa. It is possible that micro-fissures or the presence of heterogeneities (gravel) within the first sample could have contributed to the early onset of yielding.

With respect to the higher confinement samples, it is interesting to note that the change in effective confinement during shear was typically around 50% that of the actual confining stress applied to the sample. The sample sheared at a confinement of 406 kPa underwent an effective minor principal stress reduction of 51% while the sample sheared at a confinement of 809 kPa underwent a reduction of 46%. Figure 5.26 illustrates the change in effective minor principal stress during shear.

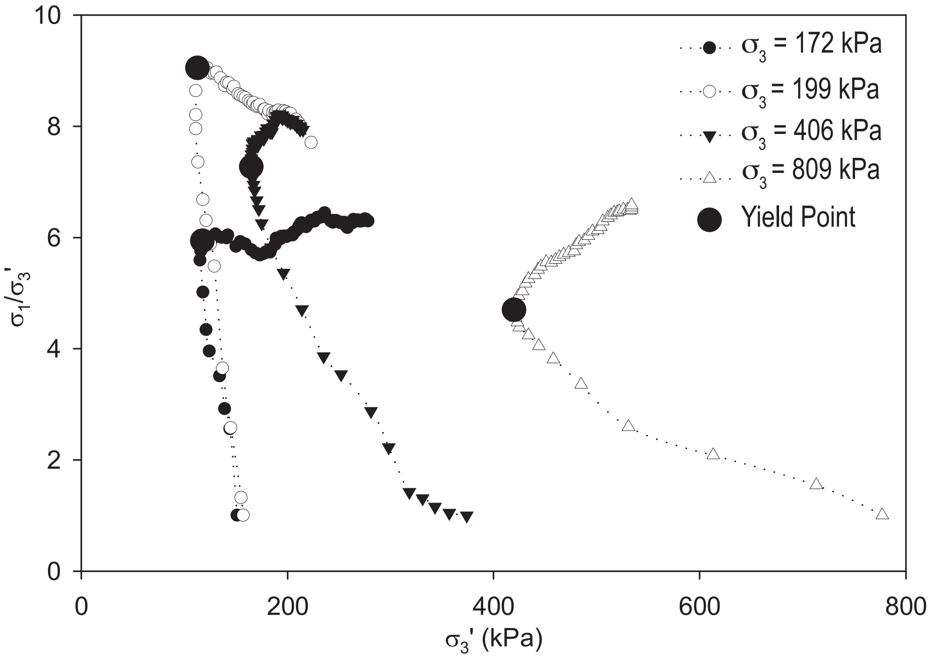

Figure 5.25 Change in effective principal stress ratio with effective minor principal stress

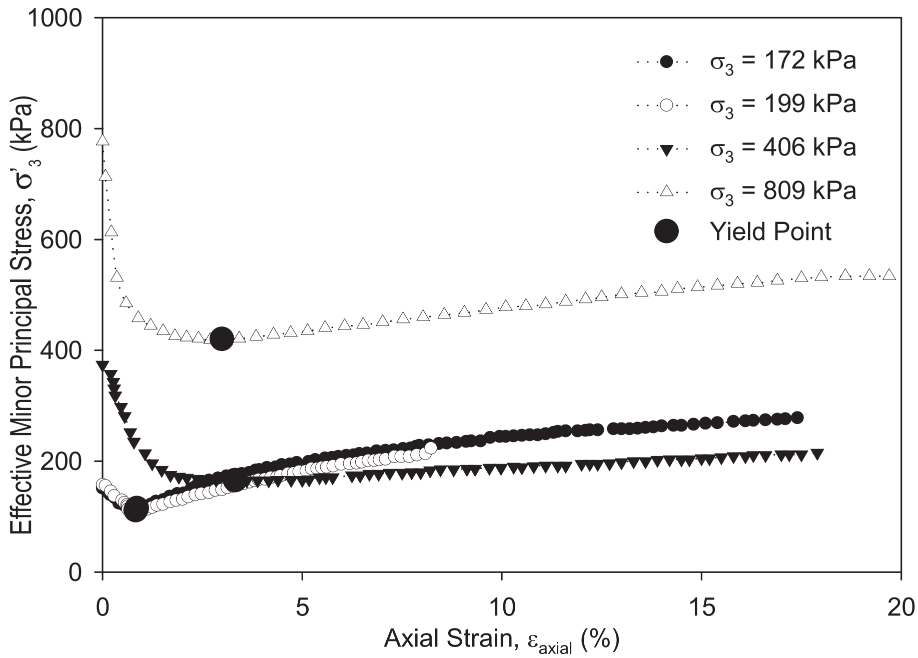

Figure 5.26 Change in effective minor principal stress during shearing

Figure 5.26 appears to provide yet another method for identifying the transition from elastic to plastic shear strains for conventional triaxial shear tests on heavily overconsolidated soils. It is interesting that three of the tests appear to approach a similar effective minor principal stress at the onset of yielding. The third triaxial test (σ_3 = 406 kPa) by Whittebolle demonstrates that the pore pressure increases by 209 kPa, which then contacted the tangential Mohr-Coulomb envelope at the transition from contraction to dilation.

Inspection of the critical state friction angle (*M*) and the angle of the tangential effective stress Mohr-Coulomb failure envelope (ϕ') suggests that the two slopes are nearly coincident. The fact that both slopes are the same suggests that at the onset of yielding, the structure of the soil (cohesion) is almost completely destroyed. When the strains required to achieve critical state are reviewed, it would appear consistent that the two tests conducted at confining stresses less than 200 kPa reach 95% of the critical state at strains corresponding with the onset of yielding. In the two tests carried out at higher confining stresses, the shear strain at the onset of yielding results in materials that are 88 and 90% of the critical state. Because the soil achieves critical state at such relatively small shear strains, it is considered appropriate to describe the post yield state by the critical state friction angle and a cohesion intercept of zero. Duncan and Wright (2005) provide a method of determining the mobilized friction angle based on the data plotted in Figure 5.25. Duncan and Wright (2005) suggest that the mobilized friction angle may be calculated as given in Equation 5.3.

$$\phi'_{\mathrm{mob}} = 2\left(\cot\sqrt{\sigma_1'/\sigma_3'}\right) - 45 \qquad \text{Equation 5.3}$$

where:

ϕ'_{mob} is the mobilized friction angle (°); and

σ_1'/σ_3' is the effective principal stress ratio.

Using Equation 5.3, the mobilized friction angle has been calculated. Because the mobilized friction angle given by Equation 5.3 was found to exceed the large-strain friction angle (critical state friction angle), the mobilized friction angle was normalized to the drained peak friction angle calculated to be 46.8° is plotted with respect to the shear strain in Figure 5.27.

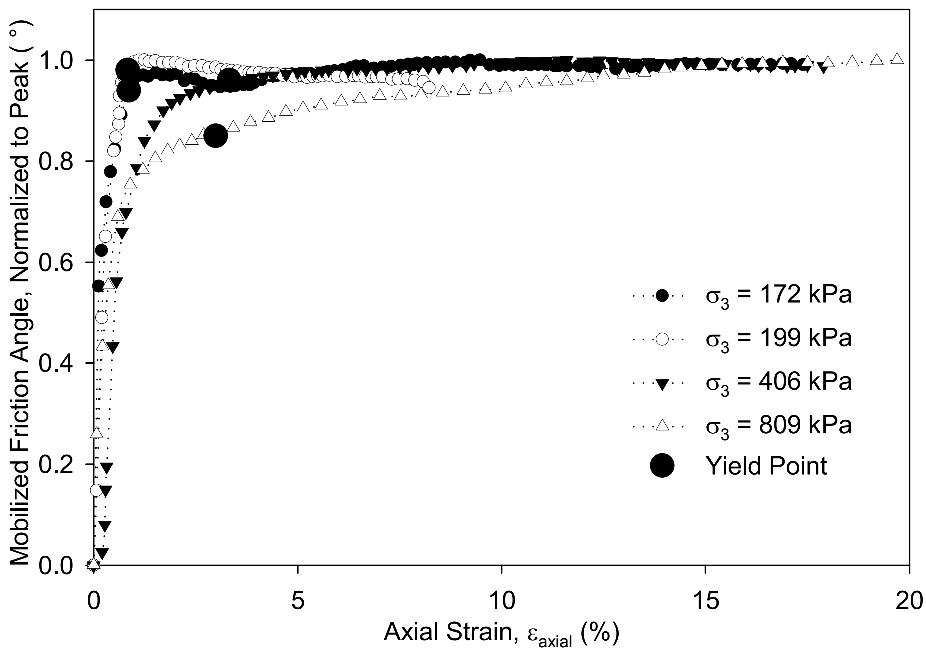

Figure 5.27 Mobilized friction angle of the glacial till based on Equation 5.3

Figure 5.27 illustrates that the hypothesis of using the critical state friction angle, post yielding appears to be reasonable as the normalized mobilized friction angles agree well with the onset of critical state.

For heavily overconsolidated soils, the shear strains at failure are limited by the pore pressure response needed to contact the effective stress failure envelope. In cases where the soil is lightly to normally consolidated, shear strains can continue until the positive pore pressures accumulate to approximately 50% of the confining stress prior to contact with the failure surface. The pore pressure development is considered very important in terms of determining an appropriate failure criterion. In applications such as tunnel excavations where there is little to no confining stresses, it is likely that the onset of yielding will occur at shear strains less than 1%. In cases where there are higher degrees of confinement such as foundation construction, the shear strain required to achieve suitable pore pressures for yielding to occur can be greater than 3%.

5.3.2 Role of Stress Path

The strength of the glacial till is highly dependent on the stress path taken prior to yielding. Medeiros (1979) clearly demonstrated that the strength of the glacial till varies considerably when strained in active or passive compression. There were also minor differences when tested under plane strain conditions. Pressuremeter testing in the glacial till has also clearly demonstrated the role of the stress path as indicated by failure strains on the order of 3 to 4% in compression and between 0.1 to 0.3% in extension. It is therefore considered crucial to establish the anticipated stress path when considering applicable failure criteria for any kind of geo-application within heavily overconsolidated soils similar to the glacial till in the City of Edmonton. The applied stress path will influence the shear strains necessary for the onset of yielding as shown in Section 5.3.1. The possible stress paths of the glacial till for various test methods are shown below in Figure 5.28.

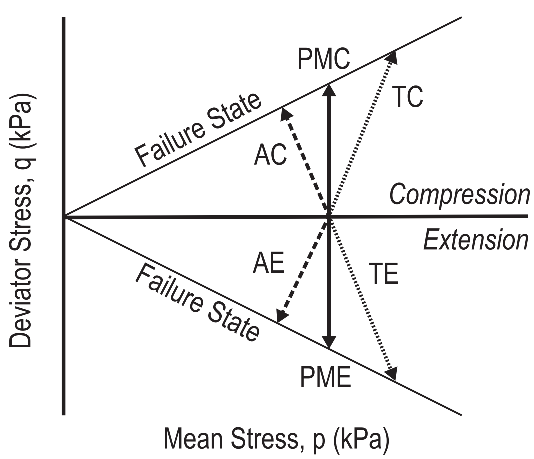

Figure 5.28 Laboratory stress path of the Edmonton glacial till

The stress paths correspond with triaxial compression (TC); active compression (AC); pressuremeter compression (PMC); triaxial extension (TE); active extension (AE) and pressuremeter extension (PME). Of all the methods, active extension is considered to be the least possible to replicate; this is because it represents tensile tests of a dog-bone shaped sample. Trimming of the Edmonton glacial till in a dog-bone shape is not considered feasible due to the high presence of smaller, micro fissures. Previous researchers in Edmonton have commented on the difficulties in trimming the till into conventional triaxial samples, the lathing of dog bone shapes adds another degree of difficulty.

The stress path experienced by the ground during tunnelling operations however differs slightly from the above lab and insitu tests. Medeiros (1979) conducted several active compression tests on the glacial till as shown in Figure 5.8. The active compression tests carried out on the glacial till indicated that yielding occurred at shear strains on the order of approximately 0.2%. The active compression test results compare well with the findings of the extensional pressuremeter tests which indicated yield strains between 0.1 to 0.3%.

Yielding of the glacial till is highly dependent on the initial stresses applied to the test samples. In the conventional triaxial tests, the compressive yield strains were dictated by the effective stress state and the pore pressure accumulation. It is for this reason that it is possible that the very low shear strains measured during the active compression tests by Medeiros (1979) might have been a function of the low confining stresses rather than the stress path taken. Had the tests been carried out at confining stresses higher than 400 kPa, it is likely that yielding would have occurred at shear strains greater than 1% but less than 3% as in conventional triaxial tests. The increased strains would then be a function of the stress path taken during loading and the fact that by simultaneously reducing confinement and increasing the vertical stress, σ_1 and σ_3 move away from one another at a constant rate until contacting the failure envelope. Provided that the sample is saturated, the Skempton 'A' parameter would be a maximum and pore pressures would also be increasing with shear stress. Failure would be therefore be initiated by a combination of pore pressure accumulation and confinement reduction.

The above failure mechanism is also relevant for tunnel construction in heavily overconsolidated soils. The differing stress paths are also a function of the initial insitu stress orientation, the excavation method and the proximity to other underground structures (initial stresses). With respect to tunnel construction, it is often more convenient to represent stress paths around the tunnel cavity in principal stress space rather than *p' - q* space as is typical for soil mechanics. Similar stress paths have been developed for a single tunnel within the Edmonton glacial till at a depth of 12 m below the ground surface. The boundary element software Examine 3D by RocScience was used to model the change in stress around a single egg shaped tunnel within the tunnel face, crown and springline. In this case the tunnel was modeled as a full-face excavation with a K_o=0.8. The calculated stress paths are shown below in Figure 5.29.

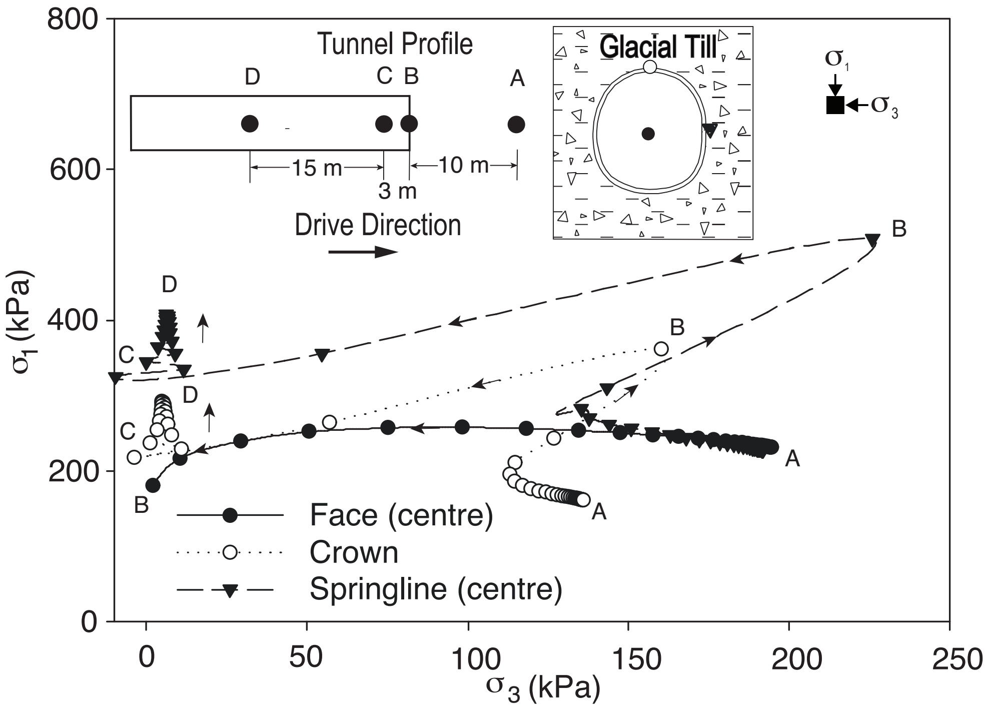

Figure 5.29 Stress path around a single tunnel within the Edmonton glacial till at a depth of 12 m below the ground surface, and a K_o=0.8

The laboratory test samples were also plotted in σ_1 - σ'_3 space in order to illustrate how the usage of conventional triaxial data to predict yielding around a tunnel cavity can be problematic. The principal stress paths of the historical laboratory testing on the Edmonton till are shown below in Figure 5.30. Because the pore pressures recorded by Whittebolle (1983) are considered, the triaxial stress paths do not extend vertically like drained tests by Medeiros (1979). The drained triaxial tests by Medeiros (1979) were strained well beyond the onset of yielding and hence extend beyond the failure envelope. The failure stresses as determined by the change in volumetric measurements (from compression to dilation) are shown as markers of increased size on the various stress paths and agree well with the predicted Mohr-Coulomb envelope with an average error of 3.3%

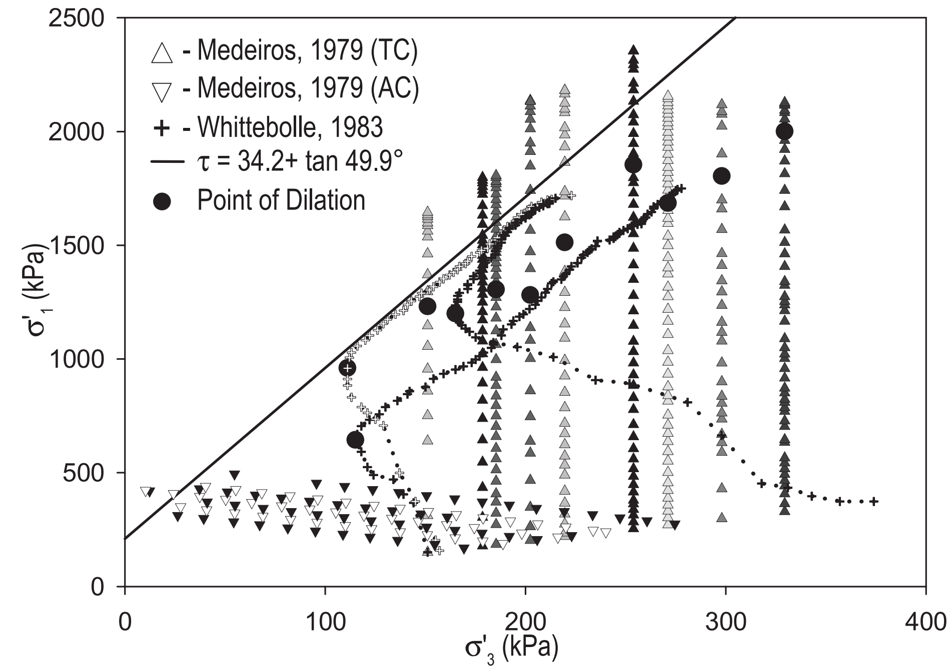

Figure 5.30 Laboratory stress paths and associated c' and ϕ' failure envelope

It is interesting to note that the active extension tests carried out by Medeiros (1979) come very close to terminating at the failure envelope in the tensile region, while the stress paths of Whittebolle (1983) tend to change direction at the contact with the failure envelope. The change in path for the conventional triaxial tests by Whittebolle (1983) is indicative of the transition from compressive to dilative behaviour of the test samples. Though not documented by Medeiros (1979), it is suspected that the active compressive samples were highly fractured upon failure and additional straining was not possible.

When Figures Figure 5.29 and Figure 5.30 are compared, it would appear that the best representation of the stress path taken by a tunnel under construction is the active compression test. This test is nearly identical to the stress path taken by the full tunnel face excavation. It also closely represents the stress path of the ground immediately prior to excavation of the tunnel springline. The stress path at the springline would be well represented by gradually increasing the vertical stress while reducing the confining stress as in the active compression tests conducted by Medeiros (1979).

When the excavation of the tunnel face is divided into sections like a header and bench, the stress paths become increasingly complex. Figure 5.31 illustrates the stress path for the center of the header, bench and crown of the same egg shaped tunnel used above in Figure 5.29.

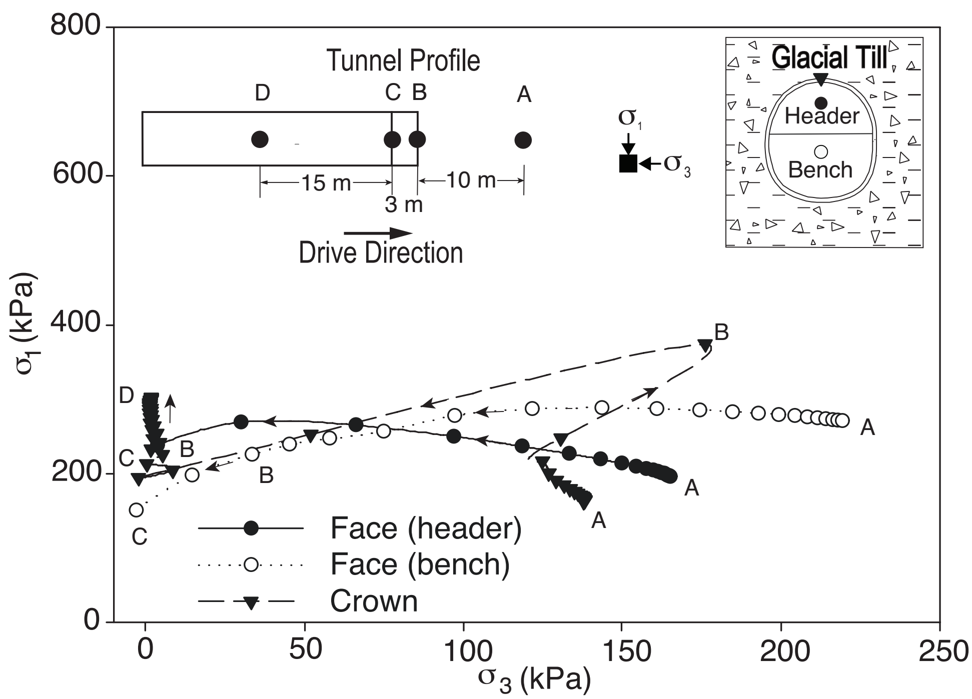

Figure 5.31 Stress path of ground within the face and crown for a tunnel excavated using a heading and bench sequence at a depth of 12 m below the ground surface and K_o=0.8

In the examples shown in Figures Figure 5.29 and Figure 5.31, the stress paths of the header and the crown are well represented by the active compression test. The bench however would be prone to block and wedge failure. The formation of blocks or wedges is due to considerable stress relaxation in the σ_1 and σ_3 directions. In the case of block or wedge failure, the stress path must contact the residual shear strength Mohr-Coulomb envelope as suggested by Skempton and La Rochelle (1965) and Bishop et al. (1965). Because the failure mechanism is discontinuity dominated, it stands to reason that yielding or block translation occurs when the stress path encounters the yield envelope of the fissures. Skempton and La Rochelle (1965) and Bishop et al. (1965) suggested that this yield surface is defined as the residual failure envelope. Figure 5.32 illustrates the calculated stress path for the springline of the tunnel in the header and the bench.

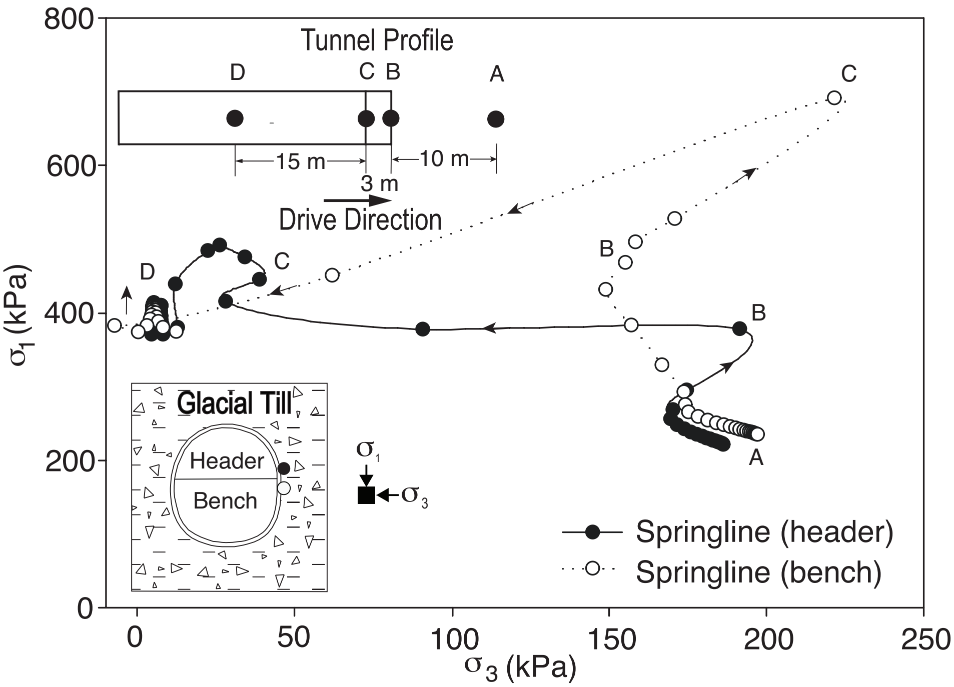

Figure 5.32 Stress path at the springline a single tunnel construction using a heading and bench excavation at a depth of 12 m below the ground surface and K_o=0.8

Figure 5.32 shows that the affect of the stress rotation on a point immediately outside of a single tunnel cavity is considerable with a large increase in the major principal stress at the tunnel face. In this case, only a test that begins in conventional triaxial compression followed by an abrupt transition to an active compression test can fully capture this type of stress path. This type of testing would be very difficult to implement and would most certainly require a servo-controlled triaxial loading frame.

5.3.3 Effect of Fissures on the Operational Strength

The role of scale affects for glacial tills was first discussed by Bishop and Little (1967) and Simons (1967) who reported on the results triaxial testing on glacial tills for differing sample sizes. Simons (1967) suggested that the study found that the measured shear strength of the till did not vary for samples greater than 100 mm in diameter. Bishop and Little (1967) disagreed with the findings of Simons and reported that the maximum representative elemental volume of the till used by Simons was more likely closer to 0.6 m. It is important to note that neither of the reports indicated what the spacing of the fissures within the soil tested were. Hand carved blocks measuring 285 mm along each edge were reportedly used for the subsequent laboratory investigation, so it is expected that the spacing of the macro fissures was greater than 300 mm. Bishop and Little (1967) suggested that there were fissures detected within the smaller 38 mm diameter samples and the measured shear strengths were not fully representative of the intact shear strength of the soil.

With respect to the measured undrained shear strength of fissured soils, Bishop et al. (1965) reported a single triaxial test on a sample of the London Clay where the test specimen failed along the surface of an unidentified internal fissure. They found that when the cohesion along the surface of the fissure was assumed to be zero, the drained friction angle of the failure surface was around 15°. This drained strength along the fissure was the same as the drained residual values of the London Clay reported by Skempton and La Rochelle (1965). The outcome of these studies suggests that the operational strength of stiff, fissured soils is controlled by the drained residual strength of the fissures.

In the North LRT tunnel excavations, measurements of the fissure spacing in the glacial till were found to be generally around 0.5 to 1.0 m apart in all horizontal directions. This is in good agreement with the findings of Medeiros (1979) who documented an open cut in the glacial till approximately 500 m to the southwest of the current study location. Understanding that the samples collected for laboratory testing do not generally incorporate the full-scale discontinuities, it is expected that the measured shear strengths from the intact laboratory samples are considerably higher than the groundmass as a whole.

Stille and Palmstrom, (2008) suggested assessing the importance of the fissuring by comparing the tunnel diameter with the spacing between the fissures referred to as Block diameter. They proposed the Continuity Factor, (CF = tunnel diameter / block diameter) to assess if the ground mass will perform as a continuum, a discontinuous continuum (highly fractured so as to be continuous) or a discontinuum. Figure 5.33 illustrates the typical fissure spacing while Figure 5.34 shows the typical block size in the North LRT twin tunnels.

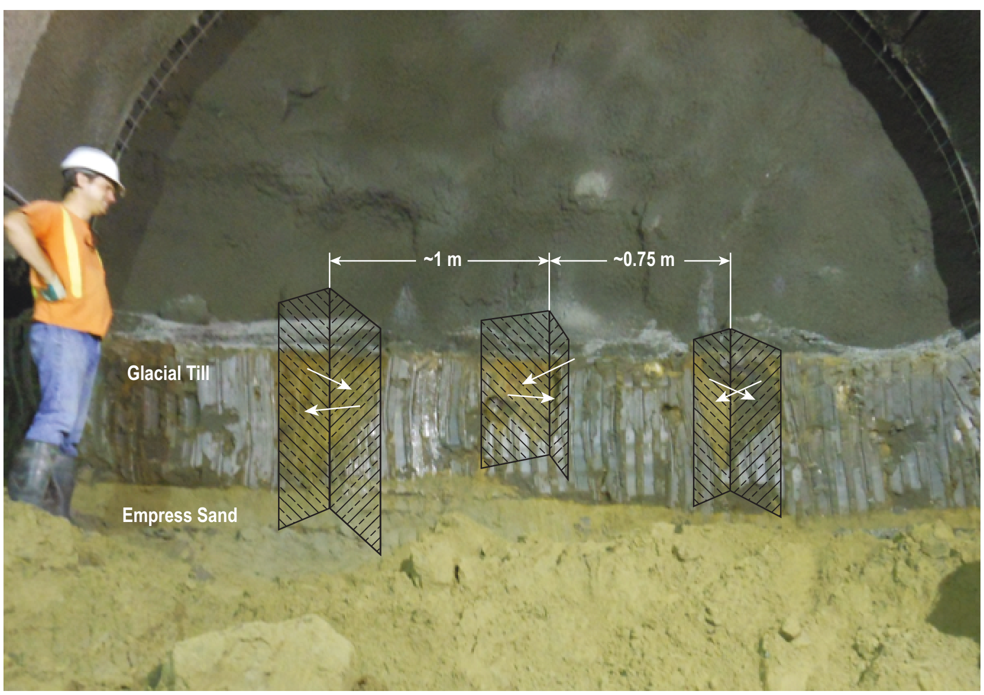

Figure 5.33 Fallen blocks and fissure planes within the lower horizons of the glacial till in the North LRT tunnels

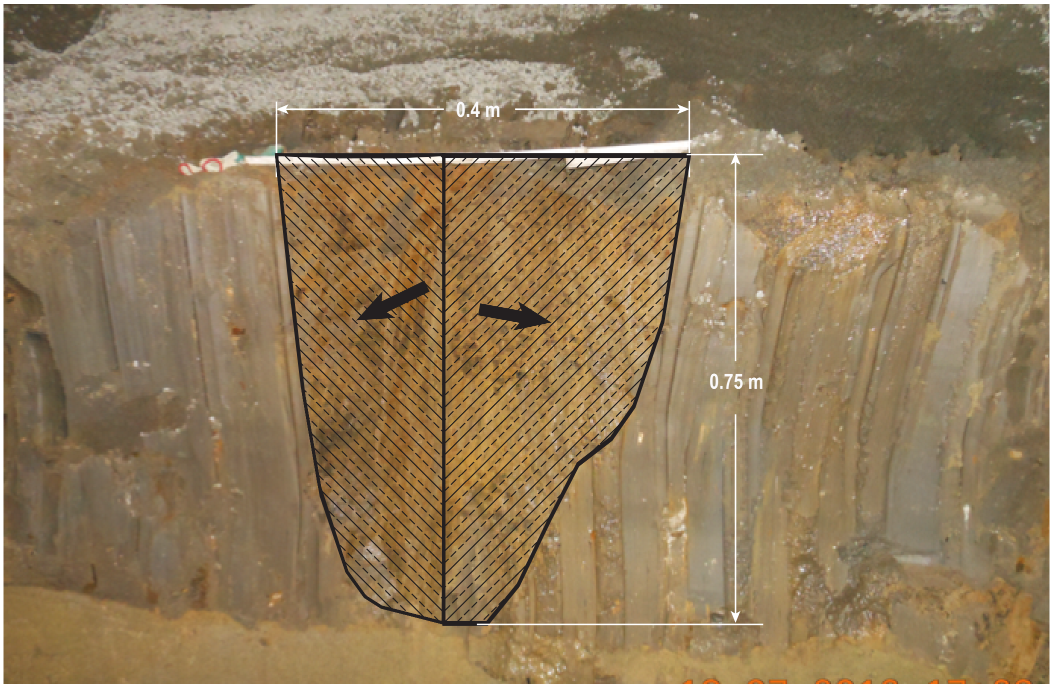

Figure 5.34 Wedge space in North LRT twin tunnels following block failure (each ruler segment is 0.1 m in length)

Figure 5.33 suggests that approximately 9 fissures spaced between 0.5 to 1.0 m apart are encountered within a typical excavation resulting in roughly 4 blocks measuring between 0.3 to 0.5 m in width. Using the approach described by Stille and Palmstrom, the CF of the North LRT tunnels was found to be approximately 14.5 to 21.5 suggesting that the ground is discontinuous. Mapping of the tunnel heading and bench supports this finding.

Considering the spacing and nature of the fissures within the glacial till, it is expected that tests greater than 1 m in size would result in a truly representative ground response. This spacing would be consistent with the recommendations of Bishop et al. (1965). It is suspected that tests on the order of 0.5 m would also likely incorporate at least one discontinuity and therefore provide relevant data in terms of the shear strength of the ground mass. If the tests by Bishop et al. (1965) and Simons (1965) were considered relevant, then a design that utilized the residual shear strength would be considered adequate for low stress conditions.

5.3.4 Role of Suction

Duncan and Dunlop (1968) reported the results of several investigations examining the role that fissures had in the failure of slopes constructed in stiff fissured clays. They indicated that the shear strength measured in rapid (undrained) tests were always higher than those with slower strain rates. They described that approximately 75% of the strength loss in long duration tests was a result of moisture migration within the samples. For constant water content, drained tests, the moisture content at the failure surface was considerably higher than that of the rest of the test specimen. This suggests that there is suction developing at the shear surface that ultimately draws water from the rest of the sample to the yield surface. This effect was pronounced up to loading durations of 7 days or longer.

Skempton and La Rochelle (1965) reported on triaxial tests investigating the same phenomenon and found that in consolidated undrained (CU) tests, the moisture content at the failure surface was virtually unchanged relative to the remainder of the sample. For the longer duration tests (7 day shearing), they found that the moisture content at the shear surface was approximately 2% higher than the rest of the sample. Skempton and La Rochelle (1965) then calculated the pore pressure along the surface of the failure plane from the drained strength parameters (c' and ϕ') using

$$s_u = {c'\cos\phi' + p'\sin\phi'} \Big/ {1 + (2A_f - 1)\sin\phi'} \qquad \text{Equation 5.4}$$

where,

s_u is the undrained strength of the soil;

p' is the spherical confining stress;

A_f is given as $A_f = u/2c$;

u is the pore pressure in the shear zone at the point of failure; and

c’ is the effective cohesion.

Using the relation given in Equation [5.4], the pore pressure along the failure plane was calculated for any undrained shear strength, s_u. When Skempton and La Rochelle (1965) calculated the pore pressure along the failure surface they found that the pore pressure was approximately 52% that measured at the ends of the sample. When the same calculations were applied to specimens loaded over a period of days, Skempton and La Rochelle (1965) determined that the pore pressures along the failure surface were nearly the same as those calculated at the sample ends. The results of the various investigations suggest that suction plays a role in determining the strength of the glacial till over the short and long-term periods.

It is expected that the increase of negative pore pressures would increase the undrained shear strength of the soil but not have a significant impact on the drained shear strength. The impact of suction on the undrained shear strength is limited by the rate of internal fissure growth that occurs during shear. As fissures grow and coalesce, the internal suction would be locally reduced as fissures come in contact with the outer portions of the sample that are at atmospheric pressure. Because rapid loading would result in localized negative pore pressures along the failure surface, as shown by Skempton and La Rochelle (1965), the strength of the soil would be dramatically increased in the short term. It also suggests that during rapid loading, the failure would approach residual values very quickly provided that the shear strength for open fissures is the same as the residual parameters as indicated by Bishop et al. (1965).

The explanation of the negative pore pressures stems from the fact that dilation of the soil will result in the expansion of voids within the soil mass. Review of the typical pore pressure response during conventional triaxial testing of the Edmonton glacial till indicates that the soil initially undergoes compression (pore pressure accumulation) followed by dilation (pore pressure reduction) as illustrated in Figure 5.24. This means that initially during loading, there is a portion of the loading curve related to micro-fissure (crack) closure and recompression of the air-filled pore spaces. The compression of the air-filled voids and total change in volume was discussed in Chapter 4. Because it is very difficult to measure the pore pressure response within a test sample during shear without changing the inherent properties of the sample, none of the above theories have been proven. The assumptions provided here have been developed understanding the stress path within a three-dimensional effective stress space. By considering the path a sample takes within the space of net stress ($\sigma_n - u_a$), suction ($u_a - u_w$) and void ratio (e), it is possible to understand the role that suction plays in the drained response of the glacial till under compression. As the net stress is increased, the suction, $u_a - u_w$, and void ratio, e are reduced towards saturation and the sample compresses. At some point, the stress path changes direction as the net stress is increased. The change in direction results in an increase in the void ratio as well as an increase in the soil suction. Because the pore-air pressure is now increasing the rate of net stress increase either slows, stops or reduces depending on the total pore-air pressure. This would in turn result in an increased void ratio of the sample as well as increased suction further contributing to the failure of the sample. It is assumed at some point, the rate of pore-air pressure surpasses the rate of stress increase that leads to the onset of cracking due to a net loss of confinement.

5.3.5 Yielding of the Glacial Till in Tunnel Construction

Traditionally, failure envelopes for frictional materials are defined as undrained, drained, or residual. However, as discussed in this chapter consideration must also be given to the strain rate, confining stress, stress path and the total strains anticipated when selecting the appropriate failure envelope. These failure envelopes and their constraints are discussed below and are summarized in Figure 5.35.

a) Undrained Envelope

Anagnostou and Kovari (1996) suggest that undrained tunneling conditions are to be expected when the permeability is less than 10^{-7} to 10^{-6} m/sec and the net tunnel excavation advance rate is 0.1-1 m/hour or more. The NLRT tunnels in the low permeability (10^{-9} m/s) till were constructed at maximum and minimum rates of 0.05 and 0.1 m/per hour respectively. This suggests that drained conditions apply according to Anagnostou and Kovari (1996) when the tunnels were excavated at its maximum rate. Figure 5.3 shows that for the North LRT glacial till, the undrained strength ranges between 118 and 438 kPa with an average of 236 kPa. The undrained shear strength utilizes the cohesion (soil fabric) as well as mobilizes negative pore pressures due to the presence of occluded pore-air within the soil.

Skempton and La Rochelle (1965) suggest that the operational undrained shear strength of overconsolidated London clay was approximately 50% of the undrained shear strength (S_u) from laboratory specimens. This could imply that for the North LRT glacial till, the operational S_u is on average 118 kPa (50% of 236 kPa). Using this value and the approach given by Vermeer and Ruse (2000) the expected factor of safety for a 6 m diameter full-face tunnel in the North LRT glacial till is approximately 3. It is important to understand that this criteria and factor of safety is only applicable for the intact soil masses and for compressive stress paths. The average undrained shear strength of the pressuremeter testing is approximately 1.5 times higher than the lab testing at 350 kPa. This may be an indication of recovered sample disturbance of the laboratory samples as the average undrained shear strength of the glacial till was calculated from the curve fitting to the inverted unloading curve.

b) Drained Envelope

When the soil is confined such as in a pillar separating the tunnels, the drained Mohr-Coulomb failure envelope should be used as the relevant yield surface. Ghaboussi and Ranken (1977) indicate that there is an increase of both vertical and confining stresses in the centre of a wide pillar following the passage of each tunnel. This type of loading is similar in nature to a conventional triaxial test. The triaxial tests by Whittebolle (1983) indicated that there were two ranges of strain resulting in yield based on the initial confining stress of the sample. The two high-pressure tests yielded due the accumulation of internal pore pressures at high strains, while the two tests at lower confining stresses required lower strains to contact the failure envelope.. This then suggests that the magnitude of initial principal stresses must be considered. Based on the findings of Whittebolle (1983), an appropriate cut off for the residual criterion during unloading is the pre-consolidation pressure, σ_p. Considering this, the total strains for yield within a pillar must be considered depending on whether the ground is over-consolidated or normally consolidated. If the soil is lightly to heavily over-consolidated, ($\sigma_v < \sigma_p$), the total stains must remain less than 1% or yielding will occur. If the ground is normally consolidated ($\sigma_v = \sigma_p$) the strains must remain below 3% or yielding can be expected to occur.

In terms of drained strength, the pressuremeter tended to underestimate the undrained shear strength when compared to the triaxial tests. On average the friction angle was estimated to be 35.5° which is approximately 70% of the values obtained from the triaxial tests. The cohesion was much more representative at an average pressuremeter cohesion of 35.3 kPa, which is within 2% of the triaxial data. There is a very strong relation between the estimation of the pressuremeter expansion yield strains and the high stress compressive yield strains. In each case, the yield strains were estimated to be approximately 3% of total strains.

c) Envelope for Fissure Strength

When fissures are encountered in a tunnel heading, the strength of the fissures will dictate the ground response. In this case, the stress path and total strains must be considered. If the ground is subjected to unloading (either active compression or extension), then the yield strains should be assumed to be 0.25% total strain. If the total strains are anticipated to exceed 0.25%, the strength of the ground should be considered as residual and wedge/block translation will dominate. Medeiros (1979) commented that the friction of the till is mobilized at much lower strains when subjected to active compression even in seemingly intact samples. Though he did not describe the failure planes or mechanisms of any sample, it is expected based on Skempton and La Rochelle (1965) and Bishop et al. (1965) that during reduction of confining stresses that micro fissures are permitted to open and eventually coalesce within the sample resulting in the failure at low strains. Considering this, it is expected that for strains greater than 0.25% during active compression or extension that the friction along the fissure surface is mobilized and therefore the residual shear strength apply. This suggests that below strains of 0.25%, the fissures remain closed and the either the undrained or drained peak strength applies depending on the excavation rate and permeability of the soil. Figure 5.29 and Figure 5.31 illustrates the reduction of stress within the tunnel face immediately prior to excavation. This distressing would potentially lead to the mobilization of friction at low strains which allows opening of the fissures and ultimately block or wedge failure similar to rock excavations.

The above criterion is summarized in Figure 5.35 and Figure 5.35.

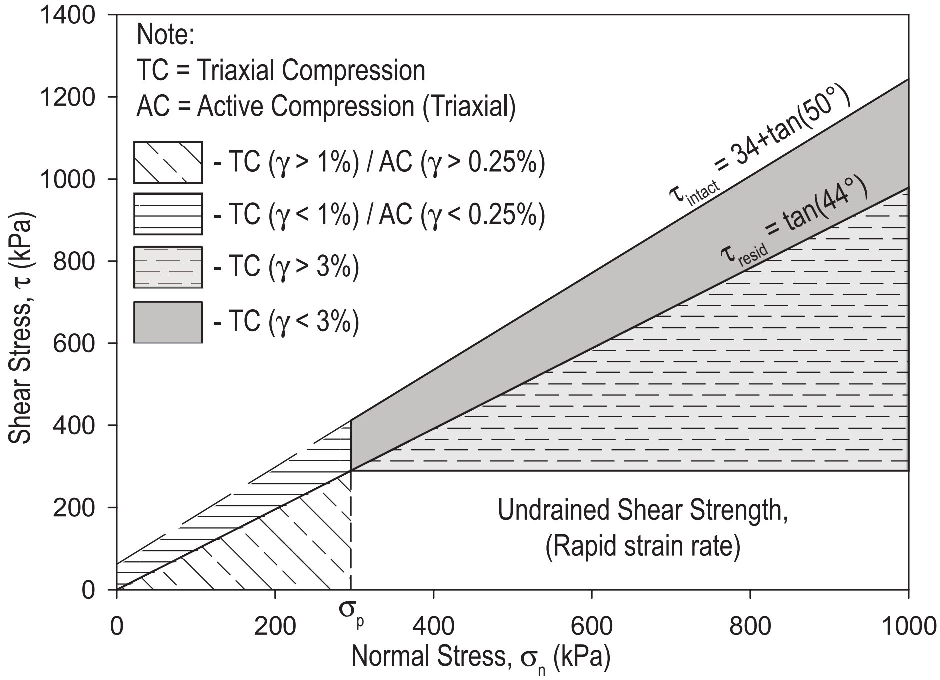

Figure 5.35 Failure envelopes for the Edmonton till considering shear strains (γ) and stress path

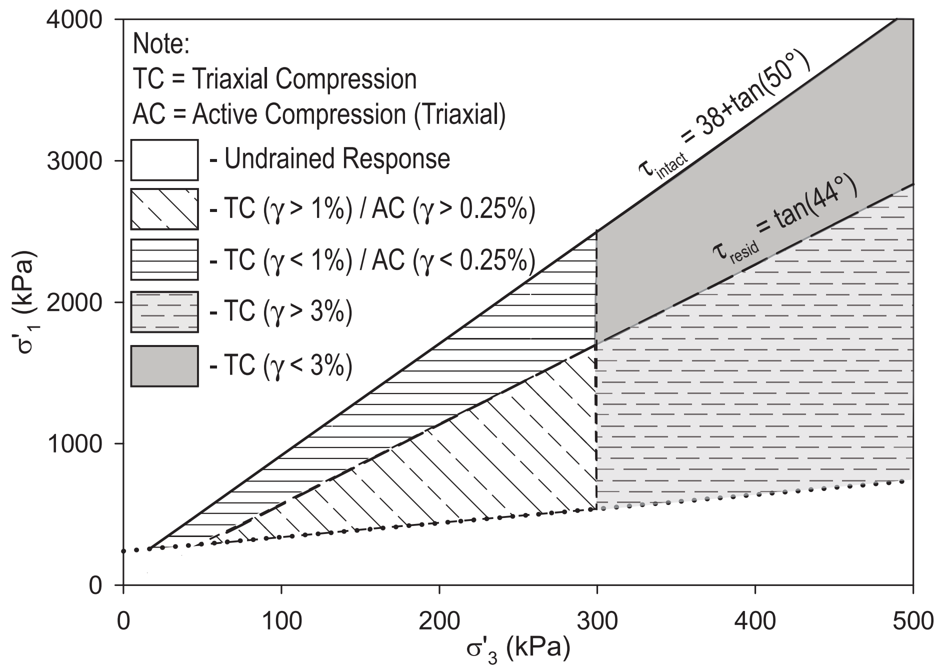

Figure 5.36 Failure envelopes for the Edmonton till considering shear strains (γ) and stress path (principal stress space)

5.4 Conclusions

This chapter presented the strength and deformation data available to date on the Edmonton glacial till and the Empress Sand. The purpose of the work was to develop yield criterion that apply to the heavily overconsolidated soils for sequentially excavated tunnelling methods. This work presents the estimation of the short term and longer-term shear strength parameters as well as the small and large strain criteria. Medeiros (1979) clearly illustrated a small aspect of defining the yield criterion for heavily overconsolidated materials by identifying how the stress path can influence when yielding occurs. The work completed in this chapter provides a more detailed understanding of the ground by supplementing the work by Medeiros (1979), El Nahhas (1981) and Whittebolle (1983) with additional insitu and laboratory testing results. This research not only highlights the effect of the stress path, but also the role that strain rate, total strains and scale affects have on predicting an appropriate yield criterion. The key points of this work are as follows:

- Undrained testing of the glacial till typically indicates a strain-hardening tendency, though there is a distinct transition in undrained strength with confinement. This transition from a weaker soil dominated by internal structure and fissures to an intact sample occurs roughly around the pre-consolidation pressure of the till;
- The undrained shear strength from laboratory and in-situ tests has been found to be between 118 and 438 kPa with an average and standard deviation of 236 and 100 kPa respectively. If the outliers are excluded, the average undrained shear strength becomes 198 kPa and the standard deviation becomes 64 kPa;
- There is a clear tendency for the glacial till to increase its strength with reduced moisture content. This is a function of the suction within the sample during rapid loading and associated inter-particle forces and aging;
- Observation of multiple plots of stress-strain data has indicated that the peak value typically occurs following the compressive phase and at the start of the dilative phase of shear;
- Usage of the volume change or pore pressure curves from triaxial tests clearly indicates the onset of yielding within a sample of glacial till. Using this as the definition for yield the effective angle of friction of the glacial till is 46.8° with an effective cohesion of 62 kPa.
- The residual friction angle (or critical state friction angle) range from 43.5 to 45.8° with an average of 44°.
- All of the testing (laboratory and in-situ) indicated that the strains to the onset of yielding were approximately 1 to 2% when the confining stress was less than the pre-consolidation pressure, between 3 to 5% in compression for normally

consolidated samples and between 0.2 and 0.5% when subjected to extension or confinement reduction;

- The laboratory strength testing on the Empress Sand has indicated that there are two distinctly different failure envelopes for a given stress path;
- The internal angle of friction for the Empress Sand under compression and direct shear was found to be 39.6°. When subjected to extension, the peak friction angle was found to be 23.9°;
- Like the glacial till, the strains at the onset of yield for the Empress sands were typically between 1 to 2% in compression or direct shear, and between 0.2 and 0.5% in extension;
- The pressuremeter indicated undrained shear strengths within the Empress sands that were typically around 600 kPa;
- No single laboratory stress path can represent the stress path taken at all points around a tunnel circumference. The active compression method however comes very close to points within the tunnel face and springlines. Based on the expected stress paths around the tunnel cavity, yielding can be expected to occur at strains of roughly 0.2 to 0.5%;
- When fissures in the glacial till are encountered in the tunnel face, the shear strength of the fissures should be considered as the lower bound failure envelope. If no laboratory tests for the fissure strength are available, then the residual strength of the intact till should be used as the fissure strength;
- When defining an appropriate yield criterion, consideration must be given to not only the stress path of the ground, but also to the strain rate, the total strains expected, the size of the excavation and the initial confining stress level;

6.0 Project Instrumentation

6.1 Introduction

As part of this research, a detailed instrumentation and monitoring program was designed to capture the ground displacements around the North LRT twin tunnels. The instrumentation monitored the ground displacements within the pillar and at the ground surface above the twin tunnels as well as the in-tunnel displacements following liner installation.

During the development of the monitoring program, consideration was given to the individual ground condition types as well as the anticipated mode(s) of failure. Thought was also given as to the method of monitoring that will provide relevant and meaningful information while minimizing the impact on the in-situ ground conditions. Dunnicliff (1993) discusses the basis for relevant and meaningful instrumentation and construction monitoring. A major concern was to provide sufficient redundancy to compare the results of one method with another. Redundancy also minimizes the risk that measurement stops should any instruments fail or become damaged throughout the course of construction.

The instrumentation and monitoring plan considered that there was no effective way to monitor the stresses within the ground without impacting the in-situ conditions. Therefore only the displacement fields within and around the tunnel cavities were monitored. All instruments installed within the ground monitored the displacements in the ground throughout all construction phases. All in-tunnel instruments only monitored the post-liner and lag tunnel construction related displacements.

The monitoring program was designed to make use of conventional and state of the art instruments. In each case, monitoring sections were designed to provide redundancy and validation for the experimental instruments. The details of the respective monitoring systems are described in greater detail in subsequent sections.

This chapter details the ground conditions encountered at each monitoring section and the measured ground displacements due to tunnel construction. The following sections provide a description and the function of the various instruments employed. Next, the results of the monitoring programs are provided followed by an assessment of each instruments' performance and reliability. Finally a discussion on the influence of the pillar width on the measurements recorded at each section is provided. This includes an analysis of the zone of influence in each formation and the resulting ground loss calculations.

6.2 Anticipated Ground Conditions

The classification of the ground conditions considered the various geologic formations that the tunnels would encounter. Following the classification, the possible failure mechanisms were determined. The Tunnelman's Ground Classification for Tunnels in Soft Ground (Terzaghi 1950, Hueur 1974, and FHWA 2009) was used to describe the anticipated ground behaviour.

The sections that were identified were the following:

- Improved glacio-lacustrine clay mixed face with glacial till and intra-till sand;
- Glacial till with intra-till sand pockets from between the improved soils to mixed face conditions;
- Mixed face glacial till and Empress Sand near the Station Lands west headwall;
- Mixed face glacial till and Empress Sand from Station Lands east headwall to 104A Avenue;

- Glacial till and intra-till sand pockets from 104A Avenue to cross over cavity;

- Glacio-lacustrine clay and fill from cross over cavity to Churchill Station.

In order to assess the efficacy of the tunnelling methods within each ground type, a monitoring cross-section was assigned to the area. Each monitoring cross-section was designed a minimum of 10 m into each ground type. This allowed for removal of any boundary conditions associated with the previous ground type.

The pillar was narrowest along the western portion of the alignment, between the West Headwall and the MacEwan Portal. In this section, the pillar width varied from 1.7 m at the West Headwall to 1.48 m at the MacEwan Portal. A photo of the pillar at the MacEwan Portal is shown below in

Figure 6.1 North LRT pillar at the MacEwan Portal

Prior to design, a basic, two-dimensional numerical model was carried out using the strength and modulus parameters given in Chapter 5 to establish the total width of the settlement trough at each location. From this data, the monitoring program and the location of the individual instruments were established.

6.3 Instrumentation

6.3.1 Cast in Place Strain Gauges

The initial liner was constructed of wet mix shotcrete and wire mesh reinforcement. As a result, cast in place strain gauges were used to measure the strains within the liner. Vibrating wire strain gauges use a thin strand of wire held in tension with end mounting blocks. The tension of the wire is altered based on the movement of the two mounting blocks relative to each other. When electrically excited, the wire vibrates at its natural frequency. As the tension in the wire changes, the natural frequency of vibration within the wire changes. An electromagnetic plucking coil, positioned at the center of the gauge both excites the tensioned wire and measures the resulting frequency. Through calibration, the vibration frequency of the tensioned wire can be rearranged to express strain as a function of frequency. Calculations to estimate the theoretical strains from the natural frequency measured during excitation are provided by GeoKon (2012).

Vibrating wire strain gauges are well known to be very stable for long periods of time within tunnel environments as shown by Smith et al., (2001). Provided that bending strains are not applied to the instrument, vibrating wire strain sensors can provide reliable measurements nearly indefinitely. The sensors were installed as close to the neutral axis of the liner as possible to minimize bending moments on the sensors. At the neutral axis, the bending moments within the liner are zero and therefore only axial strains would be measured. The neutral axis of the liner was designed to be in the centre of the shotcrete liner. The wire mesh and the vibrating wire strain gauges were installed approximately 25 mm from the sealing shotcrete layer. Therefore the strain sensors were approximately 75 mm from the tunnel profile and at the centre of the 150 mm thick shotcrete support layer.

In addition to bending moments, the strain gauges were also susceptible to temperature fluctuations. It was not anticipated that there would be any significant temperature changes throughout the construction of the tunnel. This was due to the constant ventilation system providing circulated air and heat to the work area. There would however be substantial temperature changes in the shotcrete during the curing phase. In order to compensate for the measured temperature related strains, each strain gauge was fitted with a dedicated thermistor and thermal compensation was applied as needed.

The embedded strain gauges were waterproof and the exposed end blocks had to be compatible with the surroundings for which they were installed. Therefore the strain gauges were constructed of stainless steel embedment blocks while the plucking coil and communications cables were constructed of polyethylene. The environment during installation was expected to be harsh and potentially damaging to the plastic components therefore additional protection was required. The plucking coil and communication wires were encased within small diameter poly vinyl chloride (PVC) tubing, which was then affixed to the wire mesh. It was important that the ends of the strain gauges were left exposed to ensure good embedment and bonding with the shotcrete. The signal cables exited the shotcrete and were led away from the working tunnel face. All of the instruments were connected to a dedicated datalogger to record the changes with time as well as the approach and passage of the lag tunnel. The data acquisition system was programmed to record the strain and temperature at each location at 15 minute intervals.

A photo of the installation of the strain gauges to the wire mesh prior to shotcreting is shown below in Figure 6.2.

Figure 6.2 Strain gauges attached to wire mesh prior to shotcrete placement

The primary disadvantage of the cast in place strain gauges is that they measure strain at discrete locations and cannot provide a continuous picture of the strain fields surrounding the tunnel cavity.

The strain sensors were installed at intervals of 0.45 m and extended from the shoulder furthest from the pillar to the invert nearest the pillar.

Strain gauges were installed into the liner of the lead tunnel at two separate monitoring sections along the tunnel alignment. The first location was at Northbound West Tunnel Meter 141.5 or Station 600+671.5. This was located approximately 10 m west of 101 Street and beneath Monitoring Section E. This section was wholly within the glacial till and the pillar width was 0.23D. The second location was at Southbound East Tunnel Meter 40.5 or Station 700+412.7. This position was approximately coincident with Monitoring Section D. The ground conditions through this section were mixed face with approximately half of the face composed of glacial till and the other half Empress Sand. The pillar width through this section was approximately 0.25D. Drawings showing the locations of the various monitoring sections are shown in Appendix B.

6.3.2 Optical Targets

Optical survey targets were positioned at pre-determined locations throughout the tunnel alignment. There were two optical monitoring plans that positioned the targets at different points around the circumference of the tunnel. The positions of the optical monitoring points for the various cross sections are shown below in Figure 6.3 while the locations of the monitoring sections throughout the alignment are shown in the Appendix.

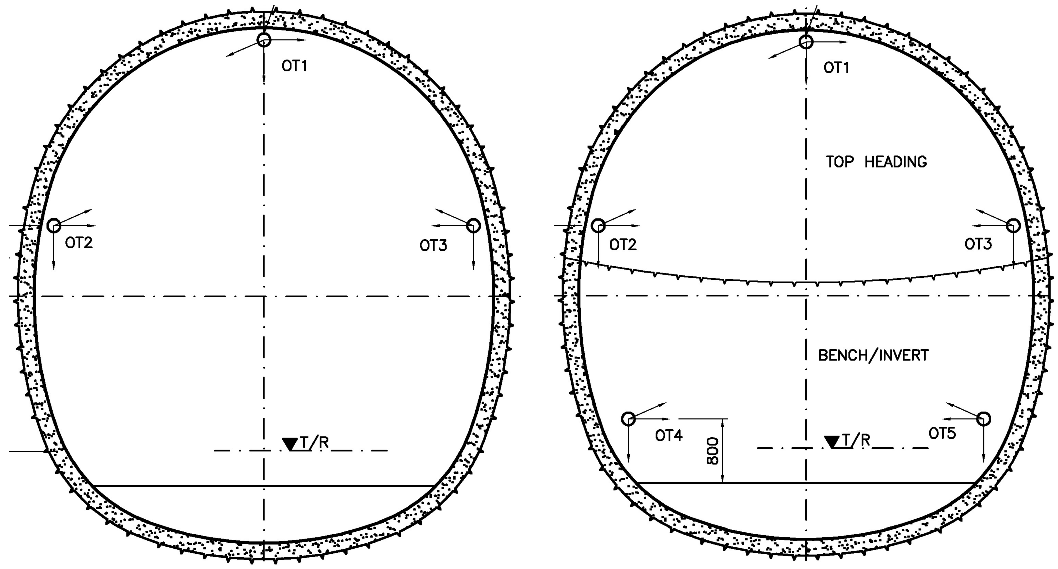

Figure 6.3 Optical target positions for in-tunnel monitoring (with permission from ILF, 2012)

The contractor installed each point was installed during tunnel liner construction. Cans with threaded inserts were tied to the wire mesh prior to shotcrete placement. The cans were protected to prevent them from filling with shotcrete. Once the cans were set and the tunnel face was secured, the optical targets were screwed into the threaded inserts and the initial reading taken by a surveyor and total station. In most cases, the initial reading was taken at least 2 m behind the tunnel face or an additional bench/invert advancement. This delayed measurement permitted some post construction displacement to occur prior to the start of monitoring.

The tunnelling contractor carried out monitoring of the optical targets, tow times a day (once every 12 hours). The contract documents specified that the surveying should provide a minimum survey accuracy of ±1 mm. However, a lack of stable benchmarks resulted in accuracies closer to ±2 mm. Post-processing of the data by the contractor corrected most errors, though some data were irreparable. The errors with readings recorded early in the tunnelling process were mostly corrected by the readings being taken by a total station positioned on arms fixed to the tunnel walls. Multiple shots of each target were then recorded from each position in order to help correct the data.

6.3.3 Shape Accel Arrays

A Shape Accel Array (SAA) consists of a series of short segments. This is similar to links of a chain that are instrumented to measure the relative displacement of each segment. SAAs use micro electro-mechanical systems (MEMS) technology to measure the change in acceleration from gravity with rotation of the instrument (tiltmeter). Using this technology, SAAs provide accurate measurements with respect to two-dimensional displacements relative to a fixed point. They are typically used as in-place inclinometers that may be connected to a dedicated data logger for regular measurements.

Bennet, et al. (2007) have shown how installation of SAAs within slopes can provide remotely monitored data of a slope. Their analysis considered the lateral movement of the slope as well as dynamic impacts from earthquakes in the region. They demonstrated that the use of SAAs can provide information similar to that of a conventional inclinometer, but without having to physically measure the displacements with an inclinometer probe. As a result, they were able to obtain much more frequent readings and interpret the data in real time from a remote location.

In terms of tunnel monitoring SAAs can be directly affixed to the tunnel liner for continual convergence monitoring. Since SAAs use tiltmeters, the accuracy of the instrument (±0.2 mm) is superior to any optical monitoring device.

One SAA was installed circumferentially within the lead tunnel at Section E. The position of the SAA was similar to that of the embedded vibrating wire strain gauges, but with a monitor spacing of 0.3 m (segment length). The circumferential SAA monitored the shape (ovalization) of the tunnel liner with the approach and passage of the lag tunnel. It was initially planned that each monitoring section would have one circumferential SAA. Due to difficulties with the contractor and an inability to procure resources for installation, only one SAA was installed circumferentially. Figure 6.4 shows the final construction of the circumferential SAA.

The in-tunnel SAA consisted of a 10 m long string with 305 mm long segments or 33 discrete monitoring locations. Due to the relatively close spacing of the segments, the SAA could be sufficiently bent to fit the tunnel cross section. In accordance with the manufacturers requirements, the SAA was encased within a PVC conduit. The orientation of the SAA within the conduit was marked for reference prior to installation within the tunnel. The SAA was affixed to the shotcrete liner by 27 mm steel brackets held in place with concrete screws. Once the PVC pipe and SAA were within the bracket, the bracket was then secured to the tunnel. Brackets were positioned every meter to minimize the potential for creep or sag of the SAA. Figure 6.4 shows that the irregular surface of the shotcrete liner prevented the SAA from being in intimate contact at all locations. The SAA was then connected to a dedicated data logger (CR1000) for continuous monitoring. The data acquisition system was programmed to record measurements hourly.

Figure 6.4 Circumferential SAA and datalogger

SAAs were also installed into two existing inclinometer casings that were installed as part of the surface-monitoring program. These instruments were used as conventional inclinometers installed within the pillar between the twin tunnels.

Because the inclinometers were located in a public area, they were subject to vandalism or theft and were consequently recorded manually. In each case, the SAAs were measured three times daily (during daylight hours). This frequency was continued as long as a tunnel face was within 1 tunnel diameter ahead of or 2 tunnel diameters behind the instrument.

6.3.4 Time Domain Reflectometry (TDR)

Time Domain Reflectometry (TDR) was used to monitor the displacements around the tunnel circumference in a fashion similar to that of the vibrating wire strain gauges and the circumferential SAA. The TDR strings were only installed in at the monitoring section within the mixed face conditions (Section D).

Time domain reflectometry uses electromagnetic pulses sent through a coaxial cable to monitor changes in signal along the length of the cable. The TDR system measures the time required for the signal pulse to return to the unit. By observing the change in time along the cable length, it is possible to monitor shear and tensile strains along the entire length of the cable. Equations governing wave propagation in coaxial cables can be derived either from circuit theory or from Maxwell's equations. Both methods will produce the same result. Dowding and O'Connor, 1988 provide the derivation of the governing equations for wave propagation within a coaxial cable.

As the electromagnetic pulse is sent through the coaxial cable, a change in signal indicates a change in resistance. This change in resistance is due to increased impedance resulting from a change in the thickness of the conducting cables. The changes in impedance result in two types of signal change, which are reflective of the two types of strains measurable with a TDR system. Elongation of the signal is indicative of tensile strains and step functions are indicative of shear strain. Because tensile strains result in necking and elongation of the cable, the signal impedance reflects this change by stretching. In general, this type of signal change is very difficult to observe as minor strains can result in nearly imperceptible changes to the total signal length. Shear strains represent localized displacements and result in a step function to the measured signal wave. Shear strains are much easier to identify than tensile strains due to their distinct and sharp steps.

One of the major difficulties on using TDR, is determining where along the cable certain signal changes are occurring. To help locate where strains are taking place, small crimps were placed into the cable at regular intervals. These crimps appear as small, but perceptible step functions and help identify the position of other induced anomalies. Dowding and O'Connor (1988) and Dowding, Su and O'Connor (1989) illustrated how the various signal shapes can be used to interpret the location and nature of displacements along a TDR cable. These researchers also demonstrated the ability of TDR to calculate the rate of shear for a given section. The above authors demonstrated importance of system calibration in order to obtain absolute values. In each case, they calibrated their system in a laboratory setting determining the displacements required to achieve distinct signal impedances. Historically, TDR has been used to locate the position of failures in pipelines (either in shear or tensile) and not the actual magnitude of the strains involved. The signal changes are generally very subtle unless large strains (>20%) occur. Therefore, quantification of the actual shear or tensile strains typically has been very difficult to assess with any degree of confidence. Though Dowding and O'Connor (1988) and Dowding, Su and O'Connor (1989) reported absolute displacements from calibrated values, there was no validation of their calculations to confirm their field measurements. To date, there is no known application of TDR technology to try to measure the circumferential changes of a tunnel following construction and liner installation.

The TDR experiments were carried out examining two types of coaxial cable. Each cable was 50 ohm coaxial cable as required by the Campbell Scientific TDR100 unit used in the experiments. The cables consisted of either a 19 mm diameter corrugated coaxial cable that were either fully sheathed or had the sheathing removed. Dowding et al. (2003) demonstrated the effect that sheathing has on bonding to the surrounding grout.

They showed that unsheathed corrugated coaxial cable provided the best bond to cement grouts.

The two cables were attached to the wire mesh prior to application of the shotcrete liner. The cables were tied to the mesh at 0.45 m increments with steel wire. The wire was tightened sufficiently to crimp the cables thus indicating the location along the length of each cable. A photo of the installation of the cables is shown below in Figure 6.5.

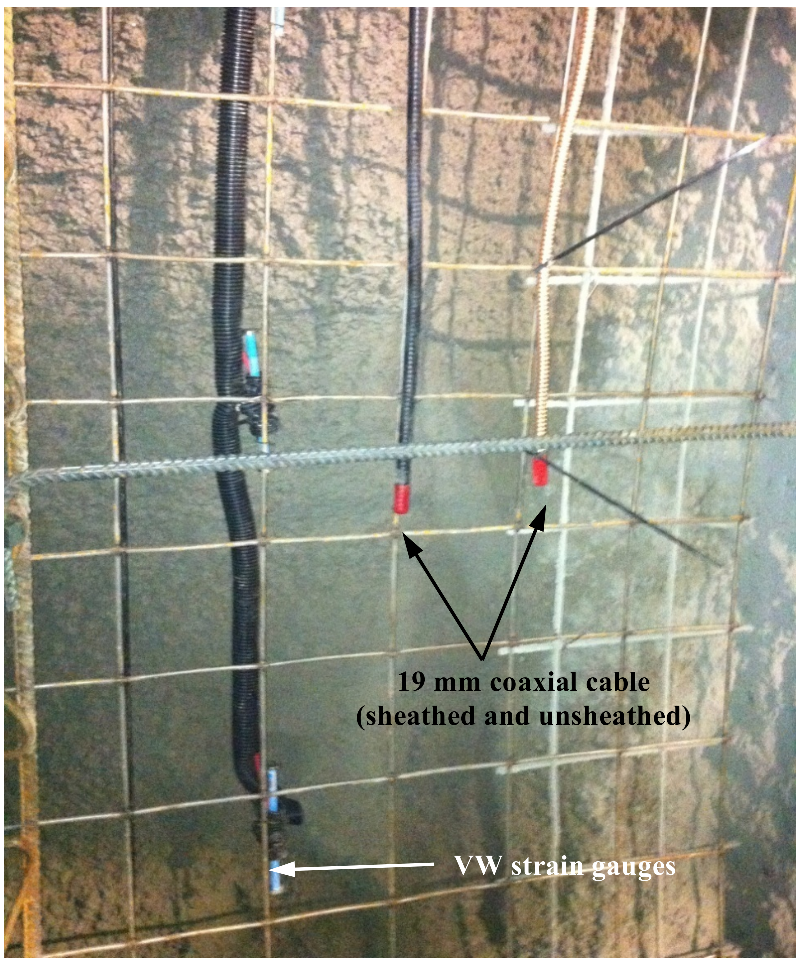

Figure 6.5. Embedded tunnel monitoring instruments

Measurements were recorded by connecting the respective coaxial cables to the TDR unit which was in turn connected to a Campbell Scientific CR1000 datalogger. The datalogger was programmed to record wavelengths in each cable hourly. Prior to initialization, the system was connected to Campbell Scientific's TDR software to assess the functionality or each cable and to determine the "cable length" as indicated by the pulse signal. The initial measurements also provided a baseline wavelength that would provide the basis for monitoring deformations.

6.3.5 Tape Extensometer

A tape extensometer was used to validate the data recorded by all of the in-tunnel instruments. Tape extensometers are commonly used in tunnels to monitor the change in diameter with time. The appeal of an extensometer is in its relative ease in use and good repeatability. The manufacturer of the instrument (Slope Indicator) suggests that the digital tape extensometer provides measurements accurate to ±0.1 mm over spans up to 30 meters (Slope Indicator, 2012). The actual error was slightly higher than the published data due to user error and was typically around ±0.25 mm.

The extensometer consists of a measuring tape with coarse measurements at fixed intervals of 50 mm. Fine measurements (less than 50 mm) are measured using modified digital callipers. Figure 6.6 shows the tape extensometer used in the research program.

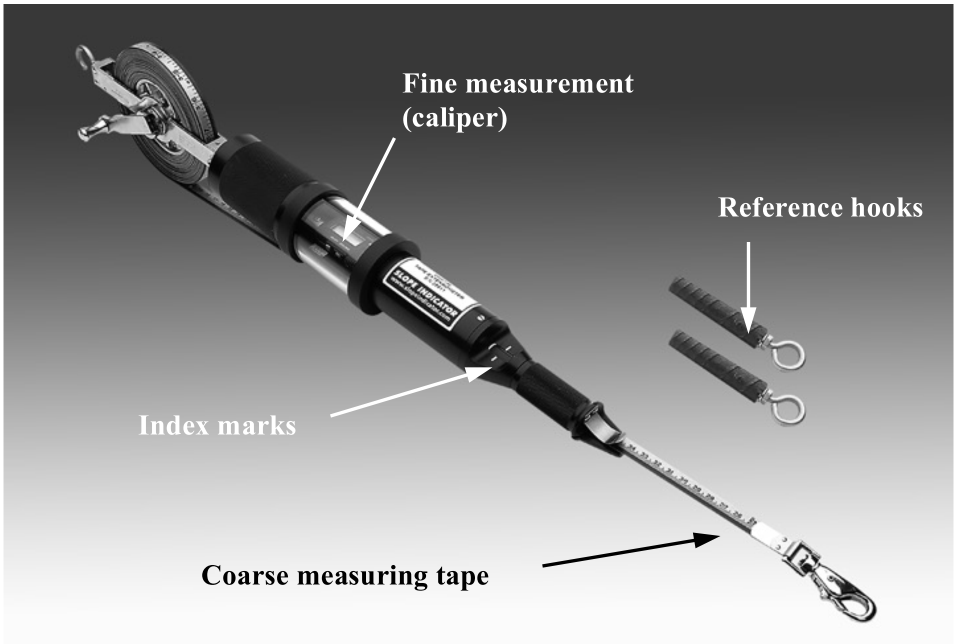

Figure 6.6 Slope Indicator tape extensometer (Slope Indicator, 2012)

Measurements are recorded by hooking the free end of the tape onto one point on the tunnel and the instrument body to another point across the tunnel diameter. Once the tape is fixed at both ends, the coarse measurement is recorded. The user then tensions a calibrated spring until index marks indicate proper tensioning of the tape. The callipers measure the displacement (in millimeters) required to tension the spring accordingly. The measurement is recorded as the sum of the tape and the digital display. In order to determine a relative error, the instrument position is reversed and the process repeated. The final measurement is then taken as the average measurement (of the two readings). Comparison of each measurement to the initial reading is then made in order to calculate the change in distance between the two reference points. Because the tunnel height was greater than 6 m, monitoring points were only installed along the tunnel sprinline. This meant that the vertical convergence could not be monitored following liner installation.

Installation consisted of the drilling of an 18.7 mm diameter pilot hole and the insertion of an expansion anchor into the pilot hole. It was necessary that a tight fit be achieved so that the anchors did not move during measurement. Because it was found that the expansion anchors did not provide satisfactory resistance, a two part epoxy was put into the pilot hole prior to the anchor. Once the anchor was set, a 25.4 mm diameter eye bolt was screwed into the anchor. In this case, a thread lock epoxy was applied to the eye bolts to eliminate the risk of the bolts unscrewing and changing position with time.

Measurements were recorded two to three times during daylight hours as the second lag tunnel approached the monitoring section. Monitoring was started a minimum of 1 tunnel diameter ahead of the lag tunnel face and continued until stable conditions were observed in the results.

6.3.6 In-Ground Monitoring

In-ground instrumentation and monitoring was implemented throughout the duration of the project. The purpose of this program was to monitor the surface settlements above and lateral displacements beside the tunnels during construction. All measurements were carried out by a licensed land surveyor or by a specialized instrumentation consultant.

The in-ground surface-monitoring program consisted of the installation and measurement of the following:

- Shallow and/or deep settlement rods installed above each tunnel crown;
- Cross sections consisting of shallow or shallow and deep settlement rods located near the start of each ground condition type;
- Multi-point extensometers installed into the cross sections where the tunnel crown was greater than 10 m below the ground surface. The monitoring points were positioned at discrete locations throughout the depth; and
- 70 mm diameter inclinometer casing installed to a depth below the tunnel invert.

An instrumentation consultant installed all of the in-ground instruments to the specifications of the contract documents. The following sections provide greater detail of each instrument and their monitoring.

6.3.6.1 Deep and Shallow Settlement Rods

Shallow settlement rods were installed to a depth of 2 m below the ground surface at 10 m intervals above each tunnel crown throughout the tunnel alignment. Where the depth to the tunnel crown was greater than 5 m below the ground surface, deep settlement rods were also installed to a depth of 2 m above each tunnel crown.

The purpose of these instruments was to observe the surface settlements during the approach and passage of each tunnel using well-established methods. The elevation of the tops of each settlement rod was measured at regular intervals to show the total settlement relative to baseline (pre-construction) readings.

The settlement points above the tunnel axis allowed for observations of the longitudinal displacements as the tunnel face approached and passed a given point. These instruments demonstrated the percentage of total ground settlement prior to excavation of the tunnel face. As stated in Chapter 2, for SEM tunnels, it is typical to observe approximately 50% of total settlements prior to excavation.

The settlement cross sections measured the depth of the settlement trough within a certain ground condition type. By fitting inverted Gaussian curves similar to those given by Peck (1969) and Suwansawat and Einstein (2007), measurement of the volume loss associated with tunnelling activities (and ultimately construction and support effectiveness) could be determined.

All settlement rods were installed using solid stem augers advanced to the design depth. A 25.4 mm diameter black iron rod with a 150 mm diameter plate at the base was set at the bottom of the borehole and 300 mm of concrete was placed on top of the plate. A friction-reducing sleeve was then placed over the black iron rod and the remaining borehole annulus was backfilled to approximately 300 mm below the ground surface with a cement-bentonite grout. A schematic drawing of a typical settlement rod installation is shown below in Figure 6.7. The locations of the installed settlement rods are shown in Appendix B.

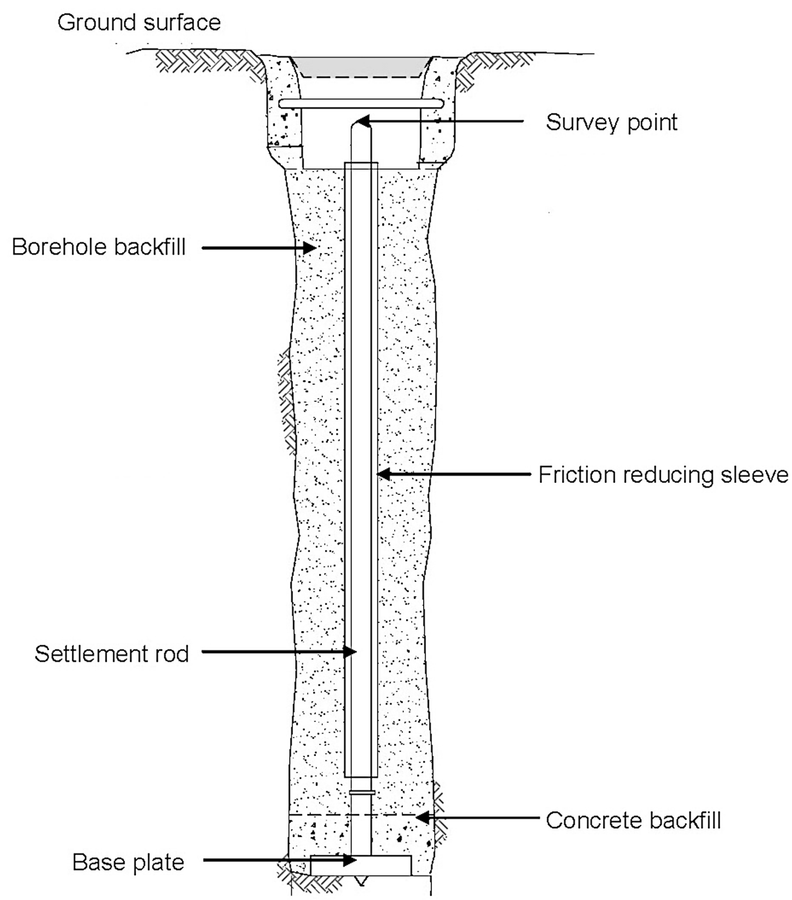

Figure 6.7. Typical deep and shallow settlement rod

The elevation at the top of each rod was then surveyed by a registered land surveyor to an accuracy of ±0.1 mm using a precise level. In most cases, this error was well adhered to as indicated by very minor fluctuations over time.

6.3.6.2 Multi-Point Extensometers

Two multi-point extensometers were installed within the pillars of the deep monitoring cross sections. The extensometers consisted of spring loaded burros type (hook) points that were expanded within the borehole following borehole excavation.

Readings of the points was carried out manually twice daily by the instrumentation consultant using a digital calliper at the instrument head. It was possible to automate the system however the consultant selected to monitor the points manually. The laboratory accuracy of the multi-point extensometers used is given as ±0.025 mm (GeoKon, 2012), however this was not found to be realistic due to the type of anchorage method used (hooks versus packer type points). The typical error as shown in the daily fluctuations was approximately ±0.25 mm. The locations and construction details of the multi-point extensometers are shown in Appendix B.

6.3.6.3 Inclinometers

Inclinometers were installed within the pillars and on the outside of the tunnel cavities at each of the monitoring cross sections. The inclinometers observed the lateral deformations of the ground due to the approach and passage of each tunnel. One inclinometer was also installed through the face of the lag tunnel at Section D (mixed face conditions). This instrument was to illustrate the deformations into the tunnel face with the approach of the lag tunnel.

In total there were 16 inclinometers installed prior to tunnel construction. All of the inclinometers were installed into boreholes drilled to the design depth or deeper using mud rotary methods. The principal (A-A') direction was aligned in the direction of the maximum displacement, which was typically perpendicular to the tunnel axes. Once in position, the inclinometers were set in place with a cement grout tremied to the base of the borehole.

Measurements were taken by the instrumentation consultant twice daily using a MEMS inclinometer probe with an accuracy of ±2 mm per 25 m of casing. The locations and typical construction of the inclinometers are shown in Appendix B. As stated in Section 6.6.3.3, two of the inclinometers within the pillar along the west alignment were replaced with Shape Accel Arrays.

6.4 Results

The results of the monitoring program are presented in the same order as those presented above in the general description of the instruments. In each case, representative curves will be presented while the complete results will be given in Appendix B.

6.4.1 Cast-in-Place Strain Gauges

6.4.1.1 Homogeneous Face Conditions (Glacial Till)

The cast in place strain gauges were installed into the shotcrete liner of the lead tunnel at two locations as discussed in Section 6.3.1. The instruments installed at Northbound Tunnel Meter (TM) 141.5 or Station 600+672 were immediately connected with the datalogger. Due to conflicts with the excavation equipment, it was requested by the contractor that the installations not be activated until the tunnel face had moved away from the monitoring location. As a result, all data was truncated and represents only the measurements taken during the approach and passage of the lag tunnel.

All instruments but one were operational throughout the entirety of the monitoring program. One strain gauge at Northbound TM 141.5 stopped working after a brief period of operation. It is possible that there was some damage to the communications wire during installation and the ingress of groundwater resulted in failure of the instrument post installation.

When the data is plotted with respect to the position of the lag tunnel face (Southbound), the data suggests that there are distinct strain patterns related to the gauge position within the liner. Figure 6.8 shows all of the data from the monitoring section within the glacial till with respect to the position of the lag tunnel face. Positive numbers indicate that the monitoring point is ahead of the face and negative distances indicate that the lag tunnel has passed the monitoring point.

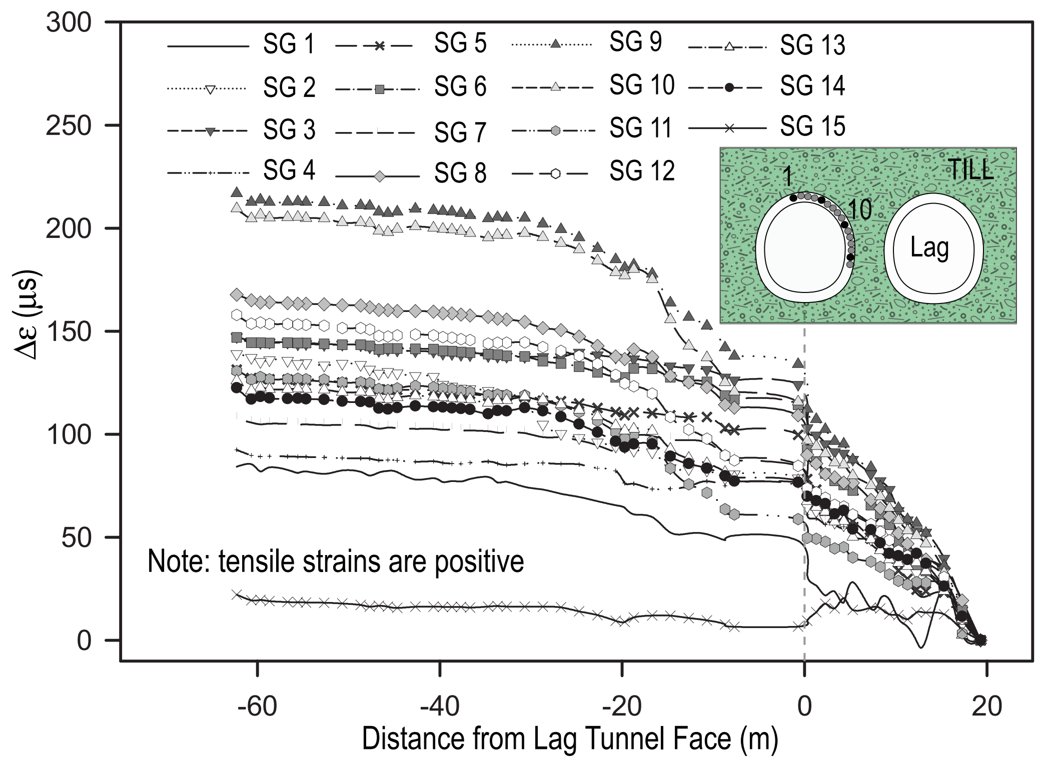

Figure 6.8 All recorded strains with respect to the lag tunnel face at Section E

Considering the stress paths given in Chapter 5, there should be three regions of strain profiles around the tunnel cavity. The different stress paths should result in differing strains in the crown, springline and invert. Figure 6.9 and Figure 6.10 provide the data for strain gauges located in the crown, springline and invert respectively.

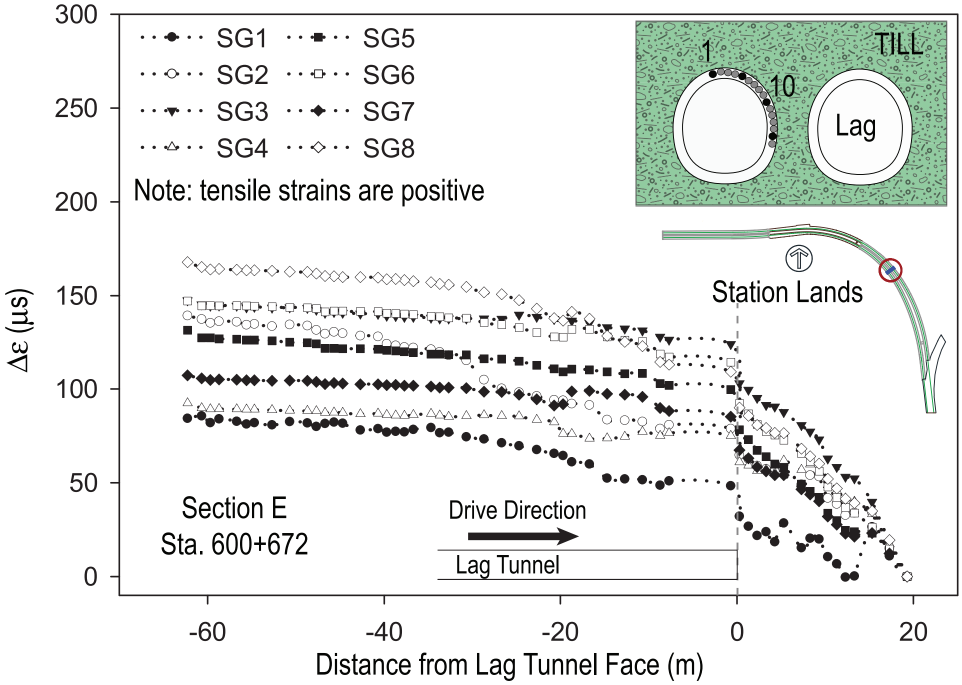

Figure 6.9. Change in strain measured in the tunnel crown (glacial till)

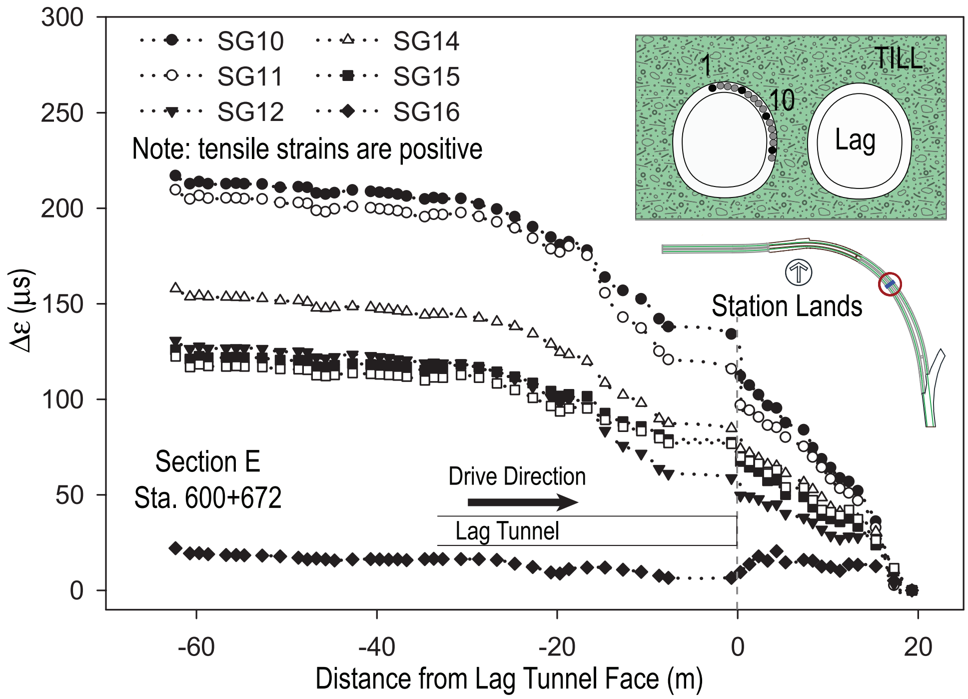

Figure 6.10. Change in strain measured in the springline and invert (glacial till)

With respect to the figures above, the rate of strain increase and impact of the lag tunnel construction are highly variable. The gauges in the crown (SG# 1 to 8) undergo moderate increases during passage of the lag tunnel and were typically around 100 to 150

$\mu\varepsilon$. The increase in strain when the lag tunnel is at the monitoring point is around 100 $\mu\varepsilon$ or approximately 65 % of the total strains.

The strain gauges located within the springline adjacent to the pillar (SG# 11 to 15) undergo considerably higher strains due to the passage of the lag tunnel when compared to those measured in the crown. The total change in strain is around 125 to 200 $\mu\varepsilon$, with higher strains occurring at the interface between the header and the bench (SG 10 and 11). As in the crown, most strains occur by the time the lag tunnel face is at the instrumentation section. In the springline, the typical strains were roughly 75 to 125 $\mu\varepsilon$ or approximately 60% of the total strains.

In the invert strain gauge (SG# 16) there is actually a drop in the measured strain resulting from the passage of the lag tunnel. The drop is approximately 10 $\mu\varepsilon$ and the total change in strain is roughly 25 $\mu\varepsilon$.

When the trends in the strains are observed, it appears that the strains continue until the lag tunnel is approximately 3 tunnel diameters from the monitoring point. After this point, the strains approach a steady state suggesting that the state of stress within the soils surrounding the two tunnels has reached equilibrium.

6.4.1.2 Mixed Face Conditions

As in the homogeneous glacial till conditions, the mixed Empress Sand and glacial till conditions resulted in several different patterns of strain with position around the tunnel. Figure 6.11 to Figure 6.14 below show the results of each zone of strain gauge with respect to the position of the lag tunnel. Like the homogeneous conditions, the passage of the lag tunnel is clearly observed as an abrupt change in strain.

The data shows that the strains measured in the crown of the tunnel are relatively uniform and minor with total changes between 50 and 100 $\mu\varepsilon$. These changes are slightly lower than those measured in the instruments installed in the crown within Section E above. The depth to the tunnel crown at both sections is approximately 13.5 m (Sta. 600+671.5) and 16 m (Sta. 700+412.7). The pillar width at Section E was 1.48 m or 0.23D, while at Section D the pillar width was 2.2 m or 0.33D. It is likely that the additional pillar width provided better stress distribution between the two tunnels at Section D and therefore reduced the strains measured in the liner.

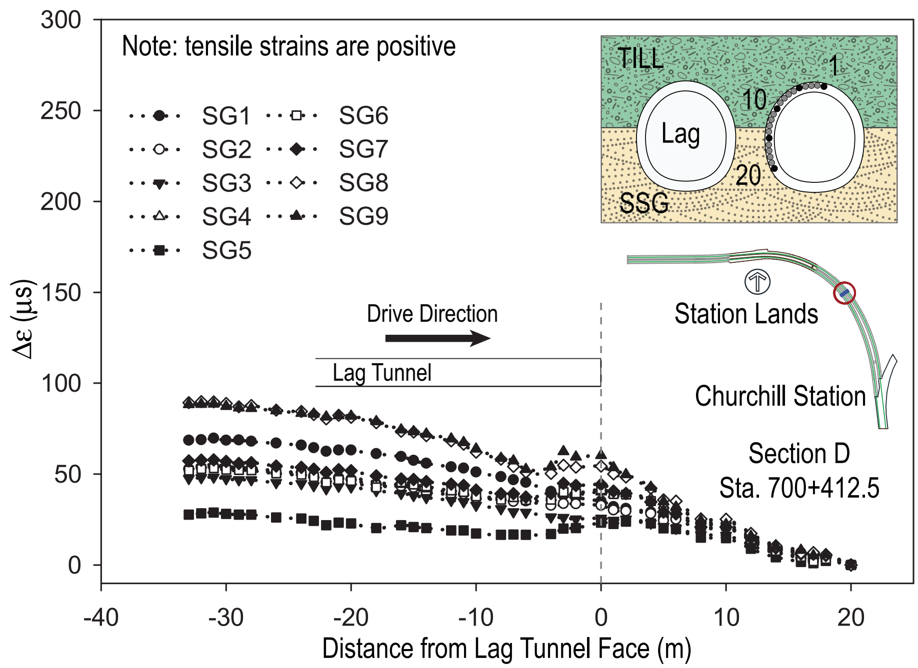

Figure 6.11. Change in strain within mixed face crown relative to the lag tunnel face

With respect to the strains measured within the glacial till at the tunnel springline (Figure 6.12), the strains are very similar to those measured at Section E (Figure 6.10). These sensors indicated total strains on the order of 100 to 150 µε, with approximately 60% of total strains occurring when the lag tunnel face is at the monitoring section.

Within the Empress Sand, the total strains are slightly higher and were typically between 150 to 250 µε. In this case, the percentage of total strains that occurred following the passage of the lag tunnel was roughly equal to those measured when the tunnel face was at the monitoring section. This may have been a result of the recompression of the previously dilated sand within the pillar. The constant rate of increase from roughly 1D ahead of to 3D past the tunnel face suggests that the change in stress is nearly constant with time. This suggests that the redistribution of stresses within the sand was solely a function of tunnel position. Based on the nature of the strains, it is likely that minor yielding occurred within the sand. In addition to displacements related to squatting of the tunnel and the lateral recompression of the pillar sands, the strains were approximately 2 times than those measured in the glacial till for the same locations.

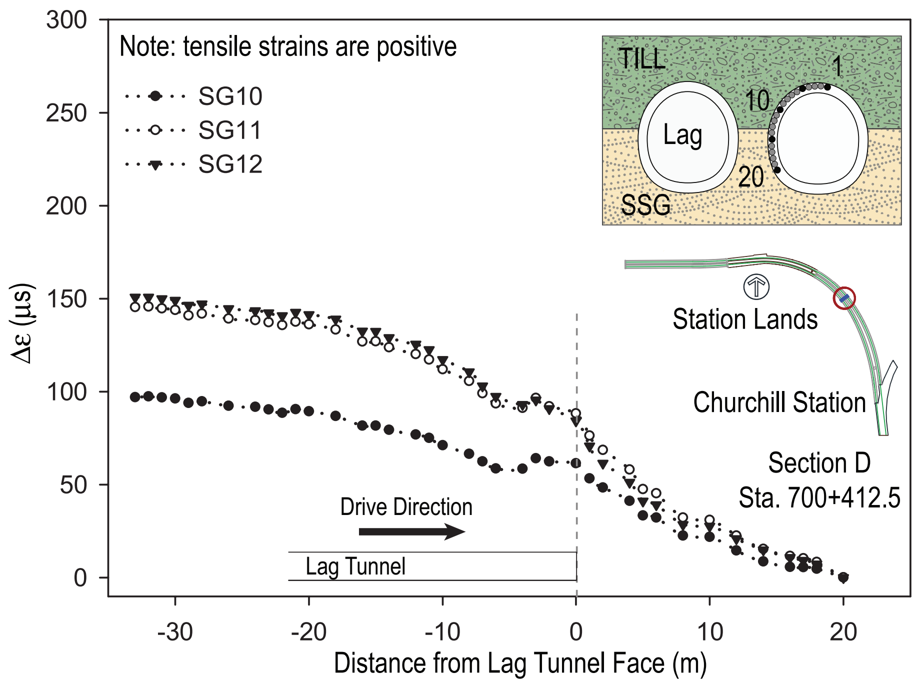

Figure 6.12. Change in strain within mixed face springline relative to the lag tunnel face

The changes in strain measured in the sensors located near the tunnel invert (Figure 6.14) indicate that the profiles are similar to those in the crown. In this case, the total strains were around 75 to 125 $\mu\varepsilon$ with approximately 50% of the total strains occurring when the lag tunnel face was at the monitoring section.

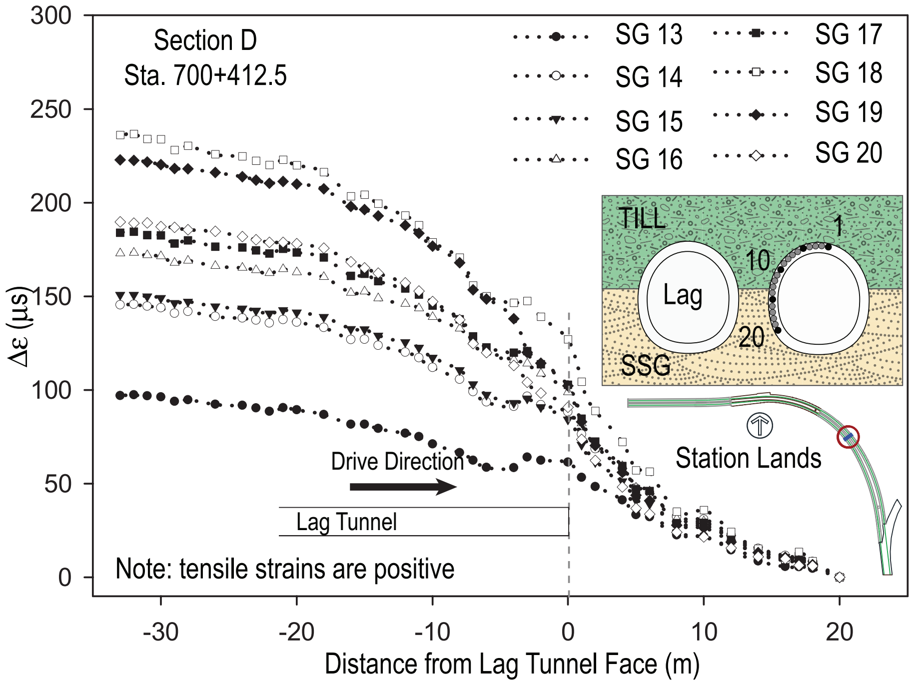

Figure 6.13. Change in strain within mixed face springline relative to the lag tunnel face

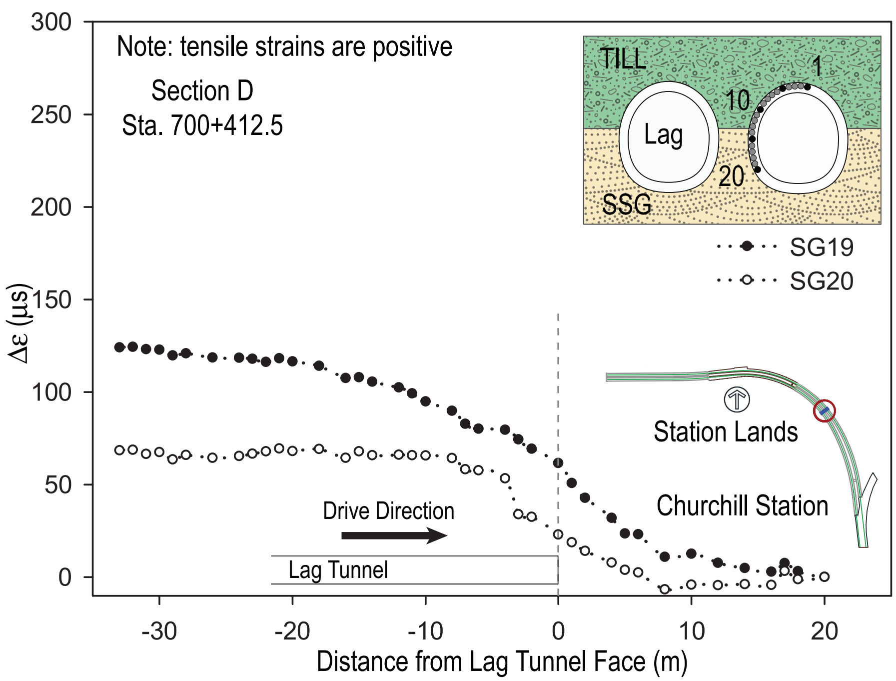

Figure 6.14. Change in strain within mixed face invert relative to the lag tunnel face

It is immediately clear that there is a distinct increase in measured strains within the Empress Sand relative to the glacial till. Most of the elevated strains however occurred near the center to lower regions of the bench within the Empress Sand. The two sensors positioned on either side of the geological unconformity and spaced 0.45 m from each other (SG#12 and 13) indicated higher strains within the glacial till. The difference in strain between the two points was approximately 50 με.

When the strains measured in the springlines are compared, the strains within the glacial till are similar to those measured in the first monitoring section (Sta. 600+671.5). The load increase from the glacial till in the springline is minor and was not likely influenced by the increase in pillar width from 0.23 to 0.33D. Considering the findings of El-Nahhas (1981), it is not likely that there was any yielding that occurred in the glacial till due to the construction of the lag tunnel. It is more likely that the measured strains are a function of the squatting of the tunnel liner resulting from tunnel construction and liner activation.

6.4.2 Optical Targets

In this section, only the convergence measured at Sections E and D (Sta. 600+671.5 and 700+412.7) will be discussed here.

6.4.2.1 Homogeneous Face Conditions (Glacial Till)

Optical targets were installed into the liner at Section E (Sta. 600+700) or 1 m ahead of the monitoring section. The targets were installed with three targets positioned at the crown and haunches of the tunnel as shown in Figure 6.3 (left). The results of the vertical and horizontal convergence monitoring in the lead tunnel at Sta. 600+670 are shown below in Figure 6.15 and Figure 6.16 respectively.

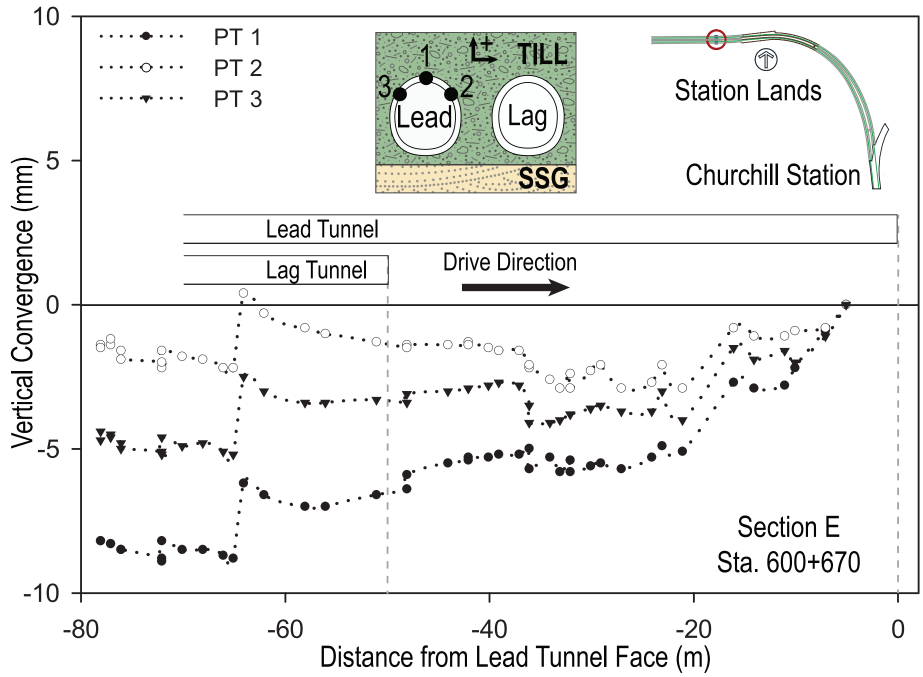

Figure 6.15. Lead tunnel vertical convergence recorded with optical targets

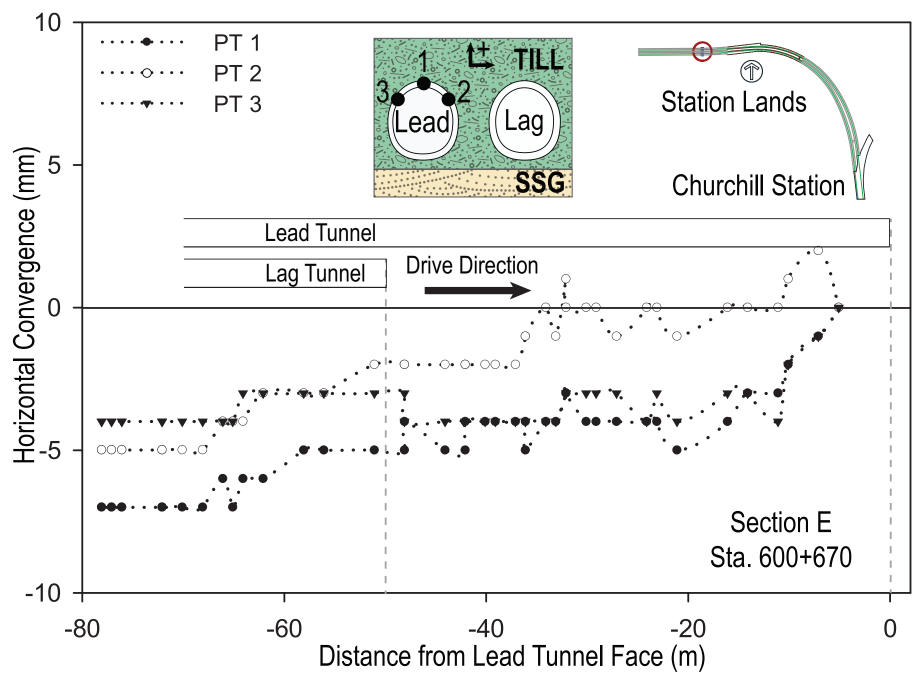

Figure 6.16. Lead tunnel horizontal convergence recorded with optical targets

Figure 6.15 and Figure 6.16 illustrate the scatter in the data throughout the monitoring program. The worst of the data is suggests that the tunnel appears to rise between +10 m and -15 m from the lag tunnel face. This is not possible and the correction applied at a distance of around -15 m from the lag tunnel face is about 2.5 mm.

The regular flat sections in the horizontal displacement would indicate that the displacements are less than the resolution of the instrument. Another error is given by the horizontal displacement of PT3, which should be positive or into the tunnel cavity. The data for the lag (Southbound) tunnel is slightly better as shown below in Figure 6.17 and Figure 6.18 for the vertical and horizontal displacements respectively.

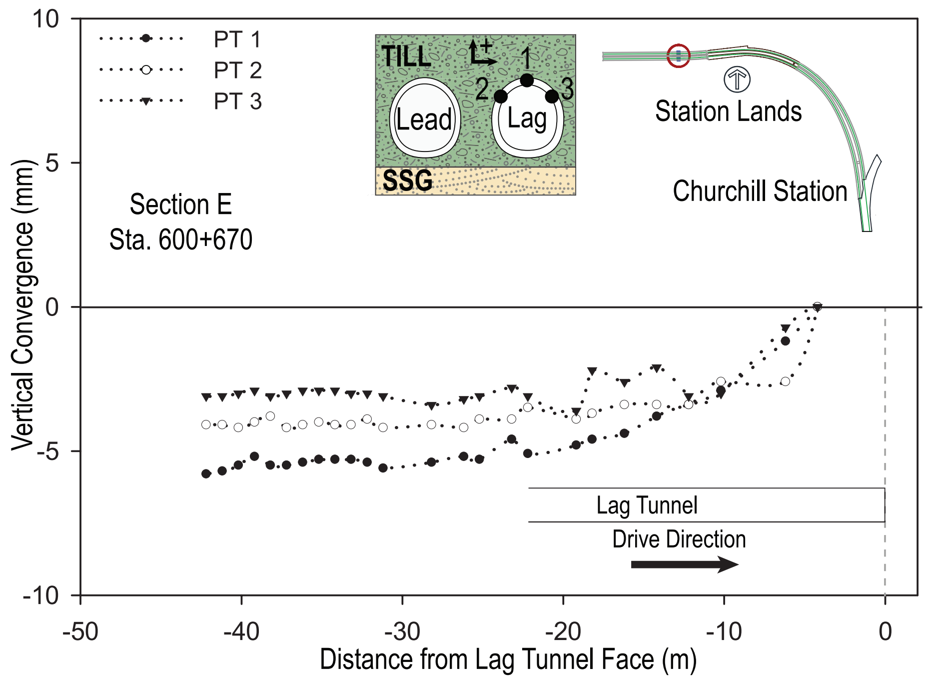

Figure 6.17. Lag tunnel vertical convergence recorded with optical targets

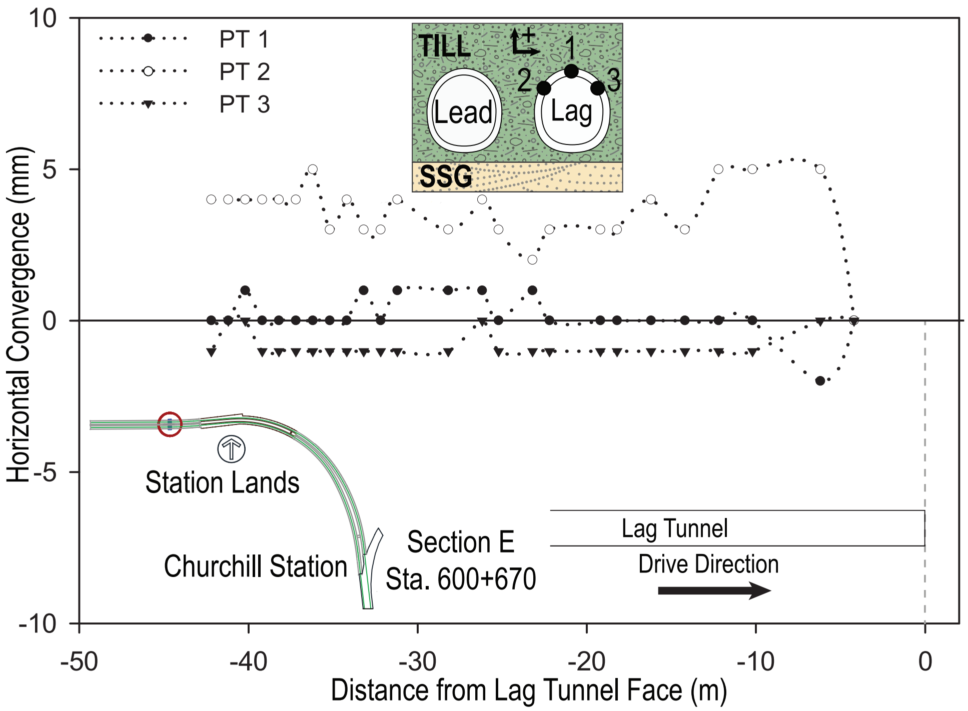

Figure 6.18. Lag tunnel horizontal convergence recorded with optical targets

The data from the lag tunnel suggests that the tunnel underwent squatting as would be expected. The vertical displacements appear to be relatively consistent with the crown settling the most (6 mm) while the pillar target undergoes the second largest settlement (4 mm). This is consistent with stresses in the pillar increasing following passage of the lag tunnel.

When the horizontal data is examined, it is interesting to note that the shortening of the horizontal diameter of the tunnel is very close to the total widening of the lead tunnel. This suggests that the ground mass moved as a whole into the lag tunnel following its construction. The movements of the lead tunnel are likely a result of elastic rebound due to unloading.

6.4.2.2 Mixed Face Conditions

The data recorded at Section D (Sta. 700+412.7) was considered to be more reliable than at Section E (Sta. 600+700). This was mainly due to the proximity of the monitoring section to the Station Lands cavity. The elevation of the cavity was static throughout the construction process and therefore provided a close benchmark for survey reference. The convergence monitoring from the two tunnels indicates that the error is likely within the ±1 mm range. The results of the vertical and horizontal convergence monitoring within the lead (Southbound) tunnel are shown below in Figure 6.19 and Figure 6.20 respectively.

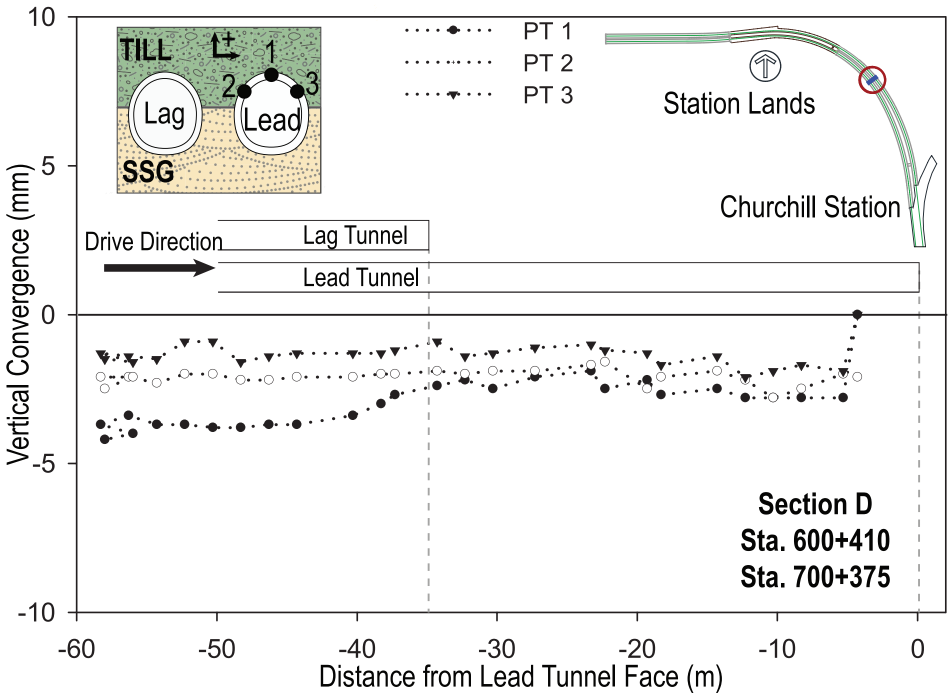

Figure 6.19. Lead tunnel vertical convergence recorded with optical targets

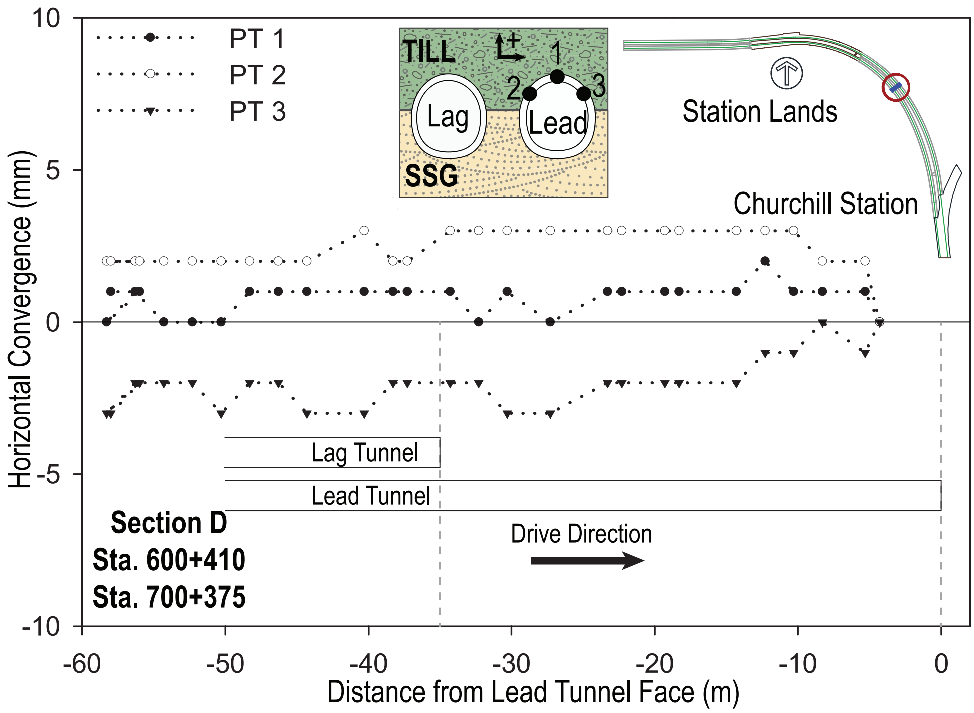

Figure 6.20. Lead tunnel horizontal convergence recorded with optical targets

The vertical displacement monitoring did not clearly detect the approach and passage of the lag tunnel. The only point that underwent additional displacements was in the tunnel crown. This point underwent an additional 1 to 1.5 mm of additional settlement following the passage of the lag tunnel. The other points are more or less static with no discernible change in vertical convergence with the passage of the second tunnel.

The horizontal convergence is slightly more telling with respect to the passage of the lag tunnel and the associated ground interactions. The point closet to the pillar (PT#2) undergoes convergence into the tunnel cavity of approximately 3 mm at its near steady state. As the lag tunnel approaches and passes the monitoring point, the convergence reverses direction slightly and reduces to approximately 2 mm. It is important to note that this recovery is within the error of the monitoring instrument and may not be real.

In terms of strains measured within the tunnel cavity, the stability of the opening can be assessed empirically using the method given by Chern et al. (1988). Observation of the tunnel convergence for the North LRT tunnels suggests that it was typically less than 8 mm along the western leg of the Northbound tunnel, though some vertical convergence values greater than 12 mm were recorded near to Churchill Station.

Assuming that the total convergence is twice the measured convergence, then a typical tunnel convergence strain is approximately 0.5%. According to Chern et al. (1988) and Hoek (2001), tunnel convergence strains less than 0.5% implies a stable, elastic response. This suggests that mobilization of the friction angle (residual shear strength) did not occur at the two monitoring points, however it is likely that some mobilization did occur at some sections in the first constructed tunnel. These strains also may have been greater in isolated locations that were not subject to monitoring. Figure 6.21 shows the data presented by Hoek (2001) updated with the information collected during the North LRT construction.

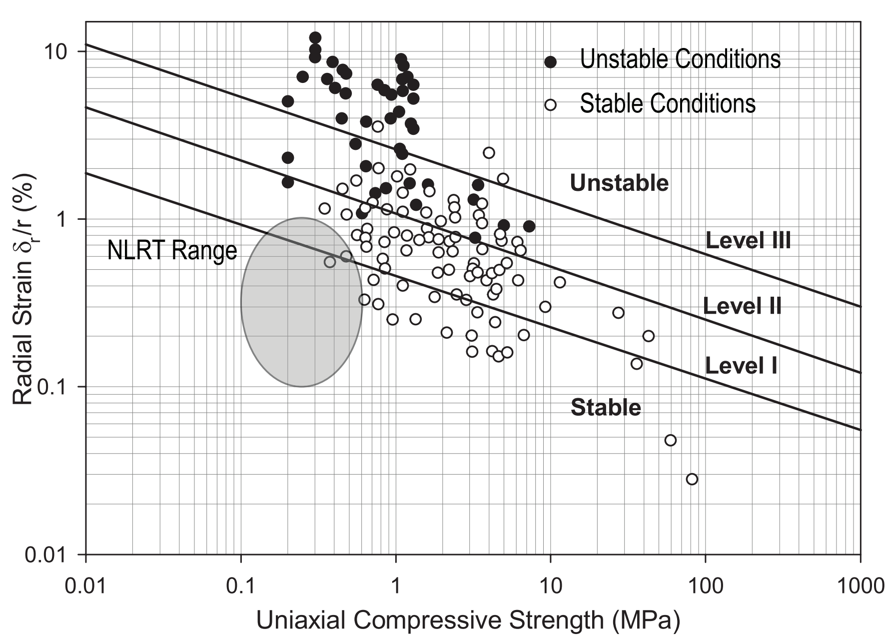

Figure 6.21. Tunnel stability based on strains and soil UCS adapted from Hoek, 2001

Considering the data given in Figure 6.21, within soils it should be assumed that strains that pass into the Level I range should be considered to be unstable. At this point, the strains associated with tunnel unloading exceed 0.5% for glacial till strengths within the typical moisture content range for the downtown area. These strains are then sufficient to mobilize the friction along the fissure surfaces and result in block and wedge formation.

6.4.2.3 Shape Accel Arrays (SAA)

At Section E (Sta. 600+671.5), the convergence of the tunnel was monitored using a circumferential SAA. The 10 m long SAA was installed starting from the shoulder furthest from the pillar in the lead (Northbound) tunnel and extended into the invert nearest the pillar. Displacements were measured relative to the starting point at the far shoulder at 305 mm intervals throughout the string. Coordinates were assigned to each segment and total displacements were calculated by monitoring the change in position relative to the first point. Based on these values, the displacements in the x and y directions could be directly computed and the resultant vector was taken as the incremental displacement.

Originally, the SAA was installed immediately behind the tunnel face and measurements were commenced within 12 hours following completion of the support ring. However the instrument was damaged the following evening and a replacement was not available until 2 weeks later. Consequently, the measurements reported herein represent the displacement of the lead tunnel from the approach and passage of the lag tunnel and not the post-support ring convergence. The initial and final shapes of the circumferential SAA are shown below in Figure 6.22; note, all displacements are exaggerated by 100 times.

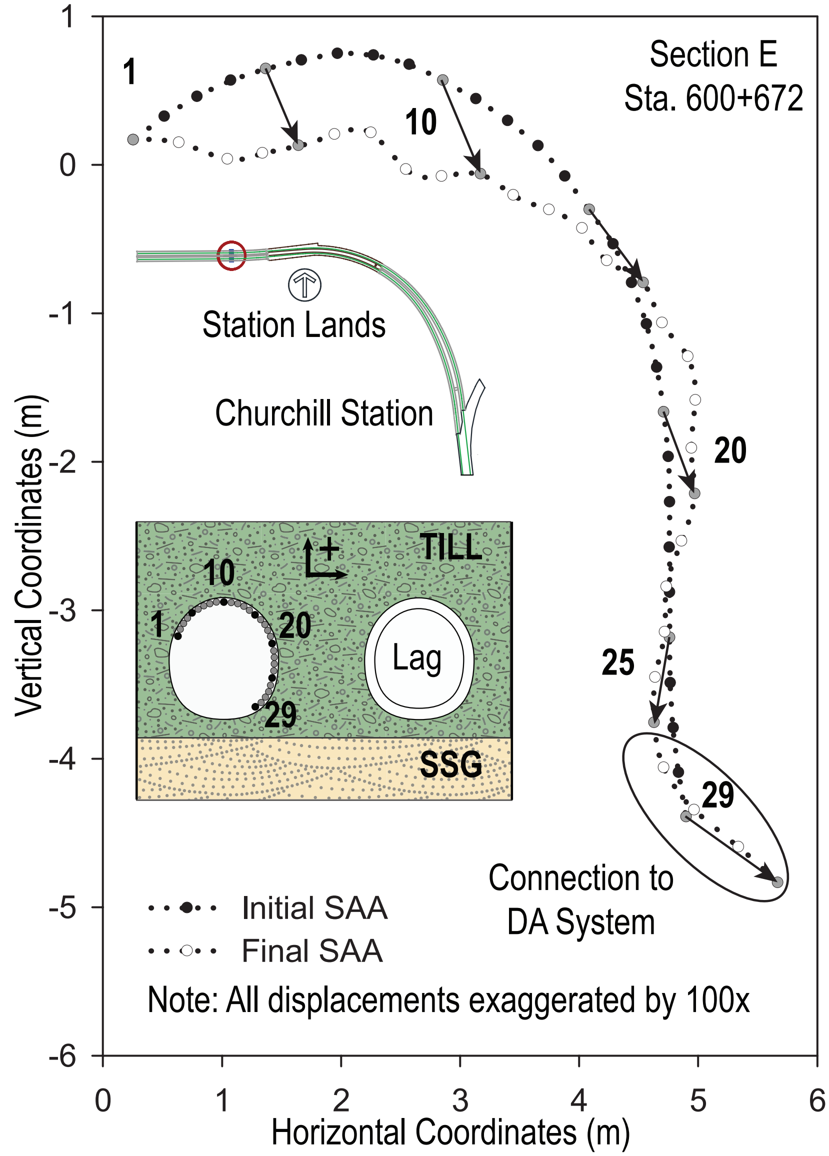

Figure 6.22. Circumferential SAA at Sta. 600+671.5

The results indicate that the tunnel underwent some squatting and some minor lateral displacements along the springline. It should be noted that all of the points above are the actual position of the SAA segments assuming that the reference point did not move. The actual location of the reference point was not surveyed and may have moved towards the lag tunnel increasing the total displacements. When the vertical and horizontal displacements are shown with respect to the lag tunnel face, the displacements fields are better illustrated. Figure 6.23 to Figure 6.30 illustrate the vertical and horizontal change in position with respect to the reference point (incremental displacement).

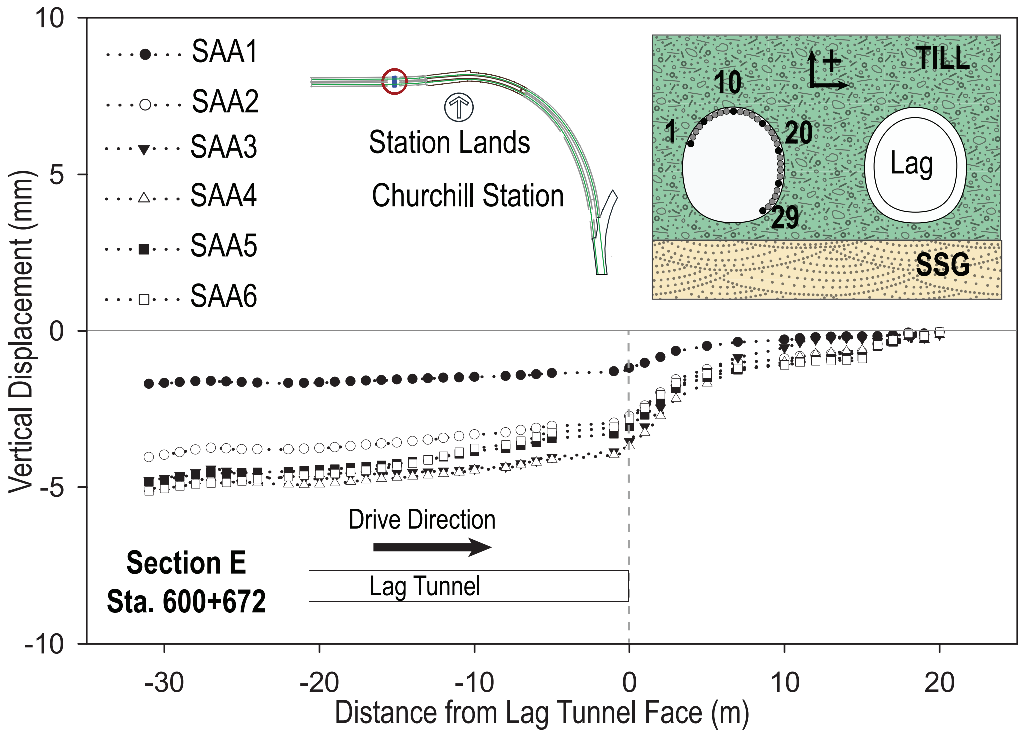

Figure 6.23. Vertical crown displacements (Points 1-6)

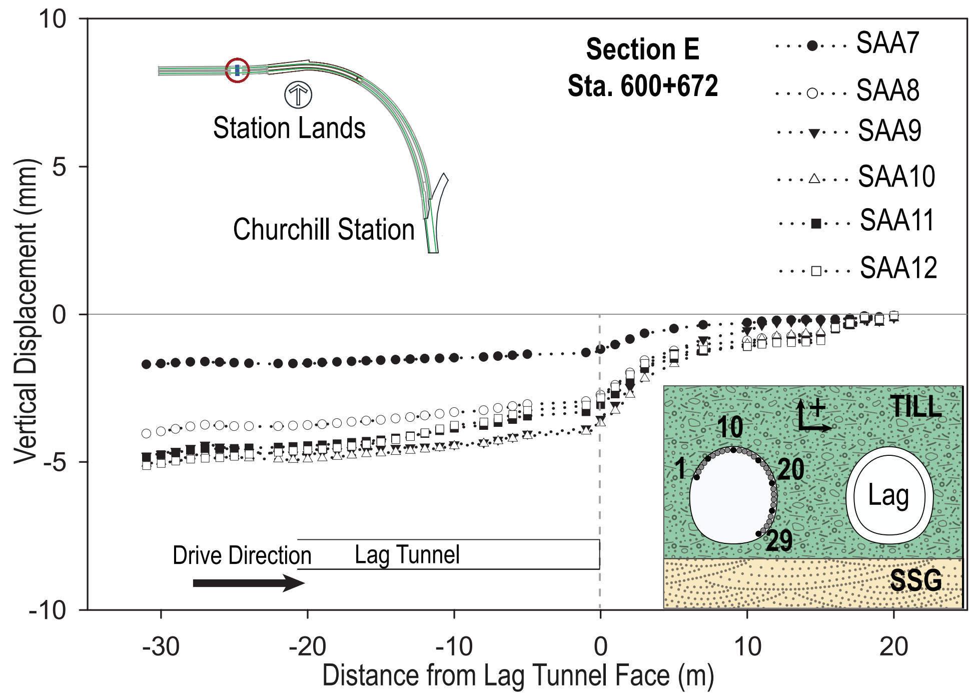

Figure 6.24 Vertical crown displacements (Points 7-12)

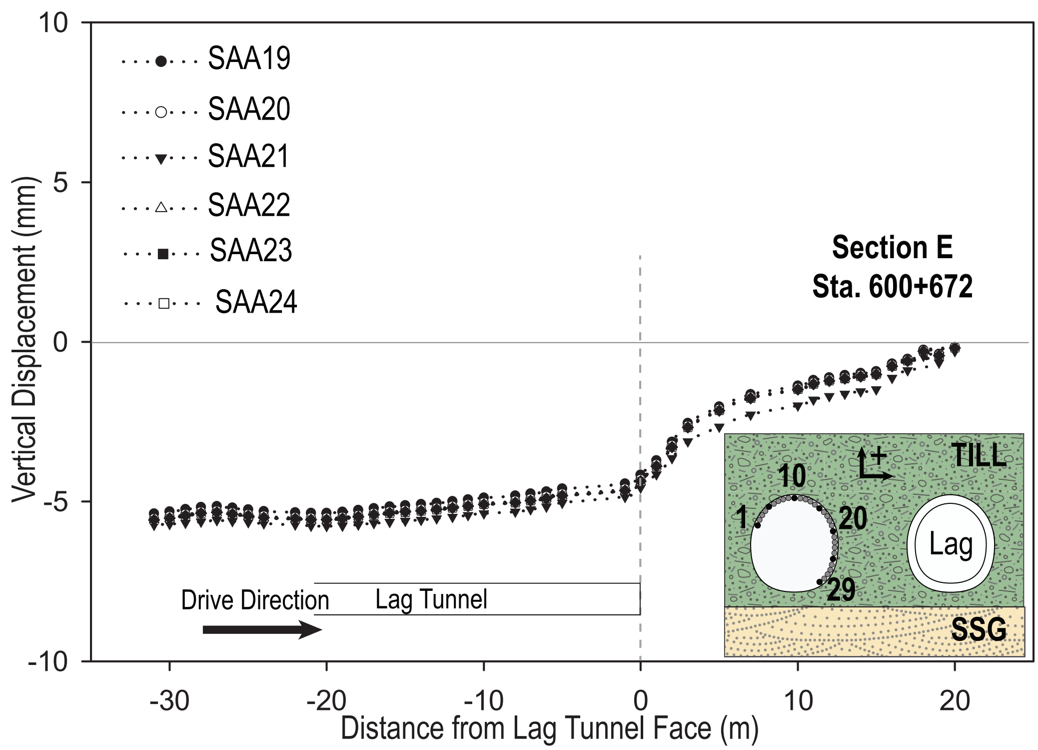

Figure 6.25. Vertical springline displacements (Points 19 to 24)

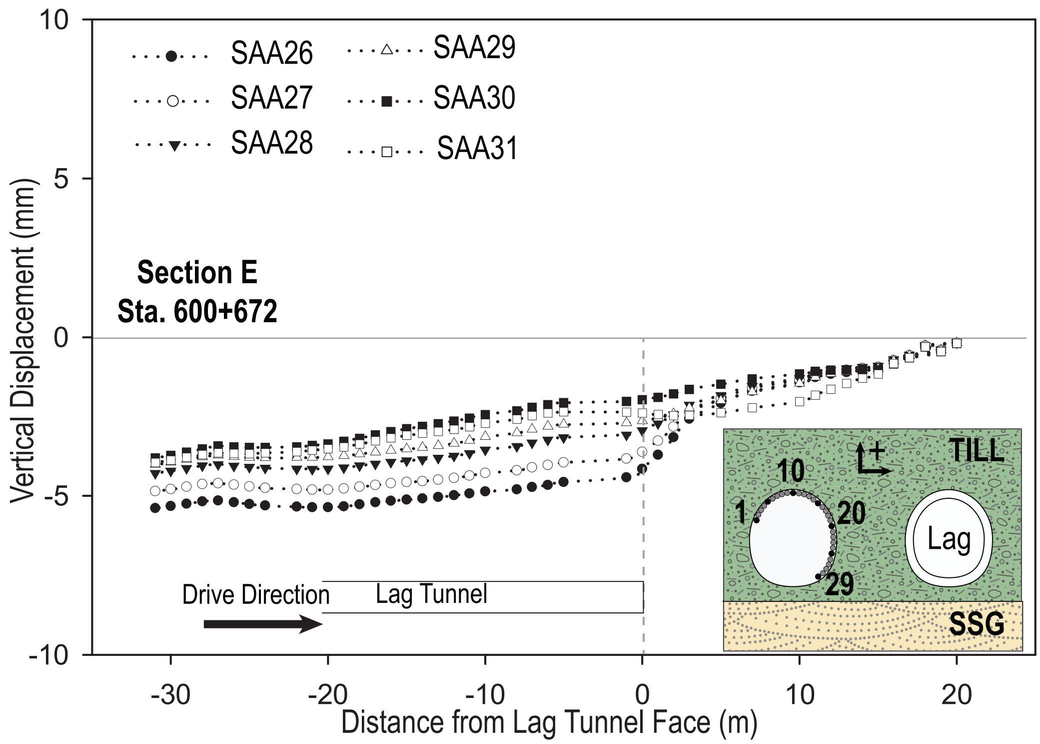

Figure 6.26. Vertical invert displacements (Points 26 to 31)

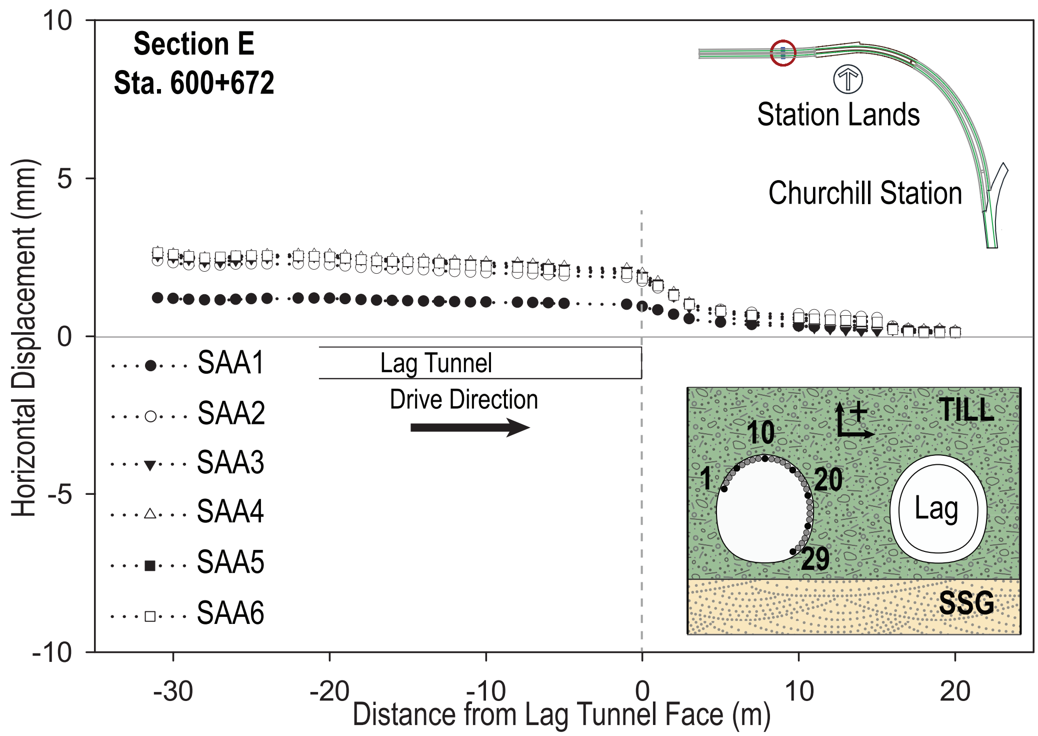

Figure 6.27. Horizontal crown displacements (Points 1-6)

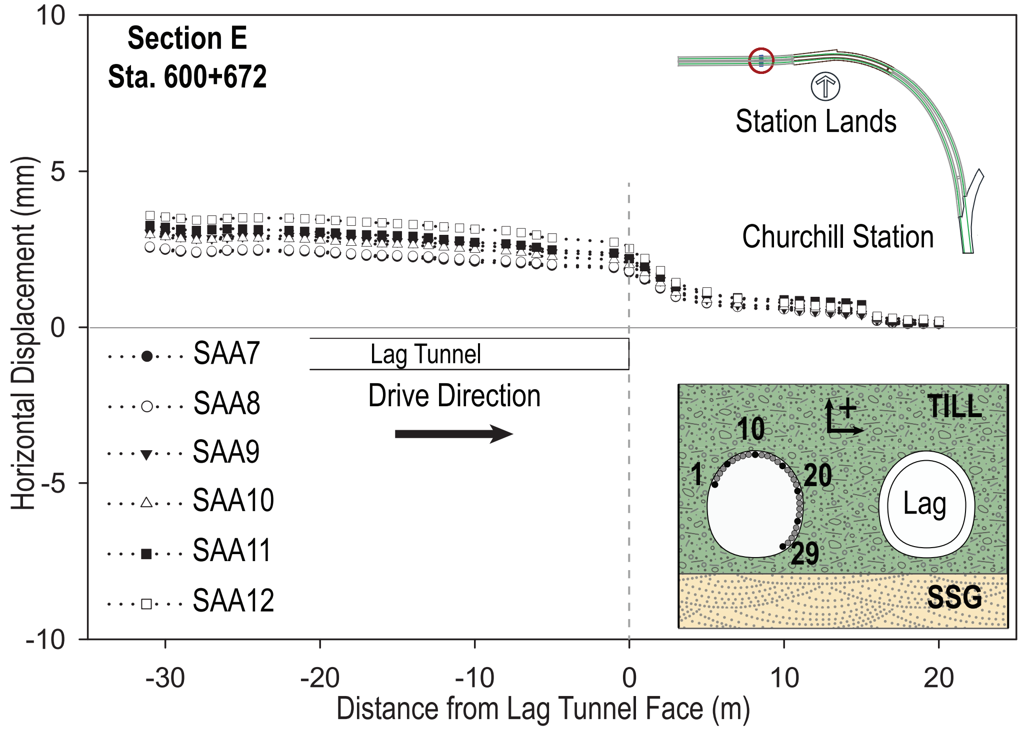

Figure 6.28. Horizontal crown displacements (Points 7-12)

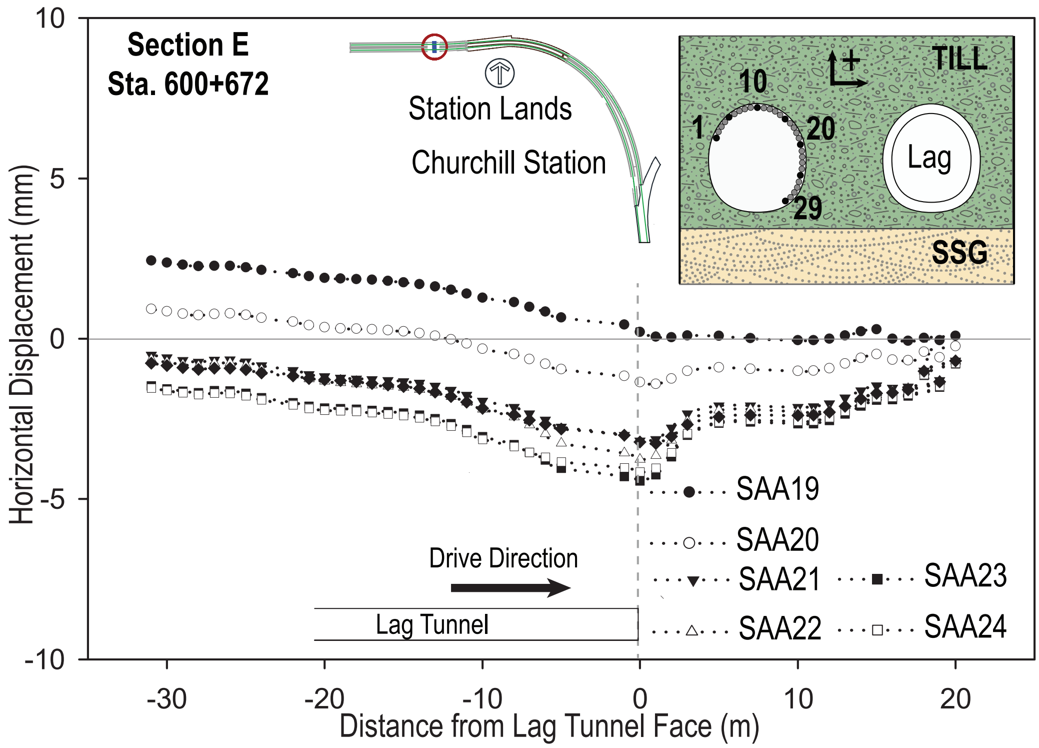

Figure 6.29. Horizontal springline displacements (Points 19-24)

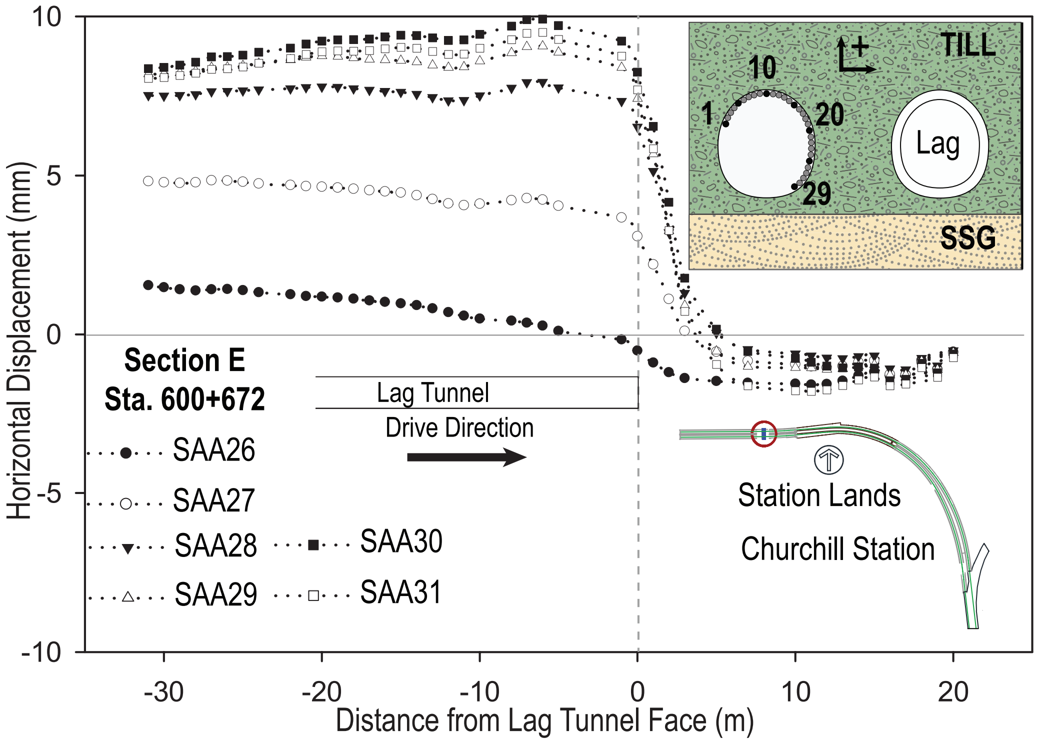

Figure 6.30. Horizontal invert displacements (Points 26-31)

The maximum vertical settlements measured by the SAA are approximately 7.6 mm at the crown, 5.7 mm at the springline and around 5.3 mm at the base of the string. The lowest segments indicated as the connection to the data acquisition system were buried below the invert backfill and only indicated a vertical displacement of around 4 mm.

The horizontal displacement varied from 4.3 mm (into the lag tunnel) at the crown; from -4.4 mm (away from the lag tunnel) to 2.5 mm (into the lag tunnel) at the springline and from 10 to 8.8 mm (into the lag tunnel) at the invert. The data shows variable the tunnel displacements are around the tunnel cavity with the approach and passage of a closely spaced lag tunnel. It also demonstrates how flexible the shotcrete liner is, as it was capable of undergoing considerable displacements with no obvious damage to the liner.

The displacements measured by the SAA suggest that there was a net movement of the lead tunnel into the lag tunnel during its approach and passage. The displacements in the springline and invert are of key interest as they show that there was a strong influence on the existing tunnel from the construction of the lag tunnel. The influence is best illustrated by the total displacements as calculated by the resultant vector of the vertical and horizontal movements. Figure 6.31 to Figure 6.34 present the incremental total displacements measured for the three groups of segments (crown, springline and invert) respectively.

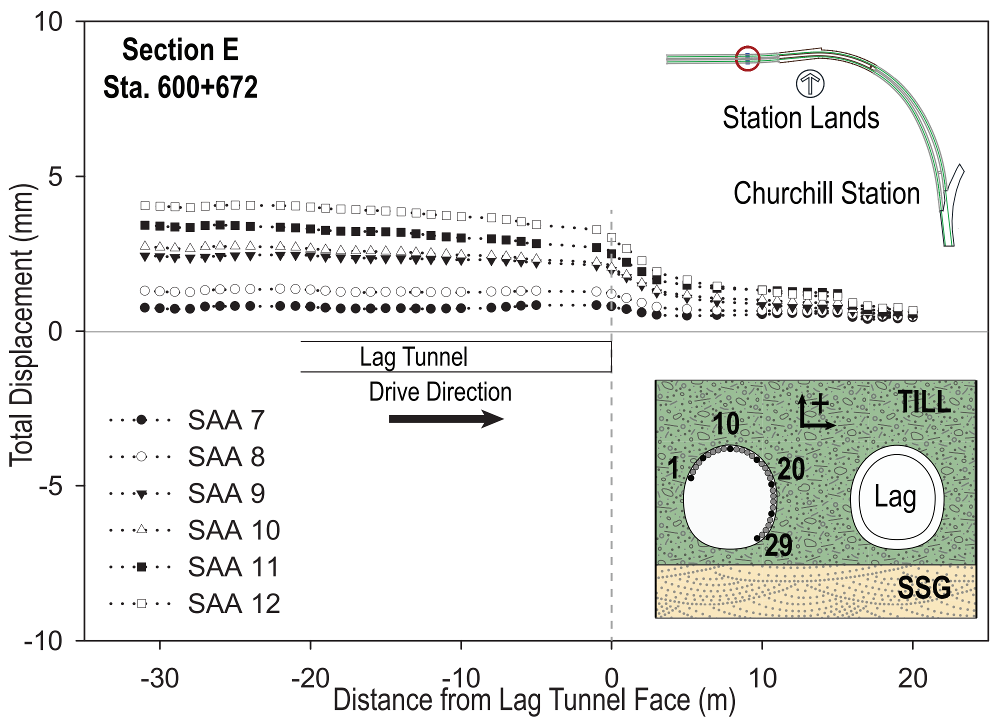

Figure 6.31. Total displacements measured at the crown (Points 7-12)

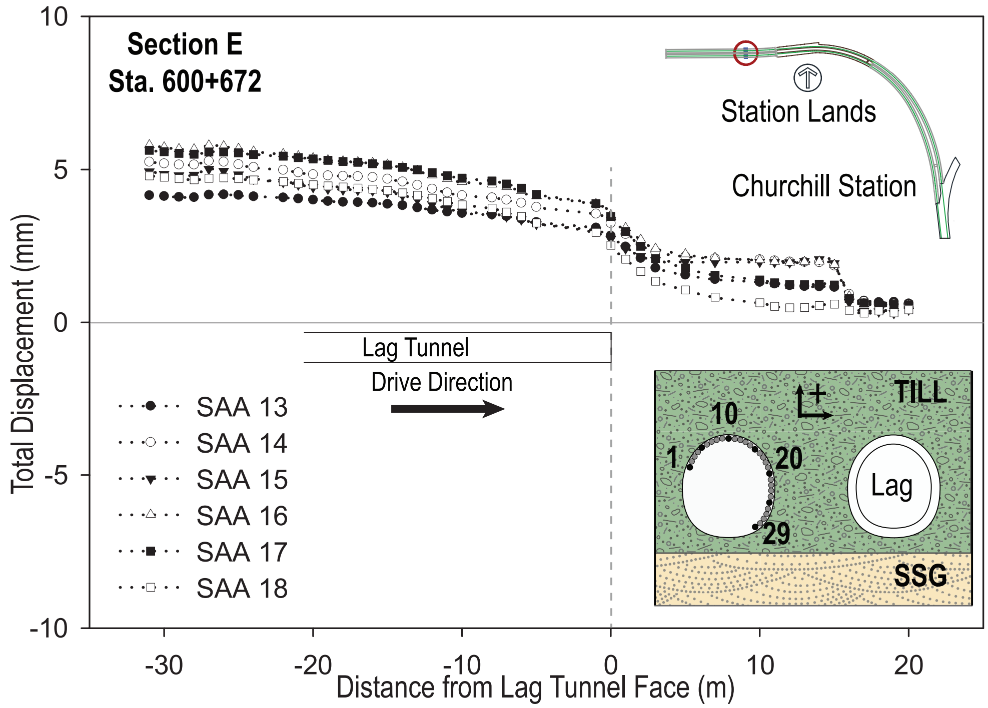

Figure 6.32. Total displacements measured at the crown (Points 7-12)

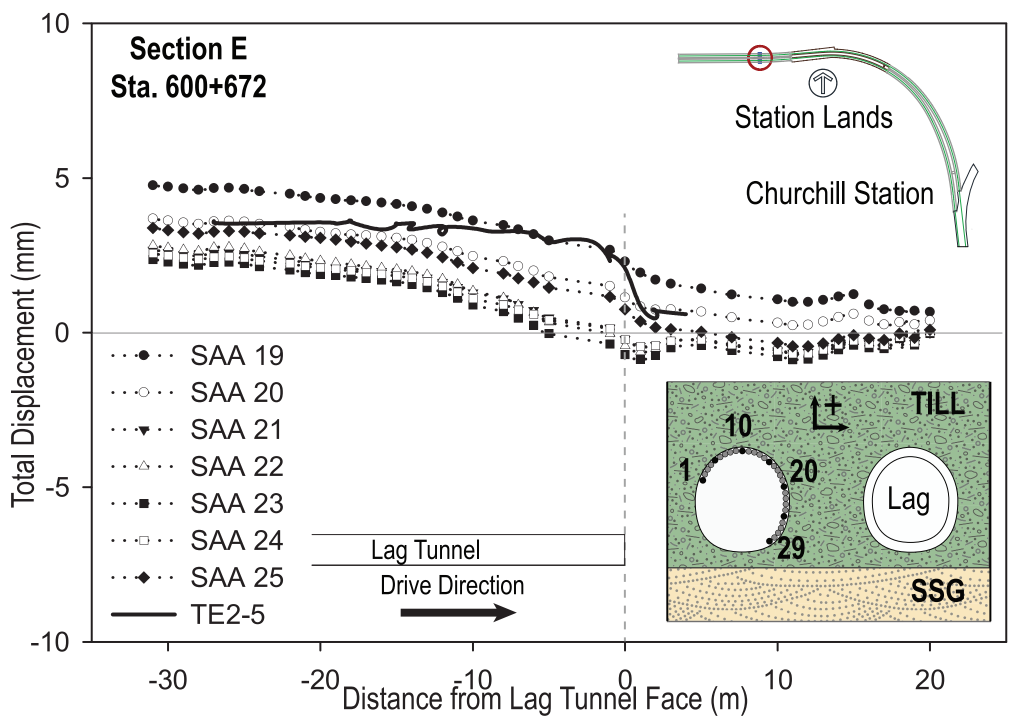

Figure 6.33. Total displacements measured at the springline (Points 19-25)

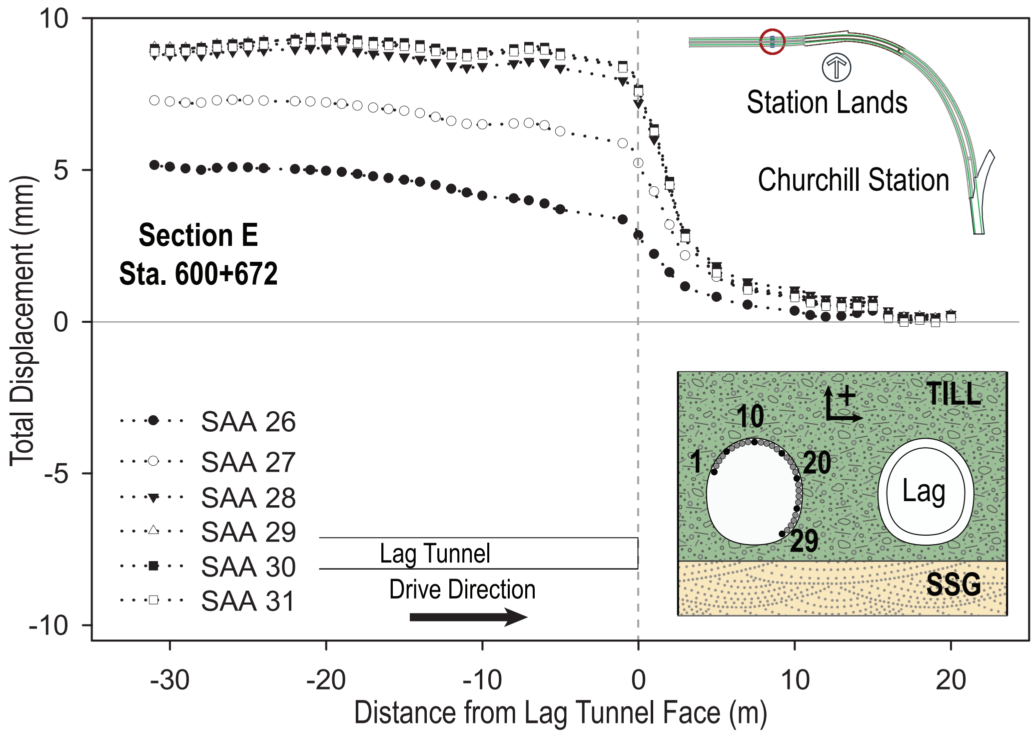

Figure 6.34. Total displacements measured at the invert (Points 26-31)

In Figure 6.33, the total displacements at the springline closely resemble those recorded by the tape extensometer, which has been shown for illustration. It is important to understand that the resultant displacements are the incremental changes of the segment position relative to the start point. These measurements are then directly comparable to those measured by the tape extensometer. The comparison is valid because the tape extensometer only measures a resultant vector relative to an assumed fixed point. In both cases, the fixed point is selected to be along the springline away from the tunnel pillar. Therefore any tunnel movements as a whole into the lag tunnel would not be detected by either method. The absolute displacements are expected to be less than 1 mm as indicated by the optical surveying of PT#3 away from the pillar (Figure 6.16). Because PT#3 was apparently constant through the construction of the lag tunnel, the displacements measured by the SAA are a result of the lag tunnel construction only. The settlement at the springline is approximately twice that reported by the optical targets. If an error of 2 mm is assigned to the optical point, the difference between the two methods becomes about 16%. This suggests that the use of the SAA to measure the real time, in-tunnel displacements is valid provided the limitations (assumed fixed point; no absolute displacements) of the instrument is well understood.

6.4.2.4 Time Domain Reflectometry (TDR)

Time domain reflectometry (TDR) was also used in a fashion similar to that of the circumferential SAA. However the coaxial cable in this case was cast directly into the shotcrete liner. The output from the TDR was a series of waveforms that illustrate peaks and valleys based on the interference of the wave pulse signal. Absolute values for displacements were estimated from laboratory calibrations on pieces of each cable prior to installation. For the calibrations, each of the cables used was subjected to incremental bending and shear forces and the corresponding signal was recorded for each step. Displacement calibrations were calculated from the corresponding signal shape and magnitude of change from the initial state. In each case, two to three waveforms were captured and the average signal was used as the value for a given location along the cable length. The resolution of the calibration curves was set for a cable/probe length of 1 m (calibration cable length) and 19 points along the cable (scaled to 256 points for a 14 m cable).

The bending calibration was carried out by recording the signal from a cable laid flat (0˚) and then the cable was bent at to an angle, and the resulting signal was recorded again. The calibration was carried out for 15˚ increments between 0 and 90°. The shear calibration was carried out by pinching the cable with a calliper to a known displacement into the cable. Like the bending, the incremental displacement and the associated signal were recorded. In each case, a line was fitted to the calibration curve and an equation was derived from the fit equation to provide values for the actual in-tunnel measurements.

An example calibration for one of the coaxial cables used in the in-tunnel monitoring considering the two deformation methods are shown below in Figure 6.35 and Figure 6.36.

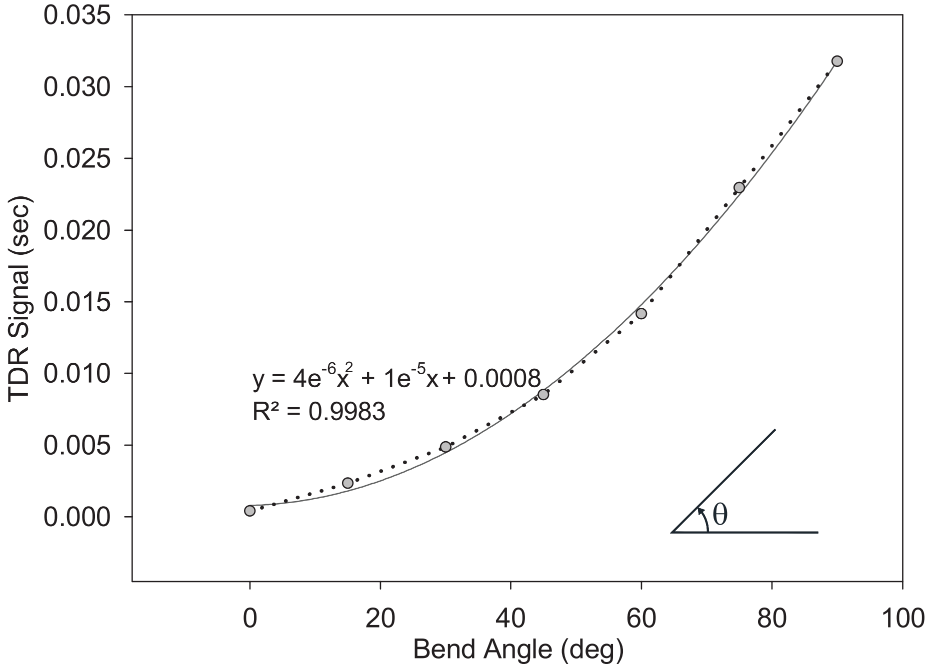

Figure 6.35. Calibration of 19 mm sheathed corrugated coaxial cable in bending

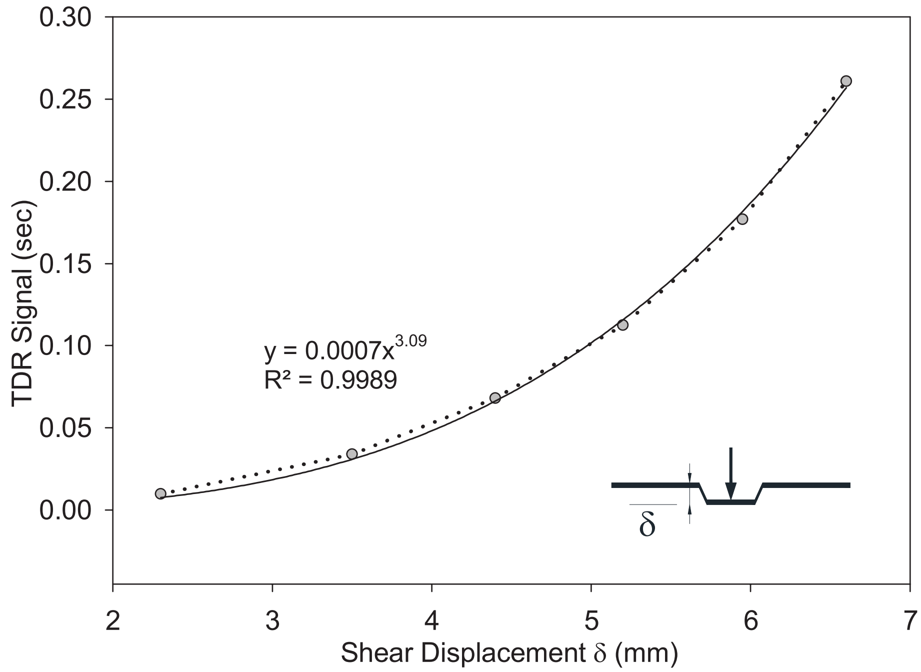

Figure 6.36. Calibration of 19 mm sheathed corrugated coaxial cable in shear

The final waveform shape recorded during the calibrations does not vary much between bending and shear. The two deformation waveforms are differentiated by the size of the anomaly within the signal. The shear signal is considerably larger than that of the bending signal. This means that when the coaxial cable is subjected to shear forces, the signal alters considerably, whereas when bending is the dominant function, the waveform deepens but the overall signal is not drastically altered. The waveform generated from the calibration tests on the above coaxial cable is shown below in Figure 6.37. Figure 6.38 presents the two final waveforms together to indicate the difference between bending and shear signal changes.

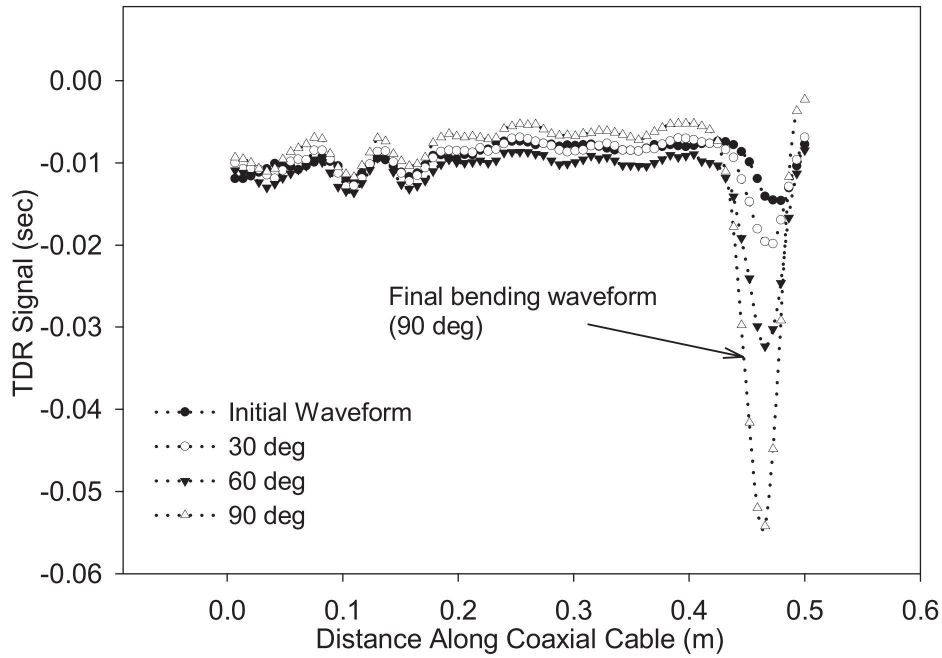

Figure 6.37. Bending calibration waveform (19 mm sheathed corrugated coaxial)

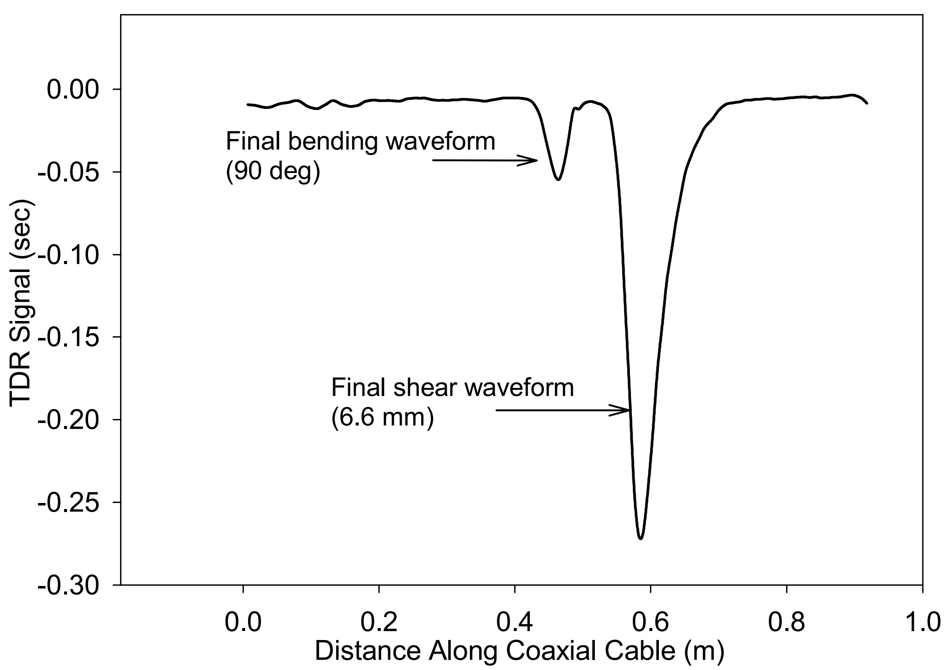

Figure 6.38. Comparison of shear and bending signal changes

Typical results of the TDR monitoring within the tunnel lining are shown below in Figure 6.39 for the 19 mm unsheathed corrugated and Figure 6.39 sheathed 19 mm diameter sheathed coaxial cables.

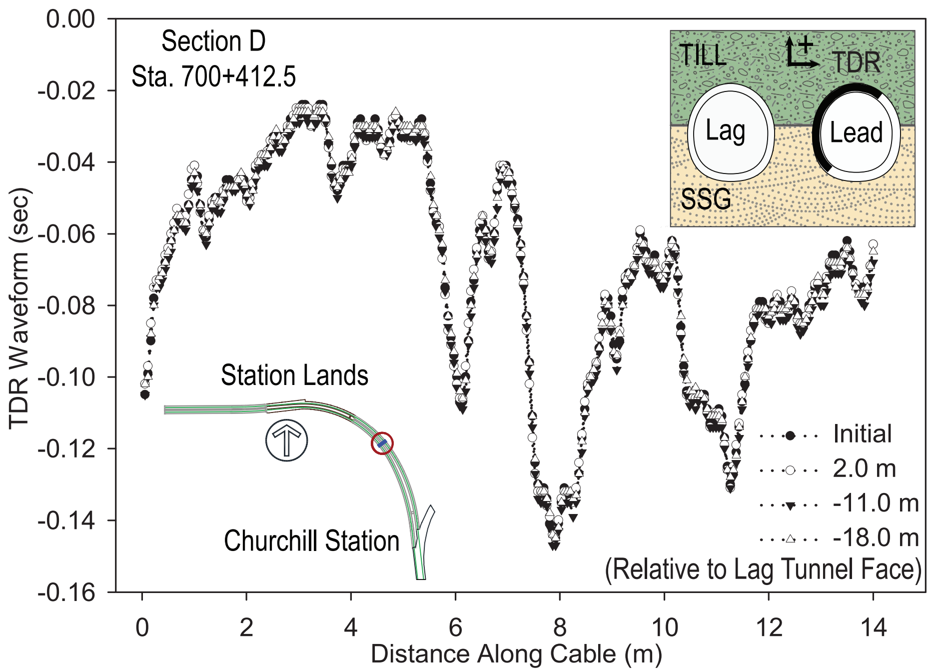

Figure 6.39. TDR waveform from unsheathed coaxial cable (25 mm diameter)

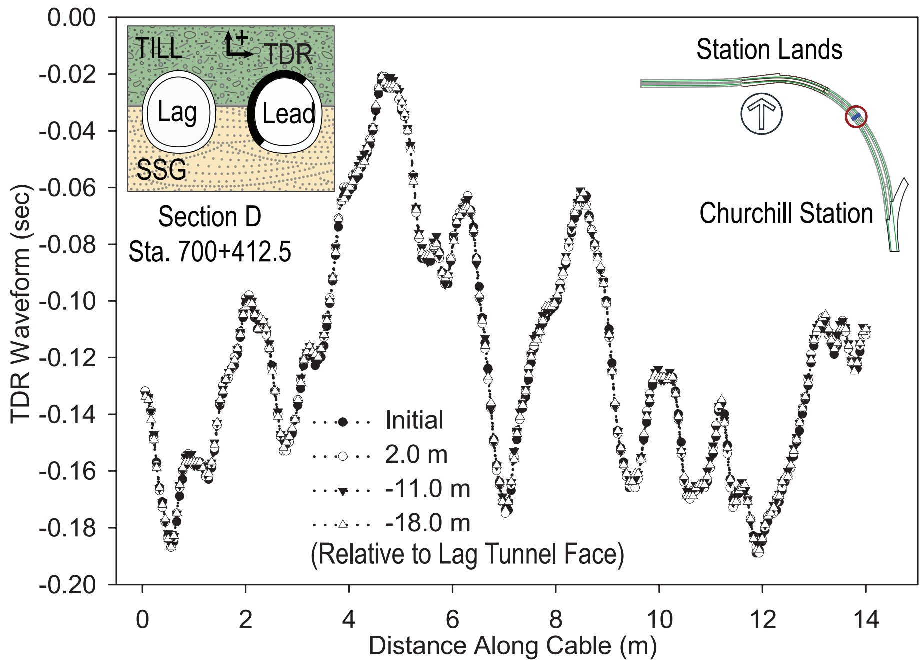

Figure 6.40. TDR waveform from sheathed coaxial cable (5 mm diameter)

The above curves do not say much in terms of displacement. It is only at the crimps can the actual changes along the cable be assessed. The crimps can be seen at regular 0.45 m intervals, which is where the cable was attached to the wire mesh with tie wire. To better isolate only the major changes that occurred along the length of the cable, the incremental difference between each scan and the initial waveform was examined. The values were then selected based on the maximum value along the string. Because the cables were crimped during installation to provide a location reference, the nature of the displacement was assumed to be increased shear (additional crimping) in each case. From this assumption, the shear displacement calibration curve was used to determine incremental displacement based on the changes to the waveforms at the locations of signal spikes. To better refine the calculations and present the data in a meaningful manner, the data was assessed only in the locations where the crimps were located. Most of the locations in between the crimps did not show any discernible change in position. This rendered the capabilities of the TDR to measure continuous strain, ineffective and therefore defeated the purpose of using the instrument. If measurements could only be made at discrete locations, then the data obtained from an SAA are more accurate and easier to interpret.

In order to make the data usable, several assumptions must be made. First, because the calculated displacements are total displacements, it was assumed that shear occurred perpendicular to liner at each location. This allowed for resolution of the vectors to generate a displacement plot similar to the circumferential SAA. By assuming this though, only a trend resulting from the approaching tunnel can be ascertained. It should be pointed out that the actual change in waveform when a step was observed were on the order of 0.001 second, which considering the calibration curve is negligible.

The TDR monitoring of the tunnel convergence at Sta. 700+412.7, shows in Figure 6.41 that the TDR tends to underestimate the displacement considerably. The displacements in Figure 6.41 have been multiplied by 100 times have been to show the changes at each step. Typically the displacement at each location is between 0.3 to 0.5 mm with some 0.7 mm changes recorded. The displacements are shown with respect to the lag tunnel face. The main observation of the TDR data is the general trend. The TDR indicates that there was an increase in shear strain following initialization, which was followed by a relaxation during approach and passage of the lag tunnel. This finding is consistent with the other monitoring instruments used during the investigation.

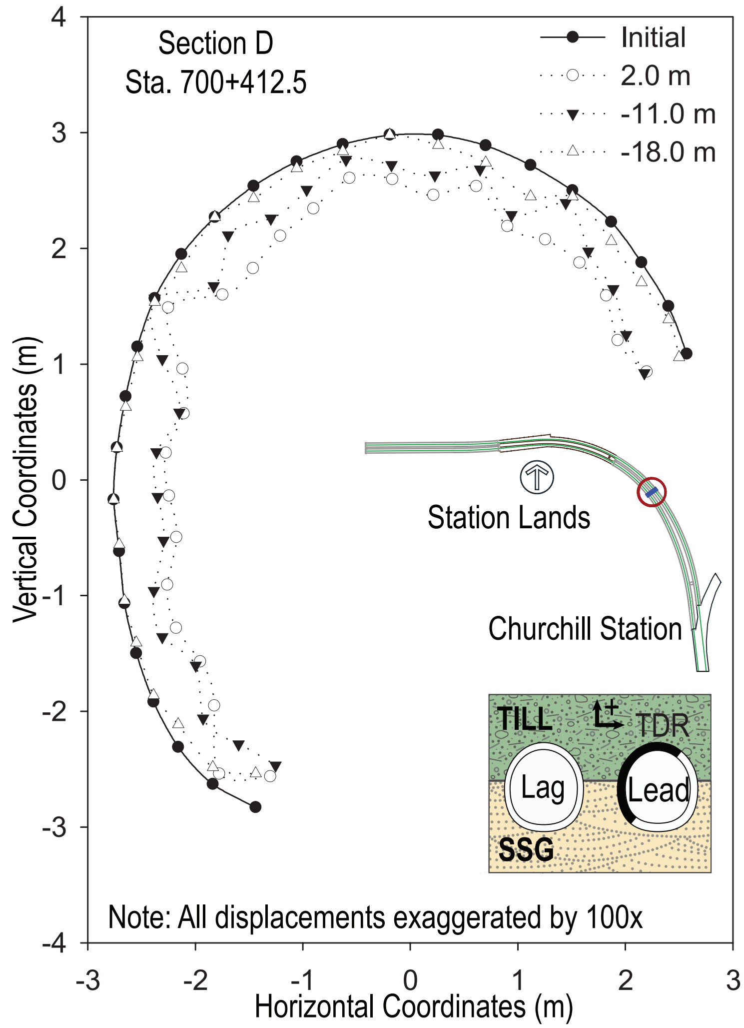

Figure 6.41. TDR circumferential displacement with lag tunnel face position

Because it was so difficult to ascertain if there was any change between readings, the comparison of which cable performed better (sheathed or unsheathed) was also difficult to determine. Based on the data, several conclusions have been drawn with respect to the use of TDR. First, the data is not easily interpreted and second, it is not clear that the measurements provide meaningful insight to the performance of the ground during tunnel construction.

6.4.3 Tape Extensometer

6.4.3.1 Homogeneous Face Conditions (Glacial Till)

Tape extensometer measurements were taken during the approach and passage of the lag tunnel. The measurements monitored the changes in the lead tunnel diameter with distance from the lag tunnel face. The results of the tape extensometer monitoring at the monitoring section installed at Sta. 600+671.5 (Section E) are shown below in Figure 6.42.

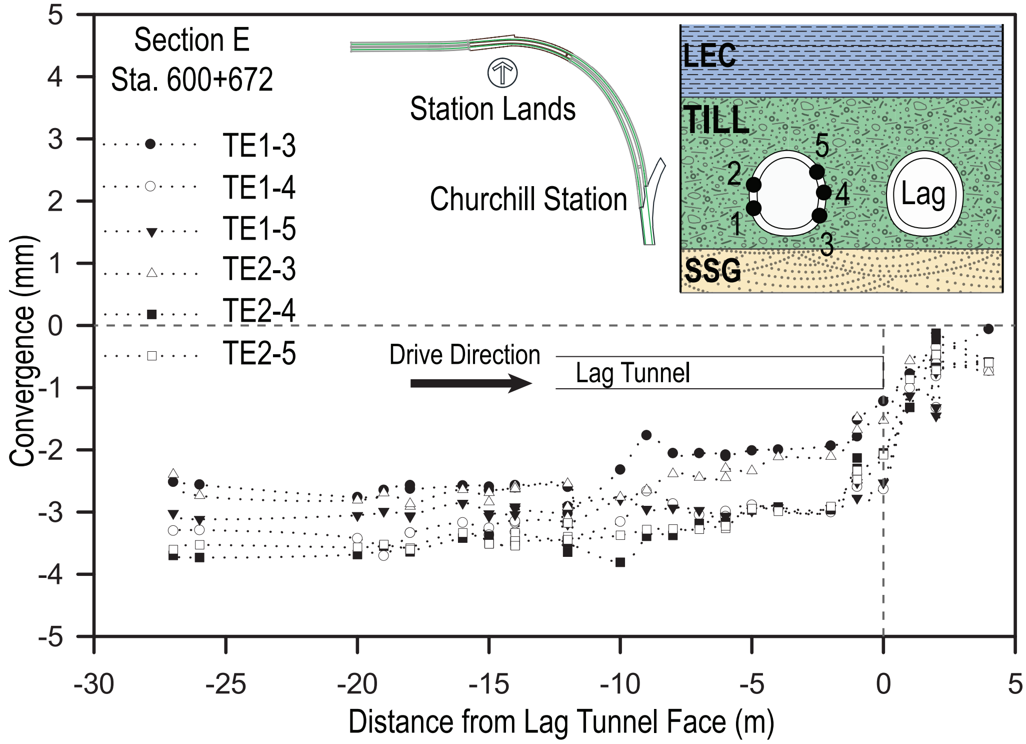

Figure 6.42. Results of glacial till tape extensometer measurements

The total widening between points TE1-4 and TE1-5 is approximately 3 to 3.5 mm, which is very similar to the widening measured between TE2-4 and TE2-5. The accuracy of the data is considered to be around ±0.25 mm based on the difference in widening measured to the same point from the two anchors. When the relative increase in diameter measured from point 1 is compared with that of the same points from point 2, the difference is only around 0.5 mm.

The results of the strain gauges can be compared to the findings of the tape extensometer with several assumptions. The first assumption is that the liner strains are elastic and all displacements may be calculated using closed form solutions for a circular opening in an elastic medium. This assumption is considered valid as the strains are extremely small and within the lower bound of the crack initiation range (σ_{ci}) for concrete. Next it is assumed that the strain gauges are installed along the neutral axis. This means that all measured strains are only axial and contributions due to bending are negligible. The final assumption is that all displacements measured by the tape extensometer occur only on the pillar side. This means that the anchor points (TE#1 and 2) do not undergo displacements due to squatting during excavation of the second tunnel. This assumption has been established as valid based on the optical survey monitoring, which indicated lateral displacements at the point furthest from the pillar of less than 1 mm.

Using the above, the displacements measured with the vibrating wire strain gauges along the tunnel springline may be calculated from

Equation 6.1.

$$u_r = \frac{\partial u_\theta}{\partial \theta} - \frac{\varepsilon_\theta}{r}$$

Equation 6.1

where

u_r is the radial displacement;

$\partial u_\theta/\partial\theta$ is the tangential displacement with respect to the change in angle; and

ε_θ/r is the change in tangential strain with respect to the initial tunnel radius.

The comparison of the two measurement methods within the glacial till only is shown below in Figure 6.43.

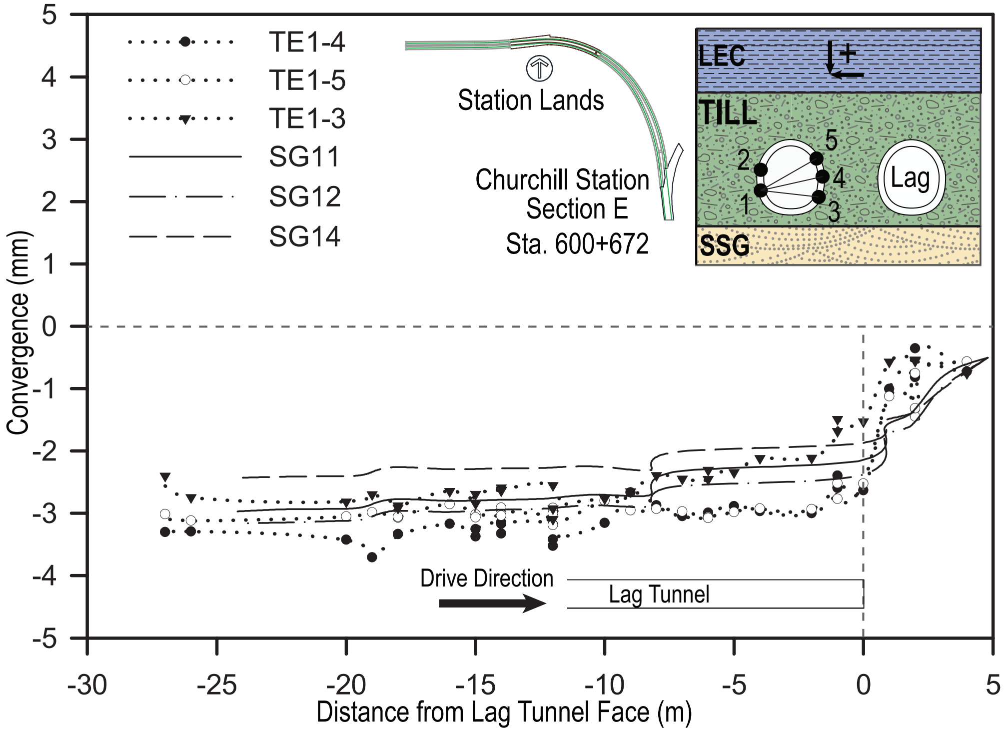

Figure 6.43. Comparison of tape extensometer measurements with liner strain gauge measurements

Figure 6.43 shows that the displacements measured from within the tunnel liner closely match those measured with the tape extensometer. It should be noted that the strain gauge measurements were taken as the average of at least five points during advancement of the lag tunnel.

6.4.3.2 Mixed Face Conditions

The displacements measured at the mixed face monitoring section (Sta. 700+412.7) are shown below in Figure 6.44.

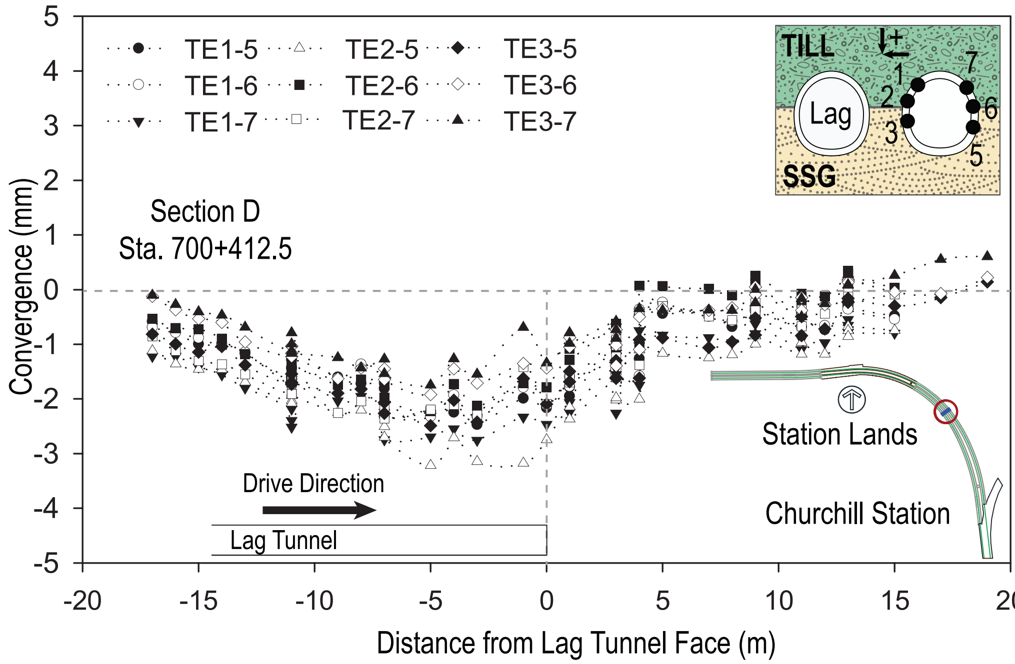

Figure 6.44. Results of mixed face tape extensometer measurements

The point TE#4 was damaged during the monitoring and the data is not shown here as a result. The displacements measured in the lead tunnel within the mixed face soil conditions show an unexpected trend. Prior to the lag tunnel reaching the monitoring points, the lead tunnel liner undergoes minor squatting and an increase in the horizontal diameter of approximately 2 mm. However, when the lag tunnel face is approximately 1.5D beyond the monitoring section, the displacements tend to approach zero. A possible reason for this trend is that as the lag tunnel approaches, the stress paths at the springline result in an increase in vertical stress. Since there is no increase in the horizontal stress, the tunnel squats and the width increases. This stress path clearly would result in increased shear stresses within the pillar similar to a UC test (σ_1 increases and σ_3 is zero). If the increased shear stress exceeds the yield surface of the Empress Sand, this would result in dilation and an increase in volume within the pillar. This volume increase may be sufficient to push the liner back to near equilibrium.

Like at Section E, the strain gauges indicate an increase in widening of the tunnel diameter similar to that of the tape extensometer. However, the decrease in the tunnel diameter following the passage of the lag tunnel does not occur immediately in the strain gauges. The strain gauges only indicate a decrease in the tunnel diameter at a distance from the lag tunnel face of approximately 30 m. Even then, the measured decrease is minimal and on the sub-millimeter range. The strain gauges also agree with the tape extensometer in that the displacements measured in the instruments within the sand show a widening approximately 1 to 2 mm greater than that of the glacial till. The comparison of the tape extensometer measurements with the strain gauge measurements is shown below in Figure 6.45.

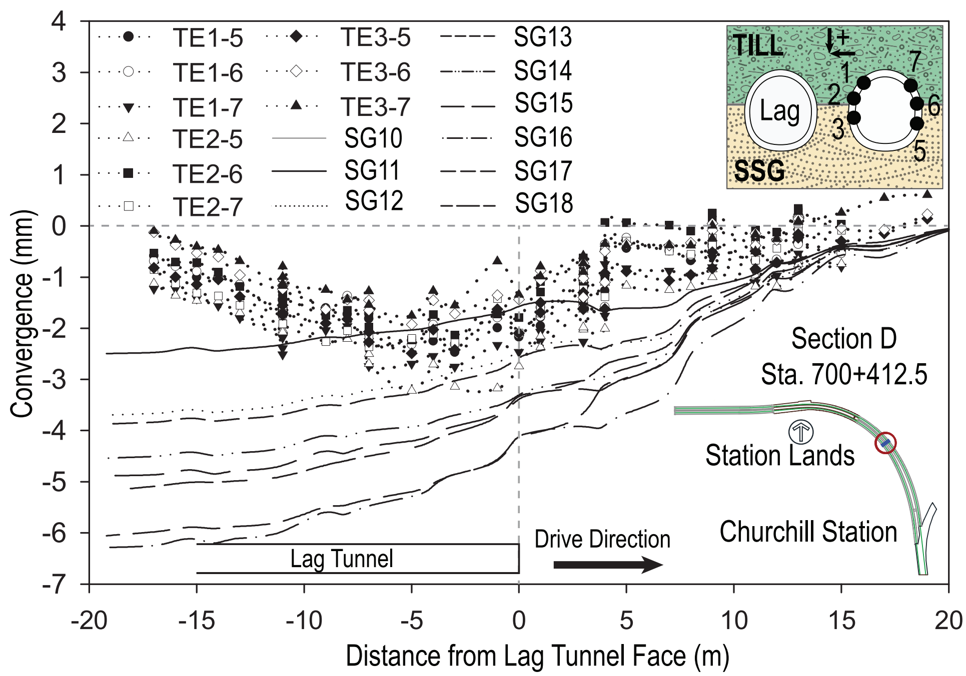

Figure 6.45. Comparison of tape extensometer measurements with liner strain gauge measurements within mixed face conditions

6.4.4 In-Ground Monitoring

6.4.4.1 Deep and Shallow Settlement – Western Alignment (Improved Soil and Glacial Till)

Of all of the monitoring methods employed, the use of the deep and shallow settlement rods was the most reliable. Because an independent, registered land surveyor monitored the points, the measurements were consistent throughout the project. Monitoring of each point commenced when either the lead or lag tunnel face was within 20 m of the point and continued until steady state conditions were observed. This provided detailed information regarding the settlement profile ahead of the tunnel face as well as on the settlement trough where a cross section was present.

The measured settlement varied based on the location of the tunnel. For much of the first leg of the tunnel, specifically the Western Northbound (lead) tunnel, the settlements were higher than those recorded elsewhere. The remainder of the settlements were generally consistent until the final breakthrough into Churchill Station. In the first leg of the tunnel, the depth to the crown varied from 0.85 m at the MacEwan Portal to around 12 m at the Epcor West Headwall. When the tunnel crown was within the improved soil, the shallow settlements above the tunnel crown were small and varied from 7.1 to 12.1 mm but were typically around 10 mm. Approximately 40 to 50% of the total settlements would occur prior to excavation of the face, which is typical for SEM tunnel construction. Figure 6.46 and Figure 6.47 illustrate the settlement profiles above the lead (Northbound) and lag (Southbound) tunnels respectively through the improved soil. In order to keep the data meaningful, the abscissa has been set to correspond with either the lead or lag tunnel face depending the monitoring point position along the alignment.

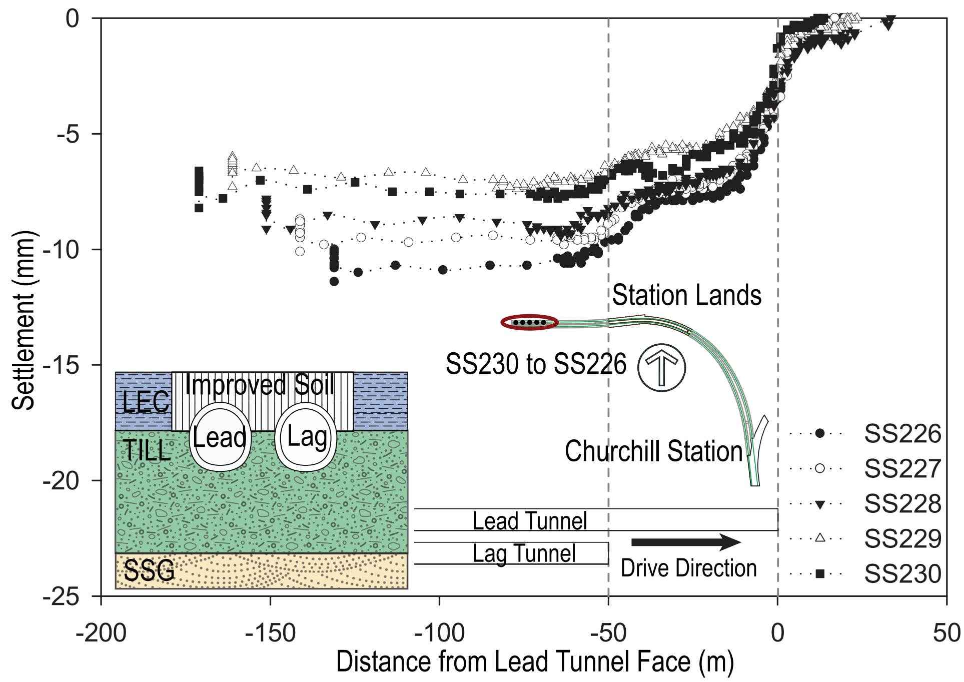

Figure 6.46. Shallow settlement in improved soil (Northbound tunnel)

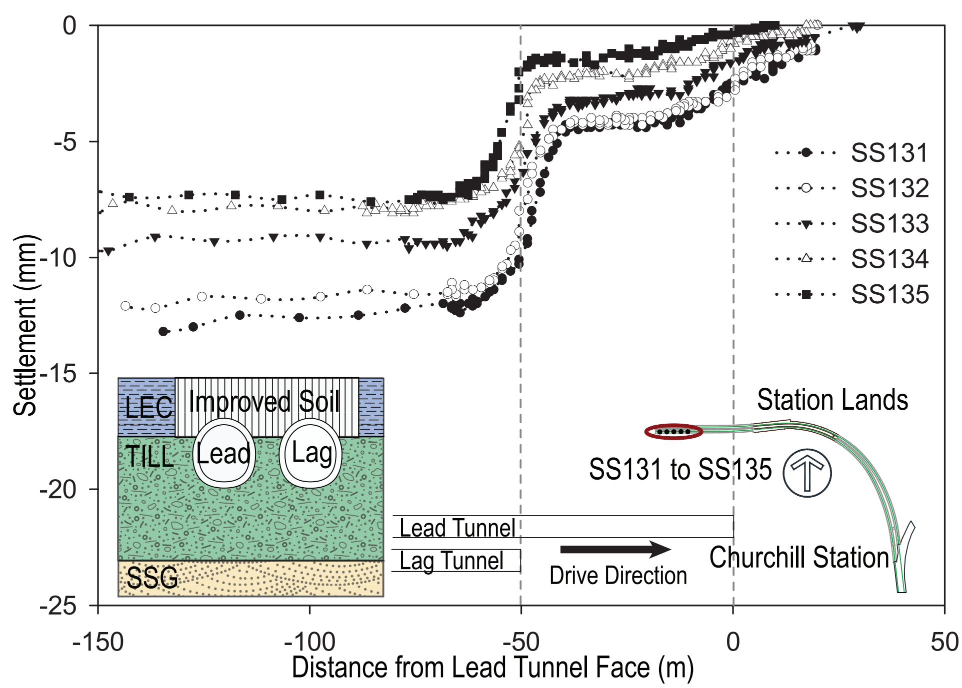

Figure 6.47. Shallow settlement in improved soil (Southbound tunnel)

The interaction between the two tunnels was quite low despite the pillar width of 0.23D as the settlement resulting from the construction of the second tunnel was typically only around 2 mm or roughly 20% of the total settlement. This is likely due to the high cementation of the improved soil, which resulted in 28-day UCS strengths greater than 2 MPa.

As the tunnels moved deeper and were wholly within the glacial till, the settlements increased considerably. This was mainly due to time lapses greater than 3 to 4 hours prior to the application of the shotcrete liner. These trends continued until near the breakthrough into the Epcor West Headwall for the lead tunnel and approximately half of the western alignment for the lag tunnel. The settlements in this section varied from 12.1 to 21.4 mm though were typically around 15 mm. Typical lead and lag tunnel settlement profiles are shown below in Figure 6.48 and Figure 6.49.

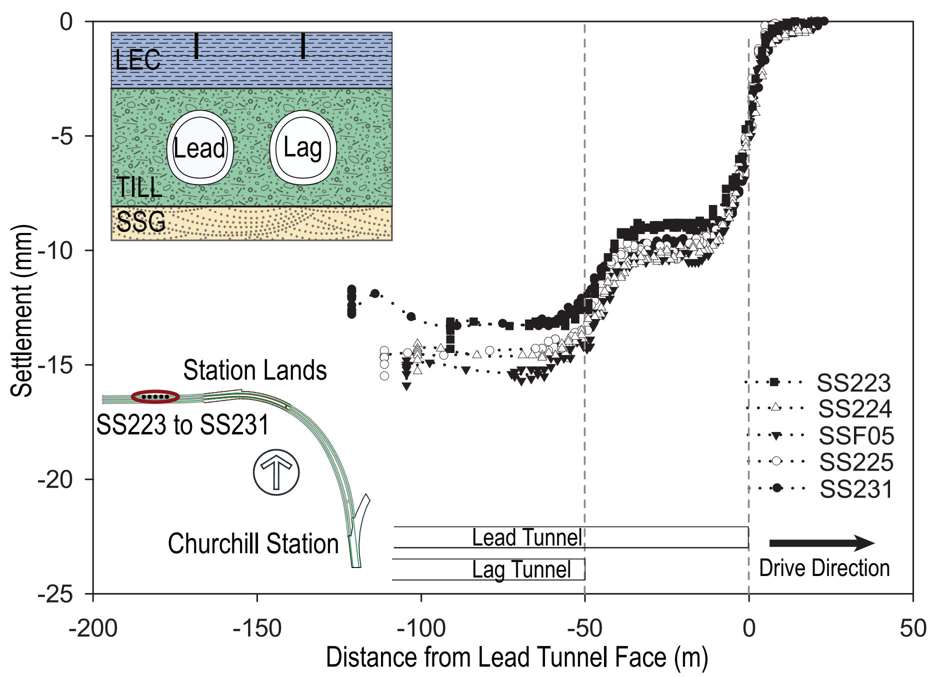

Figure 6.48. Shallow settlement above western leg lead tunnel crown (glacial till)

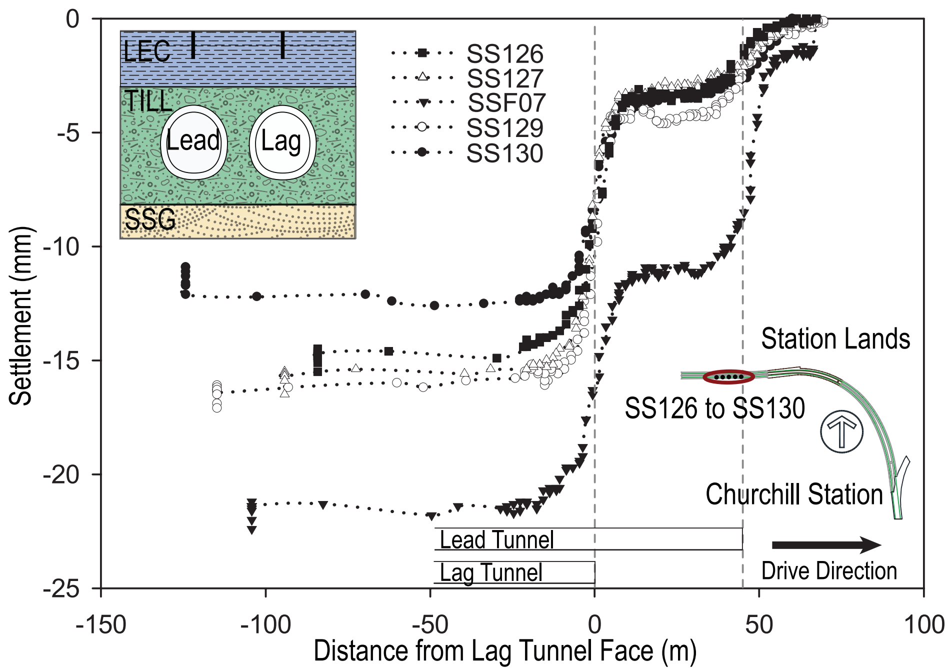

Figure 6.49. Shallow settlement above western leg lag tunnel crown (glacial till)

Like the improved soil section, approximately 50% of the total settlements for one tunnel occurred prior to the tunnel face reaching the monitoring point. When the lead tunnel was constructed, the settlement rods above the lag tunnel settled approximately 3 mm while an additional 4 to 5 mm of settlement occurred above the lead tunnel following construction of the lag tunnel. At Section F however, the interactions were abnormally high with the lead tunnel resulting in 11 mm of settlement above the unconstructed lag tunnel. Following construction of the lag tunnel, the monitoring points above the lead tunnel settled an additional 4.5 mm. These elevated settlements were likely due to continual problems with the installation of support needed to arrest displacements in a short time. This ultimately would have permitted considerable displacements to occur prior to the initialization of the shotcrete liner.

When the deep settlement in this leg of the tunnel is considered, it was found that there was little difference between the measurements recorded at the ground surface and those measured at a depth of 2 m above the tunnel crown. Typical settlement curves measured at the deep settlement rods located above the centreline of the lead and lag tunnels are shown below in Figure 6.50 and Figure 6.51 respectively.

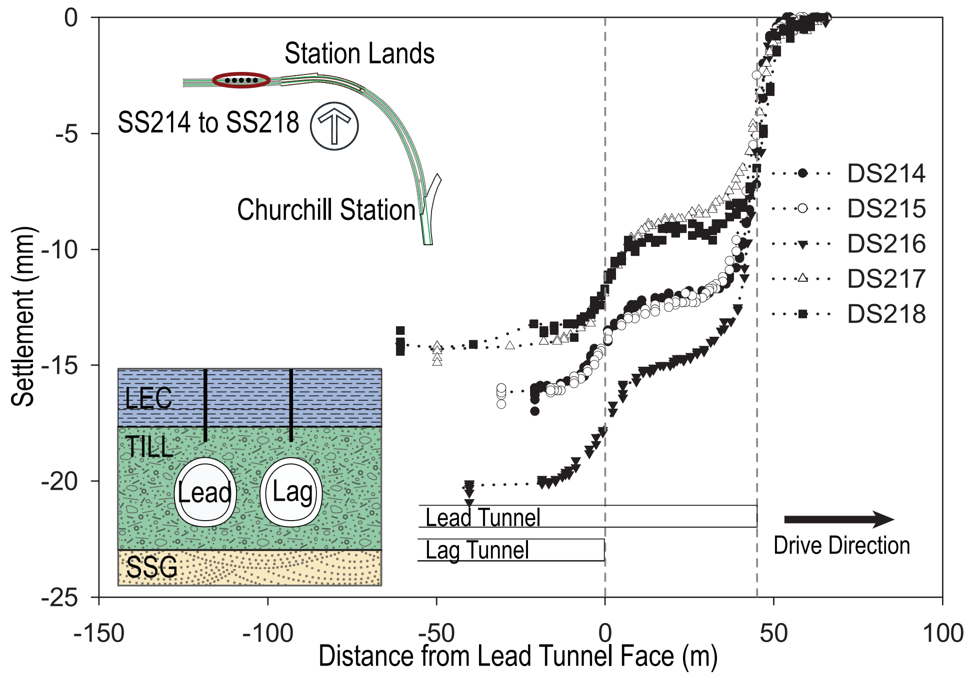

Figure 6.50. Deep settlement above the lead tunnel along western alignment

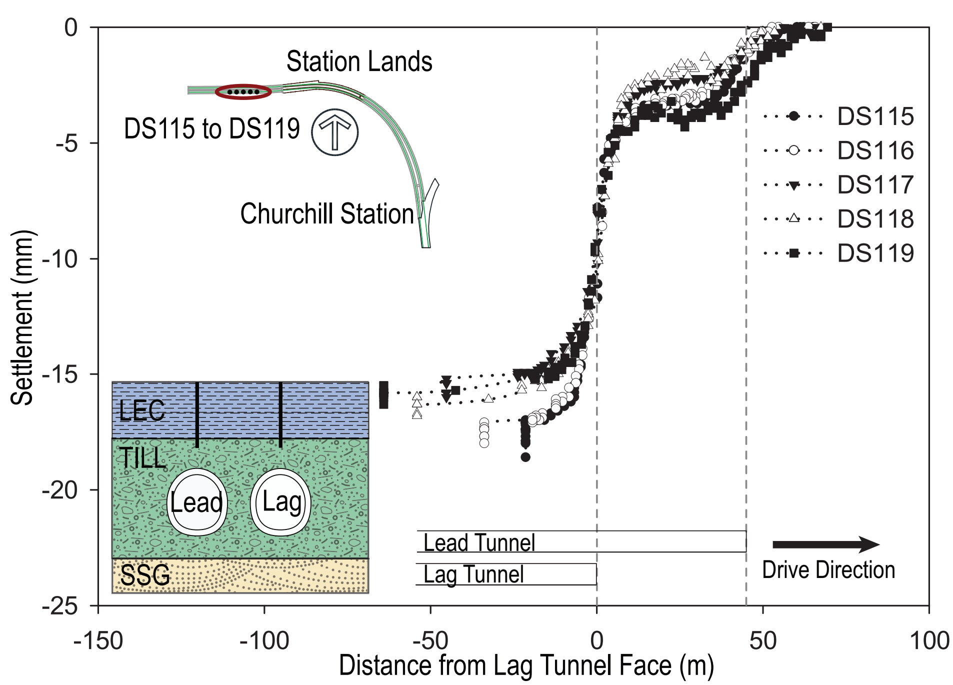

Figure 6.51. Deep settlement above the lag tunnel along western alignment

The settlements measured in the deep points ranged from 13. 4 to 19.8 mm but were typically around 16 mm. When compared to the total settlements measured in the shallow instruments in the same location, there is only a difference of around 2 mm. This suggests that the settlements were chimney like and the ground mass collapsed into the tunnel cavity mostly as a whole. If plastic deformations occurred, it is possible that translation mainly occurred along the pre-existing discontinuities (fissures). If this were the mechanism responsible for the formation of the chimney like settlements, it would be expected that there would not be significant impact outside the tunnel alignment. This is because the joints would provide a boundary and ultimately limit the zone of influence.

Observation of the two settlement monitoring cross sections confirm that the settlements were generally confined to less than one tunnel diameter outside the tunnel springline. Figure 6.52 and Figure 6.53 shows the deep and shallow settlement profiles respectively measured at Sections E and F.

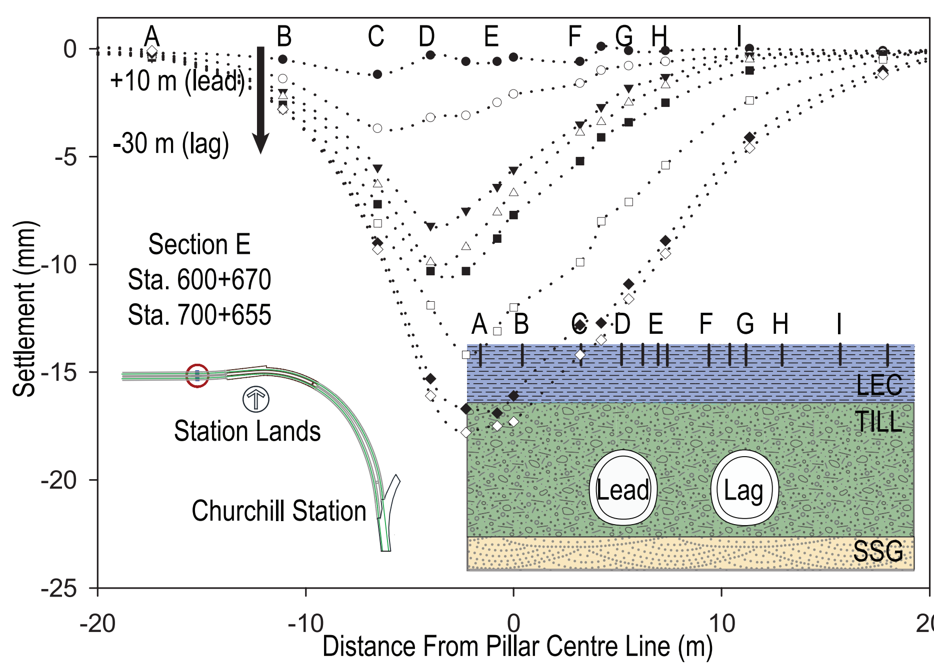

Figure 6.52. Shallow settlement trough at Section E (glacial till)

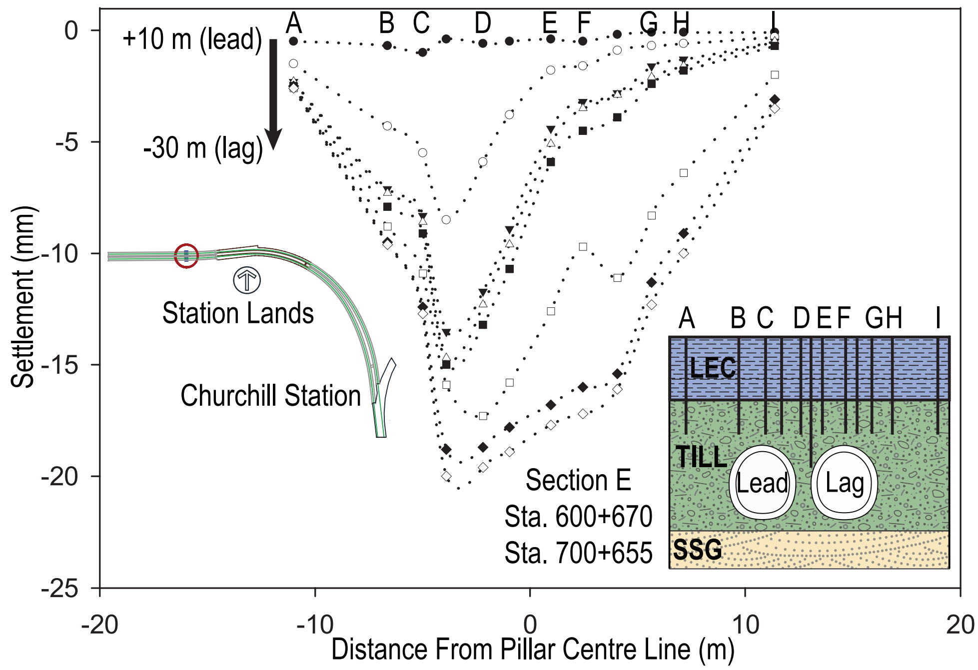

Figure 6.53. Deep settlement trough at Section E (glacial till)

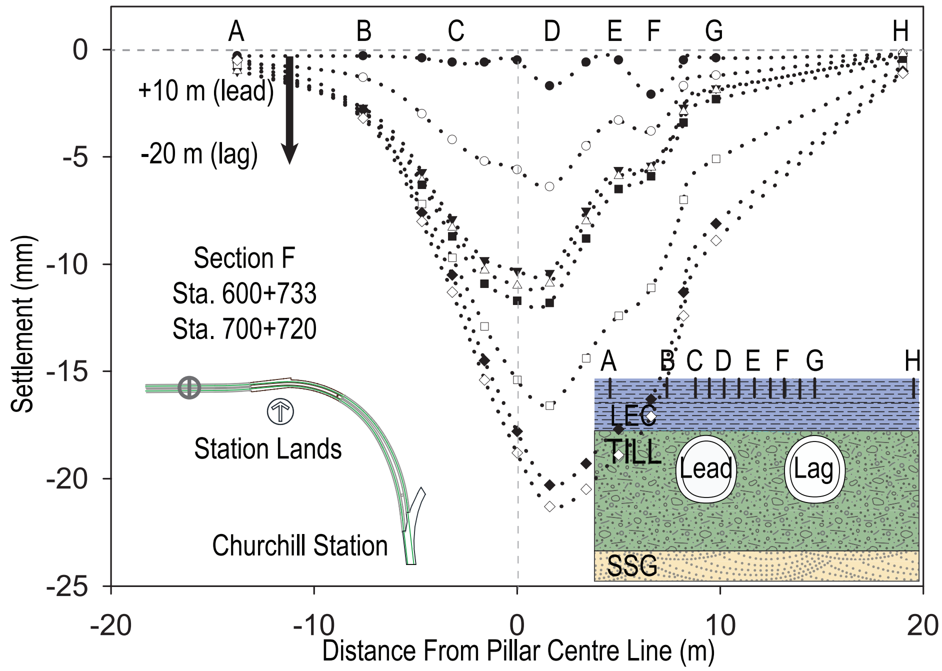

Figure 6.54 Settlement profile at Section F (glacial till)

The settlement profiles clearly show that the settlements were minimal outside the tunnel alignment. At a distance of 10 m from the centreline or 5 m (0.76D) outside the lead tunnel alignment, the settlements at Section E in the shallow and deep settlement points are approximately 2.5 mm. This corresponds with a maximum trough slope of 0.28%. The difference between the two levels is less than 0.2 mm, which is approximately the error of the monitoring system. Outside the lag tunnel, the settlements are slightly greater and are 6.0 mm at the shallow point and 5.6 mm for the deep point at a distance of 5 m (0.76D) outside the tunnel cavity. At Section F, the settlements outside the tunnel alignment fall to less than 3 mm at a distance of 1.5 m from the tunnel springlines (lead and lag). At a distance of 10 m from the tunnel springlines, the settlements are less than 1 mm.

6.4.4.2 Deep and Shallow Settlement – Eastern Alignment (Mixed Face)

In the eastern leg of the tunnel, the Southbound tunnel was constructed as the lead tunnel. Surface points could not be used to monitoring the settlements over approximately 50 m due to the presence of an existing structure above the tunnels. This eliminated the deepest monitoring points and measurements associated with the tunnel face consisting mainly of Empress Sand. Figure 6.55 and Figure 6.56 show the settlement profiles for the lead tunnel shallow and deep monitoring points respectively, above the tunnel axis within the mixed face conditions.

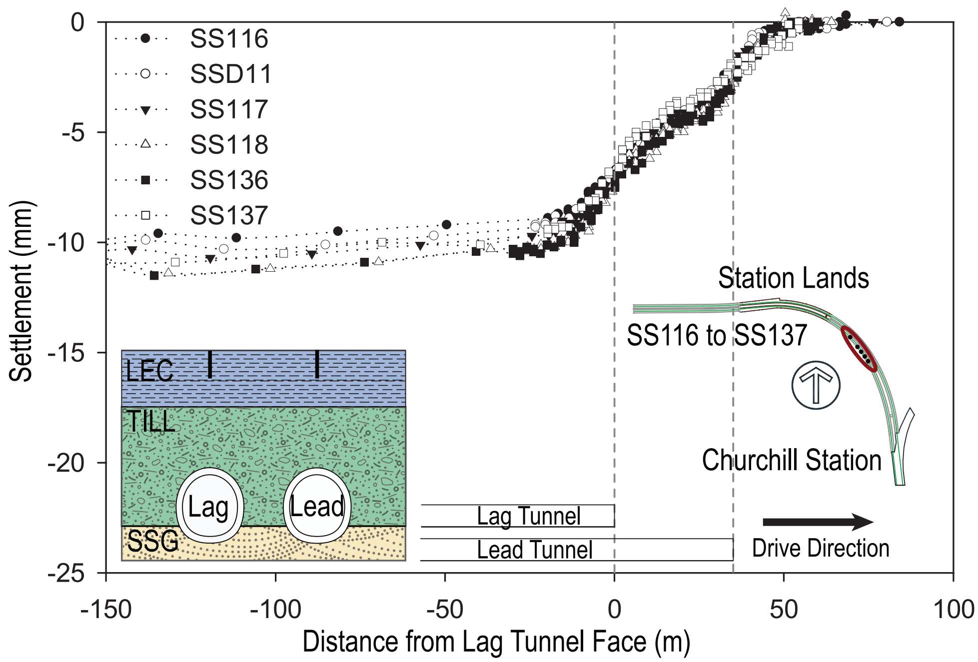

Figure 6.55. Shallow settlement above the lead tunnel in mixed face conditions

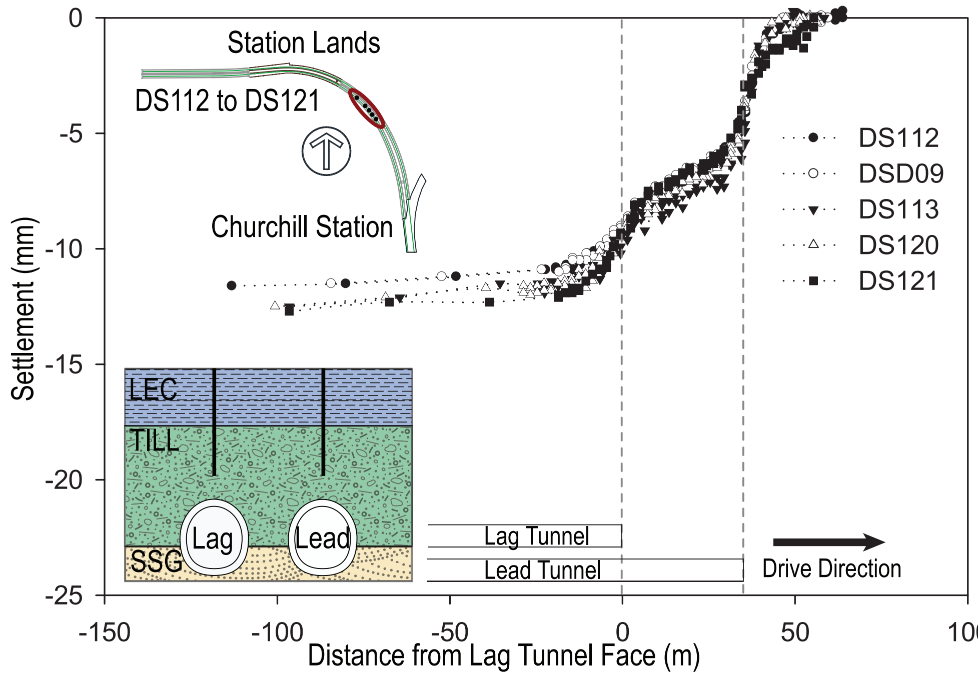

Figure 6.56. Deep settlement above the lead tunnel in mixed face conditions

The monitoring in this section indicates that typically the settlements were around 10 mm total with approximately 65% occurring due to the first tunnel alone. Of the total single tunnel settlements, around 50 to 60% occurred ahead of the tunnel face. Much like the settlements measured on the west side of the alignment, the settlements were nearly uniform with depth suggesting chimney like displacements. Considering that the separation between the base of the deep and shallow points is between 10 to 11 m, settlements of this nature are uncommon for a cohesive soil. The difference between the deep and shallow settlements at any given point is around 1.5 mm. Unlike in the western leg however, the chimney settlements were not solely confined to the tunnel alignments. It was expected due to the depth of the tunnels through this section, that the settlement trough would extend well beyond the tunnel alignment.

It should be noted that due to an obstruction at the ground surface, Section D was staggered, and the cross section above the lead tunnel was approximately 35 m down chainage from the lag tunnel. The shallow and deep settlement troughs measured at Section D are shown below in Figure 6.57 and Figure 6.58.

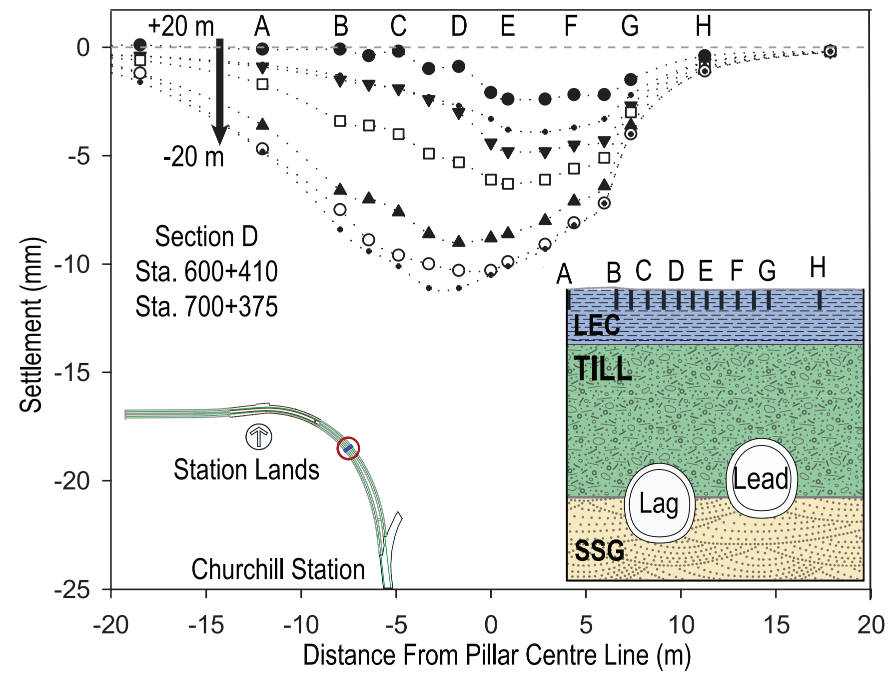

Figure 6.57. Shallow settlement trough at Section D (mixed face)

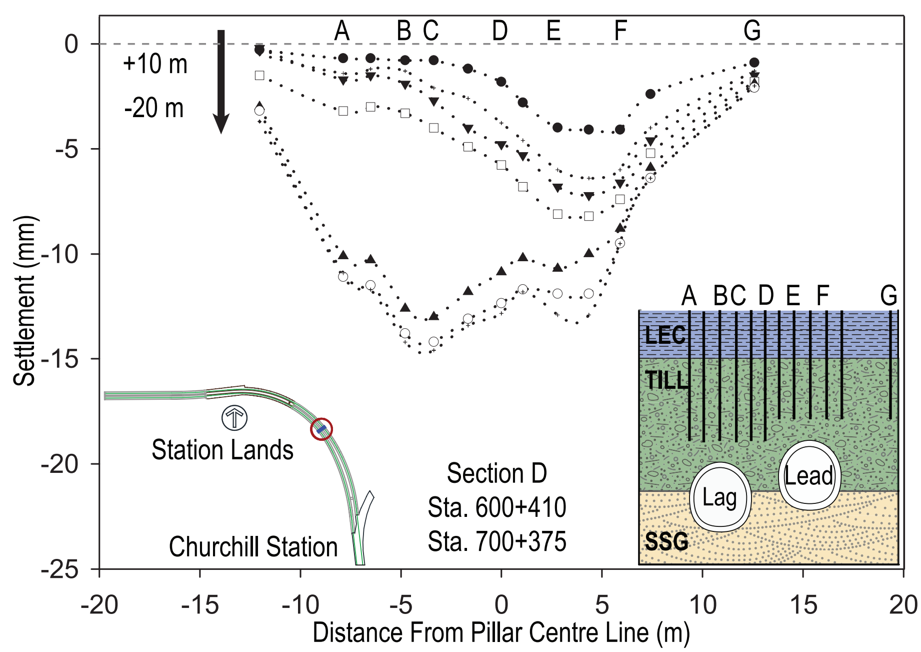

Figure 6.58. Deep settlement trough at Section D (mixed face)

The settlement trough in the shallower location (lead Southbound tunnel) resembles the troughs measured on the west side of the alignment in that the slope of the trough is very steep at a maximum of 0.24%. The surface settlement at this section is less than 5 mm just outside of the tunnel envelope or above the tunnel springline. When compared to the deeper section (lag Northbound tunnel), the slope of the trough is a maximum of 0.09%; while the surface settlements remain greater than 5 mm at a distance of 2.5 m outside of the tunnel alignment.

6.4.4.3 Deep and Shallow Settlement – Eastern Alignment (Glacial Till)

To demonstrate the influence of the pillar width, the results of Section C will be briefly discussed. The pillar width through Section C was approximately 5 m (0.76D). This afforded comparisons between Section C and E as the two cross sections were at similar depths (~10.5 m below the ground surface) and the pillar width at Section C was roughly three times that of Section E. Typical shallow and deep settlement profiles are shown below in Figure 6.59 and Figure 6.60.

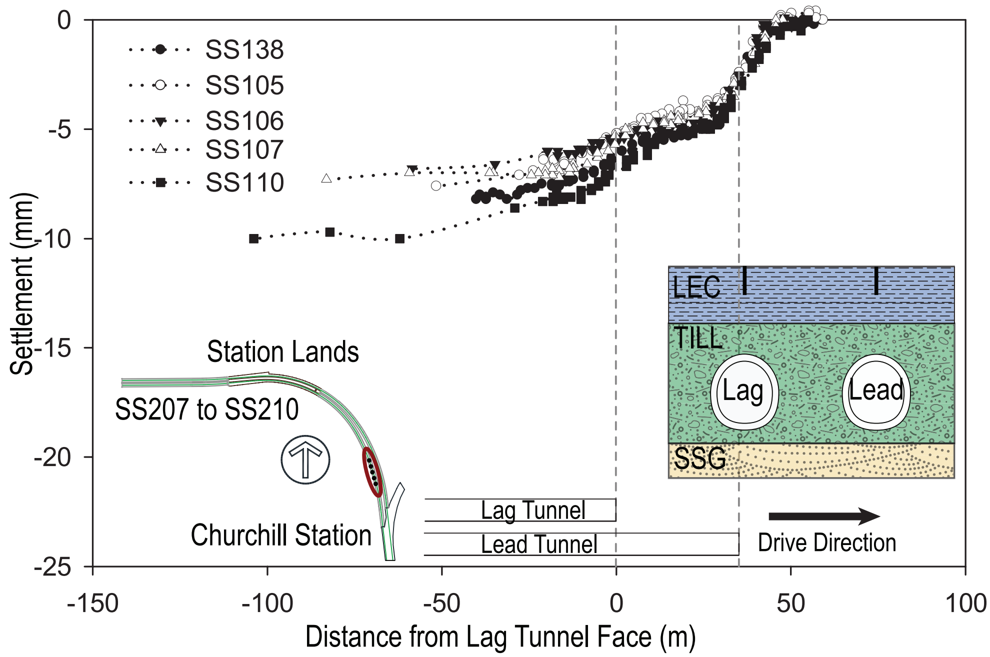

Figure 6.59. Shallow settlement over lead tunnel crown of eastern leg (glacial till)

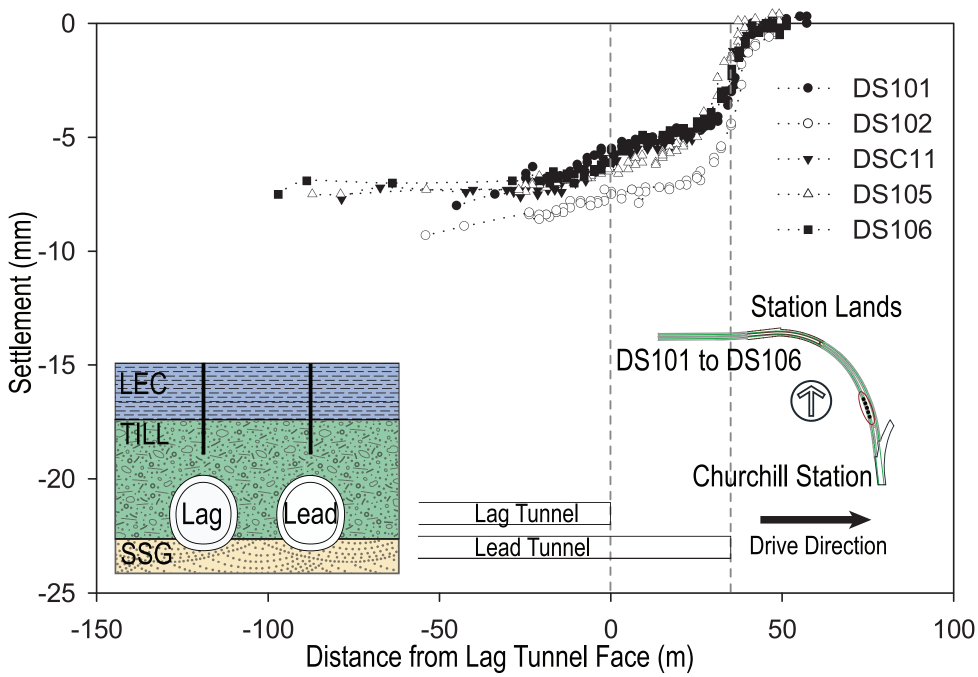

Figure 6.60. Deep settlement over lead tunnel crown of eastern leg (glacial till)

All things but the pillar width being considered equal, it is expected that the settlement profiles would be less at Section C when compared to those measured at Section E. When typical settlement profiles are compared, the settlements in the east

(Section C) are approximately 50% of those measured along the western leg (Section E). At Section C, typical settlements are around 7 to 10 mm. When compared to Section E where the settlements were around 15 to 20 mm, this indicates that the pillar width strongly influences the settlement profiles.

As with the other sections, it would also appear that the settlement is nearly uniform throughout the depth of the overburden. Settlements of around 7 mm were recorded in both the deep and shallow points above the crown through Section C. The maximum slope of the settlement trough occurs immediately outside the Northbound (lag) tunnel and is approximately 0.2%. This is slightly less than those measured elsewhere.

The settlement trough at the ground surface was gentle and extended across the entire monitoring section. This is in contrast to the previously narrow and steep troughs encountered previously. The shallow and deep settlement troughs are shown in Figure 6.61 and Figure 6.62 below. From the shallow settlement trough, it is clear that the settlements extend across the entire cross section but are minor in terms of the overall magnitude and slope.

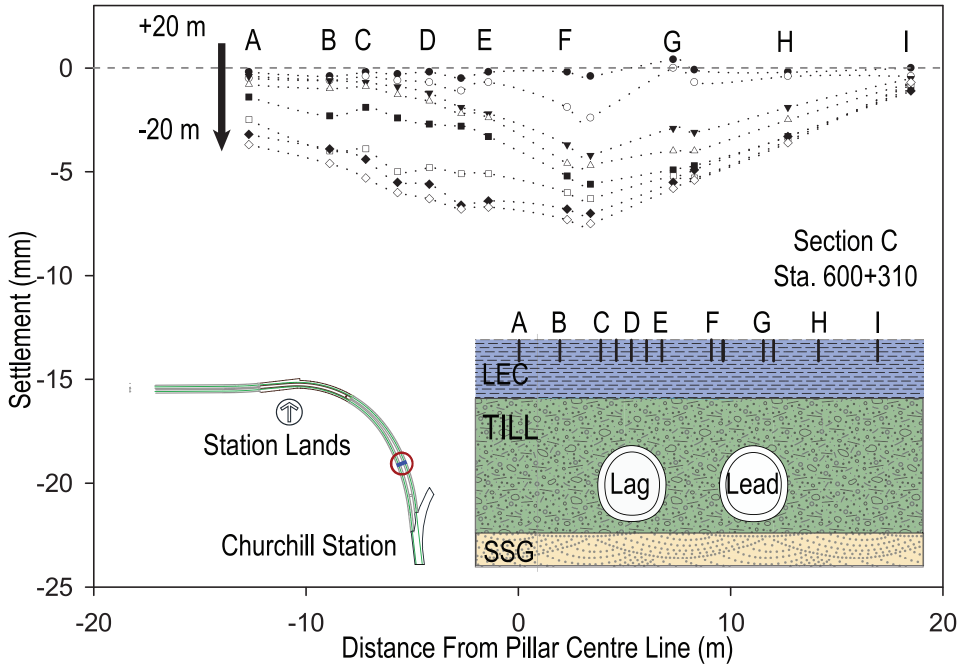

Figure 6.61. Shallow settlement trough at Section C (glacial till)

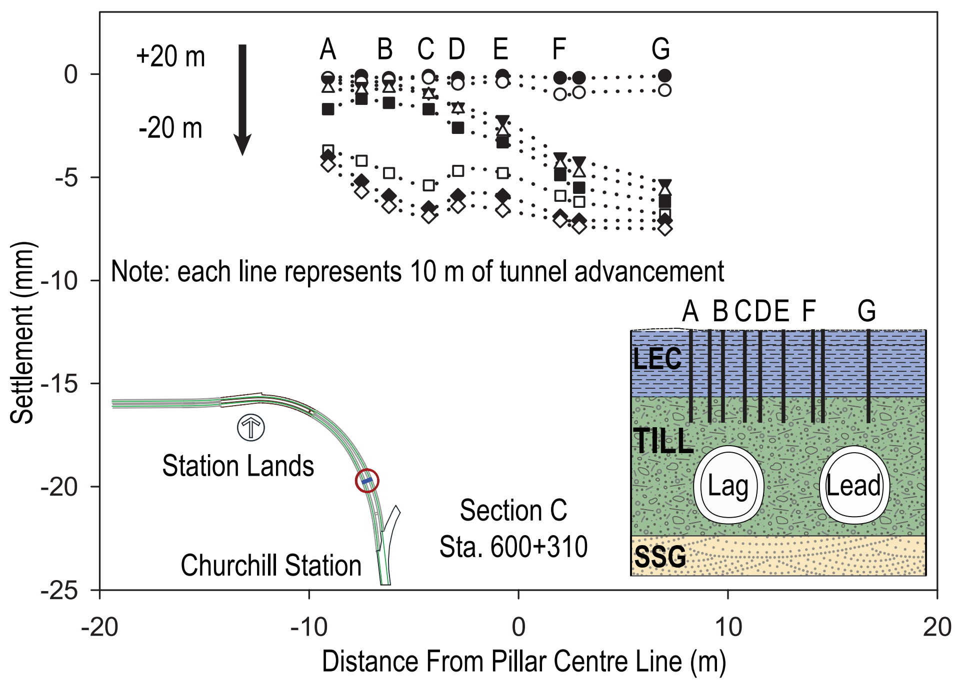

Figure 6.62. Deep settlement trough at Section C (glacial till)

6.4.5 Multi-Point Extensometers

Multi-point extensometers were used at two locations along the alignment to monitor the settlement at several depths throughout the overburden. The extensometers were located within the pillar of the two monitoring cross sections located on either side of the Station Lands Cavity (Sections D and E). Each extensometer possessed six monitoring points and one anchor located well below the tunnel invert.

From the onset, the extensometers presented difficulties for the instrumentation consultant as they were unsure how best to monitor them or how to establish a baseline measurement. A proper baseline measurement required the precise survey of the extensometer head as well as initial readings of the extensometer location. The regular measurement of the extensometer head elevation is critical, as the head will settle with the ground surface due to tunnelling activities. Provided the anchor rod is not installed between the anchor and the head, as was the case for the multi-point extensometer installed at Section E, the movement of the points was measured relative to the head. Therefore head settlements would strongly influence the recorded results. Unfortunately the consultant only measured the initial extensometer locations and not the head for a portion of the monitoring period. This meant that the head could settle and the subsequent extensometer readings would be a function of the point and the head movement. It wasn‘t until the extensometer points appeared to be moving up; a result of the head settling more than the extensometer point, that the consultant requested a daily survey of the extensometer heads. Corrections were applied to the monitoring data based on the surface settlement values as it became available. The results of the corrected multi-point extensometer monitoring at Sections E (glacial till) and Section D (mixed face) are shown below in Figure 6.63 and Figure 6.64.

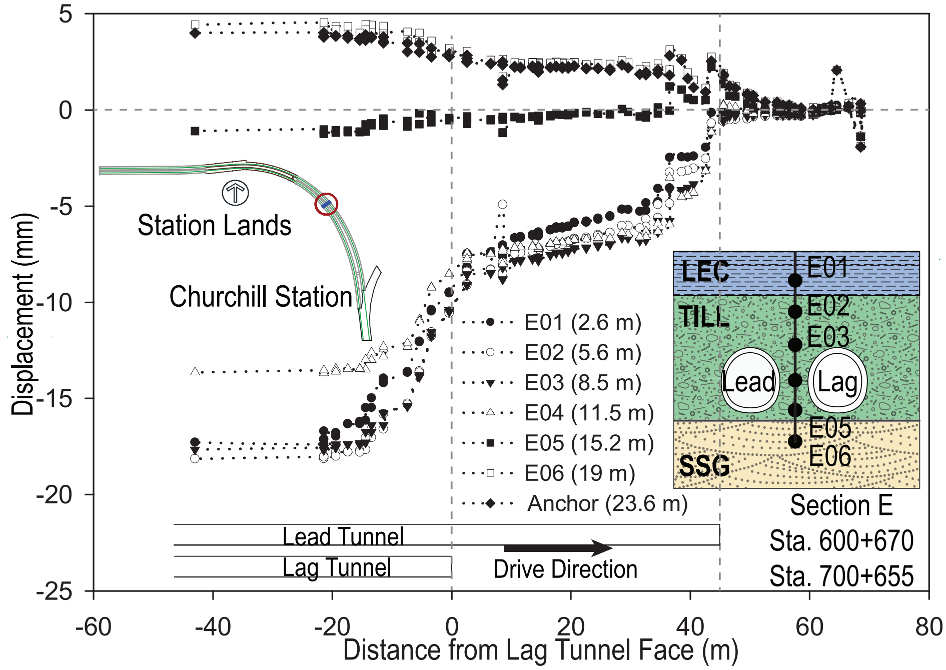

Figure 6.63. Multi-point extensometer settlement at Section E (glacial till)

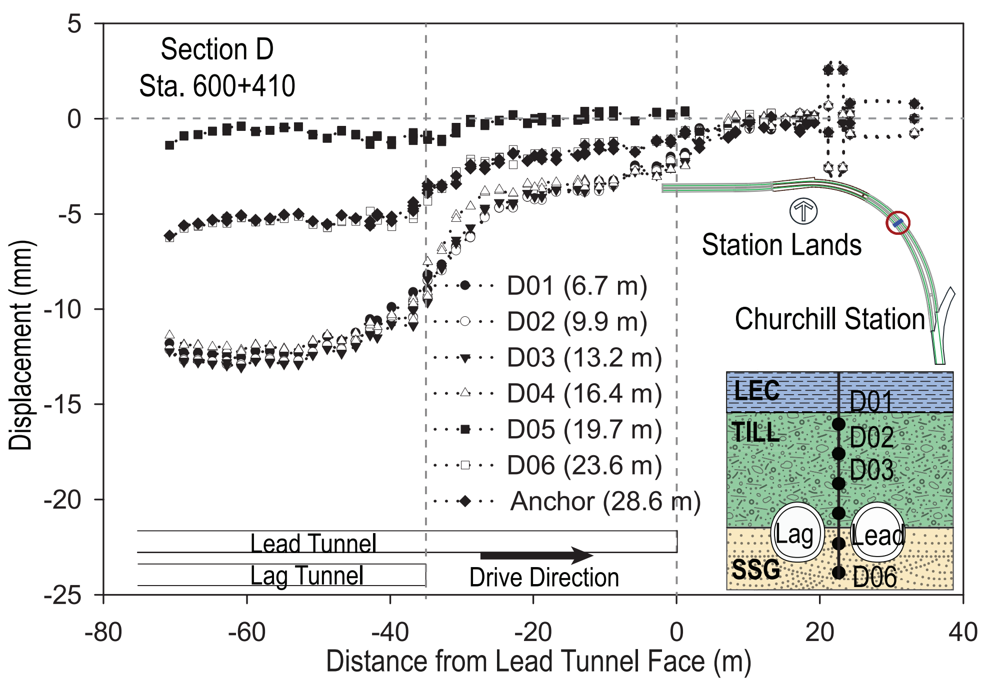

Figure 6.64. Multi-point extensometer settlement at Section D (Mixed face)

The multi-point extensometers indicate that the points located above the crown settled in a uniform fashion. Nearly all of the points above the tunnel crowns respectively settled around 17 and 12.5 mm at Sections D and E respectively. These values agree well with the findings of the surface and deep settlement monitoring at each location. Of interest is the amount of elastic rebound that occurs in the points installed below the tunnel springline at Section E. The upward movement at Section E is nearly equal at 2 mm/tunnel following the excavation of each tunnel.

At Section D, all points, including the anchor settled. This suggests that there is an increase in effective stress even at a depth below the springline of the tunnel. This is partially due to the increase in vertical stress through the pillar and the recompression of the sand following the lag tunnel excavation.

6.4.6 Lateral Displacement Monitoring

Lateral displacements were monitored throughout construction near to each tunnel springline and through the pillar at each monitoring cross section.

In two locations (Sections E and F), the inclinometers in the pillar were replaced with Shape Accel Arrays (SAAs) installed into the inclinometer casings. At Section E, the SAA was 20 m in length and extended well enough below the invert of the tunnels to consider it a fixed point. The SAA at Section F however was only 10 m in length and therefore the top of the chain was considered as fixed.

The lateral displacements will be presented in terms of the displacements at various distances from each tunnel face. The results of the lateral displacements measured in the pillar at Section E are shown below in Figure 6.65. It should be noted that the results were recorded with an SAA installed to 22 m below the ground surface.

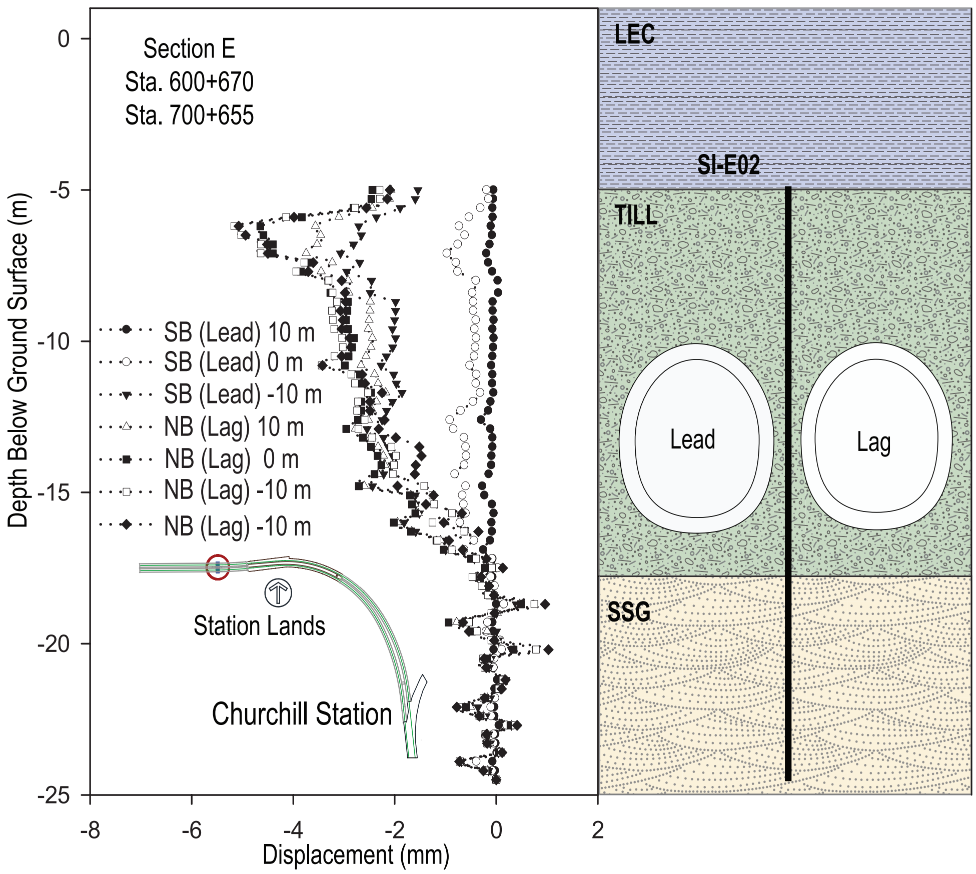

Figure 6.65. Lateral displacement of pillar at Section E (glacial till)

The lateral displacements adjacent to the lead (Northbound) tunnel recorded from the standard inclinometer are shown below in Figure 6.66.

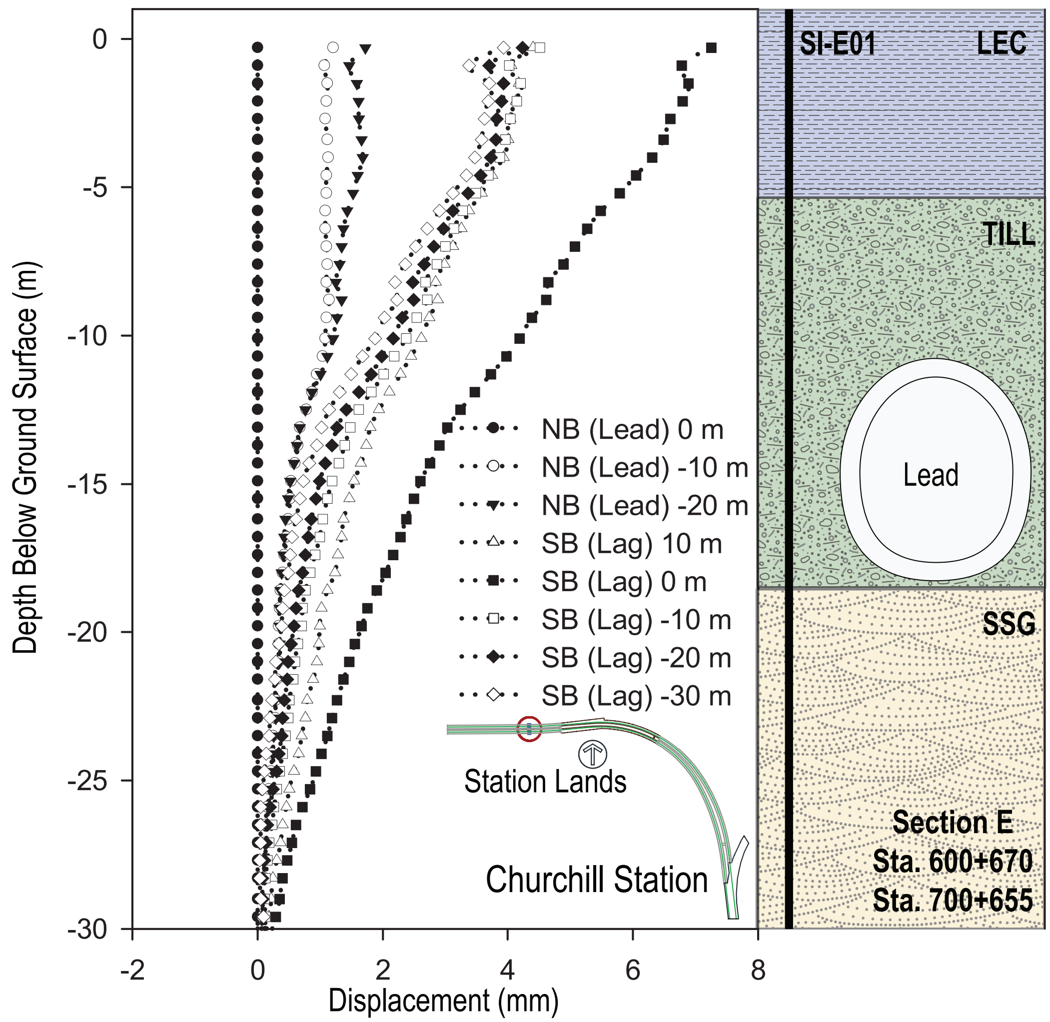

Figure 6.66. Lateral displacement outside of the lead tunnel at Section E (glacial till)

From the above figures it would appear that some form of plastic deformation is occurring within the till through Section E. Not all of the displacements in the pillar are recovered following excavation of the lag tunnel. It would therefore appear that some permanent, albeit minor, deformations have occurred. In all, approximately 0.2 to 1.5 mm of rebound occurs from the maximum lateral deformation measured at the tunnel springline. This left approximately 3 mm of total deformation remaining following completion of the tunnels through this section. When the deformations of the inclinometer installed outside of the springline of the lead tunnel are examined, it would appear that some relaxation occurs at distance from the lag tunnel. The inclinometer appeared to rebound approximately 2 to 3 mm from the maximum value following completion of the tunnels through the monitoring section. The maximum displacement occurred when the lag tunnel was in line with the inclinometer. The relaxation was measured to a distance of 30 m behind the lag tunnel face where the displacements nearly returned to zero.

The results from the pillar and the inclinometer installed outside the lead tunnel springline at Section D are shown below as Figure 6.67 and Figure 6.68.

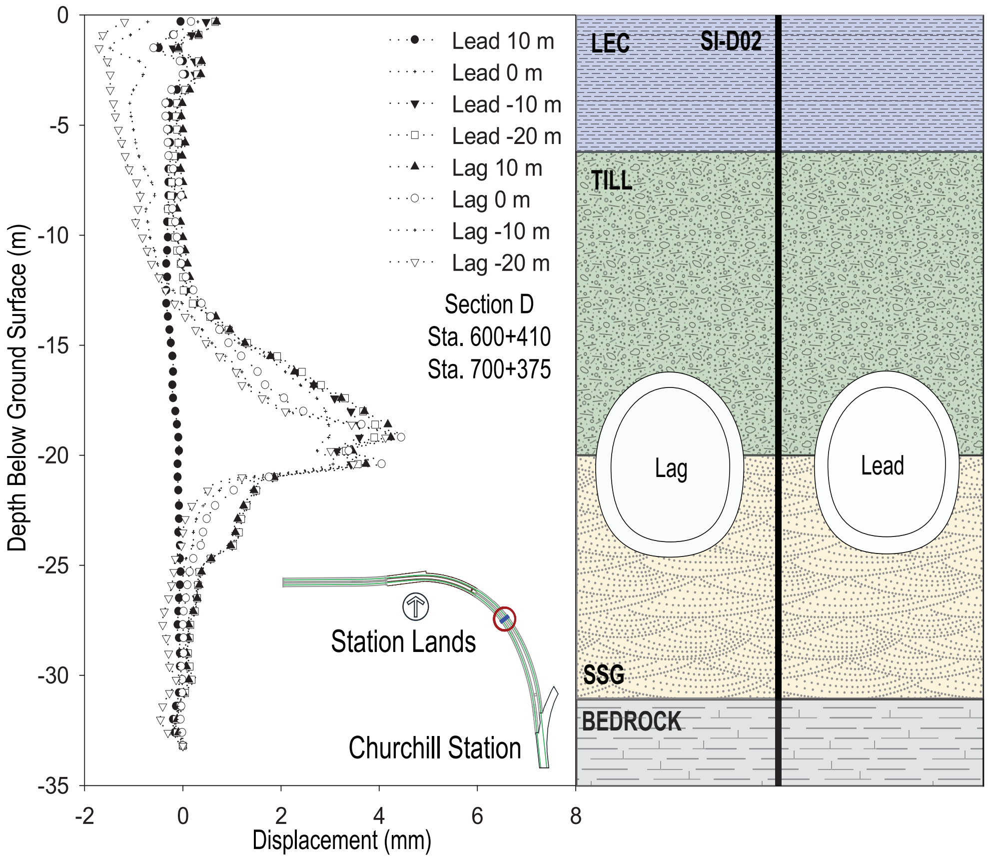

Figure 6.67. Lateral displacement of pillar at Section D (mixed face)

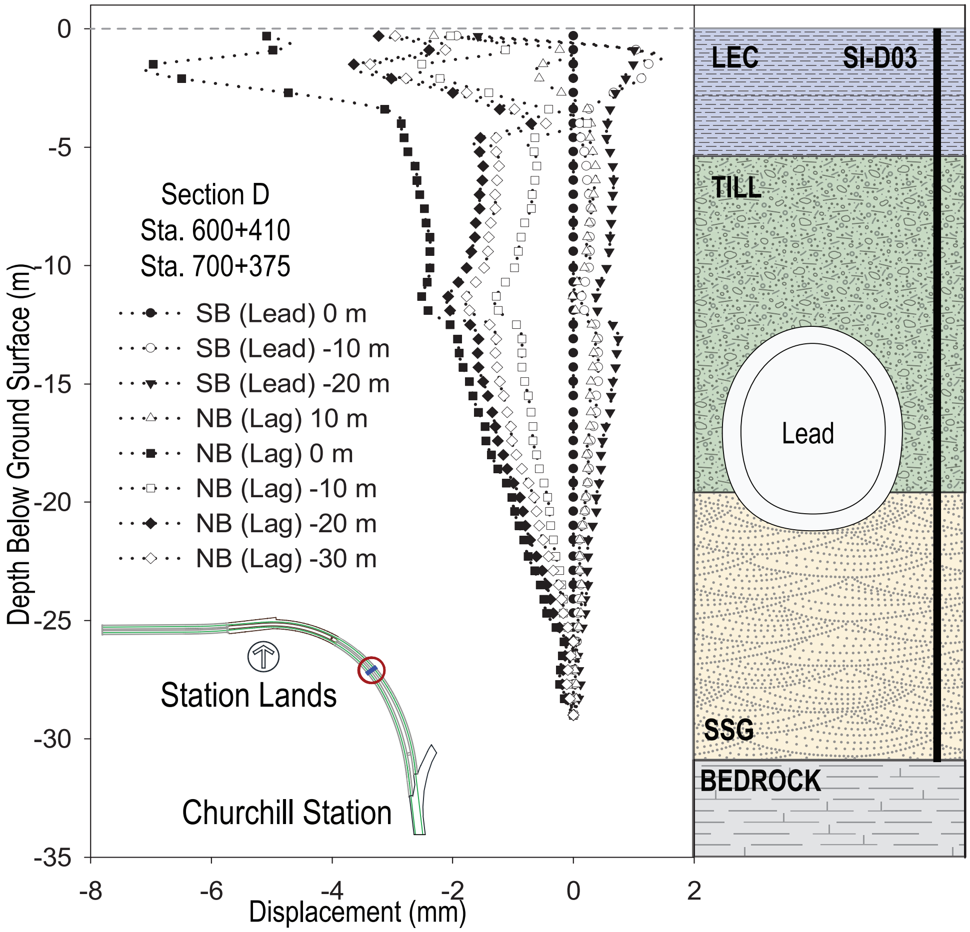

Figure 6.68. Lateral displacement outside of the lead tunnel at Section D (mixed face)

From the above figures, a trend similar to that of Section E can be observed. First within the pillar there appear to be some plastic deformations occurring through the tunnel cavity. Maximum lateral displacements occur at a depth of 19.2 m below the ground surface. This depth corresponds with the centre of the tunnel header and these displacements carry through to the top of the tunnel bench. The total maximum lateral displacements were measured to 4.5 mm and occur when the lag tunnel face is at the monitoring point. Following passage of the lag tunnel, the displacements relax approximately 0.5 to 1 mm. Therefore there is some minor relaxation that occurs as the inclinometer settles at a permanent lateral displacement of 4.1 mm. Above and below the tunnel cavity, the deformations, which occurred due to the passage of the lead tunnel, nearly recover and return to zero.

Based on the measurements within the pillar, it would appear that the materials immediately around the tunnel cavity undergo some form of permanent plastic deformation. When the shear strains measured in the inclinometers are examined, the presence of plastic deformations is better illustrated. The shear strains were measured in the inclinometers over a 1 m interval and through the face of the tunnel only. Measurement locations were selected such that one value was calculated for the header, another for the upper bench and another for the lower bench. Since the strains measured within the inclinometers nearly return to zero following the passage of the lag tunnel, it would appear that the ground performs elastically. Only in the locations where the inclinometer was located approximately 1 m from the tunnel cavity were permanent strains measured. Therefore the plastic radius likely does not exceed 1 m outside of the tunnel boundary in either the glacial till or the Empress Sand. Figure 6.69 shows the shear strains measured in SI D02 located in the pillar within the mixed face conditions.

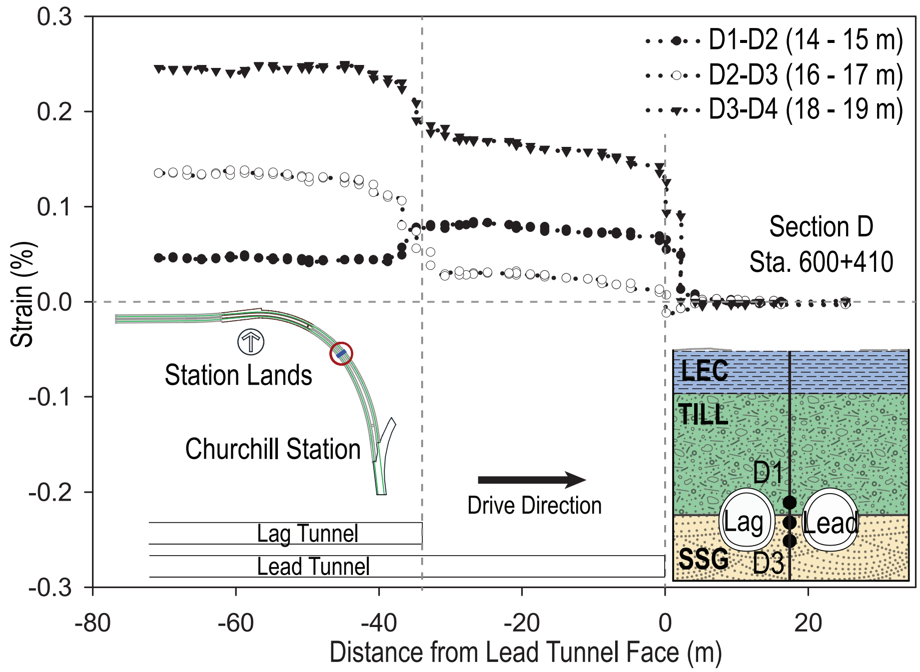

Figure 6.69. Shear strain measured in the pillar at Section D (mixed face)

The shear strains measured in the inclinometer installed within the pillar at Section D demonstrate that there are plastic deformations occurring near the crown and springline. Because the strains in the Empress Sand are in excess of the extension yield strains given as 0.2% in Chapter 4 it is assumed that yielding has occurred. The plasticity is further indicated by the permanent strains following passage of the lag tunnel. If the ground were responding as an elastic medium, symmetry would have caused the shear strains to return to zero. At the point in the crown, the strains appear to nearly return to zero suggesting elastic deformations. In the bench, approximately 65% of the strains occur following the construction of the first tunnel, while in the invert, the lead tunnel only accounts for about 15% of the total strain.

The strain rates have also been calculated and plotted in order to indicate when the majority of the strains occurred (header, bench or invert excavations). The strain rates for Section D are shown below in Figure 6.70.

Figure 6.70 indicates that the majority of strains occurred ahead of the lead tunnel face in the bench, and following construction of the lag tunnel in the lower bench. This suggests that the some form of plastic deformation had to occur for the sand to dilate and subsequently recompress. The dilation must be a result of shear failure otherwise, the displacements and strains would have returned to pre-construction values following the completion of the tunnel construction.

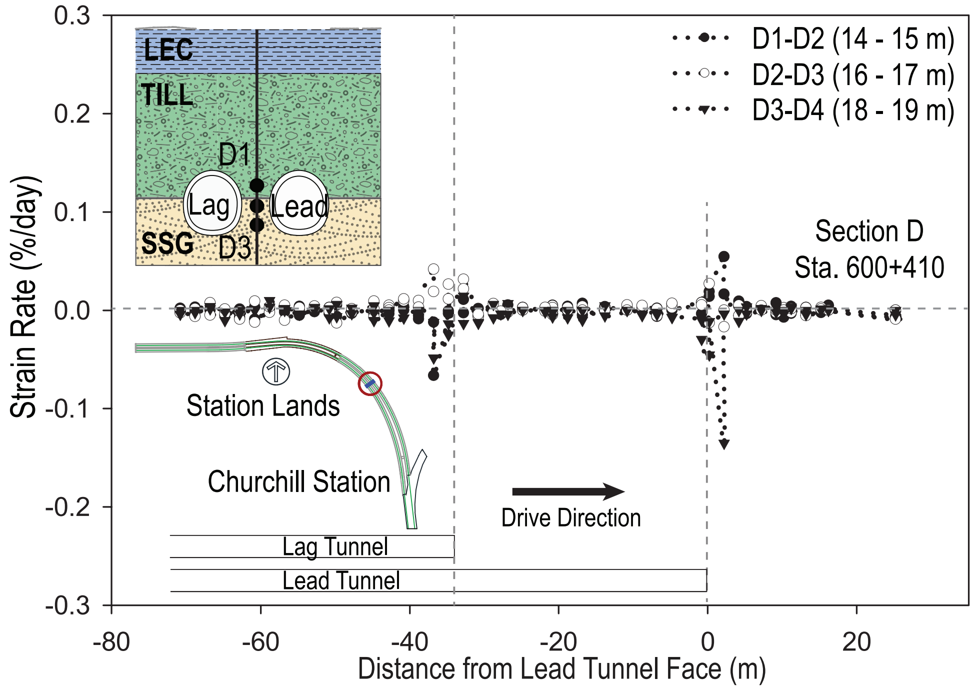

Figure 6.70. Strain rate calculated in the pillar at Section D (mixed face)

At Section C, the lateral displacements indicate nearly elastic behaviour as the displacements return to almost zero following passage of the lag tunnel. Figure 6.71 illustrates the displacements measured in the pillar. Clearly, the total displacements in the pillar are negligible as they are slightly greater than 0.3 mm following completion of the tunnels through this section. This final displacement is within the accuracy of the inclinometer probe.

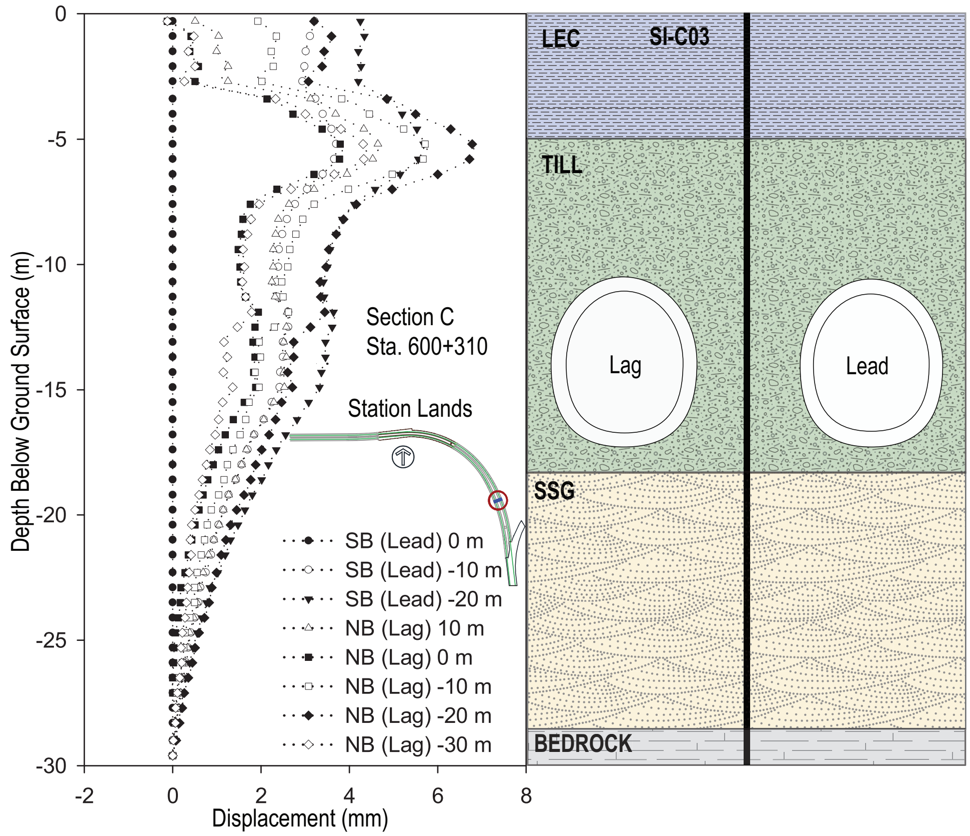

Figure 6.71. Lateral displacement of pillar at Section C (glacial till)

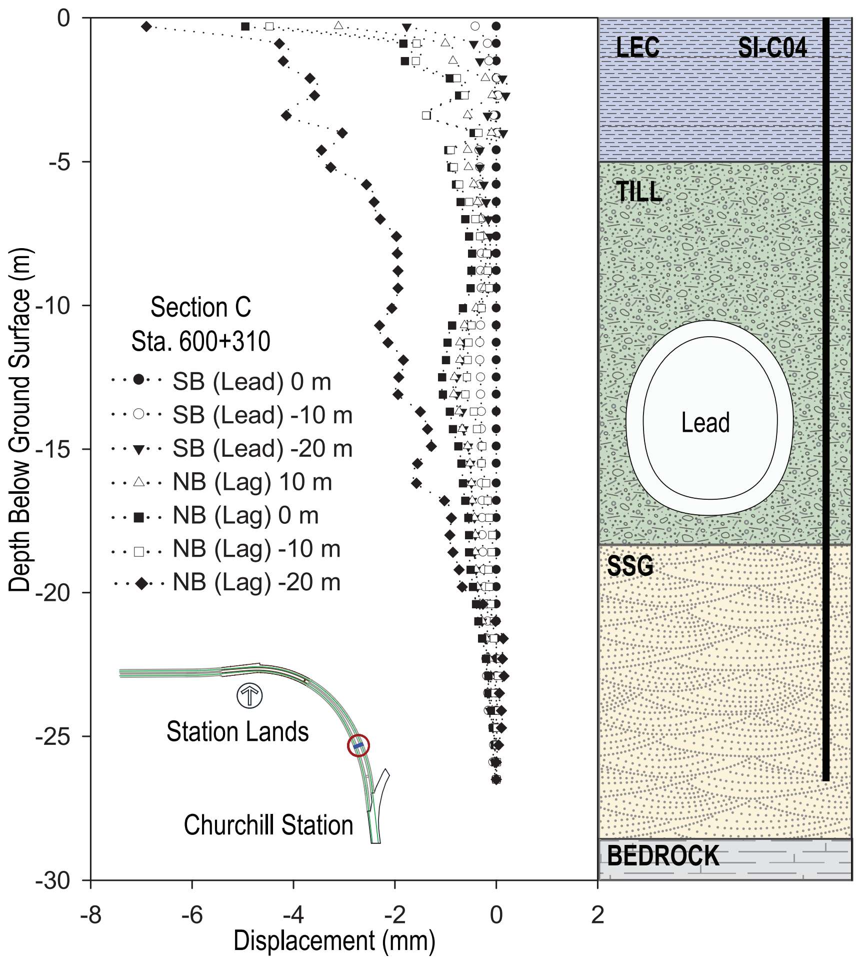

Figure 6.72. Lateral displacement outside of the lead tunnel at Section C (glacial till)

The displacements into the tunnel cavity during passage of the lead tunnel are approximately 1.5 to 2 mm while the displacements following the lag tunnel were on the order of 0.5 to 0.8 mm.

Like at Section D, the shear strains at Section C were assessed over 1 m increments through the tunnel face. The purpose was to shed light onto whether the tunnel construction within the glacial till and the added pillar width would minimize the plastic strains through the pillar. Figure 6.73 shows the shear strain profile with depth measured at Section C.

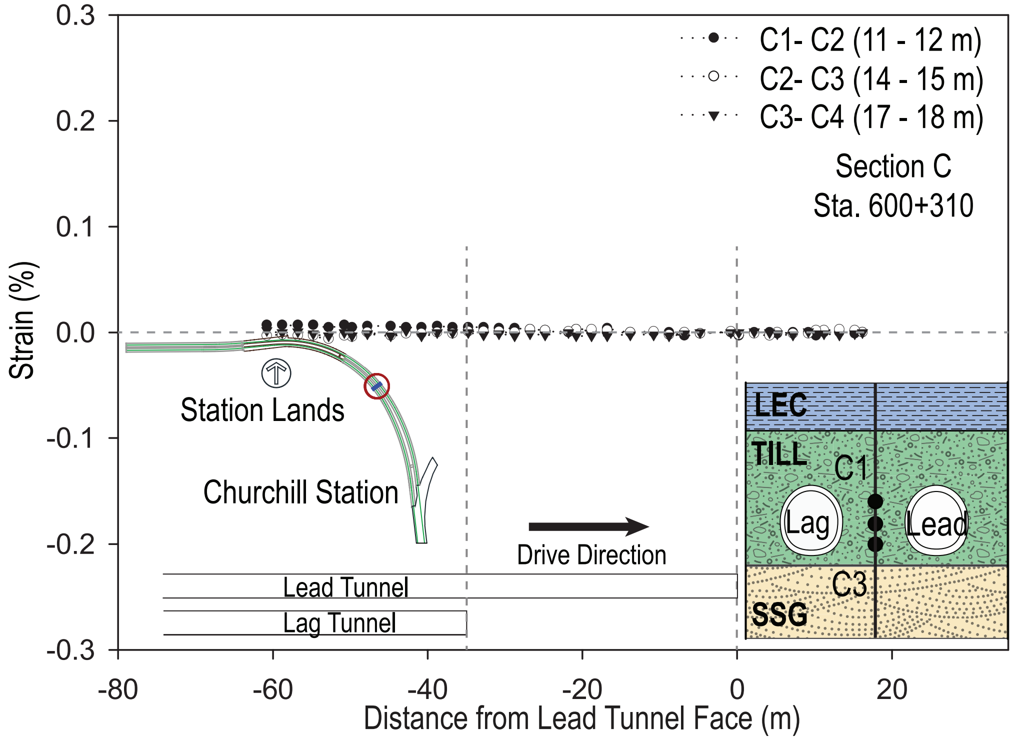

Figure 6.73. Shear strain measured in the pillar at Section C (glacial till)

Because the shear strains over a 1 m interval is only 0.01% in the header measured at Section C, yielding within the glacial till could not have occurred. This is based on a minimum active compression shear strain of 0.5% as given in Chapter 5.

In order to investigate the displacements into the tunnel face, an inclinometer was installed at Section D in the centreline of the Northbound (lag) tunnel. At the time of the installation, it was thought that the Northbound tunnel would be the lead tunnel. Therefore, installing the inclinometer through the tunnel face would result in a relatively undisturbed look into the ground movements into the tunnel face as the lead tunnel approached the point. The contractor elected to construct the Southbound tunnel first and the results of the in-face tunnel monitoring was compromised slightly. The results of the inclinometer installed through the face in the lag (Northbound) tunnel at Section D are shown below in Figure 6.74.

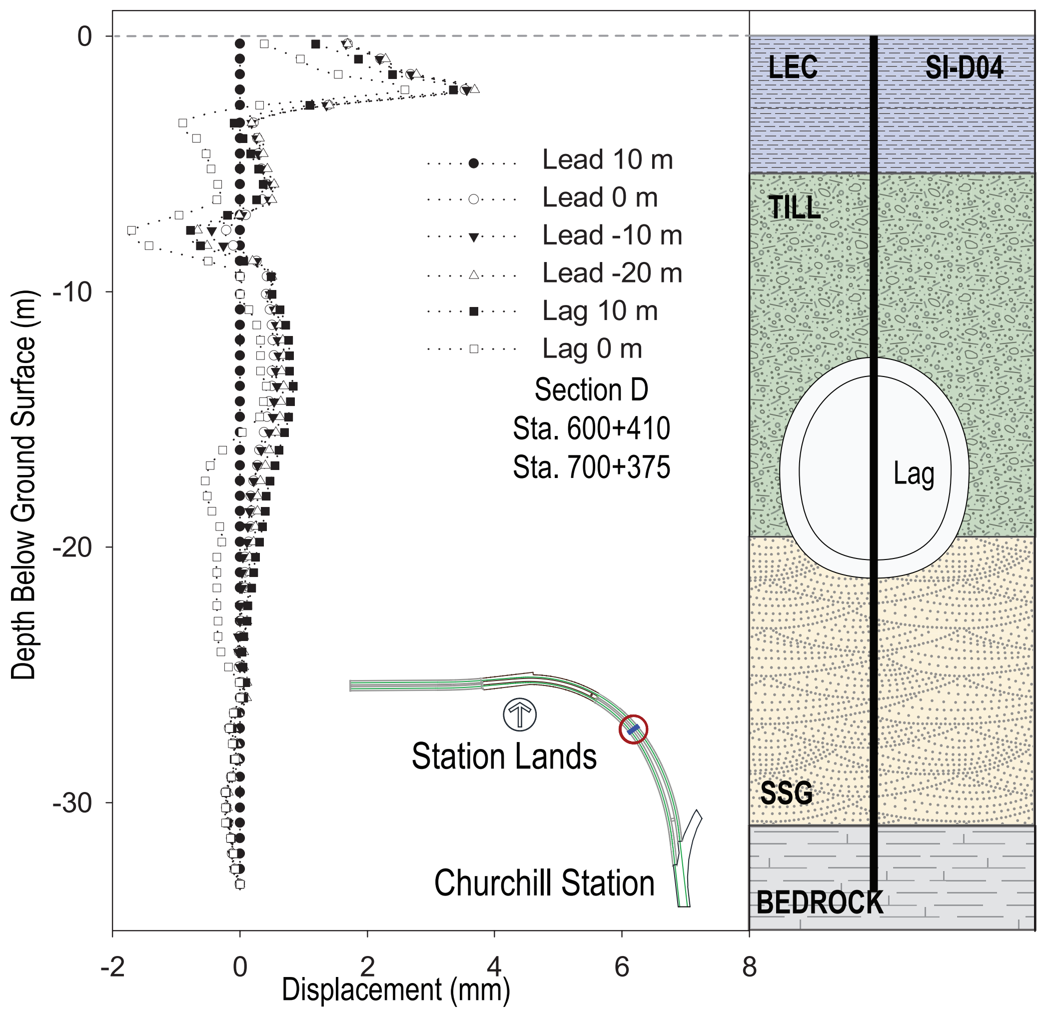

Figure 6.74. Displacement into the lag tunnel face at Section D (mixed face)

Through this section, the tunnel face is located at depths ranging from 14 to 20.7 m below the ground surface. In the data, it can be seen that there is some lateral movement of about 1.2 mm into the tunnel face from the construction of the lead tunnel. As the lag tunnel approaches the point, there is an additional 0.25 mm into the face until the last reading where the lag tunnel was 2 m from the inclinometer. At this point, there appeared to be some relaxation of the ground as the displacement into the tunnel face reduced to a maximum of 1 mm. It also appears that most displacements took place between 13.75 and 16 m below the ground surface suggesting that the majority of the face loss occurred in the header and not the bench. This is counter-intuitive to what has been shown above, since the maximum displacements were expected in the bench if the sand was yielding. The fact that the bench and invert is an additional 2 m behind the header may contribute to the reduced displacements measured in the bench.

Considering the results of the in-face monitoring, it is thought that there are more elastic deformations in the glacial till relative to the Empress Sand. This theory conforms to the findings of the pressuremeter testing given in Chapter 4 which suggested that the till had an elastic modulus around 33% that of the Empress Sand. It also suggests that yielding in the Empress Sand does not occur until the face is exposed and left unsupported and strains are permitted to exceed 0.2% in extension. In order to assess the degree of strain that was occurring in the face, the shear strains in the inclinometer were plotted over 1 m increments through the tunnel face. These strains were plotted as a function of the tunnel face position relative to the location of the inclinometer and are shown below in Figure 6.75.

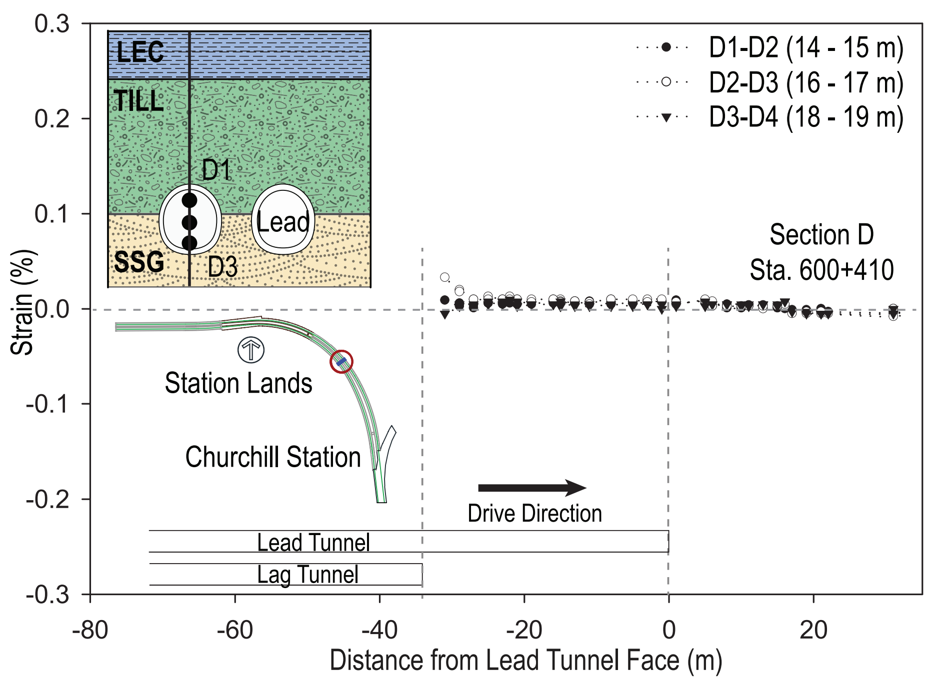

Figure 6.75. Shear strain measured in the lag tunnel face at Section D (mixed face)

The shear strains measured in inclinometer SI D04 suggest that strains only began to occur when the lag tunnel face was approximately 4 m ahead of the monitoring point. It can also be seen that the shear strains were contained mainly to the header between depths of 16 to 17 m below the ground surface.

6.5 Ground Loss and Influence of the Pillar Width

The volume loss (V_l) for the twin tunnel settlement trough was calculated using the method of superposition proposed by Suwansawat and Einstein (2007). In each case, the settlement trough measured at its steady state folowing construction of the first tunnel was subtracted from the final steady state settlement trough. An inverted Gaussian trough was fit to the measured and calculated settlement troughs and superimposed to create a fit to the final, steady state settlement trough. Once a satisfactory fit had been achieved, the volume loss at for each settlement trough was added together to provide the final ground loss as a percentage of the tunnel area. Figure 6.76 to Figure 6.82 show the measured and fitted settlement troughs at monitoring sections C to F. Monitoring Sections A and B were excluded since there was a collapse at Section A and the cross passage was located at Section B. Each of these factors was not considered to be representative of the ground conditions typical to the site.

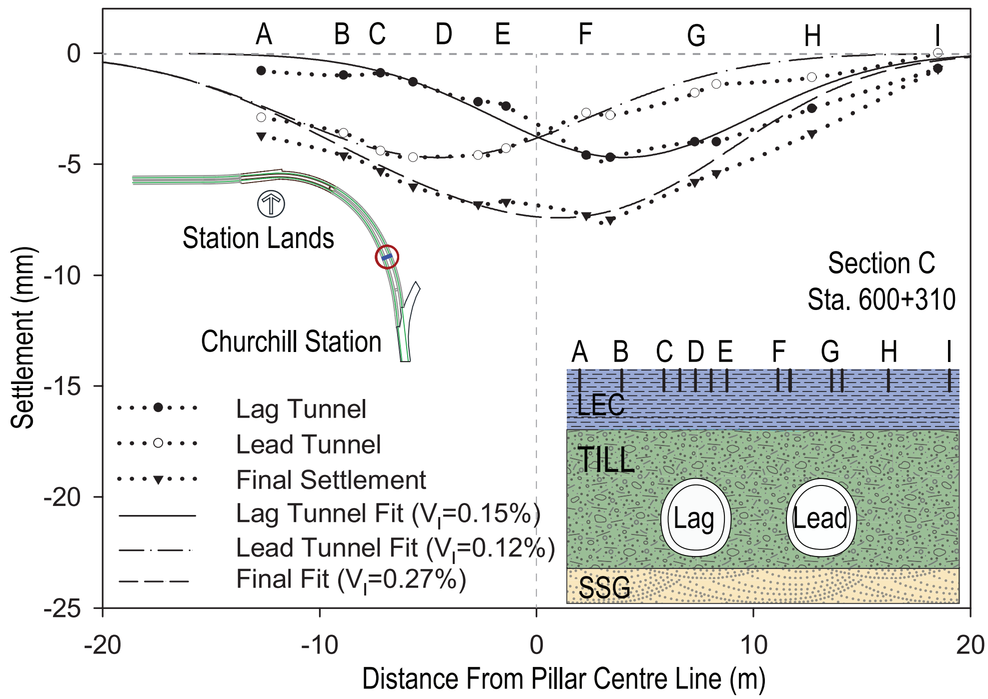

Figure 6.76. Measured and fitted shallow settlement troughs at Section C (glacial till)

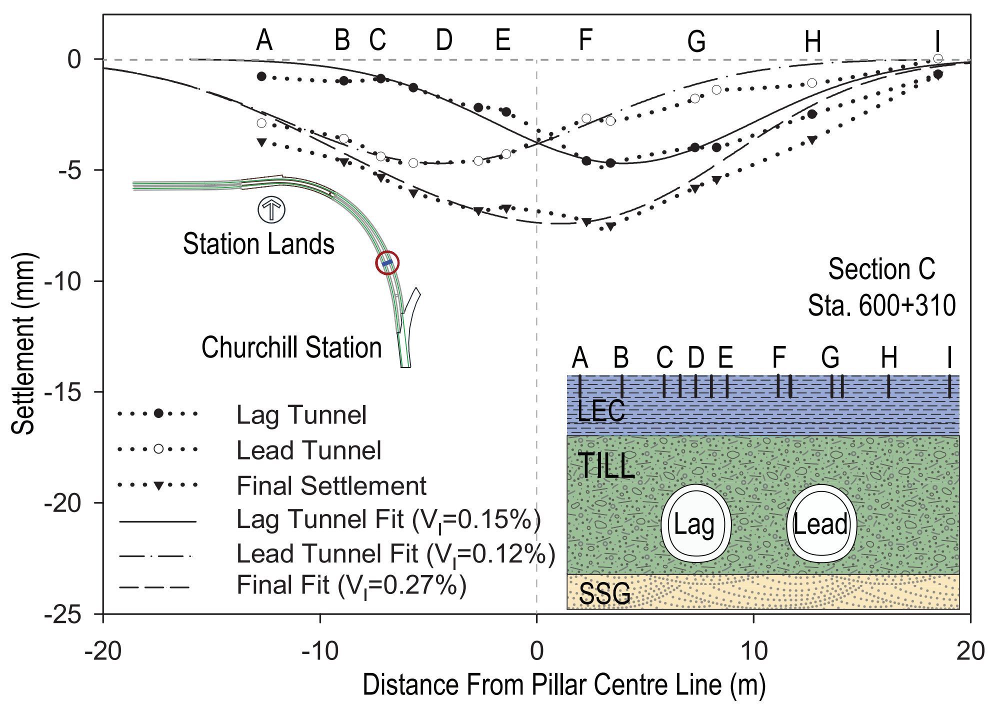

Figure 6.77. Measured and fitted deep settlement troughs at Section C (glacial till)

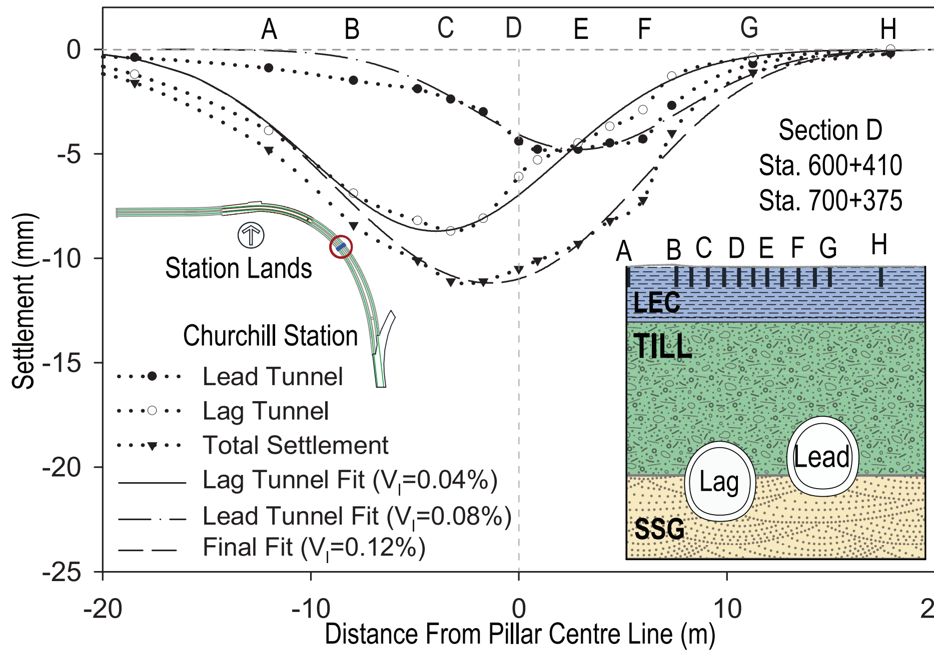

Figure 6.78. Measured and fitted shallow settlement troughs at Section D (mixed face)

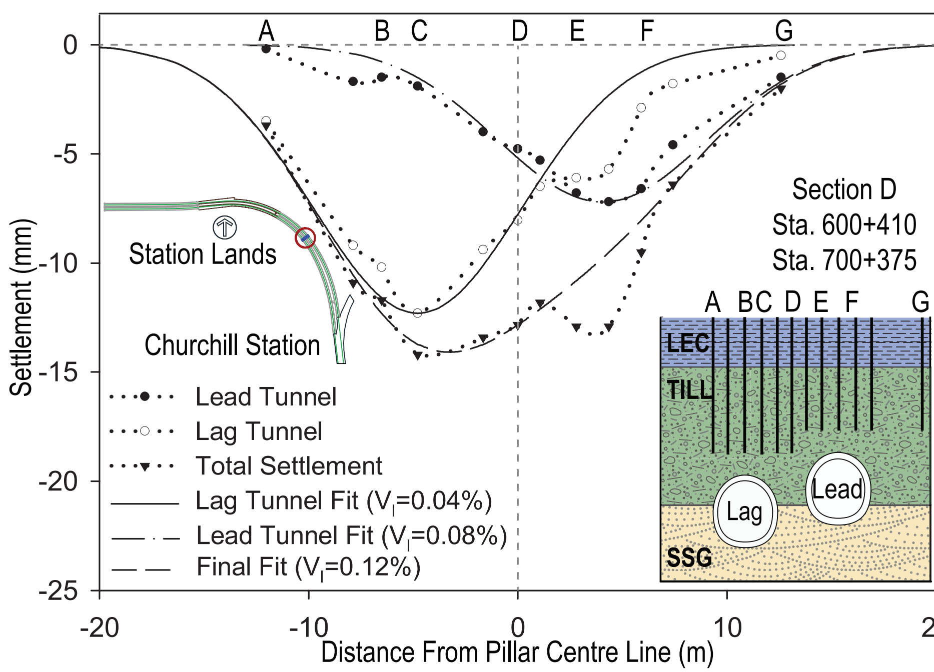

Figure 6.79. Measured and fitted deep settlement troughs at Section D (mixed face)

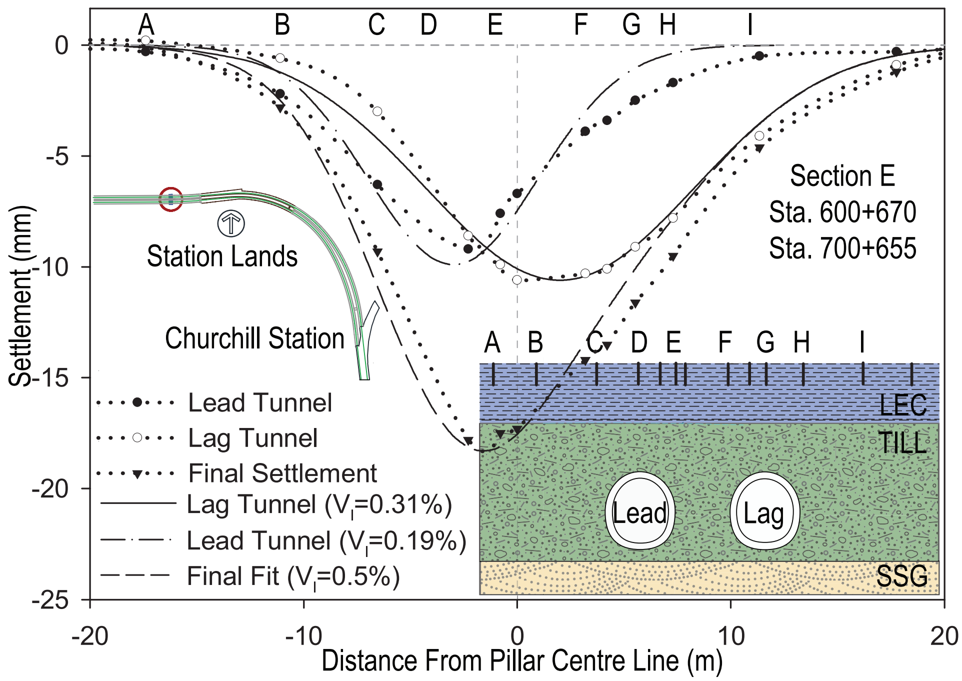

Figure 6.80. Measured and fitted shallow settlement troughs at Section E (glacial till)

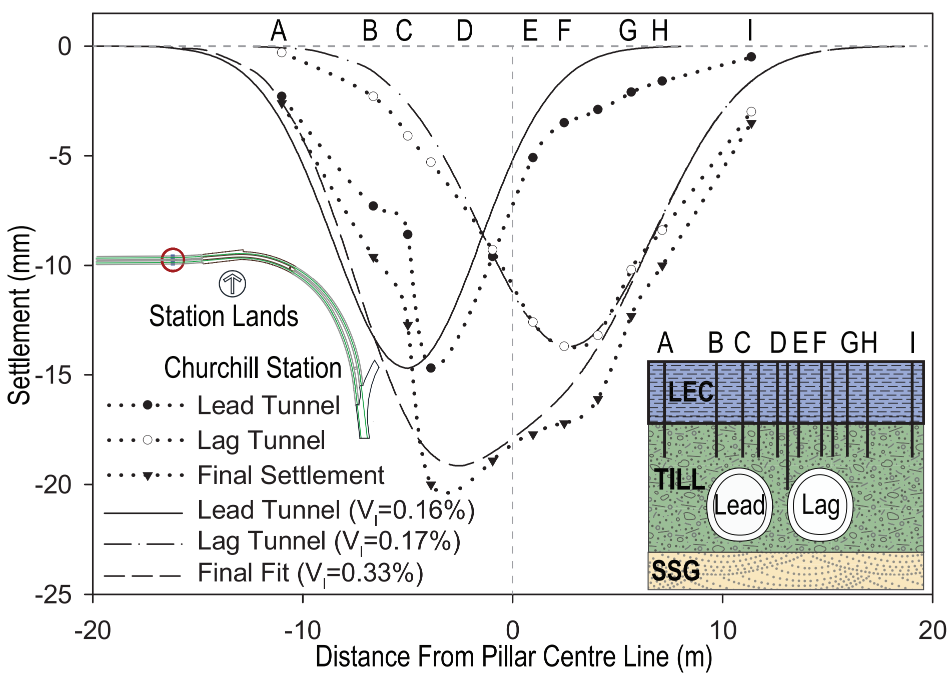

Figure 6.81. Measured and fitted deep settlement troughs at Section E (glacial till)

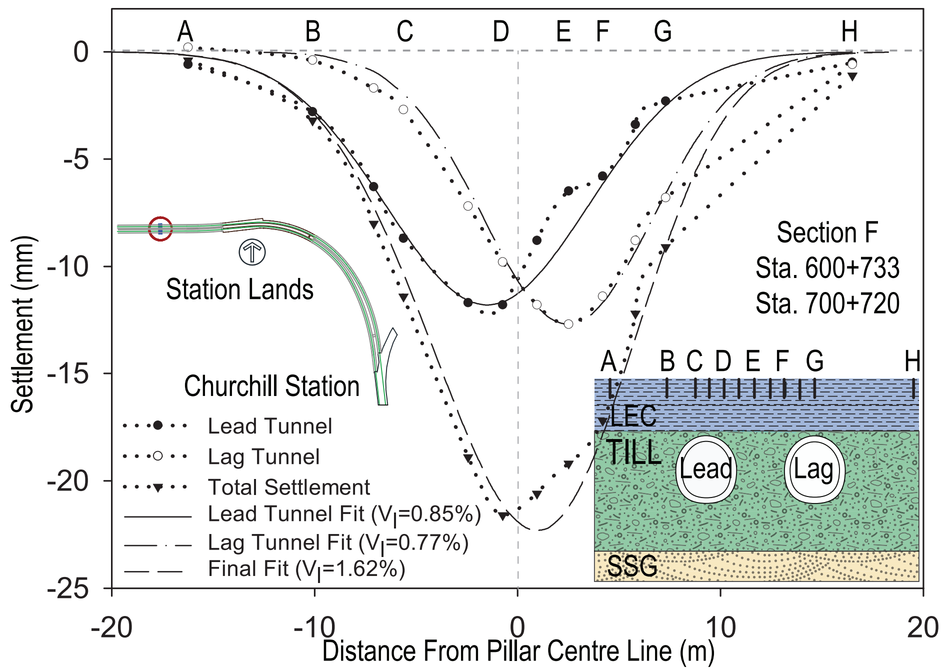

Figure 6.82. Measured and fitted shallow settlement troughs at Section F (glacial till)

From the above, it is clear that there is a good fit when the method of superposition proposed by Suwansawat and Einstein (2007) is used. Based on the above Gaussian fits, the volume loss of each settlement trough as a percentage of the tunnel face area is presented below in Table 6.1.

Section ID	Maximum Settlement (mm)	Volume Loss 1st Tunnel (%)	Volume Loss 2nd Tunnel (%)	Total Volume Loss (%)
C (Shallow)	7.5	0.15	0.12	0.27
C (Deep)	7.5	0.11	0.07	0.18
D (Shallow)	11.2	0.04	0.08	0.12
D (Deep)	14.2	0.04	0.08	0.12
E (Shallow)	17.8	0.31	0.19	0.5
E (Deep)	20	0.16	0.17	0.33
F (Shallow)	21.7	0.85	0.77	1.62

Table 6.1. Calculated volume loss as a percentage of tunnel cross sectional area

When the calculated volume loss is compared with the historical values obtained from other LRT tunnel projects throughout the City of Edmonton shown in Table 2.1, the average ground loss (with the exception of Section F) is similar to the previous projects. Section F represents the higher end of the ground loss measured throughout the city and is the second highest value next to the tunnel constructed with an open faced TBM through the outwash sands near the north shore of the North Saskatchewan River.

In order to better understand the influence of the pillar on the ground settlement, the deep settlements were plotted with respect to the pillar width. Initially only the deep settlement points were considered so that the influence of the tunnel depth could be eliminated. Because the deep settlement rods were all installed to a depth that was always 2 m above the tunnel crown, the settlements were considered to be a function of pillar width and construction methods rather than depth. Therefore it was anticipated that as the pillar width increased, the settlements would decrease. The pillar width was normalized to the effective tunnel diameter (6.5 m). The deep settlements over the twin tunnel crowns with respect to pillar width are shown below in Figure 6.83.

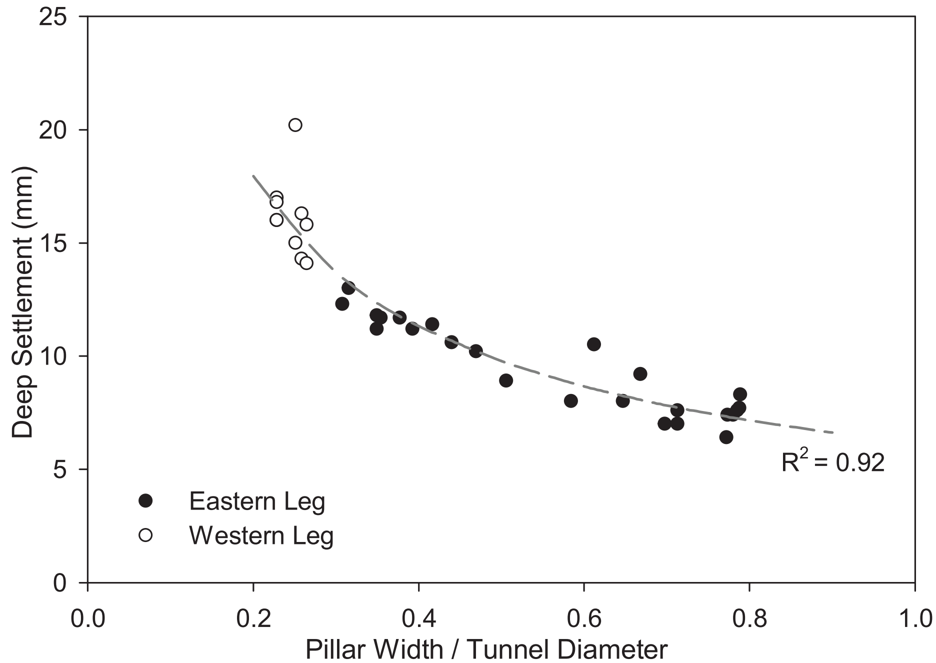

Figure 6.83. Deep settlement over tunnel crowns as a function of pillar width

It is clear that the anticipated trend is well defined based on the measurements recorded along the North LRT tunnel alignment. By examining Figure 6.83, the point where the interaction between the two tunnels should be determinate. Ranken (1978) suggested that the minimum pillar width required to reduce the interactions to zero is 2D, while for practical purposes, a spacing of 1D would be satisfactory. Figure 6.83 indicates that a spacing of 1D would be the point where interactions are reduced to a negligible point. If the criteria for interaction are set such that the percent difference in settlement is less than 10%, then the point of zero interaction occurs at a spacing of 0.6D. This criterion is considered to be satisfactory for all practical purposes as it corresponds with a change measurable settlements that are less than 0.5 mm. This suggests that there is a strong interaction and influence of one tunnel on the next in the sections where the pillar width was less than 0.6D.

The settlements throughout the tunnel alignment were then normalized relative to the depth of the tunnel (overburden thickness between tunnel crown and base of the settlement rod). This was done in an attempt to determine the strain within the overburden between the tunnel crown and settlement rod. In addition, normalization permitted the illustration of the shallow settlement points with respect to the pillar width. The results of the normalized settlements are shown below in Figure 6.84. It should be noted that the normalized settlements are shown in terms of mm (of settlement) / m (overburden thickness).

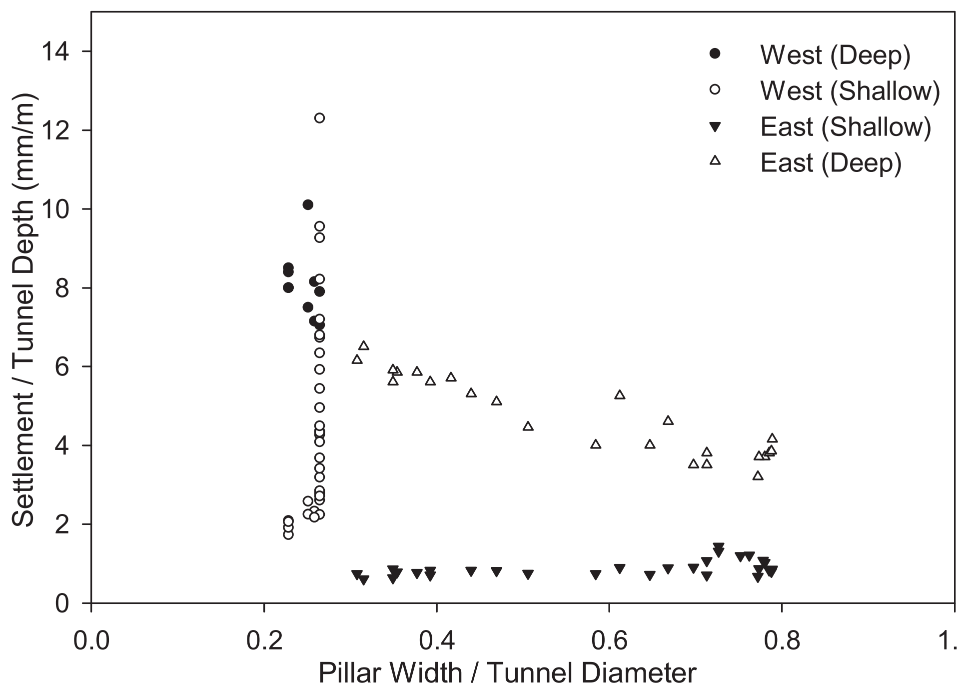

Figure 6.84 Normalized settlement with respect to pillar width

Figure 6.84 indicates that there is a definite trend in the settlement values. First, as shown in Figure 6.83, the deep settlement increases with a reduction in the pillar width. Second, the strains in the shallow settlement points all decrease with increased tunnel depth as would be expected, since as the tunnel depth increases, the resulting strains are reduced. The pillar width along the western leg decreases marginally near the Station Lands, which is the deepest section of that tunnel alignment. The eastern leg also starts out with a narrow pillar (0.29D), but also the greatest depth of the entire tunnel alignment. Because the depth influences the measured strains so much, it is only useful to examine the settlements recorded in the deep settlement points to compare the effect of pillar width.

When the deep settlement statistics are evaluated, another interesting trend is demonstrated. Figure 6.85 shows the total settlements following passage of each tunnel under a monitoring point. In order to eliminate the influence of the lead tunnel on the lag tunnel, the settlements realized during the passage of the lead tunnel were subtracted from the total settlement. This is similar to the method of superposition suggested by Suwansawat and Einstein (2007). This correction should eliminate the influence of the pillar width and indicate the impact of the construction methods on settlements alone. Like Figure 6.83, the settlements considered below are only for the deep settlement points.

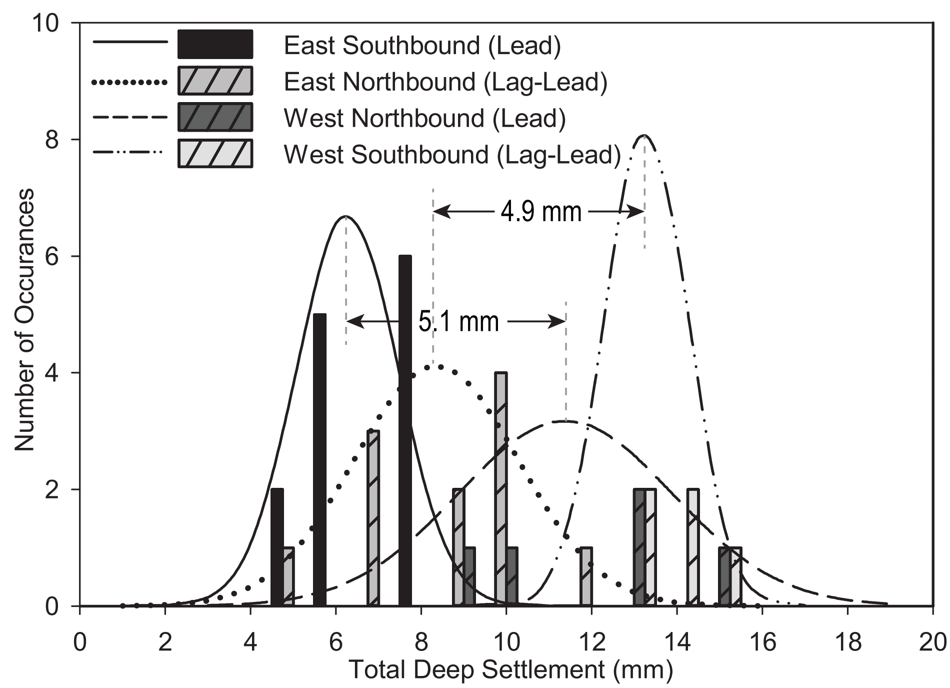

Figure 6.85 Deep settlement statistics for the east and west alignments

Figure 6.85 effectively demonstrates the construction damage due to delayed closure of the support ring. Clearly there is an improvement when the two tunnel legs are examined. It would appear that there is approximately a 5 mm improvement along the eastern leg of the alignment when compared to the west. Coupled with the knowledge that the tunnel contractor was having difficulty applying the shotcrete support in a timely fashion through the western leg, this discrepancy is not unfounded.

To see if the effect of loosening and the subsequent consolidation of the loosened material was a factor on the surface settlements, the total "damaged" settlement was calculated between the lead and lag tunnels. The respective errors for each leg are shown above as the difference in mean values of the normal distribution curves in Figure 6.85. Based on the difference in damage calculations, the effect of loosening of the soil around the lag tunnel was minimal. This is because the damage in the lead tunnel was slightly higher (5.1 mm) than the lag tunnel (4.9 mm). With this in mind, the deep settlements relative to the pillar width (Figure 6.83) have been replotted with a 5 mm "damage" correction applied to the measured settlements. The corrected data is shown as Figure 6.86. These resulting settlements are solely due to the construction of the each individual tunnel regardless of the presence of loosened near field soils around the lag tunnel cavity.

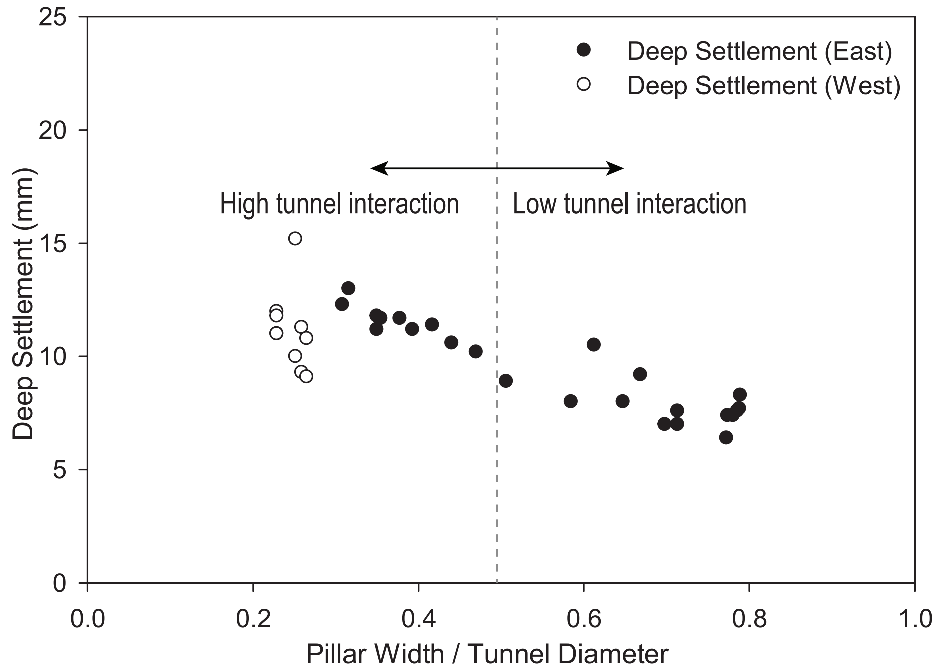

Figure 6.86. Deep settlement with western data corrected for “damage”

Figure 6.86 now shows that there is very little pillar influence within the glacial till at a pillar width of 0.5D or greater. Widths greater than 0.5D tend to show a marginal increase in ground control and therefore a slightly reduced settlement a distance of 2 m above the tunnel crown. Figure 6.86 does not suggest that there is no interaction between the two tunnels, more that the interaction between spacings of 0.5D and 0.78D does not have as great of an impact on settlement when compared to spacings of 0.23D to 0.5D.

6.6 Conclusions

The data that was accumulated throughout the tunnelling process illustrated the ground displacement profiles from within the narrow pillars of the North LRT twin tunnels. Based on the program the following conclusions have been drawn:

- The embeddable vibrating wire strain gauges worked well as the results were comparable and similar to those measured using more conventional methods. The strains that were calculated based on a mean UCS modulus of the shotcrete and the assumption that the instruments were installed along the neutral axis of the liner proved to correspond well with the findings of the tape extensometer. Historically, embeddable strain gauges tend to be destroyed during the shotcreting process. The installation methods utilized for this research program resulted in an effective system for protecting the individual instruments as well as maintain adequate contact with the shotcrete liner. Ultimately only one of the 36 strain gauges installed was found to be inoperable.

- The tape extensometer resulted in regular highly accurate and repeatable measurements of the change in tunnel diameter over several locations. Used primarily as the basis for validation of other methods, the tape extensometer proved to be a reliable monitoring system. The only major drawback of the method is that it cannot be automated since automation would require strain gauges strung across the tunnel diameter rendering access to the tunnel heading impossible.
- The results recorded from the total station and optical targets were considered to be difficult to rely on since many of the results were not generally repeatable.
- Like the vibrating wire strain gauges the circumferential Shape Accel Array installed to the inner surface of the shotcrete liner performed as intended. This tool proved to be very useful in terms of detecting sub-millimeter trends within the tunnel cavity. This data would be well supplemented if regular and accurate surveys of the reference point were recorded in order to obtain absolute displacements.
- One SAA was damaged beyond repair when it was installed immediately behind the advancing tunnel face. By either installing the SAA within the shotcrete liner or providing a metal protector around the SAA future losses may be prevented

and the initiation of the SAA can commence immediately behind the tunnel face, effectively capturing the complete convergence profile.

- The results of the time domain reflectometry (TDR) system installed within the tunnel liner were considered to be spurious at best. This system is not suitable for monitoring tunnel convergence. Interpretation was extremely difficult and prone to error both during calibration and assessment of the change in signal throughout the cable length. Therefore, use of the TDR indicated a general trend of displacement provided a number of broad assumptions were made. Application of the laboratory calibrations to obtain absolute displacements was even more suspicious. In this respect, it is not likely that the use of the TDR within the tunnel liner yielded any usable results.
- The surface-monitoring program yielded extremely useful results that demonstrated the performance of the ground tunnelled. They also indicated the efficacy of the excavation methods. The resolution and repeatability of the surface-settlement monitoring proved to be consistent throughout the program.
- The monitoring also confirmed the width of the settlement troughs associated with the construction activities were minimal and did not extend to distances more than 5 m beyond the actual tunnel alignment.
- The surface settlement monitoring also revealed that near the MacEwan Portal the settlement trough was extremely steep and chimney-like. It is possible that the presence of the fissures within the glacial till dominated the displacement profiles and the settlements were limited by the discontinuities. Therefore the settlement trough is confined to a small region around the tunnel openings as joints that have translated relative to one another bound the lateral extents of the settlement troughs. Though this mechanism is not feasible to measure in full-

scale experiments, it demonstrates the feasibility that numerical solutions involving ubiquitous joint sets will help to confirm this hypothesis.

- The pillar inclinometers proved also to be one of the most important instruments installed in the program. They were the only instruments to clearly illustrate plastic deformations. They confirmed the yield strains for a soil subjected to either extension or active compression (unloading) provided in Chapters 4 and 5. The inclinometers suggested that yielding within the ground does not occur at distances greater than 1 m from the tunnel cavity or at pillar widths greater than 0.5D.
- Ground loss associated with the tunnel construction was well represented by the method of superposition postulated by Suwansawat and Einstein (2007). With the exception of the two cross sections constructed with a pillar width of around 0.23D, the measured volume losses as a function of the tunnel face area were vast improvement to those measured in previous LRT projects throughout the city. This suggests that provided good construction methods are employed, surface settlements can be kept to extremely low levels. The volume loss measured at Section F, where the time to ring closure was considerable, suggests the importance for a construction sequence suited to the ground conditions.
- Finally, the minimum spacing required to minimize the interactions between twin tunnels constructed within the Edmonton tills is approximately 0.5D. A method has also been provided to statistically assess the damage within the ground from the lead to the lag tunnels.
- Using the new method the pillar width was effectively eliminated from the measured settlements. When the influence of the pillar was removed, it was

found that the damage for the lead tunnel (5.1 mm) was slightly higher than that of the lag tunnel (4.9 mm).

7.0 Numerical Representation of Ground Behaviour

7.1 Introduction

Extensive ground monitoring data was collected during excavation of the North LRT twin tunnels. These data, if adequate could then be used to assess the ground behaviour using back analysis. Sakurai (1983) recommended that when carrying out a back analysis of an underground opening that the model be first constructed using an elastic medium. This way, the number of unknowns and assumptions would be drastically reduced. Because the variation in Poisson's ratio is relatively small (±0.01), it leaves only the modulus of elasticity and the coefficient of lateral earth pressure at rest as the main sources of error for elastic back calculations. Based on the criteria for yielding within the Edmonton till defined in Chapter 5 as well as the strains reported in Chapter 6, it would appear likely that elastic deformations were dominant. The purpose of this work was to back analyse the measured data with the elastic parameters determined from the in-situ testing. Once a reasonable fit had been achieved, the models were then used to confirm if in fact overstressing within the ground surrounding a tunnel occurred. It was not the intention to determine absolute deformations within the tunnel cavity or help ascertain better methods for assessing liner stresses. Rather the focus was to assess if yielding was limited to the immediate vicinity of the tunnel perimeter and not the groundmass as a whole. Another aspect that was investigated was to assess the impact of a staged face excavation relative to a full-face sequence on the pillar, face and heading stability.

The three dimensional, linear elastic, numerical models for the North LRT twin tunnels were constructed using the commercial software, Fast Lagrangian Analysis of Continua 3D (FLAC 3D). These analyses were carried out for three of the four monitoring cross sections (Sections C, D and E described in Section 6).

7.1.1 Numerical Model Considerations

To assess the displacements within the ground during approach and passage of the tunnels under a specific point, the model was assembled to match the actual ground conditions as much as practical. The geology for each model was based on the borehole findings at each of the monitoring cross section locations as shown in Chapter 3. The elastic parameters were selected based on the range of values obtained during the in-situ testing carried out at the Station Lands (sCPT and pressuremeter).

The models were calculated with a primary focus on the surface settlement profiles. In each case, the trends above the crown of each tunnel and the pillar was compared to the actual monitoring data and adjusted accordingly until a fit was achieved. Once a reasonable match in the settlement data was achieved, the remaining calculated displacement fields were compared with the measured values.

7.1.2 Field Monitoring for Back-Calculation

Three monitoring cross sections were back analysed and compared with the in-ground displacements measured during the monitoring program detailed in Chapter 6. The monitoring cross sections that were analysed were Sections C, D and E respectively.

The vertical monitoring points that were used for comparison consisted of both shallow and deep settlement rods measured with a precise level during tunnel construction. The accuracy of the precise levelling system was well maintained between +/- 0.1 mm. Sections D and E utilized multipoint extensometers installed to various depths within the pillar to monitor settlements throughout the depth of the various formations.

Lateral displacements within the ground were compared to the results of monitoring within the inclinometers installed through the pillar and outside of the tunnels.

For the purpose of the back analyses, only the inclinometer outside the lead tunnel springline was considered due to symmetry.

7.2 In-tunnel displacements were monitored in the field using a combination of methods. As previously discussed, the monitoring utilized a total station and optical targets with a resolution of +/- 1mm. The optical measurements were supplemented at Sections D and E using a tape extensometer and vibrating wire strain gauges within the lead tunnel. Finally, the movement of the first tunnel into the second tunnel was also measured at Section E using an SAA installed around a portion of the tunnel circumference. All off the information above was used as the basis for the comparison for the in-tunnel back analyses.

7.3 Three Dimensional Numerical Model Construction

7.3.1 Mesh Generation

The mesh was assembled using the built in mesh generator as part of the graphical user interface in FLAC 3D. The digital cross section of the twin tunnels was saved in AutoCAD and was imported directly into the FLAC 3D extruder. The model axes were set such that the *x* and *z* coordinates represented the tunnel cross-section in the horizontal and vertical directions respectively, while the *y* direction represented the depth of the soil mass (or the extruded length of the tunnel cross section).

The mesh that was generated provided fine element sizes where accurate displacements were of importance and coarser elements near the boundaries in order to expedite the calculation process. Within the pillar and around the tunnel cavity and face, the element size was approximately 150 mm wide, 250 mm high and 500 mm deep (along the tunnel axis). There is some variation to the element size from model to model, but these constraints were kept as close as possible where displacements were considered critical. The element size around the tunnel cavities never exceeded 300 mm in the x and z directions.

The stratigraphic profiles were generated as encountered in the boreholes drilled in the field. The lateral boundaries were set such that they were equal to a minimum of 5 tunnel diameters from the outside springline of each tunnel. The depth of the model below the tunnel invert was variable, but was a minimum of 10 m (1.5D) below the invert of the tunnels.

Once the model cross section had been assembled and a mesh was generated, zone groups were created and consisted of the following:

- Lake Edmonton Clay (LEC);
- Glacial Till (Till);
- Empress Sand (SSG);
- Bedrock;
- Northbound Header (NB Header);
- Northbound Bench (NB Bench);
- Northbound Invert (NB Invert);
- Southbound Header (SB Header);
- Southbound Bench (SB Bench); and
- Southbound Invert (SB Invert).

The purpose of the grouping was to permit sequential excavation of the various tunnels throughout the model process. In the models that utilized a full-face excavation, the same groups were assigned, however all three groups (header, bench and invert) were excavated in one step. A typical cross section of the twin tunnels and soil mass is shown below in Figure 7.1.

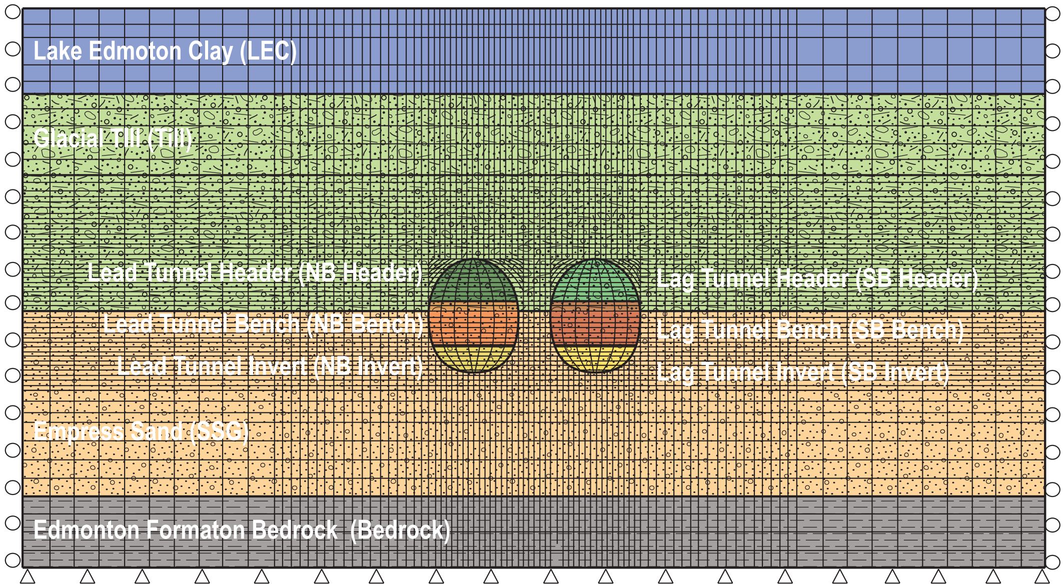

Figure 7.1. Typical mesh cross sectional arrangement in FLAC 3D

In all cases, the upper boundary was set to a free surface, which permitted displacements in all directions. Roller boundary conditions were established at the lateral (*x* and *y*) limits of the soil mass such that only vertical displacements (*z* direction) were permitted. The base of the model was fixed so that no displacements were permitted in any direction.

All models of the soil mass were extruded in the *y* direction to a length of 110 m with mesh divisions of 0.5 m or 220 elements in the *y* direction for a given soil mass. As a result, two rows of elements were removed in the *y* direction for each meter of tunnel excavated. The element resolution in the *y* direction was considered appropriate since the final stresses and displacements would be the same at steady state conditions regardless of the element depth (linear elastic).

7.3.2 Model Initiation

FLAC 3D does not require that initial stresses related to geostatic loads be imposed from the onset of the model provided that the material is homogenous and isotropic. If an initial coefficient of lateral earth pressure at rest (K_o) is desired, then stresses must be applied to the elements during initialization in order to establish the appropriate stress fields within each element. Stresses within each element are uniform and any gradients resulting from geostatic stresses are a result of gradients applied over the soil mass as a whole. Therefore prior to simulation of the tunnel excavation, geostatic stresses were assigned to the soil mass based on lithology and depths. As well as geostatic initialization, a body force and gravity was implemented for each element to mimic the self-weight of the soil during tunnel construction. The model was then calculated to assign the necessary geostatic stresses and displacements to each element. The initial displacements were then reset to zero and the monitoring points were initialized.

Geostatic stresses were also used to validate the output of the model by comparing the actual geostatic stresses with those obtained from the model. Minor deviation from the geostatic stresses produced by the model and the actual values is anticipated since the stresses are constant through each element. Because of this, the stresses calculated by the numerical model are dependent on the element size and location.

Examples of the efficacy of the numerical models with respect to the geostatic stresses are given below in Figure 7.2. The stress profiles respectively demonstrate a comparison of the modelled versus calculated vertical and horizontal stresses for each cross section modelled.

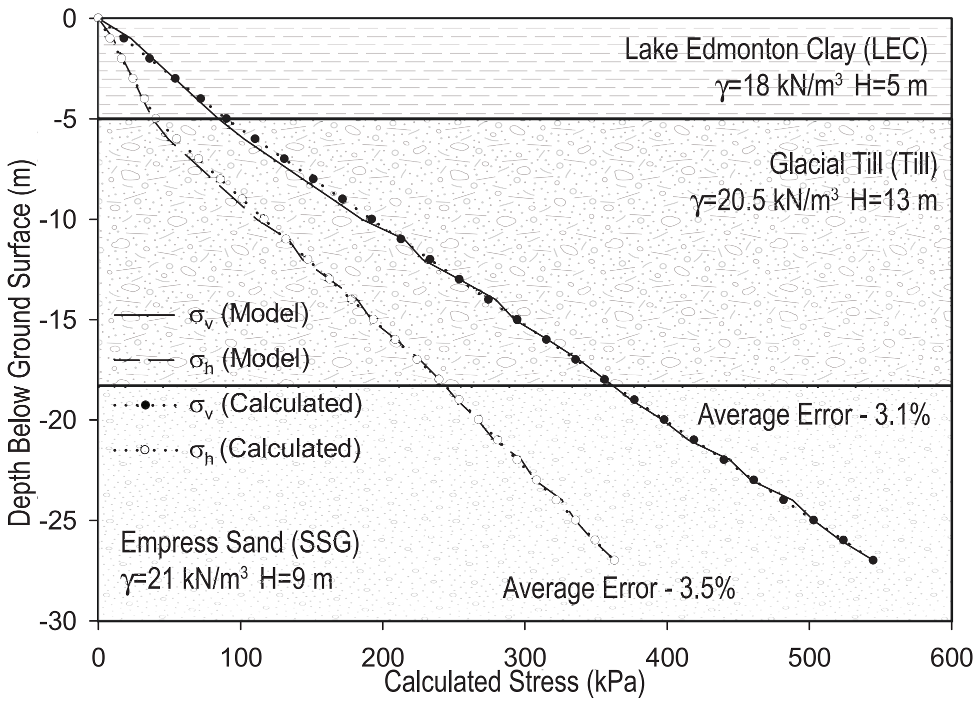

Figure 7.2. Modelled versus calculated geostatic stresses for each section

7.3.3 Excavation Sequencing

The models were programmed to follow as close as possible to the excavation sequencing used during construction. The alignment of the tunnels is shown below in Figure 7.3. The actual tunnels undergo a vertical curve of approximately 5 to 6% on both the east and west legs with the lowest point occurring at the Station Lands Cavity (Epcor Tower). When following the direction of actual tunnel construction, the west leg of the tunnel undergoes a 5 to 6% downward vertical curve while the east leg undergoes an upward 5 to 6% vertical curve. In order to expedite the modelling process, the vertical curve was neglected and instead modelled at the depth of the tunnels at each monitoring section.

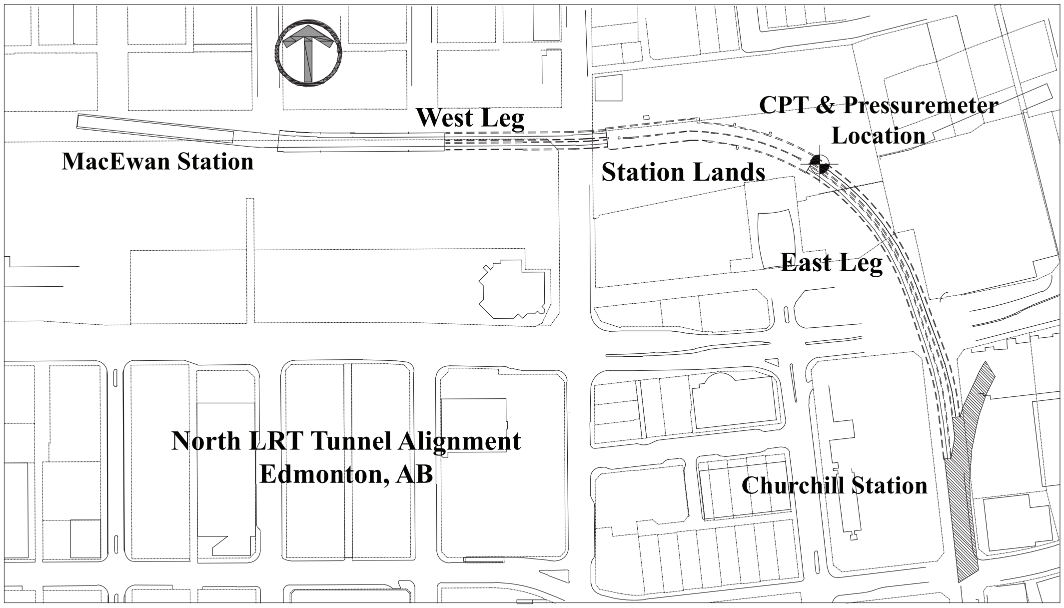

Figure 7.3 North LRT tunnel alignment

During construction, tunnel excavation was carried out in four steps. Round advancement consisted of the excavation of two headers, each 1 m in length, followed by the excavation of the bench a length of 2 m and the invert also to 2 m. Between each excavation, the round was supported by the application of wire mesh, steel sets and shotcrete. The first round however consisted of 3 heading excavations followed by 2 m of bench and invert. This ensured that the header was always at least 1 m ahead of the bench and invert.

A cross section indicating the excavation sequencing of the header/bench and invert is shown below in Figure 7.4 and a profile section illustrating the sequencing is also given below in Figure 7.5.

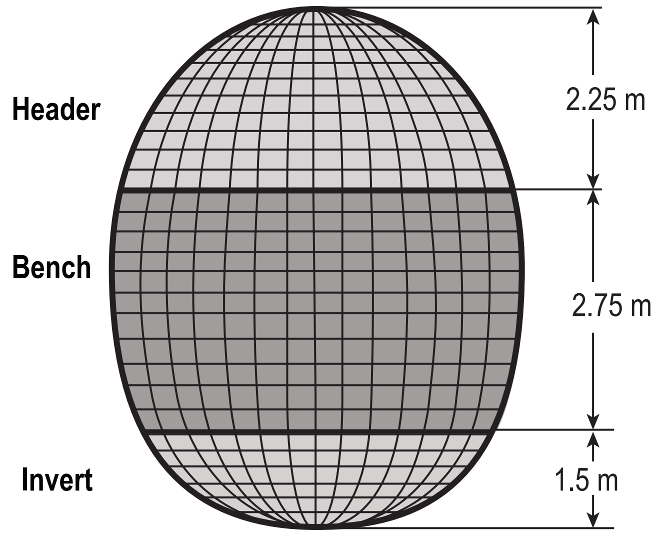

Figure 7.4. North LRT tunnel model cross section

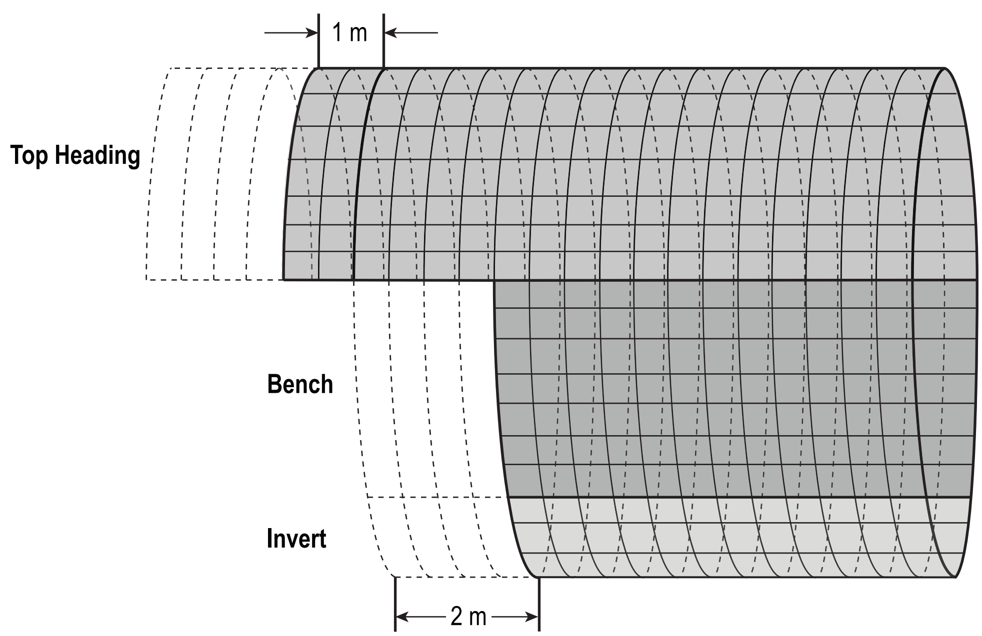

Figure 7.5. North LRT Tunnel profile and excavation sequence

The numerical models were programmed to use a common sequence for the lead tunnel until the stagger point had been reached. The stagger was kept as similar as possible to that used during construction. Once the stagger point had been achieved, then the lag tunnel was commenced with the removal of the first two headers. This was then followed by the removal of a single header in the lead tunnel. Finally, a third lag tunnel header was removed and then the sequence described above was started. It is important to note that no support was added to the numerical model between excavation steps. Because the constitutive model was linear elastic, yielding could not occur and displacements were instantaneous regardless of support.

In each case, the stagger of the tunnels was maintained as close as possible to reality through each section. Ng et al., 2004 illustrated the importance of maintaining a stagger between twin tunnel headings for ground control and settlement management. The stagger between the two tunnels varied during tunnel construction and between legs of the alignment. In the western leg of the tunnels, the actual stagger between the tunnel faces varied from between 45 to 50 m. For the numerical model, the stagger was selected as 50 m. In the eastern leg of the tunnels, the actual stagger between the lead and lag tunnel faces varied from 32 to 37 m. In the modelled sections, the stagger was selected to be 35 m.

Termination of the tunnels varied from the western leg of the tunnels (Section E) to the eastern leg of the tunnels (Sections C and D). For the numerical simulation created for Section E, excavation continued until the lead tunnel reached a distance of 100 m into the soil mass, when the lag tunnel was at a tunnel meter 50 m (30 m past the monitoring section). For the eastern leg, the model extended to a distance of 85 m into the soil mass. This distance resulted in the second tunnel achieving a tunnel length of 50 m, which is also 30 m past the monitoring section. Upon completion of the excavation sequence, the simulation was completed and the results were written to an ASCII file for post processing.

7.3.4 Soil Mass Properties

The elastic parameters used in the numerical model for each monitoring section are shown below in Table 7.1 to Table 7.3. These values have been developed based on a number of current and historical insitu and laboratory investigations carried out throughout the downtown Edmonton area. Selection of each Poisson's ratio was made based on historically published values. Though no literature was found detailing the origin of the values, practitioners throughout the city have used the same values for the better part of 60 years.

Parameter	Lowest Value	Highest Value
Unit Weight (kN/m^3)	18	-
Coefficient of Lateral Earth Pressure (K_o)	0.45	-
Poisson's Ratio (υ)	0.4	0.45
Elastic Modulus (MPa)	15	22.5

Table 7.1. Elastic parameters of the Lake Edmonton clay

Parameter	Lowest Value	Highest Value
Unit Weight (kN/m^3)	20.5	-
Coefficient of Lateral Earth Pressure (K_o)	0.75	0.85
Poisson's Ratio (υ)	0.32	0.33
Elastic Modulus (MPa)	125	200

Table 7.2. Elastic parameters of the glacial till

Parameter	Lowest Value	Highest Value
Unit Weight (kN/m^3)	21	-
Coefficient of Lateral Earth Pressure (K_o)	0.65	0.75
Poisson's Ratio (υ)	0.3	0.33
Elastic Modulus (MPa)	277	300

Table 7.3. Elastic parameters of the Empress Sand used in the numerical models

The Edmonton Formation bedrock was modelled for Section D and the elastic parameters were selected as:

Unit Weight (kN/m^3): 22;
Coefficient of Lateral Earth Pressure (K_o): 0.85;
Poisson's Ratio (υ): 0.35; and
Elastic Modulus (E): 425 MPa.

7.4 Model and Tunnel Monitoring Sections

In each simulation, the monitoring section was established at a distance of 20 m from the start of the soil mass. Because the distance to the monitoring section is greater than two tunnel diameters it is sufficient to minimize any end effects from the boundary. The location also allowed for spatial monitoring with advancement of the two tunnels as well as with the excavation sequence. Finally the location permitted for complete stabilization of the displacements and stresses (steady state conditions) following passage of each tunnel face.

7.4.1 Displacement Monitoring

7.4.1.1 Settlement Monitoring

Settlement data was uses as the initial basis for the back analyses. The settlement monitoring points within the model were established in locations similar to the actual locations and depths of the surface monitoring points. Settlement points were initialized at depths of 2 m below the ground surface and 2 m above the tunnel crowns to represent both the shallow and deep settlement points.

7.4.1.2 Lateral Displacements

Inclinometer (*x* and *y* displacement) monitoring points were initialized through the centreline of the pillar and 2 m outside of the lead tunnel (symmetry) at each monitoring section. The horizontal displacements within the model were monitored at 0.5 m increments, similar to those recorded in the field during construction. The modelled inclinometer was extended to 0.5 m above the base of the modelled soil mass so that the lateral displacements would approach zero with depth. This allowed for direct comparison with the measured cumulative displacement. The depth also ensured that there was no impact of the tunnel construction at the model boundary.

7.4.1.3 In-Tunnel Monitoring

In-tunnel monitoring was initialized to monitor the displacements of the lead tunnel due to the influence of the lag tunnel construction. As stated above, the presence of the liner within each tunnel prevented the comparison of actual in-tunnel convergence measurements. However, the numerical data are comparable to the in-tunnel instrumentation when discussing the influence of the lag tunnel. To this effect, monitoring points were initialized in the first row of elements outside the simulated tunnel cavity. In order to achieve the same resolution as the circumferential SAA installed in the lead tunnel at Section E, the monitoring points were assigned to each element surrounding the tunnel circumference. These data were then also used to compare the results obtained from the tape extensometer. In order for these comparisons to be made, it has to be assumed that both the lined lead tunnel and the simulated lead tunnel are both at a steady state prior to the approach of the lag tunnel. It must also be assumed that displacements measured after this point (either real or simulated) are solely the response of the ground associated with the lag tunnel construction.

Vibrating wire strain gauges were installed at regular intervals within the shotcrete liner to measure axial strains within the tunnel liner. With basic mathematical manipulation, the liner stresses were calculated as shown in Chapter 6. The numerical simulations were used to monitor the principal stresses within the elements surrounding the lead tunnel cavity. These data were then converted to stresses in polar coordinates in order to compare the results with the liner stresses measured by the strain gauges. As with the displacement monitoring, the numerical simulation is only valid for the data obtained during the approach and passage of the lag tunnel.

7.4.1.4 Face Displacement Monitoring

Displacement monitoring points within the model were initialized through the centre of the header, bench and invert of each tunnel face. The displacement trends were used for a general understanding of the face performance during the approach of each tunnel. These data are used solely to ascertain the percentage of elastic strain occurring in each portion of the face prior to excavation.

7.4.1.5 Stress Monitoring

Monitoring points were initialized within the soil mass to track the changes in principal stress within the centreline of the pillar; around the tunnel cavities and within the tunnel faces. Calculation of the stresses within and around the tunnels permitted comparison of the stress paths to the appropriate Mohr-Coulomb yield surface as determined in Chapter 5. All stress-monitoring points were kept coincident between the sequenced and full-face excavations to provide a basis for comparison of each construction method.

7.5 Comparison of the Field Measurements and Model Results

The data are presented using a consistent convention throughout this chapter. All numerically calculated results are presented as lines without markers and all measured values are represented by markers and dotted lines. In cases where settlement is presented in cross sectional form (across a monitoring section) or for inclinometers, the data is shown progressively as the two tunnels approach and pass the instrument array.

These data are shown at 10 m intervals starting at a distance of 20 m ahead of the lead tunnel face and continuing to a distance of 60 m behind the lead tunnel face. All distances are measured with respect to the tunnel header.

In cases where settlements are reported in profile, the settlements are presented in sets of three. These represent the settlements above the axes of the lead and lag tunnels as well as at the centreline of the pillar. In each set of data presented, the individual curves are labelled based on their position to the lead or lag tunnel as indicated in the reduced soil cross section. The abscissa for each curve changes depending on where the monitoring point is relative to the start and end of each tunnel leg. It is therefore important in each case to note the abscissa and whether the distance is to the lead or lag tunnel face.

With respect to the in-tunnel monitoring, the abscissa is reported relative to the lag tunnel face.

7.5.1 Vertical Displacements

The North LRT twin tunnels provided a unique opportunity to study the influence of the pillar spacing in that the width of the pillar varied considerably throughout the alignment. This coupled with the relative consistency of the glacial till, it allows a nearly direct comparison from one section to the next. In general, the calculated displacements were within 10% of the measured values. The larger degree of error occurred at instruments where measured settlement was less than 10 mm. Differences between the computed and measured settlements rarely exceeded 1 mm at any point in the settlement curve profiles.

7.5.1.1 Section C (Homogeneous Glacial Till – Wide Pillar)

Section C was located approximately 145 m south of the Station Lands on the eastern leg of the North LRT twin tunnels. The location of the monitoring section and location of the various monitoring points are shown in each figure. The depth to the crown of the twin tunnels through this section was approximately 10.5 m below the ground surface. The tunnel faces were entirely within the glacial till. Review of the geologic mapping for the face during tunnelling indicated that there was a considerable amount of intra-till sand within both the lead and lag faces, however the results of the sCPT testing carried out as part of the geotechnical investigation suggested that the elastic properties of the sand and the cohesive tills were very similar and were therefore modelled as one unit.

In total, the shallow vertical displacements above the lead and lag crowns and the pillar were measured to be 5.8, 6.0 and 6.7 mm respectively. The calculated shallow settlements above the South and Northbound crowns and the pillar were 5.9 and 6.3 mm respectively. Figure 7.6 compares the calculated results with the measured values.

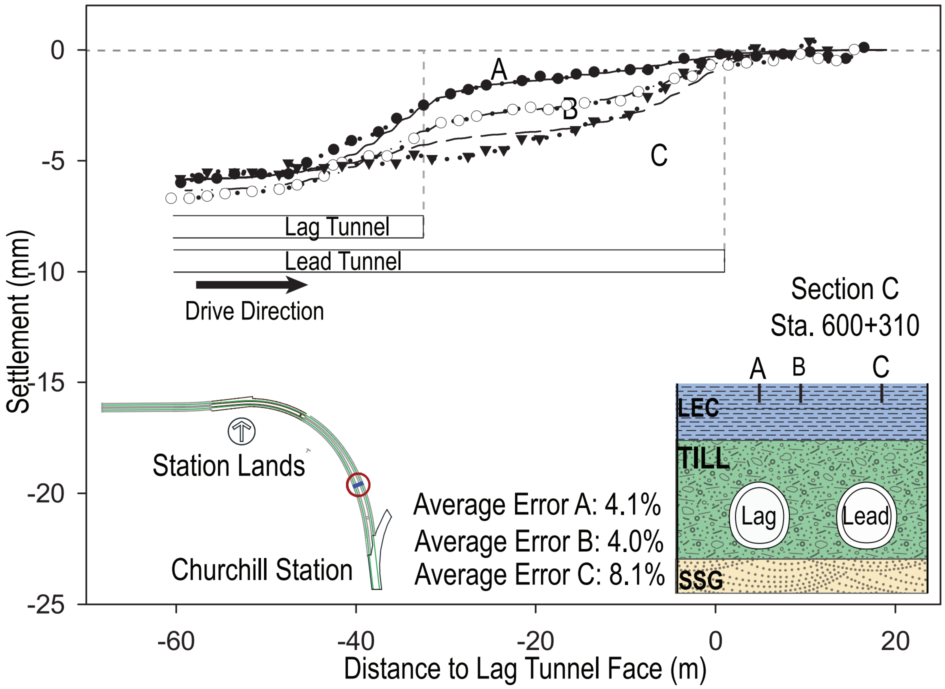

Figure 7.6. Calculated versus measured shallow settlements through Section C

When the whole cross section at Section C was considered, the calculated settlements agreed well with the measured values as shown in Figure 7.7. The average error from the numerical model to the actual values was 16.9% while the maximum and minimum errors are indicated below. The largest error occurs near to the pillar side of the lead tunnel (Points F to G). The measured settlements were slightly greater than those estimated by the numerical model. It is possible that there may have been minor yielding around the lead tunnel cavity that resulted in the minor increased settlements. It should be noted that the actual difference between the calculated and measured values is approximately only 1 mm or 13%.

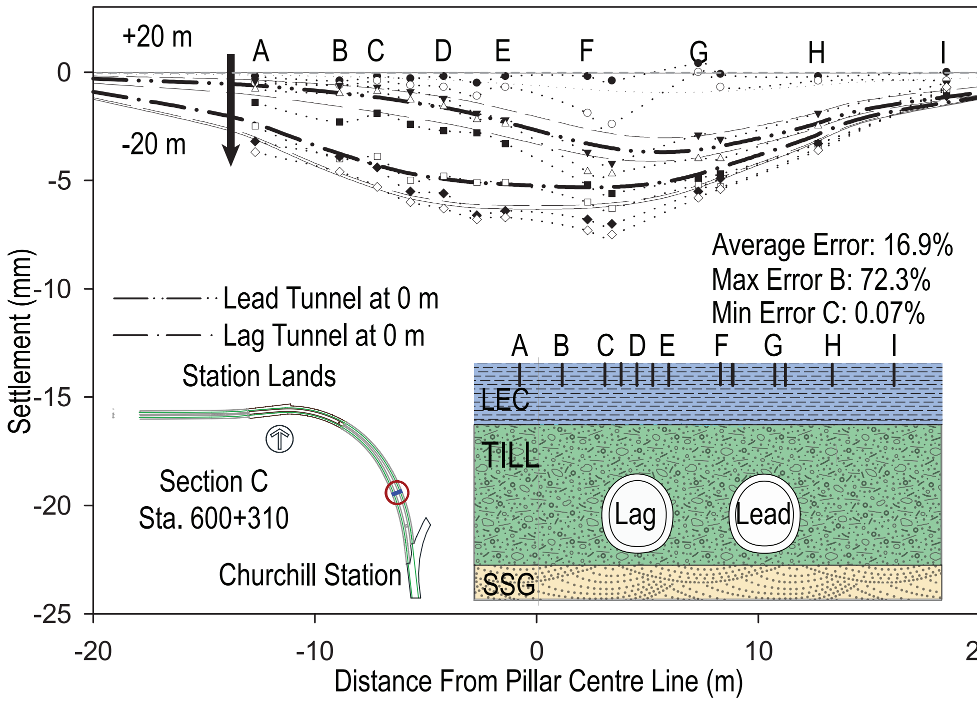

Figure 7.7. Calculated versus measured shallow settlements across Section C

For the above crown and pillar deep settlements, the average error between the calculated and measured values is around 8%. The three trends are shown below in Figure 7.8.

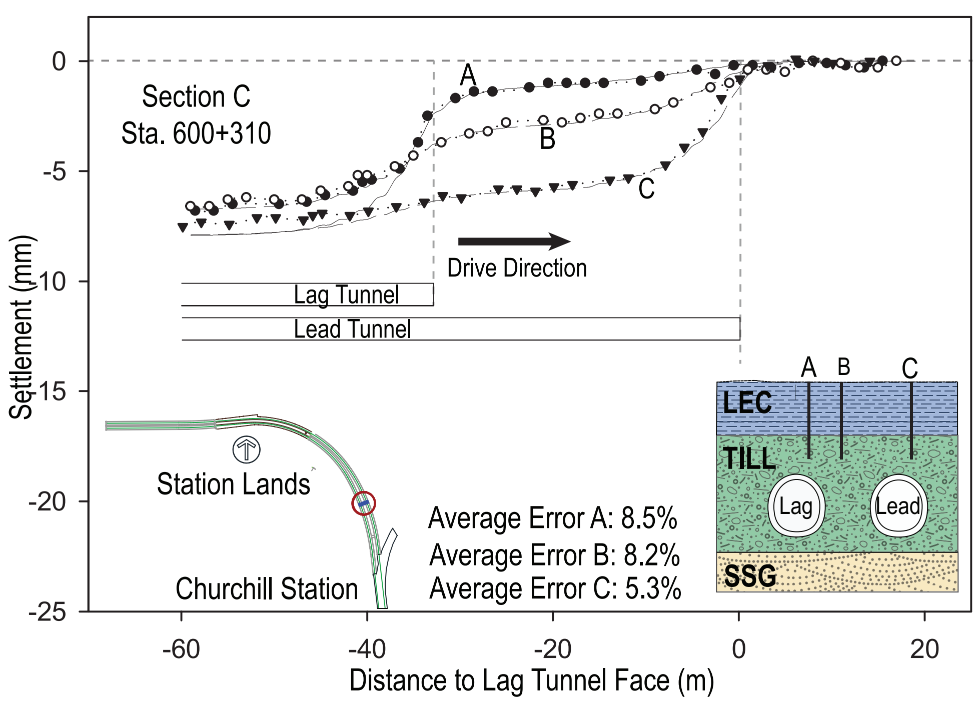

Figure 7.8. Calculated versus measured deep settlements through Section C

Figure 7.9 illustrates the deep settlement trough through Section C. It is interesting to note that the measured settlements are approximately 8% less than those predicted by the linear elastic model. The main deviation from the numerical model is only observed once the tunnel is well past the monitoring point and steady state conditions should apply. The measurements recorded at distances of 50 and 60 m from the lag tunnel correspond well with the estimated displacements at a distance of 20 m behind the lag tunnel face.

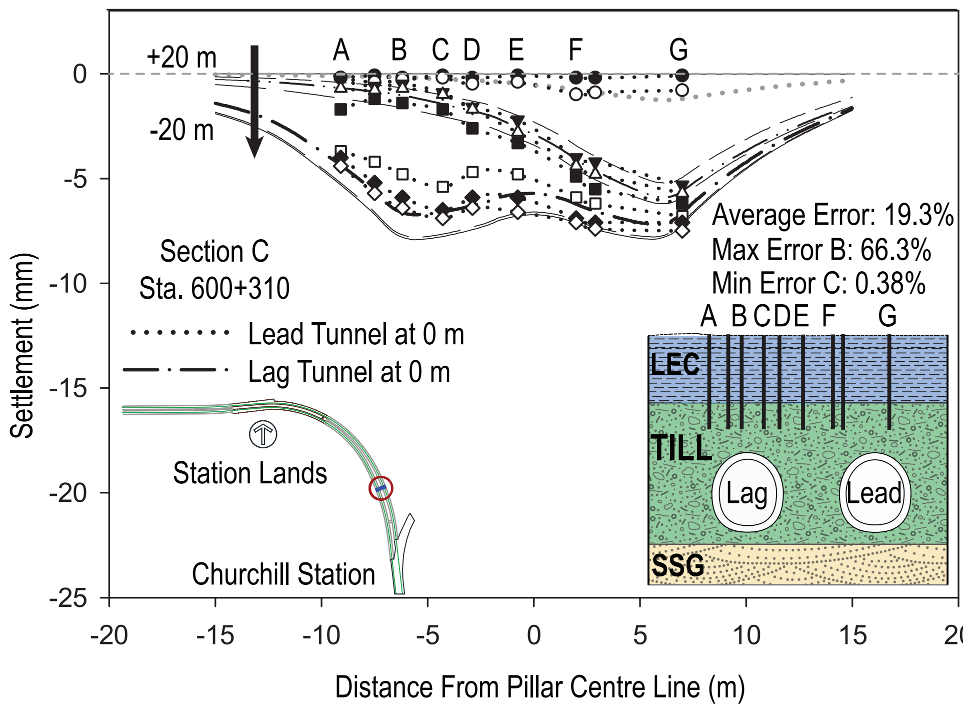

Figure 7.9. Calculated versus measured deep settlements across Section C

7.5.1.2 Section D (Mixed Face Conditions)

As described in Chapter 6, the monitoring section located within the mixed face soil conditions (Section D) was divided into two cross sections due to conflicts with subsurface structures. As a result, two numerical models were carried out to represent this section. The models were constructed to represent the ground conditions and tunnel depths at each half of the split cross-section and the data was combined for the final cross section. The two sections were located at distances of approximately 45 m (lag tunnel) and 80 m (lead tunnel) from the start of tunnelling of the eastern leg. The depth below the ground surface to the tunnel crowns at these sections was approximately 13.5 m (lead tunnel) and 16.5 m (lag tunnel).

Vertical displacements throughout the depth of the pillar were measured with a multipoint extensometer installed between the two tunnels at a distance of roughly 45 m from the start of tunnelling of this leg. Deep settlement measurements in the pillar were recorded by a multipoint extensometer point installed to a depth of 13.6 m below the ground surface. There was no shallow monitoring point within the pillar through this section as the shallowest extensometer point was 6 m below the ground surface. Figure 7.10 represents the calculated and measured shallow settlements above the tunnel crowns.

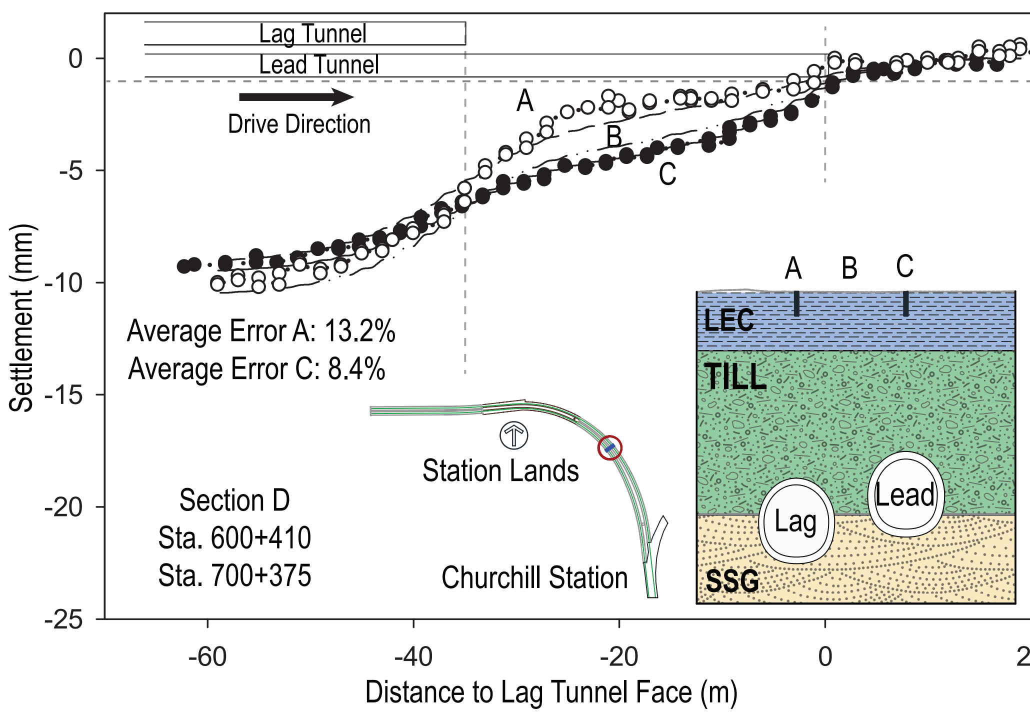

Figure 7.10. Calculated versus measured shallow settlements through Section D

Outside of the lead tunnel alignment, the calculated settlements on average exceeded those actually measured in the field by approximately 12%. The settlements were found to be uncharacteristically steep with little settlements occurring outside the tunnel alignments. Figure 7.11 illustrates the steepness in the settlement trough following excavation of the lead tunnel.

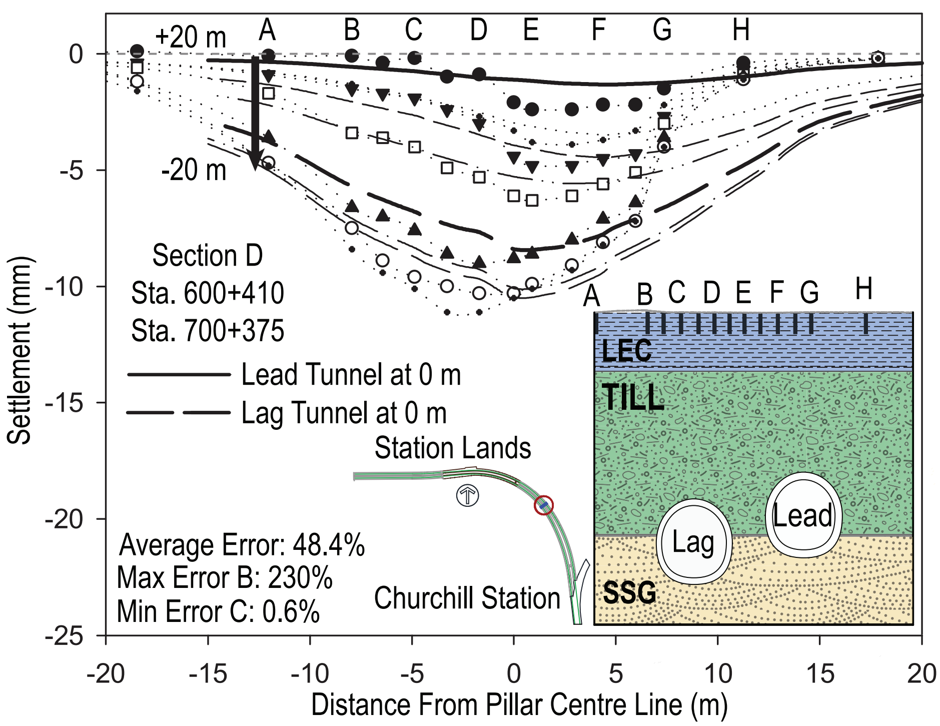

Figure 7.11. Calculated versus measured shallow settlements across Section D

Figure 7.12 illustrates a comparison of the results of the computed deep settlements with the measured values. The error through the two sections modelled at this section are a maximum of 2 mm at the start of the lead tunnel settlements and less than 0.2 mm for the final settlements. With the exception of the start of the lead tunnel, the difference between the curves did not exceed 0.5 mm. This corresponds with an average error between computed and measured values of around 10%. The error associated with the lead tunnel indicates that the settlement point “felt” the lead tunnel at a distance of approximately 1.5 tunnel diameters ahead of the tunnel face.

Approximately 65% of the total first tunnel settlements occurred prior to excavation of the tunnel cavity. This is roughly 15% higher than most cases where the pre and post excavation settlements were both approximately 50% of the total single tunnel settlements. This suggests either changed ground conditions or poor ground management during construction.

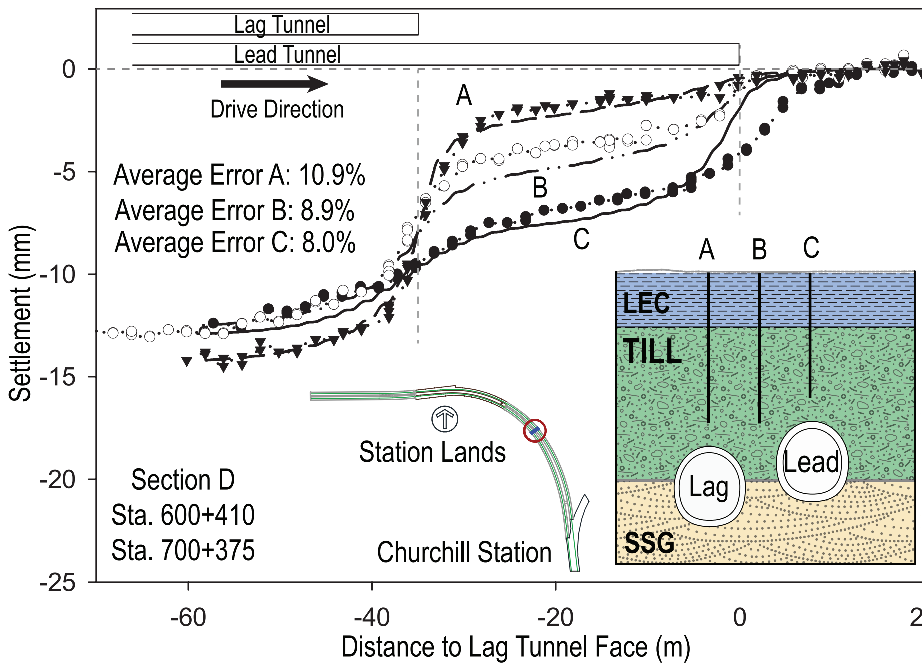

Figure 7.12. Calculated versus measured deep settlements through Section D

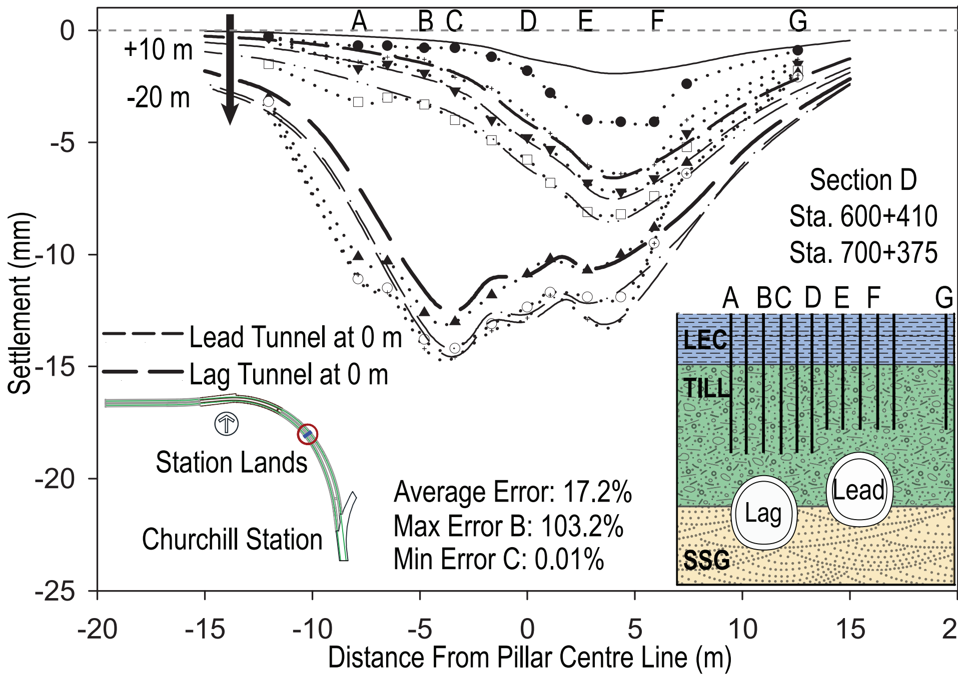

Figure 7.13. Calculated versus measured deep settlements across Section D

The measured and modelled deep settlement cross sections are shown above in Figure 7.13. It is important to note that the settlements illustrated here are from two separate models using the same elastic parameters, which reinforces the applicability of the linear elastic model used.

7.5.1.3 Section E (Homogeneous Glacial Till – Narrow Pillar)

Section E was located approximately 140 m east of the start of the tunnels along the western leg of the twin tunnel alignment. The tunnels through this section were like Section C, wholly within the glacial till. Also like Section C, the depth to the crowns was approximately 10.5 m below the ground surface. The primary difference between Sections C and E was the pillar width, which varied from 0.76D (Section C) to 0.23D (Section E).

The results of the measured and calculated shallow settlement profiles for Section E are shown below in Figure 7.14.

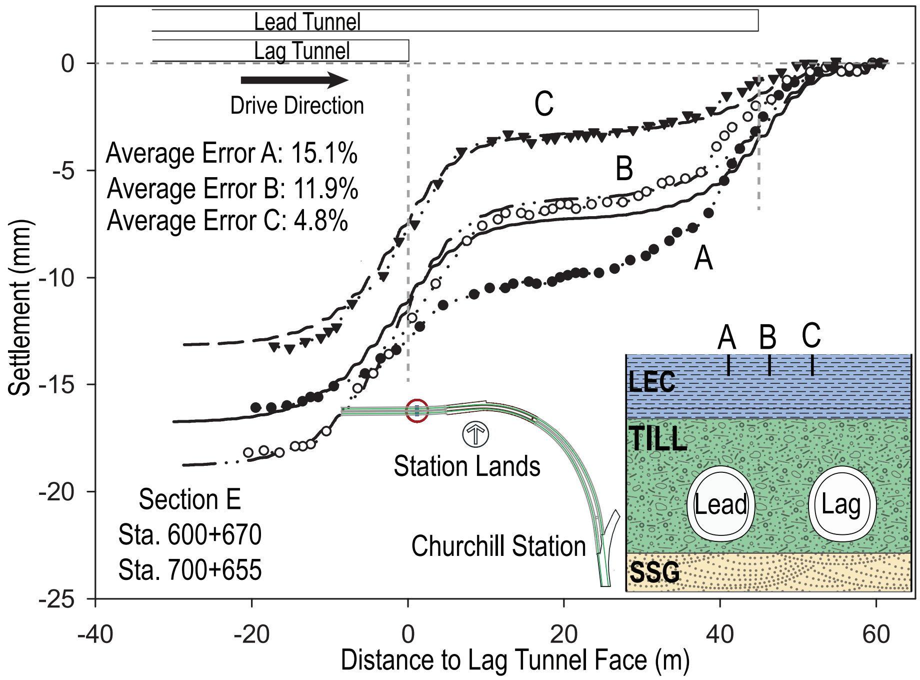

Figure 7.14. Calculated versus measured shallow settlements through Section E

Based on Figure 7.14, it is clear that there is a large discrepancy between the modelled and measured settlement values over the lead tunnel crown. It is suspected that yielding occurred around the lead tunnel during construction. This assumption can only be confirmed by examining the relevant yield surface. The computed stress path would indicate the appropriate yield surface; whether the frictional strength along the fissure surface is mobilized (residual) or if overstressing occurs (peak). Finally, the strains measured around the tunnel cavity would indicate whether peak or residual yield strains had been achieved. In this situation, an elasto-plastic numerical model would typically be implemented. However, this model may not always be relevant due to the expected stress paths around the tunnel cavity. This will be discussed in greater detail in subsequent sections.

The findings of the back-analysed pillar centreline and lag tunnel suggest that the elastic parameters given in Table 7.2 still closely represent the measured values. The average error of these two points is approximately 12 and 5% respectively. This suggests that if plastic deformations were recorded at Section E, the radius of the plastic region did not likely extend much beyond the tunnel perimeter.

As with the settlement trough at Section D, the settlement trough at Section E was also very steep beyond the tunnel cavities. The associated shallow settlement trough showing the calculated and measured settlements is shown below in Figure 7.15.

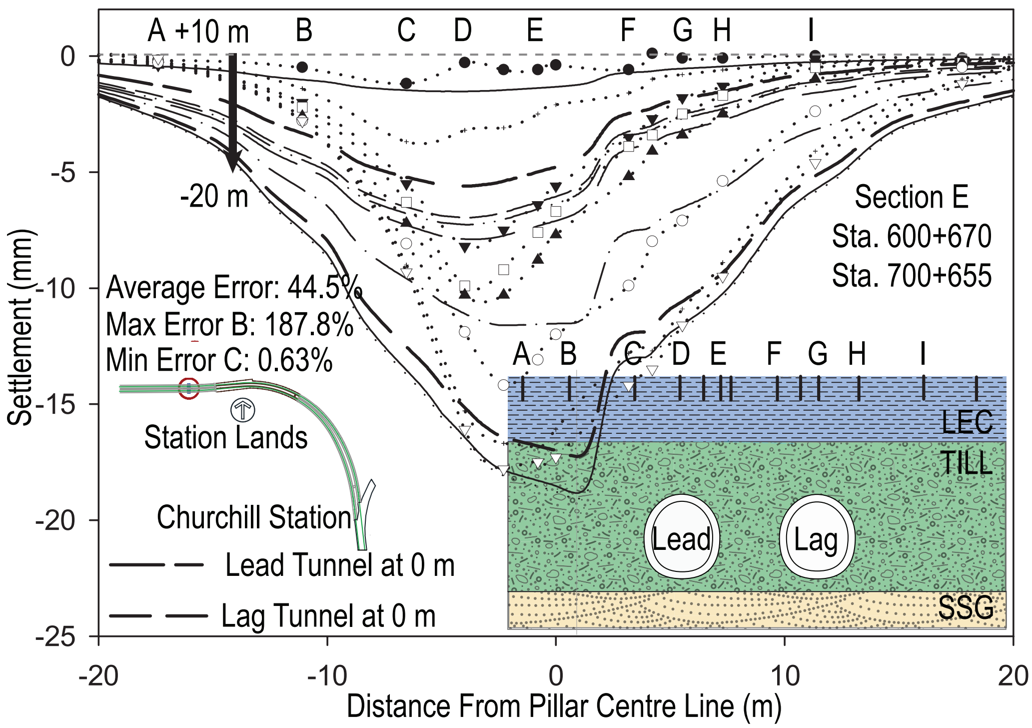

Figure 7.15. Calculated versus measured shallow settlements across Section E

When the deep settlements shown in Figure 7.16 are presented, it is clear that the elastic model does not represent the settlements measured above the lead tunnel well. The settlements measured within the pillar are from the multi-point extensometer MPE-E01 and the monitoring point installed to a depth of 11.6 m below the ground surface within the pillar near to the monitoring section. The comparison of the measured and modelled deep settlements across the monitoring section is provided below in Figure 7.17.

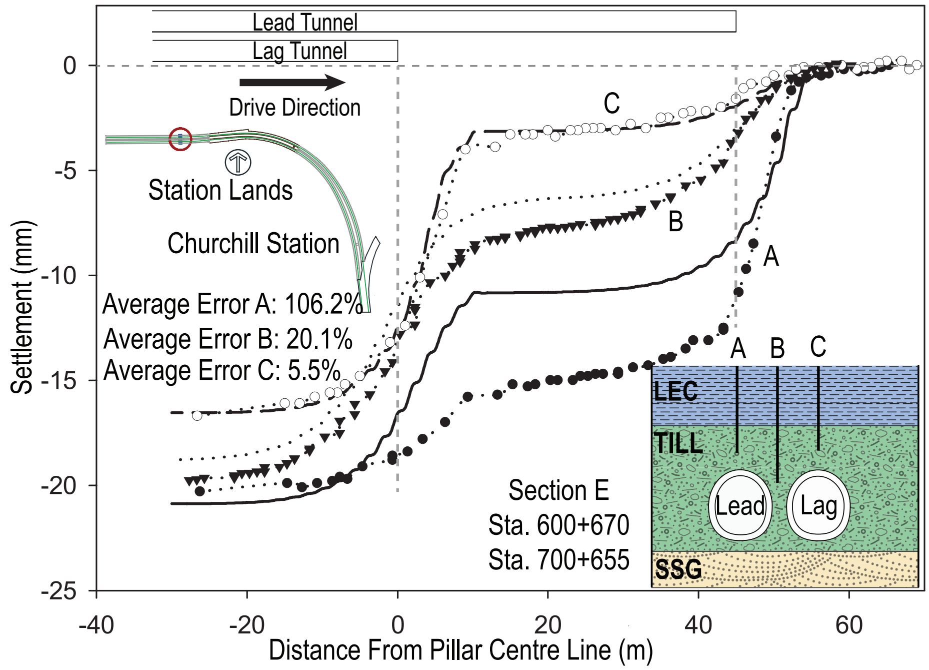

Figure 7.16. Calculated versus measured settlements through Section E above tunnel crowns and pillar

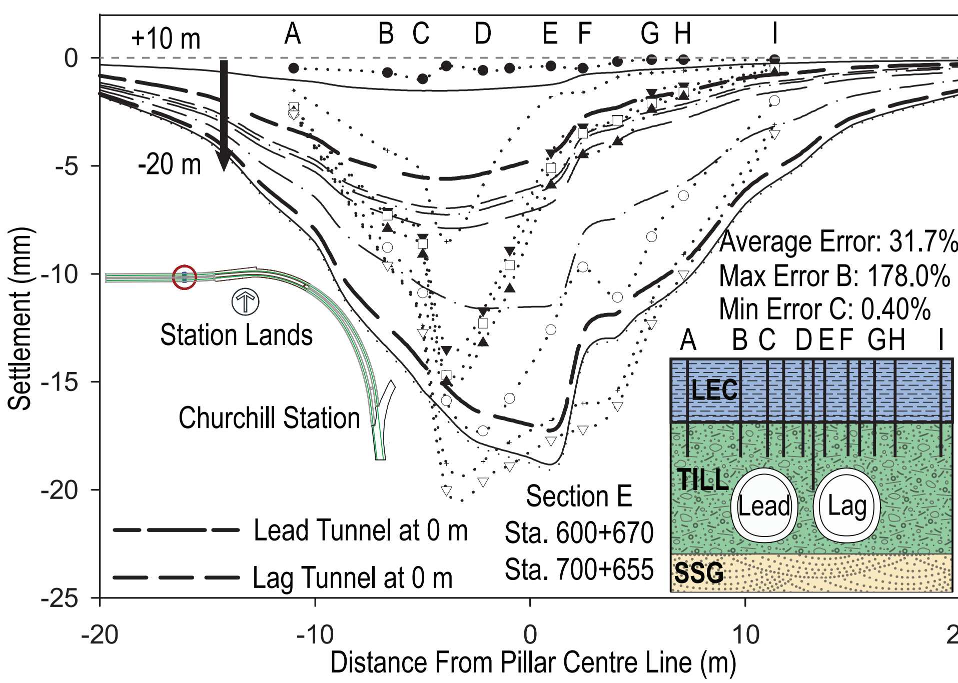

Figure 7.17. Calculated versus measured deep settlements across Section E

Again, like the shallow settlements, it is clear that the linear elastic model using the measured range of elastic parameters does not accurately represent the ground response when the pillar width is less than 0.5D. This suggests that yielding may be occurring and will need to be examined further in subsequent sections.

7.5.2 Horizontal Displacements

The numerical models produced total displacements and consequently, the results were compared to the inclinometer measured cumulative displacements. The numerical simulations were best at providing an estimate of the location of maximum and unconformity related displacements. The majority of error between the measured and calculated lateral displacements was observed near to the ground surface and always within the glacio-lacustrine clay. This aspect was consistent throughout all of the simulations.

In all cases, the modelled pillar inclinometer resulted in displacements that moved progressively away from the centreline of the pillar towards the approaching first tunnel. This movement was then followed by equal displacements back to the centreline as the second tunnel approached and passed. These findings are consistent with a linear elastic model. The measured displacements however did not always exhibit similar results. In none of the locations did the lateral displacements completely return to zero following passage of the lag tunnel, though some were close.

7.5.2.1 Section C (Homogeneous Glacial Till – Wide Pillar)

As previously stated, the tunnel depth at Section C is similar to that of Section E. Therefore any differences between the two sections will be mainly attributed to the pillar width. Figure 7.18 shows the measured and calculated displacements through the pillar at Section C.

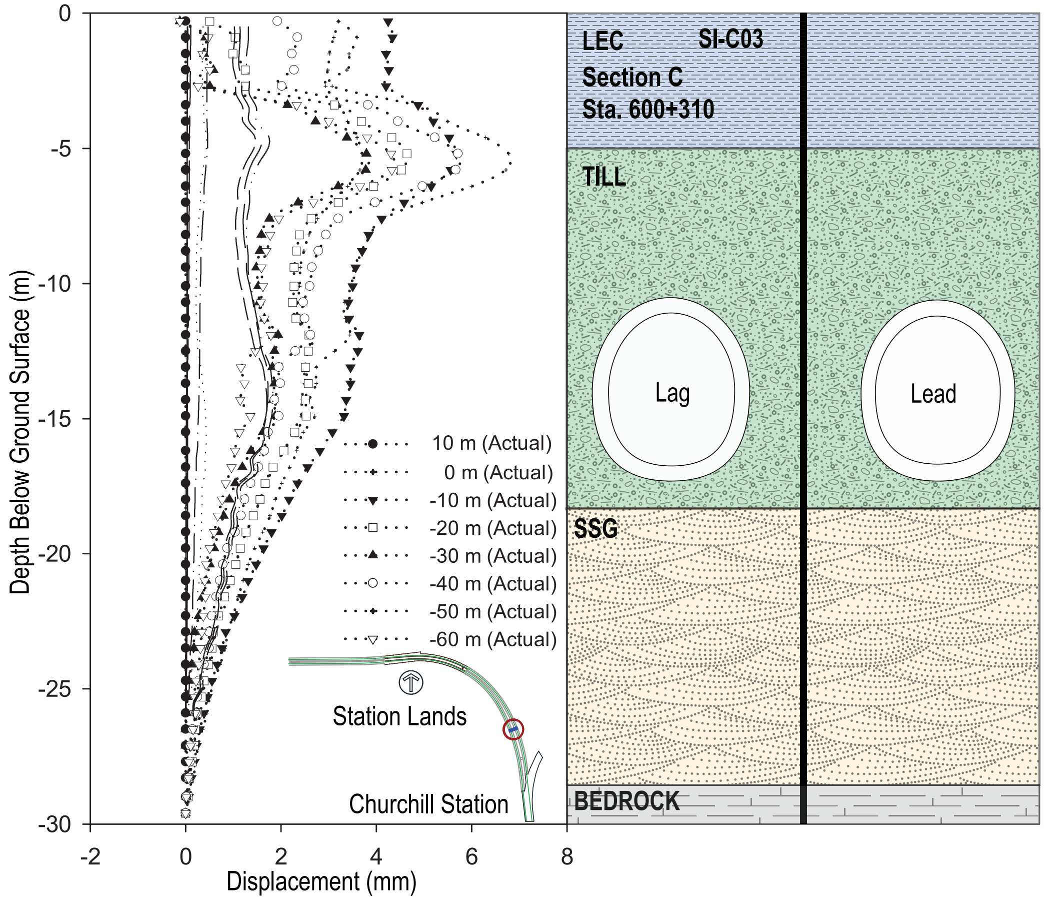

Figure 7.18. Comparison of elastic model with Section C inclinometer results

In this case the measured displacements through the tunnel face nearly return to zero following the passage of the lag tunnel. The error between the measured and computed values through the tunnel face is approximately 33%, which corresponds with a discrepancy of only 1.2 mm. The inclinometer indicated a maximum lateral displacement into the lead tunnel of 3.45 mm while the elastic model estimated 1.85 mm.

The lateral displacements on the outside of the lead tunnel are well represented by the numerical simulations as shown below in Figure 7.19. The difference between the maximum displacements within the tunnel face is only 0.2 mm. The average error between the calculated and measured values through the tunnel face is only 19%. The difference between the measured and predicted values is less than the error of the monitoring equipment and is therefore considered representative of the site conditions.

It is interesting to note that the calculated displacements exceed the measured values in a number of locations suggesting that the Poisson's ratio could be slightly less than the 0.34 used. When the Poisson's ratio was reduced to 0.33 however, the calculated lateral displacements were moderately improved in comparison to the measured values. This improvement however was at the expense of the settlement predictions, which reduced considerably and were no longer representative. This then suggests that the Poisson's ratio is well bounded by 0.33 and 0.34 with 0.34 providing a closer relation.

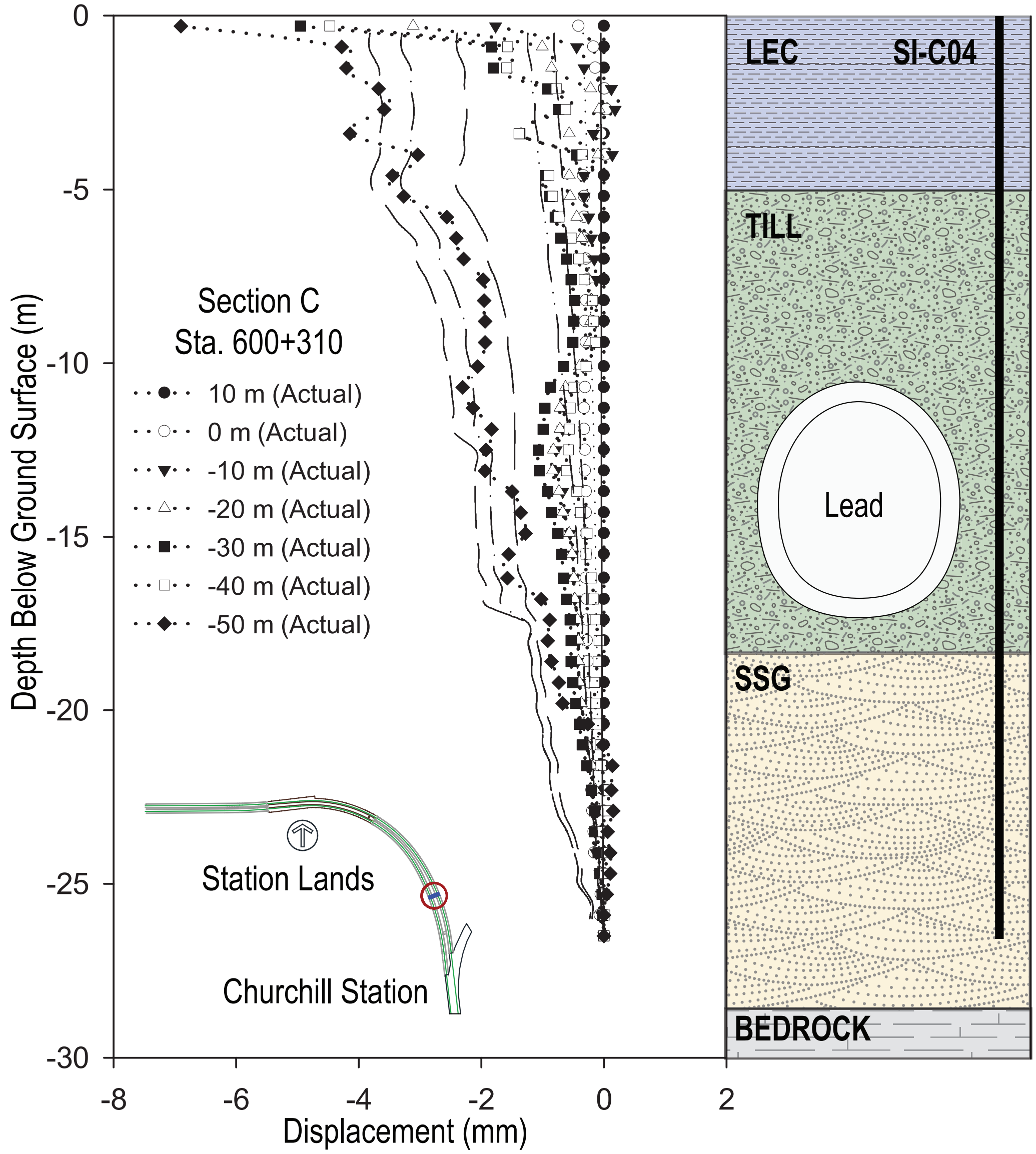

Figure 7.19. Comparison of later displacements outside lead tunnel at Section C

7.5.2.2 Section D (Mixed Face Conditions)

The lateral displacements measured in the inclinometers installed through Section D indicated that there were large differential displacements between the two materials, which comprised the tunnel face. The numerical model also confirmed this. The depth to the top of the tunnel crown was approximately 15.5 m while the top of the bench was approximately 18.0 m below the ground surface at Section D. From the figure, measurements of the inclinometer installed through the centre of the pillar suggest that the maximum displacements occurred at a depth of around 18.5 m below the ground surface. This point is nearly coincident with the centre of the tunnel bench and the unconformity of the Empress Sand and the glacial till. The calculated point of maximum displacement was also found to be at a depth of 18.5 m below the ground surface. Maximum displacements measured in the inclinometer were approximately 4.4 mm while the numerical model calculated a maximum lateral displacement of 3.6 mm for an error of 18%. The calculated and measured lateral displacements within the pillar at Section D are shown below in Figure 7.20.

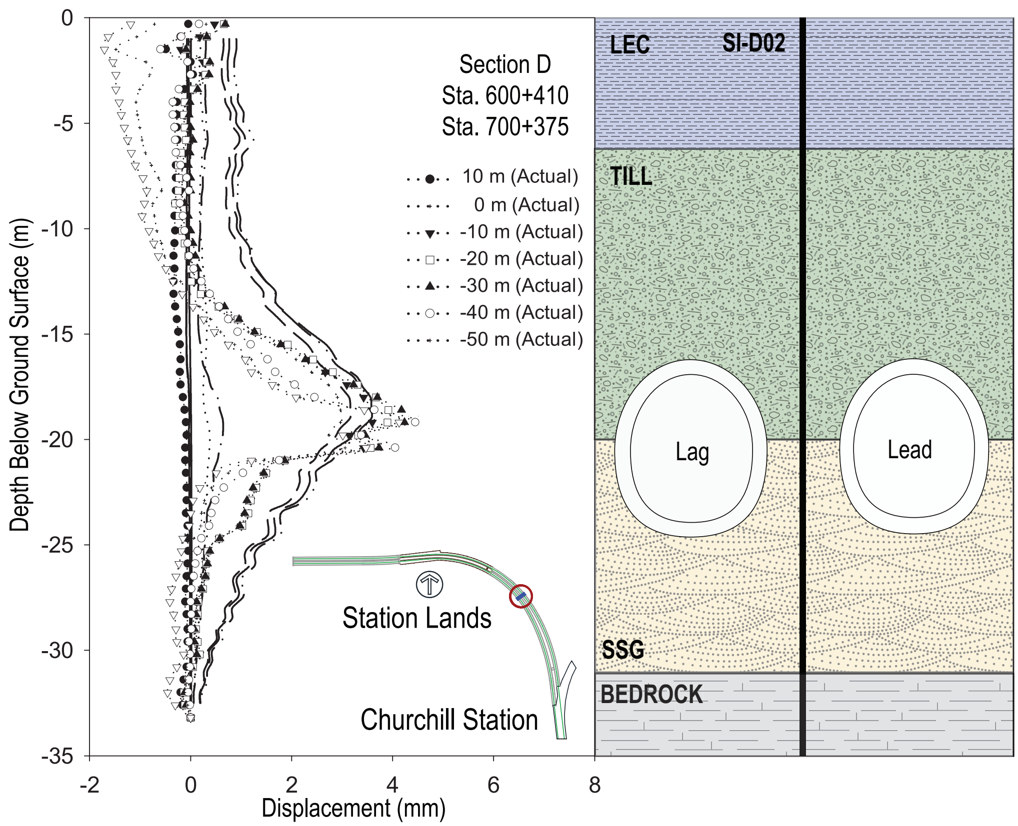

Figure 7.20. Calculated versus measured lateral displacements through the pillar at Section D

It is assumed that minor yielding took place within the pillar since the measured displacements did not return to zero following passage of the second tunnel. As discussed in Chapter 6, the shear strains also indicated final strains greater than 0.25%, which is equal with the active compressional yield strain criteria given in Chapter 5. Yielding is therefore suspected to have occurred through the height of the bench or between depths of 16 to 19 m below the ground surface.

For the lateral displacements outside the lead tunnel, the cover above the tunnel crown was approximately 14 m. The numerical model predicted that the maximum lateral displacements would occur at a depth of 14.0 m while the actual field measurements indicated a maximum displacement (through the tunnel section) at a depth of 13.9 m below the ground surface. The calculated and measured lateral displacements outside the lead tunnel at Section D are shown below in Figure 7.21.

The maximum displacement occurs in the header on the outside of the tunnel and within the bench within the pillar. This may be a function of the shape of the settlement trough. As the ground moves into the tunnel cavities, the associated displacement fields influence the inclinometer. Because the inclinometer in the pillar would be subjected to the combined displacement fields of both tunnels, the overlap of the displacement fields may be concentrated lower along the instrument. Regardless of the cause, the numerical model appeared to represent these findings reasonably well.

The maximum calculated displacements were 2.4 mm into the lead tunnel while the maximum measured displacement was 3.5 mm corresponding with an error of 31%. The average error through the tunnel face is calculated to be 12% suggesting a very strong correlation.

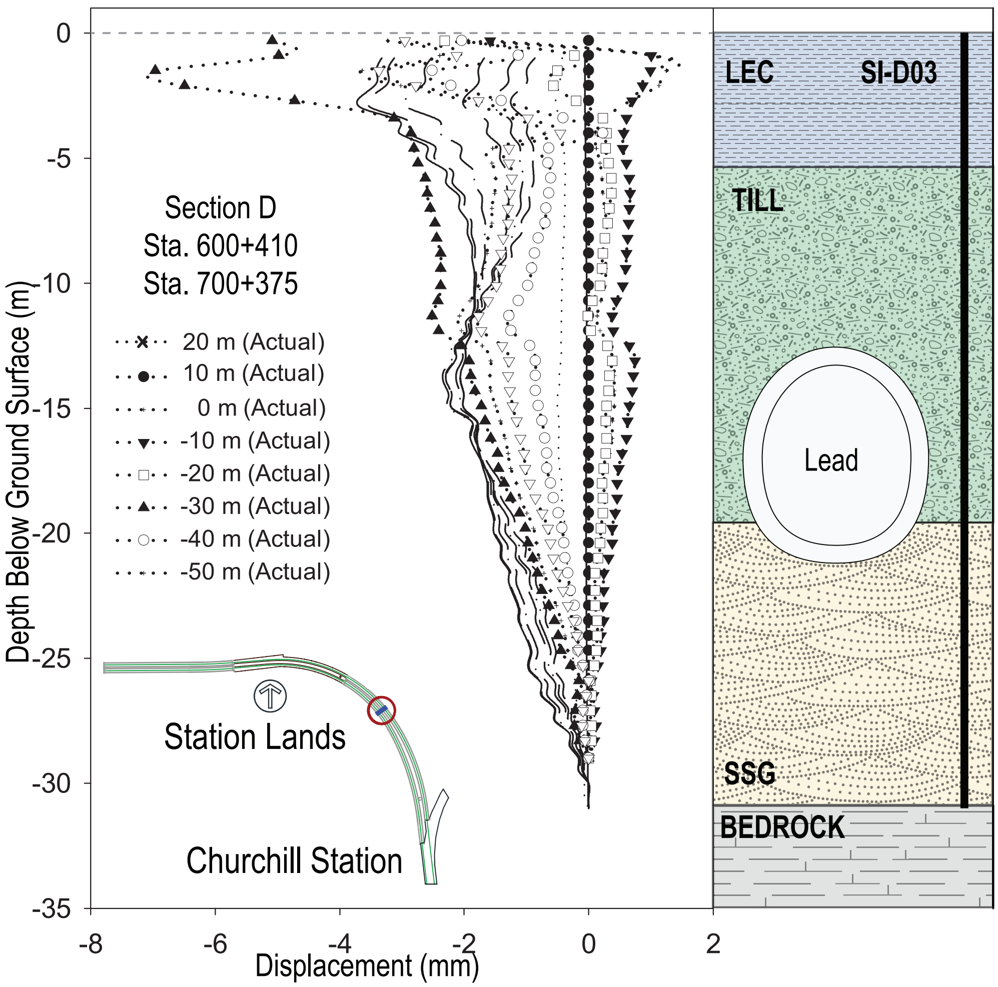

Figure 7.21. Calculated versus measured lateral displacements outside of the lead (Southbound) tunnel at Section D

The numerical model indicated the discontinuity at the ground surface corresponding with the contact with the glacio-lacustrine clay. The absolute calculated values however do not compare. It is unknown whether the measured values are real or if there was damage to the inclinometer casing. To the author's knowledge, there is no known cause for the anomaly measured at the geologic unconformity between the Lake Edmonton clay and the glacial till. The degree of lateral deformations was not observed outside the lag tunnel or anywhere else along the tunnel alignment.

7.5.2.3 Section E (Homogeneous Glacial Till – Narrow Pillar)

In the case of Section E the numerical model tended to overestimate the lateral displacements by roughly 2 times those measured in the pillar. Outside the lead tunnel however, the measured values exceeded the predicted values by nearly 3 times. The computed values therefore are not representative of the conditions encountered in the field despite the relatively strong relationship with the lag tunnel surface settlement data.

Section E possessed the narrowest pillar of the alignment, which was 1.48 m or 0.23D in width. This is in comparison to Section C where the pillar width was 5.1 m (0.76D). Therefore the calculated displacements should be considerably greater than those estimated at Section C.

The tunnel depth through this section is similar to Section C and was between depths of 11.25 and 18 m below the ground surface. The header extends to a depth of around 13.8 m below the ground surface. As stated in Chapter 6, the inclinometer in within the pillar at Section E was replaced with an SAA. A comparison of the numerical simulation and the measured displacement results are shown below in Figure 7.22

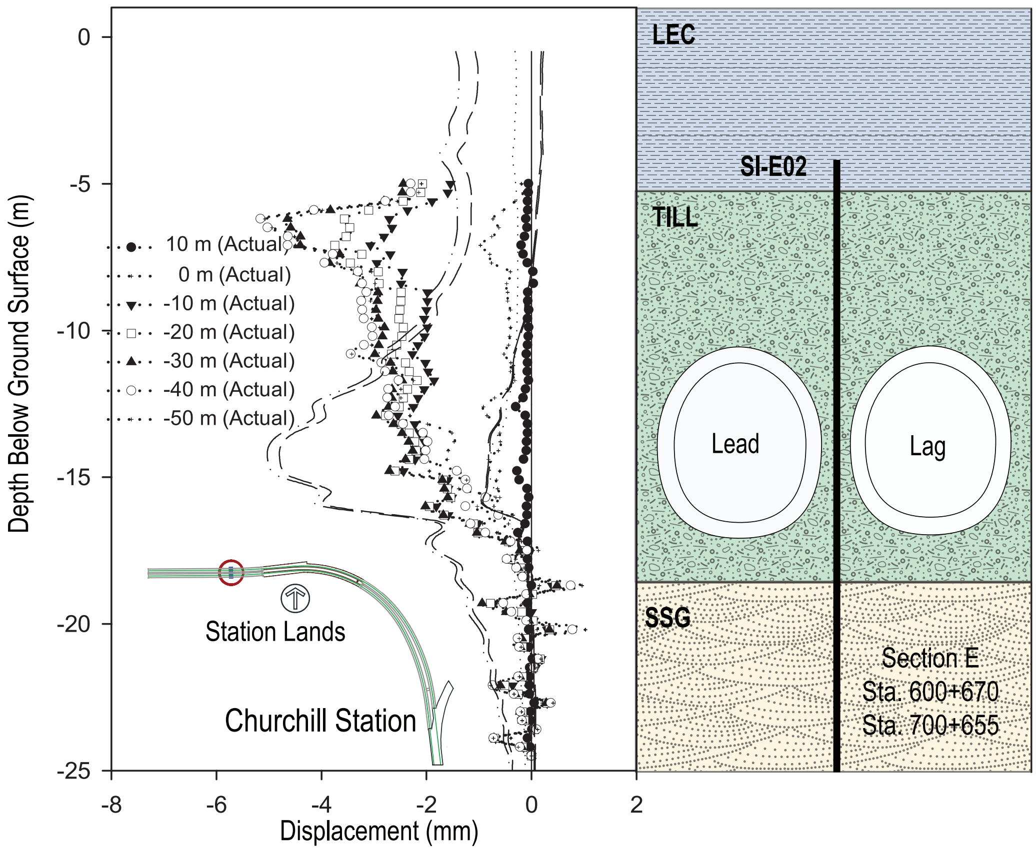

Figure 7.22. Comparison of lateral pillar displacements at Section E

Based on Figure 7.22, there is a large discrepancy between the numerical model and the measured values. The error between the maximum points within the tunnel face is approximately 2.1 mm. This corresponds with an average error through the tunnel face of approximately 81%. Considering the total displacements measured and the error at other monitoring sections is relatively high.

Figure 7.23 illustrates the comparison between the inclinometer measurements and the numerical model outside of the lead tunnel at Section E.

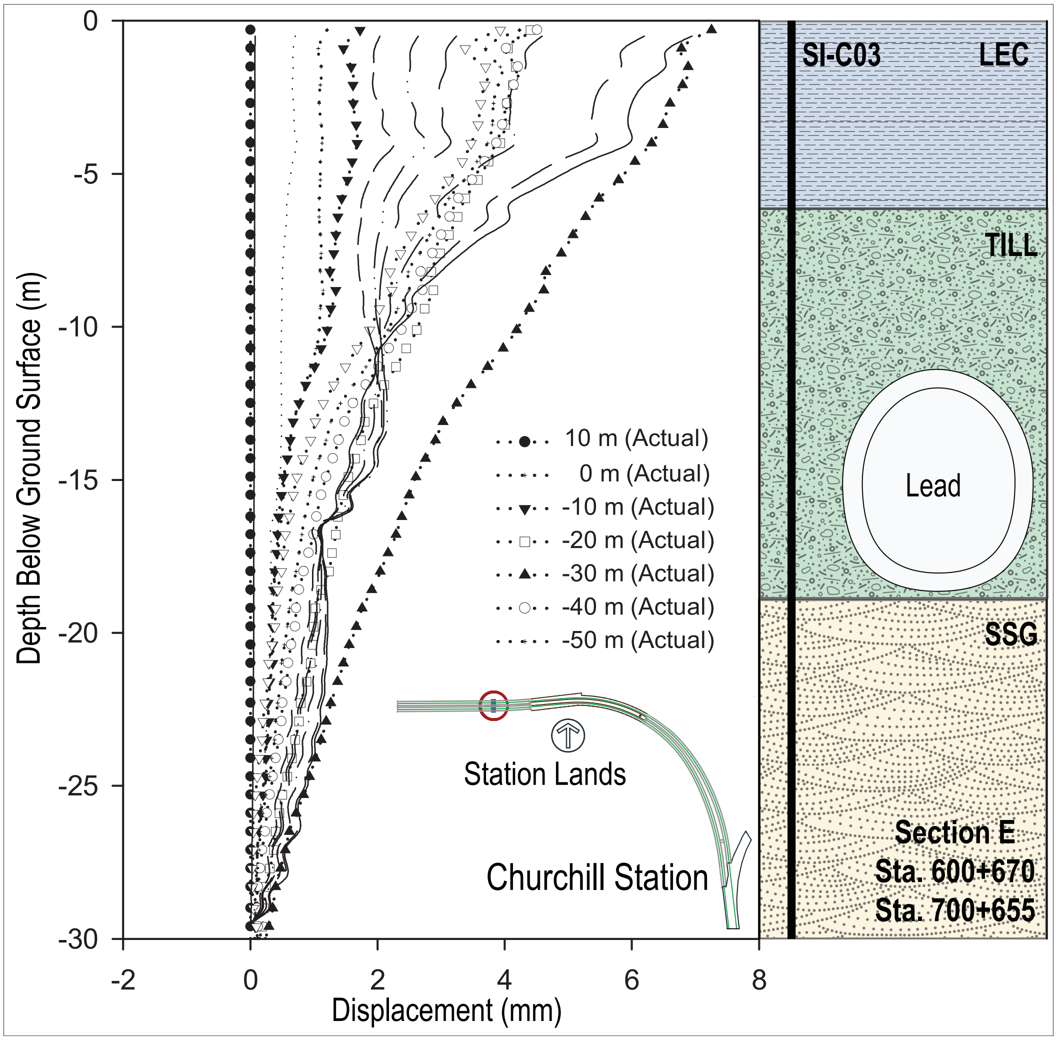

Figure 7.23. Comparison of lateral displacements outside of lead tunnel at Section E

Figure 7.23 shows that the lateral displacements exceed the elastic numerical model considerably at this section. The discrepancy between the measured and predicted values is approximately 4.5 mm at the tunnel crown and 3.5 mm at the invert.

7.5.3 Convergence

7.5.3.1 Tape Extensometer

Tape extensometer measurements were recorded within the lead tunnel to measure the change in chord length with the approach and passage of the lag tunnel. From the model convergence calculations, changes in chord length across the tunnel cavity were made in order to provide comparable values. This was done by establishing *x* and *z* coordinates at each monitoring location and tracking the change in the coordinates between two points. Once the change in coordinates was found, a resultant vector was calculated between two monitoring points across the tunnel cavity as the change in chord length.

Figure 7.24 to Figure 7.26 present the measured tape extensometer values with respect to the lag tunnel face location for Section D. Each figure also illustrates the change in chord length as calculated from the linear elastic numerical model. It should be noted that in the figures below, that a reduction in tunnel diameter is represented by positive convergence while extension is represented as negative convergence.

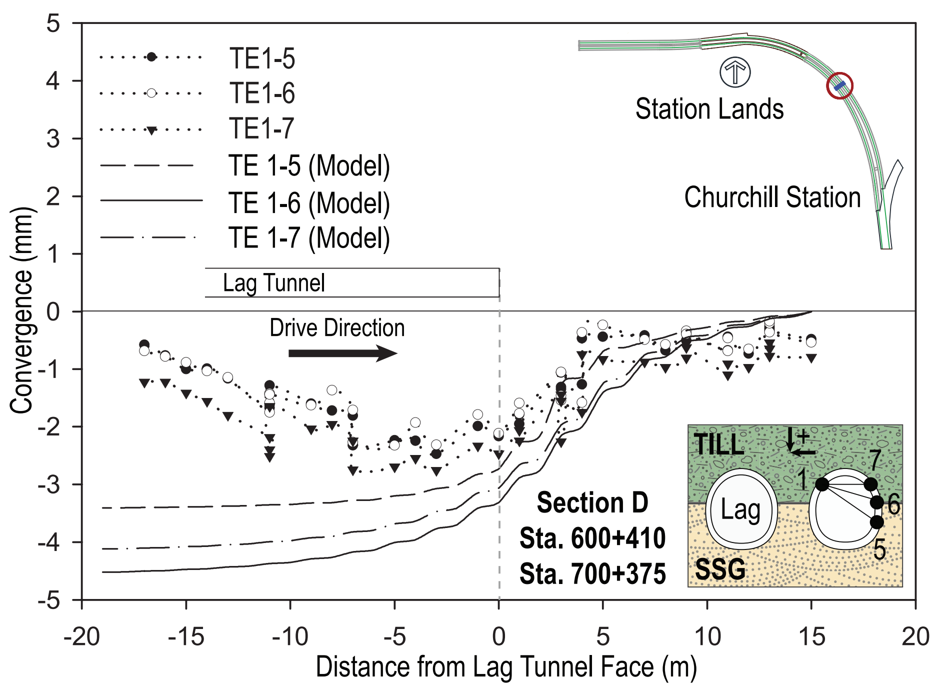

Figure 7.24. Calculated versus measured change in tunnel chord length with the approach of the lag (Northbound) tunnel at Section D

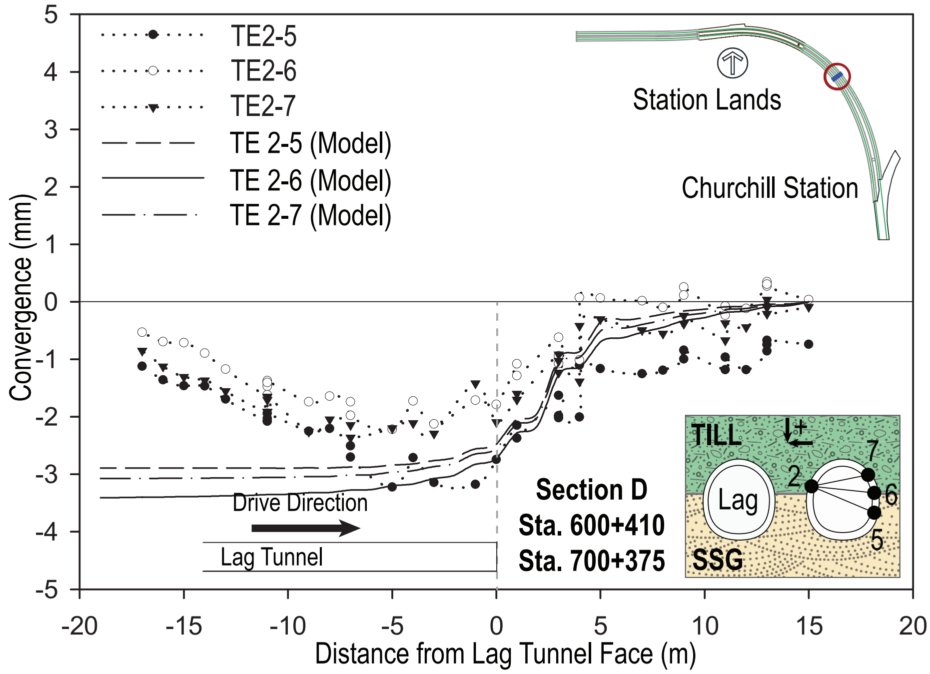

Figure 7.25. Calculated versus measured change in tunnel chord length with the approach of the lag (Northbound) tunnel at Section D

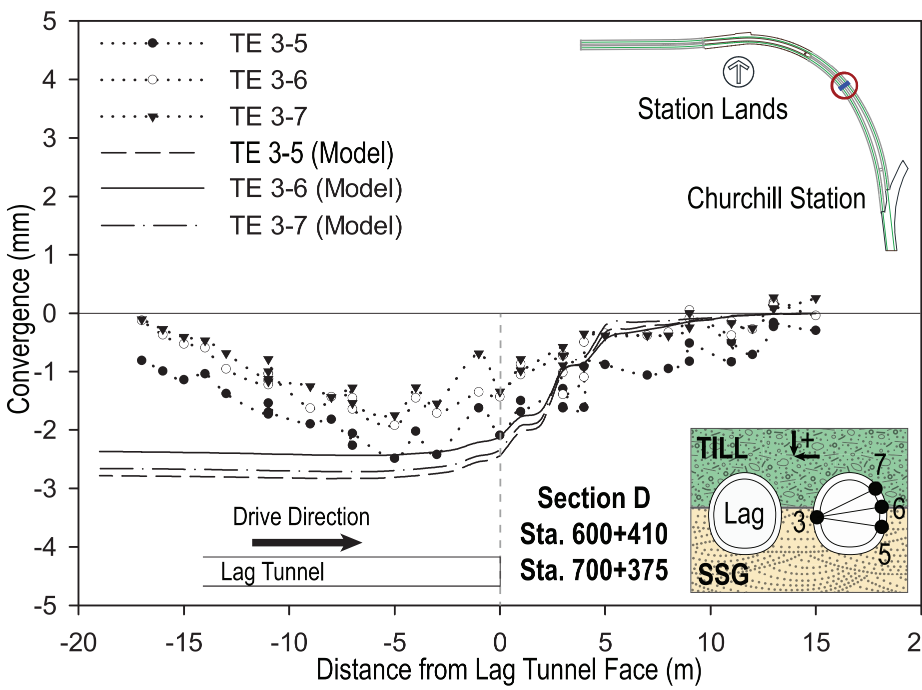

Figure 7.26. Calculated versus measured change in tunnel chord length with the approach of the lag (Northbound) tunnel at Section D

The results of the tape extensometer modelling suggest that the model reasonably predicts the displacements of the lead tunnel into the lag tunnel up to a distance of 7 m (1D) behind the lag tunnel face. It is possible that the lag tunnel liner is being activated at this point and begins to elongate in the lateral direction resulting in compaction of the pillar. It is more likely though that the displacements towards zero are a result of increased pillar stresses resulting in lateral strains during vertical compression. Review of the numerical simulation data indicates that there is some reduction in the tunnel diameter after a distance of 6 m behind the lag tunnel face. These recovery displacements are minor and are between 0.05 and 0.1 mm.

With respect to the relevance of the back analysis, the difference between the peak measured and calculated values is 0.6 to 1.1 mm or an average error of 15%. This suggests that it is likely that the lead tunnel is moving as a whole into the lag tunnel during the tunnels approach and passage.

At Section E, the results are slightly more convincing. This is due to the fact that the increase in tunnel width did not recover following passage of the lag tunnel. The measured and calculated widening of the lead tunnel due to the influence of the lag tunnel is shown below in Figure 7.27 and Figure 7.28.

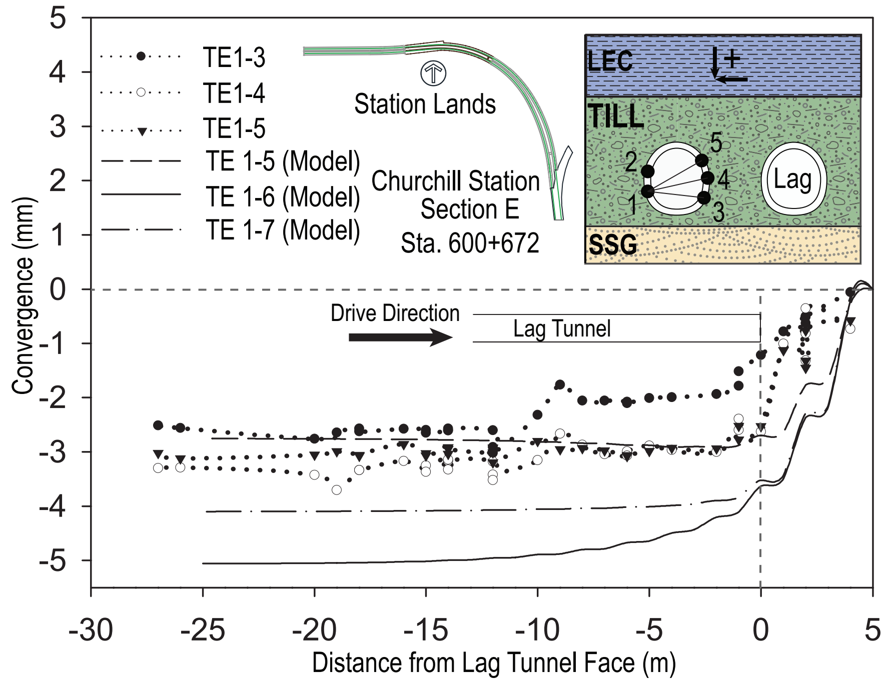

Figure 7.27 Comparison between measured and calculated lead tunnel displacements at Section E

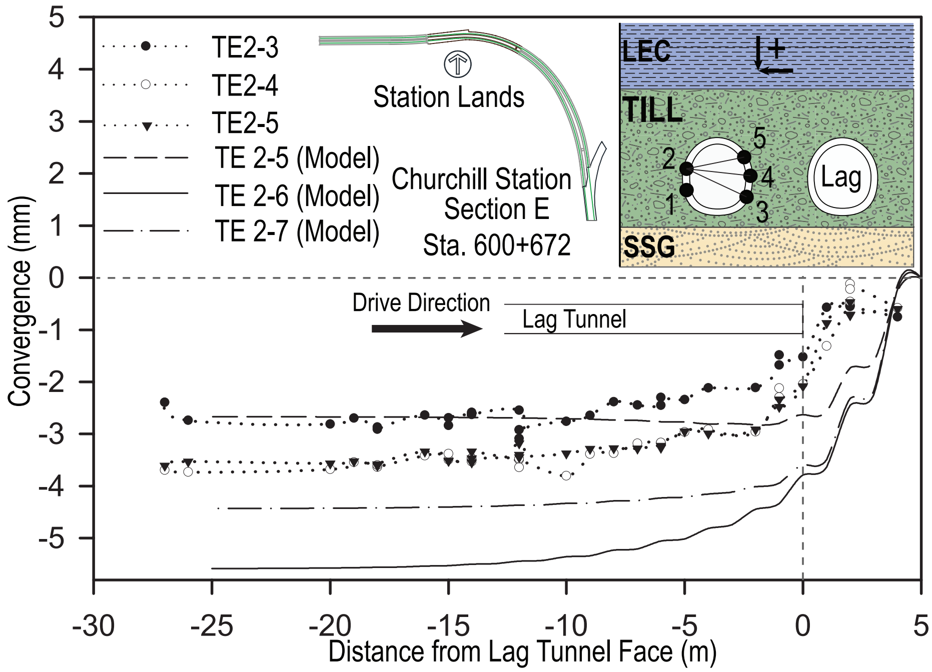

Figure 7.28 Comparison between measured and calculated lead tunnel displacements at Section E

In this case, it is clear that there is a cluster of consistent data measured in the tunnel cavity and this cluster is well represented by the chord simulated at Point 5. Using this data, the error is minor and averages only 2 to 6% suggesting a very strong correlation with the actual data. Outside this chord length, the error increases considerably ranging from 36 to 43%. Though this percentage error is very high, the actual displacements on average only differ by 1.6 to 2 mm.

7.5.4 Shape Accel Array Convergence

As discussed in Chapter 6, a Shape Accel Array (SAA) was installed around the inner circumference of the lead tunnel at Section E (Northbound West Tunnel Meter 141.5). The purpose of the SAA was to capture the displacement of the lead tunnel during construction of the lag tunnel. The results of the monitoring program were then compared with the findings of the numerical model to determine the efficacy of the monitoring method. The SAA results were separated in terms of total (circumferential), horizontal and vertical displacements.

In order to simulate the spacing for the SAA, the mesh surrounding the tunnel cavities had to be refined. In general the elements were reduced to less than 0.15 m in length, which is a reduction from around 0.25 m. This permitted displacement monitoring of each element around the circumference of the lead tunnel for comparison. It is expected that this further refinement only improved the resolution of the calculated displacements relative to the previous simulations. Because the model was linear elastic, the total displacements would not be impacted by the mesh refinement to any significant degree. Figure 7.29 illustrates the measured versus the modelled total displacements around the tunnel circumference.

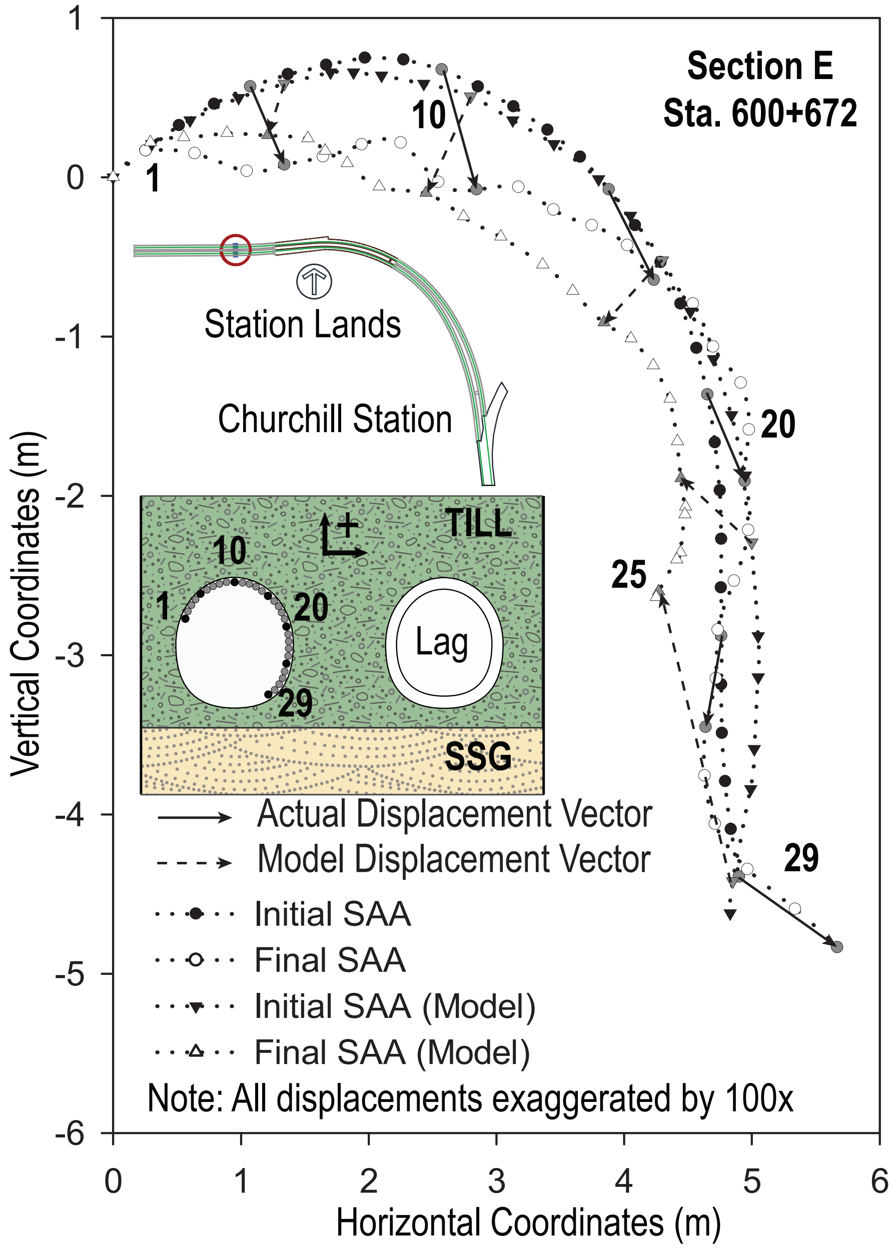

Figure 7.29. Calculated versus measured total displacements around the lead tunnel with the approach of the lag (Northbound) tunnel at Section E

From Figure 7.29, when the vertical displacements dominate the measured displacement vectors, the model does a good job reproducing the SAA data. However, when the horizontal displacements are the dominant vector, then the model has significant difficulty in producing similar values. It is important to note that the model predicted a rise in the tunnel through the springline (shortening of the tunnel height) following passage of the lag tunnel. This is in agreement with elastic rebound of the ground following unloading. This is in comparison to the SAA, which measured what is expected and that is a continual downward trend with time at all points.

Figure 7.30 through to Figure 7.33 show measured and calculated horizontal and vertical displacements for the SAA at Section E. The figures below represent charts of best and worst case scenarios. The remaining figures are provided in Appendix C.

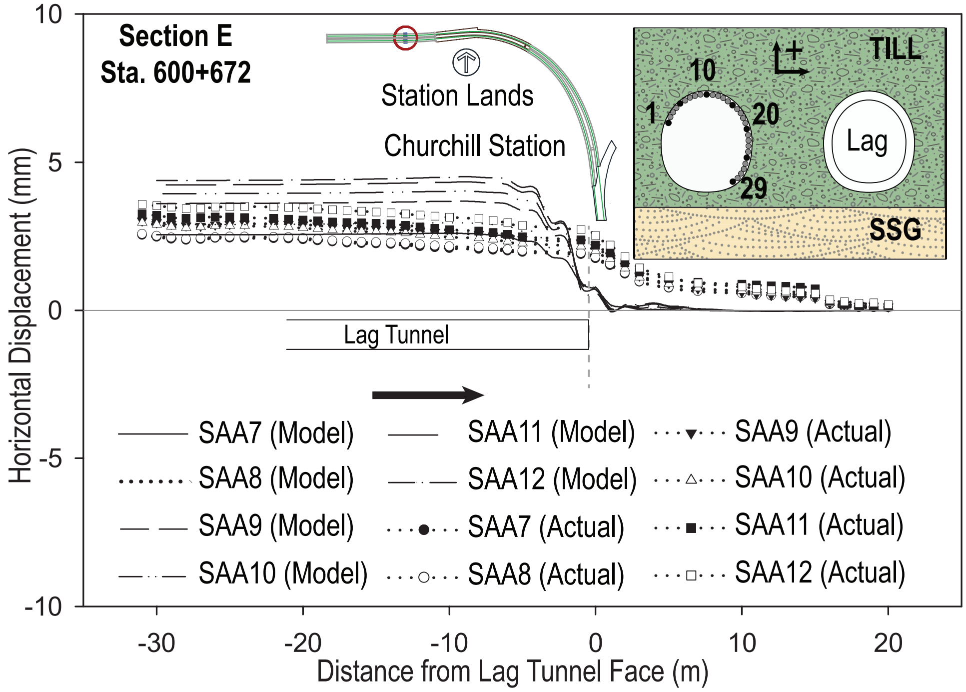

Figure 7.30. Best case calculated versus measured horizontal displacements around the lead tunnel with the approach of the lag tunnel at Section E

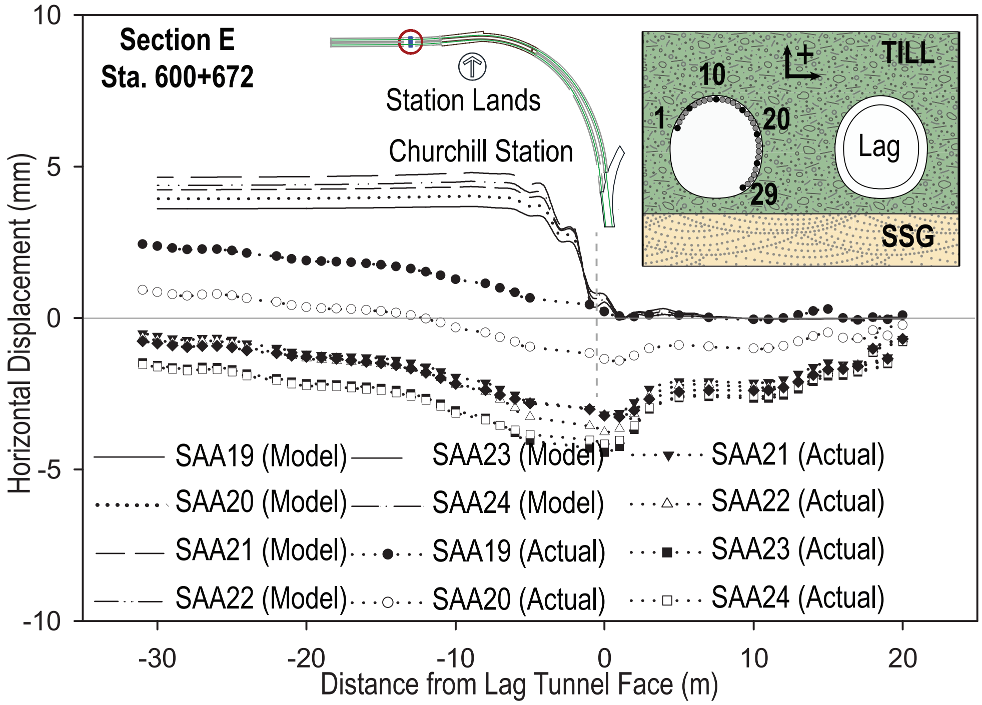

Figure 7.31. Worst case calculated versus measured horizontal displacements around the lead tunnel with the approach of the lag tunnel at Section E

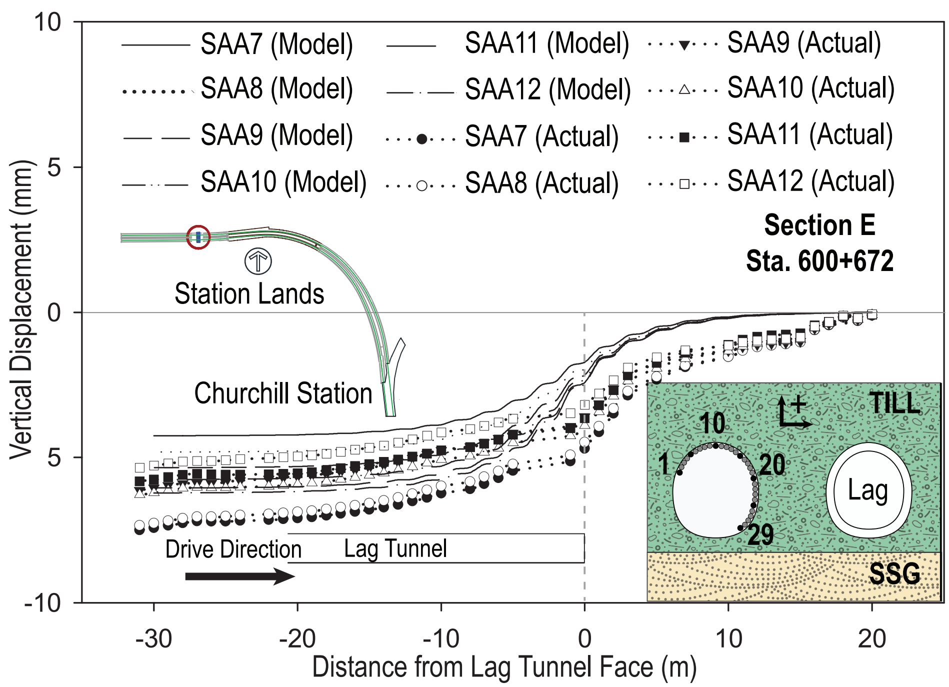

Figure 7.32. Best case calculated versus measured vertical displacements around the lead tunnel with the approach of the lag tunnel at Section E

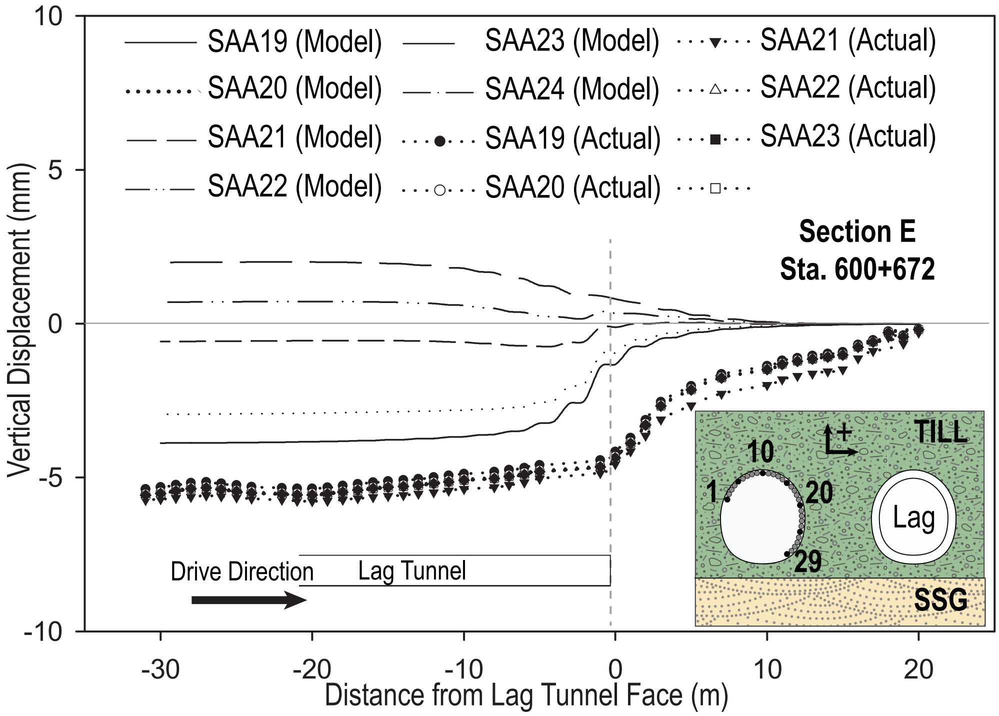

Figure 7.33. Worst case calculated versus measured vertical displacements around the lead tunnel with the approach of the lag tunnel at Section E

The above figures demonstrate that the elastic model does not reasonably represent the displacements measured by the SAA in any location except the crown. If only the crown displacements are considered, the only major error between the calculated and measured values occurs during the approach of the lag tunnel where the lead tunnel begins to respond to the release of stress at the start of the monitoring or 20 m ahead of the lag tunnel face. In all the average best-case error is between 16 and 22% while the worst-case error though the springline/invert is more than 200%.

7.5.5 Stresses and Strains around the Tunnel Cavity

The stresses surrounding the tunnel cavity have been estimated from the results of the vibrating wire strain gauge monitoring installed within the shotcrete liner. The numerical model was used to compare the change in σ_1 at each location with that of the change in calculated stress within the liner. For the calculation of the internal stresses within the shotcrete liner, it was assumed that the instruments were installed along the neutral axis and all strains were axial. As a result the stresses measured at each location were calculated assuming only an axial strain and a shotcrete stiffness of 26 MPa. The area of the shotcrete liner was also assumed as 75 mm per unit length. This depth corresponds with the thickness of shotcrete acting on the instrument or half of the temporary liner thickness.

The results presented below are from the monitoring section installed within mixed face conditions (Section D). At this location, the glacial till comprised approximately 0.5 to 0.7 m of the upper portion of the tunnel bench. In the numerical model, the glacial till was set as 0.7 m into the tunnel bench. The results from the second monitoring section (Section E) are provided in Appendix C.

When the calculated and measured values of liner stress are plotted, there are four distinct stress regions around the tunnel cavity. The first region is within the tunnel crown, which in this case extended from the shoulder furthest from the pillar to the shoulder closest to the pillar. Figure 7.34 illustrates the location of the installed strain gauges, which were coincident with the numerically modelled locations. It should be noted that tensile stresses are positive in accordance with structural sign conventions. This stress orientation is the opposite of conventional geotechnical sign conventions.

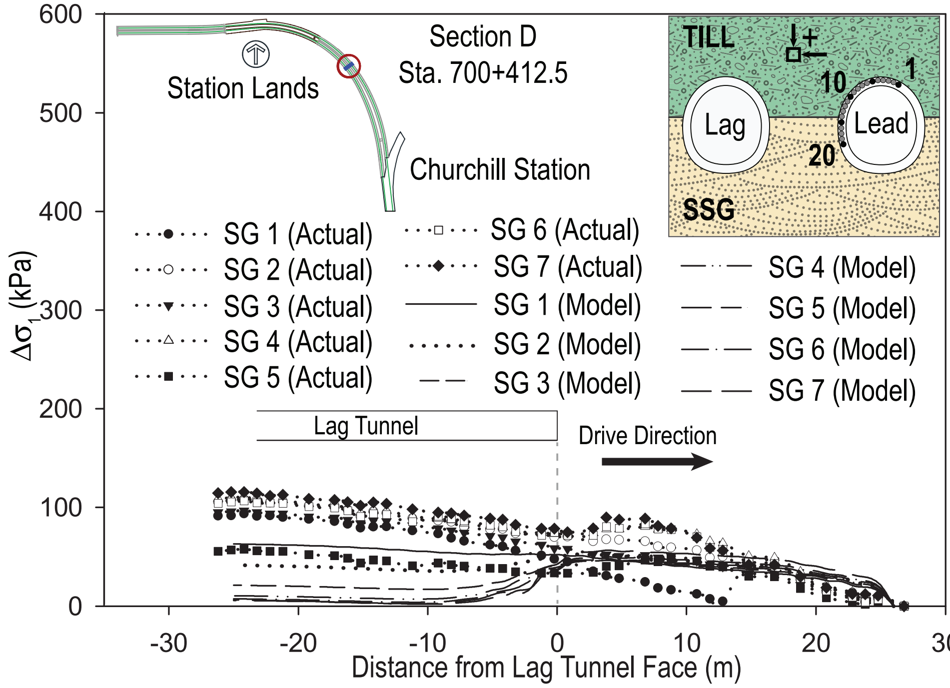

Figure 7.34. Calculated versus measured change in liner stress within the crown segment with the approach of the lag (Northbound) tunnel at Section D

From Figure 7.34, the numerical model did not accurately represent the trend of the measured values as the points moved from the far side of the tunnel towards the pillar (SG1 to SG7). The model indicates that the change in tangential stress approaches zero as the vertical stress approaches zero at the tunnel boundary with the passage of the lag tunnel. There remains some minor tensile stress within the elements, however these values are between 0 and 70 kPa and at their maximum represent the lower bound of the measured stresses. The stress trend calculated in the numerical simulation was not observed with the strain gauges. The instruments detected a slight reduction in tensile stress when the face of the lag tunnel was at the monitoring point. The tensile stresses gradually increased with distance from the lag tunnel face. This trend corresponds with increased vertical displacement of the crown into the tunnel cavity or squatting.

The next region involved the instruments installed from the pillar side shoulder to the springline within the glacial till. The locations of these instruments are shown below in Figure 7.35. As discussed in Chapter 6, the main purpose of these instruments was to detect any differences in the strain profiles between the mixed face conditions.

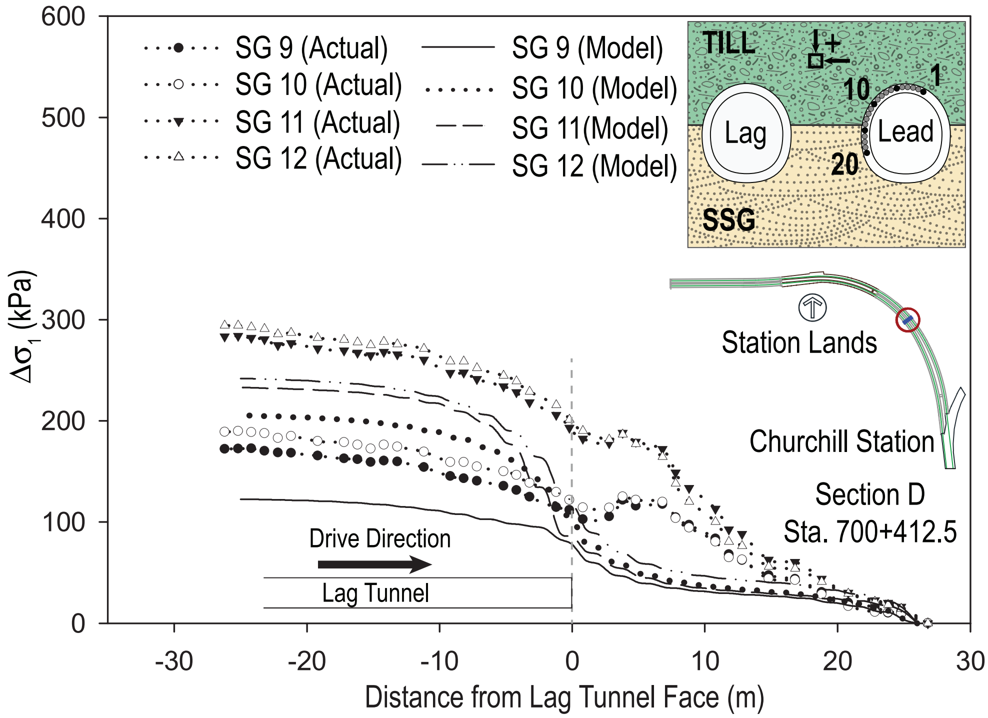

Figure 7.35. Calculated versus measured change in liner stress within the till springline segment with the approach of the lag (Northbound) tunnel at Section D

Through the springline of the tunnel within the till, the stresses are reasonably well represented by the model. The error between the predicted and measured values was approximately 50 to 60 kPa or roughly 17 to 25%.

Note that the strain gauges detected the passage of the lag tunnel with a slight drop in stress that later began to accumulate afterwards. Following the break in the slope of the second leg of stress change appears to approach the initial slope before developing a near constant stress at around two tunnel diameters past the lag tunnel. The numerical model does not detect a similar trend during passage of the lag tunnel, only subtle breaks in the curve related to the tunnel face excavation sequence used in the simulation.

The third section is where the strain gauges are installed within the tunnel springline through the Empress Sand. Figure 7.36 illustrates the measured and calculated values for comparison.

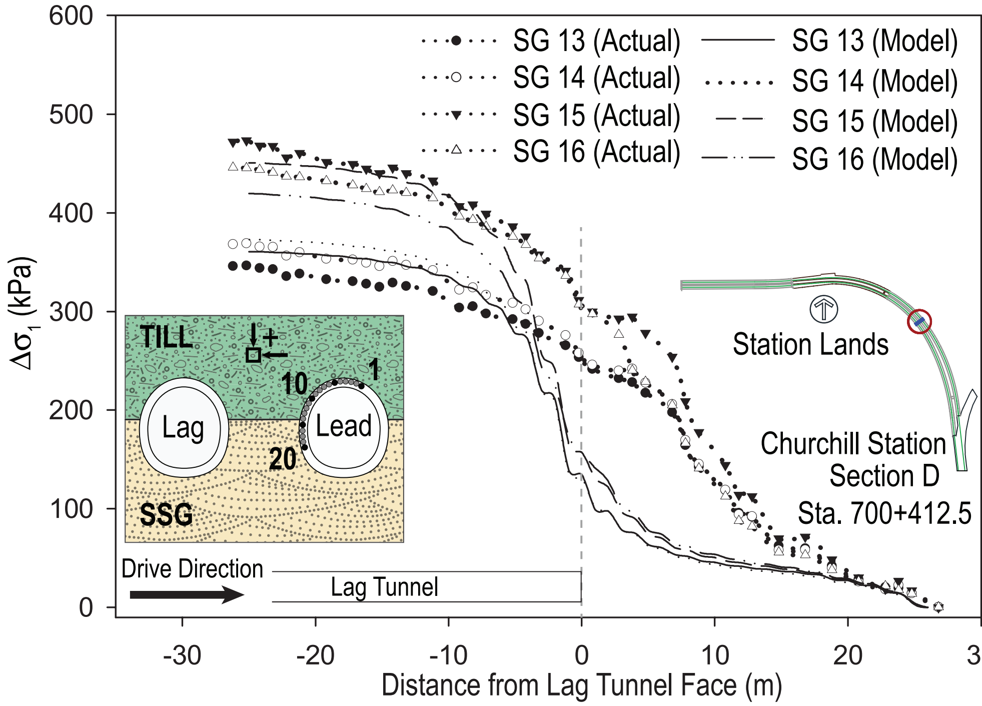

Figure 7.36. Calculated versus measured change in liner stress within the sand springline segment with the approach of the lag (Northbound) tunnel at Section D

Like the gauges within the springline in the glacial till, the numerical model closely represents the final stress measurements within the Empress Sand. In this section, the degree of error between the predicted and measured stresses is less than the glacial till and is typically between 15 and 20 kPa or roughly 5 to 10%. The major difference between the two models appears to be where the tunnel begins to detect the approach of the lag tunnel. The data shows that the strain gauges actually start to accumulate stress at the springlines when the lag tunnel is approximately 1.5D away from the monitoring point. The model predicts most of the stress increases to occur within 1D ahead of and behind the tunnel face.

The final stress region is where the instruments were installed near to or within the invert of the tunnel. These points were provided additional confinement during tunnel construction since the invert was subsequently backfilled following completion of the support ring. Measurements from the strain gauges within this section were expected to result in the least degree of strain when compared to the other points. Figure 7.37 below illustrates the calculated stresses recorded from the various instruments as well as provides a comparison of the calculated stress values through this section.

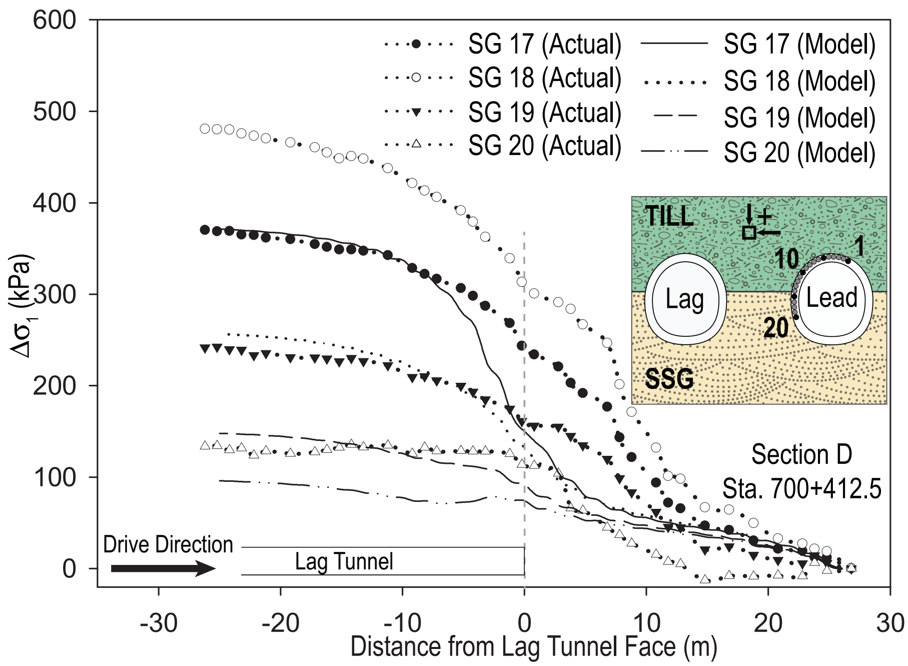

Figure 7.37. Calculated versus measured change in liner stress within the invert segment with the approach of the lag (Northbound) tunnel at Section D

From Figure 7.37, it appears that the numerical model is not as accurate as the previous models when compared to the measured values. In general, the trends are well represented in that the stress measured immediately above the invert backfill was higher than the maximum value recorded at the tunnel springline. It is however possible that the invert backfill may have influenced the change in shape of the liner through this section and therefore altered the measurements in the strain gauges. Overall, the maximum error through this section was typically between 37 to 109 kPa or 25 to 32% differences.

There was a discernible increase in measured strain with the instruments installed within the Empress Sand relative to those installed within the glacial till despite the increased stiffness of the soil. This finding is counterintuitive and it would be expected that the liner displacements within the sand would be less than those within the till. In an attempt to confirm the results by understanding how the liner strained (and thus the calculated stresses within the liner), the displacements at each of the strain gauge locations were modelled and calculated in terms of polar tangential strain ($\varepsilon_{\theta\theta}$). Because no liner was used in the numerical model, the displacements in the elements located immediately outside the tunnel cavity were used for comparison. The size of the elements used to calculate the displacements were typically 0.15 m wide by 0.25 m high and 0.5 m deep. Also FLAC 3D produces displacements only in the *x*, *y* and *z* directions and the results had to be manipulated to produce tangential strains similar to those measured by the strain gauges. By using the equation for tangential strain of a circle given as Equation 7.1, the change in strain at each location was calculated in polar coordinates.

$$\varepsilon_{\theta\theta} = \frac{1}{r}\frac{\partial u_\theta}{\partial_\theta} + \frac{u_r}{r}$$ Equation 7.1

where,
r is the tunnel radius;
∂u_θ is the change in circumferential displacement; and
u_r is the radial displacement.

This method assumes that the shape of the tunnel is circular; that the angle θ is measured counter clockwise from the horizontal and that the tunnel axis was assumed as the origin. The corresponding radii (r) and angles (θ) were then calculated for each point based on the established origin. The change in the strain was calculated incrementally throughout the approach and passage of each tunnel. Figure 7.38 to Figure 7.41 shows the results of the strain calculations from the numerical model and a comparison with the measured changes at Section D.

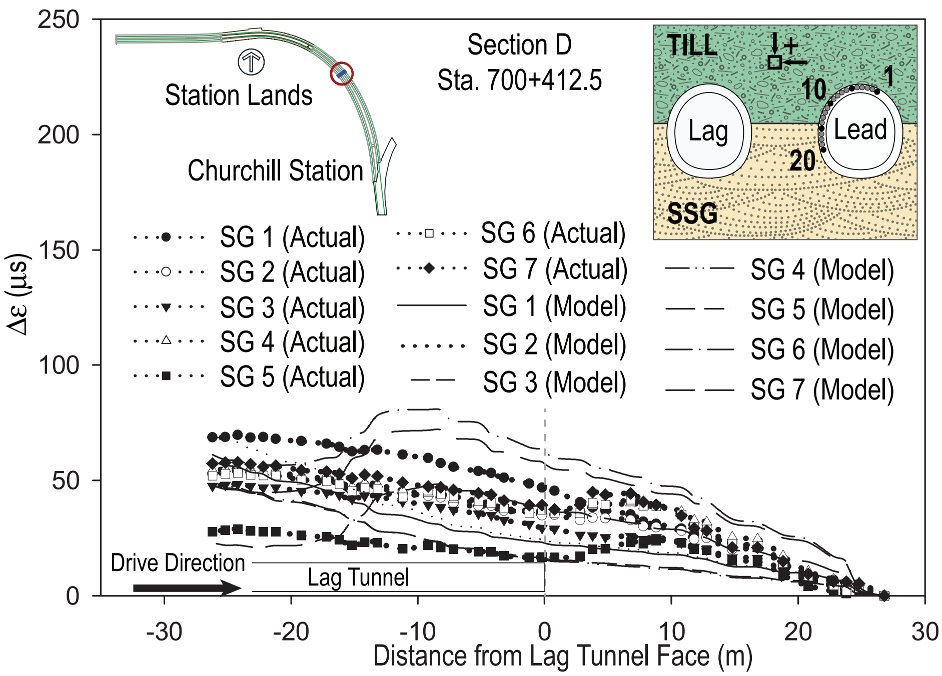

Figure 7.38. Calculated versus measured change in tangential stains within the crown segment with the approach of the lag (Northbound) tunnel at Section D

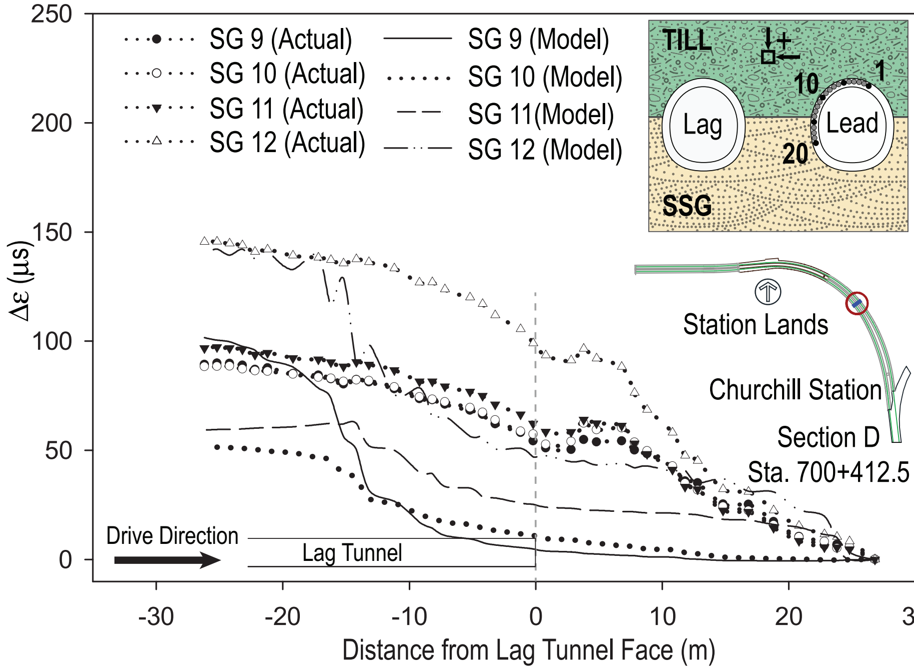

Figure 7.39. Calculated versus measured change in tangential stains within the till springline segment with the approach of the lag (Northbound) tunnel Section D

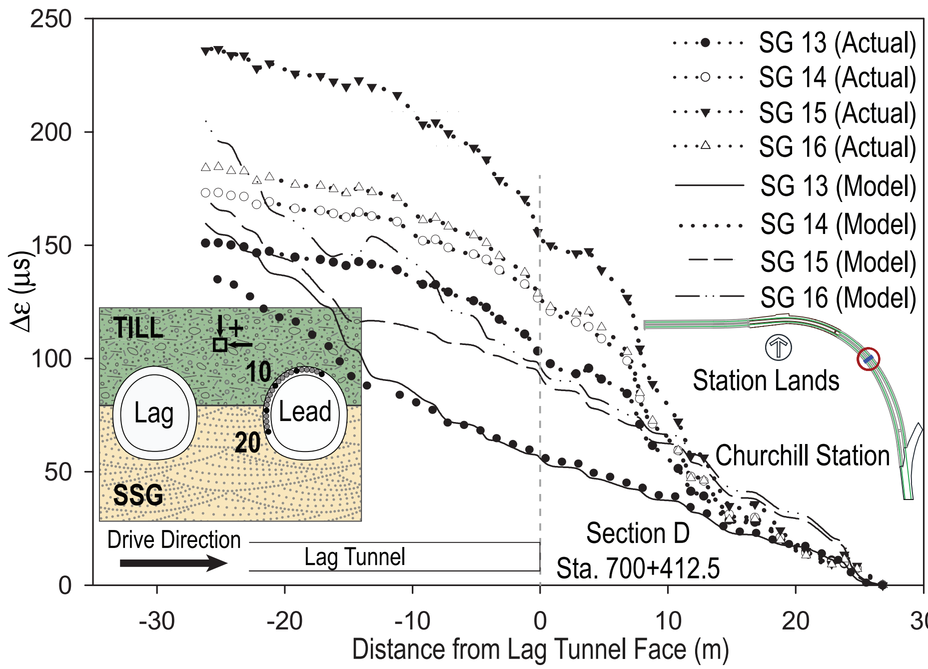

Figure 7.40. Calculated versus measured change in tangential stains within the sand springline segment with the approach of the lag (Northbound) tunnel Section D

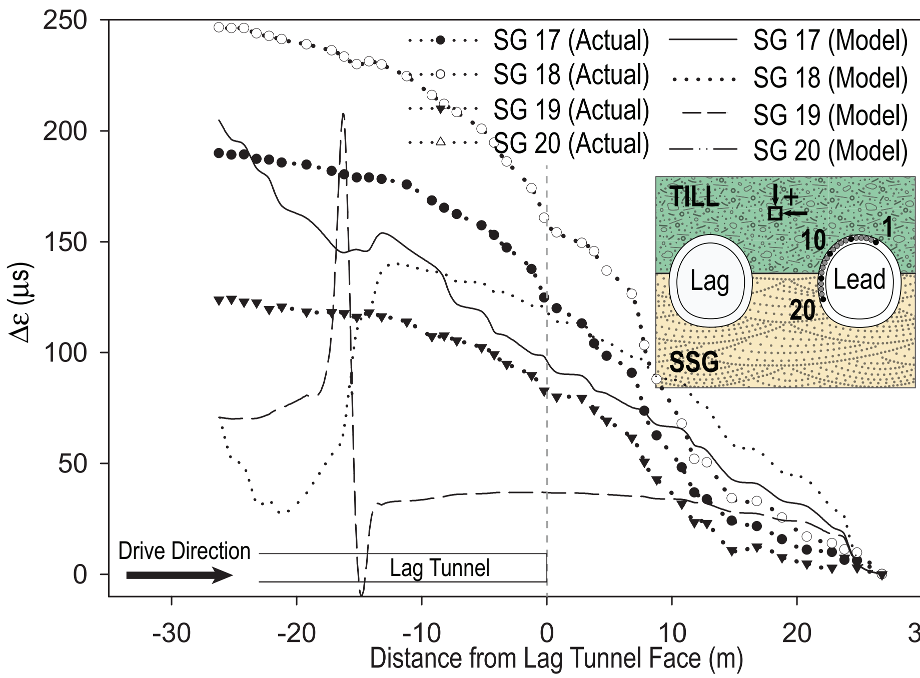

Figure 7.41. Calculated versus measured change in liner stress within the invert segment with the approach of the lag (Northbound) tunnel at Section D

As with the calculated stresses, it is obvious that the calculated strains only represent the measured strains in specific areas around the tunnel circumference. The best correlations are in the crown and in the springlines. There is a clear disconnect with the calculated values in the invert values. The reason for the discontinuous response of the numerical model within the invert is not known.

7.5.6 Applicability of the Numerical Model

Observation of the results of the model indicates that a linear elastic model is applicable for back analysis in only certain areas around the tunnel cavity. Considering this, it is important to discuss the relevance of each location prior to assessing why a monitoring method may not be well represented by the model.

With respect to the settlements, the three dimensional linear elastic numerical model reasonably replicates the displacements measured during the actual tunnelling activities. Typically the error between the simulated and actual results was minor and less than 20%. In the cases of the settlement above the tunnel crown, the differences were even less and were typically around 10%.

When the lateral displacements were modeled, the percent difference between the measured and calculated values were high (around 25 to 35%). The actual difference between the two however was typically within 1 to 2 mm of error. The major source of error occurred at Section E where the pillar width was at a minimum of 0.23D.

Inside the tunnel cavity (displacement due to the construction of the lag tunnel), the efficacy of the numerical model was dependent on the position of the monitoring point. When the point was located within the crown of the tunnel, the displacements were well represented. When the monitoring point was in the springline or the invert however, the displacement vectors were not representative. The same observations may be applied to the strains measured within the liner as well as the stresses that were calculated based on the measured strains.

Now that the applicability and limitations of the numerical model to back analyse the field monitoring results is understood, a further analysis of the calculated stress paths to determine the reasons for the numerical limitations is now discussed.

7.6 Localized Yielding

Given the inconsistent relation of the linear elastic model to the actual field response, it appears important to use the information obtained to illustrate when the numerical simulations used in this study are appropriate. To achieve this goal, the stress paths of the around the tunnel cavities have been plotted in a similar format to those in Chapter 5 (σ_1 / σ_3 space). These data are then compared with the glacial till effective residual failure envelope defined in Chapter 5 as c'= 0 kPa and ϕ'=44.2°.

For the Empress sand, the effective, extensional failure envelope has been assigned as the appropriate yield surface. This is because during unloading in tunnel construction, the stress path is similar to the active compression tests conducted by Medeiros (1979). These paths would indicate if and when overstressing of the soil occurs. In addition, it will clearly demonstrate when and to what extent unloading occurs. This information coupled with the strains measured during the field monitoring, should give a clear image of what the depth into the ground and away from the tunnel cavity, yielding can be expected.

Finally, the validity of a continuous numerical model is assessed. It is expected that when yielding does occur, it is during unloading where the active compression / extension yield strain criteria dominate. By yielding due to unloading, the pre-existing fissures can be expected to dilate and the mobilized friction angle will prevail. This suggests that the main form of failure for tunnels within a heavily overconsolidated, fissured soils such as the Edmonton till may be best considered as a discontinuous medium depending on the size of the excavation relative to the spacing and orientation of the fissures.

7.6.1 Glacial till

7.6.1.1 Tunnel Springline and Pillar

The stress paths within the glacial till were assessed at Sections C and E due to the similarity in the overlying stratigraphy and depth to the tunnels. The width of the pillar at Section C is also wide enough that there is expected to be substantial differences between the points located at the springline of the tunnels versus those in the middle of the pillar. The stress paths at the springline of the lead and lag tunnels at the narrow pillar section (Section E) are shown below in

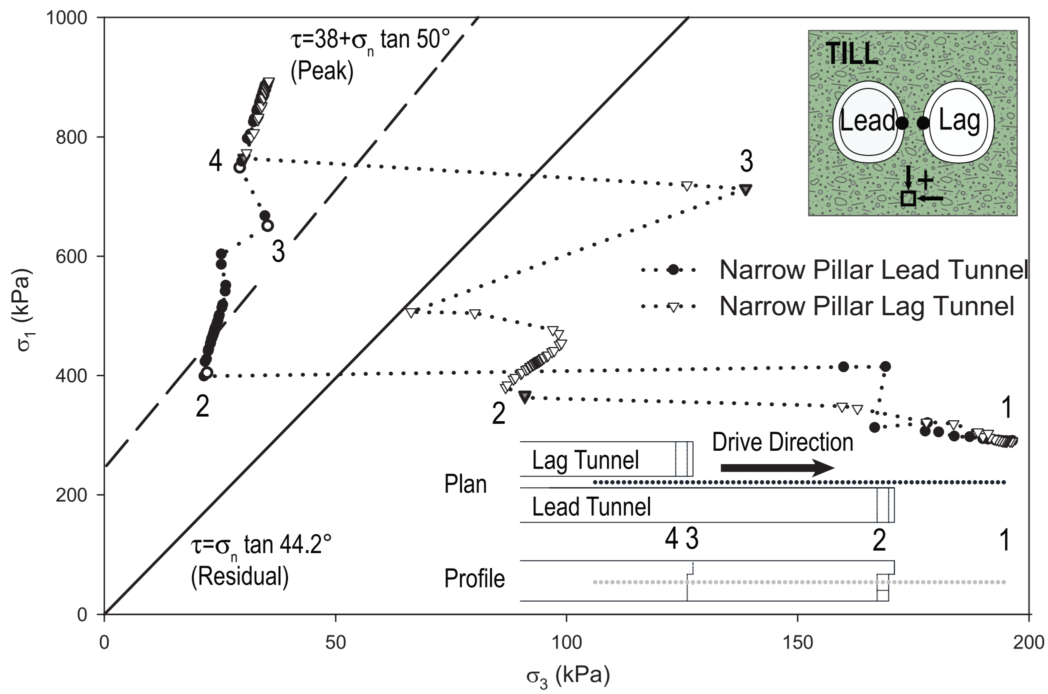

Figure 7.42 Stress path at tunnel springline at Section E

Using the stress paths at Section E, it appears that the hypothesis that yielding near to the tunnel was valid. This is assuming that the strains around the tunnel perimeter exceeded 0.25%. Using the same model, the strains were monitored at the same location with the approach and passage of each tunnel. The calculated strains are shown below in Figure 7.43.

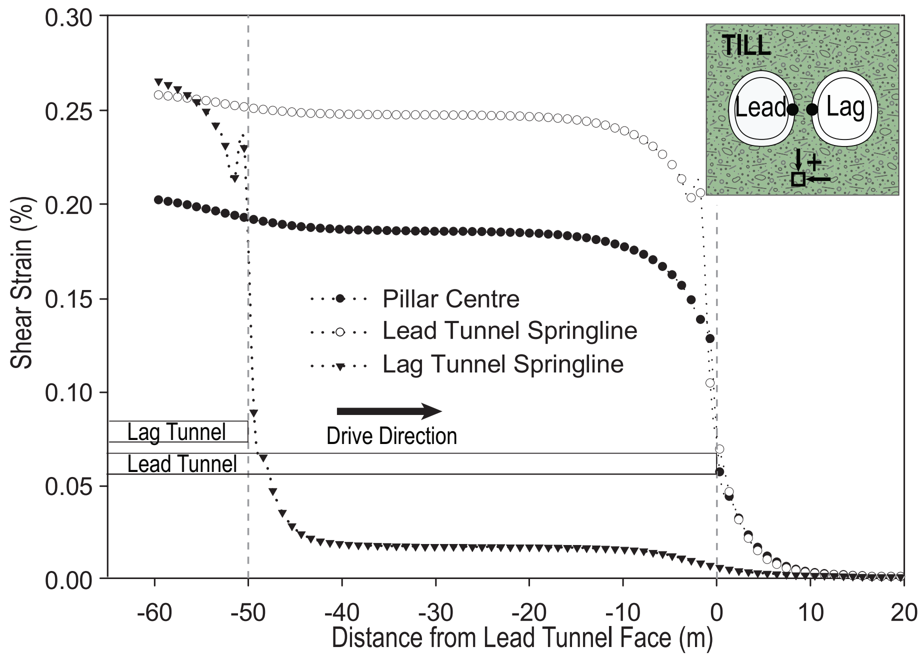

Figure 7.43 Shear strains within the narrow pillar at Section E

What Figure 7.43 illustrates is the potential for block translation to occur. Because the shear strains at the springlines exceed the 0.25% criteria, the friction along the surface of the fissures can become mobilized and therefore the residual failure envelope is valid. The point in the centre of the pillar is slightly below 0.2%. It is therefore not expected that the residual envelope would dictate the yield surface at this point. Also, dilation followed by block translation cannot occur while the pillar is intact. Considering this, the decision of whether the yield surface is drained or undrained should be determined using the methods described Anagnostou and Kovari (1996) regardless of unloading occurring.

At Section C, it was hypothesized that yielding does not occur within the pillar to any extent beyond the immediate tunnel boundary. At this section, the stress paths have also been plotted from the lag tunnel to the centre of the pillar as shown in Figure 7.44. The stress path of the point at the springline of the lead tunnel is also shown for reference.

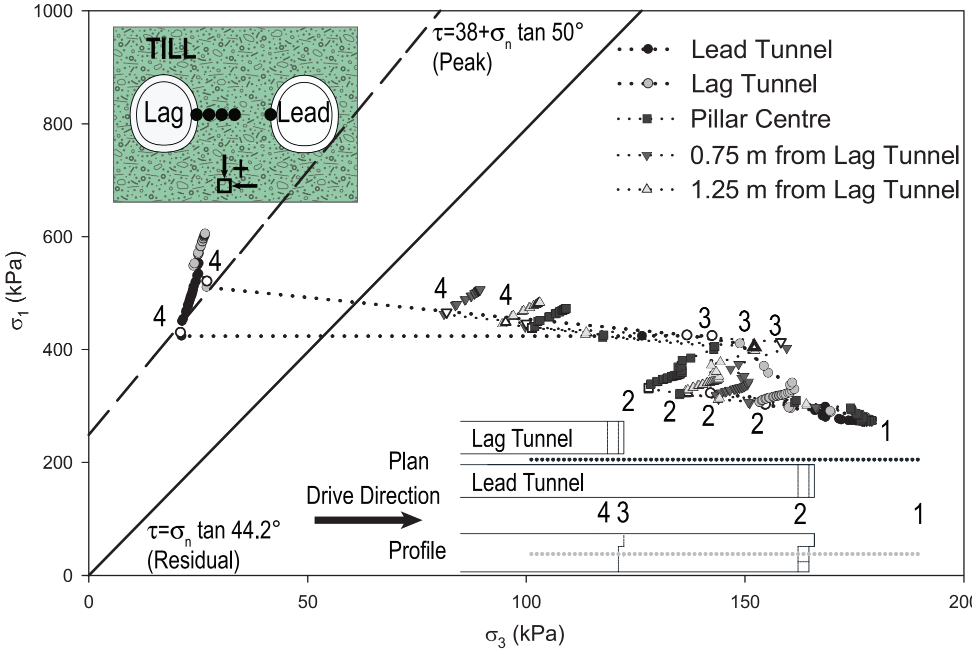

Figure 7.44 Stress paths near to the lag tunnel at Section C

Figure 7.44 demonstrates that there is only the potential for yielding at the perimeter of the tunnel cavity when the pillar width is greater than 0.5D. At a distance of 0.75 m from the tunnel cavity, the material only begins to approach the residual shear strength envelope. This also shows that there is no possibility of overstressing at these locations either. It should be noted that there is no discernable differences between the stress path at the centre of the pillar and a point approximately 0.5 m from the centre of the pillar.

In order to determine whether block failure can occur, the shear strains at the tunnel springlines need to be examined. The strains adjacent to the lead and lag tunnels as well as the centre of the wide pillar at Section C are shown in Figure 7.45.

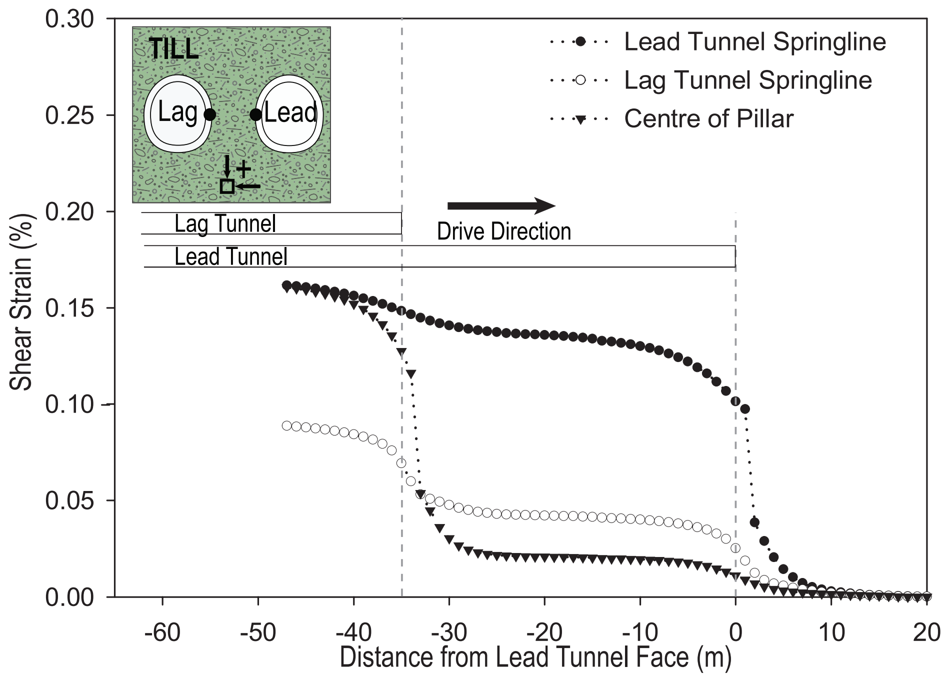

Figure 7.45 Shear strains within the wide pillar at Section C

Figure 7.45 demonstrates that though the points around the tunnel circumference exceed the residual shear strength yield surface, they do not strain sufficiently to mobilize the friction along the surface of the fissures. Therefore, the ground does not dilate sufficiently to permit block translation or wedge formation.

Since the stress paths and the strain fields have indicated that yielding is not occurring to any appreciable distance around the tunnel cavities provided the pillar width is sufficient, the linear elastic model should be considered adequate. The usage of the residual model in conjunction with the yield shear strain criteria also indicates that the predominate failure mechanism is not overstressing as is commonly assumed by most designers when tunnelling in soils.

Based on this knowledge, it would appear that the use of limit equilibrium software that utilizes the fissure spacing and orientation relative to the tunnel orientation is more relevant than a continuous numerical model when determining the stability of the unsupported tunnel cutting in similar soils. This type of software obviously cannot indicate the degree of surface settlements, but can indicate the general stability of the unsupported tunnel cutting at the crown and springlines. It also functions to indicate the typical and maximum block and wedge sizes that may form.

7.6.2 Wedges in Fissured Glacial Till

An analysis of wedge formation in the North LRT tunnel cavities was undertaken using the commercial RocScience software UnWedge. This software package assesses the risk of wedge failure around the perimeter of cavities advanced through fissured/jointed materials. For this model, the stereonet provided in Chapter 3 was used the orientation of the fissures. A state of zero stress was used since this case would provide the least confinement on any intersecting joints and the ensuing blocks/wedges. The persistence was assigned a maximum of 1.5 m allowing for the tunnel liner and an unsupported cutting of only 1 m. The maximum wedge size was calculated to have a volume of 0.16 m^3 and a mass of 335 kg. The factor of safety against this large block falling was calculated to be 1.8. An image of the calculated wedges assuming the given conditions above is shown below in Figure 7.46

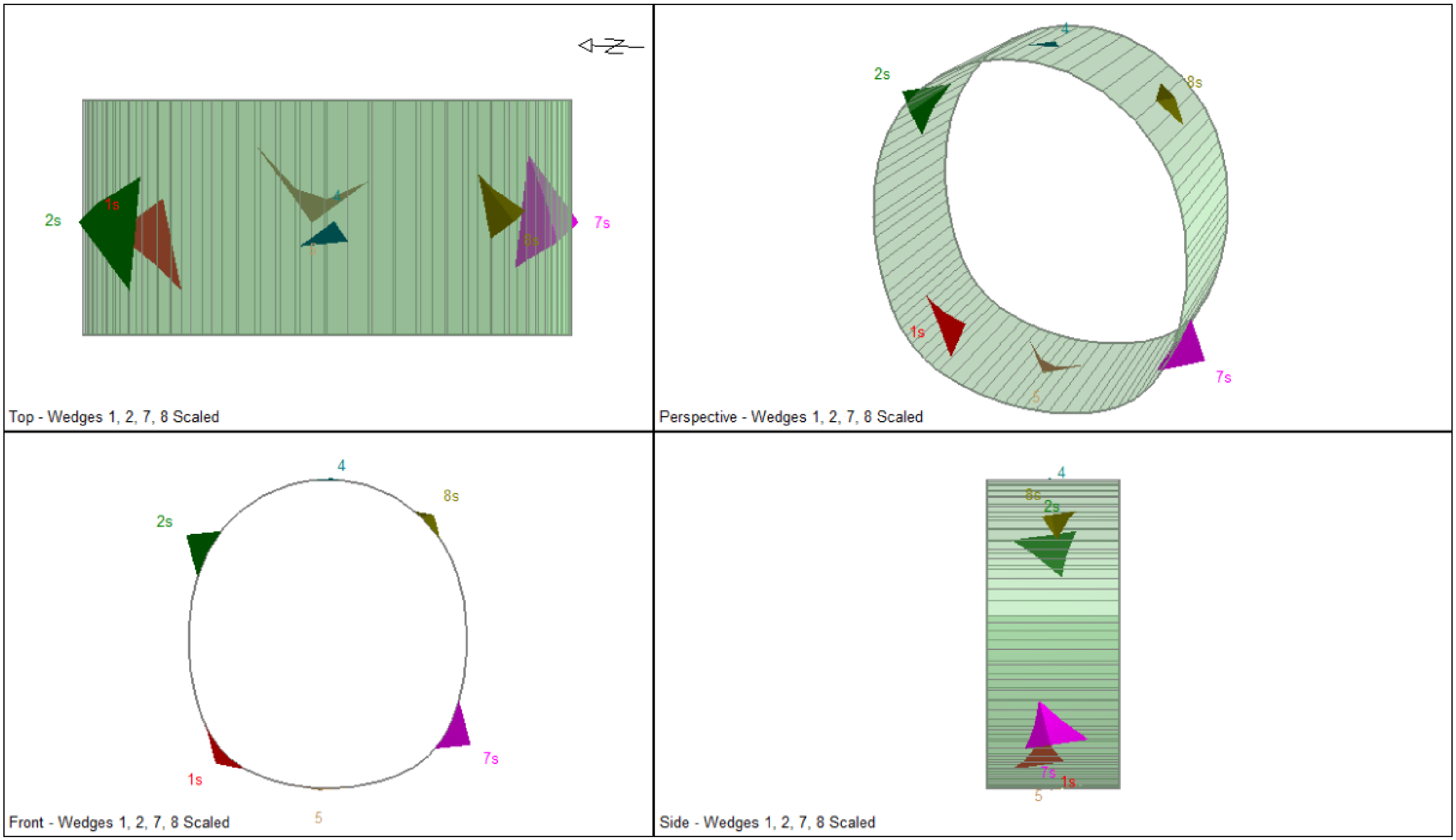

Figure 7.46. Scaled wedge failures assuming a 1 m long unsupported cutting

It was relatively common to see similar sized wedges form around the tunnel perimeter, however these were not generally considered to be instabilities since they did not represent an indication of yielding in the conventional sense. An example of a similar wedge failure is shown at a location similar to Wedge #8 above as shown in Plate 7.1. Note that the actual size of the wedges that formed are relatively small and did not appear to generally exceed 0.01 m^3.

Plate 7.1. Wedge failure near far shoulder (Wedge #8) of Southbound West (TM 111.7 m)

7.6.2.1 Tunnel Face Stress Paths

The stress path of the ground within the tunnel face was also calculated. Like with the perimeter of the tunnel cavity, it is expected that yielding occurred and the linear elastic data does not accurately demonstrate the displacement fields. The data was then used to assess the theory of block or wedge translation within the bench rather than conventional overstressing. In each simulation, the stresses were monitored within the centre of the header and bench during the approach of each tunnel. For this analysis, only the ground response at Section E will be evaluated as this indicated the worst-case scenario based on the results shown above. The calculated stress paths at Section E relative to the residual shear strength of the glacial till is shown below in Figure 7.47.

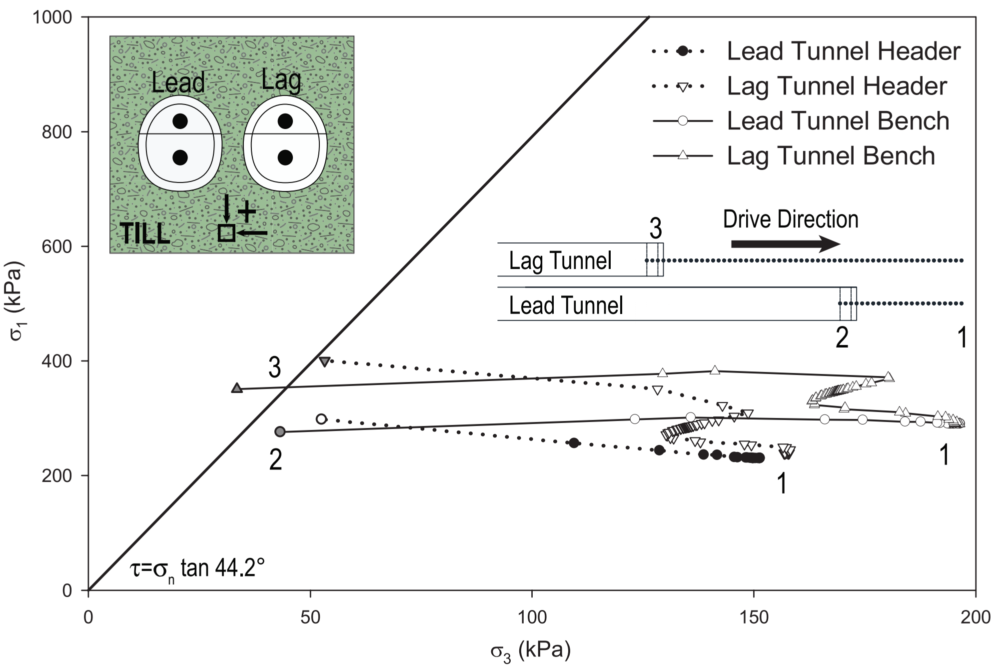

Figure 7.47 Stress path of points within the header and bench at Section E

It would appear that the only potential for yielding within the face occurs in the bench of the lag tunnel. The header of the lag tunnel and the bench of the lead tunnel approach the residual yield surface, but do not cross it. It is important to note that there is a considerable drop in confinement within the bench following the excavation of the header. Again the strains play a role in fully capturing whether failure within the bench would actually be possible. As with the springline, the strains within the face were calculated at the same positions as the stress analysis and are shown below in Figure 7.48.

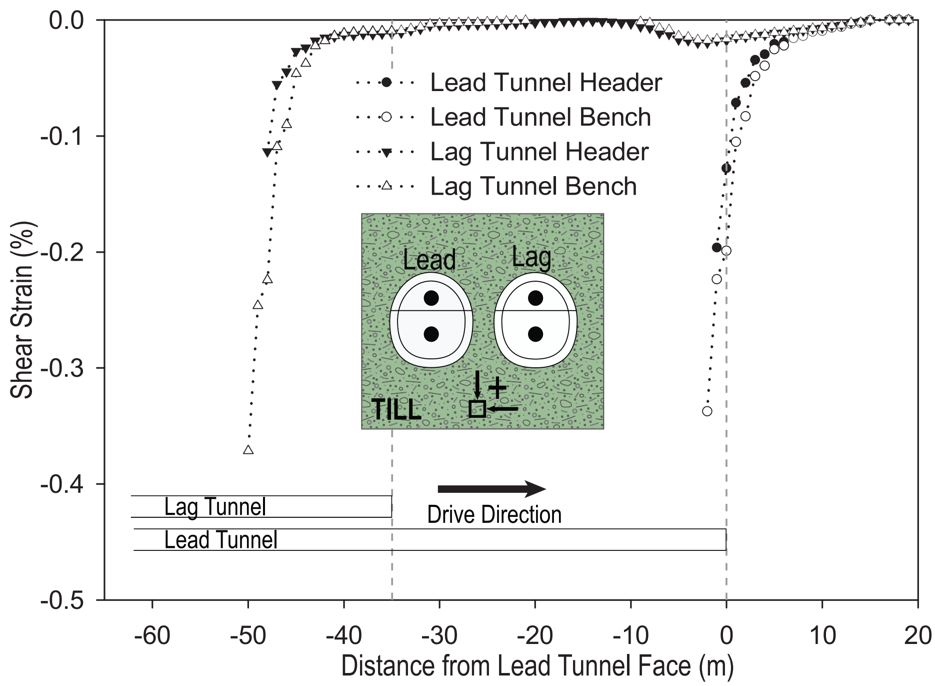

Figure 7.48 Strains at points within the tunnel face at Section E

With the strains shown in Figure 7.48, it is apparent that only the benches in each tunnel have the potential for the friction to be mobilized. With the stress paths shown in Figure 7.47, it is considered that bench yielding in terms of block / wedge formation is incipient. Yielding of the lead tunnel face has a high potential since the strains exceed the 0.25% criteria and closely approach the residual yield surface.

Like the tunnel perimeter at the springline would indicate that the dominant failure mechanism would be block / wedge translation along the surface of intersecting fissures. This would then imply that the best method of analysis would not be a continuous numerical solution as yielding does not occur as overstressing. The limit equilibrium approach would therefore likely provide more useful information regarding the likely failure surfaces and the size of blocks formed during exposure. The commercial software SWedge by RocScience was used to determine the factor of safety for small and large block formation within the bench of the glacial till.

The large wedges had some form of shearing that occurred along one or more faces of the failed wedge. This was due to the weight of the wedge overstressing the intact soil where a discontinuity was not present. Figure 7.49 illustrates the largest wedge that occurred in the bench within the glacial till. The measured fissure orientation and spacing relative to the tunnel drive were used in the model. The shape of the wedge illustrated below Figure 7.49 is very similar to the largest wedge observed in the bench during construction. A photograph of the actual wedge failure recorded in the western leg of the Northbound tunnel is shown below in Figure 7.50.

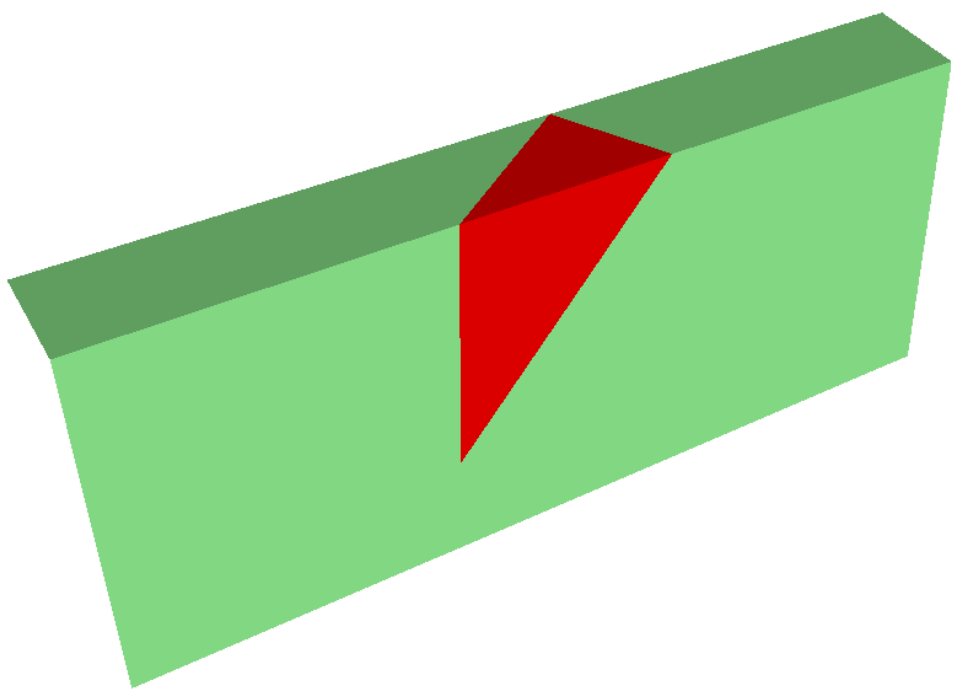

Figure 7.49. Estimated wedge size within the glacial till bench in the North LRT tunnels (bench width is 1 m)

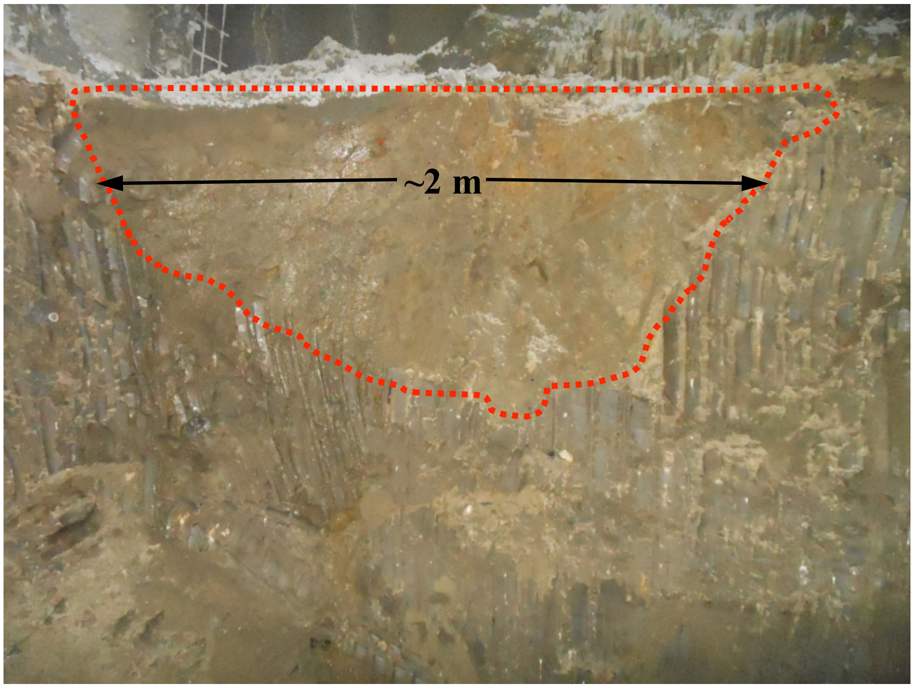

Figure 7.50. Failure within the glacial till in the Northbound (lead) tunnel at Station 600+716.6 (tunnel meter 98.7)

Based on the results of the SWedge analysis, the factor of safety against a large wedge formation like this using a deterministic method is approximately 1.2. This results in a wedge that is approximately 750 kg and around 0.37 m^3. This block grows considerably if the bench length is extended beyond the maximum 3 m. If the volume of the blocks was set to 0.03 m^3, which was the typical size observed in the North LRT tunnels, the factor of safety against wedge failure is approximately 1.1 or failure is incipient. This agrees well with the findings in the tunnels since most blocks of this size were loosened during excavation and could easily be pulled out by hand.

7.6.3 Empress Sand

7.6.3.1 Tunnel Springline and Pillar

The analyses that were used to determine yielding around the tunnel cavity and face of the glacial till were used to assess the stability of the tunnel within the Empress sand. Medeiros (1979) had demonstrated that the extensional yield strains were very similar to that of the glacial till and on the order of 0.25%. The pressuremeter testing reported in Chapter 4 indicate that the yield shear strains in the Empress sand in extension are around 0.15 to 0.2%. The yield strain criterion are therefore set to 0.2% in active compression / extension due to the lack of cohesion that is needed to overcome. Because the extensional failure envelope is vastly lower than that of the residual shear strength, the extensional envelope was compared to the numerically calculated stress paths. The stress paths of the springline at the geologic unconformity with the overlying glacial till is shown below in Figure 7.51.

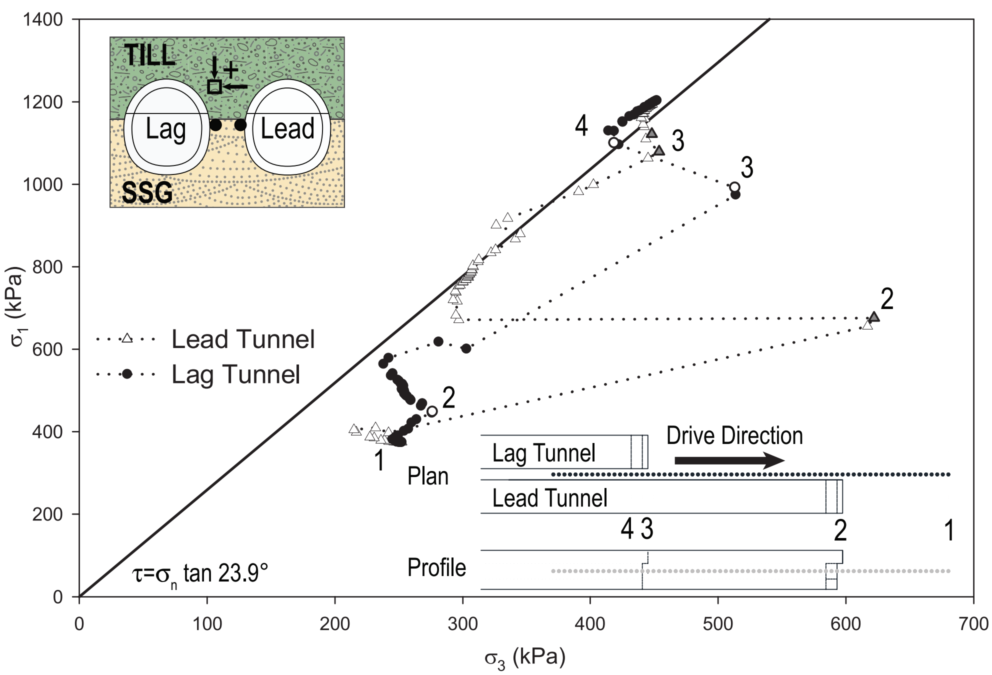

Figure 7.51 Stress path within the Empress sand at Section D

Figure 7.51 demonstrates that yielding should only be anticipated at the springline within the lag tunnel. Point 2 suggests that there is a substantial reduction in confinement within the bench following excavation of the header, however the stress path does not cross the yield surface until well after the liner is installed. Point 4 indicates that yielding would be expected.

The stress path across the pillar was also examined to determine the extent of yielding that may occur within the Empress sand. Like the stress paths at the unconformity with the glacial till, the springline stress paths were compared to the extensional yield surface. It is expected however that the points within the pillar should be in fact compared to the peak shear strength of the Empress sand. This is because there is confinement of the ground at these locations and the applied stresses would be similar to compressive shear. The extensional failure surface however does provide a lower bound of the strength. The stress path of the Empress sand at the tunnel springlines are shown below in

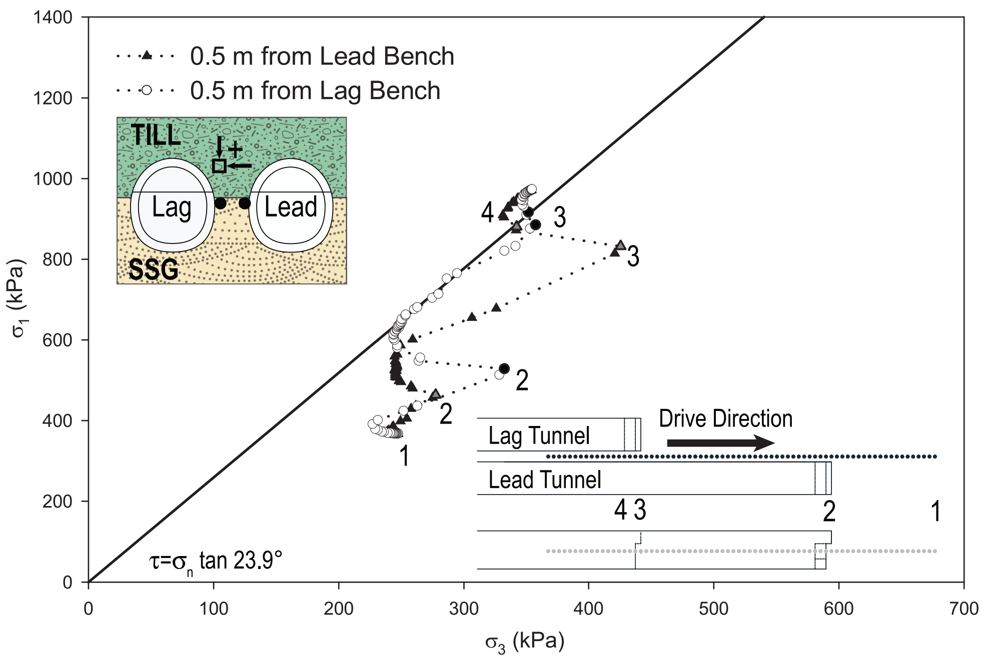

Figure 7.52 Stress path across the pillar within the Empress sand (Section D)

As with the springline stress paths, it is expected that yielding would only occur near to the lag tunnel springline at a depth of 0.5 m from the tunnel cavity. To this end, it is expected that yielding would not occur at this location and the linear elastic numerical model would be applicable.

7.6.3.2 Tunnel Face – Bench

Finally the stability of the mixed face tunnel face within the bench has been assessed. As with the glacial till, the stress paths within the bench have been compared to the extensional yield surface. The calculated strains within the bench were then examined to determine the applicability of the numerical model for the tunnel face. Figure 7.53 shows the calculated stress path of the Empress sand bench at Section D.

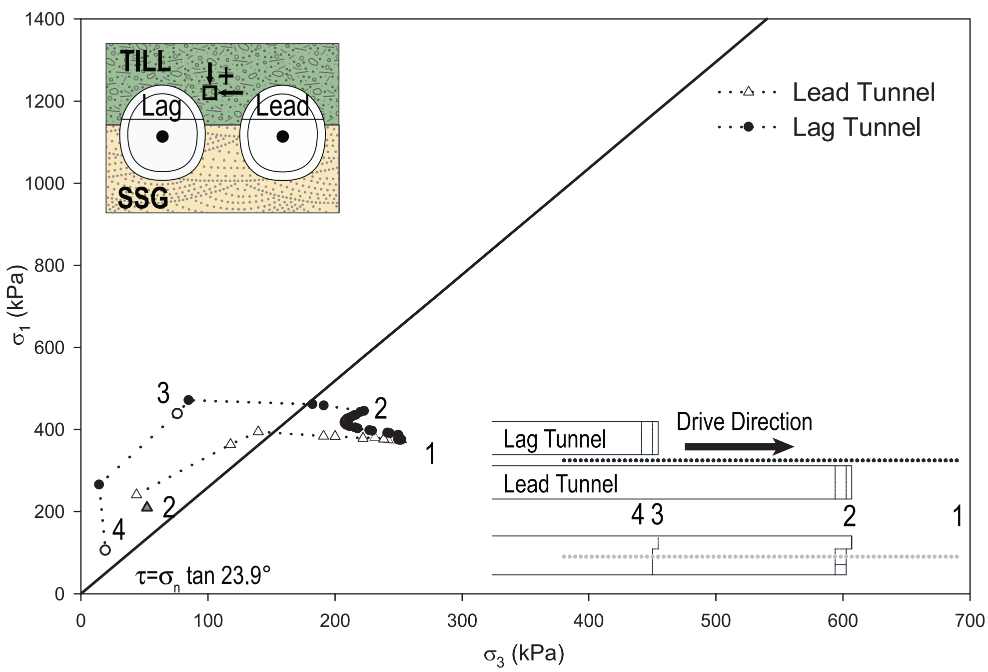

Figure 7.53 Stress path within the Empress sand bench (Section D)

Figure 7.53 demonstrates that yielding within the bench composed of the Empress sand should occur in both tunnel faces. This suggests that the displacements calculated from the linear elastic model are not representative and therefore the models should not be used to determine the ground loss into the tunnel face. The numerical simulations do demonstrate that there was likely yielding that occurred during excavation of the twin tunnels due to the presence of the bench. The likelihood of the onset of yielding is supported by the strains measured within the centre pillar inclinometer, which indicated shear strains greater than 0.2% through the bench section of the pillar. The yielding of the face, coupled with the yielding of the springline adjacent to the lag tunnel suggest that the numerical models provide an method for determining when and where failure can be expected.

7.7 Conclusions

Based on the data collected during the instrumentation and monitoring section and the results of the back analysis of the three dimensional numerical modelling the following conclusions have been drawn:

- The three dimensional, continuous, linear elastic numerical models represented the ground displacements within and around the tunnel cavities provided the pillar width was greater than 0.5D as outlined in Chapter 6.
- Where the pillar width was less than 0.5D, the surface settlements and lateral displacements were well represented. Near tunnel displacements were not well replicated as a linear elastic model can accurately model the stresses post yielding, but stains and displacements are no longer representative.
- In two locations (Sections C and E), the measured settlement troughs were very steep and narrow. In neither of these locations was the three dimensional linear elastic model capable of reproducing these results and is not applicable.
- A comparison of the convergence data measured within the tunnel cavities is not well represented in the numerical model. This is because the convergence measurements would only commence following the installation of the support. Because the numerical model does not include the presence of a liner system, any post-liner displacements are not comparable.
- The numerical simulations provide a satisfactory representation of the displacements of one tunnel due to the influence of the second tunnel. The

models were most accurate within the crown, while the least accuracy was encountered along the springline adjacent to the pillar.

- The stresses calculated from the measured embedded strain gauges within the liner of the lead tunnel were well represented by the numerical simulations. Because the calculated stresses were due solely to the approach and passage of the lag tunnel alone, they are well represented by the model.
- Stress paths of the ground calculated from the numerical models are adequate for determining whether yielding can be anticipated to occur around the tunnel cavity. This is provided that the strains associated with the stress paths indicate the applicability of the selected yield surface.
- If the mode of failure within materials similar to the glacial till is expected to occur due to the mobilization of friction along the pre-existing fissures, then the usage of a continuous numerical model such as finite element or finite difference is not sufficient for determining where and how failure will occur. In these instances, then limit equilibrium models that utilize the tunnel and fissure orientation should be used to determine the overall stability of the unsupported cutting.
- When the stress paths indicate that yielding in either active compression or extension is to occur, then the near tunnel displacements must not be used. However, the displacements outside the anticipated yield zone such as surface settlements may still be well represented.
- The above suggests that the usage of the linear elastic numerical simulation used in this analysis are applicable for tunnels within the glacial till and Empress sand, provided the pillar width is greater than 0.5D.

8.0 Conclusions and Recommendations for Future Research

8.1 Conclusions

The work presented in this research project has demonstrated that prediction of the yield criterion for heavily overconsolidated soils is not straightforward and does not generally adhere well to conventional soil mechanics. First and foremost when determining an applicable yield surface for the ground, consideration needs to be given to the geology of the stratigraphy. Presence of glaciers may have altered the ground not only by compressing it to an overconsolidated state, but may have also worked to create regular fissures similar to jointing in rocks. The fissures are likely a result of permafrost conditions that desiccated the soils by drawing groundwater to the freezing front. This in turn has generated regular primary and secondary fissure systems that can dominate the type of yielding present in an excavation. As a result, the orientation and size of the excavation relative to the fissure orientation and spacing must be considered. As was demonstrated, the development of a representative element volume (REV) can be very difficult with conventional geotechnical testing programs.

This work has documented the presence and nature of the intra-till sands within the downtown area. Previously, the sand pockets have been thought of as only ubiquitous throughout the glacial till formation. The recent construction of the North LRT tunnels has revealed that the sand pockets may be more complex than initially thought. The recent investigation has indicated that the sand pockets are likely the upper horizons of the Empress sand that had been incorporated into the glacial deposits as frozen slabs. Additionally, the sand pockets have likely been altered and deformed through the extrusion of the clay till into the slabs of frozen sand as indicated by the presence of dipirism. Boudinage has also been observed within the sands suggesting that they were under significant stress during their deposition within the till. New documentation on the orientation and spacing of the fissures within the city of Edmonton has also been provided. This information supplements the existing data provided by Shaw (1982) and provides information for the downtown area. Based on this information, it is hypothesised that a relevant REV for the Edmonton glacial till should be taken as roughly 2 m. Evidence of glacial tectonic actions within the glacial till has also been presented. This evidence indicates that the till was randomly pushed by glaciers resulting in the bending of the deposits and ultimately alteration of the measured fissure orientations.

Additional pressuremeter testing has been carried out within the heavily overconsolidated formations within the City of Edmonton. These tests have helped define the elastic parameters for the various formations using state of the art technology and practices. The testing has also helped bound the drained and undrained strength criteria for the glacial till and Empress sand. Through examination of the data obtained form the pressuremeter testing, new methods for determining the horizontal coefficient of consolidation, coefficient of horizontal volume change and horizontal coefficient of hydraulic conductivity have also been developed. These values have been typically very difficult to obtain for most soils and the methods developed utilize well-established methods for analyzing field data. Comparison of the test results obtained from the test site has shown that they agree well with the values obtained by Morgenstern and Thomson (1971). The tests by Morgenstern and Thomson (1971) used samples obtained from nearby the site and should closely resemble those tested during the current investigation. As part of the pressuremeter interpretation, previous interpretation methods have been called into question and a new form of analysis is given to help understand the limitations of previous practices. Conventionally, the undrained shear strength of the soil is determined using the methods provided by Gibson and Anderson (1961). The new method of interpretation demonstrates that in heavily overconsolidated unsaturated soils the undrained analysis given by Gibson and Anderson (1961) can result in significant errors. This is because Gibson and Anderson (1961) assumes an undrained state from the onset of loading, this implies that there is no volume changes that occur under loading. In unsaturated soils, there are volume changes that can occur during the initial stages of loading. These volume changes can account for up to 40 to 50% of the total loading and must be accounted for. A new method for determining when the onset of saturation based on the Hilf (1959) method as well as the amount of volume change that can be expected during loading is provided. The applicability of the methods is provided and have been shown to be well bounded for heavily overconsolidated materials.

Laboratory experimentation using soils similar in nature to the Edmonton glacial till or the Empress sands also only present a narrow indication of the appropriate yield criterion. Because the stress strain curves of most test samples indicate strain-hardening behaviours regardless of the confining stress, the definition of the onset of yielding was required. Therefore, a definition of yielding for experimental data has also been presented. This definition examined the pore pressure trends within various test samples. Ultimately, the point of dilation within the samples, or the reversal of the pore pressures from positive to negative states has been assigned to represent the onset of yielding for a given sample. Medeiros (1979) also demonstrated the importance of probing stress paths on the glacial till to determine an appropriate yield surface. Therefore, numerous laboratory experiments probing the yield surface using a number of stress paths are considered crucial. Even with a variation to the applied stress path, this research has shown that the failure envelope may not always be relevant when designing underground structures. Understanding the influence of the strain fields on the yield criterion has also proven important. The influence of the strain fields has been shown not only by the laboratory experiments, but also by the recently conducted pressuremeter testing. This illustrated that the shear strains required for yielding were considerably less in extension than those measured during the expansion of the borehole. These extensional yield strains coincided very well with the shear strains at the onset of yield in the active compression and extensional lab experiments carried out by Medeiros (1979). As a result, yield criteria for both the Edmonton glacial till and the Empress sands have been developed for a variety of stress paths. It has therefore been established that yield criterion for the Edmonton glacial till should be defined based on not only the stresses within the ground but also on the anticipated stress path and strains following excavation. A chart detailing the different modes required for defining yield has been provided. The chart demonstrates that for stresses less than the pre-consolidation pressure, the residual shear strength envelope should dictate any stress cases that result in either tension or unloading. This envelope defines the mobilized frictional envelope, which has been assumed based on Skempton and La Rochelle (1965) to define the friction angle of the fissure surface. By defining yield in this fashion, the yield surface related to block and wedge formation can be easily defined. For scenarios where stresses increase or confinement is provided, then the conventionally defined peak yield surface is used. Finally the conventional strength envelope that is typically defined as either drained or undrained (effective or total stress) is delimitated by the pre-consolidation pressure. At confining stresses below the pre-consolidation pressure, the effective stress failure envelope should be selected. Above the pre-consolidation pressure (normally consolidated soils) the failure surface should be defined by the criteria given by Anagnostou and Kovari (1996).

The results of the instrumentation program implemented during the construction of the North LRT twin tunnels are also provided. These instruments have shed important light onto the influence of the pillar width within the Edmonton soils. Previously (Ottoviani and Barla, 1974; Ghaboussi and Ranken, 1977, Addenbrooke and Potts, 1996 and Ng et al., 2004) have demonstrated the influence of reduced pillar width on the influence of lead tunnel. This study has shown that for an intermediate material such as the Edmonton glacial till, that the conventional thinking of requiring a pillar width of at least 1 tunnel diameter is not necessary to control yielding. The current investigation has demonstrated that even with a pillar width of as little as 0.23D, that surface settlements are minimal and generally confined to the tunnel alignments. This suggests that care must be taken to ensure that surface structures are positioned at least outside of the anticipated settlement trough. This is because the settlement trough has been shown to be very steep at its limits and could result in excessive differential settlements. Calculation of the volume loss of the ground due to tunnel construction has been provided using the method of Suwansawat and Einstein (2007). This method agrees very well between the measured and analytical methods and shows that the ground loss within the city of Edmonton is generally very low provided good ground control is provided. Finally, the measured deep and surface settlements have demonstrated that the minimum spacing required to minimize the interactions between twin tunnels constructed within the Edmonton tills is approximately 0.5D. This criteria was developed based on the rapid increase of settlements above a given tunnel crown following excavation of that tunnel for the pillar width at that section. A method has also been provided to statistically assess the damage within the ground from the lead to the lag tunnels. Using the new method the pillar width was effectively eliminated from the measured settlements. When the influence of the pillar was removed, it was found that the damage for the lead tunnel (5.1 mm) was slightly higher than that of the lag tunnel (4.9 mm).

The last portion of this research involved the back analysis of the measured displacements using a linear elastic numerical model. The thee-dimensional finite difference model used the elastic parameters determined during the field investigation to back analyse the measured displacements. From these analyses, the viability of each model was determined. It has been concluded that a linear elastic numerical model is appropriate for determining the displacements within the Edmonton glacial till and the Empress sand, provided the pillar width exceeds the 0.5D limits determined in the monitoring chapter, or are at some distance from the tunnel cavities. The displacements related to the influence of the lag tunnel are also generally relevant provided the calculated displacements consider the ground and lead tunnel movements into the lag tunnel as a whole. These displacements accurately indicate the movement of the lead tunnel into the lag tunnel during the approach and passage of the lag tunnel. It has also been shown that the criteria established in Chapter 5 are applicable to the assessment of whether yielding within and around the tunnel cavity occurs. Conventional analysis models the ground using the most likely Mohr-Coulomb yield surface and determines the extent of yielding. This model was not designed to determine the extent of yielding, but rather to determine whether usage of the residual (glacial till) and extensional (Empress sand) yield surfaces were relevant based on the stress path. Combination of the residual yield surface and the calculated strains associated with each monitoring point indicated the applicability of using a continuous model to assess stability of an unsupported tunnel cutting. These methods indicated that within the glacial till, unloading occurs resulting in the dilation of the pre-existing fissures followed by the formation of blocks /wedges within the tunnel cavity. This type of failure lends itself to analysis by various limit equilibrium methods rather than conventional continuous elasto-plastic models. Application of various limit equilibrium models has shown that there is a strong agreement with the block and wedge failures observed within the North LRT tunnels.

8.2 Recommendations for Future Research

This research has illustrated the need for several additional investigations. First it is considered crucial to determine the role that suction has on the various yield surfaces. To date, the degree of suction of the pore-air spaces within the glacial till is not known. This has been shown by Fredlund and Morgenstern (1977) to play a pivotal role in the peak strength and the associated shear strains of various unsaturated soils. This research determined the failure criterion based on previously obtained investigations and additional laboratory and in-situ data. With the addition of laboratory experimentation that probes the influence of suction within the unsaturated glacial till, a full picture of the true effective stress of the material may be ascertained. This investigation should include not only a series of laboratory tests on the till, but also should examine the influence of tunnel construction on the development of suction at scale. It is hypothesized based on the current work, that as tunnels are constructed, dilation of the ground within the excavated damaged zone around the tunnel would result in suctions and increased strength. These changes in the pore-air pressure would also likely limit the strains fields into tunnel cavities. Based on the stress paths demonstrated in this thesis, it is expected that the degree of suction around the tunnel cavity should vary considerably and may provide an additional aspect to the failure criteria provided herein.

Another aspect that was not investigated in this research program includes the measurement and calculation of the poro-elastic response of the ground prior to excavation of the tunnel cavities. It is expected that there is a slight increase in the pore pressures during the approach of the tunnel face followed by a rapid drop to negative once excavation is complete. This is evidenced by the definition of yielding provided in Chapter 5. As yielding was defined as having occurred when the pore pressures reversed from positive to negative, it is likely that this also occurs within the excavated damaged zone around the tunnel cavities. Comparison of the pore pressure response around the tunnel cavity to the three-dimensional pore pressure response solutions provided by Biot (1941) would likely yield additional information as to the performance of the ground during tunnelling activities.

The last topic that should be investigated is the stability of the tunnel heading using a discrete element model (DEM). This type of model allows for the formation of blocks and wedges within the bench or around the tunnel cavity following dilation of the pre-existing fissures. It is hoped that this model will illustrate the influence of the fissures on the chimney-like settlement profiles measured during the construction of the North LRT. These settlement profiles were not well represented by the continuous model and it is hypothesized that the settlements are bounded by the fissures and therefore create behaviour typically encountered in cohesionless deposits. It is possible that a finite element model that utilizes ubiquitous joints or a Voronoi mesh may better define how failure is occurring. This type of model would require a strong definition of the frictional criteria along the surface of the pre-existing fissures. It may be beneficial to conduct large-scale direct shear tests similar to those conducted by Marsland (1973). This would help to not only define the frictional characteristics of the fissures, but also to determine an accurate REV for the glacial till. This information could then be related to the continuity factor for a given excavation, which would complete the definition of the yield surface for the Edmonton glacial till.

References

Addenbrooke, T. I. (1996). *Numerical analysis of tunnelling in stiff clay.* Unpublished PhD, University of London (Imperial College of Science Technology and Medicine),

Addenbrooke, T., & Potts, D. (1996). Twin tunnel construction—ground movements and lining behaviour. *Geotechnical Aspects of Underground Construction in Soft Ground, 446*

Addenbrooke, T., & Potts, D. (2001). Twin tunnel interaction: Surface and subsurface effects. *International Journal of Geomechanics, 1*(2), 249-271.

Aitchison, G. (1960). Relationships of moisture stress and effective stress functions in unsaturated soils. Paper presented at the *Pore Pressure and Suction in Soils,* London, England. pp. 47 - 52.

Anagnostou, G., & Kovári, K. (1994). The face stability of slurry-shield-driven tunnels. *Tunnelling and Underground Space Technology, 9*(2), 165-174.

Anagnostou, G., & Kovari, K. (1996). Face stability conditions with earth-pressure-balanced shields. *Tunnelling and Underground Space Technology, 11*(2), 165-173.

ASTM Standard D2435-11. (2011). Standard test methods for one-dimensional consolidation properties of soils using incremental loading. *ASTM International Standards*. 1-15.

Atkinson, J., & Mair, R. (1981). Soil mechanics aspects of soft ground tunnelling. *Ground Engineering, 14*(5)

Atkinson, J., Potts, D., & Schofield, A. (1977). Centrifugal model tests on shallow tunnels in sand. *Tunnels and Tunnelling, 9*(1), 59-64.

Balanko, L. A., Morgenstern, N. R., & Yacyshyn, R. (1982). Tangent pile wall, edmonton convention centre. Paper presented at the *Application of Walls to Landslide Control Problems,* pp. 108-123.

Barla, G., & Ottoviani, M. (1974). Stresses and displacements around two adjacent circular openings near to the ground surface. *Proceedings of the Third International Congress on Rock Mechanics,* Denver, CO., *II.* pp. 975-980.

Bayrock, L., & Hughes, G. M. (1962). *Surficial geology of the Edmonton district, Alberta* Research Council of Alberta.

Bayrock, L., & Berg, T. (1966). *Geology of the city of Edmonton*, Alta.: Research Council of Alberta.

Bishop, A. W. (1954). The use of pore-pressure coefficients in practice. *Geotechnique*, *4*(4), 148-152.

Bishop, A. (1961). The measurement of pore pressure in the triaxial test. Paper presented at the *Pore Pressure and Suction in Soils,* London, England. pp. 38 - 46.

Bishop, A. W., Kumapley, N., & El-Ruwayih, A. (1975). The influence of pore-water tension on the strength of clay. *Philosophical Transactions of the Royal Society of London.Series A, Mathematical and Physical Sciences, 278*(1286), 511-554.

Bishop, A., & Blight, G. (1963). Some aspects of effective stress in saturated and partly saturated soils. *Geotechnique, 13*(3), 177-197.

Bishop, A., Webb, D., & Lewin, P. (1965). Undisturbed samples of London clay from the Ashford common shaft: Strength–effective stress relationships. *Geotechnique, 15*(1), 1-31.

Bishop, A. W., & Little, A. L. (1967). The influence of the size and orientation of the sample on the apparent strength of the London Clay at Maldon, Essex. In *Proceedings of the Geotechnical Conference on Shear Strength of Natural Soils and Rocks. Oslo, Norway*. 19-22.

Bjerrum, L., & Eide, O. (1956). Stability of strutted excavations in clay. *Geotechnique, 6*(1), 32-47.

Blight, G. E. (1965). A study of effective stresses for volume change. *Moisture Equilibira and Moisture Changes in Soils beneath Covered Areas,* pp. 259 - 269.

Bowles Joseph, E. (1996). Foundation analysis and design. McGraw Hill, New York.

Branco, P. (1981). *Behaviour of a shallow tunnel in till.* Unpublished MSc, University of Alberta, Broms, B. B., & Brennermark, H. (1967). Stability of clay at vertical openings. *Journal of the Soil Mechanics and Foundation Engineering Division of the ASCE, 93*(1), 71-94.

Carter, J. P., Randolph, M. F., & Wroth, C. P. (1979). Stress and pore pressure changes in clay during and after the expansion of a cylindrical cavity. *International Journal for Numerical and Analytical Methods in Geomechanics*, *3*(4), 305-322

Carter, J. P., Booker, J. R., & Yeung, S. K. (1986). Cavity expansion in cohesive frictional soils. *Geotechnique*, *36*(3), 349-358.

Chapman, D., Ahn, S., & Hunt, D. V. (2007). Investigating ground movements caused by the construction of multiple tunnels in soft ground using laboratory model tests. *Canadian Geotechnical Journal, 44*(6), 631-643.

Chapman, D., Rogers, C., & Hunt, D. (2003). Investigating the settlement above closely spaced multiple tunnel constructions in soft ground. Paper presented at the *Proceedings of the ITA World Tunnelling Congress in Amsterdam, Saveur (Ed), 2.* pp. 629-635.

Chern, J., Shiao, F., & Yu, C. (1998). An empirical safety criterion for tunnel construction. Paper presented at the *Proceedings of the Regional Symposium on Sedimentary Rock Engineering, Taipei, Taiwan,* pp. 222-227.

Clarke, B. G., Carter, J. P., & Wroth, C. P. (1979). In situ determination of the consolidation characteristics of saturated clays. *Design Parameters in Geotechnical Engineering, Proceedings of the 7th European Conference of Soil Mechanics and Foundation Engineering*. Vol. 2, 207 - 211.

Clarke, B. G. (1995). *Pressuremeters in geotechnical design*. CRC Press.

Cording, E. J., & Hansmire, W. H. (1975). Displacements around soft ground tunnels. *Proceedings of the 5th PanAmerican Conference on Soil Mechanics and Foundation Engineering,* Buenos Aires. *, 4.* pp. 571-633.

Deere, D. U., Peck, R. B., Parker, H. W., Monsees, J. E., & Schmidt, B. (1969). *Design of tunnel support systems* No. Report for U.S. Department of Transportation, Office of

High Speed Ground Transportation, Contract No. 3-0152), Order No. PB 183799 from NTIS, Springfield, VA. 22151).

DeJong, J. (1971). *Foundation displacements of multi-storey structures.* Unpublished PhD, University of Alberta,

DeJong, J., & Harris, M. (1971). Settlements of two multistory buildings in edmonton. *Canadian Geotechnical Journal, 8*(2), 217-235.

Dowding, C. H., Su, M., & O'Connor, K. (1988). Principals of time domain reflectometometry applied to measurement of rock mass deformation. Paper presented at the *International Journal of Rock Mechanics and Mining Sciences & Geomechanics Abstracts, , 25.* (5) pp. 287-297.

Dowding, C. H., Dussud, M. L., Kane, W. F., & O'Connor, K. M. (2003). Monitoring deformation in rock and soil with TDR sensor cables. *Geotechnical News, 21*(2), 51-59.

Doohan, J., & McLean, D. B. (1975). *North east rail rapid transit line*. No. 934-36-08-09), EBA Engineering Consultants Ltd.

Duncan, J. M., & Dunlop, P. (1968). *Slopes in stiff-fissured clays and shales* (No. TE-68-6). California University Berkley Office of Research Services.

Dunnicliff, J. (1993). *Geotechnical instrumentation for monitoring field performance* John Wiley & Sons.

Eisenstein, Z., & Sorenson, K. L. (1986). Tunnelling for the south LRT extension in Edmonton, Alberta. *Tunnelling Association of Canada Annual Publication,*

Eisenstein, Z., El-Nahhas, F., & Thompson, S. (1981). Strain field around a tunnel in stiff soil. Paper presented at the *Proceedings of the International Conference on Soil Mechanics and Foundation Engineering, 10th. , 1.* (Conf Paper)

Eisenstein, Z., & Thomson, S. (1978). Geotechnical performance of a tunnel in till. *Canadian Geotechnical Journal, 15*(3), 332-345.

Thomson, S., & El-Nahhas, F. (1980). Field measurements in two tunnels in Edmonton, Alberta. *Canadian Geotechnical Journal*, 17, 20-33.

El-Nahhas, F. (1981). *The behaviour of tunnels in stiff soils.* Unpublished PhD, University of Alberta.

El-Nahhas, F., & Harris, M. C. (1981). *South LRT extension geotechnical report no. 10 – government centre station detailed geotechnical investigation.* Thurber Consultants Ltd.

Fredlund, D. (1969). Consolidometer test procedural factors affecting swell properties. Paper presented at the *Proceedings of the Second International Conference on Expansive Clay Soils, Texas A & M Press, College Station, TX,* pp. 435-456.

Fredlund, D. G., & Dahlman, A. E. (1971). Statistical geotechnical properties of glacial Lake Edmonton sediments. *First International Conference on Applications of Statistics and Probability to Soil and Structural Engineering,* Hong Kong. pp. 204 - 228.

Fredlund, D. G., & Morgenstern, N. R. (1977). Stress state variables for unsaturated soils. *Journal of Geotechnical and Geoenvironmental Engineering, 103*(ASCE 12919)

Fredlund, D. G., Rahardjo, H. & Fredlund, M. D., (2012). *Unsaturated soil mechanics in engineering practice.*

Gasparre, A., Nishimura, S., Coop, M., & Jardine, R. (2007). The influence of structure on the behaviour of london clay. *Géotechnique, 57*(1), 19-31.

Ghaboussi, J., & Ranken, R. E. (1977). Interaction between two parallel tunnels. *International Journal for Numerical and Analytical Methods in Geomechanics, 1*(1), 75-103.

Gibson, R., & Anderson, W. (1961). In situ measurement of soil properties with the pressuremeter. *Civil Engineering and Public Works Review, 56*(658), 615-618.

Hansmire, W. H. (1975). *Field measurements of ground displacements about a tunnel in soil* . Unpublished PhD, University of Illinois at Urbana-Champaign,

Hansmire, W. H., & Cording, E. J. (1985). Soil tunnel test section: Case history summary. *Journal of Geotechnical Engineering, 111*(11), 1301-1320.

Harris, M. C., Chatterji, P. K., Tweedie, R. W., & Kack, G. J. (January 16, 1986). *South light rail transit extension - phase II; in situ testing at proposed university station site; geotechnical report no. 3* No. 3). Edmonton, AB.

Hoek, E. (2001). Big tunnels in bad rock. *Journal of Geotechnical and Geoenvironmental Engineering, 127*(9), 726-740.

Hight, D., Gasparre, A., Nishimura, S., Minh, N., Jardine, R., & Coop, M. (2007). Characteristics of the london clay from the terminal 5 site at heathrow airport. *Géotechnique, 57*(1), 3-18.

Hilf, J.W. (1948). Estimating construction pore pressures in rolled earth dams. *Proceedings 2nd International Conference on Soil Mechanics and Foundation Engineering*, Rotterdam, Vol. 111, pp. 234-240.

Ho, D. Y., & Fredlund, D. G. (1982). A multistage triaxial test for unsaturated soil. *ASTM Geotechnical Testing Journal*, *5*(1/2).

Houlsby, G., Clarke, B., & Wroth, C. (1986). Analysis of the unloading of a pressuremeter in sand. Paper presented at the *Proceedings of the Pressuremeter and its Marine Applications: 2nd International Symposium. Philadelphia: ASTM Publication,* pp. 245-262.

Hughes, J.M.O., Wroth, C.P., & Windle, D. (1977). Pressuremeter tests in sands. *Geotechnique*, *27*(4), 455-477.

Hunt, D. (2004). *Predicting the ground movements above twin tunnels constructed in London clay.* Unpublished PhD, University of Birmingham.

Kathol, C., & McPherson, R. A. (1975). *Urban geology of Edmonton* Alberta Research Council.

Kerfoot, D. E. (1972). Thermal contraction cracks in an arctic tundra environment. *Arctic,* 142-150.

Kimura, T., & Mair, R. (1981). Centrifugal testing of model tunnels in soft clay. Paper presented at the *Proceedings of the 10th International Conference on Soil Mechanics and Foundation Engineering,* pp. 319-322.

Kjartanson, B. H., Shields, D. H. & Domaschuk, L. (1990). Pressuremeter creep testing in ice: calibration and test procedures. *Geotechnical Testing Journal, ASTM*, 13(1), 3-9

Koungelis, D., & Augarde, C. (2004). Interaction between multiple tunnels in soft ground. Paper presented at the *Developments in Mechanics of Structures and Materials: Procs. 18th Australasian Conference, Perth, Australia,* pp. 1031-1036.

Lachenbruch, A. H. (1962). Mechanics of thermal contraction cracks and ice-wedge polygons in permafrost. *Geological Society of America Special Papers, 70*, 1-66.

Lambe, T. W., & Whitman, R. V. (1969). Soil mechanics: Series in soil engineering.

Lo, K. Y. (1970). The operational strength of fissured clays. *Geotechnique*, *20*(1), 57-74.

Mair, R., & Taylor, R. (1997). Theme lecture: Bored tunnelling in the urban environment. *Of XIV ICSMFE, 4*, 2353-2385.

Mair, R., Taylor, R., & Burland, J. (1996). Prediction of ground movements and assessment of risk of building damage due to bored tunnelling. Paper presented at the *Fourth International Symposium of International Conference of Geotechnical Aspects of on Underground Construction in Soft Ground,* pp. 713-718.

Marsland, A. (1973). *Large in-Situ Tests to Measure the Properties of Stiff Fissured Clays,*

Marsland, A., & Butler, M. E. (1968). *Strength measurements on stiff fissured Barton clay from Fawley (Hampshire)* Building Research Station, Ministry of Public Building and Works.

Marsland, A. (1971). *Large in-situ tests to measure the properties of stiff fissured clays* (No. CP 1/73), In *Proceedings of the First Australian-New Zealand Conference on Geomechanics*, Melbourne, Vol 1, 180-189.

Marsland, A. (1971). The shear strength of stiff fissured clays (CP21/71). In *Proceedings of the Roscoe Memorial Symposium*, Cambridge University Engineering Department.

Marsland, A., & Randolph, M. F. (1977). Comparisons of the results from pressuremeter tests and large in-situ plate tests in London clay. *Geotechnique 27*(2), 217-243.

Martin, C. D. (2010). *Technical note: Ground strength, ground behaviour and primary excavation support for the NLRT SEM tunnels.* Unpublished Report to the City of Edmonton.

Matheson, D. S. (December 8, 1969). *Report on a tunnel roof fall in till* No. SM 4). Edmonton, AB.

Matheson, D. S. (1970). A tunnel roof failure in till. *Canadian Geotechnical Journal, 7*(3), 313-317.

May, R., & Thomson, S. (1978). The geology and geotechnical properties of till and related deposits in the edmonton, alberta, area. *Canadian Geotechnical Journal, 15*(3), 362-370.

Mayne, P. W. (2001). Stress-strain-strength-flow parameters from enhanced in-situ tests. Paper presented at the *Proc. Int. Conf. on in Situ Measurement of Soil Properties and Case Histories, Bali,* pp. 27-47.

Medieros, L. V. (1979). *Deep excavations in stiff soils.* Unpublished PhD, University of Alberta.

Morgan, A. V. (1972). Late Wisconsinan ice-wedge polygons near Kitchener, Ontario, Canada. *Canadian Journal of Earth Sciences, 9*(6), 607-617.

Morgenstern, N., & Thomson, S. (1971). Comparative observations on the use of the pitcher sampler in stiff clay. *American Society for Testing and Materials, Special Technical Publication, 483*, 180-191.

Morrison, N. (1972). *Investigation of foundaton deformations using an in situ pressure probe.* Unpublished Master of Science, University of Alberta Civil and Environmental Engineering, Edmonton, AB.

Mohamad, H. (2008). *Distributed optical fibre strain sensing of geotechnical structures.* Unpublished PhD, Cambridge University,

Muir Wood, A. M., & Gibb, F. R. (1971). Design and construction of the cargo tunnel at Heathrow airport, London. Paper presented at the *ICE Proceedings, 48.* (1) pp. 11-34.

Neal, J. T., Langer, A. M., & Kerr, P. F. (1968). Giant desiccation polygons of great basin playas. *Geological Society of America Bulletin, 79*(1), 69-90.

Ng, C. W., Lee, K., & Tang, D. K. (2004). Three-dimensional numerical investigations of new Austrian tunnelling method (NATM) twin tunnel interactions. *Canadian Geotechnical Journal, 41*(3), 523-539.

Palmer, A. C. (1972). Undrained plane-strain expansion of a cylindrical cavity in clay: a simple interpretation of the pressuremeter test. *Geotechnique*, *22*(3), 451-457.

Peck, R. B. (1969). Deep excavations and tunneling in soft ground," proceedings". Paper presented at the *7th International Conference on Soil Mechanics and Foundation Engineering, Mexico City, Mexico, , 1.* pp. 225-290.

Peck, R. (1969). Advantages and limitations of the observational method in applied soil mechanics. *Geotechnique, 19*(2)

Phelps, D. J., & Brandt, J. R. (1989). Design and construction of tunnels for the Edmonton LRT. *Tunnelling Association of Canada Annual Publication,* , 45-59.

Phelps, D. J., Brandt, J. R., & Eisenstein, Z. (1988). Design and construction of closely spaced tunnels for the Edmonton subway. *International Congress on Tunnels and Water,* Madrid, Spain. pp. 273 - 281.

Randolph, M. F., Carter, J. P., & Wroth, C. P. (1979). Driven piles in clay - the effects of installation and subsequent consolidation. *Geotechnique*, *29*(4), 361-393.

Randolph, M. F., & Wroth, C. P. (1979). An analytical solution for the consolidation around a driven pile. *International Journal for Numerical and Analytical Methods in Geomechanics*, *3*(3), 217-229.

Ranken, R. E. (1978). *Analysis of ground-liner interactions for tunnels* . Unpublished PhD, University of Illinois at Urbana-Champaign,

Rankin, W. (1988). Ground movements resulting from urban tunnelling: Predictions and effects. *Geological Society, London, Engineering Geology Special Publications, 5*(1), 79-92.

Sakurai, S. (1981). Direct strain evaluation technique in construction of underground opening. Paper presented at the 22nd U.S. Symposium on Rock Mechanics (USRMS), June 29 - July 2, 1981, Cambridge, MA.

Satija, B., & Gulhati, S. (1979). Strain rate for shearing testing of unsaturated soil. *Proceedings 6th Asian Regional Conference Soil Mechanics and Foundation Engineering, Singapore,* 83-86.

Schiffman, R.L., & Gibson, R.E. (1964). Consolidation of nonhomogeneous clay layers. *Journal of the Soil Mechanics and Foundations Division*, 90(5), 1-30.

Schofield, A. N. (1980). Cambridge geotechnical centrifuge operations. *Geotechnique, 30*(3), 227-268.

Shaw, J. (1982). Melt-out till in the Edmonton area, Alberta, Canada. *Canadian Journal of Earth Sciences, 19*(8), 1548-1569.

Simons, N. E. (1967). Discussion on shear strength of stiff clay. In *Proceedings of the Geotechnical Conference* (Vol. 2, pp. 159-160).

Skempton, A. W. (1954). The pore-pressure coefficients A and B. *Geotechnique*, *4*(4), 143-147.

Skempton, A. (1960). Effective stress in soils, concrete, and rocks. *Pore Pressure and Suction in Soils,* 4-16.

Smith, L. B., & Harris, M. C. (1980). *South LRT extension geotechnical report no. 5 - insitu pressuremeter tests; 104th and 107th street stations* No. 14-31-1)Thurber Consultants Ltd.

Soliman, M., & Cherniawski, M. J. (2010). *Final geotechnical report; Edmonton north LRT extension - Churchill station to MacEwan station* No. Vol. 1(1)), AMEC Earth and Environmental.

Stalker, A. M. (1968). Geology of the terraces at Cochrane, Alberta. *Canadian Journal of Earth Sciences, 5*(6), 1455-1466.

Stille, H., & Palmström, A. (2008). Ground behaviour and rock mass composition in underground excavations. *Tunnelling and Underground Space Technology, 23*(1), 46-64.

Suwansawat, S., & Einstein, H. H. (2007). Describing settlement troughs over twin tunnels using a superposition technique. *Journal of Geotechnical and Geoenvironmental Engineering, 133*(4), 445-468.

Terzaghi, K. V. (1936). The shearing resistance of saturated soils and the angle between the planes of shear. In *Proceedings of the 1st International Conference on Soil Mechanics and Foundation Engineering*, Vol. 1, 54-56.

Terzaghi, K. (1943). Earth pressure and shearing resistance of plastic clay: A symposium: Liner-plate tunnels on the Chicago (IL) subway. *Transactions of the American Society of Civil Engineers, 108*(1), 970-1007.

Terzaghi, K., Peck, R.B., Mesri, G. (1996). *Soil mechanics in engineering practice*. John Wiley & Sons.

Thomson, S. (1969). *A summary of laboratory results on Lake Edmonton clay*, Internal Note: SM2), Department of Civil Engineering University of Alberta.

Thomson, S., Martin, R., & Eisenstein, Z. (1982). Soft zones in the glacial till in downtown Edmonton. *Canadian Geotechnical Journal, 19*(2), 175-180.

Tweedie, R. W., Harris, M. C., Gerber, G. E., & Eisenstein, Z. (1989). Ground and structure monitoring for the Edmonton SLRT - phase II tunnels. *Tunnelling Association of Canada Annual Publication,* 61-72.

Vermeer, P., & Ruse, N. (2000). Face stability when tunneling in soil and homogeneous rock. *Proceedings Developments in Theoretical Soil Mechanics,* 123-138.

Vermeer, P. A., Ruse, N., & Marcher, T. (2002). Tunnel heading stability in drained ground. *Felsbau, 20*(6), 8-18.

Warren, P. S. (1954). Some glacial features of central Alberta. *Roy. Soc. Canada Trans*, *48*, 75-85.

Westgate, J. (1968). Linear sole markings in pleistocene till. *Geological Magazine, 105*(6), 501-505.

Westgate, J. A. (1969). The quaternary geology of the Edmonton area, Alberta. In *Pedology and Quaternary Research Symposium, National Research Council of Canada* (pp. 129-152).

Wittebolle, R. J. (1983). *The influence of microfabric on the engineering properties of glacial till.* Unpublished MSc, University of Alberta.

Withers, N. J., Howie, J., Hughes, J. M. O., & Robinson, P. K. (1989). Performance and analysis of cone pressuremeter tests in sands. *Géotechnique*, *39*(3), 433-454.

Wroth, C.P. & Hughes, J.M.O. (1973). An instrument for the in situ measurement of the properties of soft clays. In *Proceedings of the 8th International Conference of Soil Mechanics and Foundation Engineering (Moscow),* 1(2), 487 – 494.

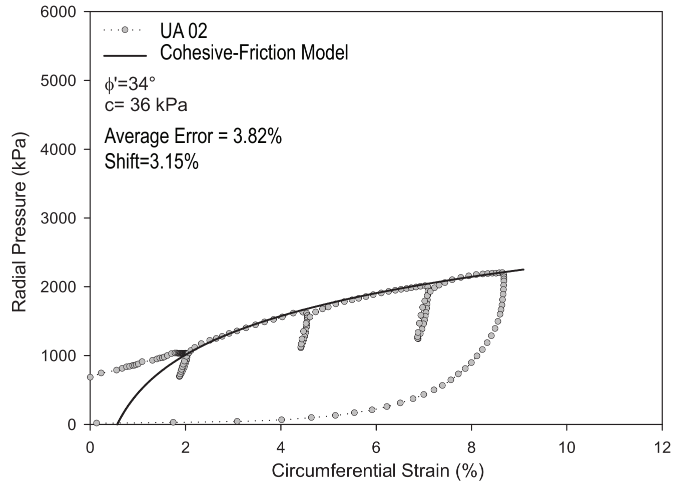

Figure A.1 Cohesive frictional model fit (UA 02)

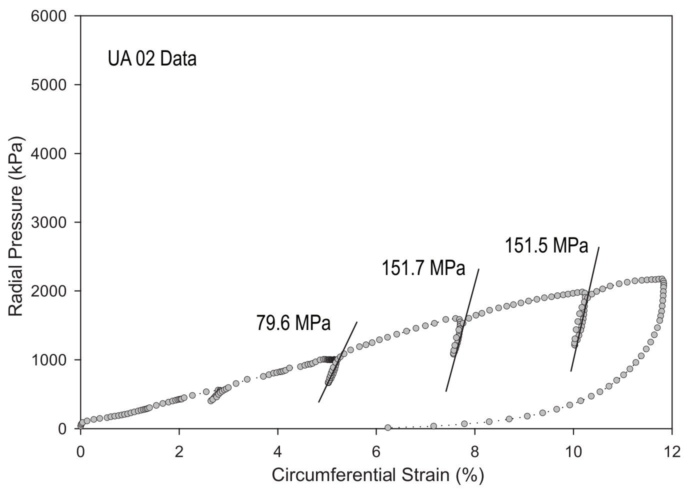

Figure A.2 Field data and shear modulus calculations (UA 02)

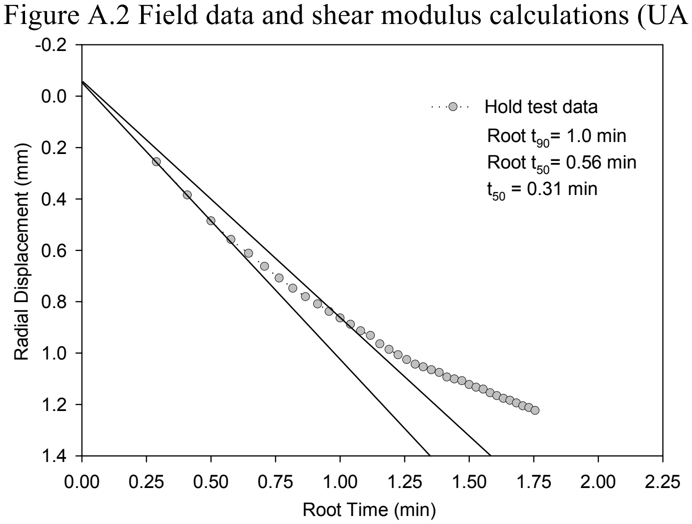

Figure A.3 Hold test data and t_{90} calculation (UA 02)

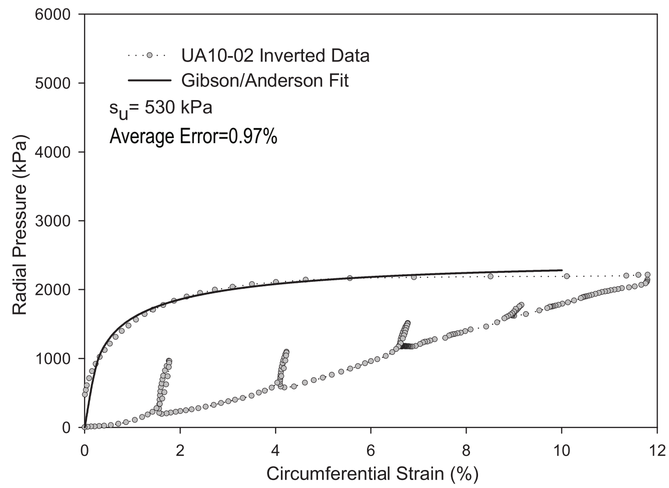

Figure A.4 Inverted undrained shear strength analysis (UA 02)

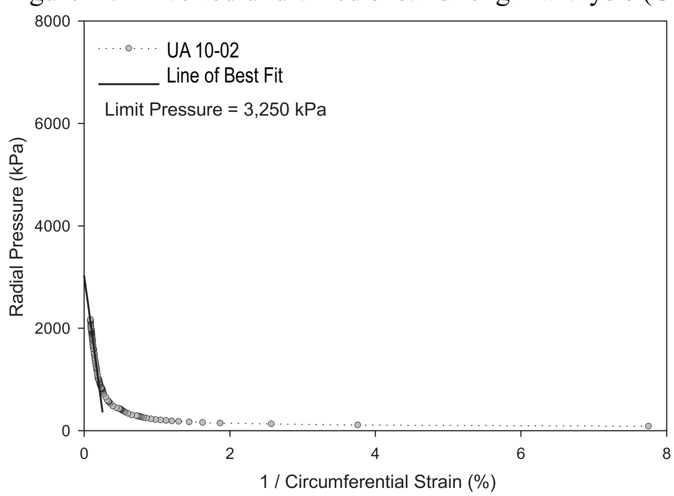

Figure A.5 Limit pressure calculation (UA 02)

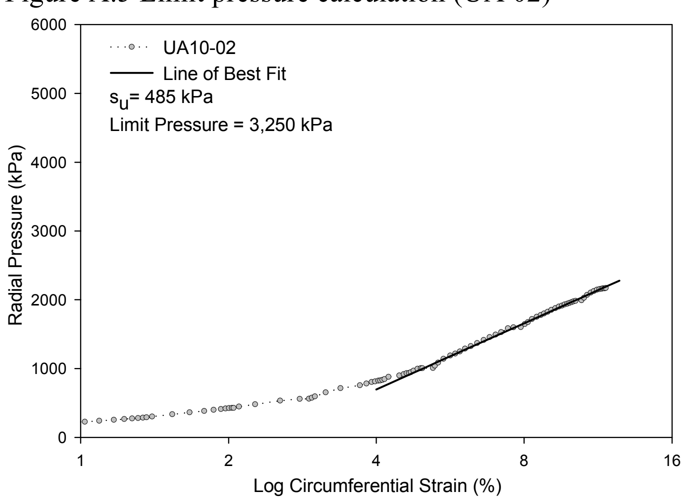

Figure A.6 Undrained shear strength; log method (UA 02)

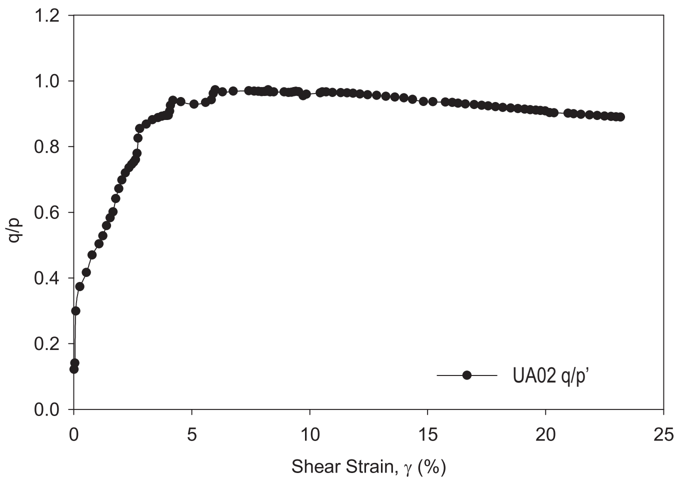

Figure A.7 Principal stress ratio versus shear strain (UA 02)

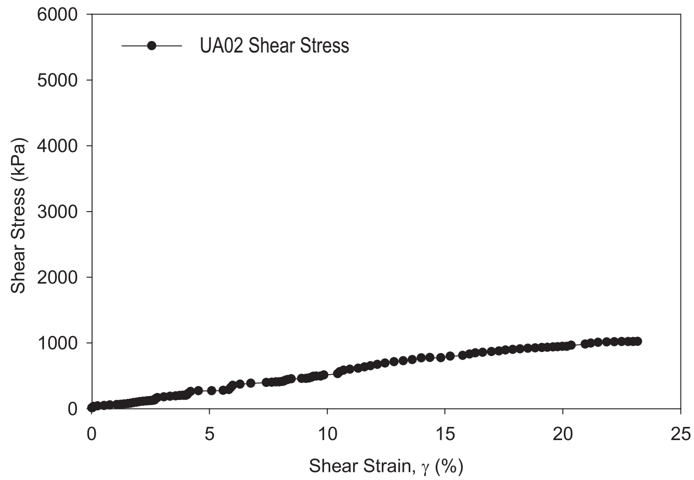

Figure A.8 Shear stress versus shear strain (UA 02)

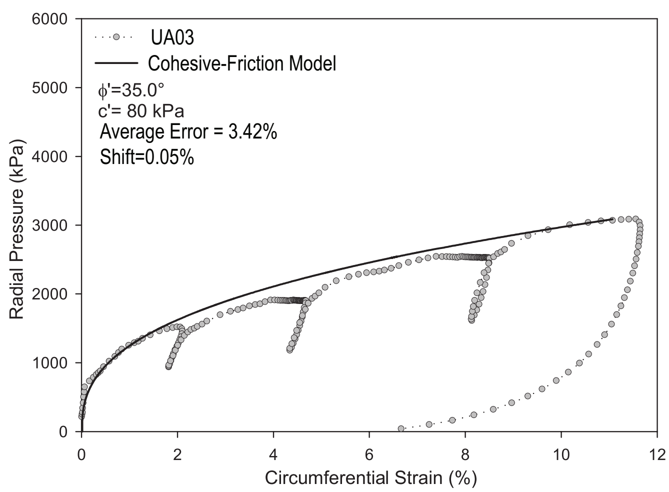

Figure A.9 Cohesive frictional model fit (UA 03)

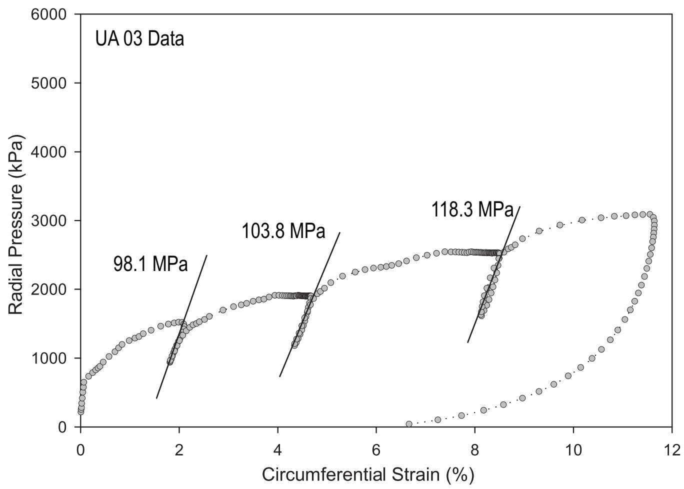

Figure A.10 Field data and shear modulus calculations (UA 03)

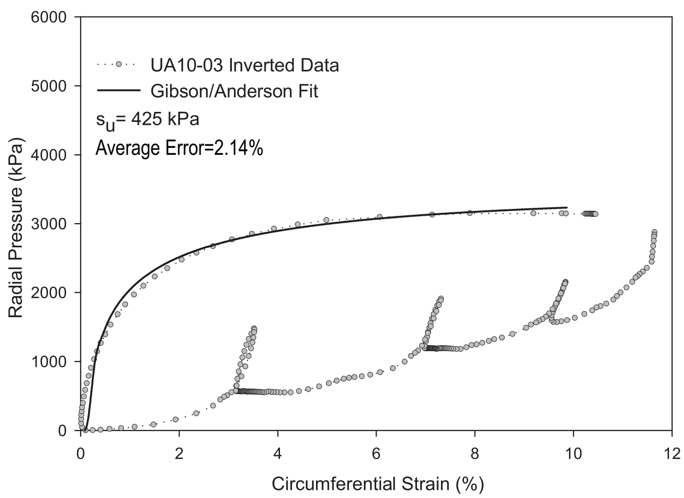

Figure A.11 Inverted undrained shear strength analysis (UA 03)

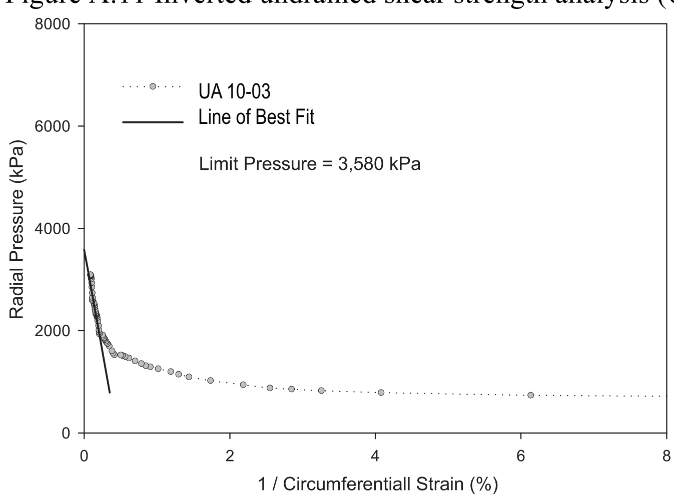

Figure A.12 Limit pressure calculation (UA 03)

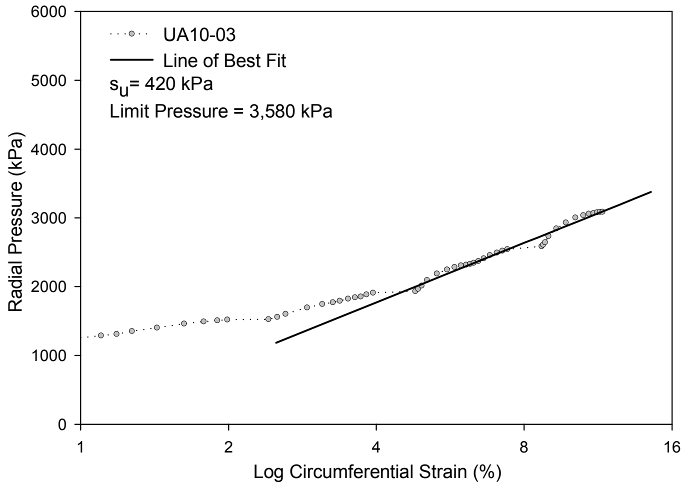

Figure A.13 Undrained shear strength; log method (UA 03)

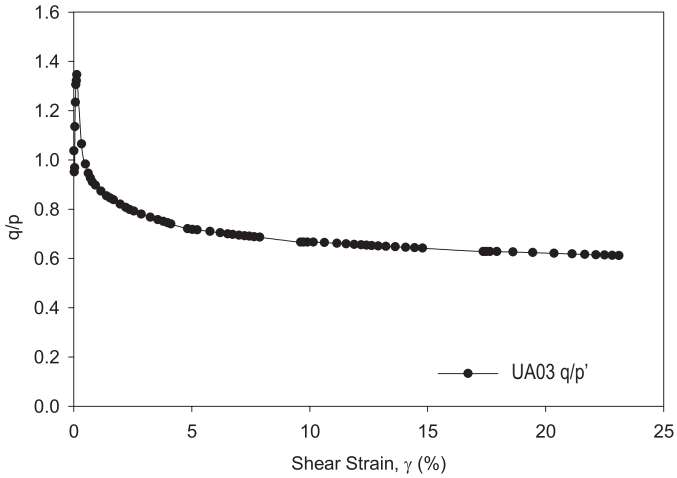

Figure A.14 Principal stress ratio versus shear strain (UA 03)

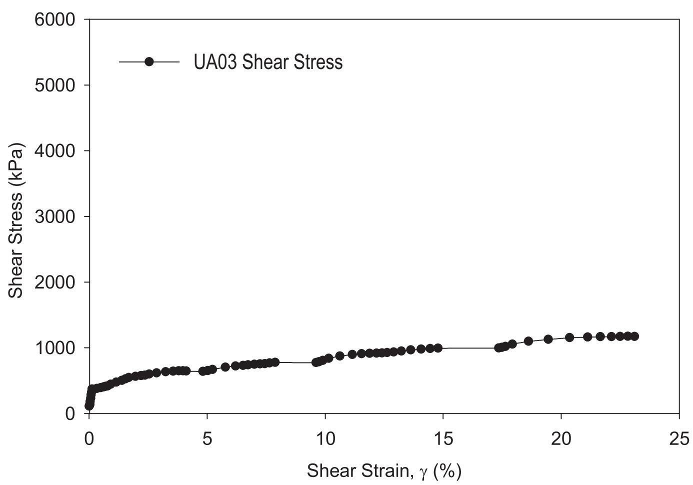

Figure A.15 Shear stress versus shear strain (UA 03)

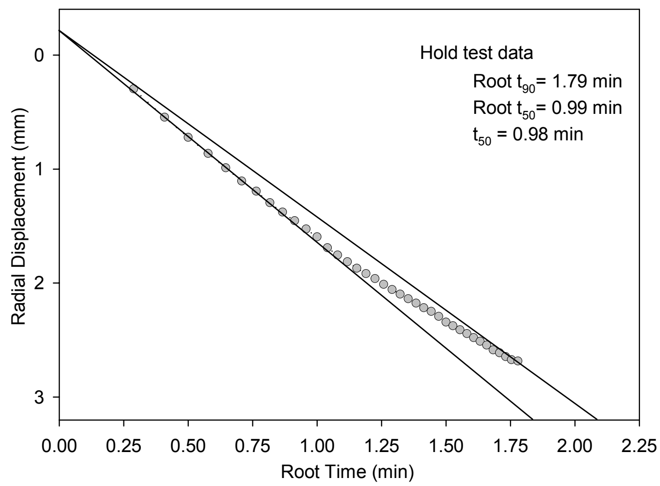

Figure A.16 Hold test data and t_{90} calculation (UA 03)

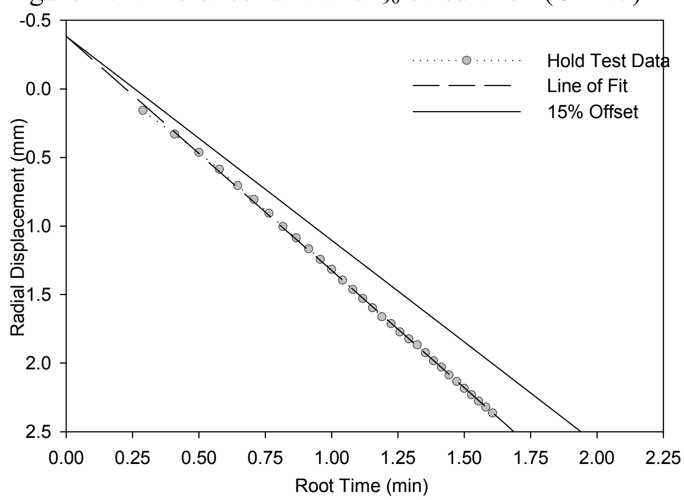

Figure A.17 Hold test data and t_{90} calculation (UA 03)

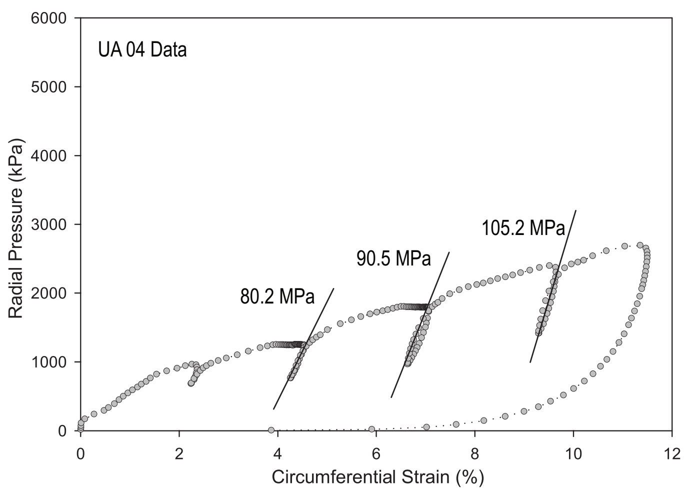

Figure A.18 Field data and shear modulus calculations (UA 04)

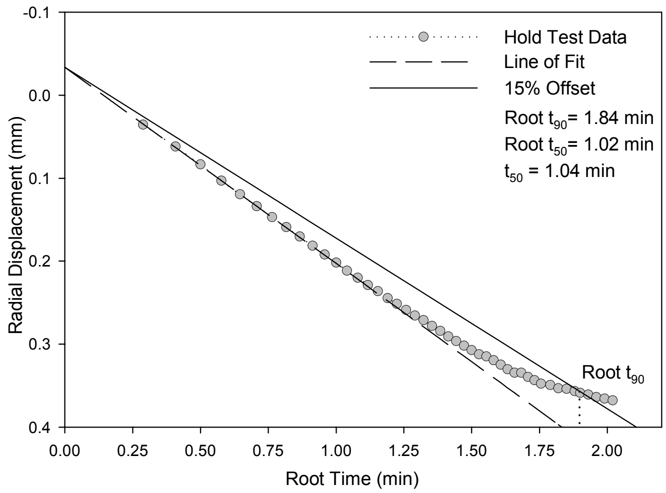

Figure A.19 Hold test data and t_{90} calculation (UA 04)

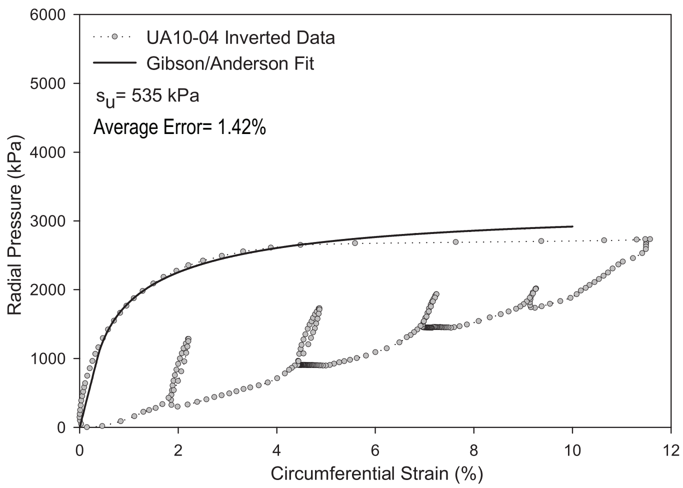

Figure A.20 Inverted undrained shear strength analysis (UA 04)

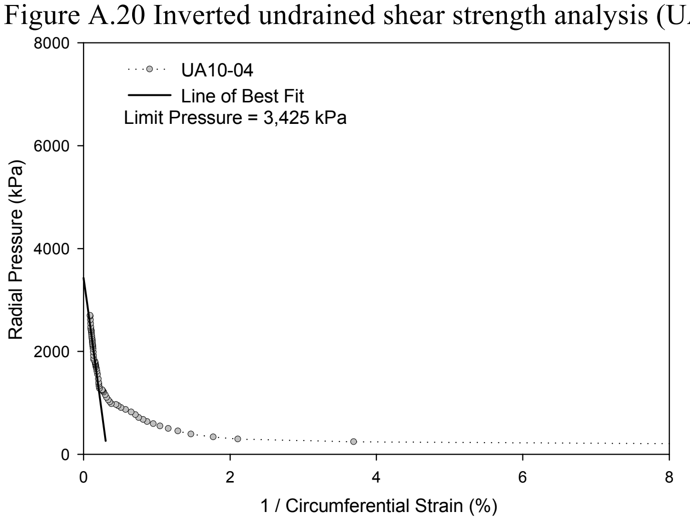

Figure A.21 Limit pressure calculation (UA 04)

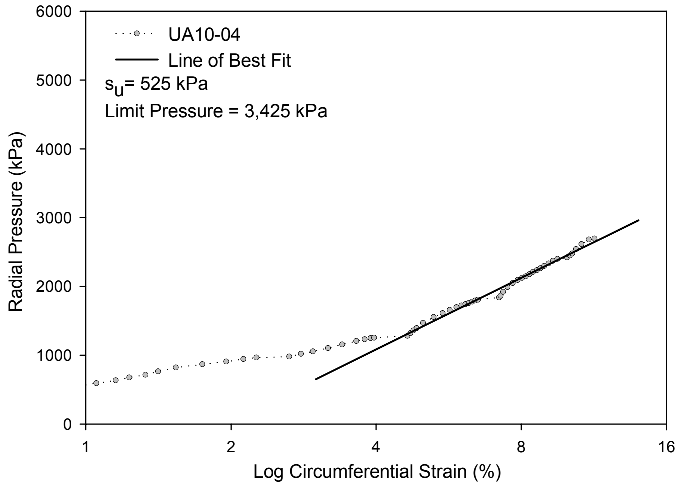

Figure A.22 Undrained shear strength; log method (UA 04)

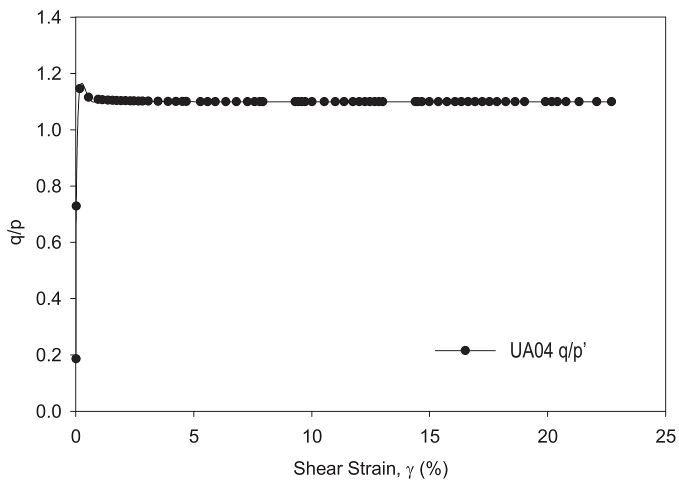

Figure A.23 Principal stress ratio versus shear strain (UA 04)

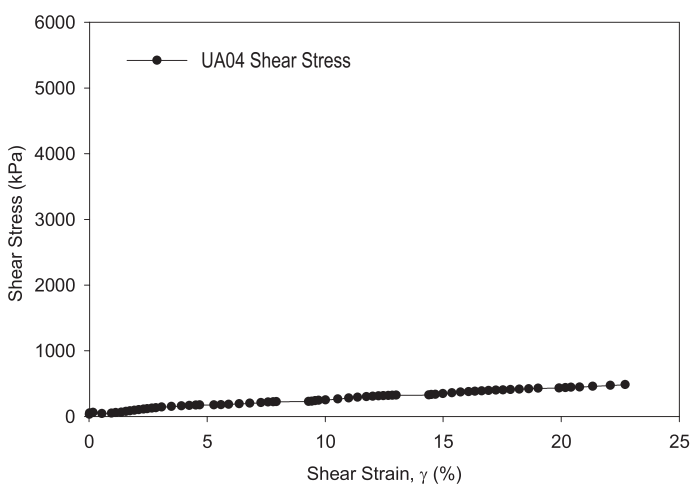

Figure A.24 Shear stress versus shear strain (UA 04)

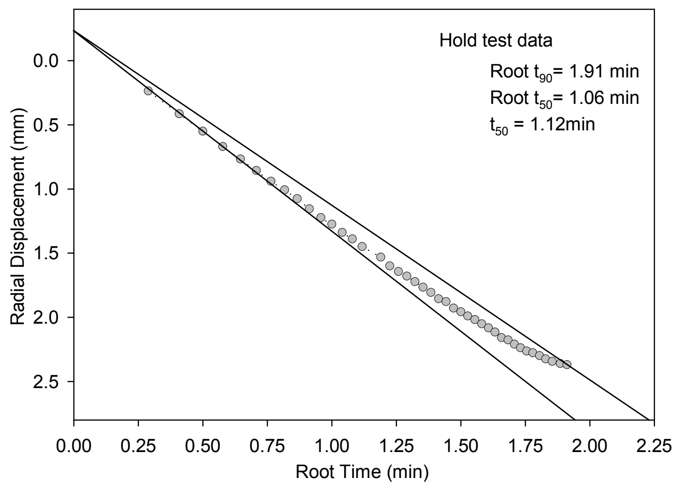

Figure A.25 Hold test data and t_{90} calculation (UA 05)

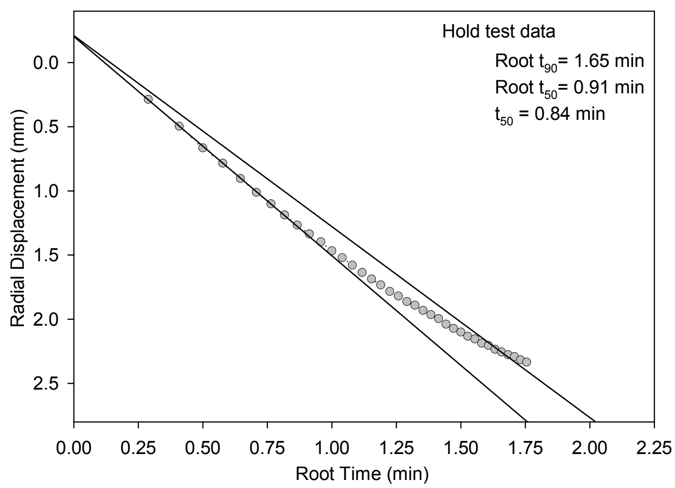

Figure A.26 Hold test data and t_{90} calculation (UA 05)

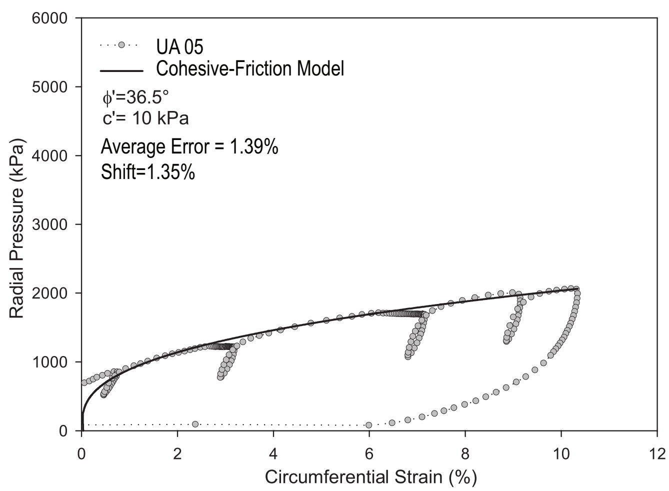

Figure A.27 Cohesive frictional model fit (UA 05)

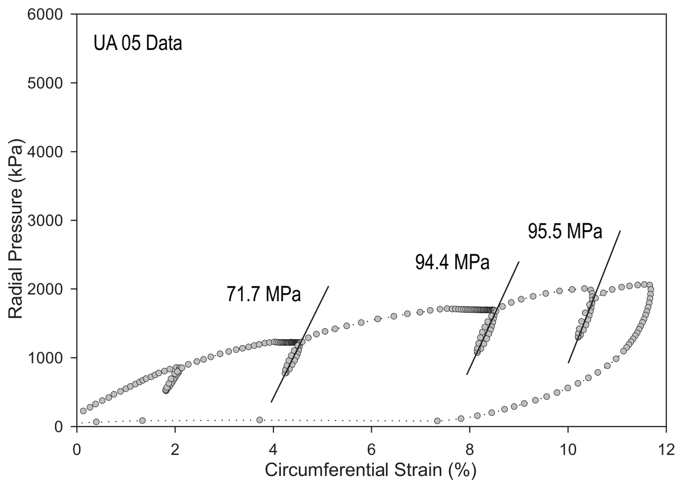

Figure A.28 Field data and shear modulus calculations (UA 05)

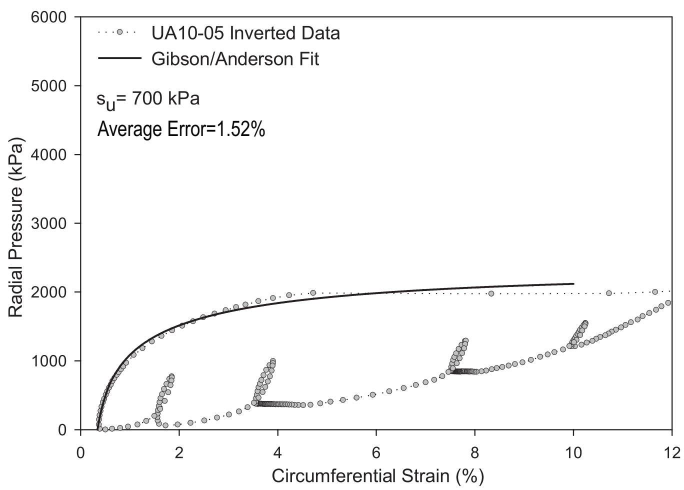

Figure A.29 Inverted undrained shear strength analysis (UA 05)

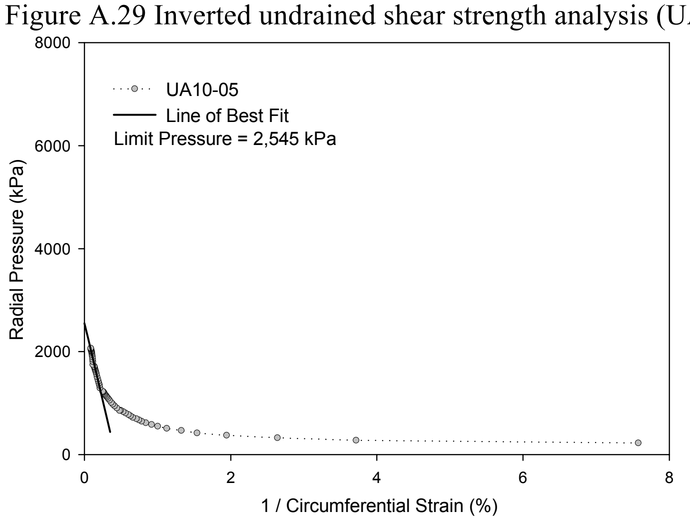

Figure A.30 Limit pressure calculation (UA 05)

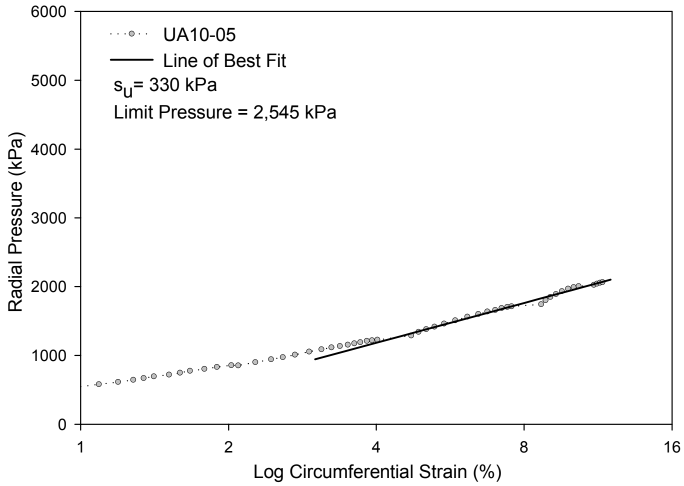

Figure A.31 Undrained shear strength; log method (UA 05)

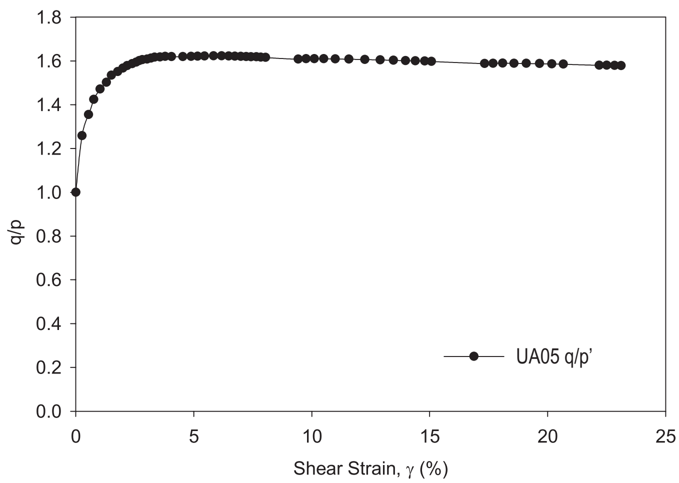

Figure A.32 Principal stress ratio versus shear strain (UA 05)

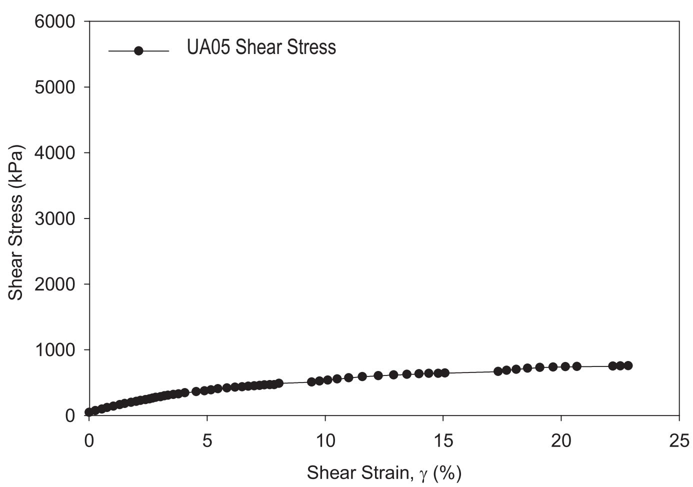

Figure A.33 Shear stress versus shear strain (UA 05)

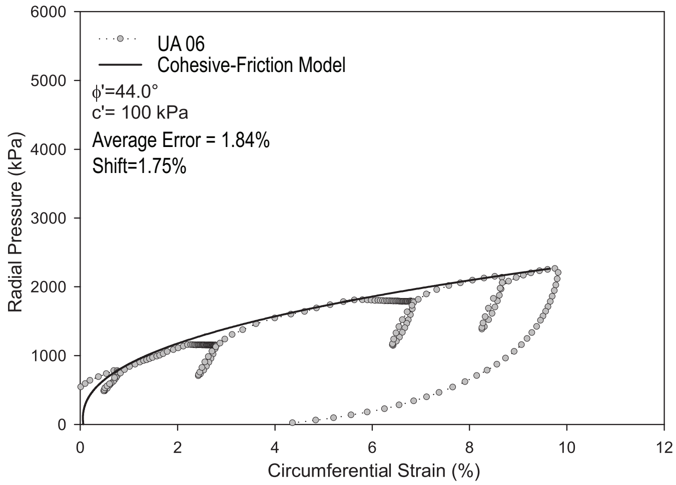

Figure A.34 Cohesive frictional model fit (UA 06)

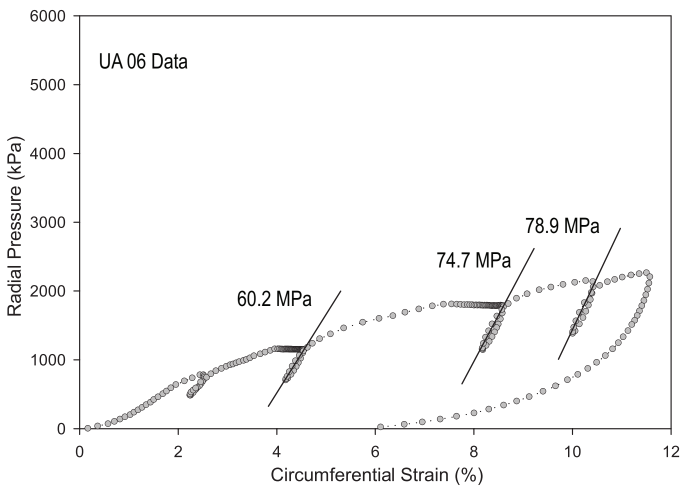

Figure A.35 Field data and shear modulus calculations (UA 06)

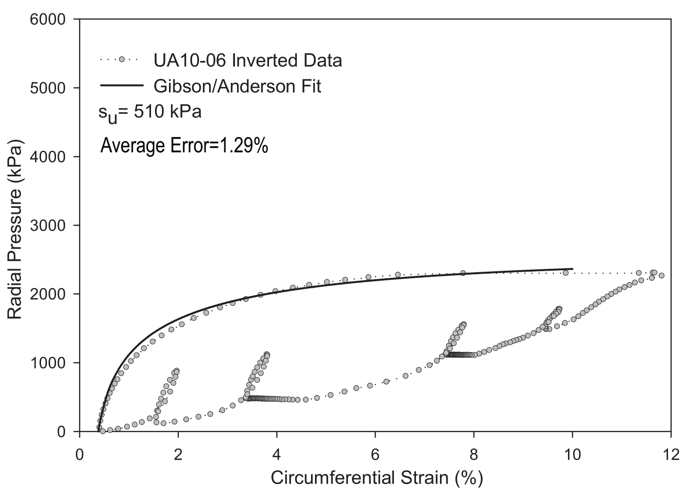

Figure A.36 Inverted undrained shear strength analysis (UA 06)

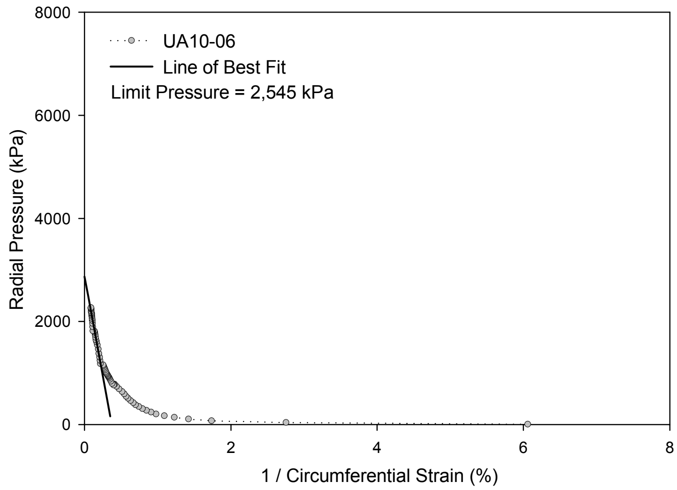

Figure A.37 Limit pressure calculation (UA 06)

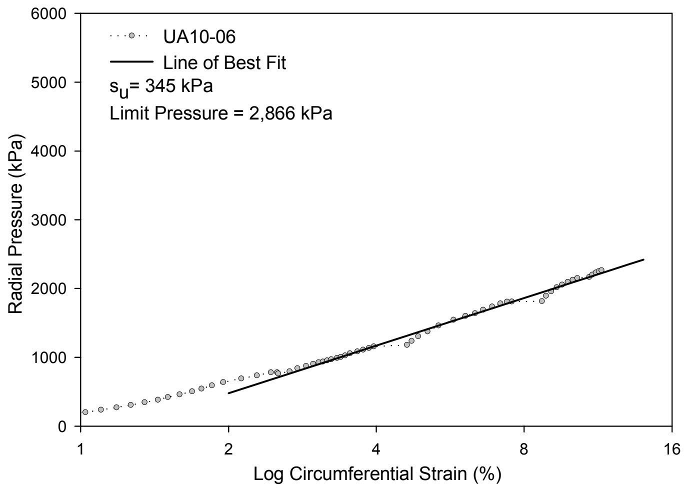

Figure A.38 Undrained shear strength; log method (UA 06)

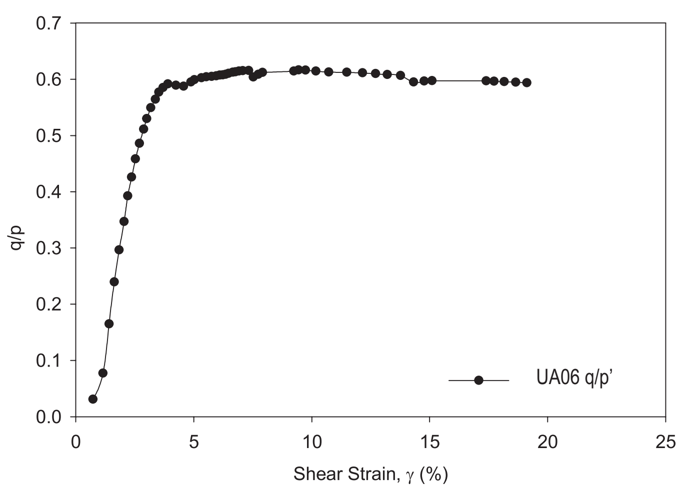

Figure A.39 Principal stress ratio versus shear strain (UA 06)

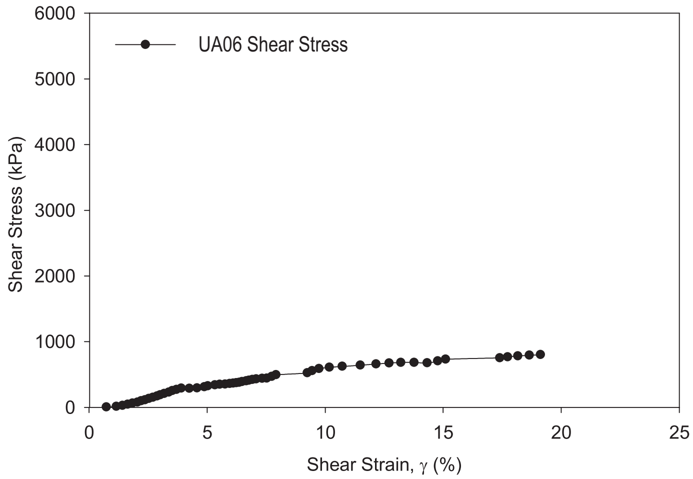

Figure A.40 Shear stress versus shear strain (UA 06)

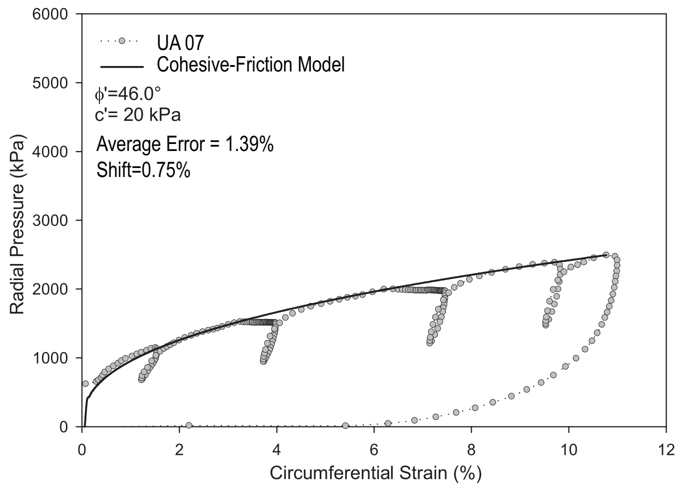

Figure A.41 Cohesive frictional model fit (UA 07)

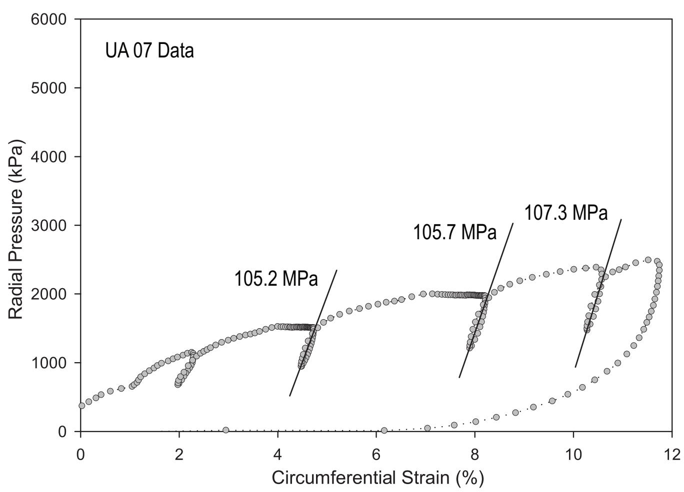

Figure A.42 Field data and shear modulus calculations (UA 07)

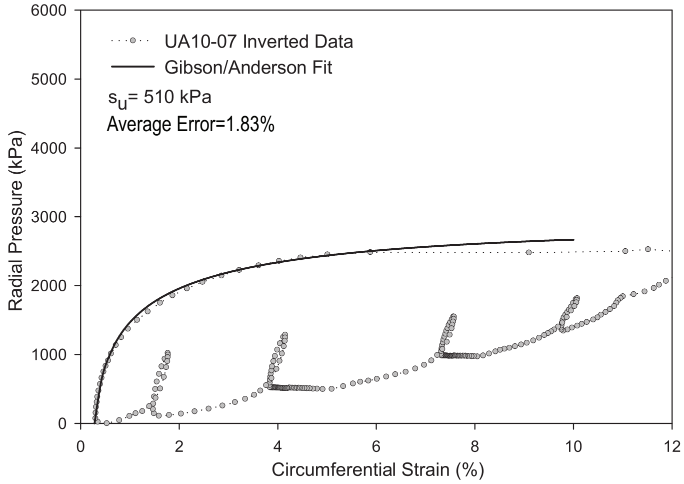

Figure A.43 Inverted undrained shear strength analysis (UA 07)

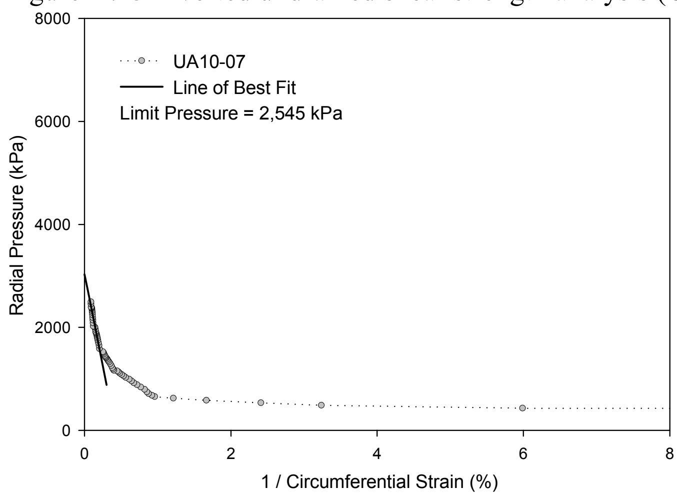

Figure A.44 Limit pressure calculation (UA 07)

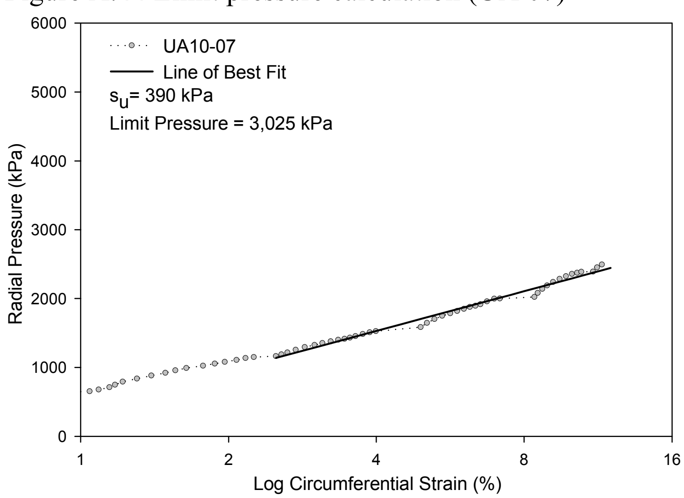

Figure A.45 Undrained shear strength; log method (UA 07)

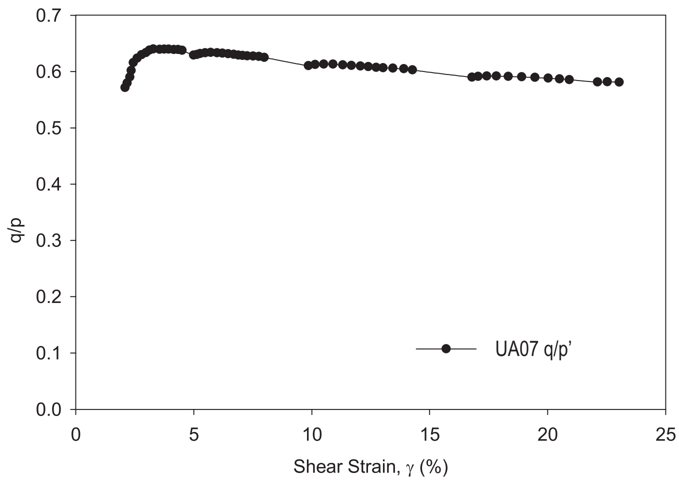

Figure A.46 Principal stress ratio versus shear strain (UA 07)

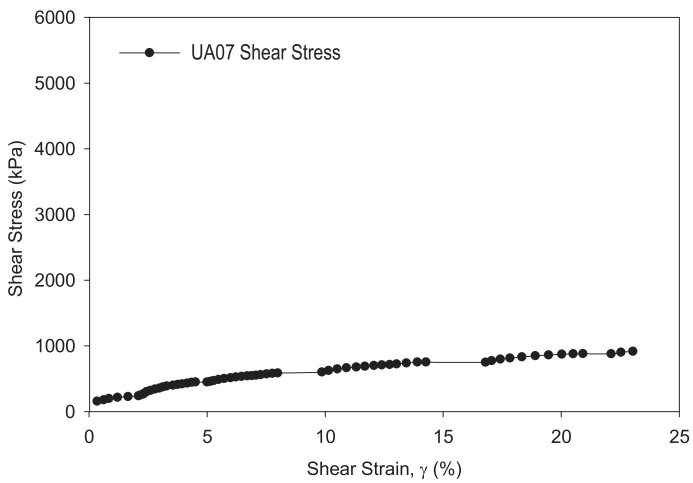

Figure A.47 Shear stress versus shear strain (UA 07)

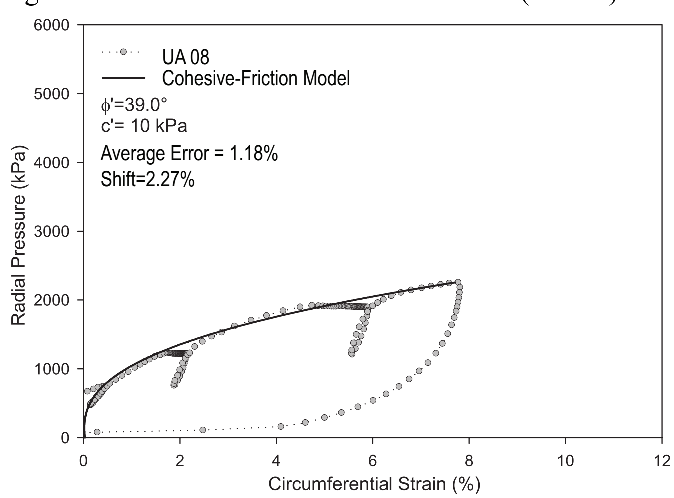

Figure A.48 Cohesive frictional model fit (UA 08)

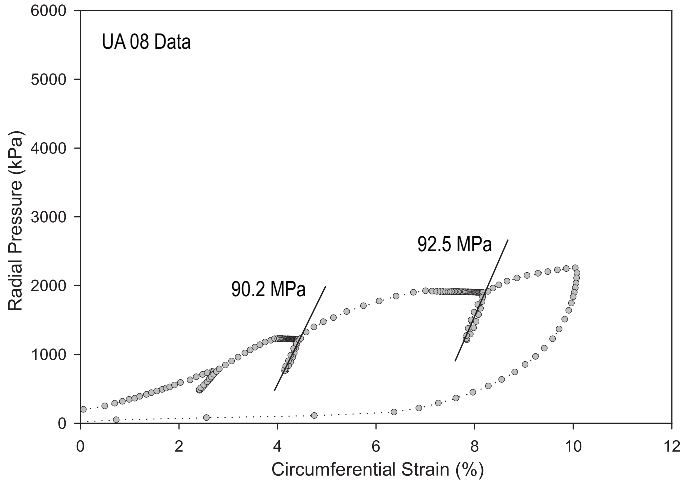

Figure A.49 Field data and shear modulus calculations (UA 08)

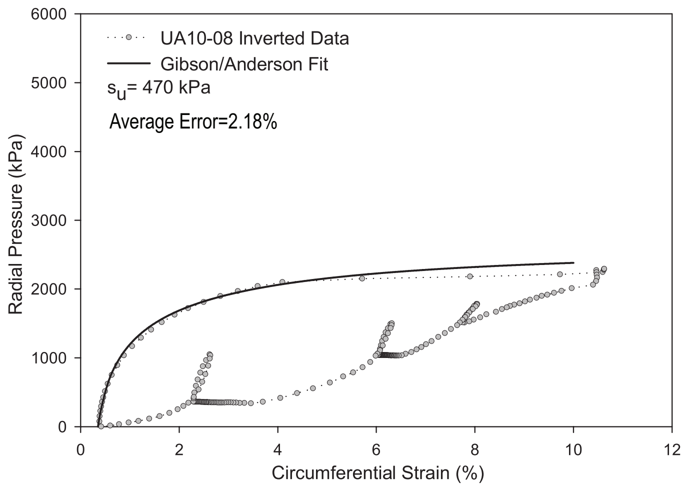

Figure A.50 Inverted undrained shear strength analysis (UA 08)

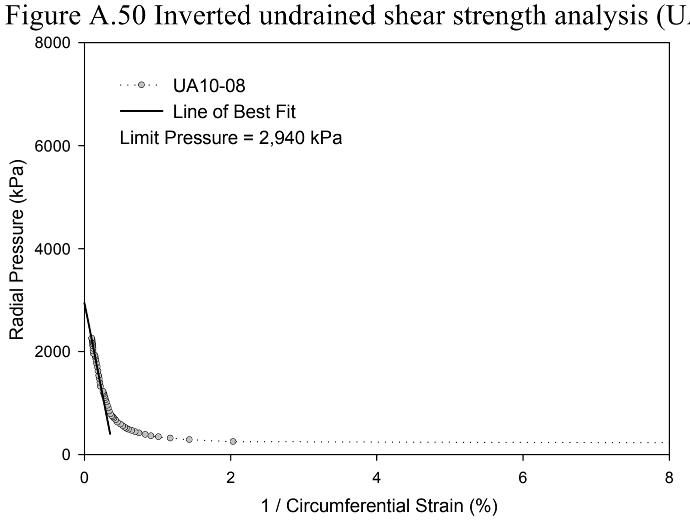

Figure A.51 Limit pressure calculation (UA 08)

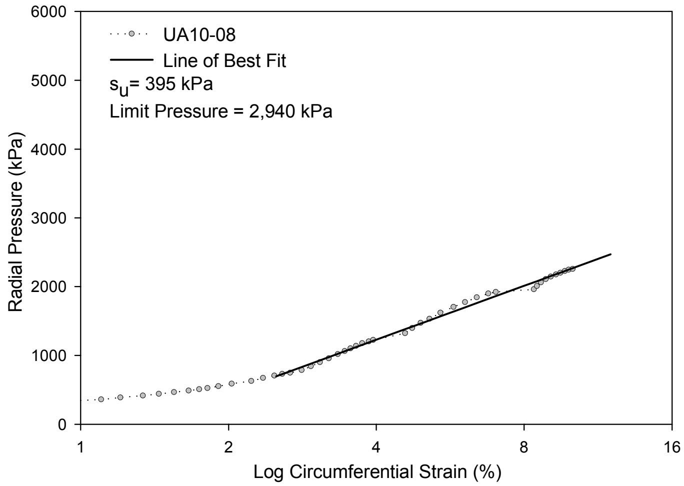

Figure A.52 Undrained shear strength; log method (UA 08)

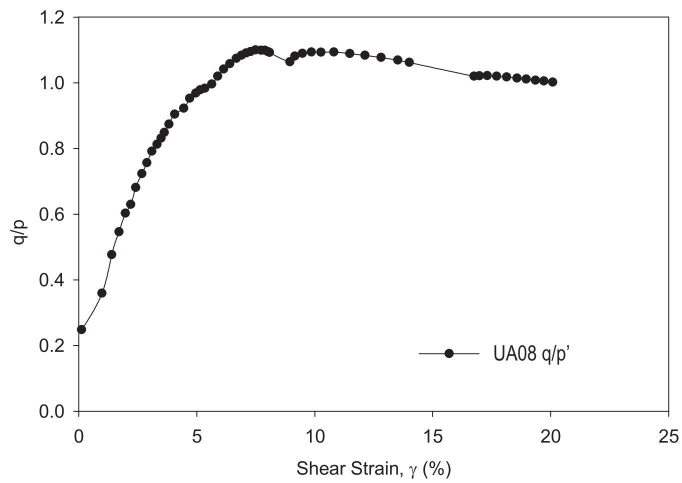

Figure A.53 Principal stress ratio versus shear strain (UA 08)

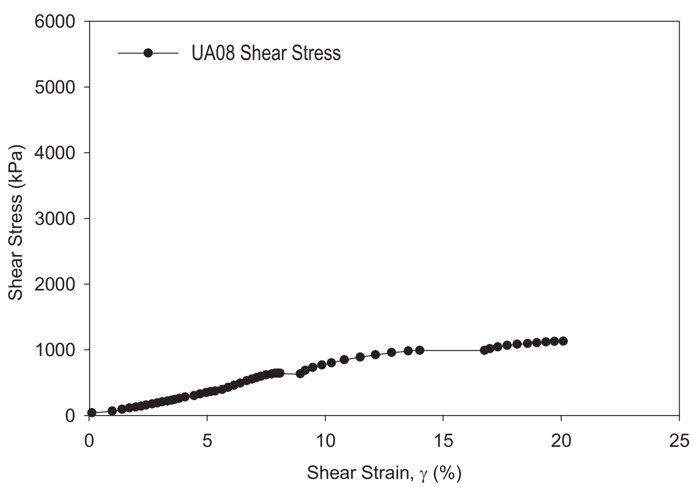

Figure A.54 Shear stress versus shear strain (UA 08)

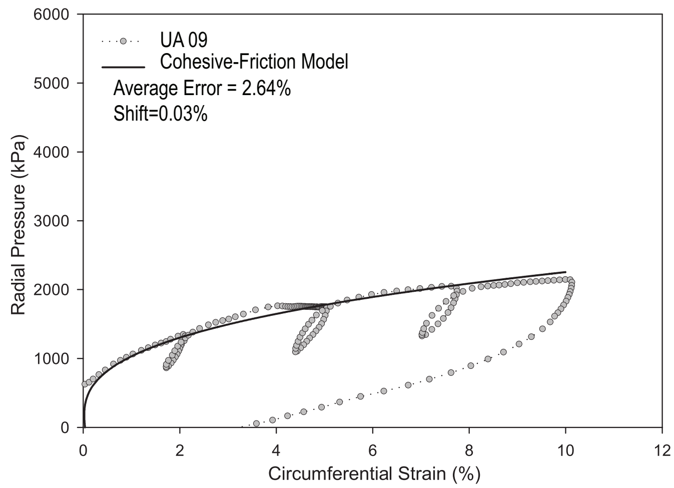

Figure A.55 Cohesive frictional model fit (UA 09)

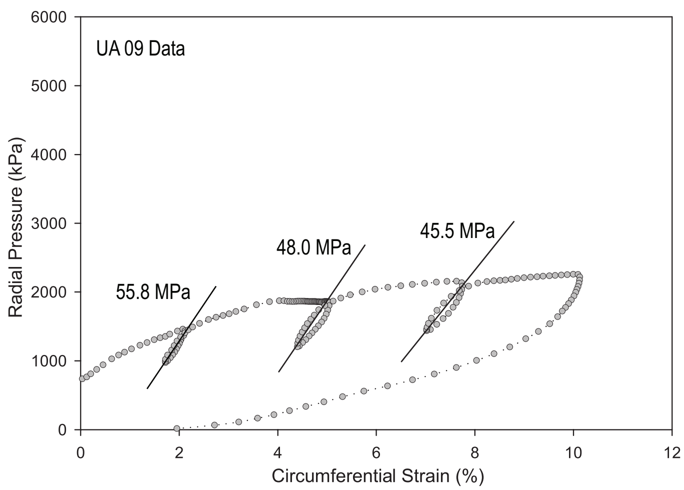

Figure A.56 Field data and shear modulus calculations (UA 09)

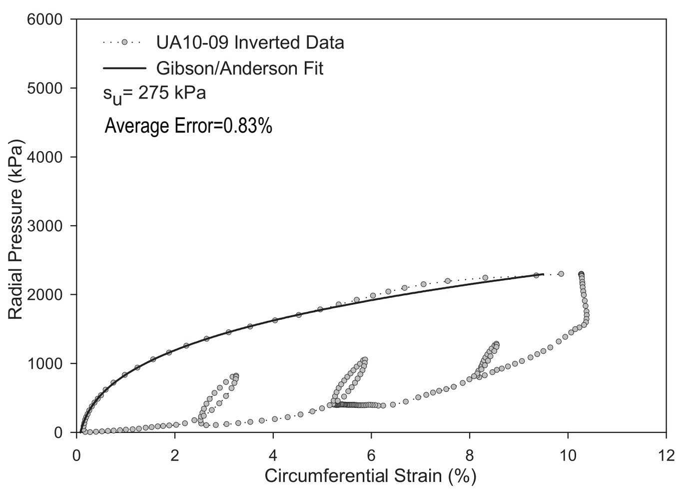

Figure A.57 Inverted undrained shear strength analysis (UA 09)

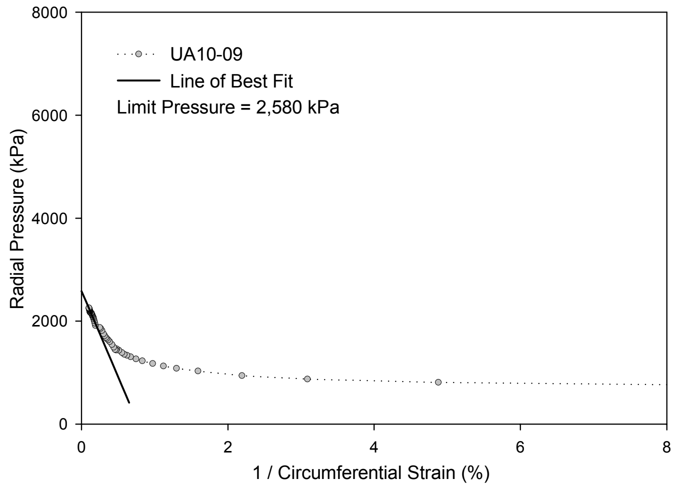

Figure A.58 Limit pressure calculation (UA 09)

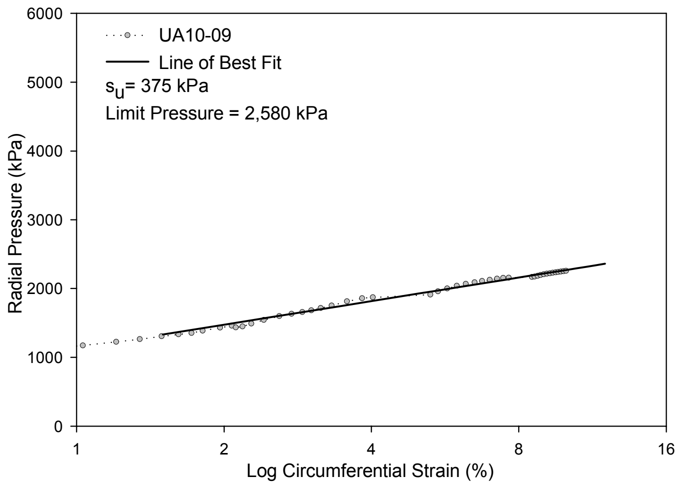

Figure A.59 Undrained shear strength; log method (UA 09)

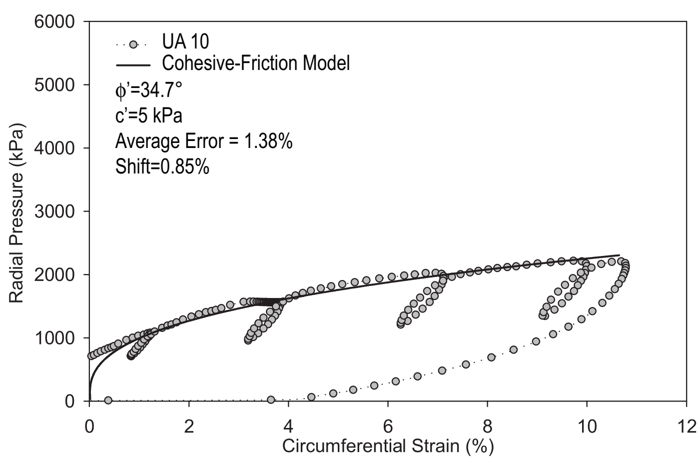

Figure A.60 Cohesive frictional model fit (UA 10)

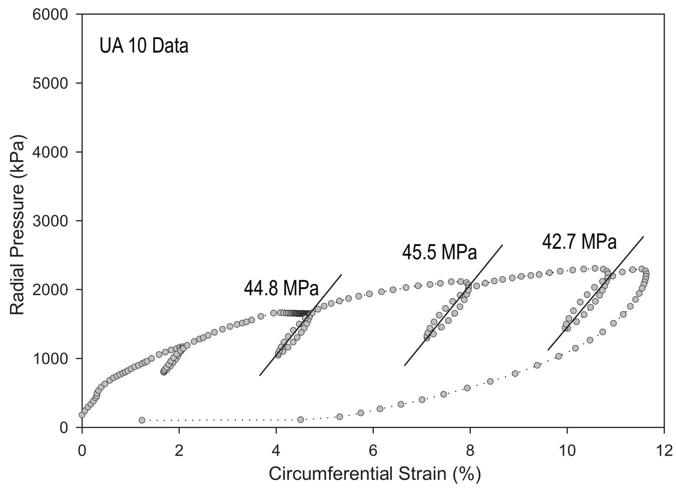

Figure A.61 Field data and shear modulus calculations (UA 10)

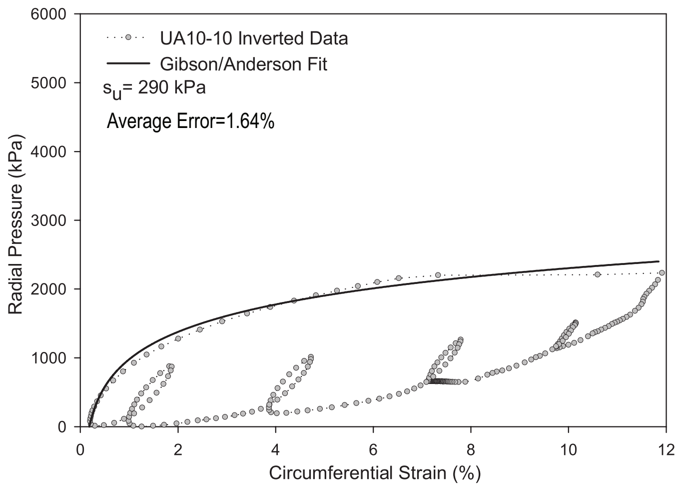

Figure A.62 Inverted undrained shear strength analysis (UA 10)

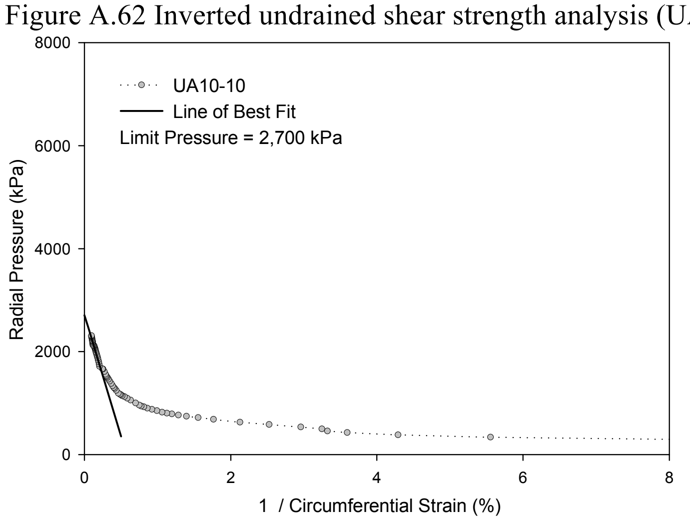

Figure A.63 Limit pressure calculation (UA 10)

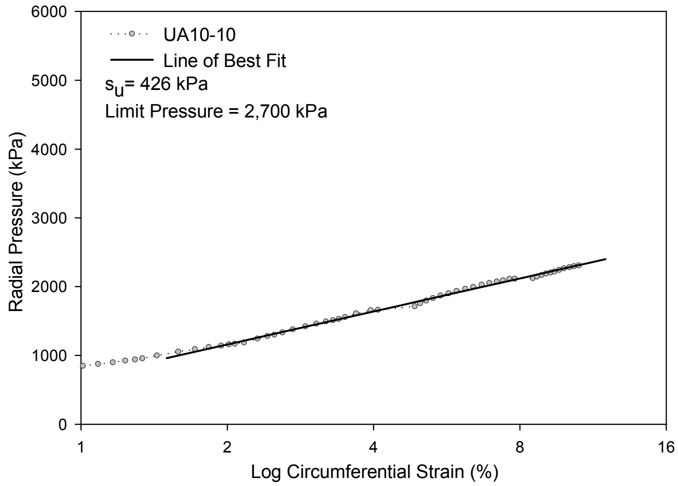

Figure A.64 Undrained shear strength; log method (UA 10)

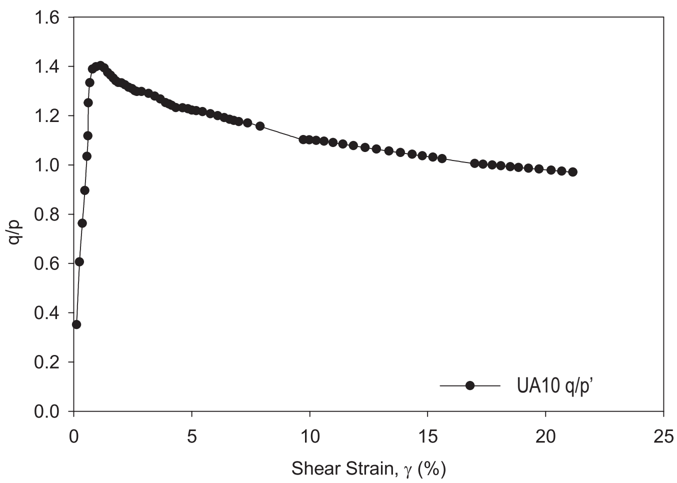

Figure A.65 Principal stress ratio versus shear strain (UA 10)

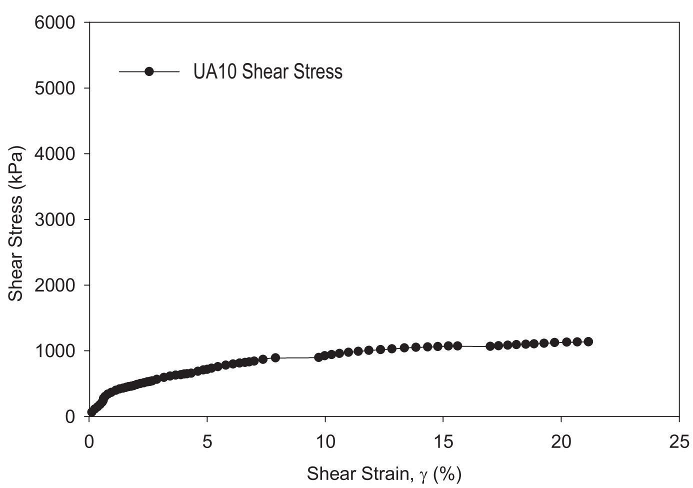

Figure A.66 Shear stress versus shear strain (UA 10)

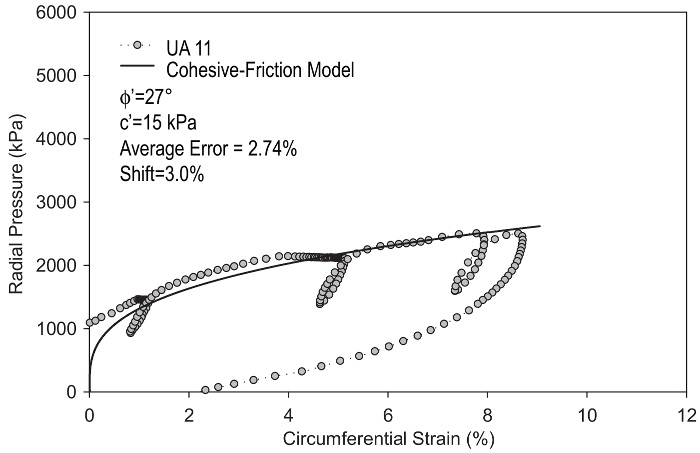

Figure A.67 Cohesive frictional model fit (UA 11)

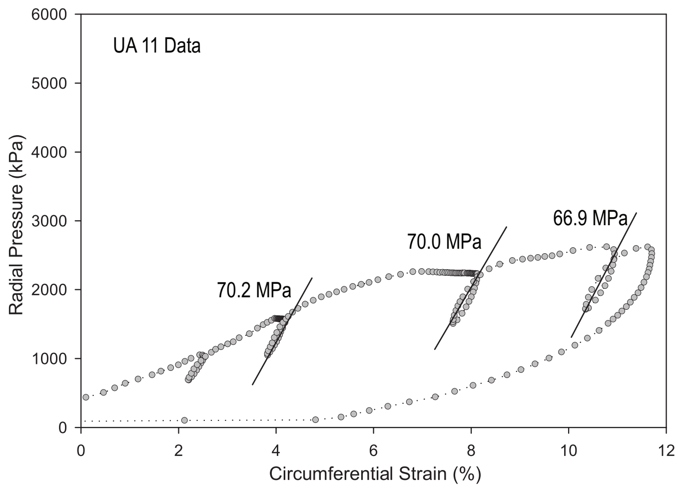

Figure A.68 Field data and shear modulus calculations (UA 11)

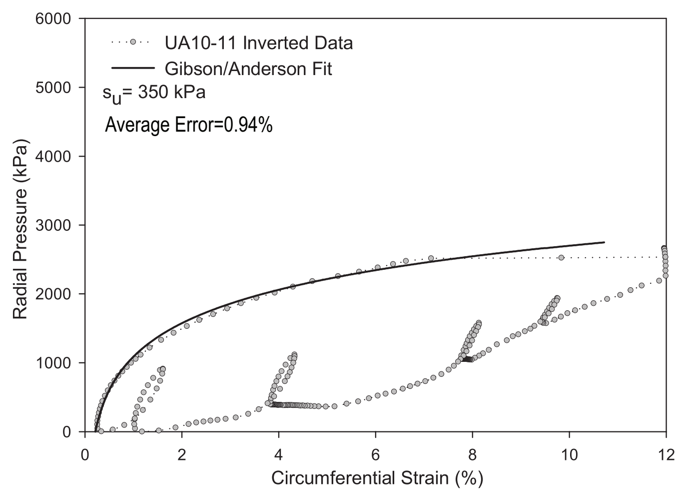

Figure A.69 Inverted undrained shear strength analysis (UA 11)

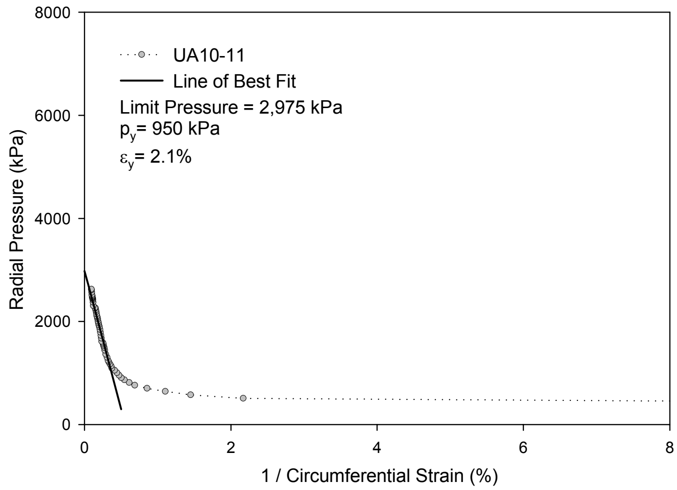

Figure A.70 Limit pressure calculation (UA 11)

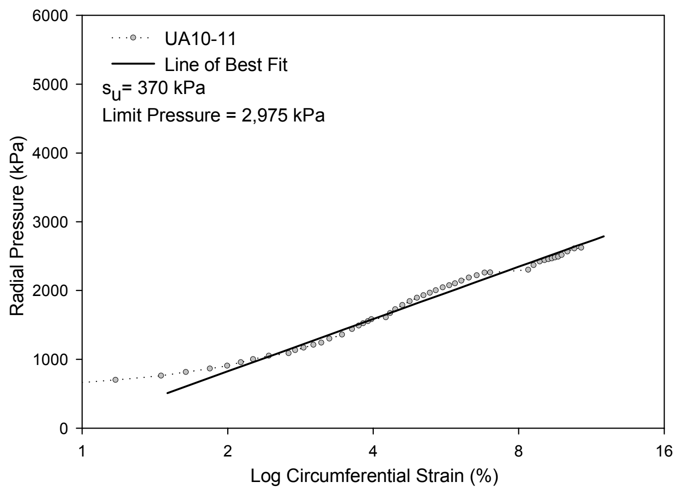

Figure A.71 Undrained shear strength; log method (UA 11)

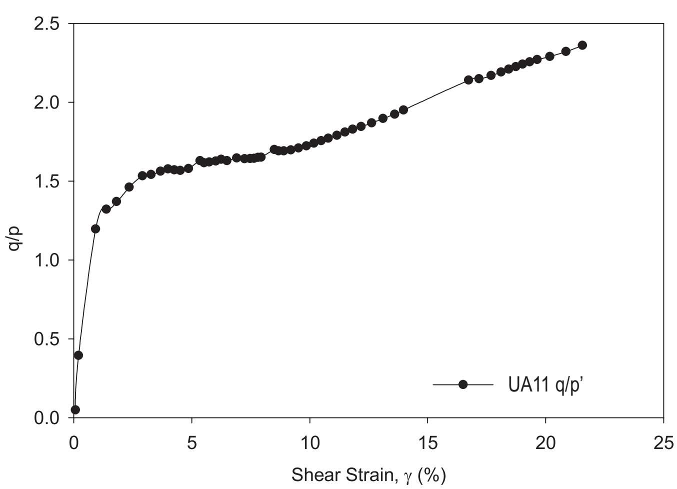

Figure A.72 Principal stress ratio versus shear strain (UA 11)

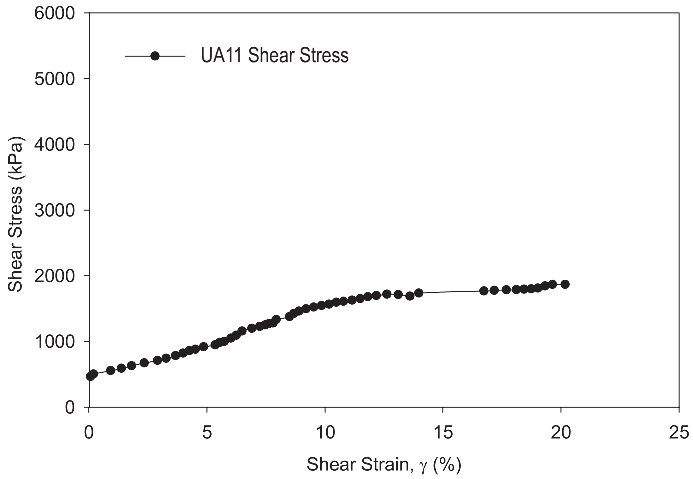

Figure A.73 Shear stress versus shear strain (UA 11)

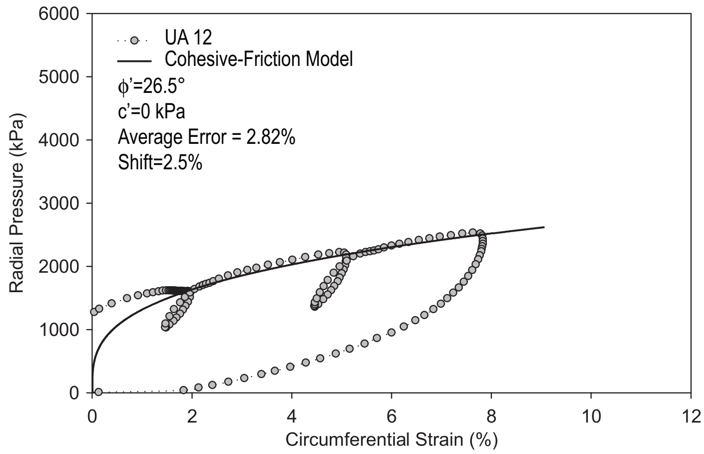

Figure A.74 Cohesive frictional model fit (UA 12)

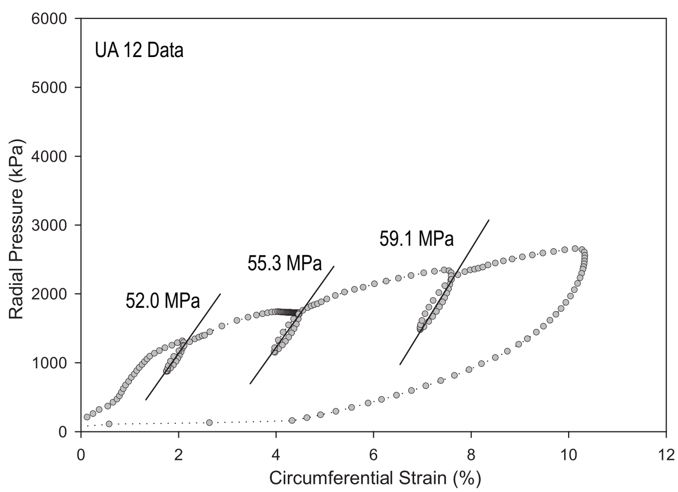

Figure A.75 Field data and shear modulus calculations (UA 12)

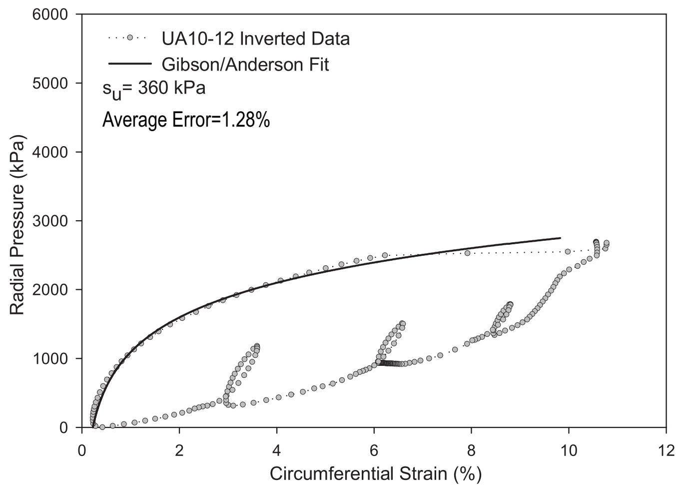

Figure A.76 Inverted undrained shear strength analysis (UA 12)

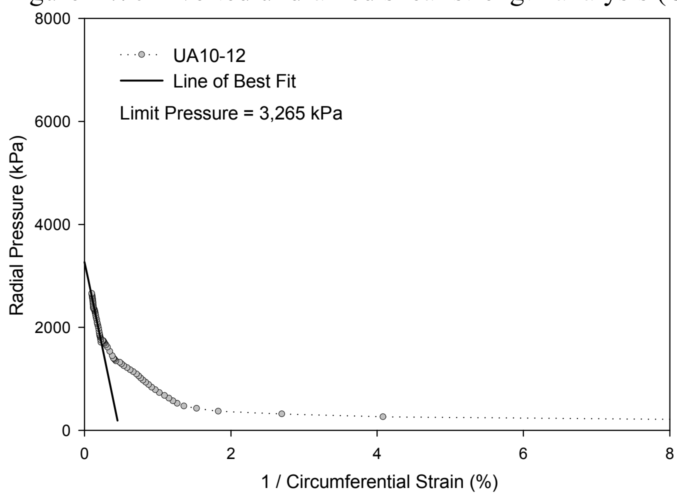

Figure A.77 Limit pressure calculation (UA 12)

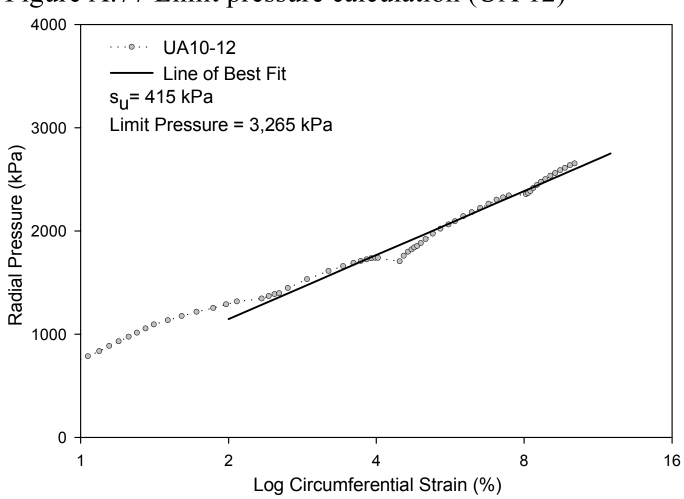

Figure A.78 Undrained shear strength; log method (UA 12)

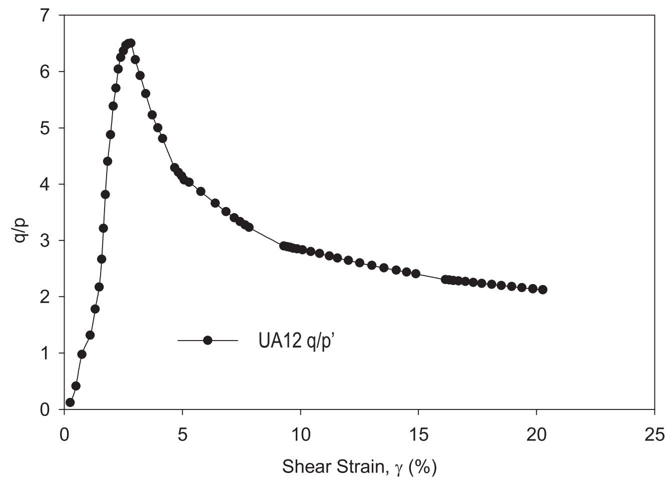

Figure A.79 Principal stress ratio versus shear strain (UA 12)

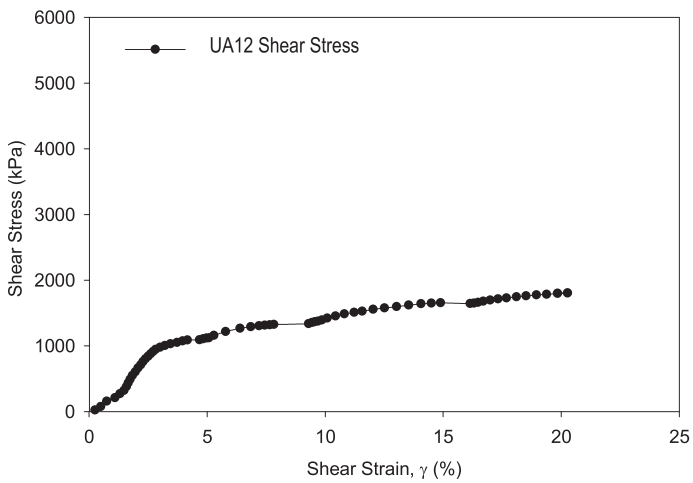

Figure A.80 Shear stress versus shear strain (UA 12)

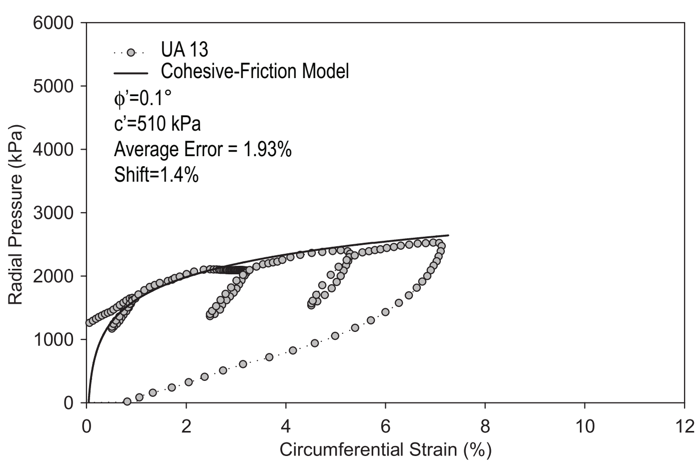

Figure A.81 Cohesive frictional model fit (UA 13)

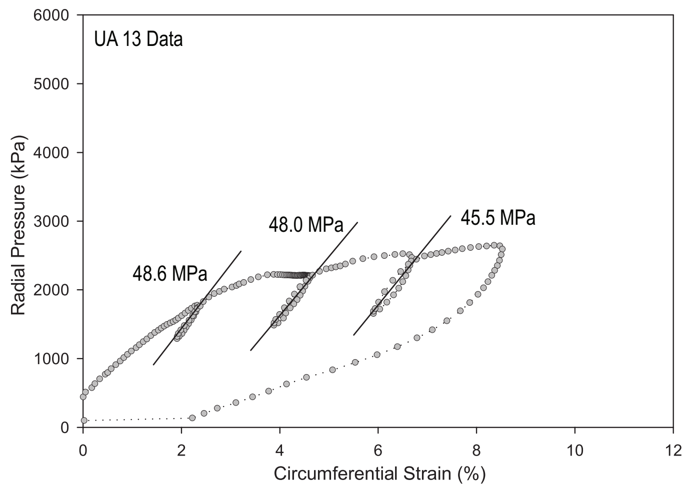

Figure A.82 Field data and shear modulus calculations (UA 13)

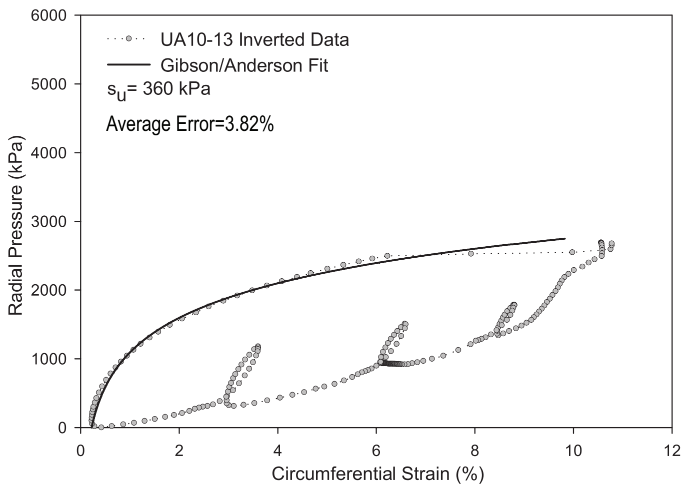

Figure A.83 Inverted undrained shear strength analysis (UA 13)

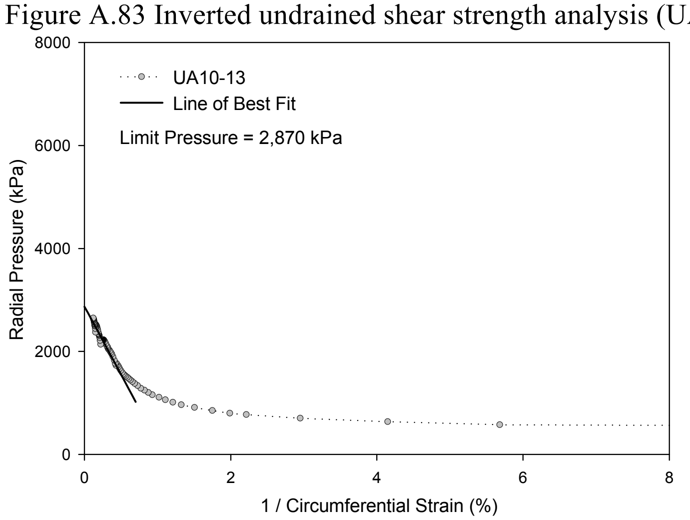

Figure A.84 Limit pressure calculation (UA 13)

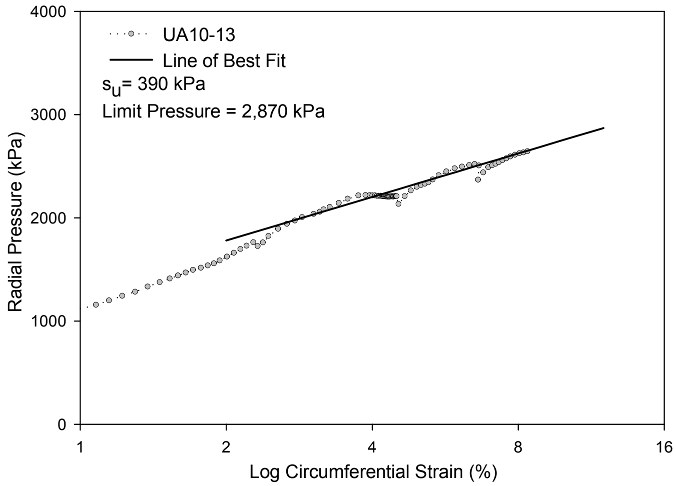

Figure A.85 Undrained shear strength; log method (UA 13)

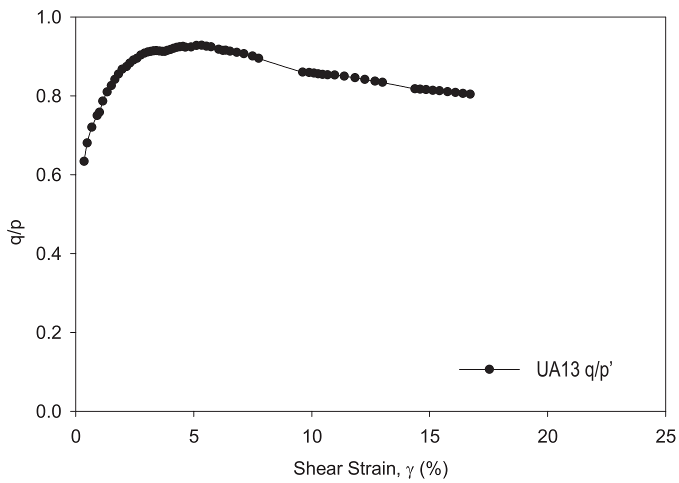

Figure A.86 Principal stress ratio versus shear strain (UA 13)

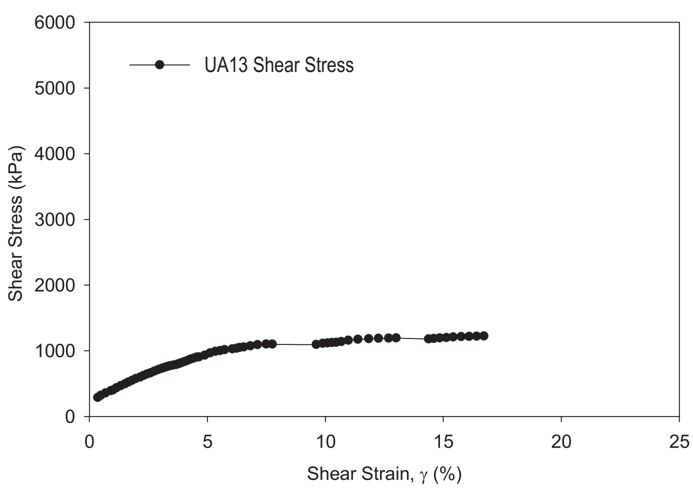

Figure A.87 Shear stress versus shear strain (UA 13)

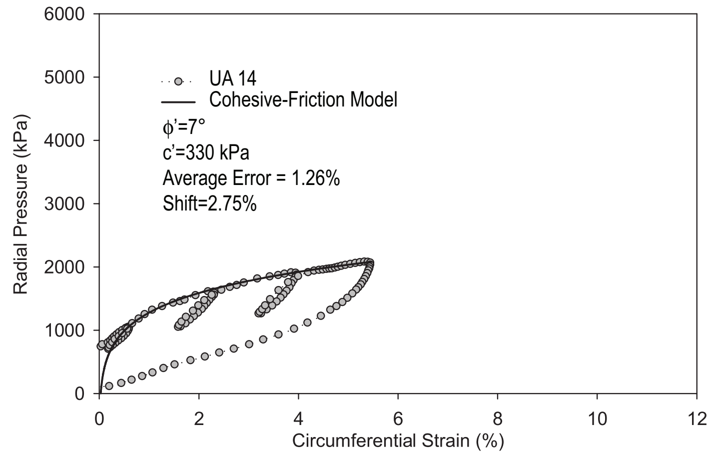

Figure A.88 Cohesive frictional model fit (UA 14)

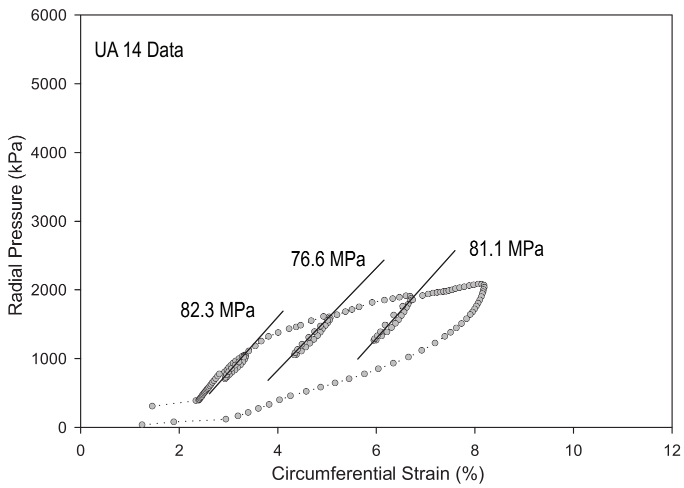

Figure A.89 Field data and shear modulus calculations (UA 14)

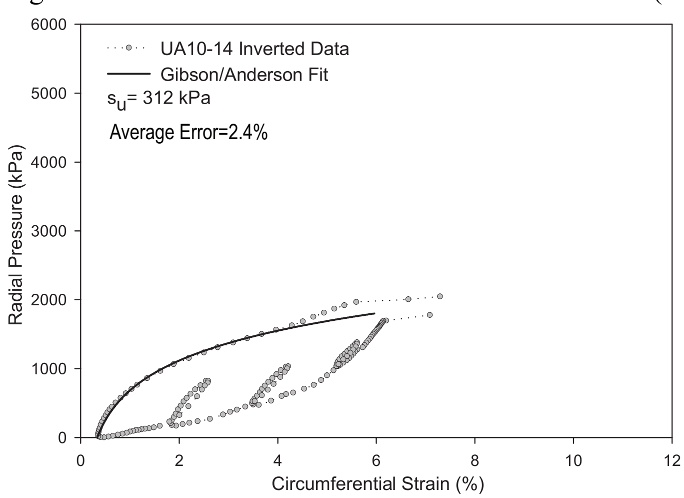

Figure A.90 Inverted undrained shear strength analysis (UA 14)

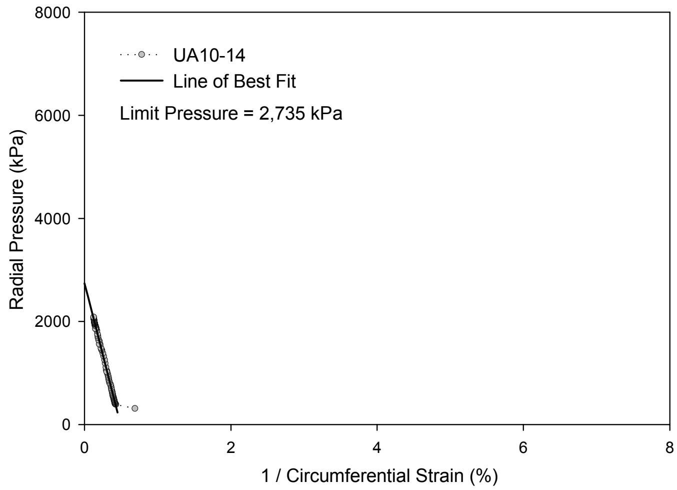

Figure A.91 Limit pressure calculation (UA 14)

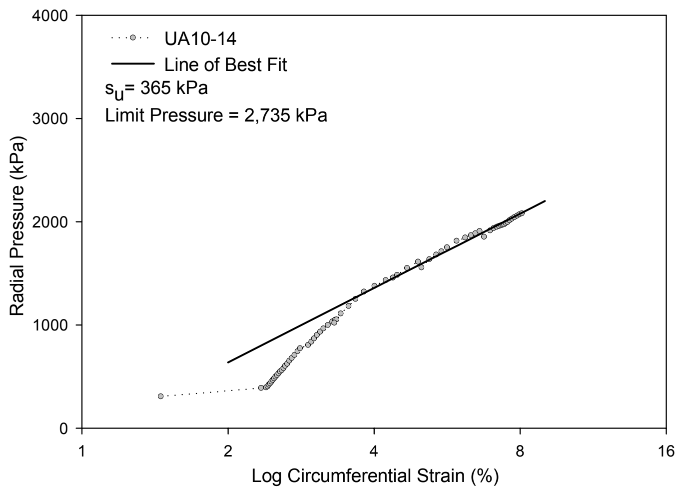

Figure A.92 Undrained shear strength; log method (UA 14)

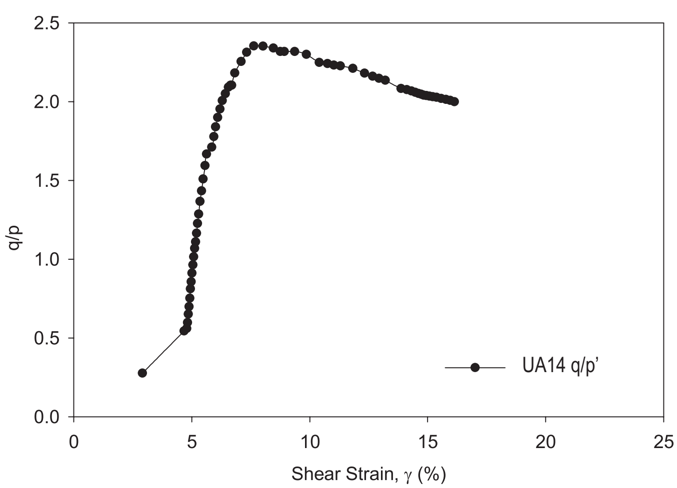

Figure A.93 Principal stress ratio versus shear strain (UA 14)

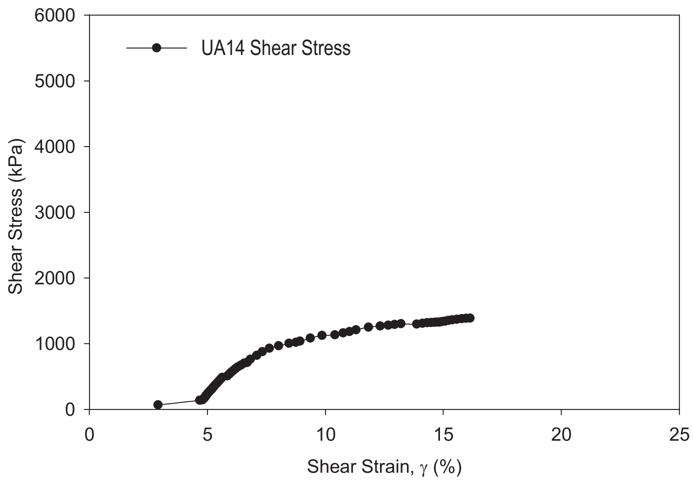

Figure A.94 Shear stress versus shear strain (UA 14)

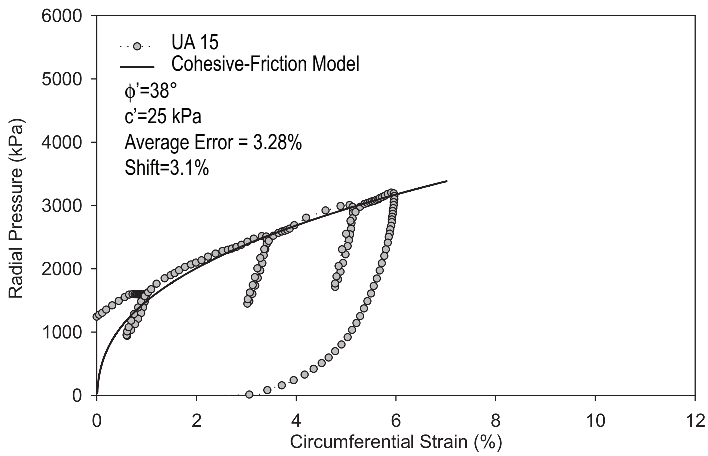

Figure A.95 Cohesive frictional model fit (UA 15)

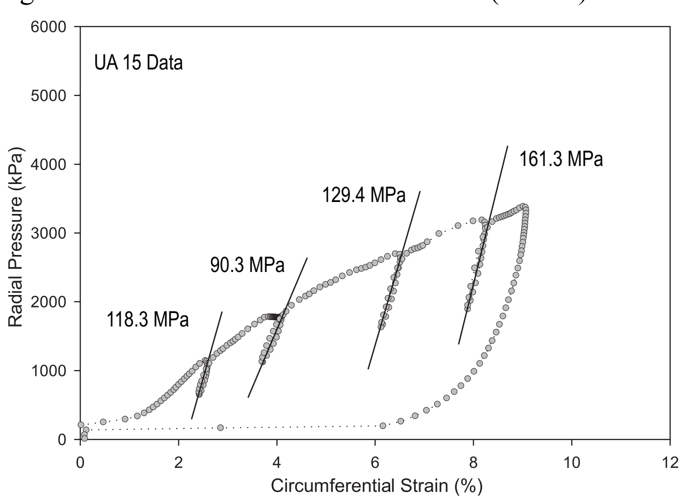

Figure A.96 Field data and shear modulus calculations (UA 15)

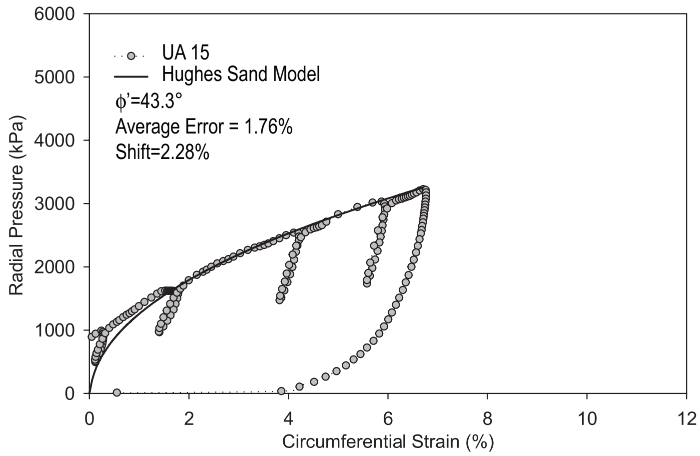

Figure A.97 Hughes frictional model fit (UA 15)

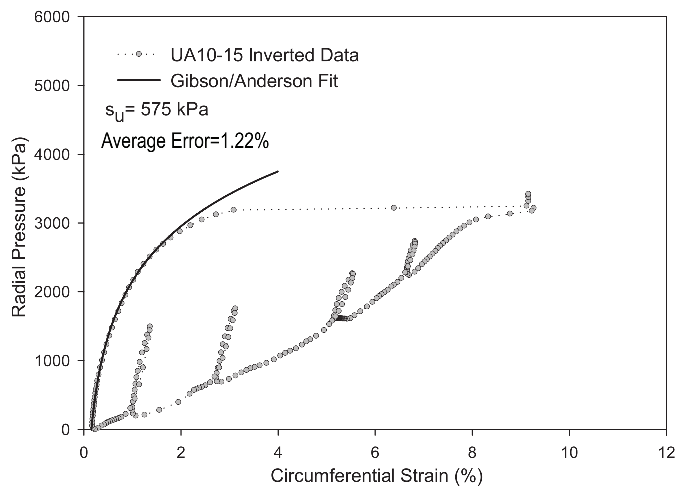

Figure A.98 Inverted undrained shear strength analysis (UA 15)

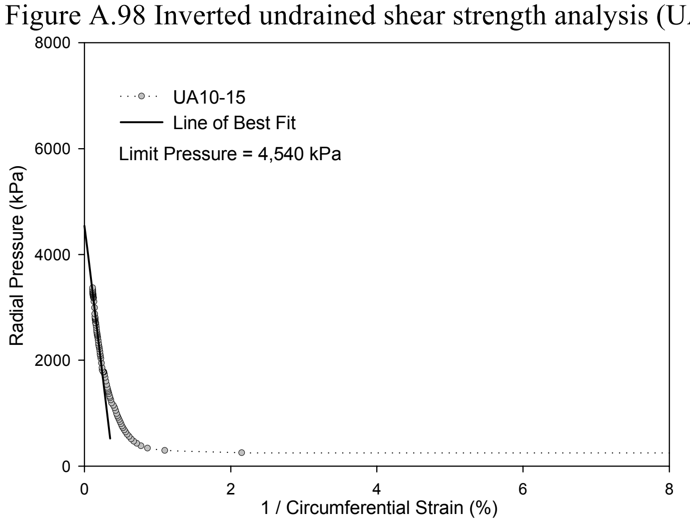

Figure A.99 Limit pressure calculation (UA 15)

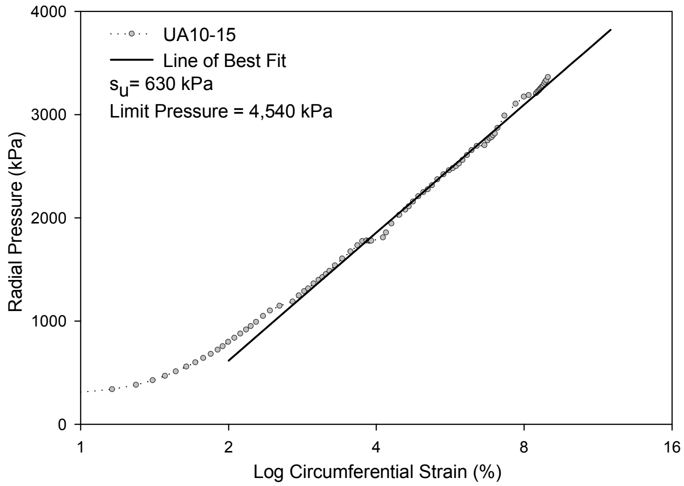

Figure A.100 Undrained shear strength; log method (UA 15)

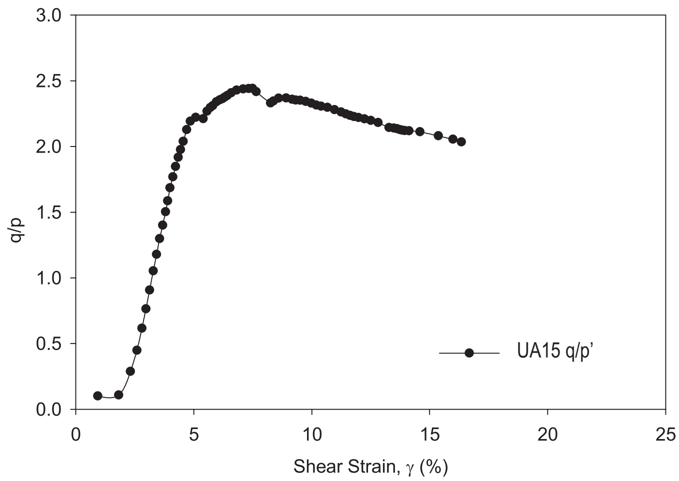

Figure A.101 Principal stress ratio versus shear strain (UA 15)

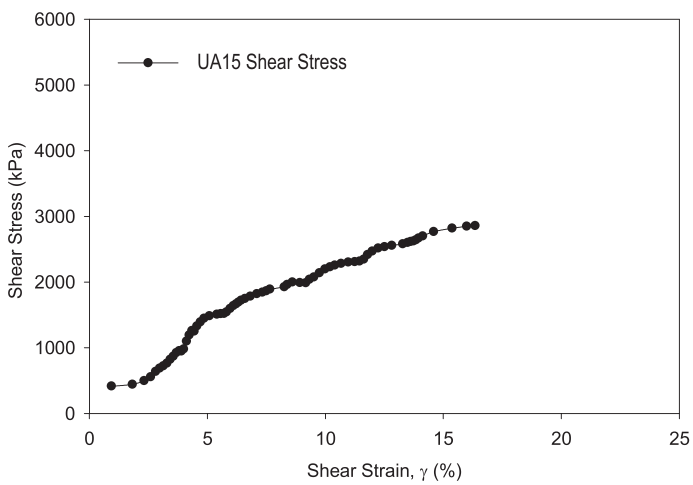

Figure A.102 Shear stress versus shear strain (UA 15)

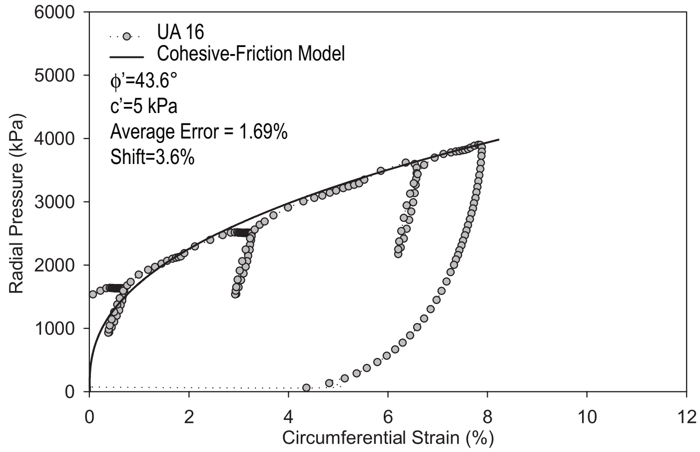

Figure A.103 Cohesive frictional model fit (UA 16)

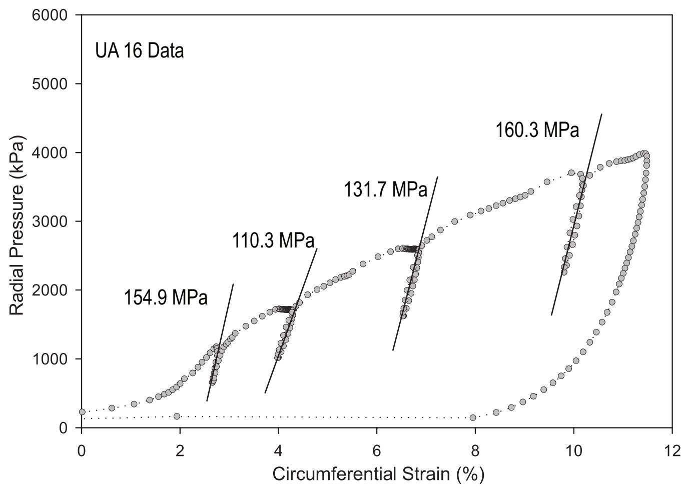

Figure A.104 Field data and shear modulus calculations (UA 16)

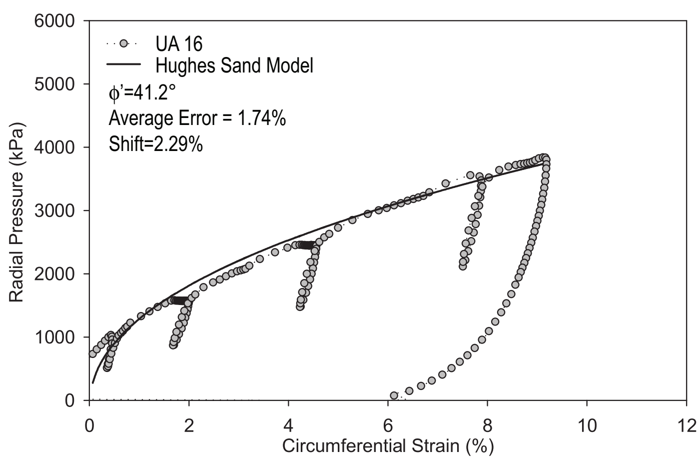

Figure A.105 Hughes frictional model fit (UA 16)

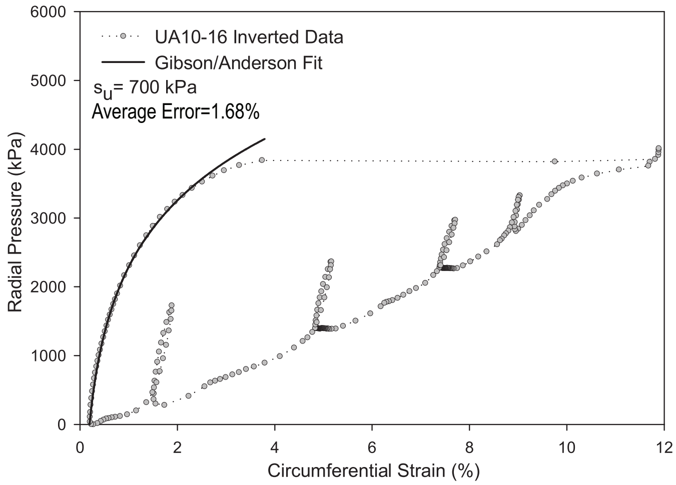

Figure A.106 Inverted undrained shear strength analysis (UA 16)

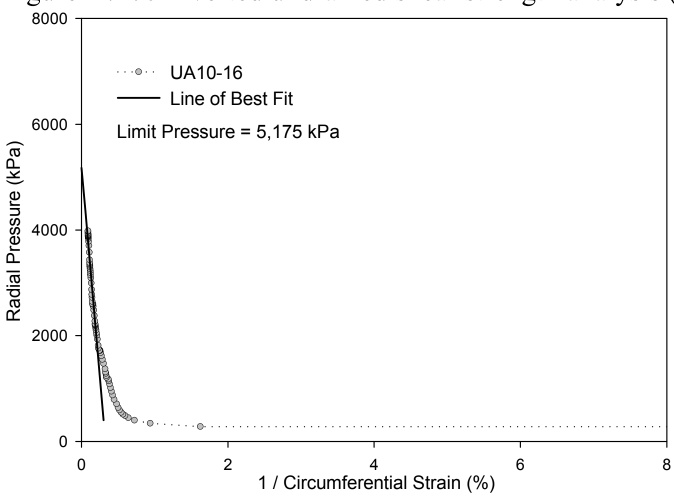

Figure A.107 Limit pressure calculation (UA 16)

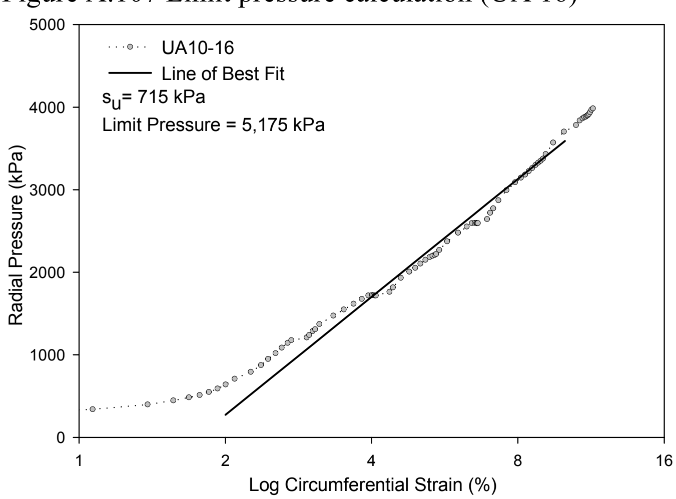

Figure A.108 Undrained shear strength; log method (UA 16)

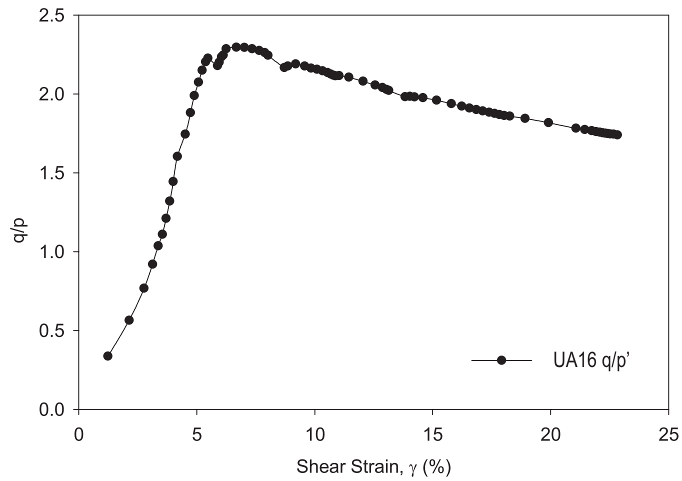

Figure A.109 Principal stress ratio versus shear strain (UA 16)

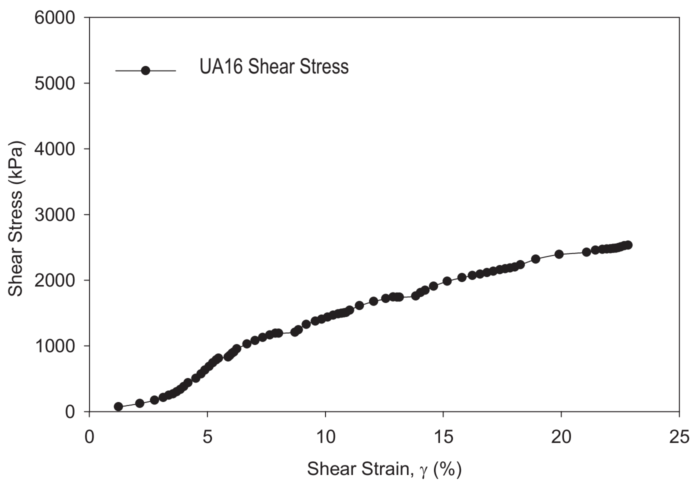

Figure A.110 Shear stress versus shear strain (UA 16)

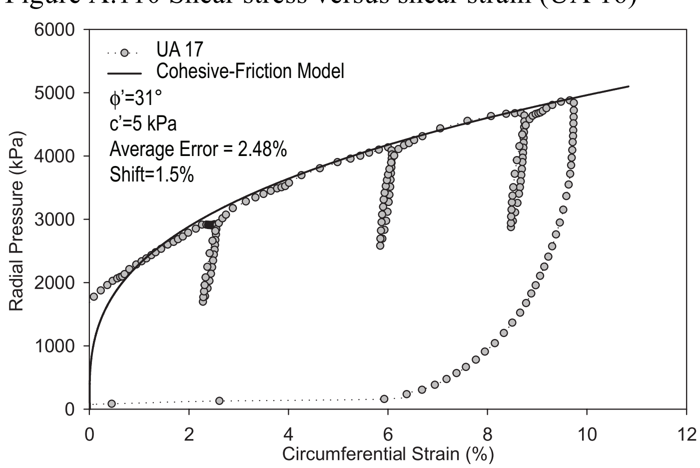

Figure A.111 Cohesive frictional model fit (UA 17)

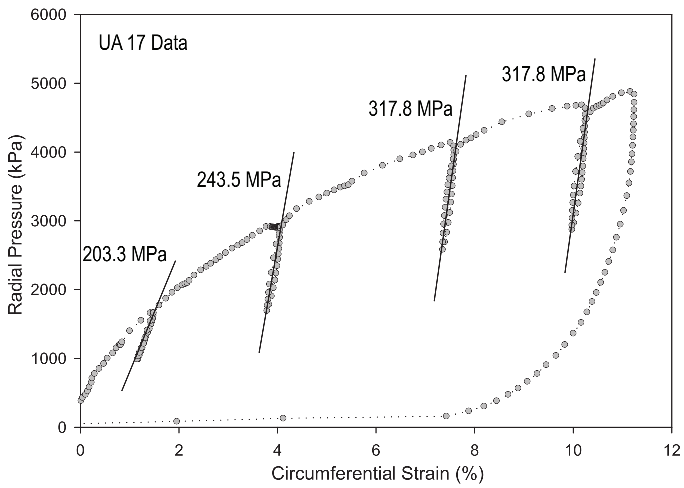

Figure A.112 Field data and shear modulus calculations (UA 17)

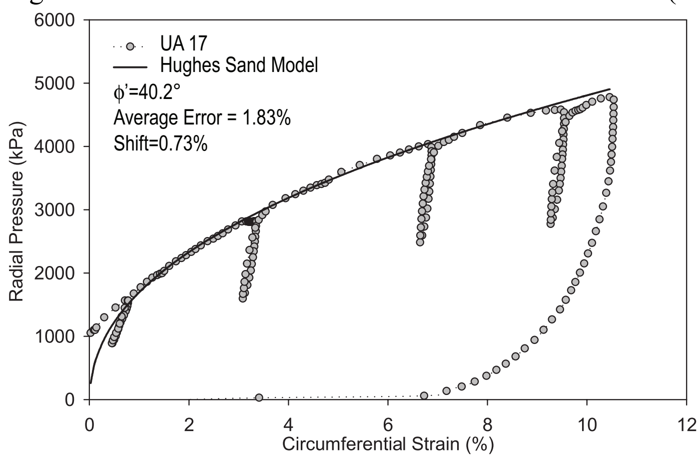

Figure A.113 Hughes frictional model fit (UA 17)

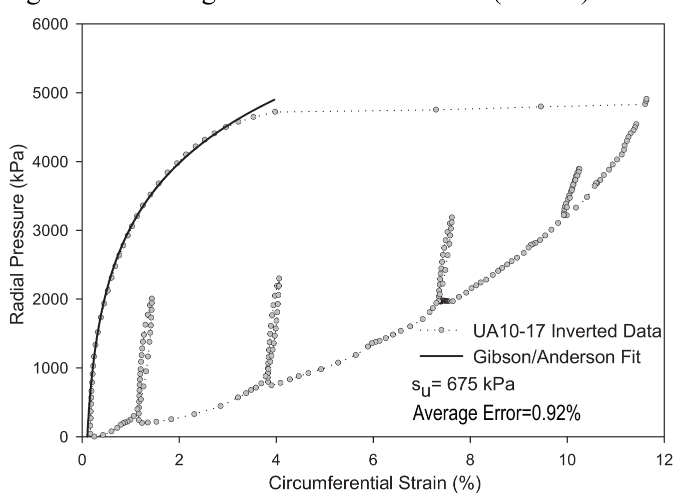

Figure A.114 Inverted undrained shear strength analysis (UA 17)

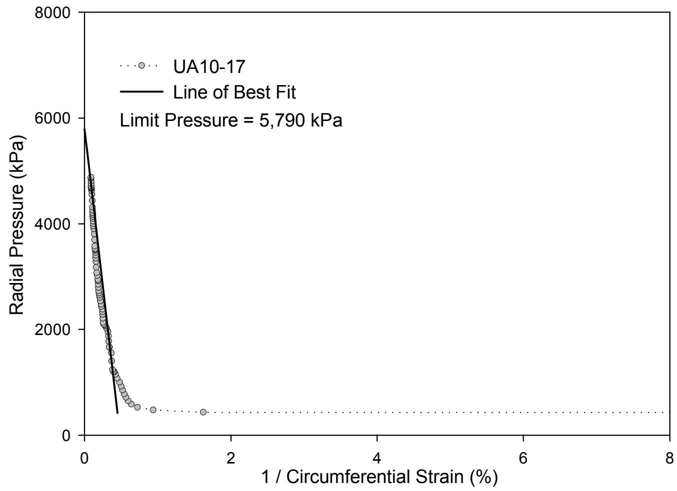

Figure A.115 Limit pressure calculation (UA 17)

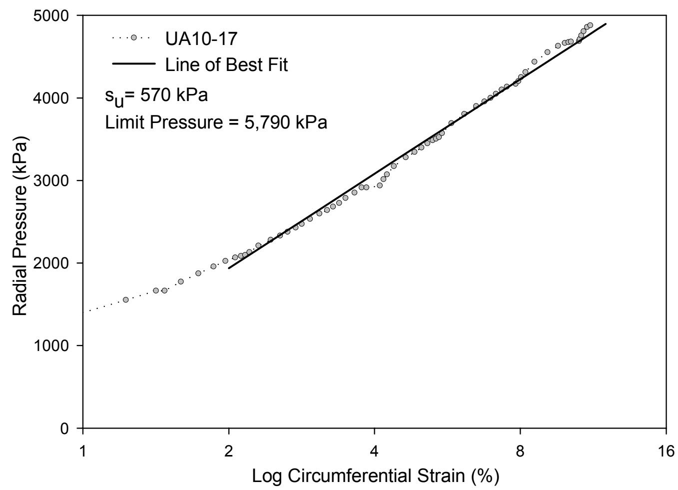

Figure A.116 Undrained shear strength; log method (UA 17)

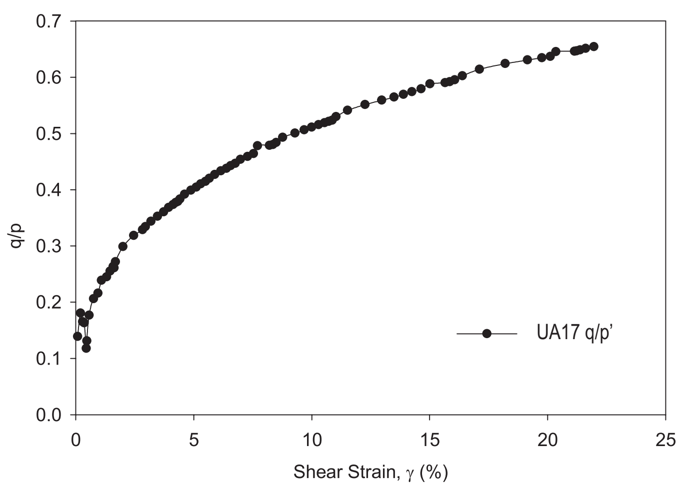

Figure A.117 Principal stress ratio versus shear strain (UA 17)

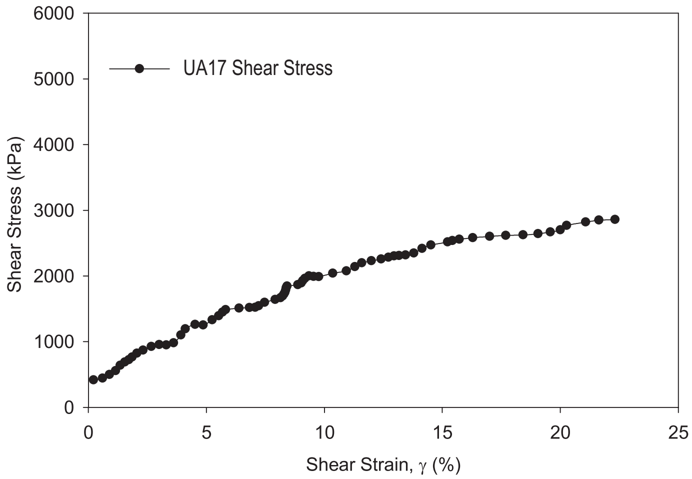

Figure A.118 Shear stress versus shear strain (UA 17)

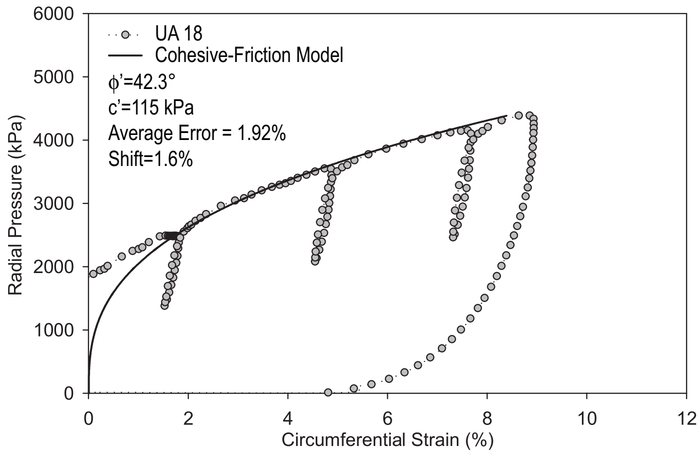

Figure A.119 Cohesive frictional model fit (UA 18)

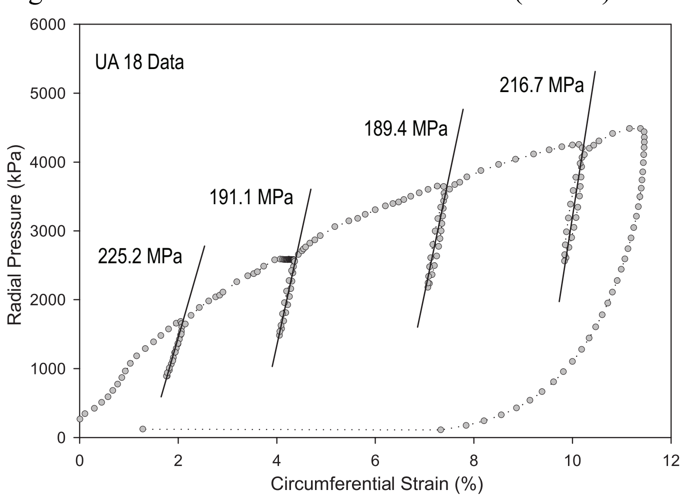

Figure A.120 Field data and shear modulus calculations (UA 18)

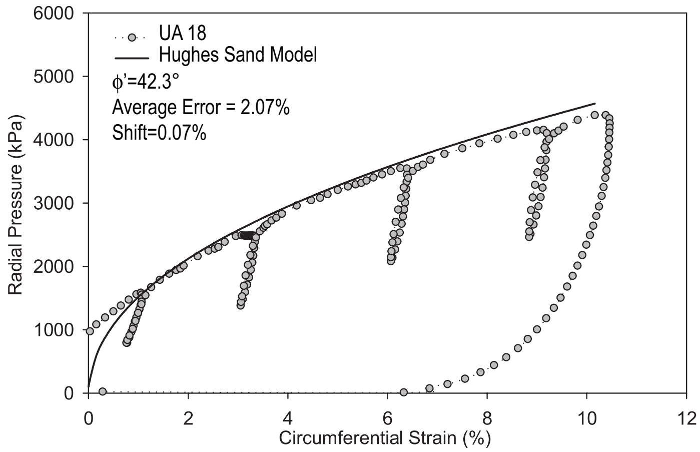

Figure A.121 Hughes frictional model fit (UA 18)

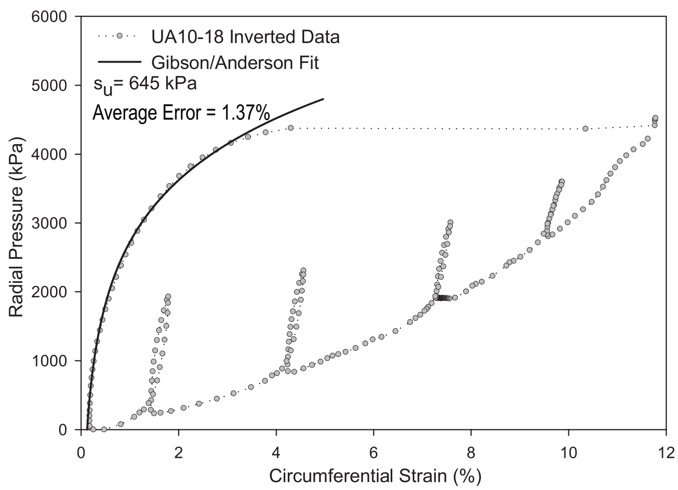

Figure A.122 Inverted undrained shear strength analysis (UA 18)

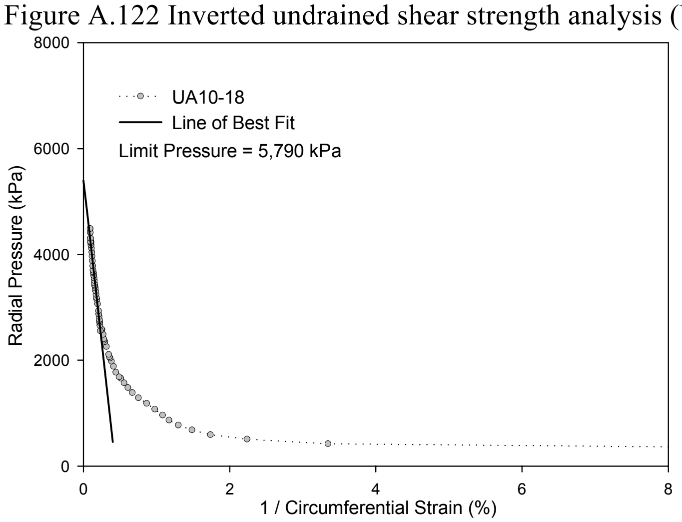

Figure A.123 Limit pressure calculation (UA 18)

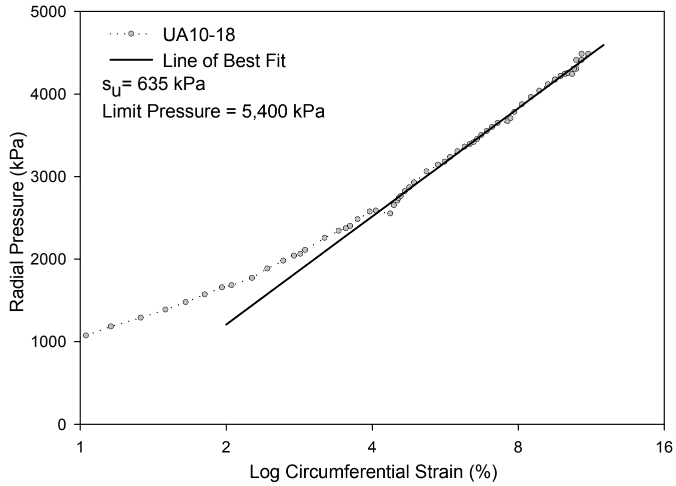

Figure A.124 Undrained shear strength; log method (UA 18)

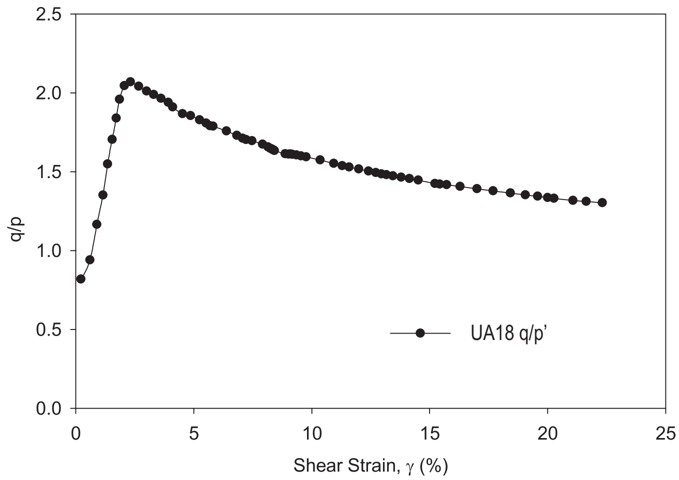

Figure A.125 Principal stress ratio versus shear strain (UA 18)

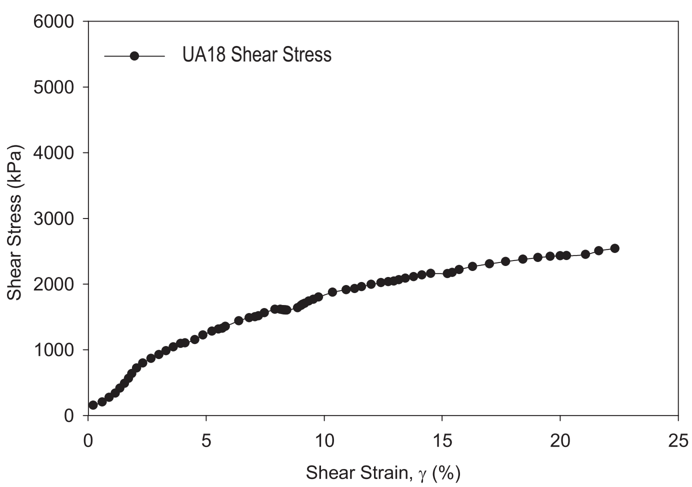

Figure A.126 Shear stress versus shear strain (UA 18)

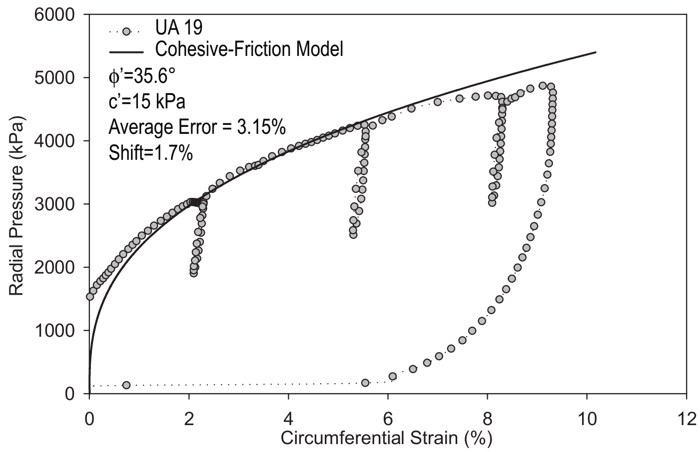

Figure A.127 Cohesive frictional model fit (UA 19)

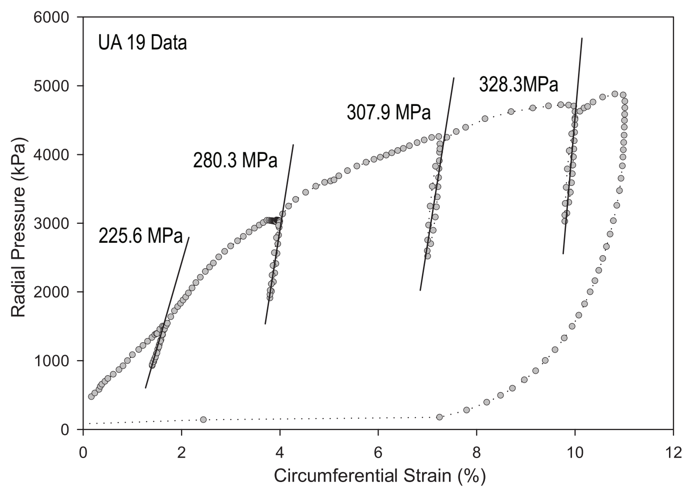

Figure A.128 Field data and shear modulus calculations (UA 19)

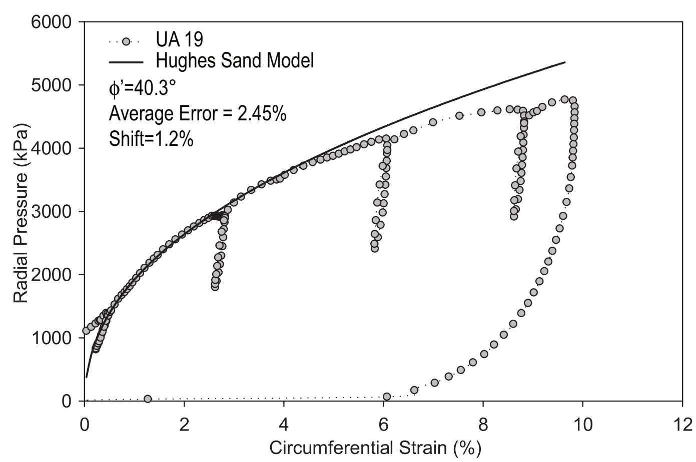

Figure A.129 Hughes frictional model fit (UA 19)

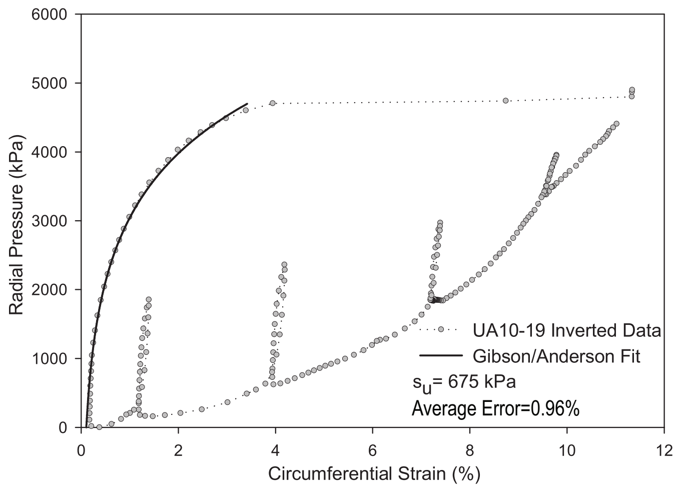

Figure A.130 Inverted undrained shear strength analysis (UA 19)

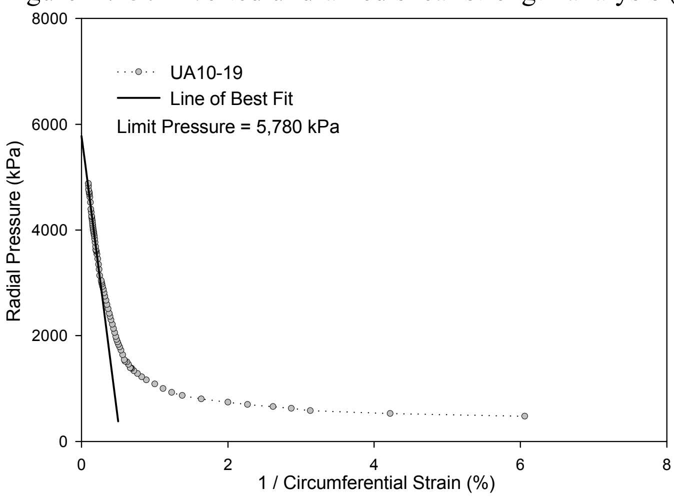

Figure A.131 Limit pressure calculation (UA 19)

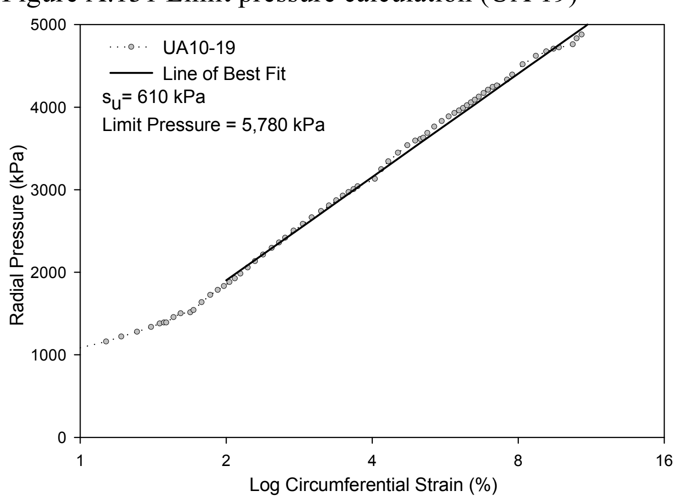

Figure A.132 Undrained shear strength; log method (UA 19)

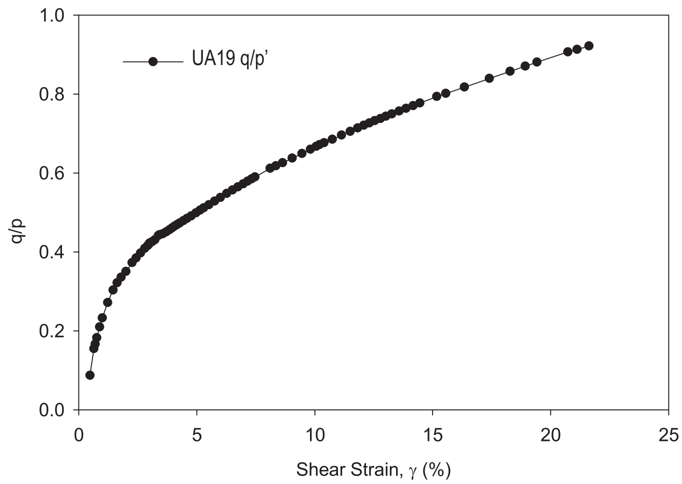

Figure A.133 Principal stress ratio versus shear strain (UA 19)

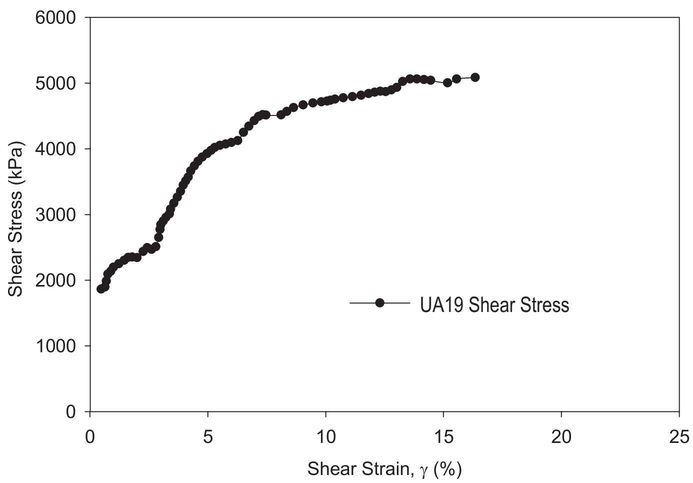

Figure A.134 Shear stress versus shear strain (UA 19)

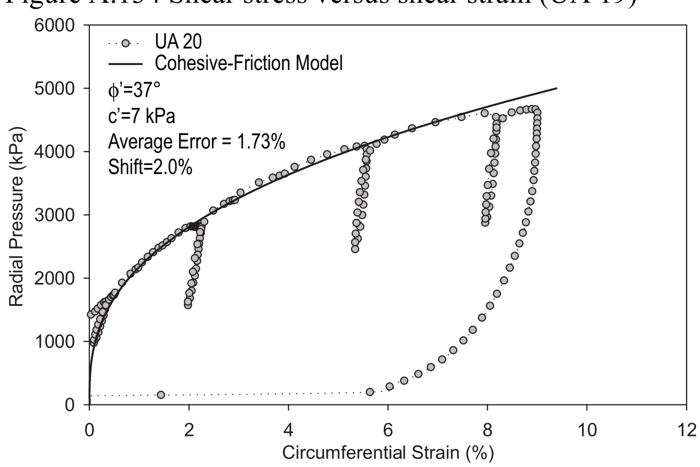

Figure A.135 Cohesive frictional model fit (UA 20)

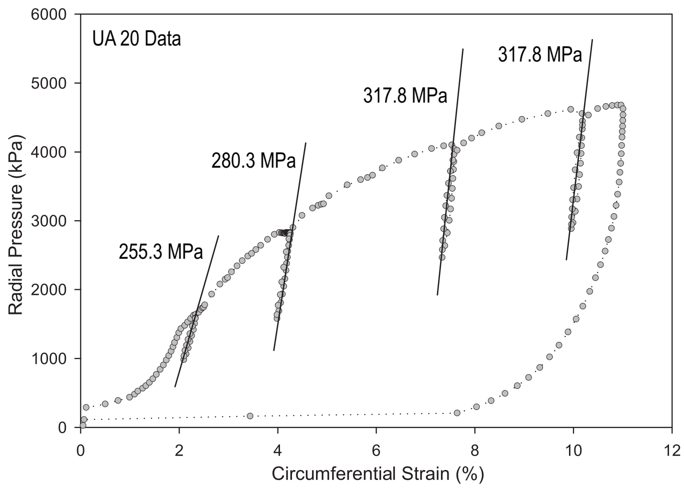

Figure A.136 Field data and shear modulus calculations (UA 20)

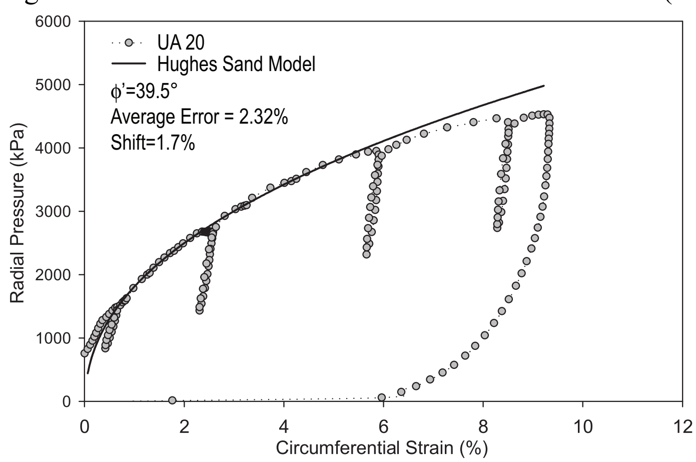

Figure A.137 Hughes frictional model fit (UA 20)

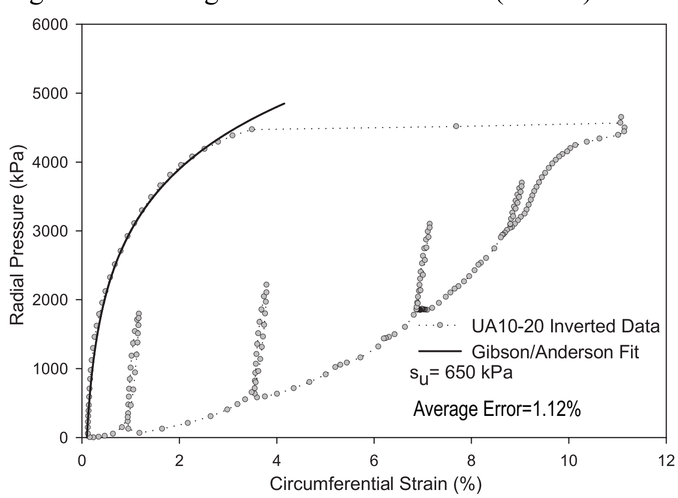

Figure A.138 Inverted undrained shear strength analysis (UA 20)

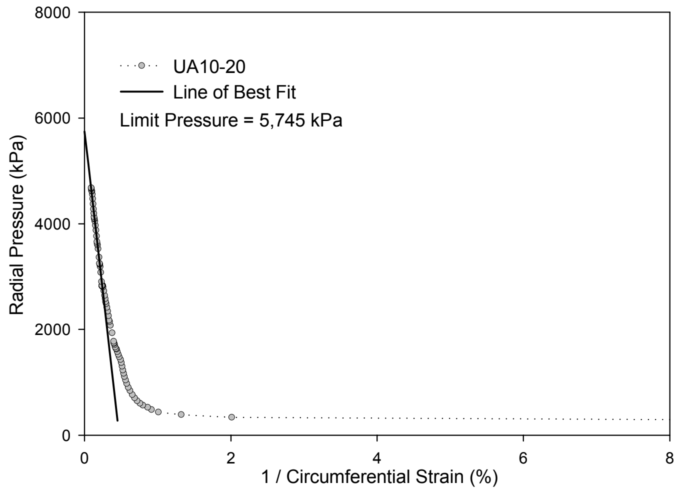

Figure A.139 Limit pressure calculation (UA 20)

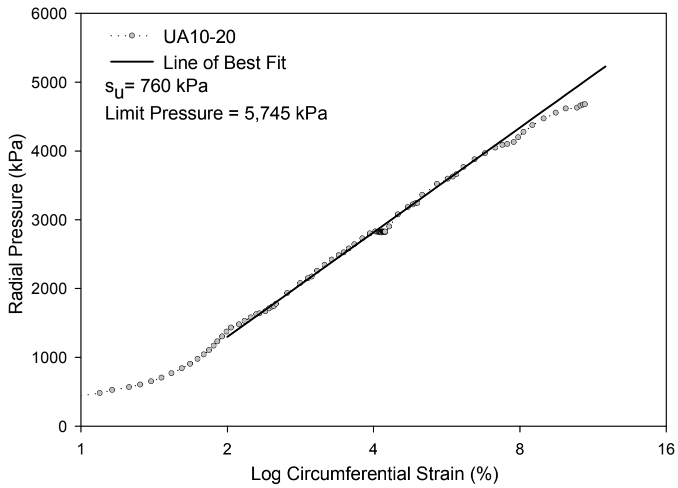

Figure A.140 Undrained shear strength; log method (UA 20)

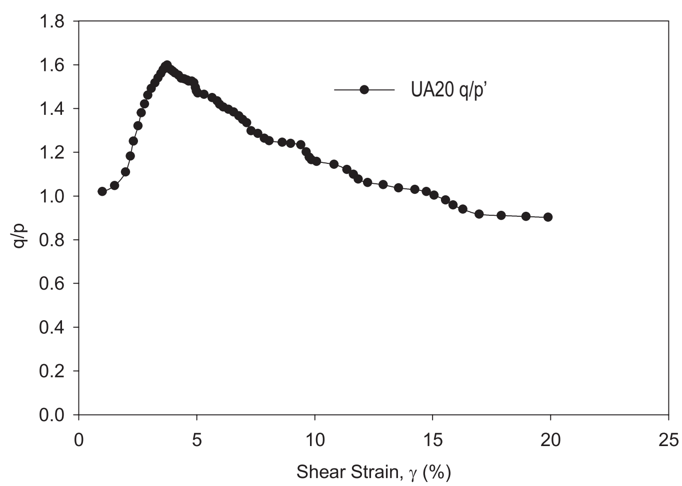

Figure A.141 Principal stress ratio versus shear strain (UA 20)

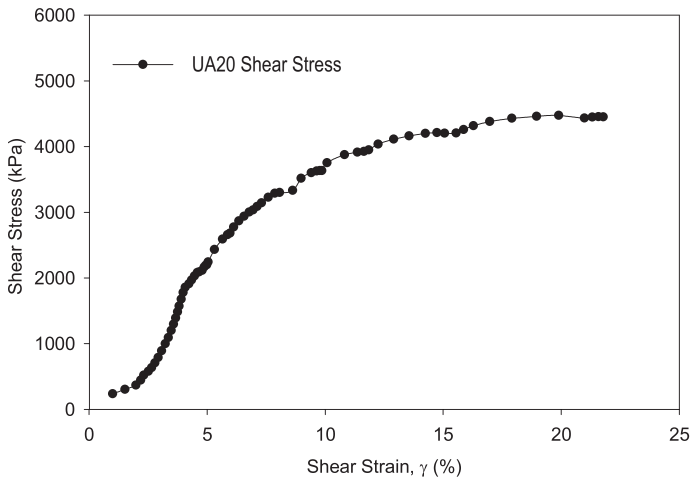

Figure A.142 Shear stress versus shear strain (UA 20)

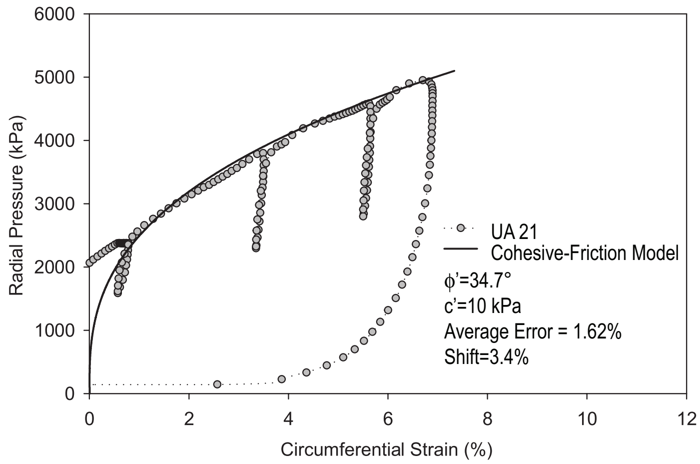

Figure A.143 Cohesive frictional model fit (UA 21)

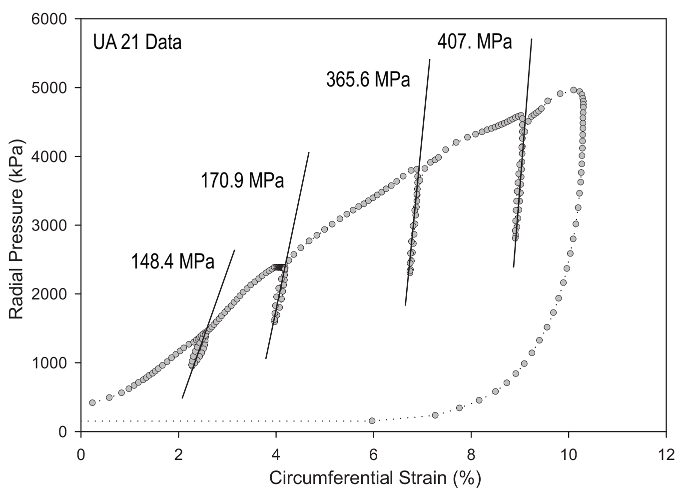

Figure A.144 Field data and shear modulus calculations (UA 21)

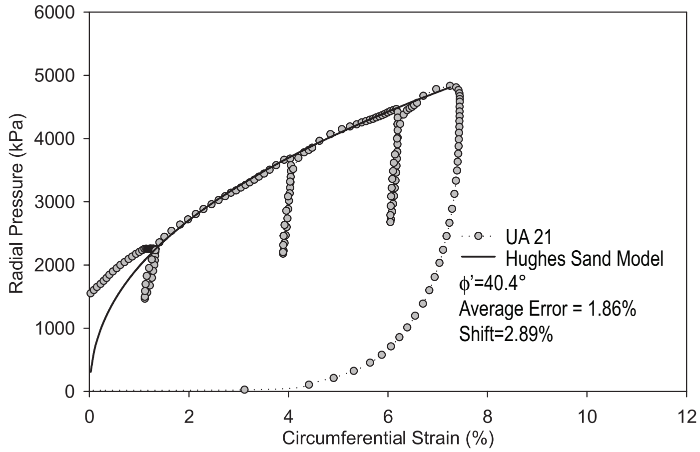

Figure A.145 Hughes frictional model fit (UA 21)

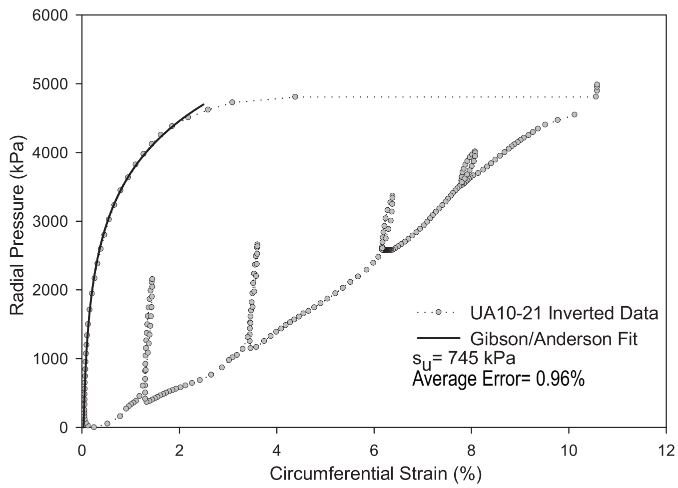

Figure A.146 Inverted undrained shear strength analysis (UA 21)

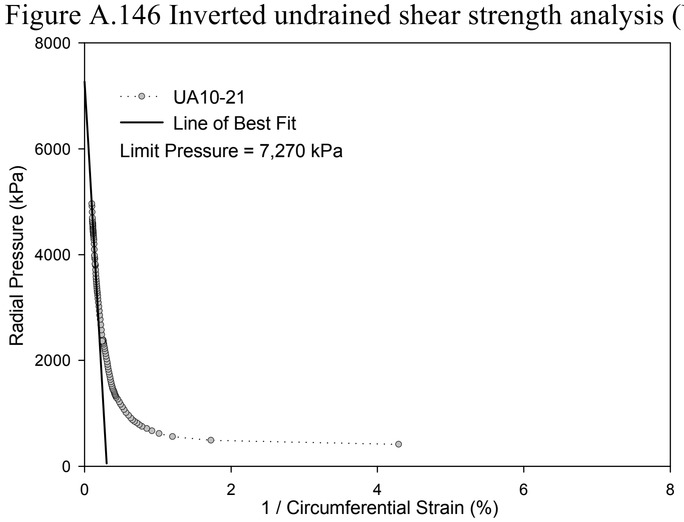

Figure A.147 Limit pressure calculation (UA 21)

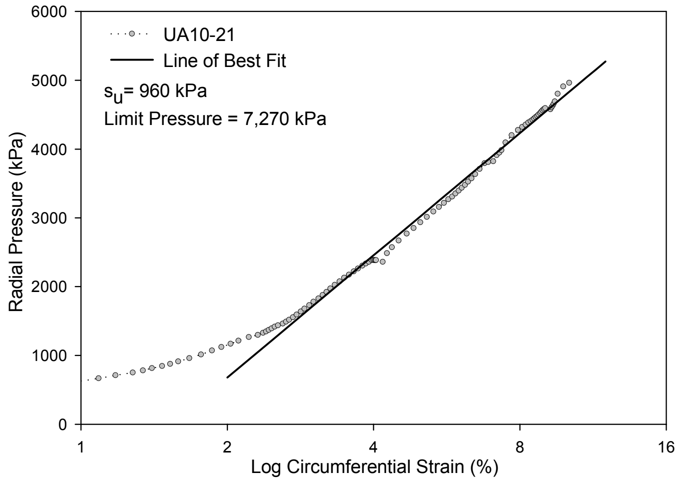

Figure A.148 Undrained shear strength; log method (UA 21)

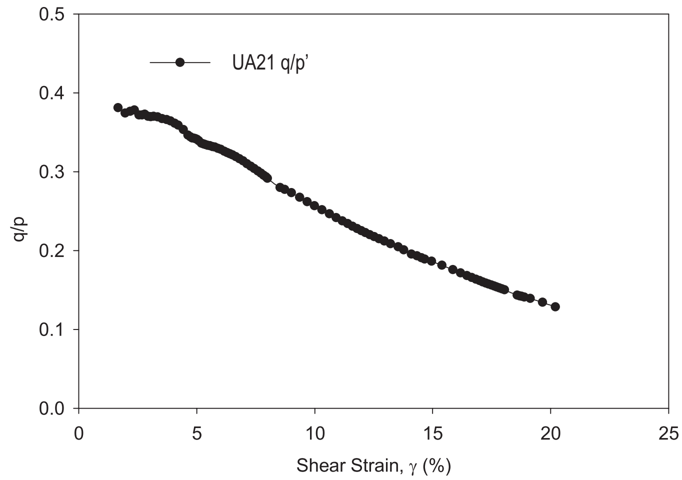

Figure A.149 Principal stress ratio versus shear strain (UA 21)

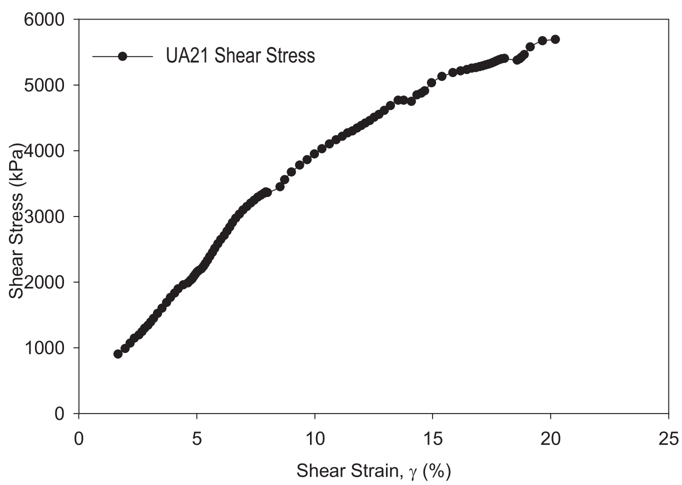

Figure A.150 Shear stress versus shear strain (UA 21)

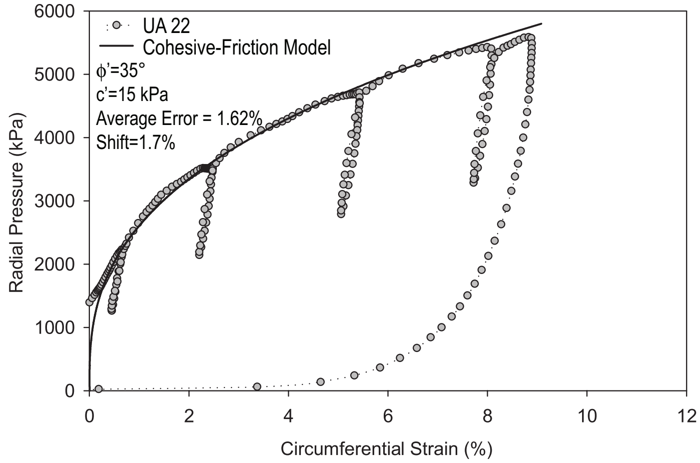

Figure A.151 Cohesive frictional model fit (UA 22)

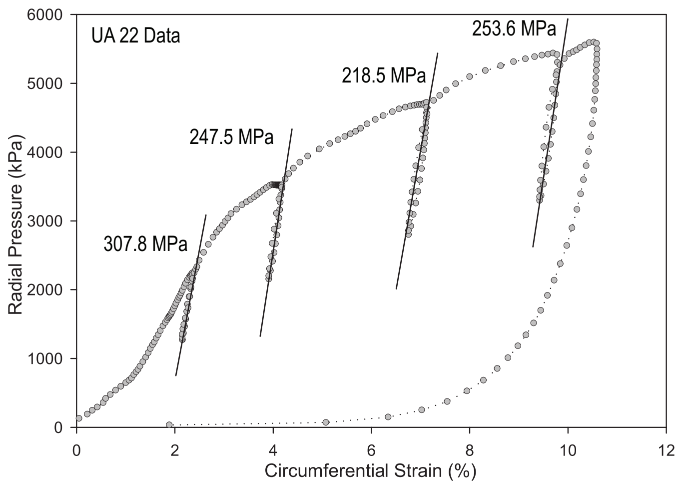

Figure A.152 Field data and shear modulus calculations (UA 22)

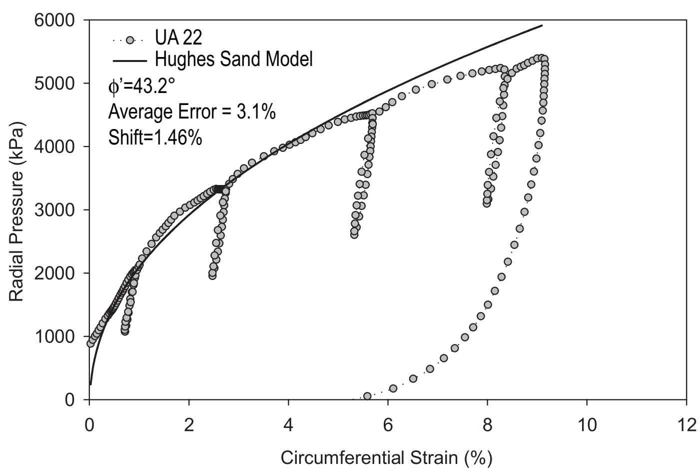

Figure A.153 Hughes frictional model fit (UA 22)

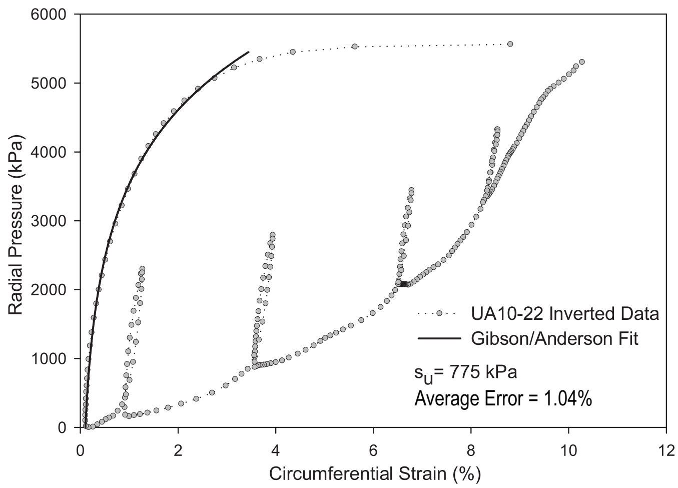

Figure A.154 Inverted undrained shear strength analysis (UA 22)

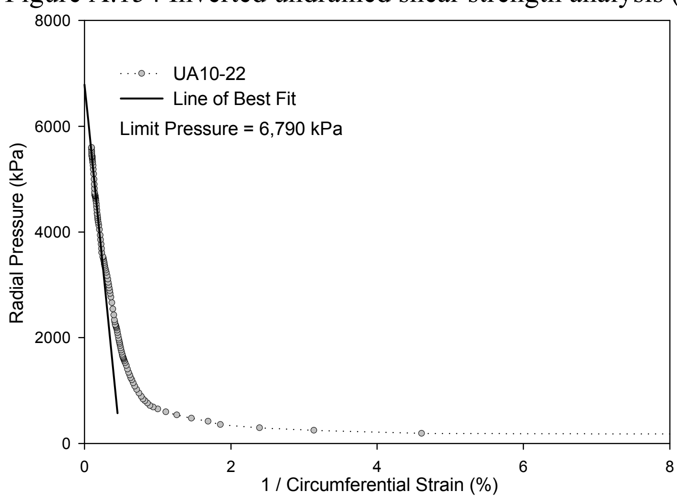

Figure A.155 Limit pressure calculation (UA 22)

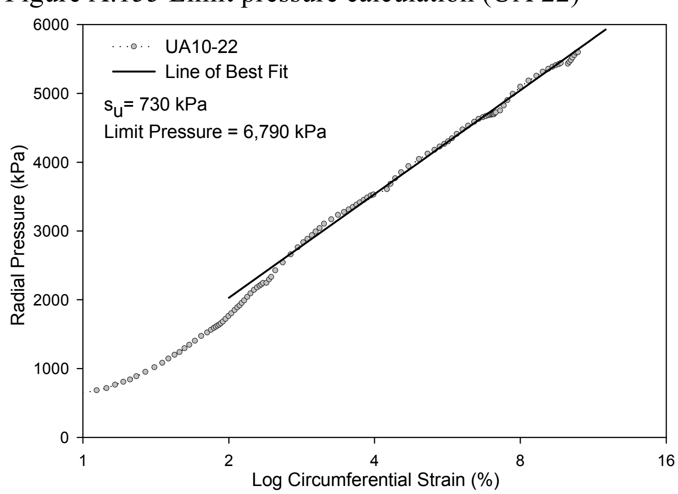

Figure A.156 Undrained shear strength; log method (UA 22)

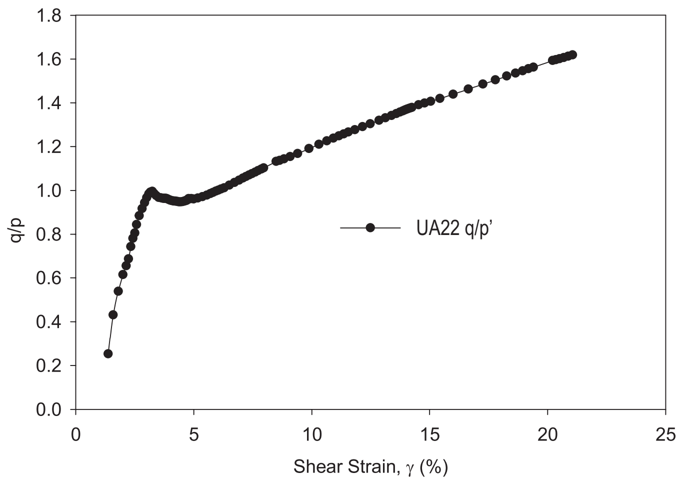

Figure A.157 Principal stress ratio versus shear strain (UA 22)

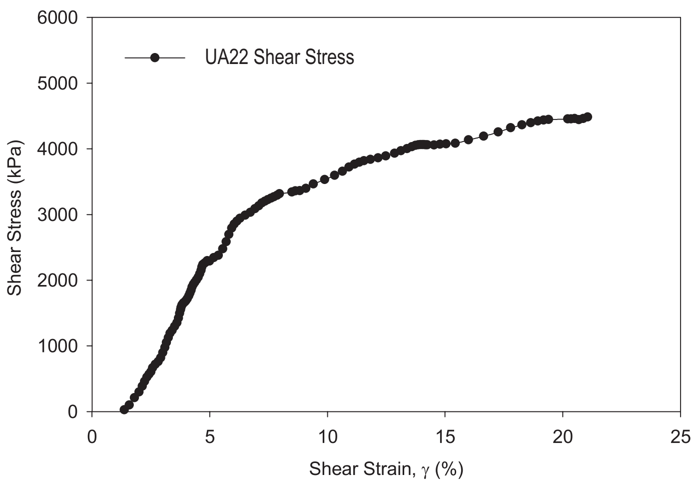

Figure A.158 Shear stress versus shear strain (UA 22)

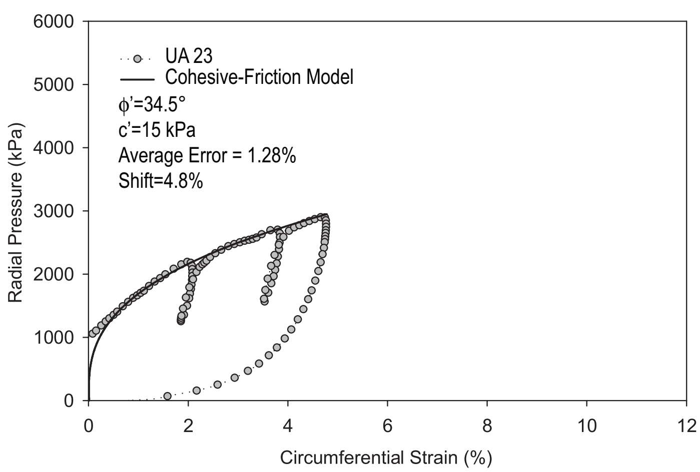

Figure A.159 Cohesive frictional model fit (UA 23)

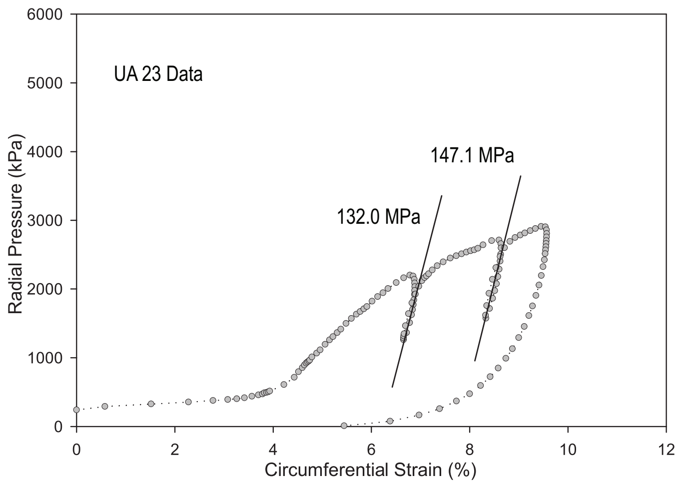

Figure A.160 Field data and shear modulus calculations (UA 23)

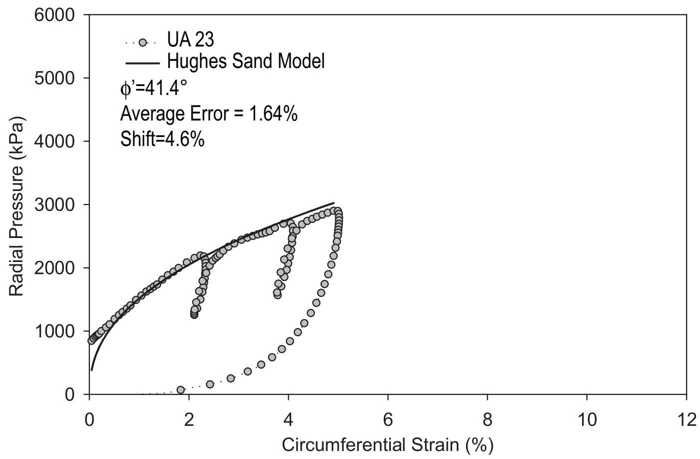

Figure A.161 Hughes frictional model fit (UA 23)

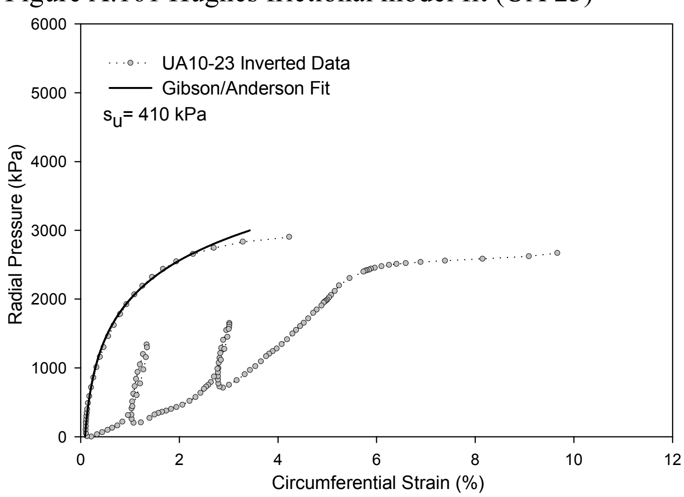

Figure A.162 Inverted undrained shear strength analysis (UA 23)

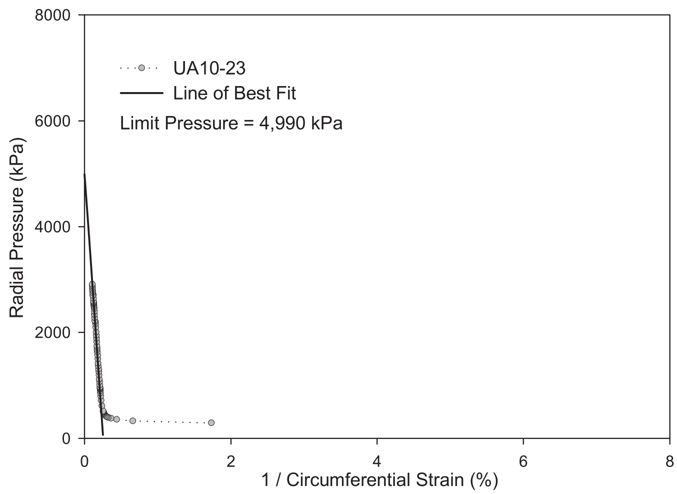

Figure A.163 Limit pressure calculation (UA 23)

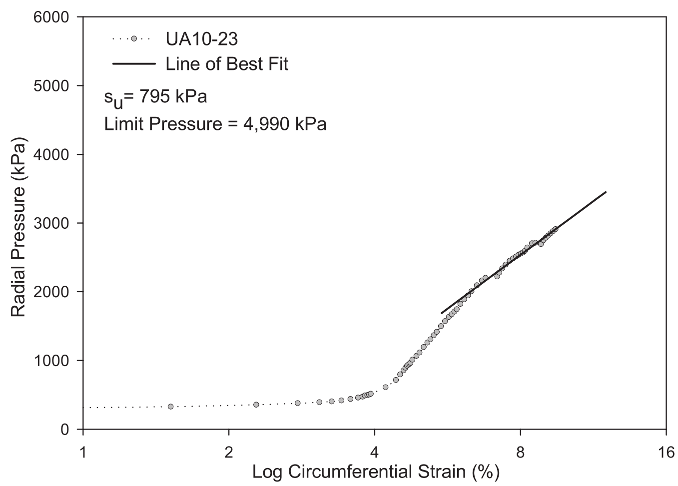

Figure A.164 Undrained shear strength; log method (UA 23)

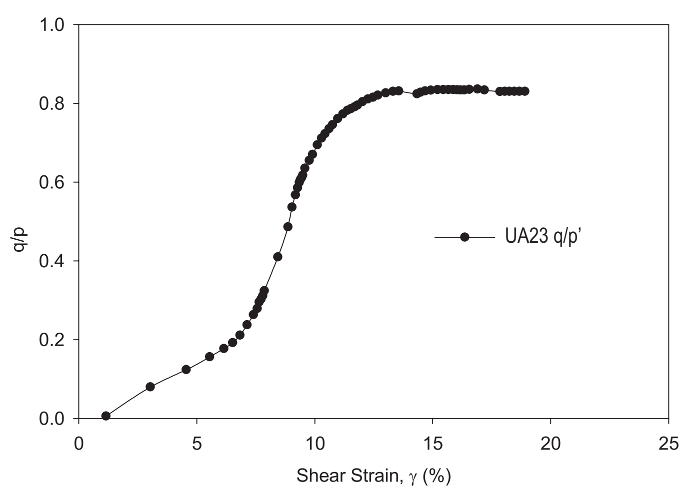

Figure A.165 Principal stress ratio versus shear strain (UA 23)

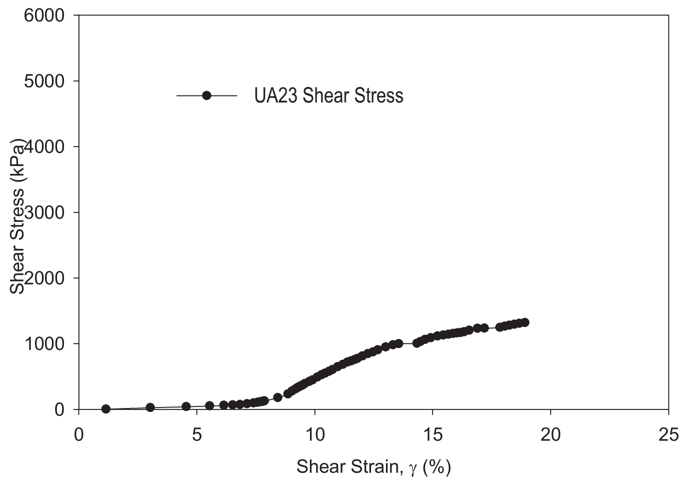

Figure A.166 Shear stress versus shear strain (UA 23)

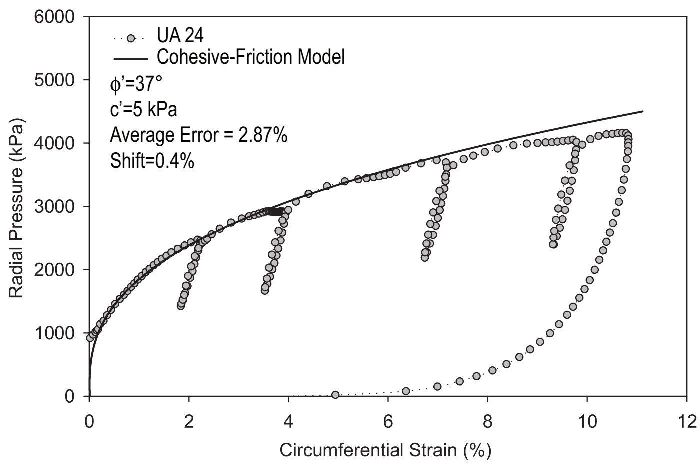

Figure A.167 Cohesive frictional model fit (UA 24)

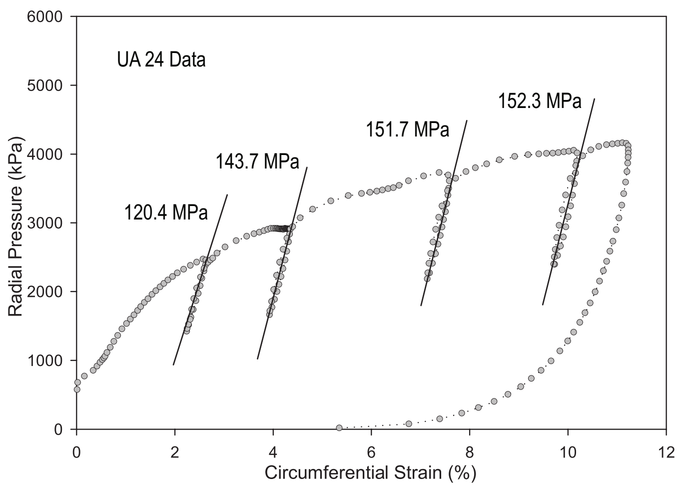

Figure A.168 Field data and shear modulus calculations (UA 24)

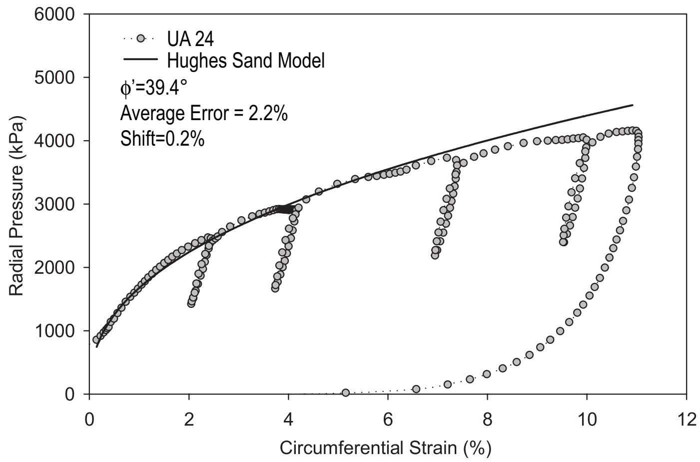

Figure A.169 Hughes frictional model fit (UA 24)

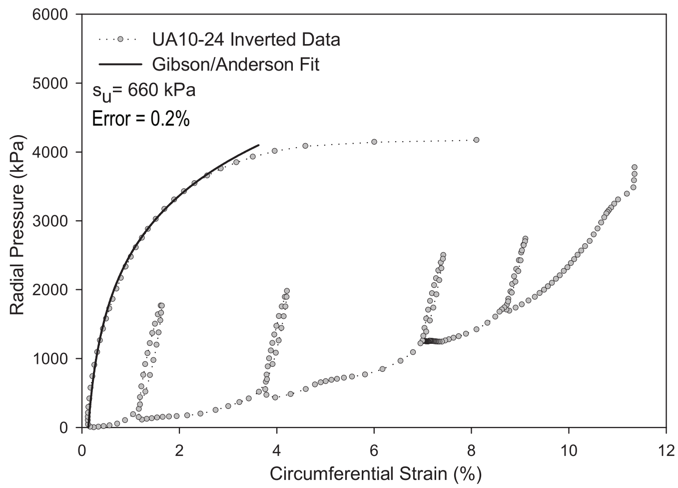

Figure A.170 Inverted undrained shear strength analysis (UA 24)

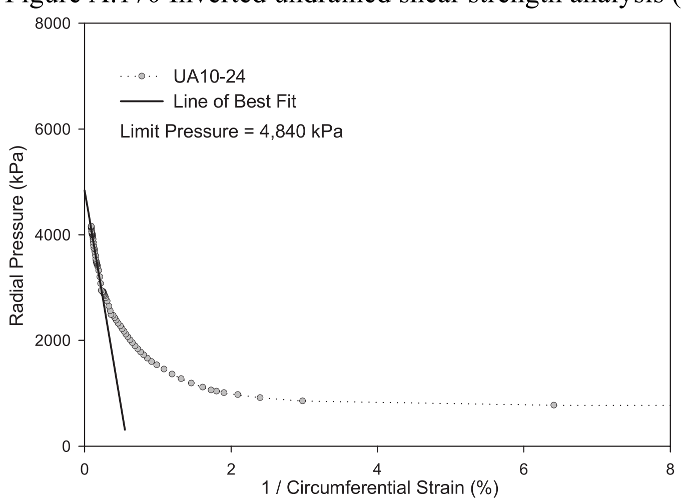

Figure A.171 Limit pressure calculation (UA 24)

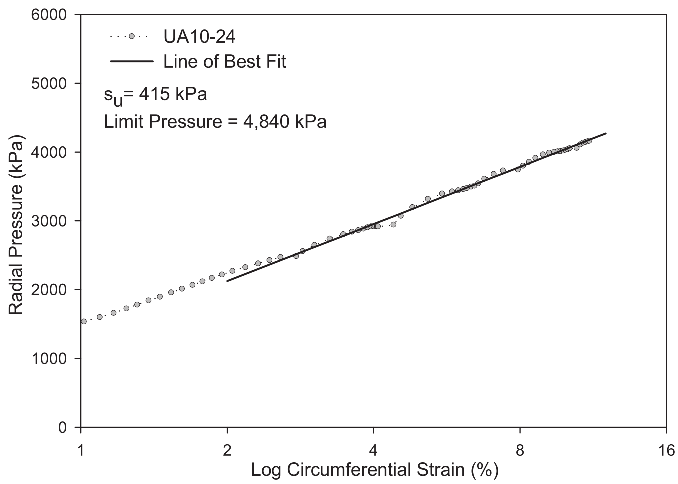

Figure A.172 Undrained shear strength; log method (UA 24)

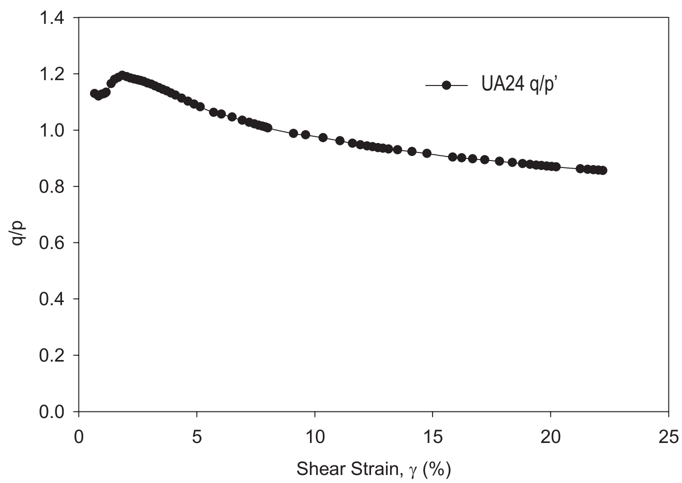

Figure A.173 Principal stress ratio versus shear strain (UA 24)

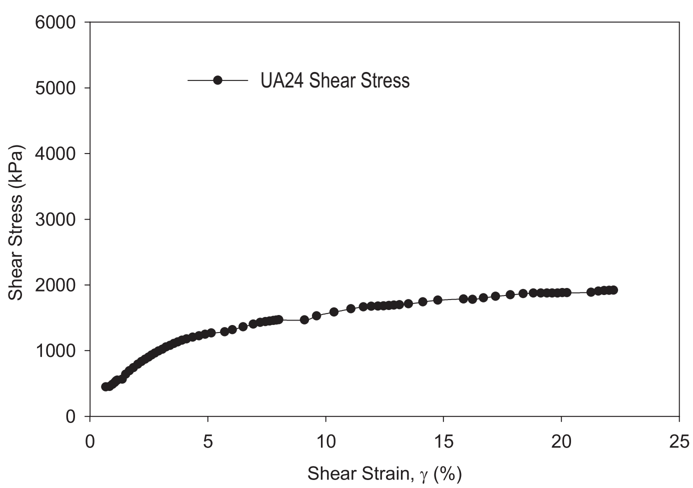

Figure A.174 Shear stress versus shear strain (UA 24)

Appendix B: Field Data

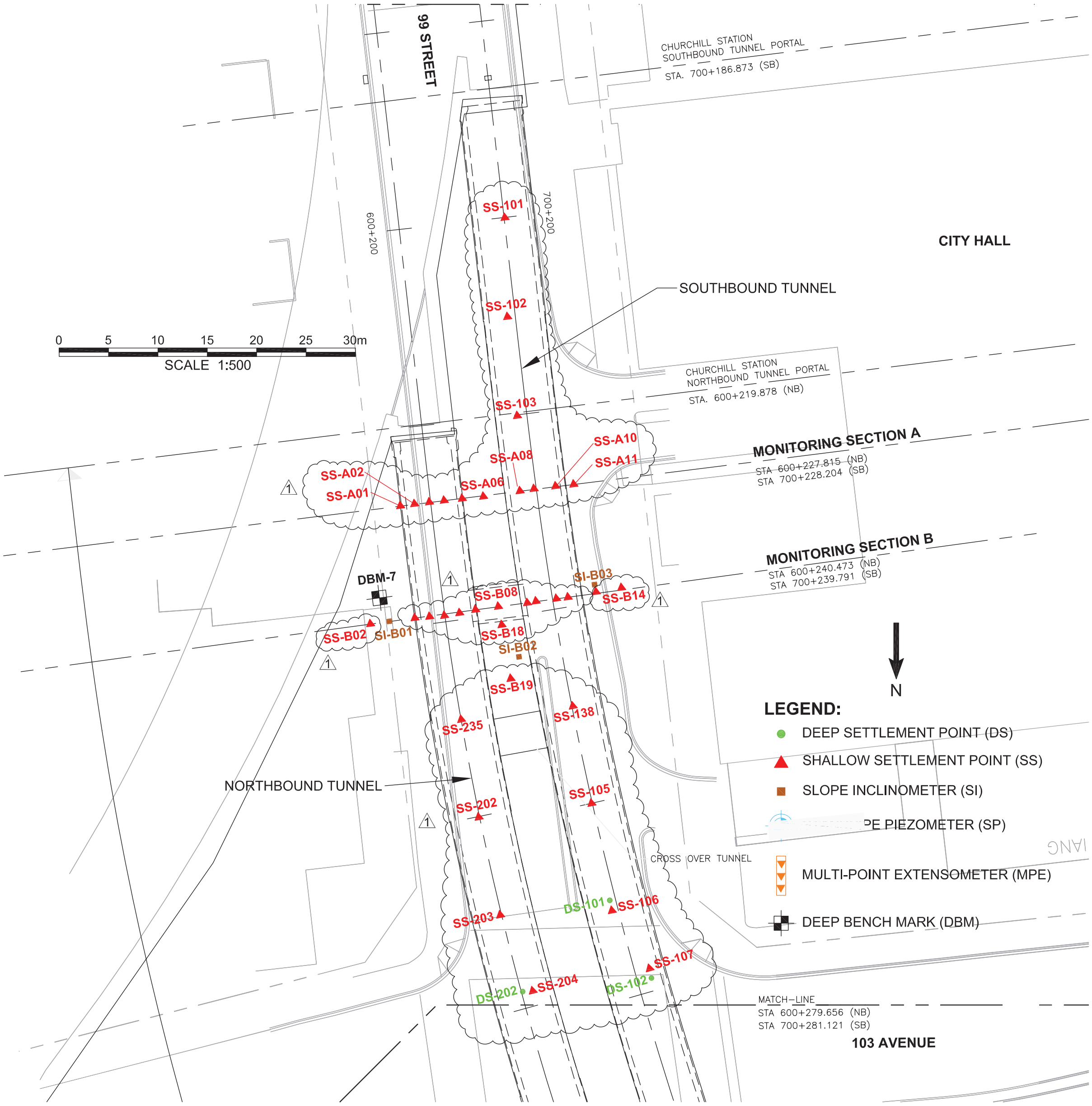

Figure B.01 Site plan showing instrument locations (1 of 3)

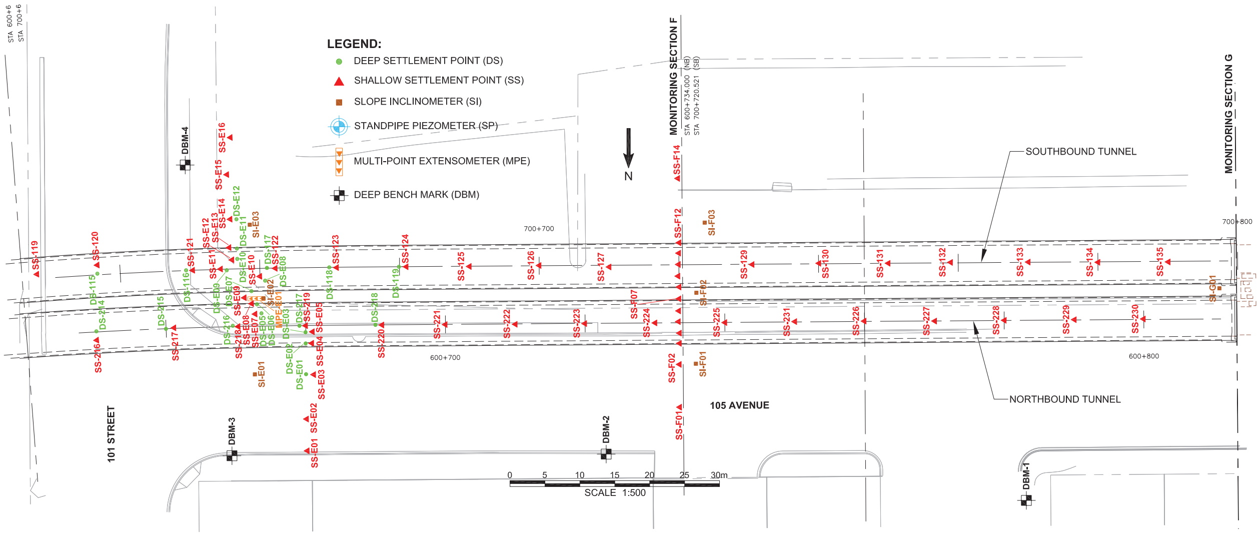

Figure B.02 Site plan showing instrument locations (2 of 3)

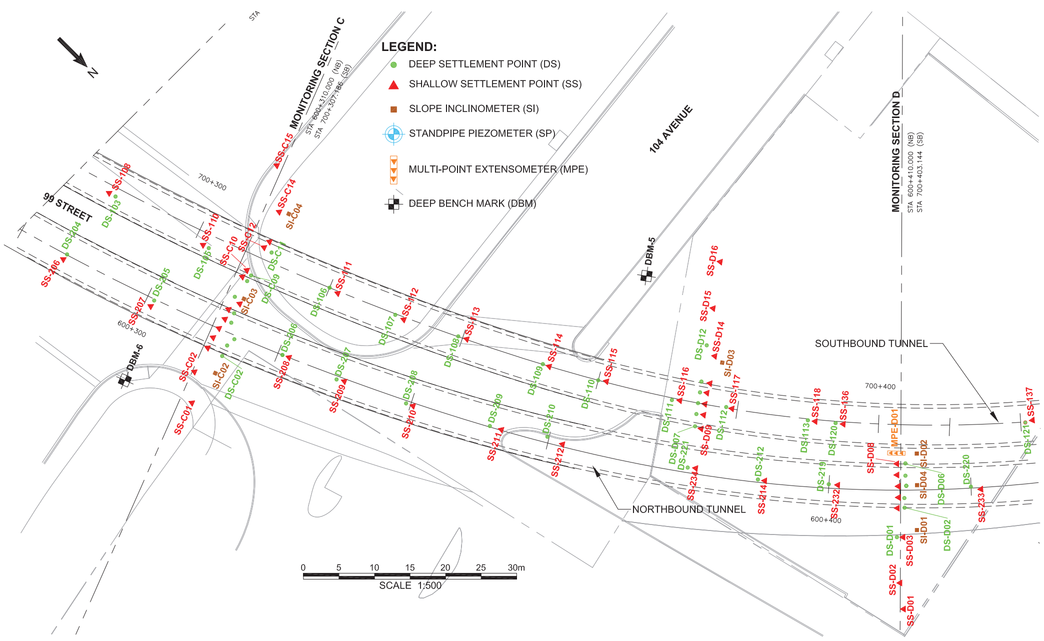

Figure B.03 Site plan showing instrument locations (3 of 3)

Optical Convergence

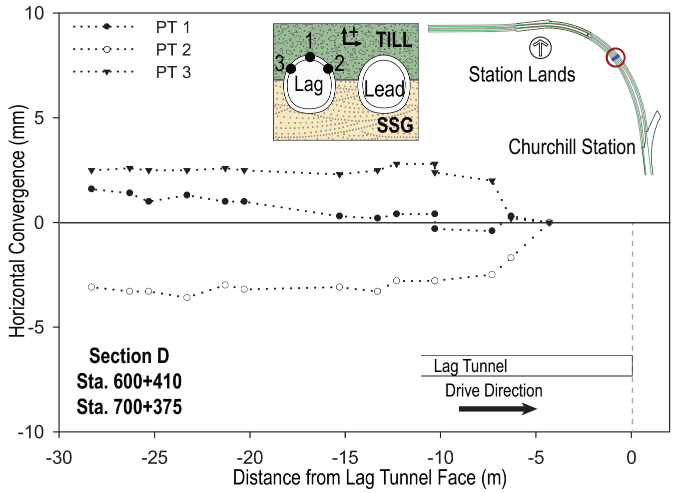

Figure B.04 Horizontal convergence Section D (lag tunnel)

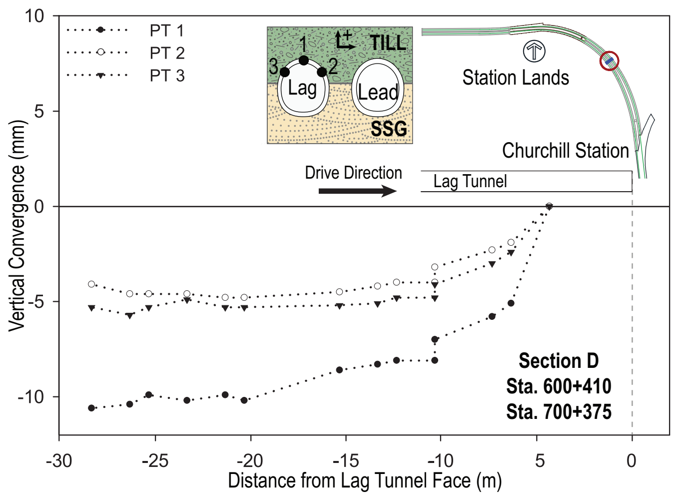

Figure B.05 Vertical convergence Section D (lag tunnel)

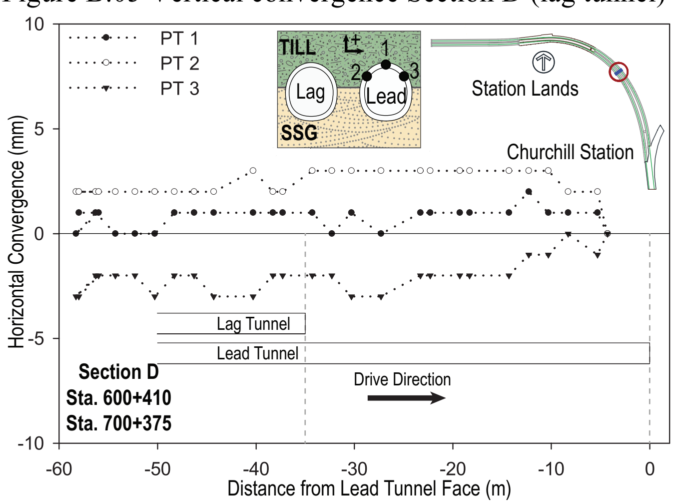

Figure B.06 Horizontal convergence Section D (lead tunnel)

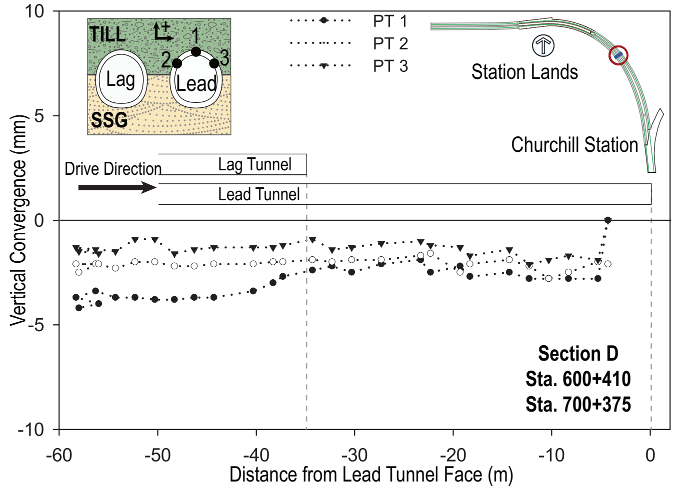

Figure B.07 Horizontal convergence Section D (lag tunnel)

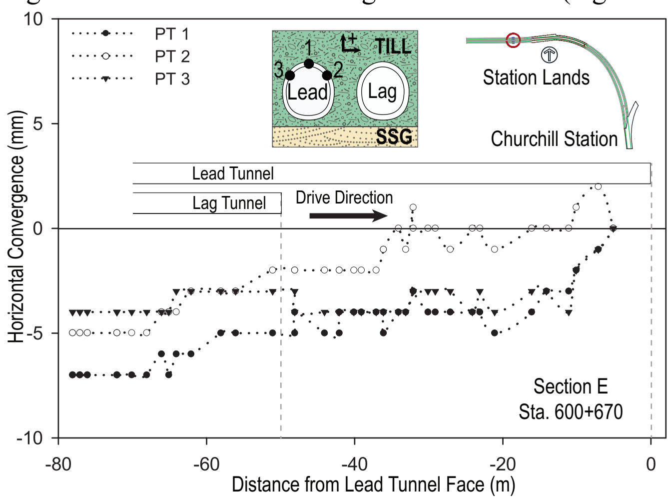

Figure B.08 Horizontal convergence Section E (lead tunnel)

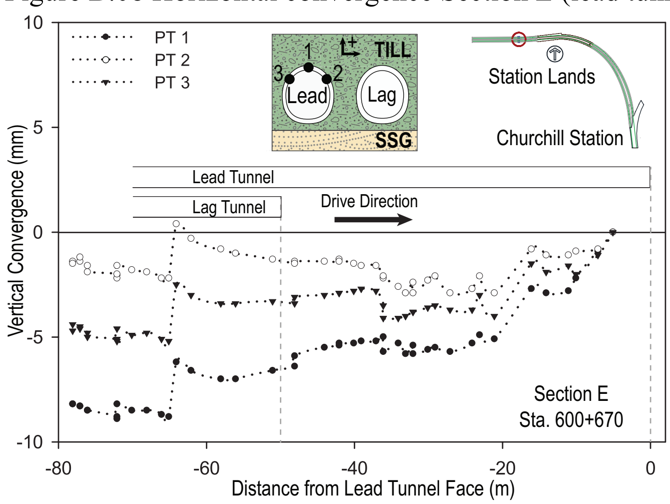

Figure B.09 Vertical convergence Section E (lead tunnel)

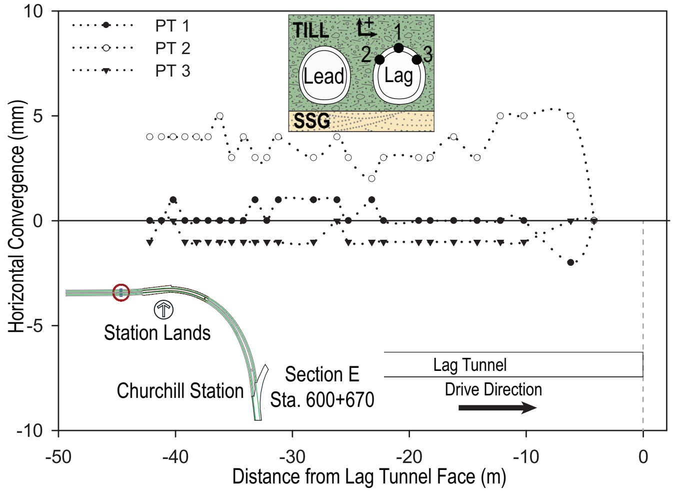

Figure B.10 Horizontal convergence Section E (lag tunnel)

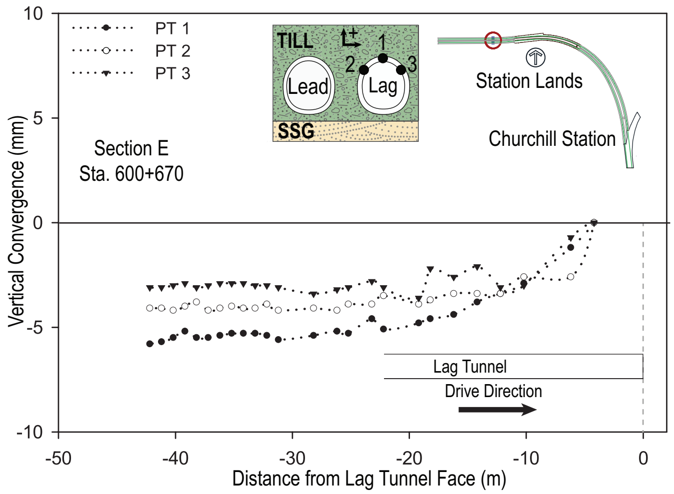

Figure B.11 Vertical convergence Section E (lead tunnel)

Tape Extensometer

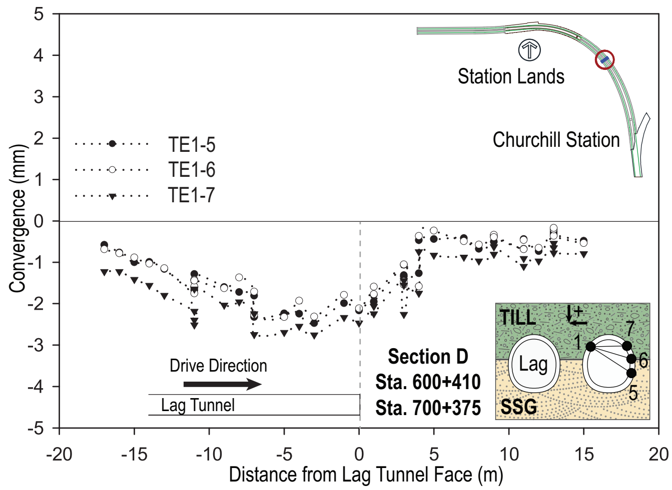

Figure B.12 Tape extensometer convergence Section D (Point 1)

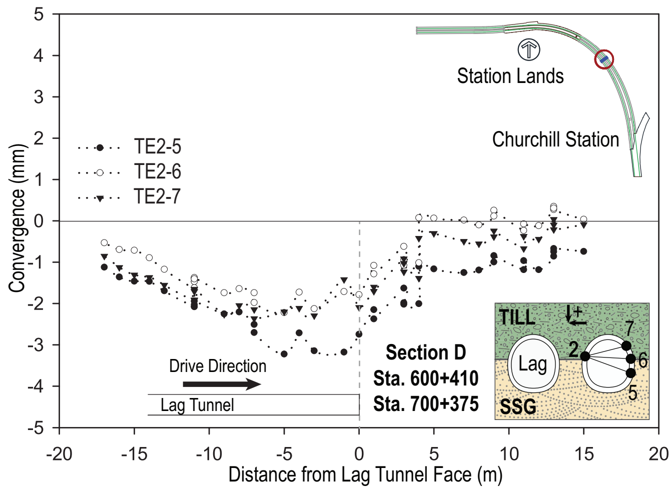

Figure B.13 Tape extensometer convergence Section D (Point 2)

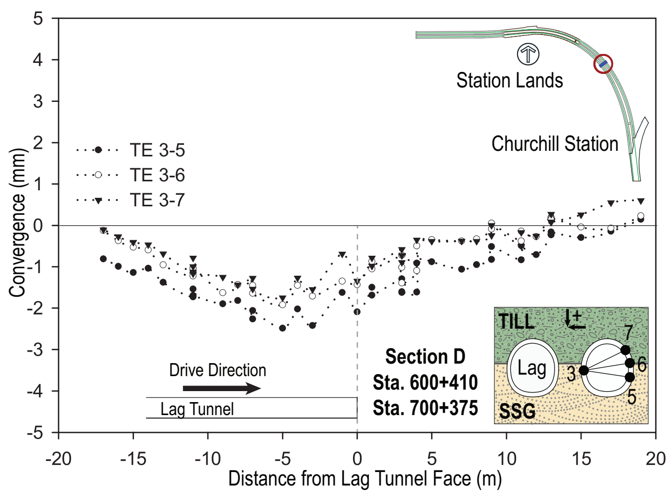

Figure B.14 Tape extensometer convergence Section D (Point 3)

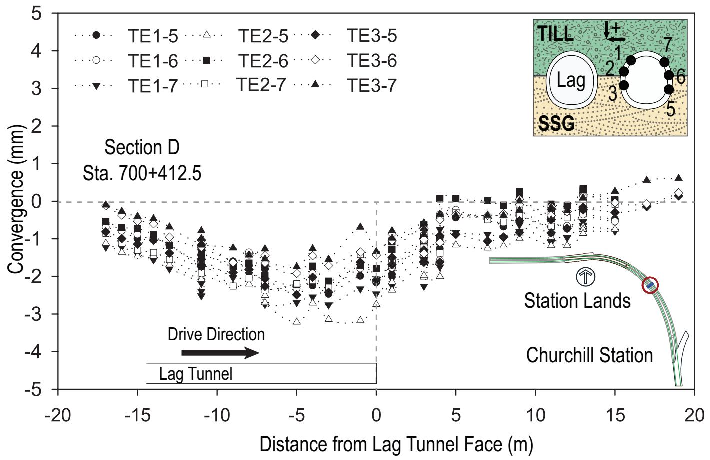

Figure B.15 Tape extensometer convergence Section D (All points)

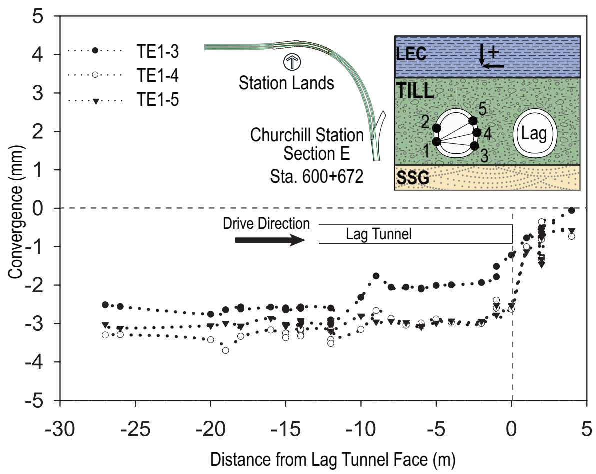

Figure B.16 Tape extensometer convergence Section E (Point 1)

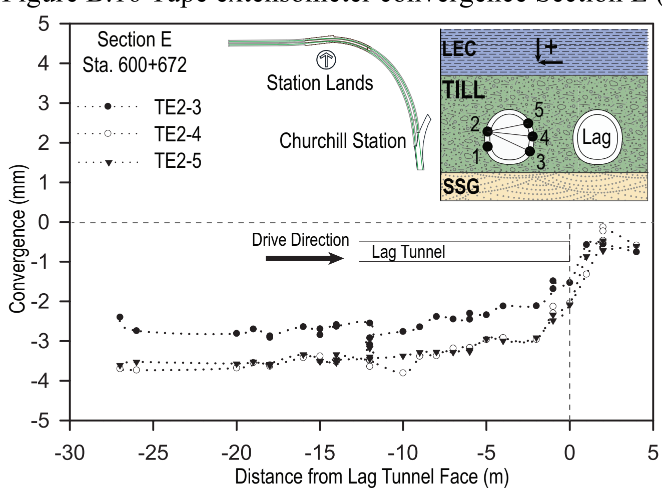

Figure B.17 Tape extensometer convergence Section E (Point 2)

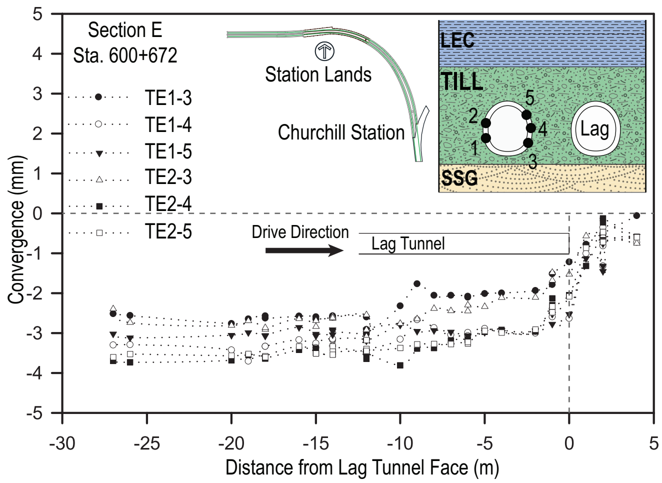

Figure B.18 Tape extensometer convergence Section E (All Points)

Circumferential SAA

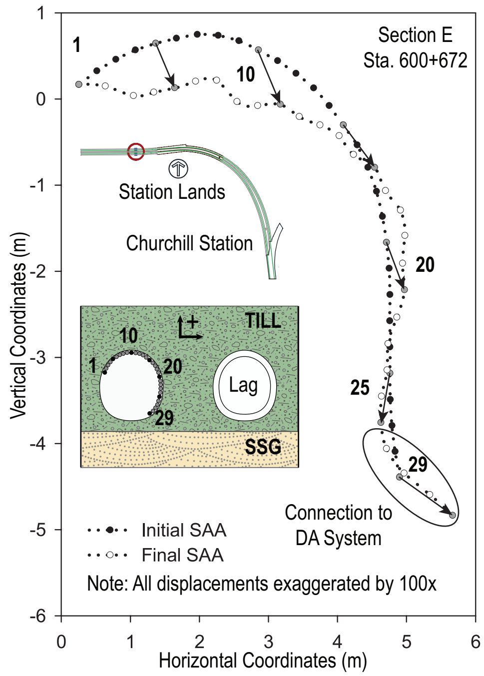

Figure B.19 Circumferential SAA measurements Section E (All Points)

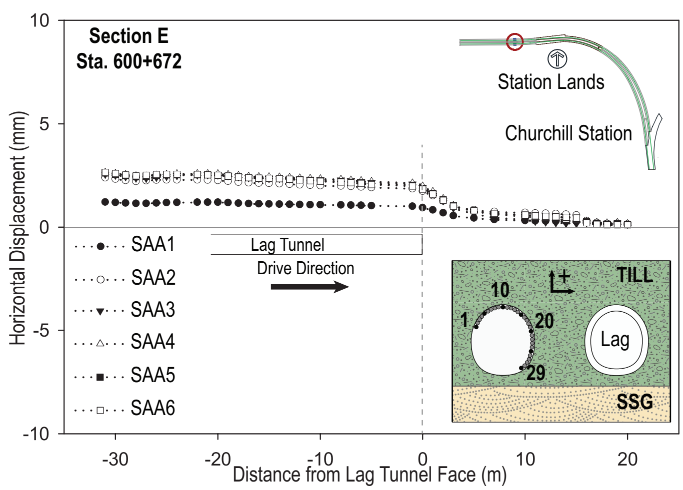

Figure B.20 Circumferential SAA measurements – Horizontal (Points 1-6)

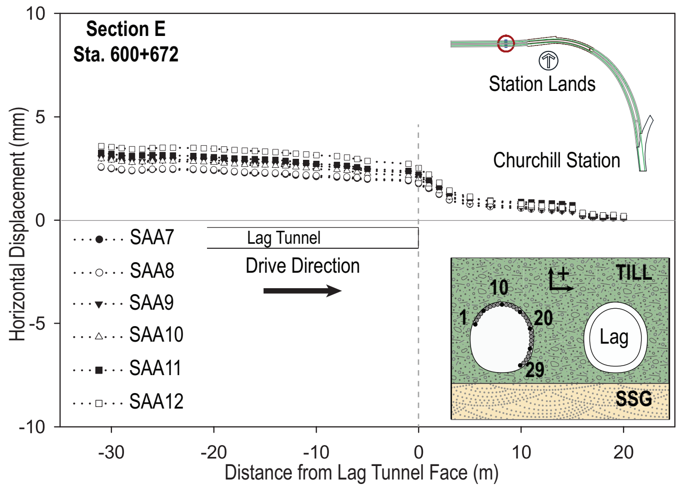

Figure B.21 Circumferential SAA measurements – Horizontal (Points 7-12)

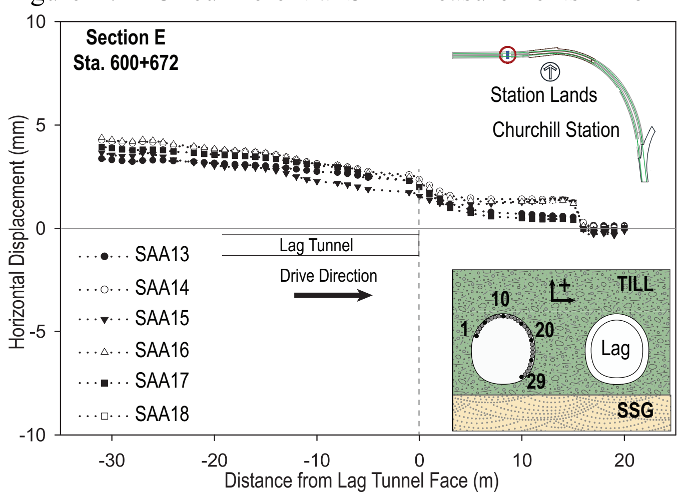

Figure B.22 Circumferential SAA measurements – Horizontal (Points 13-18)

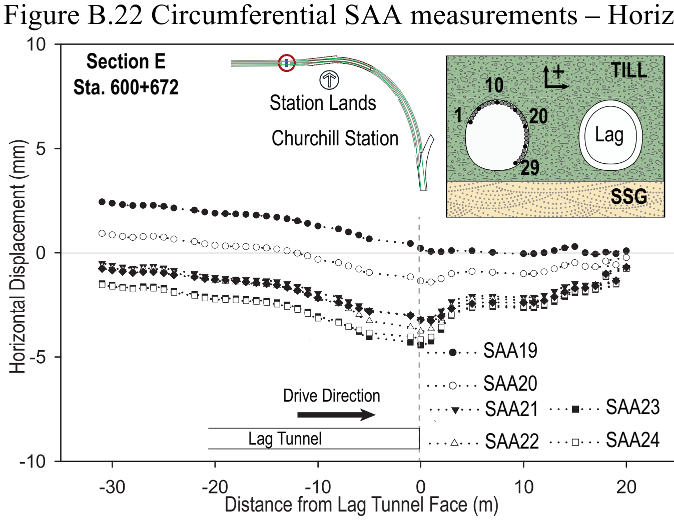

Figure B.23 Circumferential SAA measurements – Horizontal (Points 19-24)

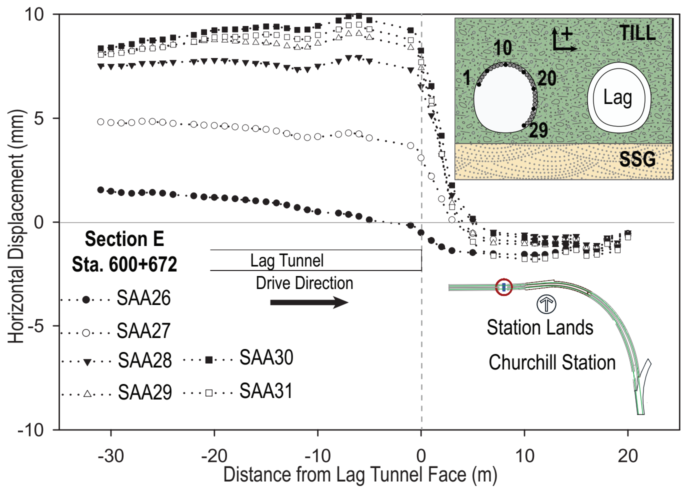

Figure B.24 Circumferential SAA measurements – Horizontal (Points 25-31)

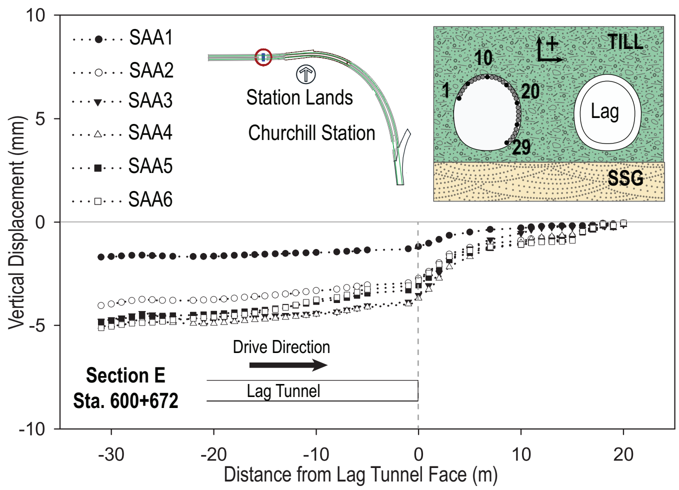

Figure B.25 Circumferential SAA measurements – Vertical (Points 1-6)

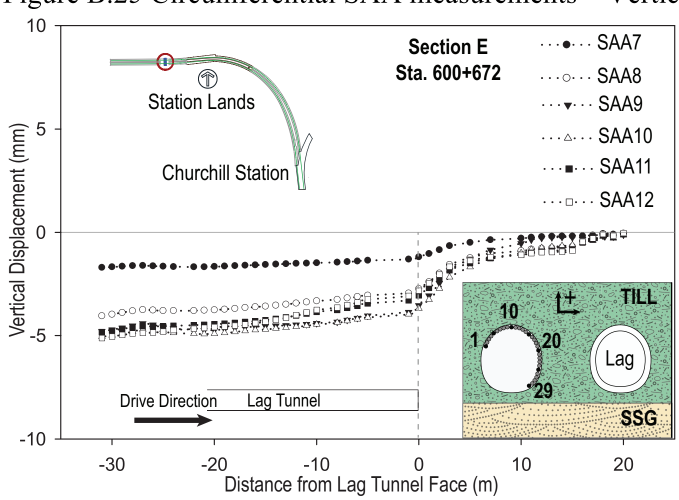

Figure B.26 Circumferential SAA measurements – Vertical (Points 7-12)

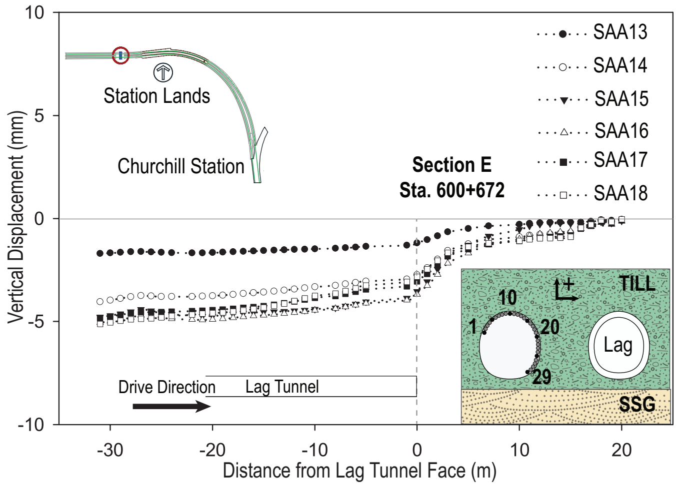

Figure B.27 Circumferential SAA measurements – Vertical (Points 13-18)

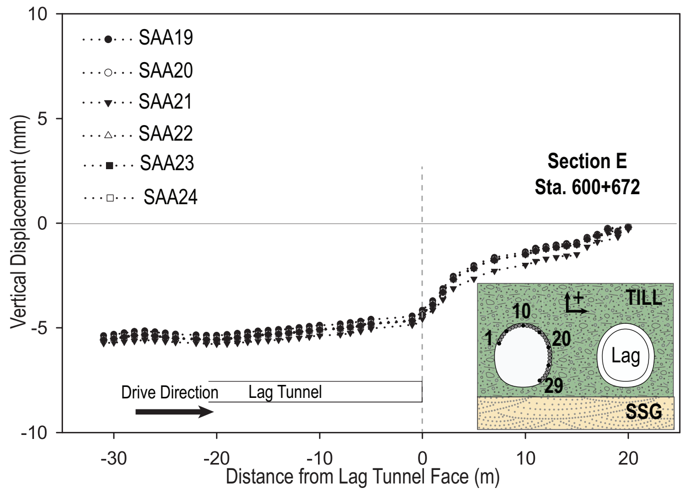

Figure B.28 Circumferential SAA measurements – Vertical (Points 19-24)

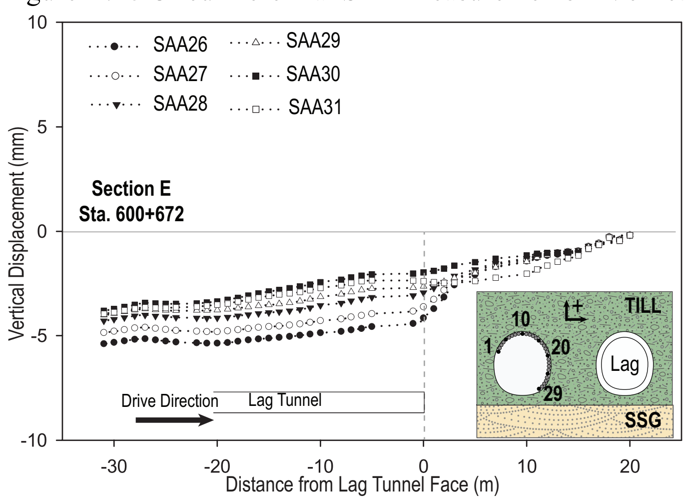

Figure B.29 Circumferential SAA measurements – Vertical (Points 25-31)

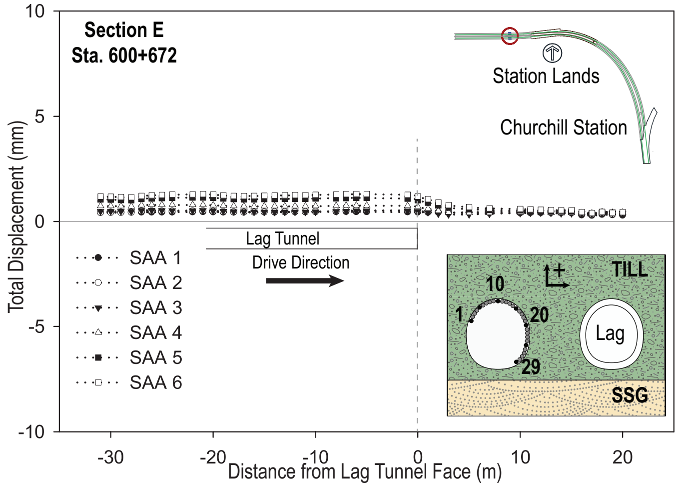

Figure B.30 Circumferential SAA measurements – Total displacement (Points 1-6)

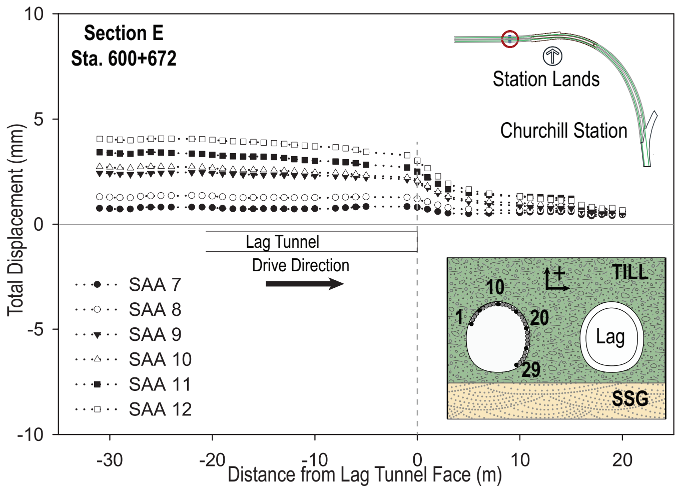

Figure B.31 Circumferential SAA measurements – Total displacement (Points 7-12)

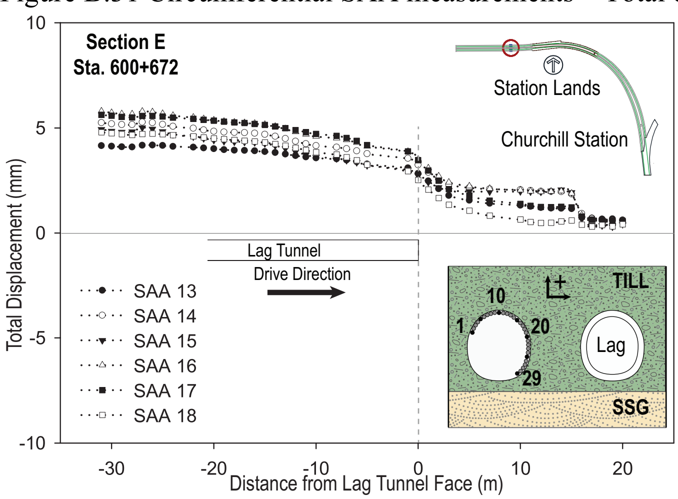

Figure B.32 Circumferential SAA measurements – Total displacement (Points 13-18)

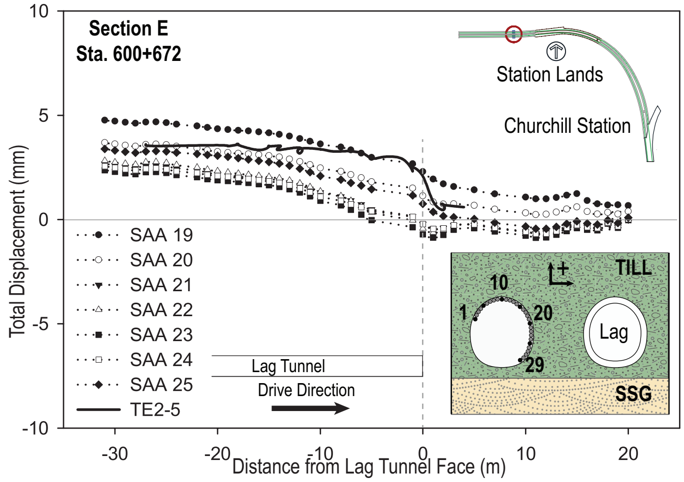

Figure B.33 Circumferential SAA measurements – Total displacement (Points 19-24)

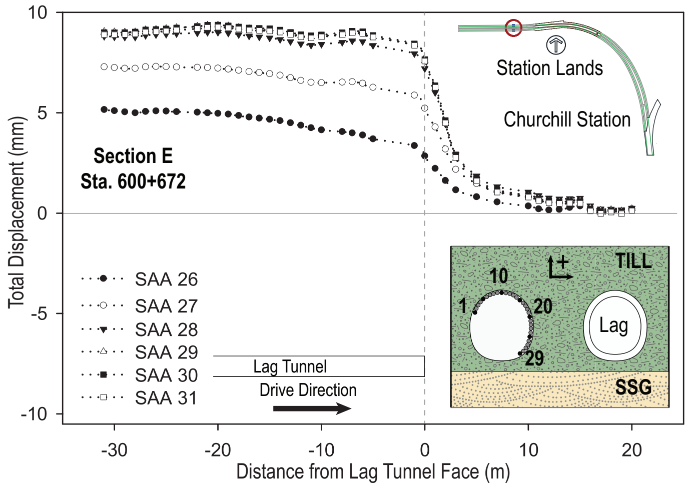

Figure B.34 Circumferential SAA measurements – Total displacement (Points 25-31)

Strain Gauge Measurement – Strain

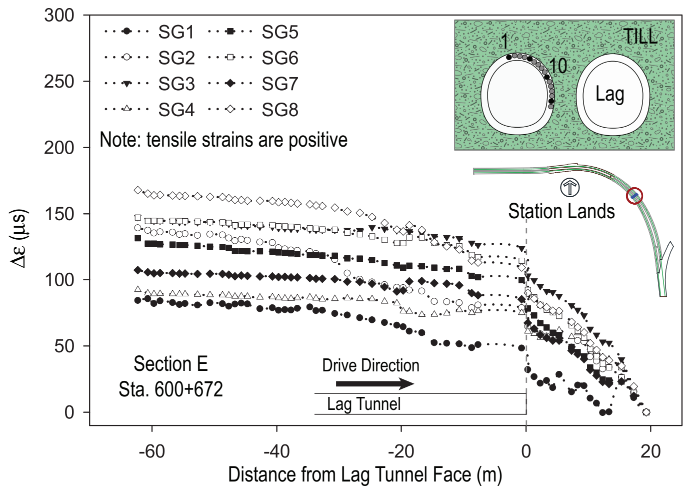

Figure B.35 Strain gauge measurements, Section E (Points 1-8)

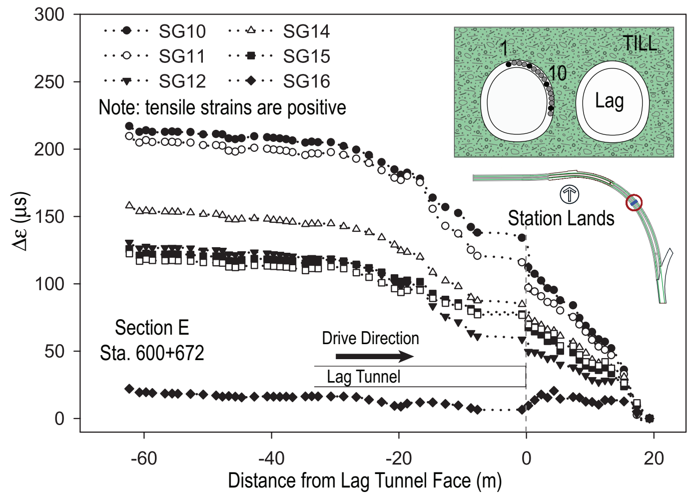

Figure B.36 Strain gauge measurements, Section E (Points 9-16)

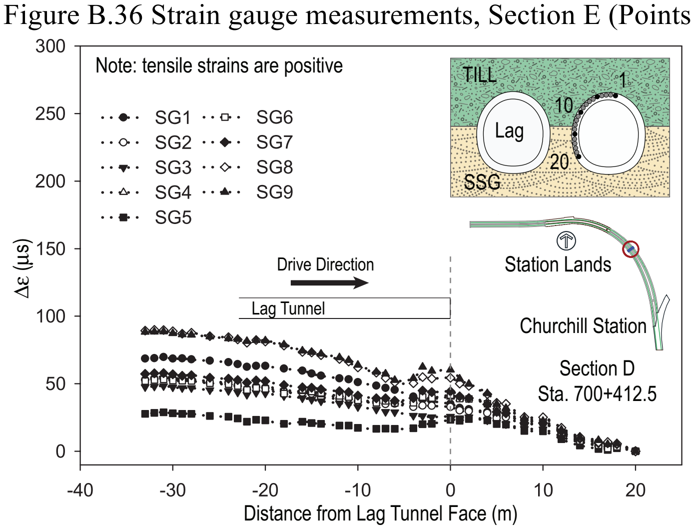

Figure B.37 Strain gauge measurements, Section D (Points 1-9)

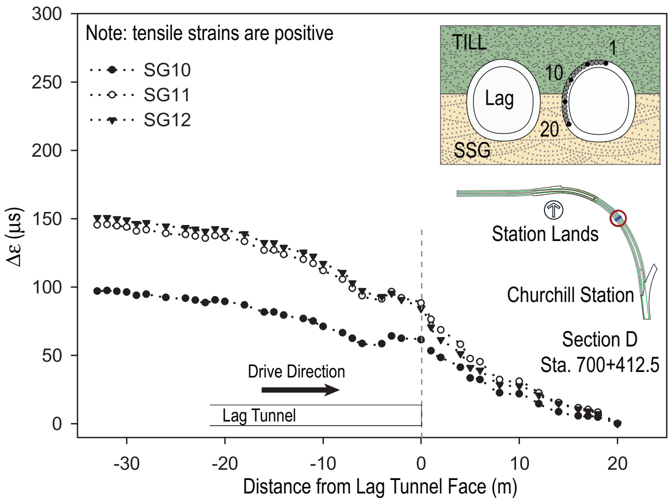

Figure B.38 Strain gauge measurements, Section D (Points 10-12)

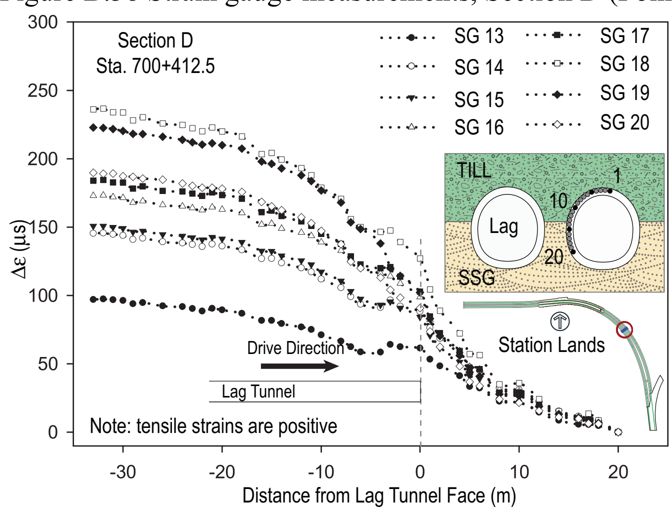

Figure B.39 Strain gauge measurements, Section D (Points 13-18)

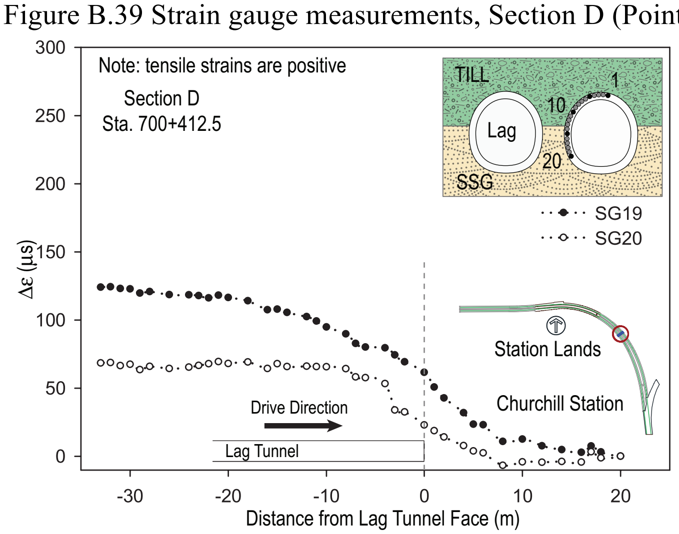

Figure B.40 Strain gauge measurements, Section D (Points 19-20)

Strain Gauge Measurement – Stress

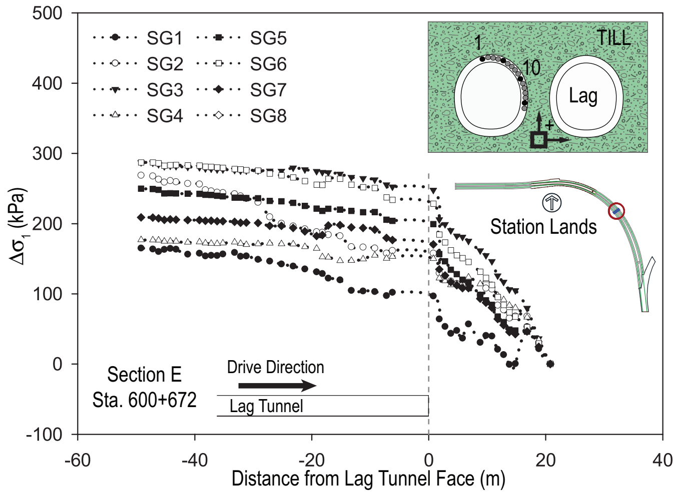

Figure B.41 Strain gauge measurements, Section E (Points 1-8)

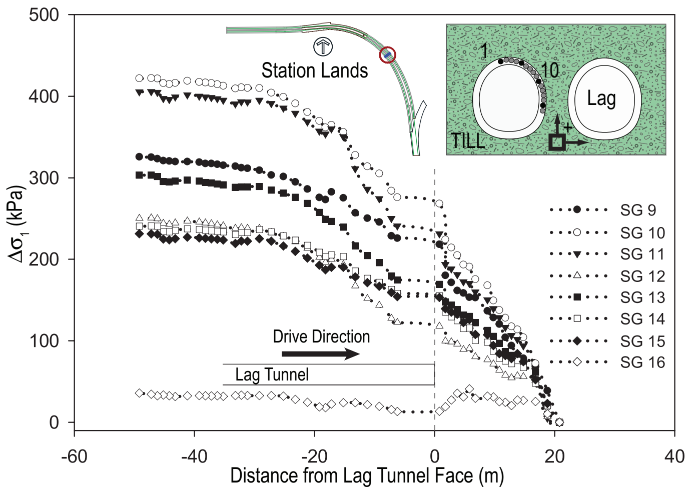

Figure B.42 Strain gauge measurements, Section E (Points 9-16)

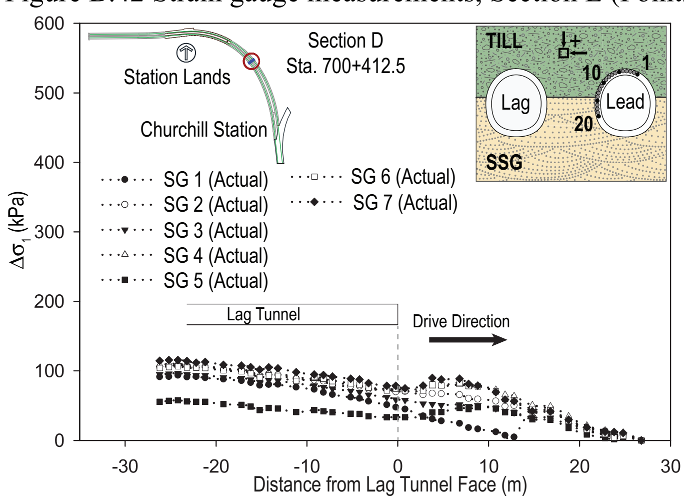

Figure B.43 Strain gauge measurements, Section D (Points 1-7)

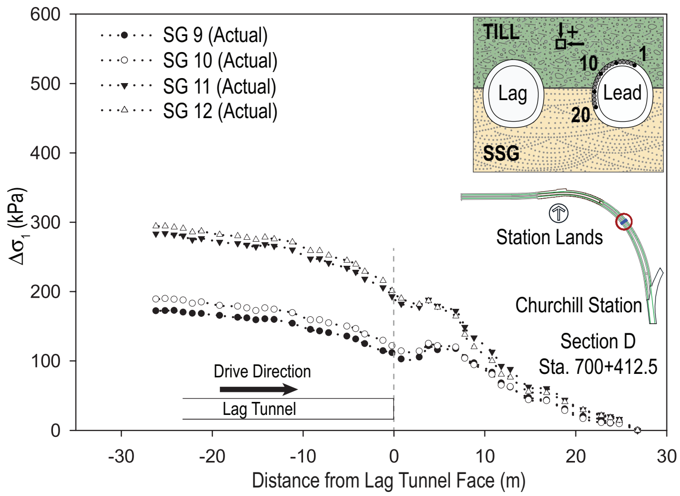

Figure B.44 Strain gauge measurements, Section D (Points 9-12)

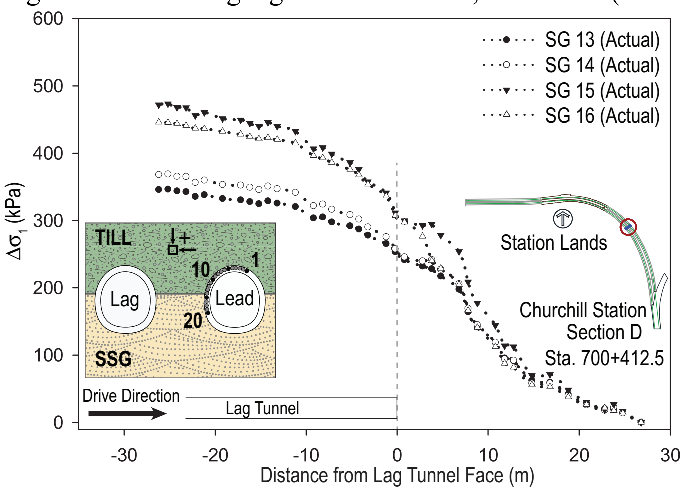

Figure B.45 Strain gauge measurements, Section D (Points 13-16)

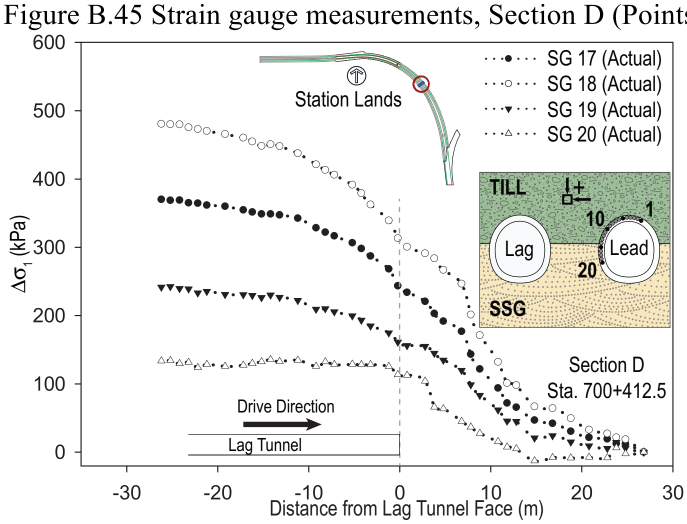

Figure B.46 Strain gauge measurements, Section D (Points 16-20)

Settlement Data

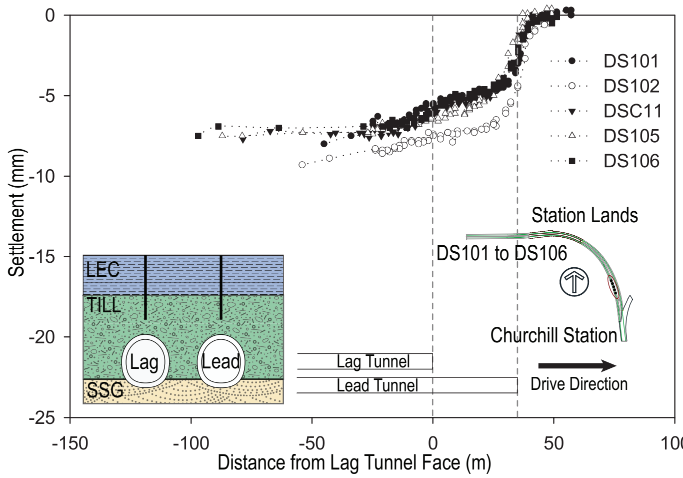

Figure B.47 Deep settlement profiles (Points DS101 to DS106)

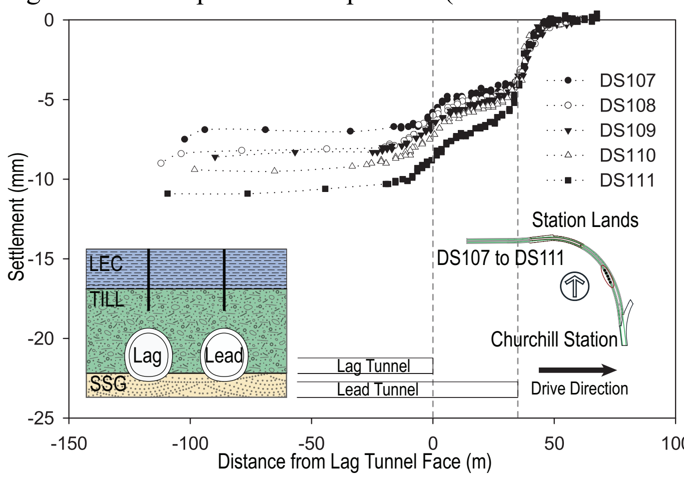

Figure B.48 Deep settlement profiles (Points DS107 to DS111)

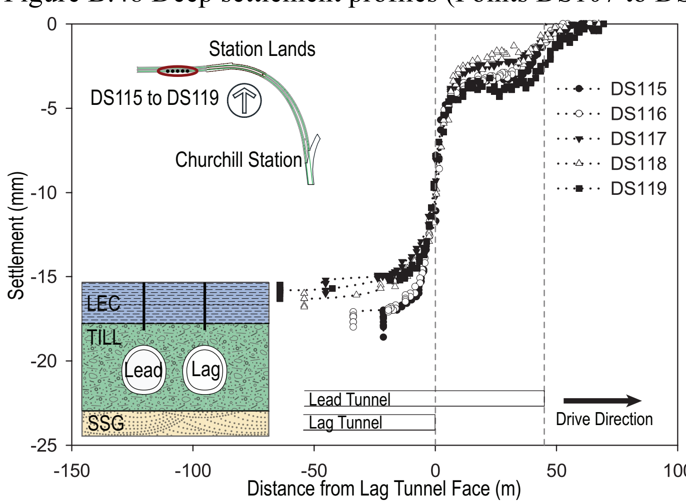

Figure B.49 Deep settlement profiles (Points DS115 to DS119)

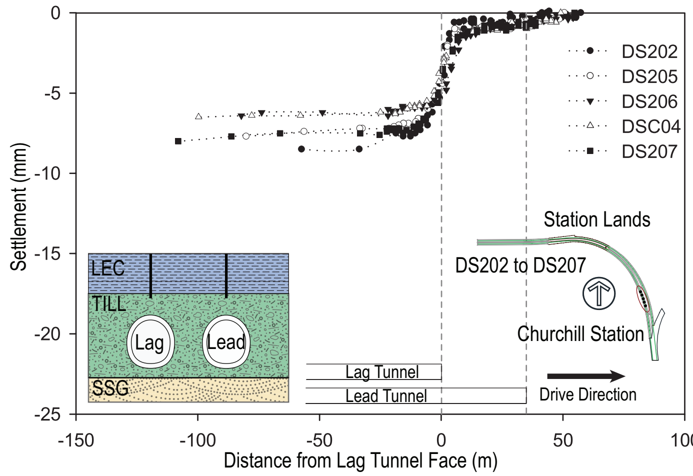

Figure B.50 Deep settlement profiles (Points DS202 to DS207)

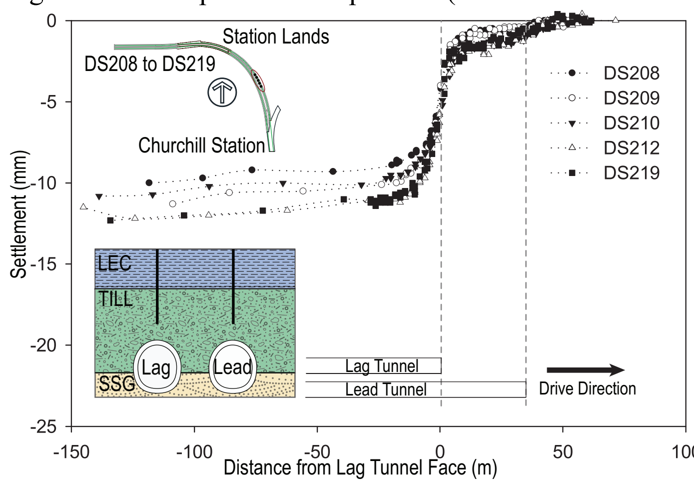

Figure B.51 Deep settlement profiles (Points DS208 to DS219)

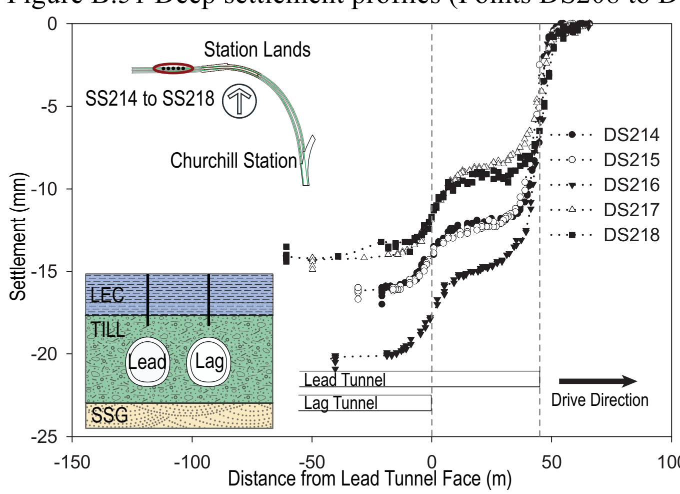

Figure B.52 Deep settlement profiles (Points DS214 to DS218)

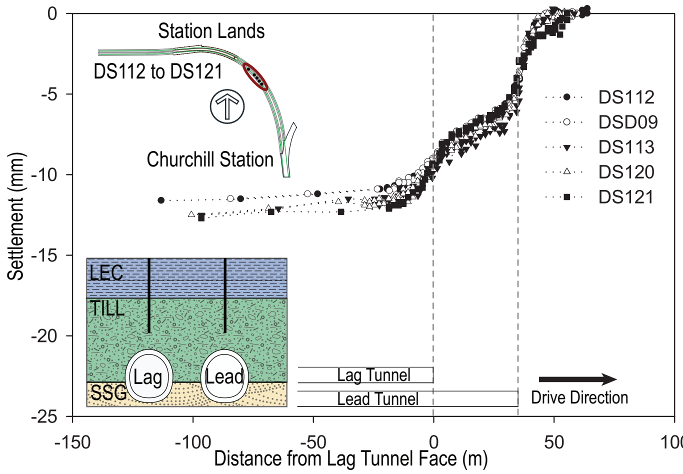

Figure B.53 Deep settlement profiles (Points DS112 to DS121)

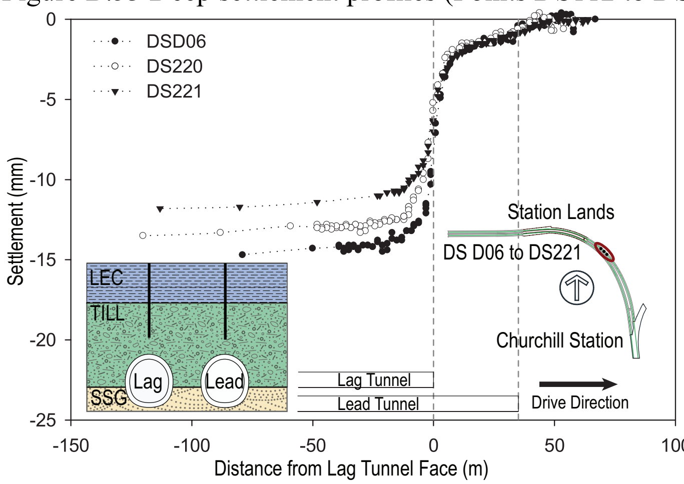

Figure B.54 Deep settlement profiles (Points DSD06 to DS221)

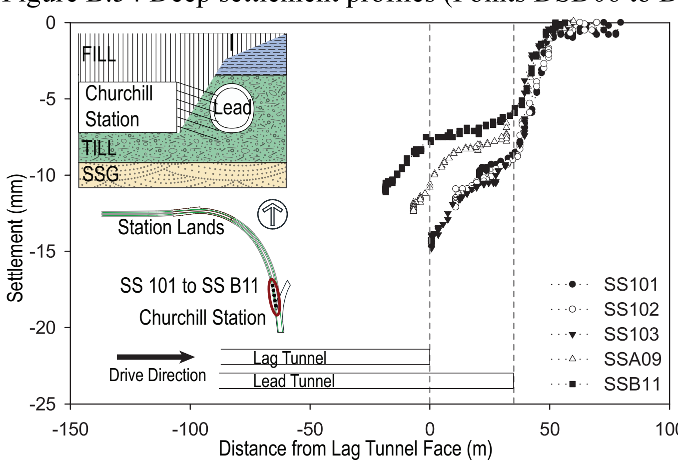

Figure B.55 Shallow settlement profiles (Points SS101 to SSB11)

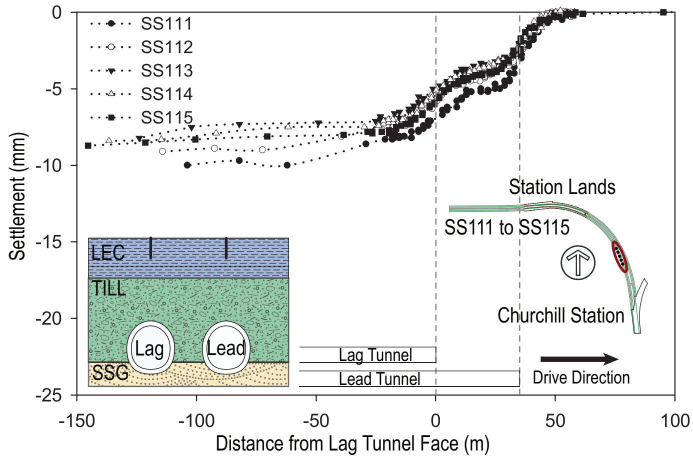

Figure B.56 Shallow settlement profiles (Points SS111 to SS115)

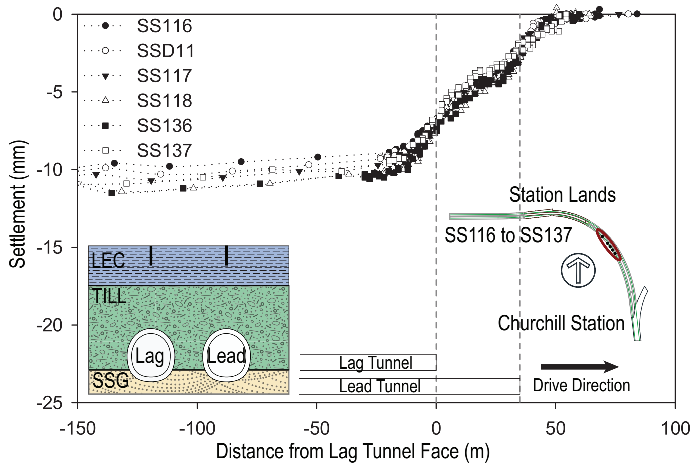

Figure B.57 Shallow settlement profiles (Points SS116 to SS137)

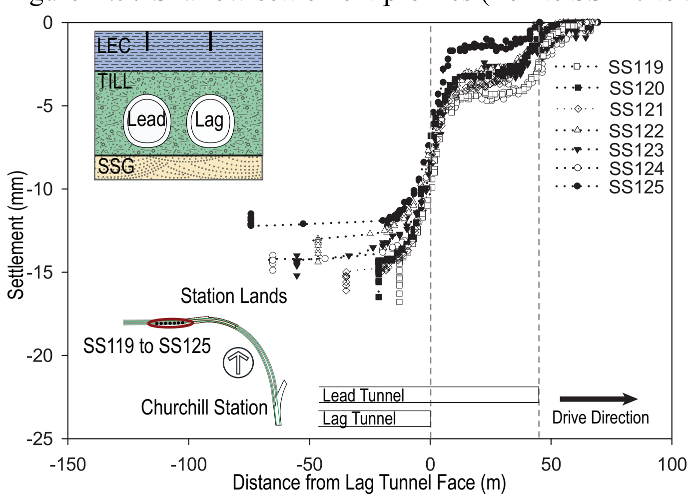

Figure B.58 Shallow settlement profiles (Points SS119 to SS125)

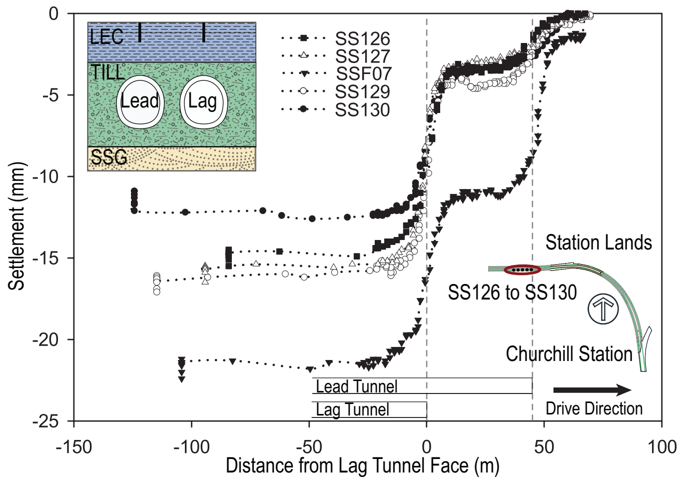

Figure B.59 Shallow settlement profiles (Points SS126 to SS130)

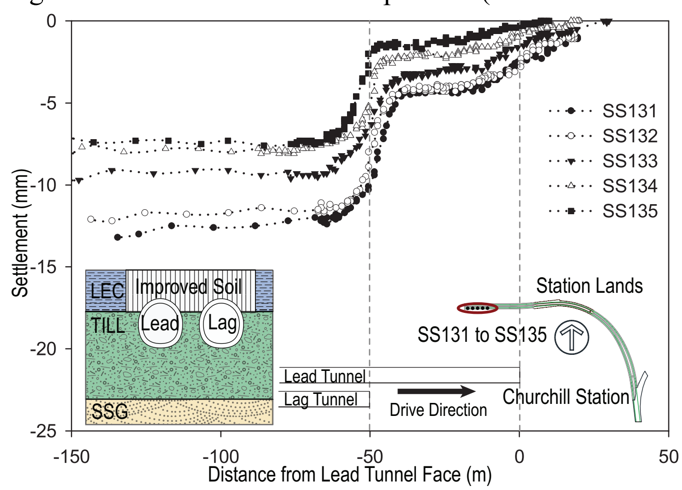

Figure B.60 Shallow settlement profiles (Points SS131 to SS135)

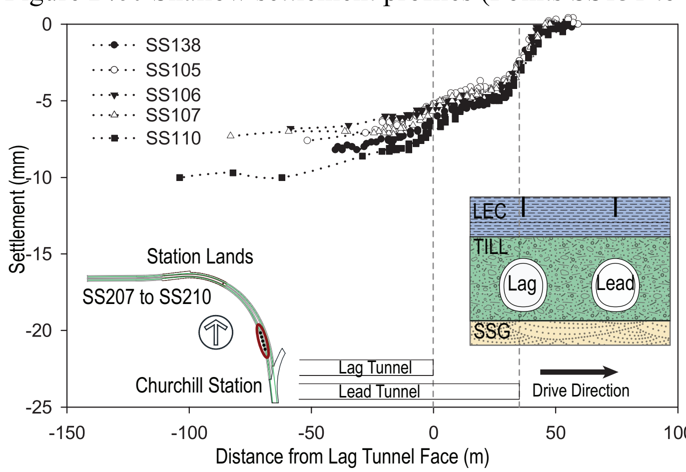

Figure B.61 Shallow settlement profiles (Points SS138 to SS110)

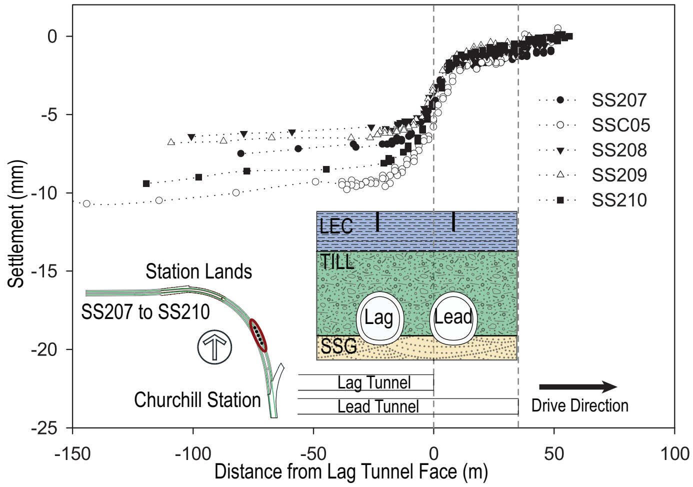

Figure B.62 Shallow settlement profiles (Points SS207 to SS210)

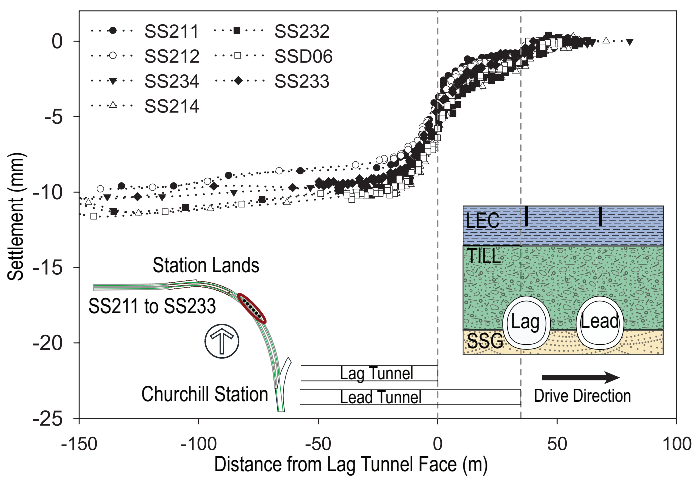

Figure B.63 Shallow settlement profiles (Points SS211 to SS233)

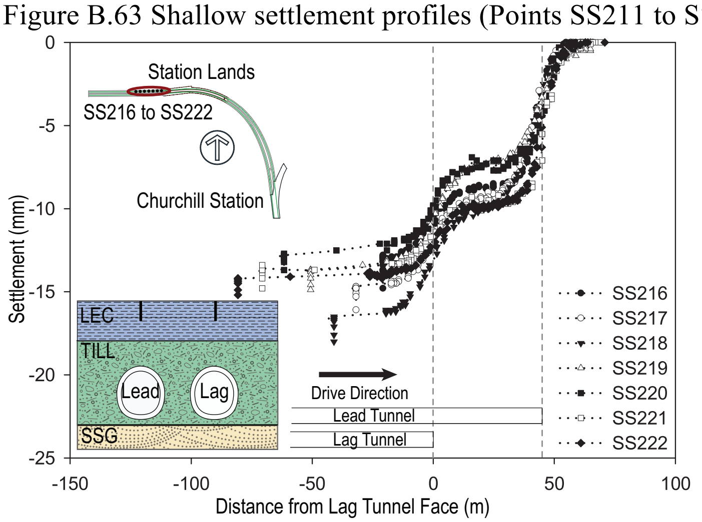

Figure B.64 Shallow settlement profiles (Points SS216 to SS222)

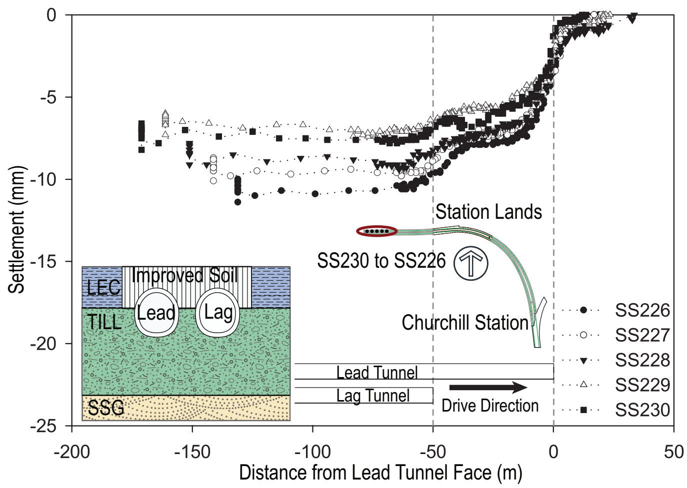

Figure B.65 Shallow settlement profiles (Points SS226 to SS230)

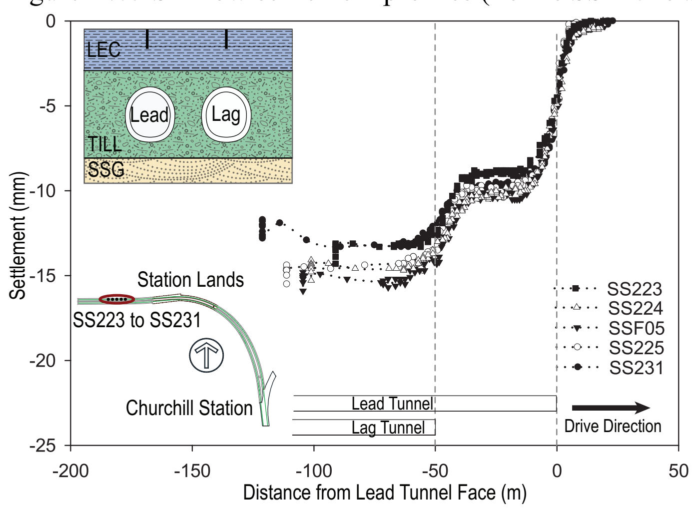

Figure B.66 Shallow settlement profiles (Points SS223 to SS231)

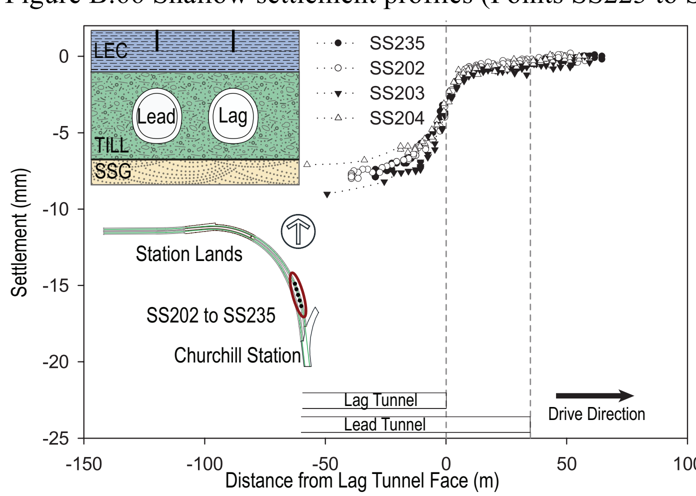

Figure B.67 Shallow settlement profiles (Points SS235 to SS204)

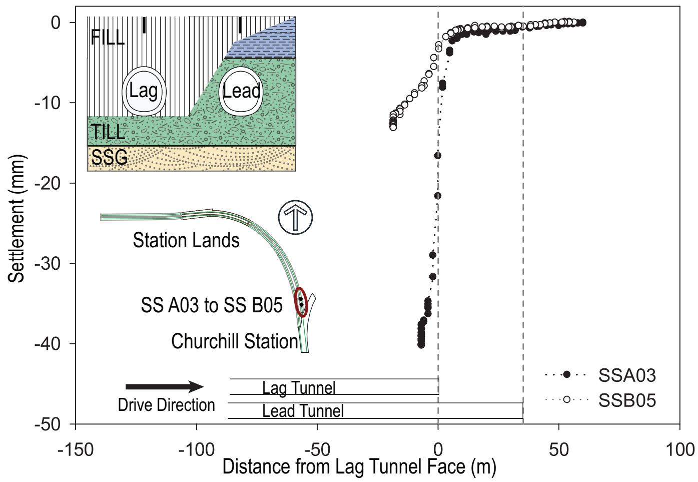

Figure B.68 Shallow settlement profiles (Points SSA03 to SSB05)

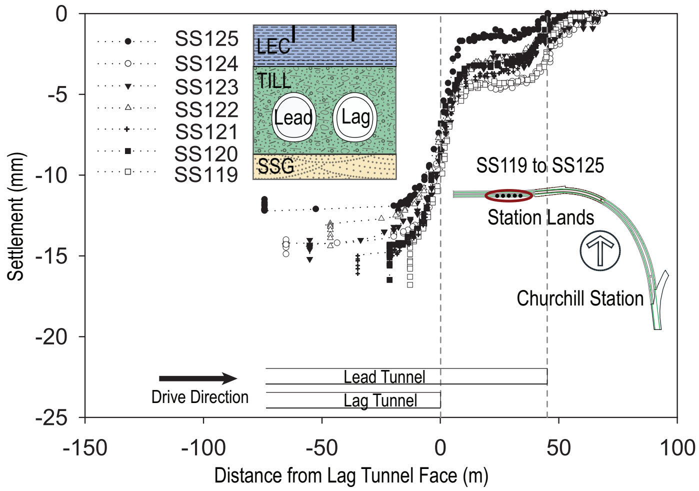

Figure B.69 Shallow settlement profiles (Points SS125 to SS119)

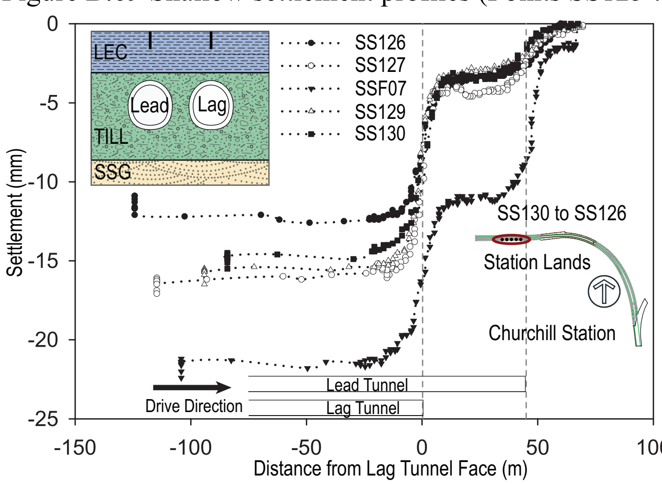

Figure B.70 Shallow settlement profiles (Points SS126 to SS130)

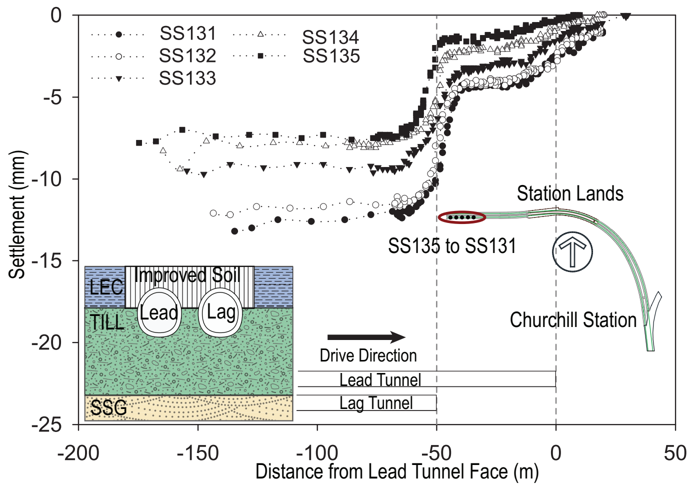

Figure B.71 Shallow settlement profiles (Points SS131 to SS135)

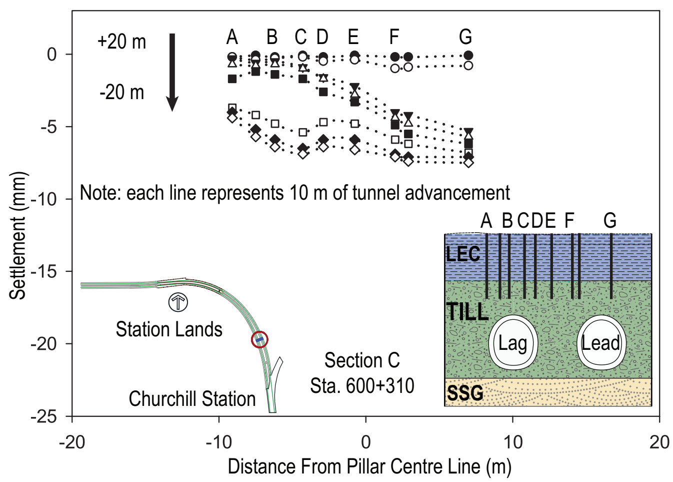

Figure B.72 Deep settlement cross section (Section C)

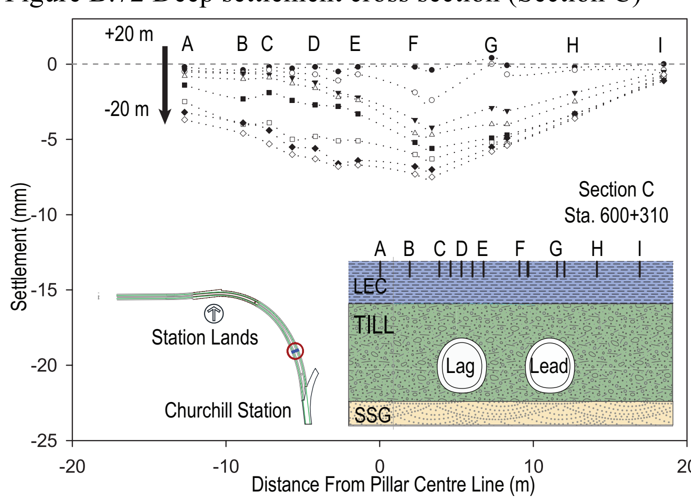

Figure B.73 Shallow settlement cross section (Section C)

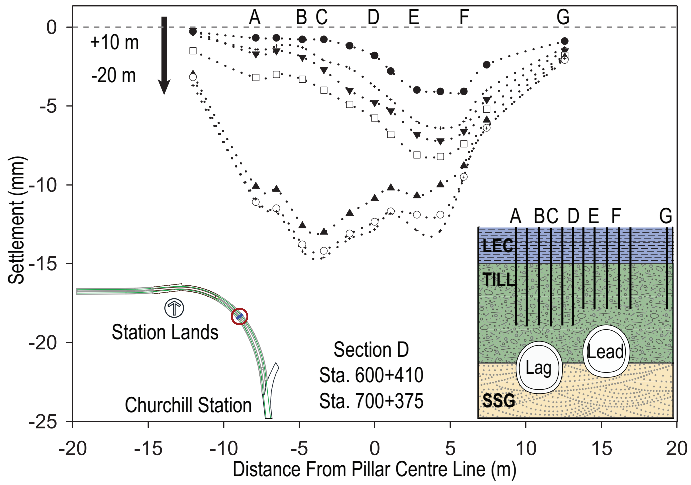

Figure B.74 Deep settlement cross section (Section D)

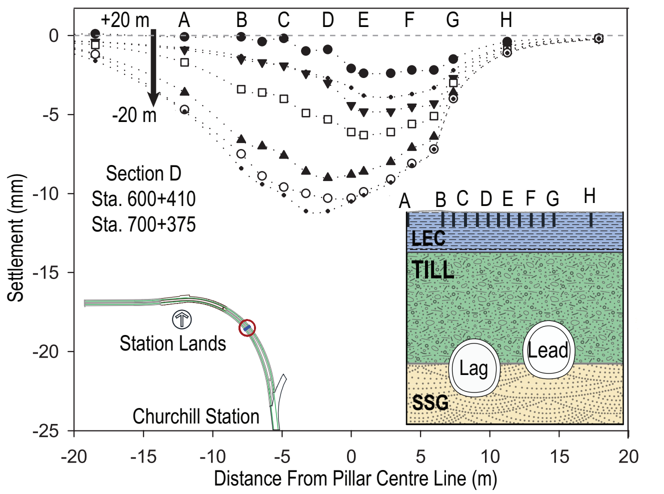

Figure B.75 Shallow settlement cross section (Section D)

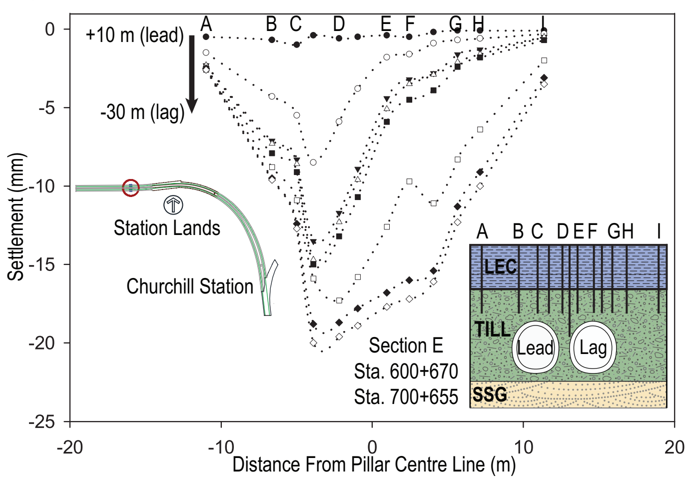

Figure B.76 Deep settlement cross section (Section E)

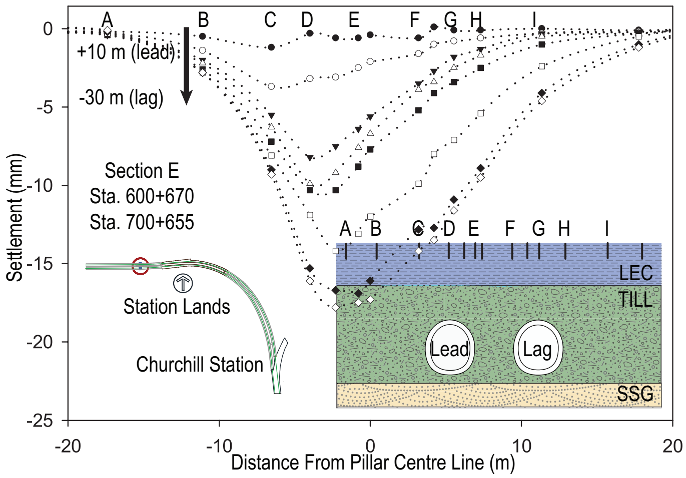

Figure B.77 Shallow settlement cross section (Section E)

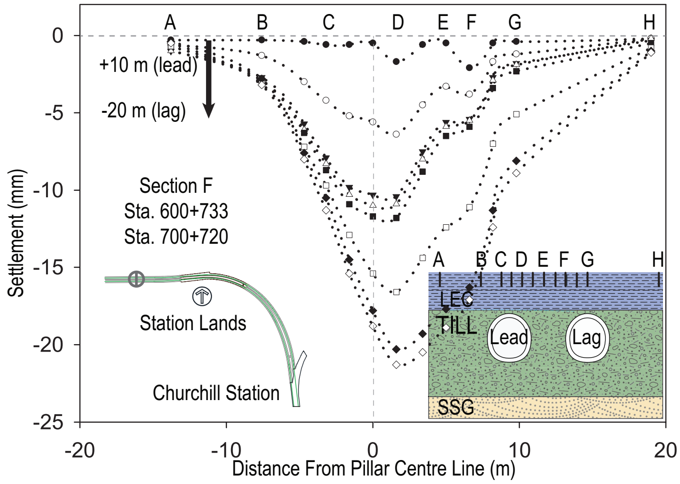

Figure B.78 Shallow settlement cross section (Section F)

Inclinometers

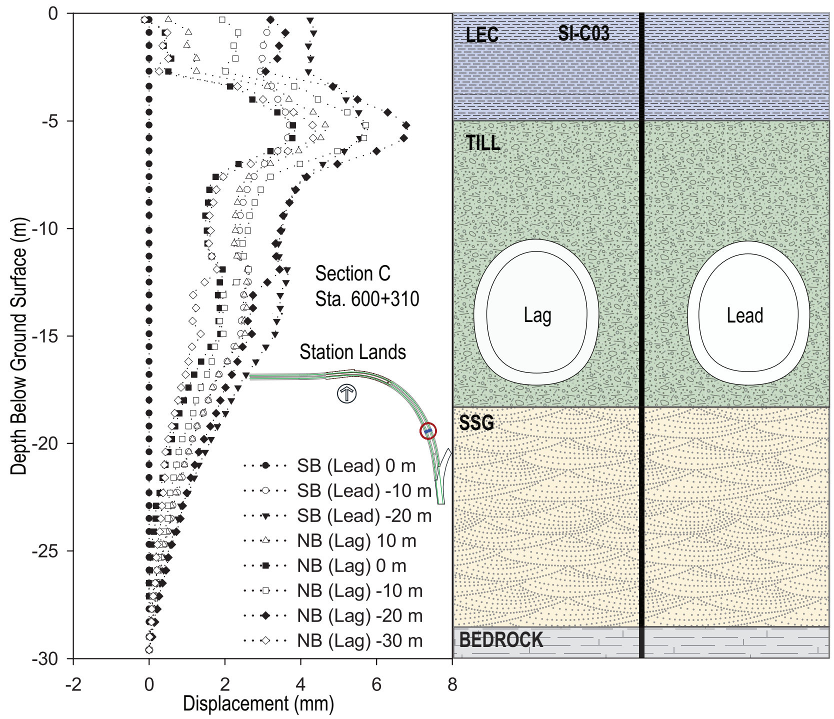

Figure B.79 Centreline inclinometer measurements (Section C)

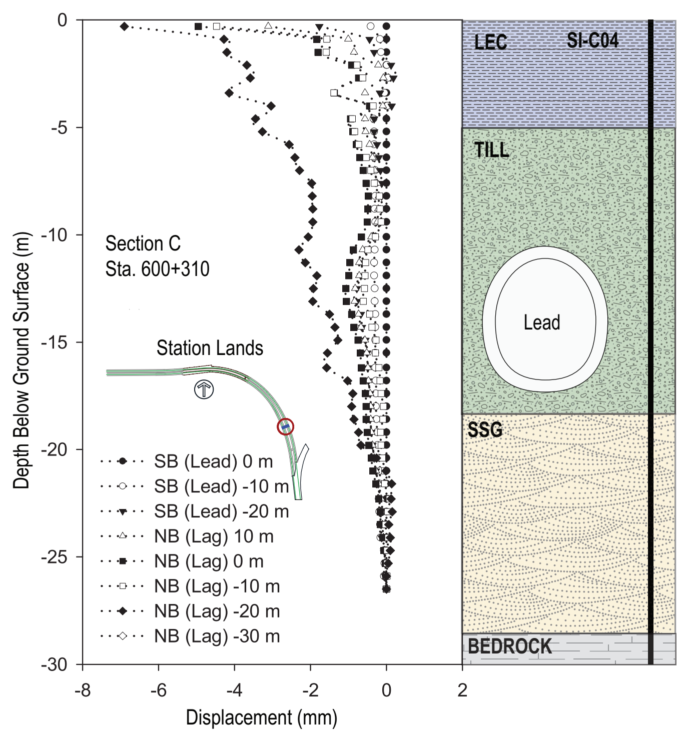

Figure B.80 Lead tunnel inclinometer measurements (Section C)

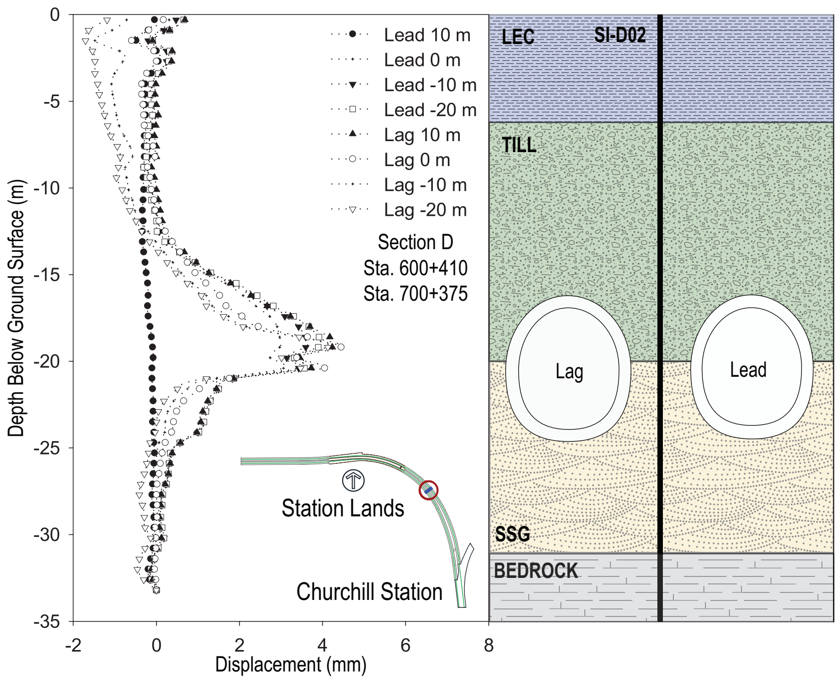

Figure B.81 Centreline inclinometer measurements (Section D)

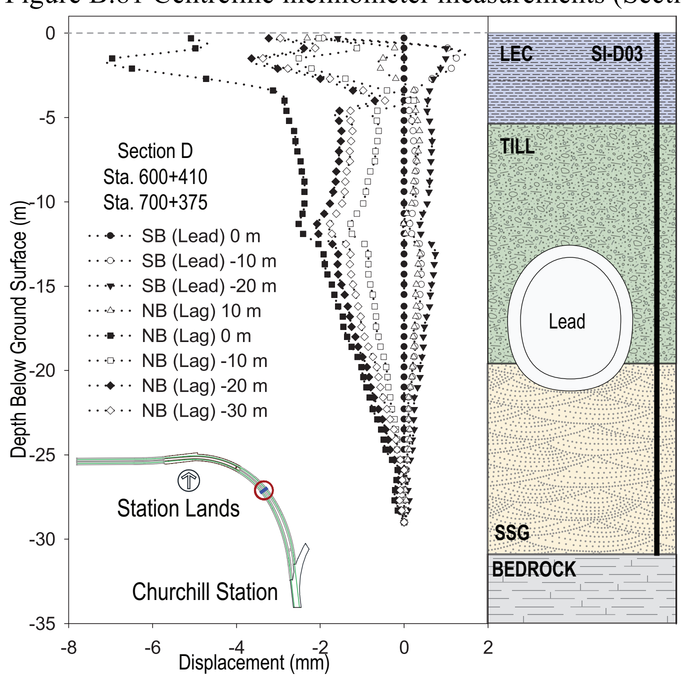

Figure B.82 Lead tunnel inclinometer measurements (Section D)

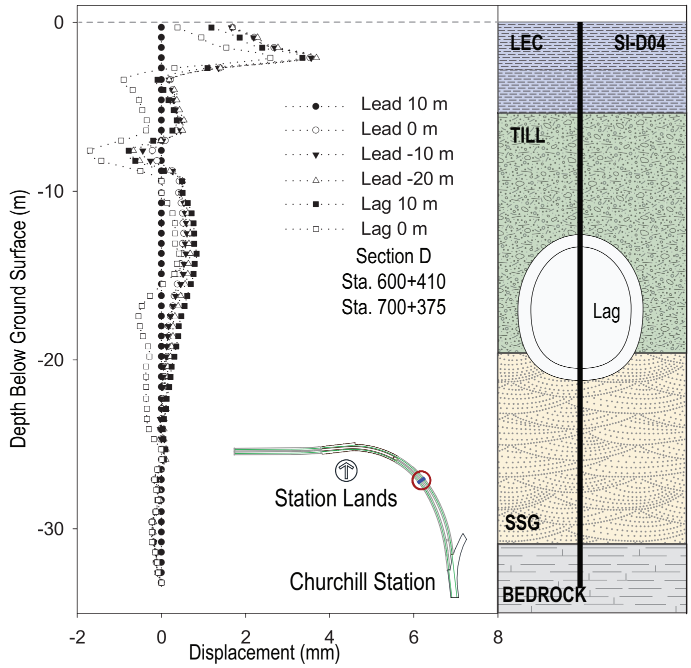

Figure B.83 Tunnel face inclinometer measurements (Section D)

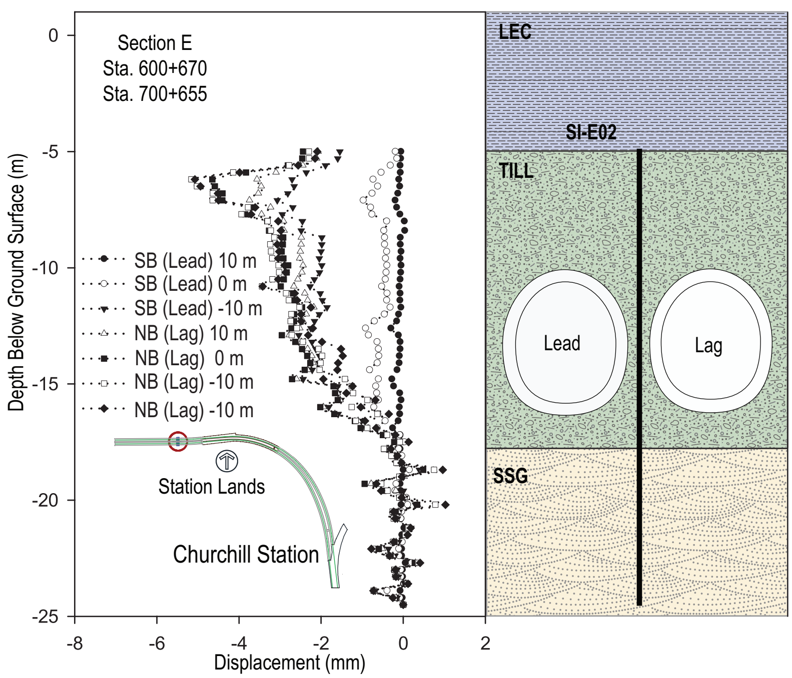

Figure B.84 Centreline inclinometer measurements (Section E)

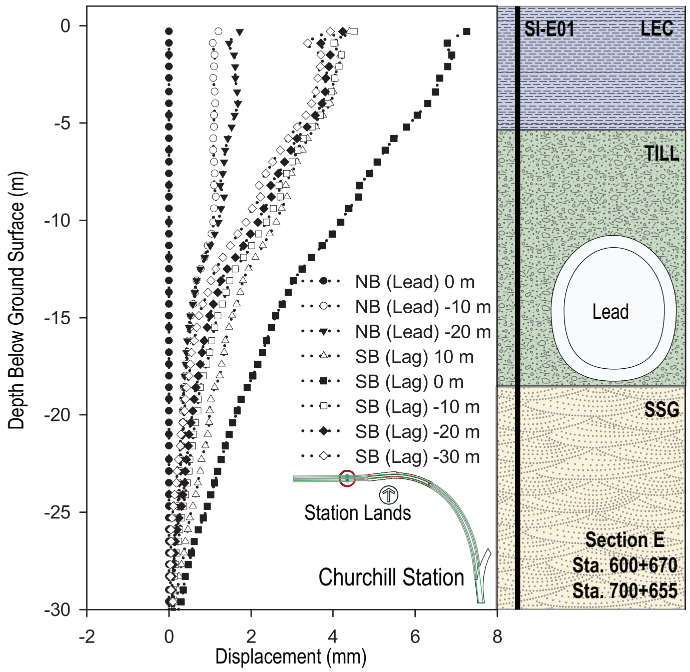

Figure B.85 Lead tunnel inclinometer measurements (Section E)

Appendix C: Numerical Model Results and Field Data

Settlements

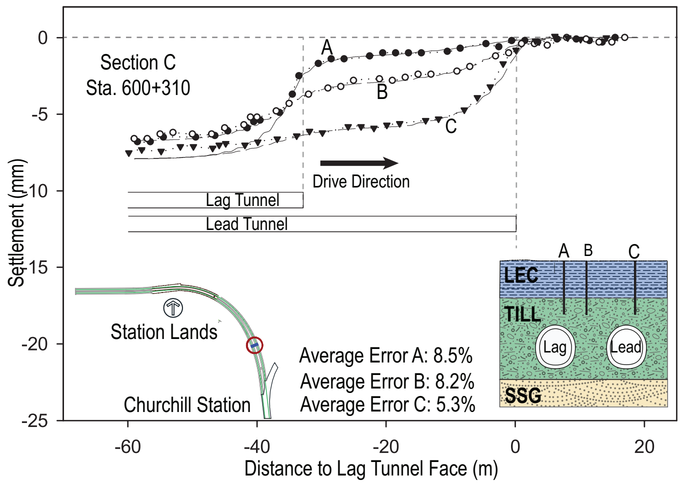

Figure C.01 Deep settlements over tunnel axis and centreline (Section C)

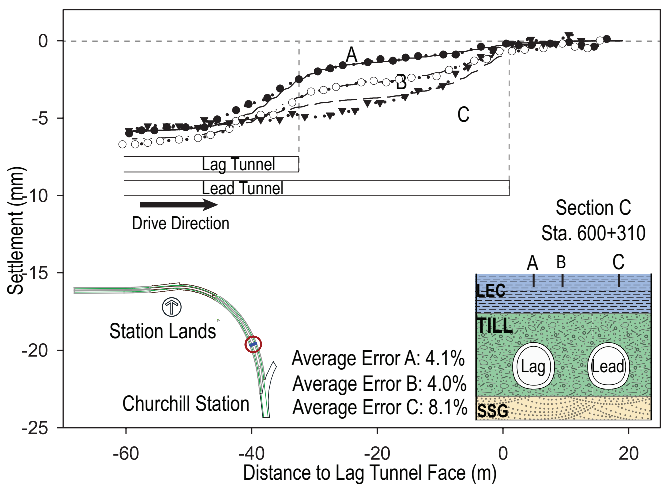

Figure C.02 Shallow settlements over tunnel axis and centreline (Section C)

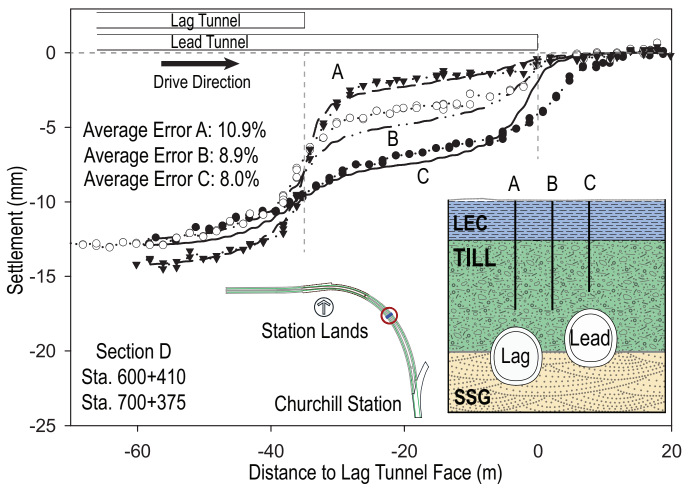

Figure C.03 Deep settlements over tunnel axis and centreline (Section D)

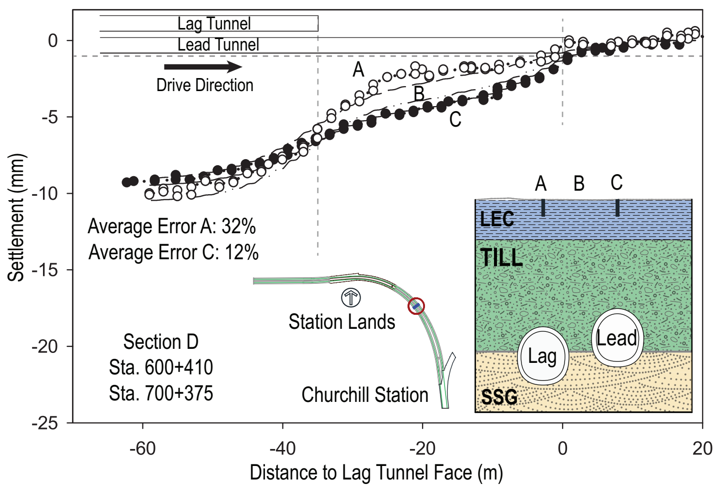

Figure C.04 Shallow settlements over tunnel axis and centreline (Section D)

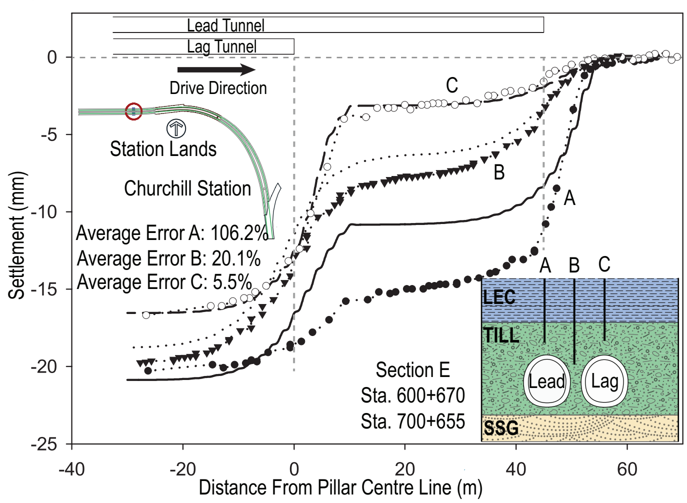

Figure C.05 Deep settlements over tunnel axis and centreline (Section E)

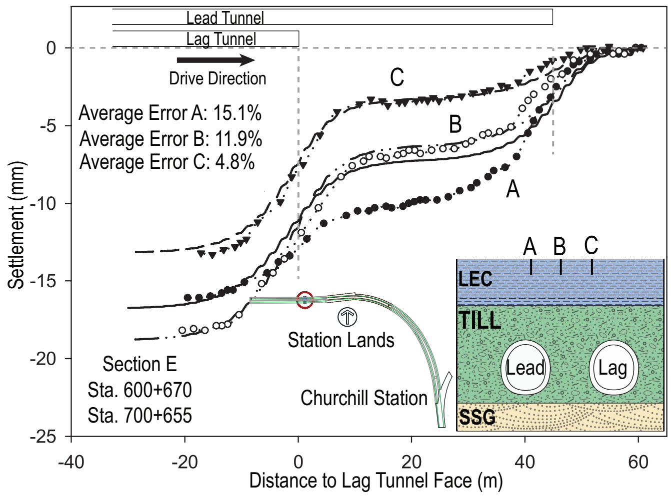

Figure C.06 Shallow settlements over tunnel axis and centreline (Section E)

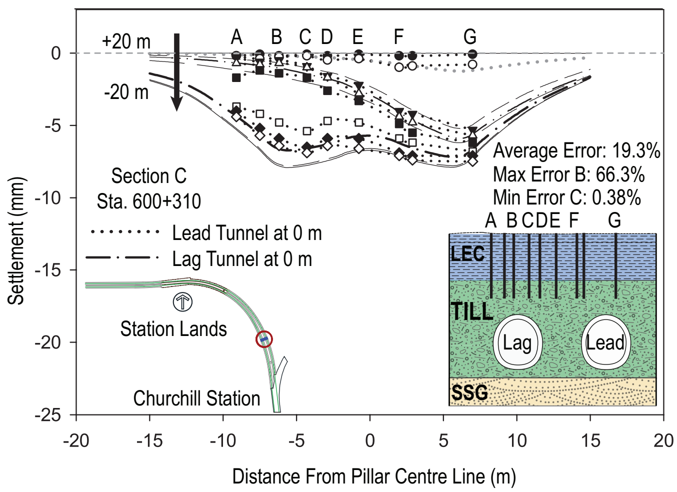

Figure C.07 Deep cross-sectional settlements (Section C)

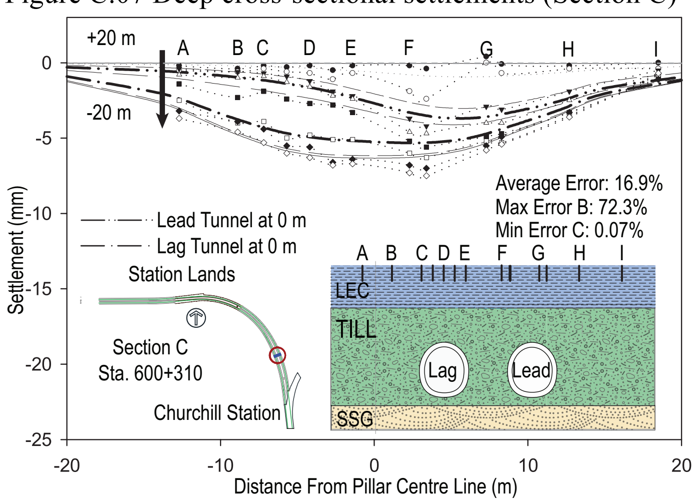

Figure C.08 Shallow cross-sectional settlements (Section C)

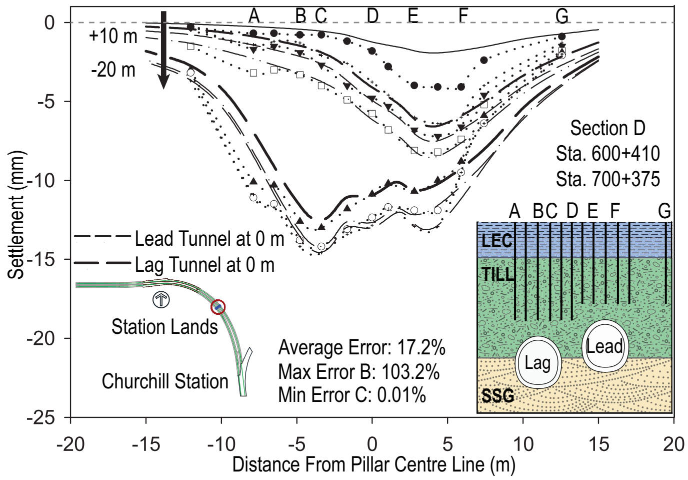

Figure C.09 Deep cross-sectional settlements (Section D)

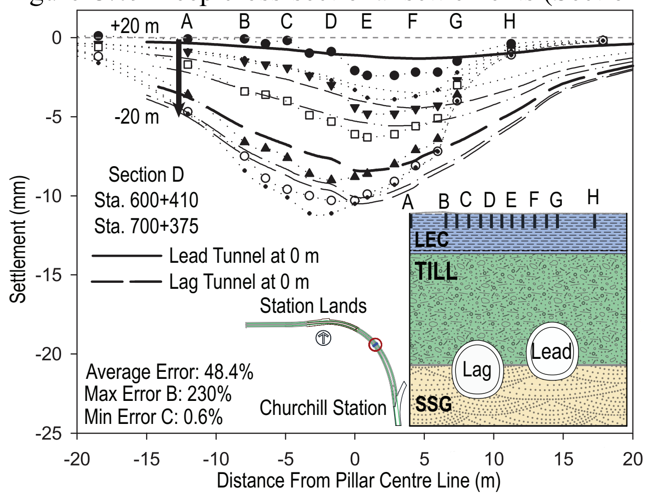

Figure C.10 Shallow cross-sectional settlements (Section D)

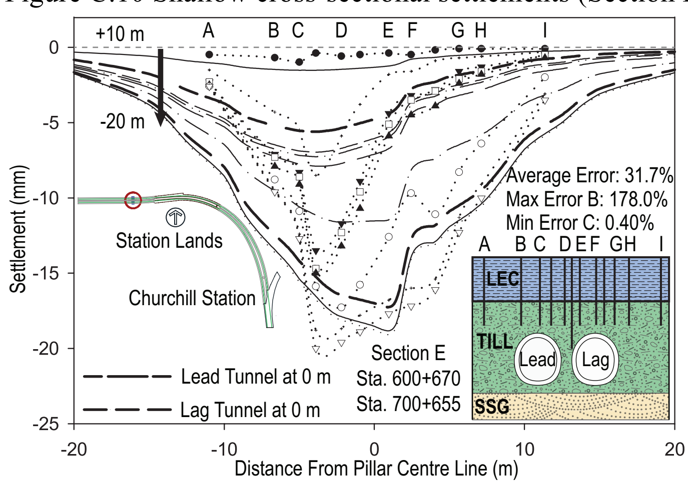

Figure C.11 Deep cross-sectional settlements (Section E)

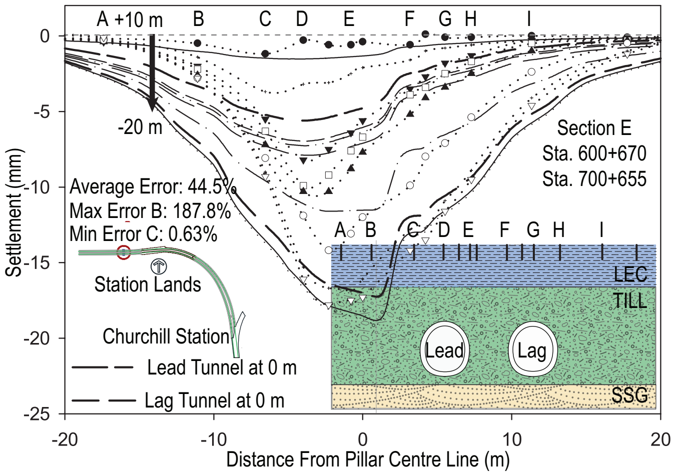

Figure C.12 Shallow cross-sectional settlements (Section E)

Strain Gauges – Strains

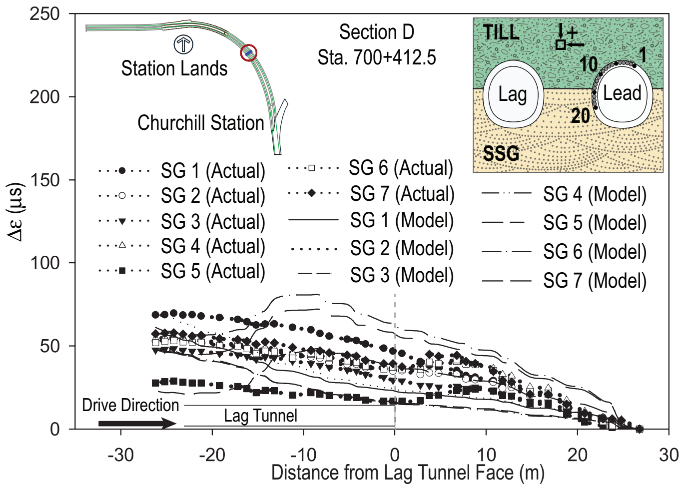

Figure C.13 Comparison of strain gauge results, Section D (Points 1-8)

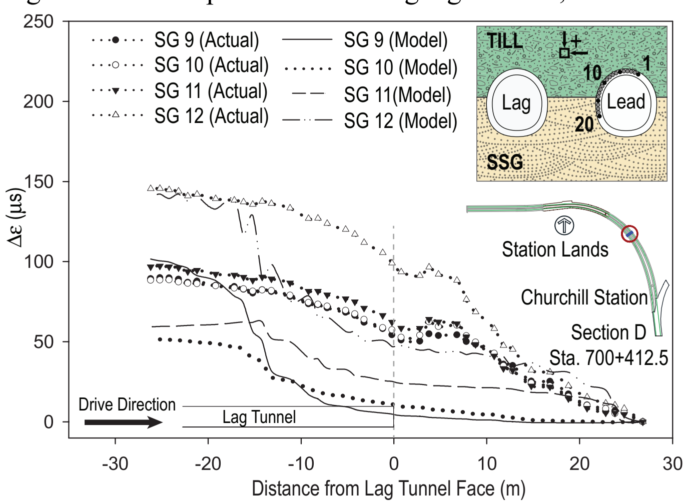

Figure C.14 Comparison of strain gauge results, Section D (Points 9-12)

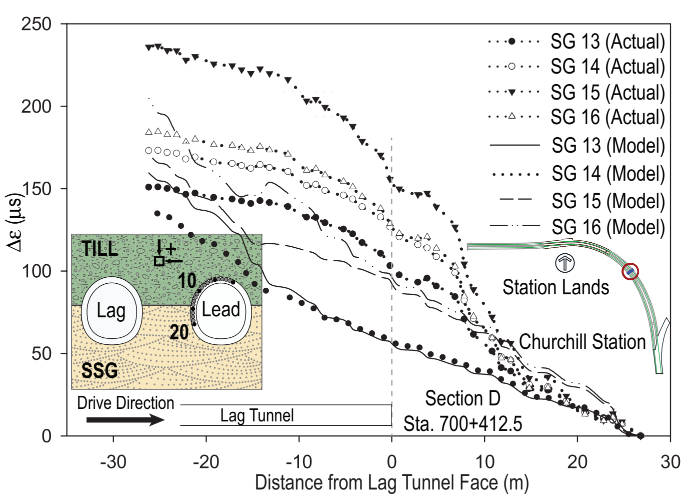

Figure C.15 Comparison of strain gauge results, Section D (Points 13-16)

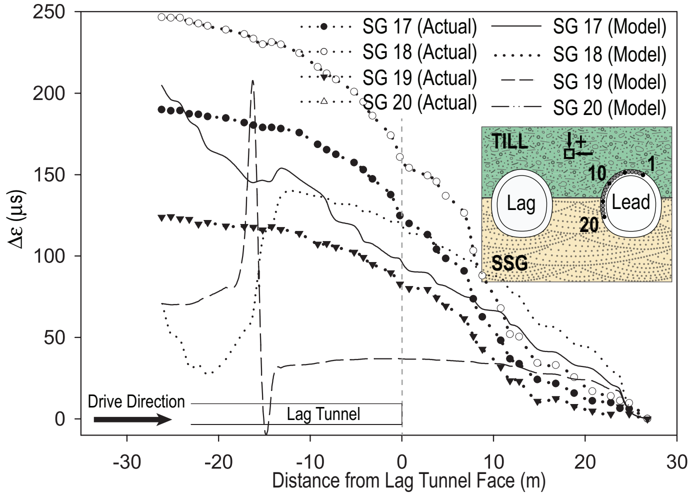

Figure C.16 Comparison of strain gauge results, Section D (Points 17-20)

Strain Gauges – Stress

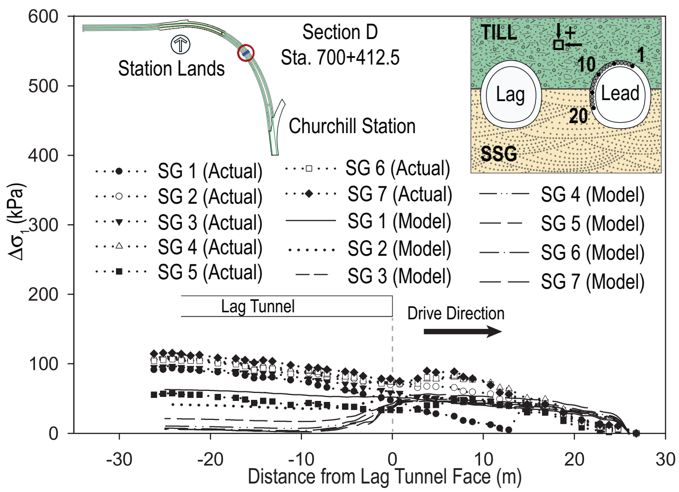

Figure C.17 Comparison of strain gauge results, Section D (Points 1-8)

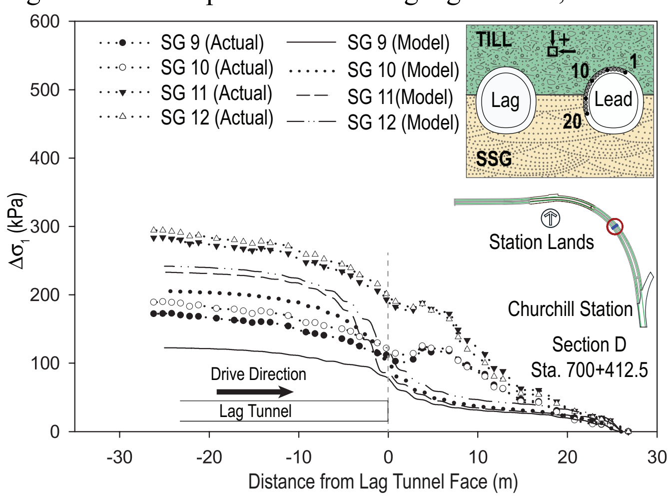

Figure C.18 Comparison of strain gauge results, Section D (Points 9-12)

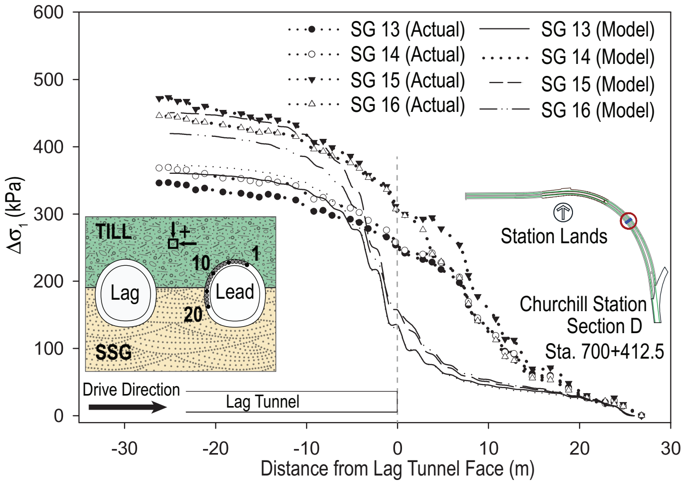

Figure C.19 Comparison of strain gauge results, Section D (Points 13-16)

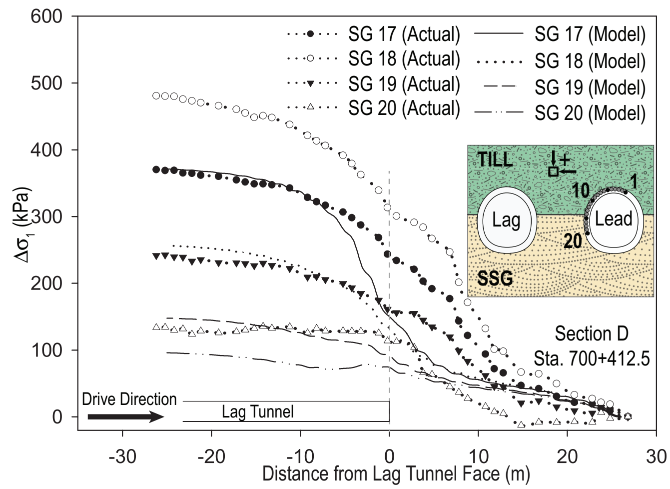

Figure C.20 Comparison of strain gauge results, Section D (Points 17-20)

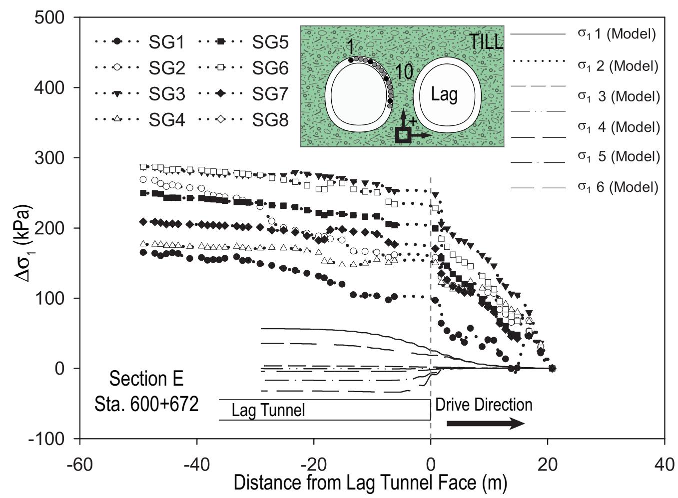

Figure C.21 Comparison of strain gauge results, Section E (Points 1-8)

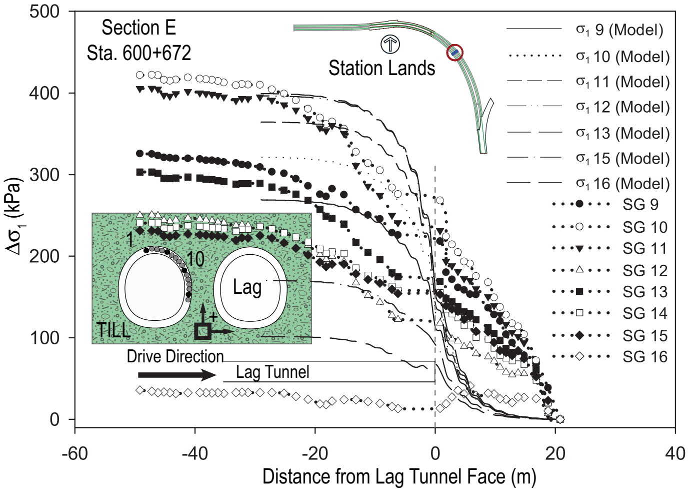

Figure C.22 Comparison of strain gauge results, Section E (Points 1-8)

Tape Extensometer

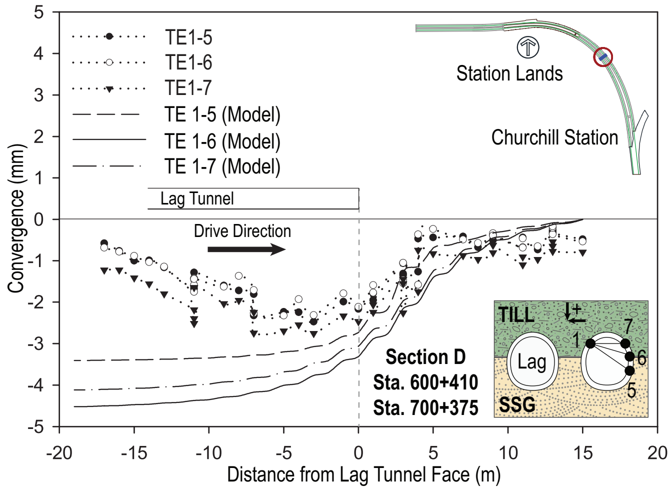

Figure C.23 Comparison of tape extensometer convergence Section D (Point 1)

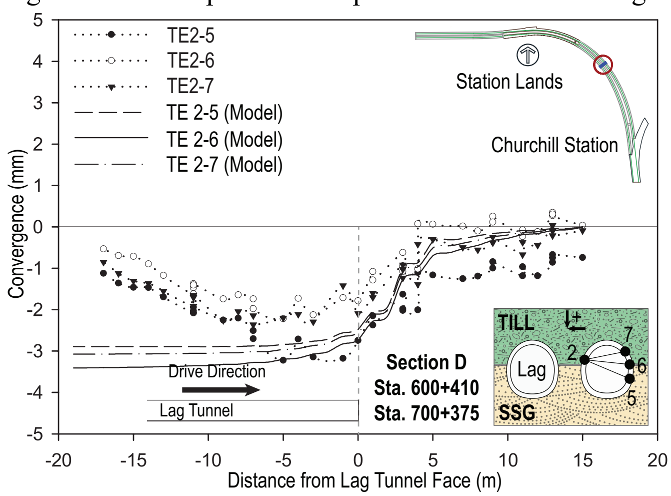

Figure C.24 Comparison of tape extensometer convergence Section D (Point 2)

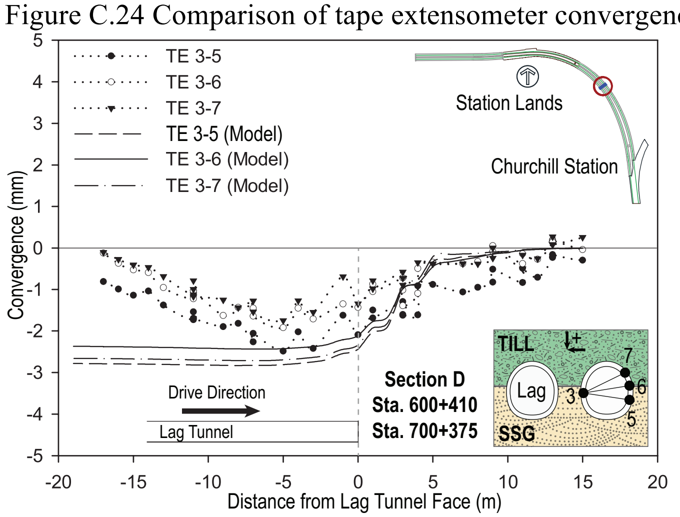

Figure C.25 Comparison of tape extensometer convergence Section D (Point 3)

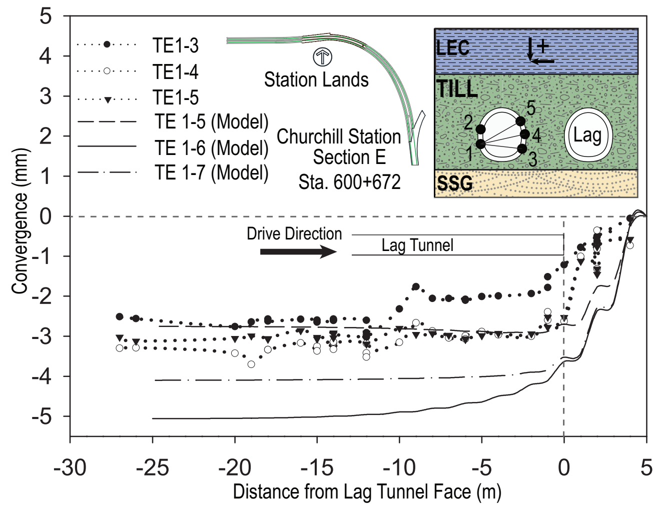

Figure C.26 Comparison of tape extensometer convergence Section D (Point 1)

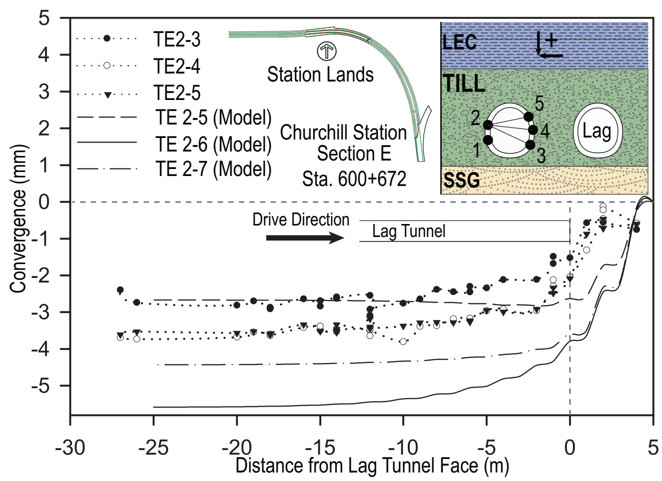

Figure C.27 Comparison of tape extensometer convergence Section D (Point 2)

Shape Accel Array

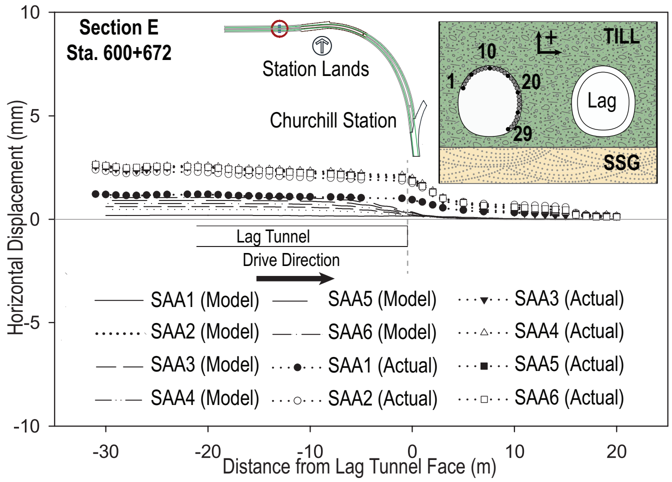

Figure C.28 Comparison of horizontal circumferential SAA (Points 1-6)

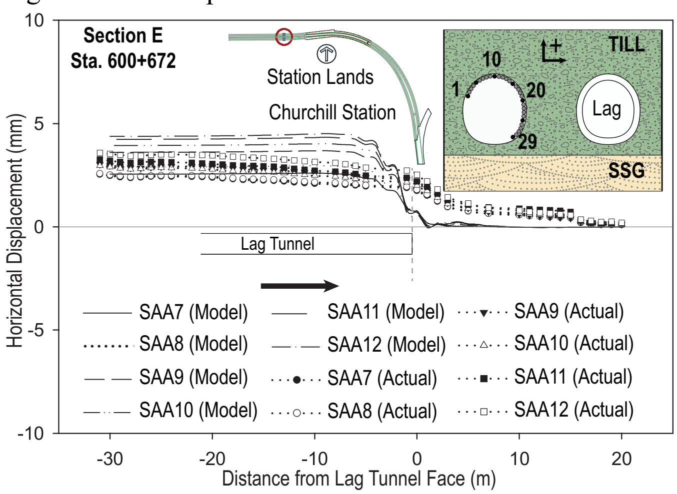

Figure C.29 Comparison of horizontal circumferential SAA (Points 7-12)

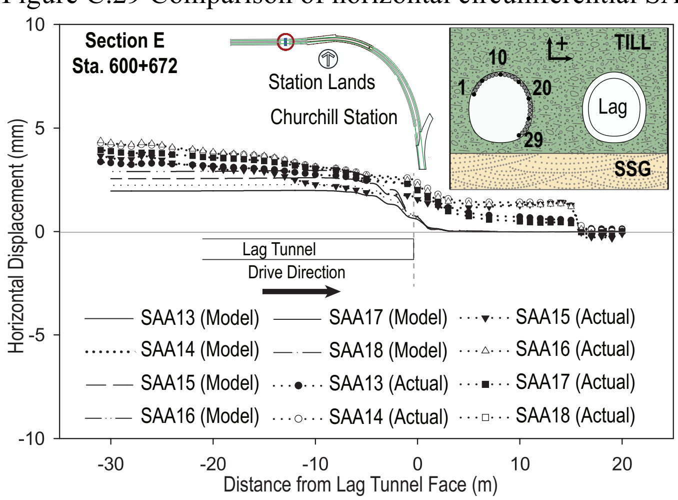

Figure C.30 Comparison of horizontal circumferential SAA (Points 13-18)

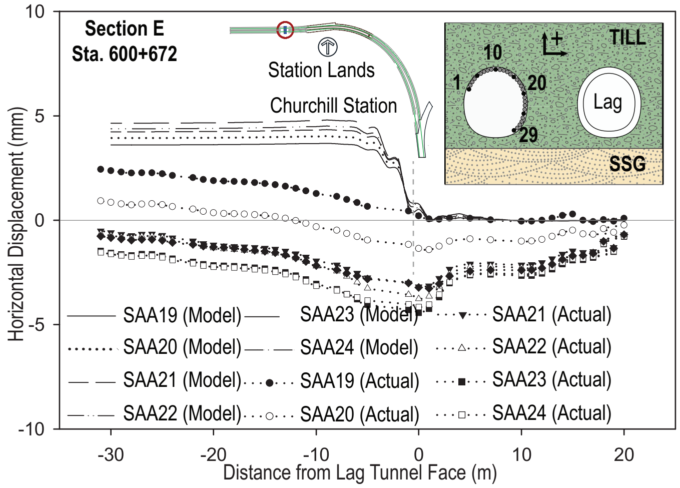

Figure C.31 Comparison of horizontal circumferential SAA (Points 19-24)

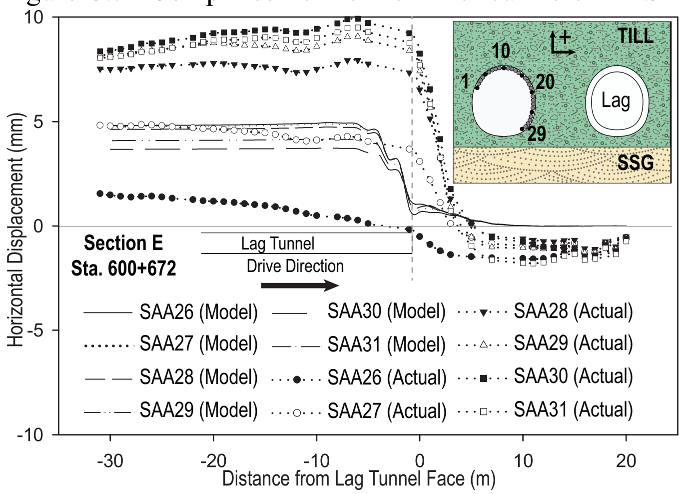

Figure C.32 Comparison of horizontal circumferential SAA (Points 25-31)

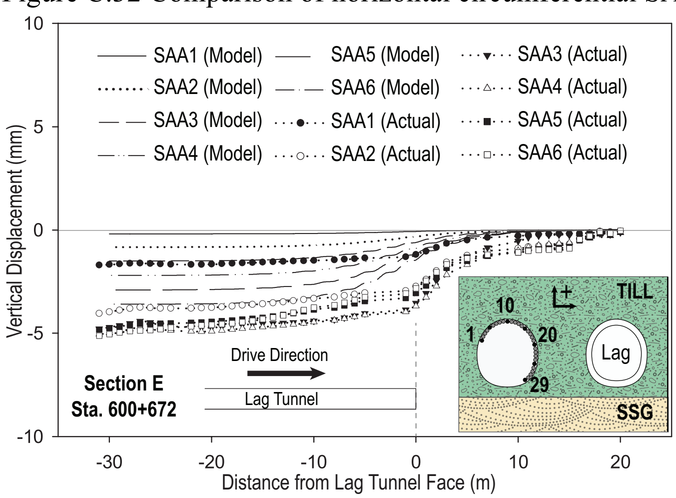

Figure C.33 Comparison of vertical circumferential SAA (Points 1-6)

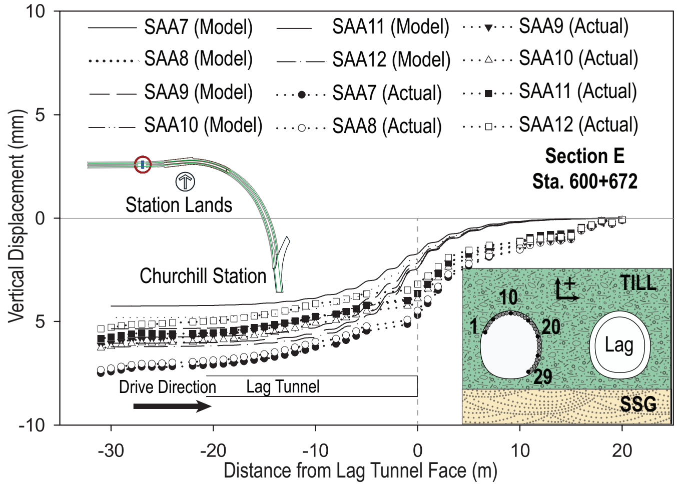

Figure C.34 Comparison of vertical circumferential SAA (Points 7-12)

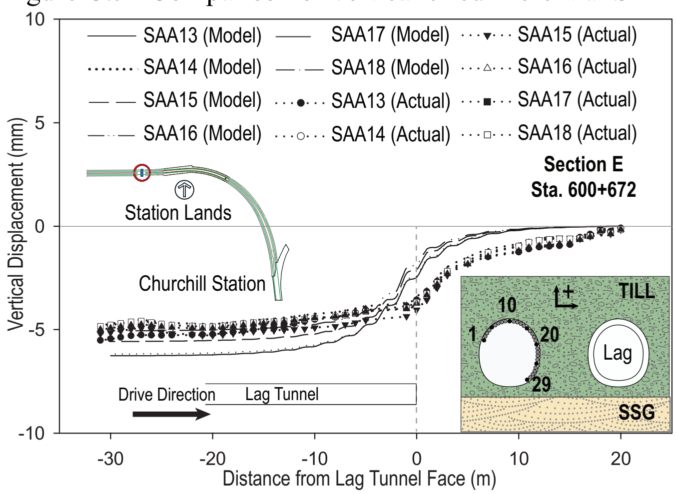

Figure C.35 Comparison of vertical circumferential SAA (Points 13-18)

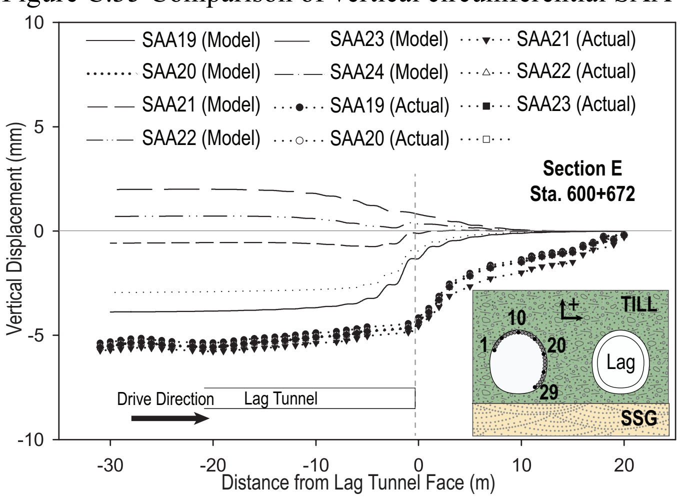

Figure C.36 Comparison of vertical circumferential SAA (Points 19-24)

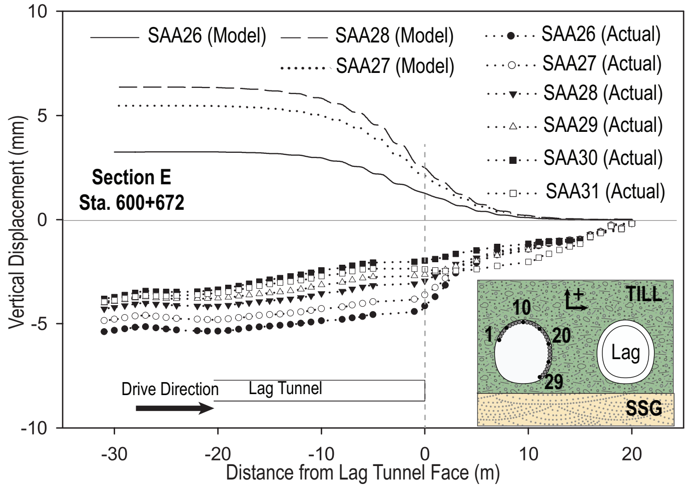

Figure C.37 Comparison of vertical circumferential SAA (Points 25-31)